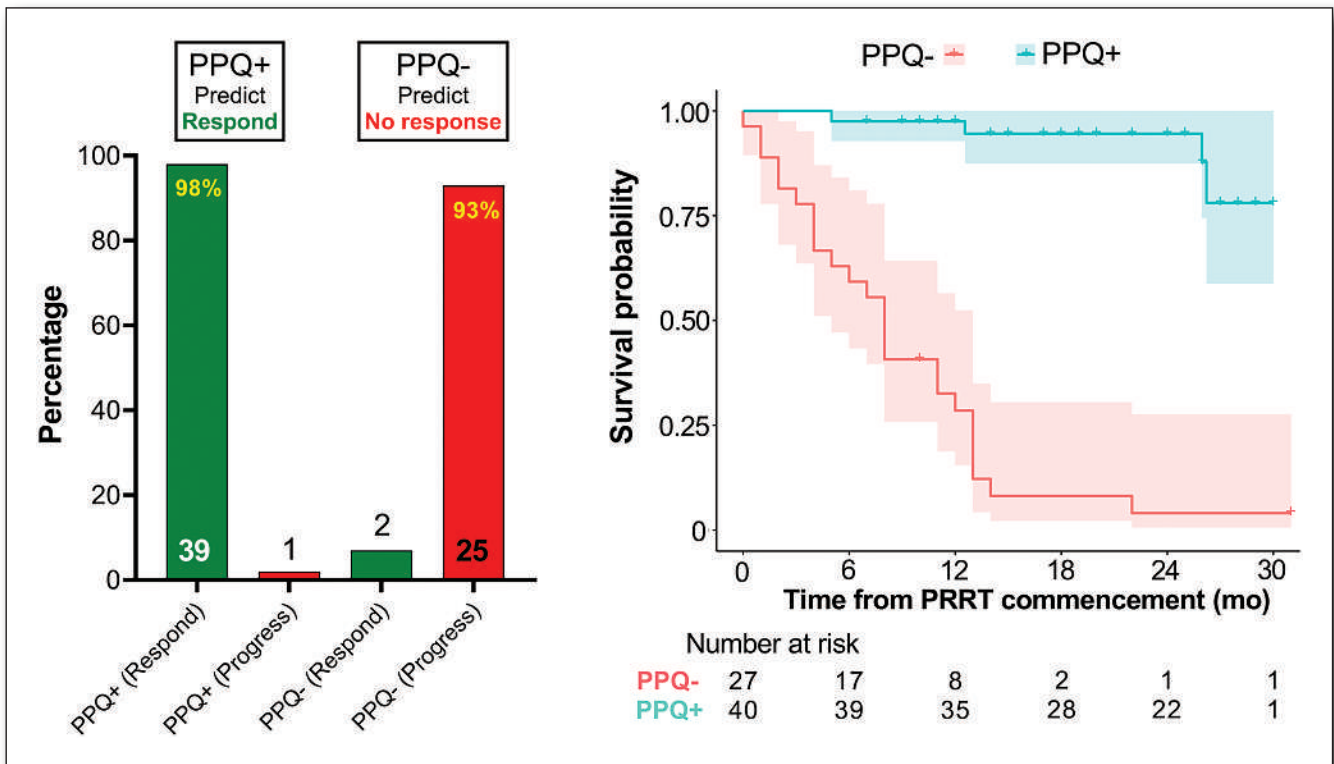


FEATURED ARTICLE

Interim Analysis of a Prospective Validation of 2 Blood-Based Genomic Assessments (PPQ and NETest) to Determine the Clinical Efficacy of ¹⁷⁷Lu-DOTATATE in Neuroendocrine Tumors. Lisa Bodei et al. See page 567.



[¹⁷⁷Lu]Lu-ofatumumab therapy: a promising human anti-CD20 antibody disseminated non-Hodgkin lymphoma. Kyuhwan Shim et al. See page 542.



**ALZHEIMER'S[®]
ASSOCIATION**

AAIC>23

**ADVANCE DEMENTIA RESEARCH
AND ACCELERATE YOUR CAREER.**

Register by May 12 and save.

Join researchers, clinicians and dementia professionals from all career stages in Amsterdam, Netherlands, and online, at the Alzheimer's Association International Conference[®] (AAIC[®]). Share your work and accelerate your career at the largest and most influential international conference on dementia science.

AAIC 2023: JULY 16-20, AMSTERDAM, NETHERLANDS, AND ONLINE

Educational Workshops and Preconferences: July 14-15

Exhibits: July 16-19

Register at alz.org/AAIC-JNM.

EDITOR'S PAGE

- 503 Amyloid Imaging–Based Food and Drug Administration Approval of Lecanemab to Treat Alzheimer Disease—What Lasts Long Finally Becomes Good?**
Henryk Barthel

DISCUSSIONS WITH LEADERS

- 505 Nuclear Medicine from a Novel Perspective: Buvat and Weber Talk with OpenAI's ChatGPT**
Irène Buvat and Wolfgang Weber

STATE OF THE ART

- 508 Functional Imaging of Chemobrain: Usefulness of Nuclear Medicine in the Fog Coming After Cancer**
Agostino Chiaravalloti, Luca Filippi, Marco Pagani, and Orazio Schillaci

CONTINUING EDUCATION

- 515 Role of ¹⁸F-FDG PET/CT in Large Vessel Vasculitis and Polymyalgia Rheumatica**
Riemer H.J.A. Slart, Pieter H. Nienhuis, Andor W.J.M. Glaudemans, Elisabeth Brouwer, Olivier Gheysens, and Kornelis S.M. van der Geest

HOT TOPICS

- 522 The Latest Advances in Peptide Receptor Radionuclide Therapy for Gastroenteropancreatic Neuroendocrine Tumors**
Elif Hindié, Eric Baudin, Rodney J. Hicks, and David Taieb

APPROPRIATE USE CRITERIA

- 525 Summary: Appropriate Use Criteria for Lymphoscintigraphy in Sentinel Node Mapping and Lymphedema/Lipedema**
Kevin J. Donohoe, Brett J. Carroll, David K. V. Chung, Elizabeth H. Dibble, Emilia Diego, Francesco Giammarile, Frederick D. Grant, Stephen Y. Lai, Hannah Linden, Megan E. Miller, et al.

ONCOLOGY

Clinical

- 529 Real-Life Experience in the Treatment of Intrahepatic Cholangiocarcinoma by ⁹⁰Y Radioembolization: A Multicenter Retrospective Study**
Benedikt M. Schaarschmidt, Roman Kloeckner, Thomas Dertnig, Aydin Demircioglu, Lukas Müller, Timo Alexander Auer, Daniel Pinto dos Santos, Verena Steinle, Matthias Miederer, Bernhard Gebauer, et al.
- 536 Prognostic Value of ¹⁸F-FDG PET/CT in Diffuse Large B-Cell Lymphoma Treated with a Risk-Adapted Immunochemotherapy Regimen**
Laure Michaud, Kurt Bantilan, Audrey Mauguen, Craig H. Moskowitz, Andrew D. Zelenetz, and Heiko Schöder

Basic

- 542 ■ FEATURED BASIC SCIENCE ARTICLE. Cure of Disseminated Human Lymphoma with [¹⁷⁷Lu]Lu-Ofatumumab in a Preclinical Model**
Kyuhan Shim, Mark S. Longtine, Diane S. Abou, Mark J. Hoegger, Richard S. Laforest, Daniel L.J. Thorek, and Richard L. Wahl
- 549 ²²⁵Ac-MACROPATATE: A Novel α -Particle Peptide Receptor Radionuclide Therapy for Neuroendocrine Tumors**
A. Paden King, Nicholas T. Gutsche, Natarajan Raju, Stanley Fayn, Kwamena E. Baidoo, Meghan M. Bell, Colleen S. Olkowski, Rolf E. Swenson, Frank I. Lin, Samira M. Sadowski, et al.
- 555 Preclinical Evaluation of ⁸⁹Zr-Desferrioxamine-Bexmarilimab, a Humanized Antibody Against Common Lymphatic Endothelial and Vascular Endothelial Receptor-1, in a Rabbit Model of Renal Fibrosis**
Olli Moisio, Jenni Virta, Emrah Yatkin, Heidi Liljenbäck, Senthil Palani, Riikka Viitanen, Maxwell W.G. Miner, Vesa Oikonen, Tuula Tolvanen, Danielle J. Vugts, et al.

THERANOSTICS

Clinical

- 561 Radioiodine Ablation of Thyroid Remnants in Patients with Graves' Orbitopathy**
Michael Oeverhaus, Jana Koenen, Nikolaos Bechrakis, Mareile Stöhr, Ken Herrmann, Wolfgang P. Fendler, Anja Eckstein, and Manuel Weber
- 567 ■ FEATURED ARTICLE OF THE MONTH. Interim Analysis of a Prospective Validation of 2 Blood-Based Genomic Assessments (PPQ and NETest) to Determine the Clinical Efficacy of ¹⁷⁷Lu-DOTATATE in Neuroendocrine Tumors**
Lisa Bodei, Nitya Raj, Richard K. Do, Audrey Mauguen, Simone Krebs, Diane Reidy-Lagunes, and Heiko Schöder
- 574 ■ BRIEF COMMUNICATION. Safety and Survival Outcomes of ¹⁷⁷Lu-Prostate-Specific Membrane Antigen Therapy in Patients with Metastatic Castration-Resistant Prostate Cancer with Prior ²²³Ra treatment: The RALU Study**
Kambiz Rahbar, Markus Essler, Kim M. Pabst, Matthias Eiber, Christian la Fougère, Vikas Prasad, Philipp Rassek, Ergela Hasa, Helmut Dittmann, Ralph A. Bundschuh, et al.
- 579 Phase III Study of ¹⁸F-PSMA-1007 Versus ¹⁸F-Fluorocholine PET/CT for Localization of Prostate Cancer Biochemical Recurrence: A Prospective, Randomized, Crossover Multicenter Study**
Pierre Olivier, Anne-Laure Giraudet, Andrea Skanjeti, Charles Merlin, Pierre Weinmann, Ines Rudolph, Alexander Hoepfing, and Mathieu Gauthé
- 586 Differences in Failure-Free Survival After Salvage Radiotherapy Guided by Conventional Imaging Versus ¹⁸F-Fluciclovine PET/CT in Postprostatectomy Patients: A Post Hoc Substratification Analysis of the EMPIRE-1 Trial**
Ismahel O. Lawal, Ashesh B. Jani, Omotayo A. Adediran, Subir Goyal, Olayinka A. Abiodun-Ojo, Vishal R. Dhere, Charles V. Marcus, Shreyas S. Joshi, Viraj A. Master, Pretesh R. Patel, et al.
- 592 A Pilot Study of ⁶⁸Ga-PSMA11 and ⁶⁸Ga-RM2 PET/MRI for Evaluation of Prostate Cancer Response to High-Intensity Focused Ultrasound Therapy**
Heying Duan, Pejman Ghanouni, Bruce Daniel, Jarrett Rosenberg, Guido A. Davidzon, Carina Mari Aparici, Christian Kunder, Geoffrey A. Sonn, and Andrei Iagaru

598 **¹⁸F-PSMA Cerenkov Luminescence and Flexible Autoradiography Imaging in a Prostate Cancer Mouse Model and First Results of a Radical Prostatectomy Feasibility Study in Men**

Pedro Fragoso Costa, Lukas Püllen, Claudia Kesch, Ulrich Krafft, Stephan Tschirdewahn, Alexandros Moraitis, Jan Philipp Radtke, Saskia Ting, Michael Nader, Jasmin Wosniack, et al.

605 **Prognostic Value of Tumor Volume Assessment on PSMA PET After ¹⁷⁷Lu-PSMA Radioligand Therapy Evaluated by PSMA PET/CT Consensus Statement and RECIP 1.0**

Felix Kind, Ann-Christin Eder, Cordula A. Jilg, Philipp E. Hartrampf, Philipp T. Meyer, Juri Ruf, and Kerstin Michalski

611 **A Single-Arm, Low-Dose, Prospective Study of ¹⁷⁷Lu-EB-PSMA Radioligand Therapy in Patients with Metastatic Castration-Resistant Prostate Cancer**

Guochang Wang, Jie Zang, Yuanyuan Jiang, Qingxing Liu, Huimin Sui, Rongxi Wang, Xinrong Fan, Jingjing Zhang, Zhaohui Zhu, and Xiaoyuan Chen

618 **Three-Time-Point PET Analysis of ⁶⁸Ga-FAPI-46 in a Variety of Cancers**

Mahnoosh Naeimi, Peter L. Choyke, Katharina Dendl, Yuriko Mori, Fabian Staudinger, Tadashi Watabe, Stefan A. Koerber, Manuel Röhrich, Jürgen Debus, Clemens Kratochwil, et al.

623 ■ **INVITED PERSPECTIVE. Could FAP-Targeted Molecular Imaging Replace ¹⁸F-FDG for Standard-of-Care Oncologic PET?**

Raghava Kashyap and Aravind S. Ravi Kumar

625 **Response Prediction Using ¹⁸F-FAPI-04 PET/CT in Patients with Esophageal Squamous Cell Carcinoma Treated with Concurrent Chemoradiotherapy**

Xinying Hu, Tao Zhou, Jiazhong Ren, Jinghao Duan, Hongbo Wu, Xiaoli Liu, Zhengshuai Mu, Ning Liu, Yuchun Wei, and Shuanghu Yuan

632 **¹⁸F-AIF-NOTA-Octreotide Outperforms ⁶⁸Ga-DOTATATE/ NOC PET in Neuroendocrine Tumor Patients: Results from a Prospective, Multicenter Study**

Elin Pauwels, Frederik Cleeren, TERENCE Tshibangu, Michel Koole, Kim Serdons, Lennert Boeckxstaens, Jeroen Dekervel, Timon Vandamme, Willem Lybaert, Bliede Van den Broeck, et al.

Basic

639 **Preclinical Evaluation of ⁶⁸Ga- and ¹⁷⁷Lu-Labeled Integrin $\alpha_v\beta_6$ -Targeting Radiotheranostic Peptides**

Tanushree Ganguly, Nadine Bauer, Ryan A. Davis, Cameron C. Foster, Rebecca E. Harris, Sven H. Hausner, Emilie Roncali, Sarah Y. Tang, and Julie L. Sutcliffe

CARDIOVASCULAR

Clinical

645 **Myocardial External Efficiency in Asymptomatic Severe Primary Mitral Regurgitation Using ¹¹C-Acetate PET**

Jens Sorensen, Johannes Bergsten, Tomasz Baron, Lovisa Holm Orndahl, Tanja Kero, Tomas Bjerner, Eva-Maria Hedin, Hendrik J. Harms, Rafael Astudillo, and Frank A. Flachskampf

AI/ADVANCED IMAGE ANALYSIS

Basic

652 **Deep Learning Coronary Artery Calcium Scores from SPECT/CT Attenuation Maps Improve Prediction of Major Adverse Cardiac Events**

Robert J.H. Miller, Konrad Pieszko, Aakash Shanbhag, Attila Feher, Mark Lemley, Aditya Killekar, Paul B. Kavanagh, Serge D. Van Kriekinge, Joanna X. Liang, Cathleen Huang, et al.

PHYSICS AND INSTRUMENTATION

Basic

659 **Fast and Accurate Amyloid Brain PET Quantification Without MRI Using Deep Neural Networks**

Seung Kwan Kang, Daewoon Kim, Seong A Shin, Yu Kyeong Kim, Hongyoon Choi, and Jae Sung Lee

ILLUSTRATED POST

667 **Detecting CXCR4 Expression in Meningioma on ⁶⁸Ga-Pentixafor PET/MRI**

Simone Krebs, Jazmin Schwartz, Christian Grommes, Robert J. Young, Heiko Schöder, and Marius E. Mayerhoefer

DEPARTMENTS

9A Recruitment

10A This Month in JNM

Tc 99m: The **core** of nuclear medicine imaging^{1,2}

EFFICIENT AND RELIABLE³

- Greater than 50 years of TechneLite[®] generator manufacturing expertise³
- Our 5th generation of dry-column technetium-99m generator advances³
- 100% Assay and Mo-99 breakthrough testing³
- 100% terminal sterilization following filling and in-process test elutions³



INDICATIONS AND USAGE:

The TechneLite[®] generator is a source of sodium pertechnetate Tc 99m for use in the preparation of FDA-approved diagnostic radiopharmaceuticals, as described in the labeling of these diagnostic radiopharmaceutical kits.

Sodium Pertechnetate Tc 99m Injection is used IN ADULTS as an agent for:

- Thyroid Imaging
- Salivary Gland Imaging
- Urinary Bladder Imaging (direct isotopic cystography) for the detection of vesico-ureteral reflux
- Nasolacrimal Drainage System Imaging

Sodium Pertechnetate Tc 99m Injection is used IN CHILDREN as an agent for:

- Thyroid Imaging
- Urinary Bladder Imaging (direct isotopic cystography) for the detection of vesico-ureteral reflux

CONTRAINDICATIONS: None known.

Important Safety Information:

Allergic reactions including anaphylaxis have been reported infrequently following the administration of Sodium Pertechnetate Tc 99m Injection.

WARNINGS:

Radiation risks associated with the use of Sodium Pertechnetate Tc 99m Injection are greater in children than in adults and, in general, the younger the child, the greater the risk owing to greater absorbed radiation doses and longer life expectancy. These greater risks should be taken firmly into account in all benefit-risk assessments involving children. Long-term cumulative radiation exposure may be associated with an increased risk of cancer.

PRECAUTIONS:

Since the eluate does not contain an antimicrobial agent, it should not be used after 12 hours from the time of TechneLite[®], Technetium Tc 99m Generator, elution. After the termination of the nasolacrimal imaging procedure, blowing the nose and washing the eyes with sterile distilled water or an isotonic sodium chloride solution will further minimize the radiation dose. As in the use of any radioactive material, care should be taken to minimize radiation exposure to patients and occupational workers. Radiopharmaceuticals should be used only by physicians who are qualified by training and experience and who are licensed in the safe handling of radionuclides.

Please see following page(s) for brief Prescribing Information. Full Prescribing Information may be accessed at <https://www.lantheus.com/assets/TechneLite-PI-513160-0719mktg.pdf>

References:

1. World Nuclear Association, <http://www.world-nuclear.org/information-library/non-power-nuclear-applications/radioisotopes-research/radioisotopes-in-medicine.aspx> Accessed April 1, 2019 2. FDA News Release, February 8, 2018, <https://www.fda.gov/news-events/newsroom/press-announcements/ucm595990.htm> Accessed April 1, 2019 3. Quality data on file, Lantheus Medical Imaging, Inc.



FOR DIAGNOSTIC USE

BRIEF SUMMARY

Please see Full Prescribing Information available at https://www.lantheus.com/assets/TechneLite-PI-_513160-0719mktg.pdf for complete information.

INDICATIONS AND USAGE:

The Technelite generator is a source of sodium pertechnetate Tc 99m for use in the preparation of FDA-approved diagnostic radiopharmaceuticals, as described in the labeling of these diagnostic radiopharmaceutical kits. Sodium Pertechnetate Tc 99m Injection is used IN ADULTS as an agent for:

- Thyroid Imaging
- Salivary Gland Imaging
- Urinary Bladder Imaging (direct isotopic cystography) for the detection of vesico-ureteral reflux.
- Nasolacrimal Drainage System Imaging

Sodium Pertechnetate Tc 99m Injection is used IN CHILDREN as an agent for:

- Thyroid Imaging
- Urinary Bladder Imaging (direct isotopic cystography) for the detection of vesico-ureteral reflux.

CONTRAINDICATIONS: None known.

WARNINGS: Radiation risks associated with the use of Sodium Pertechnetate Tc 99m Injection are greater in children than in adults and, in general, the younger the child, the greater the risk owing to greater absorbed radiation doses and longer life-expectancy. These greater risks should be taken firmly into account in all benefit-risk assessments involving children.

Long-term cumulative radiation exposure may be associated with an increased risk of cancer.

PRECAUTIONS:**General**

As in the use of any radioactive material, care should be taken to minimize radiation exposure to the patient consistent with proper patient management and to ensure minimum radiation exposure to occupational workers.

Since the eluate does not contain an antimicrobial agent, it should not be used after 12 hours from the time of TECHNELITE®, Technetium Tc 99m Generator elution.

After the termination of the nasolacrimal imaging procedure, blowing the nose and washing the eyes with sterile distilled water or an isotonic sodium chloride solution will further minimize the radiation dose.

Radiopharmaceuticals should be used only by physicians who are qualified by training and experience in the safe handling of radionuclides and whose experience and training have been approved by the appropriate government agency authorized to license the use of radionuclides.

Carcinogenesis, Mutagenesis, Impairment of Fertility

No animal studies have been performed to evaluate carcinogenic potential or whether Sodium Pertechnetate Tc 99m affects fertility in males or females.

Pregnancy

Animal reproductive studies have not been conducted with Sodium Pertechnetate Tc 99m. It is also not known whether Sodium Pertechnetate Tc 99m can cause fetal harm when administered to a pregnant woman or can affect reproduction capacity. Sodium Pertechnetate Tc 99m Injection should be given to a pregnant woman only if clearly needed.

Ideally examinations using radiopharmaceuticals, especially those elective in nature, of a woman of childbearing capability should be performed during the first few (approximately 10) days following the onset of menses.

Nursing Mothers

Sodium Pertechnetate Tc 99m is excreted in human milk during lactation; therefore formula feedings should be substituted for breast feeding.

This radiopharmaceutical preparation should not be administered to pregnant or lactating women unless expected benefits to be gained outweigh the potential risks.

Pediatric Use

See INDICATIONS and DOSAGE AND ADMINISTRATION sections. Also see the description of additional risks under WARNINGS.

Geriatric Use

Clinical studies of Technelite® did not include sufficient numbers of subjects aged 65 and over to determine whether they respond differently from younger subjects. Other reported clinical experience has not identified differences in responses between the elderly and younger patients. In general, dose selection for an elderly patient should be cautious, usually starting at the low end of the dosing range, reflecting the greater frequency of decreased hepatic, renal, or cardiac function, and of concomitant disease or other drug therapy.

ADVERSE REACTIONS: Allergic reactions including anaphylaxis have been reported infrequently following the administration of Sodium Pertechnetate Tc 99m Injection.

Lantheus Medical Imaging

331 Treble Cove Road

N. Billerica, MA 01862 USA

For Ordering Call Toll-Free: 800-299-3431

All other business: 800-362-2668

(In Massachusetts and International, call 978-667-9531)

Patent: <http://www.lantheus.com/patents/index.html>

**LANTHEUS™**

513160-0719
PM-US-TE-0004

Printed in U.S.A.

July 2019

The Official Publication of **SNMMI**

Publications Committee

TODD E. PETERSON, PhD, FSNMMI

Chair

CAROLYN J. ANDERSON, PhD, FSNMMI

PAIGE B. BENNETT, MD

JOYITA DUTTA, PhD

MICHAEL M. GRAHAM, PhD, MD, FACR,

FSNMMI

HOSSEIN JADVAR, MD, PhD, FACNM,

FSNMMI

STEVEN M. LARSON, MD, FACNM

HEINRICH R. SCHELBERT, MD, PhD, FSNMMI

HEIKO SCHÖDER, MD, MBA, FSNMMI

DAVID M. SCHUSTER, MD

JESSICA WILLIAMS, CNMT, RT(N),

FSNMMI-TS

HARVEY A. ZIESSMAN, MD, FSNMMI

Ex officio

JOHANNES CZERNIN, MD, FSNMMI

MUNIR GHESANI, MD, FACNM, FACR

ARNOLD M. STRASHUN, MD, FSNMMI

KATHY S. THOMAS, MHA, CNMT,

PET, FSNMMI-TS

HENRY F. VANBROCKLIN, PhD, FSNMMI

Associate Director of Communications

SUSAN ALEXANDER

Senior Copyeditor

SUSAN NATH

Senior Publications & Marketing Service Manager

STEVEN KLEIN

Editorial Production Manager

PAULETTE MCGEE

Editorial Project Manager

MARK SUMIMOTO

Director of Communications

REBECCA MAXEY

CEO

VIRGINIA PAPPAS

MISSION STATEMENT: *The Journal of Nuclear Medicine* advances the knowledge and practice of molecular imaging and therapy and nuclear medicine to improve patient care through publication of original basic science and clinical research.

JNM (ISSN 0161-5505 [print]; ISSN 2159-662X [online]) is published monthly by SNMMI, 1850 Samuel Morse Drive, Reston, VA 20190-5316. Periodicals postage is paid at Herndon, VA, and additional mailing offices. Postmaster, send address changes to *The Journal of Nuclear Medicine*, 1850 Samuel Morse Drive, Reston, VA 20190-5316. The costs of publication of all nonsolicited articles in *JNM* were defrayed in part by the payment of page charges. Therefore, and solely to indicate this fact, these articles are hereby designated "advertisements" in accordance with 18 USC section 1734.

DISCLOSURE OF COMMERCIAL INTEREST: Johannes Czernin, MD, editor-in-chief of *The Journal of Nuclear Medicine*, has indicated that he is a founder of Sofie Biosciences and holds equity in the company and in intellectual property invented by him, patented by the University of California, and licensed to Sofie Biosciences. He is also a founder and board member of Trethera Therapeutics and holds equity in the company and in intellectual property invented by him, patented by the University of California, and licensed to Triangle. He also serves on the medical advisory board of Actinium Pharmaceuticals and on the scientific advisory boards of POINT Biopharma, RayzeBio, and Jubilant Pharma and is a consultant for Amgen. No other potential conflicts of interest were reported. Manuscripts submitted to *JNM* with potential conflicts are handled by a guest editor.

EDITORIAL COMMUNICATIONS should be sent to: Editor-in-Chief, Johannes Czernin, MD, *JNM* Office, SNMMI, 1850 Samuel Morse Drive, Reston, VA 20190-5316. Phone: (703) 326-1185; Fax: (703) 708-9018. To submit a manuscript, go to <https://submit-jnm.snmjournals.org>.

BUSINESS COMMUNICATIONS concerning permission requests should be sent to the publisher, SNMMI, 1850 Samuel Morse Drive, Reston, VA 20190-5316; (703) 708-9000; home page address: jnm.snmjournals.org. Subscription requests and address changes should be sent to Membership Department, SNMMI at the address above. Notify the Society of change of address and telephone number at least 30 days before date of issue by sending both the old and new addresses. Claims for copies lost in the mail are allowed within 90 days of the date of issue. Claims are not allowed for issues lost as a result of insufficient notice of change of address. For information on advertising, contact Team SNMMI (Kevin Dunn, Rich Devanna, and Charlie Meitner; (201) 767-4170; fax: (201) 767-8065; TeamSNMMI@cunnasso.com). Advertisements are subject to editorial approval and are restricted to products or services pertinent to nuclear medicine. Closing date is the first of the month preceding the date of issue.

INDIVIDUAL SUBSCRIPTION RATES for the 2023 calendar year are \$633 within the United States and Canada; \$680 elsewhere. Make checks payable to the SNMMI. CPC IPM Sales Agreement No. 1415158. Sales of individual back copies from 1999 through the current issue are available for \$60 at <http://www.snmml.org/subscribe> (subscriptions@snmml.org; fax: (703) 667-5134). Individual articles are available for sale online at <http://jnm.snmjournals.org>.

COPYRIGHT © 2023 by the Society of Nuclear Medicine and Molecular Imaging. All rights reserved. No part of this work may be reproduced or translated without permission from the copyright owner. Individuals with inquiries regarding permission requests, please visit <http://jnm.snmjournals.org/site/misc/permission.xhtml>. Because the copyright on articles published in *The Journal of Nuclear Medicine* is held by the Society, each author of accepted manuscripts must sign a statement transferring copyright (available for downloading at <http://jnm.snmjournals.org/site/misc/ifora.xhtml>). See Information for Authors for further explanation (available for downloading at <http://www.snmjournals.org/site/misc/ifora.xhtml>).

The ideas and opinions expressed in *JNM* do not necessarily reflect those of the SNMMI or the Editors of *JNM* unless so stated. Publication of an advertisement or other product mentioned in *JNM* should not be construed as an endorsement of the product or the manufacturer's claims. Readers are encouraged to contact the manufacturer with any questions about the features or limitations of the products mentioned. The SNMMI does not assume any responsibility for any injury or damage to persons or property arising from or related to any use of the material contained in this journal. The reader is advised to check the appropriate medical literature and the product information currently provided by the manufacturer of each drug to be administered to verify the dosage, the method and duration of administration, and contraindications.

EDITOR-IN-CHIEF

Johannes Czernin, MD
University of California at Los Angeles
Los Angeles, California

IMMEDIATE PAST EDITOR

Dominique Delbeke, MD, PhD
Vanderbilt University Medical Center
Nashville, Tennessee

ASSOCIATE EDITORS, CONTINUING EDUCATION

Hossein Jadvar, MD, PhD, MPH, MBA, FACNM, FSNMMI
University of Southern California
Los Angeles, California
Lale Kostakoglu, MD, MPH
University of Virginia Health System
Charlottesville, Virginia

ASSOCIATE EDITORS

Ramsey Derek Badawi, PhD
UC Davis Medical Center
Sacramento, California
Henryk Barthel, MD, PhD
Leipzig University
Leipzig, Germany
Frank M. Bengel, MD
Hannover Medical School
Hannover, Germany
Lisa Bodei, MD, PhD
Memorial Sloan Kettering Cancer Center
New York, New York
Irene Buvat, PhD
Université Paris Sud
Orsay, France
Jérémie Calais, MD
University of California at Los Angeles
Los Angeles, California
Sharmila Dorbala, MBBS
Brigham and Women's Hospital
Lexington, Massachusetts
Alexander E. Drzezga, MD
University Hospital of Cologne
Cologne, Germany
Jan Grimm, MD, PhD
Memorial Sloan Kettering Cancer Center
New York, New York
Ken Herrmann, MD, MBA
Universitätsklinikum Essen
Essen, Germany
Thomas A. Hope, MD
University of California, San Francisco
San Francisco, California
Jason S. Lewis, PhD
Memorial Sloan Kettering Cancer Center
New York, New York
David A. Mankoff, MD, PhD
University of Pennsylvania
Philadelphia, Pennsylvania
Heiko Schöder, MD
Memorial Sloan Kettering Cancer Center
New York, New York
Wolfgang Weber, MD
Technical University of Munich
München, Germany

SERIES EDITOR, FOCUS ON MI

Carolyn J. Anderson, PhD
University of Missouri
Columbia, Missouri

SERIES EDITOR, HOT TOPICS

Heinrich R. Schelbert, MD, PhD
University of California at Los Angeles
Los Angeles, California

CONSULTING EDITORS

Nancy Knight, PhD
University of Maryland School of Medicine
Baltimore, Maryland
Barry A. Siegel, MD
Mallinckrodt Institute of Radiology
St. Louis, Missouri
Arnold M. Strashun, MD
SUNY Downstate Medical Center
Scarsdale, New York
H. William Strauss, MD
Memorial Sloan Kettering Cancer Center
New York, New York

ASSOCIATE EDITORS (INTERNATIONAL)

Gerald Antoch, MD
Dusseldorf, Germany

Richard P. Baum, MD, PhD

Bad Berka, Germany
Ambros J. Beer, MD
Ulm, Germany
François Bénard, MD, FRCPC
Vancouver, Canada
Thomas Beyer, PhD
Vienna, Austria
Andreas K. Buck, MD, PhD
Würzburg, Germany
Ignasi Carrió, MD
Barcelona, Spain
June-Key Chung, MD
Seoul, Korea
Stefano Fanti, MD
Bologna, Italy
Markus Hacker, MD
Wien, Austria
Rodney J. Hicks, MD, FRACP
Melbourne, Australia
Michael S. Hofman, MBBS, FRACP
Melbourne, Australia
Ora Israel, MD
Haifa, Israel
Andreas Kjaer, MD, PhD, DMSc
Copenhagen, Denmark
Adriaan A. Lammertsma, PhD
Amsterdam, The Netherlands
Michael Lassman, PhD
Würzburg, Germany
Helmut R. Mäcke, PhD
Freiburg, Germany
Wim J.G. Oyen, MD, PhD
Milan, Italy
John O. Prior, MD, PhD
Lausanne, Switzerland
Osman Ratib, MD, PhD
Geneva, Switzerland
Mike Sathekge, MBChB, MMed, PhD
Pretoria, South Africa
Markus Schwaiger, MD
München, Germany
Andrew M. Scott, MD
Heidelberg, Australia
Nagara Tamaki, MD, PhD
Kyoto, Japan
Jia-He Tian, PhD
Beijing, China
Mei Tian, MD, PhD
Hangzhou, China

EDITORIAL CONSULTANTS

Martin S. Allen-Auerbach, MD
Los Angeles, California
Magnus Dahlbom, PhD
Los Angeles, California
Andrew Quon, MD
Los Angeles, California
Christiaan Schiepers, MD, PhD
Los Angeles, California
Daniel H. Silverman, MD, PhD
Los Angeles, California
Roger Slavik, PhD
Winterthur, Switzerland

EDITORIAL BOARD

Diane S. Abou, PhD
St. Louis, Missouri
Hojjat Ahmadzadehfar, MD
Dortmund, Germany
Valentina Ambrosini, MD, PhD
Bologna, Italy
Norbert Avril, MD
Cleveland, Ohio
Shadfar Bahri
Los Angeles, California
Jacques Barbet, PhD
Saint-Herbalin, France
Bradley Jay Beattie, PhD
New York, New York
Matthias Richard Benz, MD
Los Angeles, California
Elie Besserer-Offroy, PhD, FACSc
Los Angeles, California
Pradeep Bhambhvani, MD
Birmingham, Alabama
Angelika Bischof-Delaloye, MD
Lausanne, Switzerland

Christina Bluemel, MD

Würzburg, Germany
Ronald Boellaard, PhD
Groningen, The Netherlands
Nicolaas Bohnen, MD
Ann Arbor, Michigan
Wesley E. Bolch, PhD
Gainesville, Florida
Elias H. Botvinick, MD
San Francisco, California
Winfried Brenner, MD, PhD
Berlin, Germany
Richard C. Brunken, MD
Cleveland, Ohio
Ralph Buchert, PhD
Hamburg, Germany
Alfred Buck, MD
Menzingen, Switzerland
Denis B. Buxton, PhD
Bethesda, Maryland
Weibo Cai, PhD
Madison, Wisconsin
Federico Caobelli, MD
Basel, Switzerland
Giuseppe Carlucci, PhD
Los Angeles, California
Richard E. Carson, PhD
New Haven, Connecticut
Paolo Castellucci, MD
Bologna, Italy
Francesco Ceci, MD, PhD
Turin, Italy
Juliano J. Cerci
Curitiba, Brazil
Delphine Chen, MD
Seattle, Washington
Xiaoyuan Chen, PhD
Singapore
Simon R. Cherry
Davis, California
Arturo Chiti, MD
Rozzano, Italy
Peter M. Clark, PhD
Los Angeles, California
Christian Cohade, MD
Montreal, Canada
Ekaterina (Kate) Dadachova, PhD
Saskatoon, Canada
Issa J. Dahabreh, MD
Boston, Massachusetts
Heike Elisabeth Daldrup-Link, MD, PhD
Stanford, California
Farrokh Dehdashti, MD
St. Louis, Missouri
Robert C. Delgado-Bolton, MD, PhD
Logroño, Spain
Thorsten Derlin, MD
Hannover, Germany
Elisabeth G.E. de Vries, PhD
Groningen, The Netherlands
Marcelo F. Di Carli, MD
Boston, Massachusetts
David W. Dick, PhD
Iowa City, Iowa
Vasken Dilisizian, MD
Baltimore, Maryland
Jacob Dubroff, MD, PhD
Philadelphia, Pennsylvania
Janet F. Eary, MD
Bethesda, Maryland
W. Barry Edwards, PhD
Columbia, Missouri
Matthias Eiber, MD
Munich, Germany
David Eidelberg, MD
Manhasset, New York
Georges El Fakhri, PhD
Boston, Massachusetts
Peter J. Ell, MD
London, United Kingdom
Keigo Endo, MD
Nantan, Japan
Einat Even-Sapir, MD, PhD
Tel Aviv, Israel
Frederic H. Fahey, DSc
Boston, Massachusetts



CREATING HOPE THROUGH INNOVATION

At Eisai, everything we do is guided by a simple principle: patients and their families come first. We spend time with them. We listen and we learn about their lives, their desires and their greatest needs. *We call this human health care or hhc*, giving first thoughts to patients and their families and helping increase the benefits health care provides.

Our hhc mission is what drives us to discover innovative solutions and therapies that help address unmet needs within the communities that we seek to serve.

hhc
human health care

TO LEARN MORE, PLEASE VISIT WWW.EISAI.COM/US

EDITORIAL BOARD, continued**Melpomeni Fani, PhD, MSc**

Basel, Switzerland

Andrea Farolfi, MD

Bologna, Italy

Wolfgang Peter Fendler, MD

Essen, Germany

James W. Fletcher, MD

Indianapolis, Indiana

Amy M. Fowler, MD, PhD

Madison, Wisconsin

Kirk A. Frey, MD, PhD

Ann Arbor, Michigan

Andrei Gafita

Los Angeles, California

Victor H. Gerbaudo, PhD, MSHCA

Boston, Massachusetts

Frederik L. Giesel, MD, PhD, MBA

Düsseldorf, Germany

Karolien Goffin, MD, PhD

Leuven, Belgium

Serge Goldman, MD, PhD

Brussels, Belgium

Stanley J. Goldsmith, MD

New York, New York

Martin Gotthardt, MD, PhD

Nijmegen, The Netherlands

Michael Graham, MD, PhD

Iowa City, Iowa

David Groheux, MD, PhD

Paris, France

Uwe A. Haberkorn, MD

Heidelberg, Germany

Mathieu Hatt, PhD, HDR

Brest, France

Wolf-Dieter Heiss, MD

Cologne, Germany

Karl Herholz, MD

Manchester, United Kingdom

Thomas F. Heston, MD

Las Vegas, Nevada

John M. Hoffman, MD

Salt Lake City, Utah

Carl K. Hoh, MD

San Diego, California

Jason P. Holland, DPhil

Zurich, Switzerland

Roland Hustinx, MD, PhD

Liege, Belgium

Andrei H. Iagaru, MD

Stanford, California

Masanori Ichise, MD

Chiba, Japan

Heather A. Jacene, MD

Boston, Massachusetts

Francois Jamar, MD, PhD

Brussels, Belgium

Jae Min Jeong, PhD

Seoul, Korea

John A. Katzenellenbogen, PhD

Urbana, Illinois

Zohar Keidar, MD, PhD

Haifa, Israel

Kimberly A. Kelly, PhD

Charlottesville, Virginia

Laura M. Kenny, MD, PhD

London, United Kingdom

Fabian Kiessling, MD

Aachen, Germany

E. Edmund Kim, MD, MS

Orange, California

Francoise Kraeber-Bodéré, MD, PhD

Nantes, France

Clemens Kratochwil, MD

Heidelberg, Germany

Kenneth A. Krohn, PhD

Portland, Oregon

Brenda F. Kurland, PhD

Pittsburgh, Pennsylvania

Constantin Lapa, MD

Augsburg, Germany

Suzanne E. Lapi, PhD

Birmingham, Alabama

Steven M. Larson, MD

New York, New York

Dong Soo Lee, MD, PhD

Seoul, Korea

Jeffrey Leyton, PhD

Sherbrooke, Canada

Xiang-Guo Li, PhD

Turku, Finland

Hannah M. Linden, MD

Seattle, Washington

Martin A. Lodge, PhD

Baltimore, Maryland

Katharina Lückerath, PhD

Los Angeles, California

Susanne Lütje, MD, PhD

Bonn, Germany

Umar Mahmood, MD, PhD

Boston, Massachusetts

H. Charles Manning, PhD

Nashville, Tennessee

Giuliano Mariani, MD

Pisa, Italy

Chester A. Mathis, PhD

Pittsburgh, Pennsylvania

Alan H. Maurer, MD

Philadelphia, Pennsylvania

Jonathan McConathy, MD, PhD

Birmingham, Alabama

Alexander J.B. McEwan, MD

Edmonton, Canada

Yusuf Menda, MD

Iowa City, Iowa

Philipp T. Meyer, MD, PhD

Freiburg, Germany

Matthias Miederer, MD

Mainz, Germany

Erik Mittra, MD, PhD

Portland, Oregon

Christine E. Mona, PhD

Los Angeles, California

Dae Hyuk Moon, MD

Seoul, Korea

Jennifer Murphy, PhD

Los Angeles, California

Helen Nadel, MD, FRCPC

Stanford, California

Matthias Nahrendorf, MD, PhD

Boston, Massachusetts

Yuji Nakamoto, MD, PhD

Kyoto, Japan

David A. Nathanson, PhD

Los Angeles, California

Nghi C. Nguyen, MD, PhD

Dallas, Texas

Sridhar Nimmagadda, PhD

Baltimore, Maryland

Egbert U. Nitzsche, MD

Aarau, Switzerland

Daniela E. Oprea-Lager, MD, PhD

Amsterdam, The Netherlands

Medhat M. Osman, MD, PhD

Saint Louis, Missouri

Christopher J. Palestro, MD

New Hyde Park, New York

Miguel Hernandez Pampaloni, MD, PhD

San Francisco, California

Neeta Pandit-Taskar, MD

New York, New York

Ashwin Singh Parihar, MBBS, MD

Saint Louis, Missouri

Michael E. Phelps, PhD

Los Angeles, California

Gerold Porenta, MD, PhD

Vienna, Austria

Sophie Poty, PhD

Montpellier, France

Edwin (Chuck) Pratt, PhD, MS Eng

New York, New York

Daniel A. Pryma, MD

Philadelphia, Pennsylvania

Valery Radchenko, PhD

Vancouver, Canada

Caius G. Radu, MD

Los Angeles, California

Isabel Rauscher, MD

Munich, Germany

Nick S. Reed, MBBS

Glasgow, United Kingdom

Mark Rijpkema, PhD

Nijmegen, The Netherlands

Steven P. Rowe, MD, PhD

Baltimore, Maryland

Mehran Sadeghi, MD

West Haven, Connecticut

Orazio Schillaci, MD

Rome, Italy

Charles Ross Schmidtlein, PhD

New York, New York

David M. Schuster, MD

Atlanta, Georgia

Travis Shaffer, PhD

Stanford, California

Sai Kiran Sharma, PhD

New York, New York

Anthony F. Shields, MD, PhD

Detroit, Michigan

Barry L. Shulkin, MD, MBA

Memphis, Tennessee

Yu Shyr, PhD

Nashville, Tennessee

Albert J. Sinusas, MD

New Haven, Connecticut

Riemer H.J.A. Slart, MD, PhD

Groningen, The Netherlands

Piotr Slomka, PhD, FACC

Los Angeles, California

Simon John Christoph Soerensen, MD

Stanford, California

Ida Sonni, MD

Los Angeles, California

Michael G. Stabin, PhD

Richland, Washington

Lisa J. States, MD

Philadelphia, Pennsylvania

Sven-Erik Strand, PhD

Lund, Sweden

Rathan M. Subramaniam, MD, PhD, MPH

Dunedin, New Zealand

John Sunderland, PhD

Iowa City, Iowa

Suleman Surti, PhD

Philadelphia, Pennsylvania

Julie Sutcliffe, PhD

Sacramento, California

David Taieb, MD, PhD

Marseille, France

Laura H. Tang, MD, PhD

New York, New York

Ukihide Tateishi, MD, PhD

Tokyo, Japan

James T. Thackeray, PhD

Hannover, Germany

Mathew L. Thakur, PhD

Philadelphia, Pennsylvania

Alexander Thiel, MD

Montreal, Canada

Daniel L.J. Thorek, PhD

St. Louis, Missouri

David W. Townsend, PhD

Singapore

Timothy Turkington, PhD

Durham, North Carolina

Gary A. Ulaner, MD, PhD

Irvine, California

David Ulmert, MD, PhD

Los Angeles, California

Lena M. Unterrainer, MD, MHBA

Munich, Germany

Christopher H. van Dyck, MD

New Haven, Connecticut

Douglas Van Nostrand, MD

Washington, District of Columbia

Patrick Veit-Haibach, MD

Toronto, Canada

Nerissa Viola-Villegas, PhD

Detroit, Michigan

John R. Votaw, PhD

Atlanta, Georgia

Richard L. Wahl, MD

St. Louis, Missouri

Anne Marie Wallace, MD

La Jolla, California

Martin A. Walter, MD

Geneva, Switzerland

Rudolf A. Werner, MD

Wuerzburg, Germany

Andreas G. Wibmer, MD

New York, New York

Anna M. Wu, PhD

Duarte, California

Randy Yeh, MD

New York, New York

Hyewon (Helen) Youn, PhD

Seoul, Korea

Pat B. Zanzonico, PhD

New York, New York

Brian M. Zeglis, PhD

New York, New York

Robert Zeiser, MD

Freiburg, Germany

Hong Zhang, MD, PhD

Hangzhou, China

Hongming Zhuang, MD, PhD

Philadelphia, Pennsylvania

Sibylle I. Ziegler, PhD

Munich, Germany

ASSISTANT TO THE EDITOR**Joshua N. Wachtel**

Los Angeles, California

Learn more about becoming a Value Initiative Industry Alliance Member Company:



valueinitiative.snmmi.org



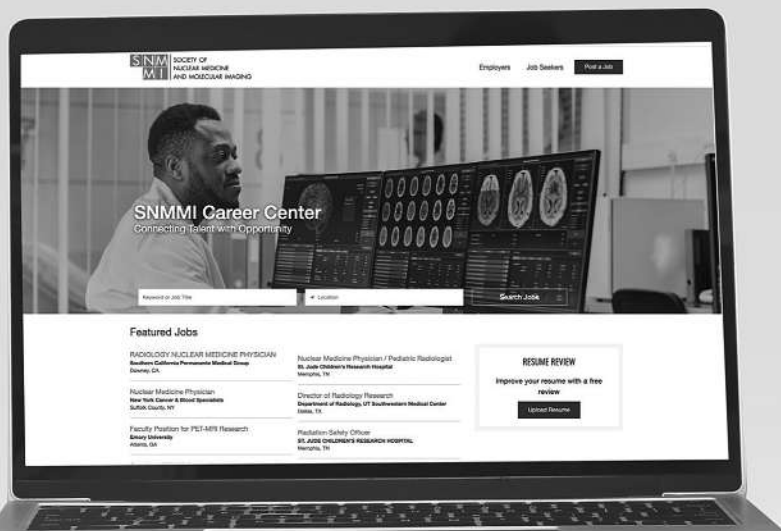
JOHNS HOPKINS
MEDICINE
Division Of Nuclear Medicine
And Molecular Imaging

The Russell H. Morgan Department of Radiology and Radiological Science at The Johns Hopkins University School of Medicine invites applications for a faculty position as a Nuclear Medicine Physician or Nuclear Radiologist in a dynamic and state-of-the-art environment. The Division of Nuclear Medicine and Molecular Imaging is seeking a full-time faculty member with ABR and/or ABNM board certifications to support our mission in clinical service, teaching and research with an emphasis on development and implementation of new agents for PET and theranostics. Salary and academic rank will be commensurate with experience and qualifications.

For further information please contact Martin Pomper, M.D., Ph.D. (mpomper@jhmi.edu). Johns Hopkins University is an equal opportunity, affirmative-action employer.

Explore SNMMI's Online Career Center!

Explore the benefits of SNMMI's online career center by logging in or creating a new account today.



careercenter.snmmi.org

**Note: Single sign-on has been enabled for this platform and you can use your member login credentials to access the Career Center. If you are unsure of your password, to go to the SNMMI password reset link to create a new password.*

Discussions with leaders: Buvat and Weber test ChatGPT's familiarity with nuclear medicine knowledge and practice in an extended virtual conversation. *Page 505*

Chemotherapy and cognitive impairment: Chiaravalloti and colleagues summarize brain imaging findings relevant to subsequent cognitive effects in patients undergoing chemotherapy for common oncologic diseases. *Page 508*

PET imaging in vasculitis: Slart and colleagues provide an educational overview of the diagnostic role of ^{18}F -FDG PET/CT in patients with large-vessel vasculitis, medium-sized vessel vasculitis, and polymyalgia rheumatica. *Page 515*

PRRT and NETs: Hindié and colleagues offer a brief review of the latest advances in peptide-receptor radionuclide therapy of neuroendocrine tumors of gastroenteropancreatic origin, including clinical trial results and promising combination therapies. *Page 522*

AUC summary for lymphoscintigraphy: Donohoe and members of a collaborative work group summarize the key points of appropriate use criteria (AUC) developed for lymphoscintigraphy in sentinel lymph node mapping and in lymphedema, including clinical scenarios. *Page 525*

Radioembolization in cholangiocarcinoma: Schaarschmidt and colleagues identify clinical and tumor-associated factors in improved median overall survival in patients with intrahepatic cholangiocarcinoma receiving radioembolization at 5 major tertiary-care centers. *Page 529*

PET in large B-cell lymphoma: Michaud and colleagues assess the prognostic value of ^{18}F -FDG PET/CT parameters at baseline, interim, and end of treatment in patients with diffuse large B-cell lymphoma. *Page 536*

[^{177}Lu]Lu-Ofatumumab lymphoma therapy: Shim and colleagues report on in vitro studies, dosimetry, tumor targeting, and therapeutic efficacy with this radiolabeled human anti-CD20 antibody in a murine model of disseminated non-Hodgkin lymphoma. *Page 542*

^{225}Ac -MACROPATATE for NETs: King and colleagues detail the design and production of a novel radioconjugate capable of chelating ^{225}Ac at room temperature and assess in vitro and in vivo studies of its potential for α -particle targeted peptide-receptor radionuclide therapy. *Page 549*

^{89}Zr -DFO-bexmarilimab PET: Moisisio and colleagues evaluate a humanized monoclonal antibody against common lymphatic endothelial and vascular endothelial receptor-1 in a rabbit model of renal fibrosis. *Page 555*

Thyroid remnant ablation in GO: Oeverhaus and colleagues report on responses after ablation of thyroid remnants with radioactive iodine therapy in patients with unstable Graves' orbitopathy after subtotal thyroidectomy. *Page 561*

PPQ/NETest validation for PRRT: Bodei and colleagues look at 2 predictive markers for response to and monitoring of peptide-receptor radionuclide therapy in neuroendocrine tumors and evaluate the predictive contributions of tissue-based genetic alterations. *Page 567*

Sequencing ^{223}Ra and ^{177}Lu -PSMA: Rahbar and colleagues document safety and survival outcomes in patients with bone-predominant metastatic castration-resistant prostate cancer treated with ^{177}Lu -PSMA after ^{223}Ra therapy. *Page 574*

^{18}F -PSMA versus ^{18}F -fluorocholine PET/CT: Olivier and colleagues compare ^{18}F -PSMA-1007 PET/CT and ^{18}F -fluorocholine PET/CT for localization of suspected biochemical recurrence of prostate cancer and for associated clinical management. *Page 579*

^{18}F -Fluciclovine PET-guided radiotherapy: Lawal and colleagues analyze data from the EMPIRE-1 study, which compared fluciclovine PET/CT and conventional imaging in guiding prostate cancer salvage radiotherapy, here stratifying by protocol-specified criteria and comparing failure-free rates. *Page 586*

^{68}Ga -PSMA11 and ^{68}Ga -RM2 PET for HIFU: Duan and colleagues evaluate a novel approach using both ^{68}Ga -RM2 and ^{68}Ga -PSMA11 PET/MRI in patients with localized prostate cancer before and after high-intensity focused ultrasound therapy to assess target tumor localization and response to treatment. *Page 592*

Translation of ^{18}F -PSMA CLI and FAR CLI: Fragoso Costa and colleagues assess the value of Cerenkov luminescence imaging with flexible autoradiography and with ^{18}F -PSMA-1007 in pre-clinical studies and in patients with high-risk prostate cancer. *Page 598*

Systematic PSMA PET response assessment: Kind and colleagues analyze the suitability of a semiautomatic prognostic approach by comparing ^{18}F -PSMA-1007 with ^{68}Ga -PSMA-11 PET/CT data for prediction of overall survival in patients with prostate cancer before ^{177}Lu -PSMA radioligand therapy. *Page 605*

^{177}Lu -EB-PSMA RLT in mCRPC: Wang and colleagues investigate the safety and therapeutic efficacy of radioligand therapy with ^{177}Lu -EB-PSMA in patients with previously treated metastatic castration-resistant prostate cancer. *Page 611*

^{68}Ga -FAPI-46 at 3 time points: Naeimi and colleagues monitor uptake on PET at 10 min, 1 h, and 3 h after ^{68}Ga -FAPI-46 administration in a spectrum of tumor types, with resulting implications for improving workflow and patient wait times. *Page 618*

FAP-based PET imaging: Kashyap and Ravi Kumar review the current status and future promise of fibroblast-activation protein inhibitor-based imaging, including the ability to address specific limitations of ^{18}F -FDG PET and to provide both new and complementary biologic insights. *Page 623*

^{18}F -FAPI-04 PET/CT response prediction in LA-ESCC: Hu and colleagues examine whether ^{18}F -AIF-NOTA-fibroblast-activation protein inhibitor-04 PET/CT can predict short-term outcomes in patients with locally advanced esophageal squamous cell carcinoma treated with concurrent chemoradiotherapy. *Page 625*

^{18}F -AIF-OC versus ^{68}Ga -DOTA-SSA PET: Pauwels and colleagues detail the results of a multicenter trial comparing the diagnostic performances of ^{18}F - and ^{68}Ga -labeled somatostatin analog PET tracers in patients with neuroendocrine tumors. *Page 632*

Theranostic peptides targeting integrin $\alpha_v\beta_6$: Ganguly and colleagues describe development and testing of a novel $\alpha_v\beta_6$ -targeting peptide, ^{68}Ga -DOTA-5G, and its DOTA-albumin-binding moiety for PET/CT imaging and with ^{177}Lu labeling for treatment. *Page 639*

Myocardial efficiency in mitral regurgitation: Sorensen and colleagues use ^{11}C -acetate PET to noninvasively measure myocardial mechanical external efficiency, the energetic ratio of external cardiac work and left ventricular oxygen consumption. *Page 645*

Deep learning for CAC on SPECT/CT: Miller and colleagues evaluate CT attenuation correction quantification derived from SPECT/CT myocardial perfusion maps using a deep learning model, including correlation with expert annotations and associations with major adverse cardiovascular events. *Page 652*

Spatial normalization with deep learning: Kang and colleagues present a novel method for automatic quantification of amyloid PET using deep learning-based spatial normalization of PET images, which does not require MR or CT images of the same patient. *Page 659*

CXCR4 expression in meningioma: Krebs and colleagues report on a clinical experience detecting C-X-C chemokine receptor 4 expression in meningioma with ^{68}Ga -pentixafor PET. *Page 667*

Amyloid Imaging–Based Food and Drug Administration Approval of Lecanemab to Treat Alzheimer Disease—What Lasts Long Finally Becomes Good?

Henryk Barthel

Leipzig University Medical Center, Leipzig, Germany

Alzheimer disease (AD) is a devastating neurologic condition of high socioeconomic relevance. Although today this disease can be accurately diagnosed during a lifetime, especially with the help of molecular imaging approaches such as amyloid PET, tau PET or ^{18}F -FDG PET, no disease-modifying treatment is yet available. The search for a drug able to positively influence the course of AD is a long story of frustration. This search thankfully took a positive turn with the U.S. Food and Drug Administration (FDA) approval of lecanemab (Leqembi; Eisai and Biogen) on January 6, 2023 (1). Lecanemab is currently also undergoing evaluation for approval by the European Medicines Agency.

The Tokyo (Japan)-based pharmaceutical company Eisai and the Cambridge (Massachusetts)-based biotech company Biogen developed lecanemab. It is a humanized IgG1 monoclonal antibody that mainly targets larger β -amyloid oligomers (so-called protofibrils). The approval of this drug was the outcome of the FDA's Accelerated Approval pathway, applicable in cases of unmet medical need and if a drug has shown a favorable effect on a surrogate of clinical efficacy. In this case, of note, the reduction of amyloid PET quantitative readouts via lecanemab as shown in a placebo-controlled phase 2 study was accepted by the FDA as a suitable clinical efficacy surrogate. In this study, subjects with mild cognitive impairment or mild AD dementia underwent brain MRI and, importantly, amyloid PET imaging to establish amyloid positivity. Included patients received an intravenous infusion of the drug (up to 10 mg/kg body weight) once every 2 wk or placebo. It was convincingly shown that lecanemab is indeed able to remove amyloid aggregates from the brain.

Consequently, the above phase 2 study methods are replicated in the lecanemab prescribing information. In terms of side effects, potential amyloid removal-related imaging abnormalities need to be monitored by MRI, apart from potential drug infusion-related side effects. The need of a priori amyloid testing is based on the well-known fact that not all patients fulfilling the clinical criteria of AD dementia indeed suffer from an amyloidopathy (2). In other words, the amyloid "gate-keeper" test provides evidence for the presence of the drug target and thus avoids the prescription of a drug that will not only not work in amyloid-negative patients (and lecanemab will

likely cost around \$26,000 USD per patient per year), but also potentially have side effects.

After aducanumab, lecanemab is the second FDA-approved anti-amyloid drug to treat AD. In distinction from the controversial clinical efficacy data (followed by the controversial FDA approval and nonapproval by the European Medicines Agency) with aducanumab, for lecanemab there are convincing results in the clinical efficacy phase 3 study program. In this phase 3 study, the drug was given

for 18 mo in the treatment arm, demonstrating a slowing of cognitive decline by 27%. In absolute numbers, this equals a difference of 0.45 points on the Clinical Dementia Rating-Sum of Boxes (a valuable dementia severity measure covering a wider range of memory, orientation, personal care, and other symptoms or problems) between the treatment and placebo arms (3). Although some neurologists express concern about the relevance of this achieved primary endpoint to an individual patient (4,5), and concerns are also raised about the vascular events safety profile of the drug (6), most clinicians in the field seem to be positive about these clinical efficacy data (7–9). The FDA is currently reviewing these lecanemab phase 3 clinical efficacy data. In parallel, another anti-amyloid antibody, donanemab, developed by Eli Lilly, likewise appears to be making good progress in its development program (10).

Regardless, the lecanemab development pipeline convincingly showed the value of amyloid imaging in identifying patients in whom the actual drug target is present and who, as such, qualify for respective drug prescription on a disease pathology ground. Here, amyloid PET also provides a perfect baseline amyloid state readout, which can be used as a starting point for follow-up imaging to monitor the biologic drug effect. As such, it is conceivable that amyloid removal might differ from patient to patient with regard to speed and intensity. Thus, providing that such intraindividual biologic drug effect differences are indeed of relevance, amyloid imaging might allow for a truly personalized, PET-guided drug administration regimen.

In addition, the positive clinical effect of lecanemab evidences the validity of the amyloid cascade hypothesis. This hypothesis proposes the aggregation of β -amyloid in the brain representing the initial event in AD triggering a cascade of other processes, finally resulting in neurodegeneration and cognitive decline (11). Excitingly, now—with the lecanemab development program



Henryk Barthel

Received Mar. 2, 2023; revision accepted Mar. 2, 2023.
For correspondence or reprints, contact Henryk Barthel (henryk.barthel@medizin.uni-leipzig.de).
Published online Mar. 23, 2023.
COPYRIGHT © 2023 by the Society of Nuclear Medicine and Molecular Imaging.
DOI: 10.2967/jnumed.123.265667

data—we seem to have one missing piece to the puzzle in hand to better understand this devastating disorder on pathobiochemical grounds. It would be the logical next step to apply anti-amyloid drugs in earlier or prodromal AD stages, that is, at a time point in which tau accumulation and neurodegeneration have not yet started, thus preventing (instead of slowing down existing) cognitive deterioration and providing ultimate proof of the amyloid cascade theory.

The Society of Nuclear Medicine and Molecular Imaging (SNMMI) recently welcomed the FDA's decision to approve lecanemab (12) and echoed that amyloid PET imaging is very well suited both for qualifying patients for drug prescription and for evaluating the drug effect on a biologic ground. The SNMMI will also discuss a respective reimbursement with the Centers for Medicare & Medicaid Services (CMS), with some promising preliminary feedback from the CMS (13). Together with the Alzheimer's Association, the SNMMI is also working on updating the Appropriate Use Criteria for amyloid imaging (14) by including PET imaging to qualify patients for anti-amyloid drug prescription. Our molecular imaging community will need to prepare to fulfil the future requirements of anticipated widespread employment of lecanemab in terms of amyloid tracer, PET scanner, and PET imaging staff availability. Now, more than ever, it is the right time to support the SNMMI and other involved bodies in their respective efforts, for the good of our patients.

REFERENCES

1. FDA grants accelerated approval for Alzheimer's disease treatment. FDA website. www.fda.gov/news-events/press-announcements/fda-grants-accelerated-approval-alzheimers-disease-treatment. January 6, 2023. Accessed March 6, 2023.

2. Barthel H, Seibyl J, Sabri O. The role of positron emission tomography imaging in understanding Alzheimer's disease. *Expert Rev Neurother*. 2015;15:395–406.
3. van Dyck CH, Swanson CJ, Aisen P, et al. Lecanemab in early Alzheimer's disease. *N Engl J Med*. 2023;388:9–21.
4. Mahase E. Lecanemab trial finds slight slowing of cognitive decline, but clinical benefits are uncertain. *BMJ*. 2022;379:o2912.
5. Lecanemab for Alzheimer's disease: tempering hype and hope (editorial). *The Lancet*. 2022;400:P1899.
6. Reardon S. FDA approves Alzheimer's drug lecanemab amid safety concerns. *Nature*. 2023;613:227–228.
7. Alzheimer's Association statement on lecanemab phase 3 full results. Alzheimer's Association website. www.alz.org/news/2022/statement-lecanemab-phase-three-full-results. Accessed March 6, 2023.
8. Treating Alzheimer's: a new era begins with lecanemab. Alzheimer's Association website. www.alz.org/media/Documents/joint-letter-alzheimers-scientists-lecanemab.pdf. Accessed March 6, 2023.
9. Lowe D. Lecanemab and Alzheimer's: more data. www.science.org/content/blog-post/lecanemab-and-alzheimer-s-more-data. November 30, 2022. Accessed March 6, 2023.
10. Donanemab. Alzforum website. www.alzforum.org/therapeutics/donanemab. Updated February 6, 2023. Accessed March 6, 2023.
11. Hardy JA, Higgins GA. Alzheimer's disease: the amyloid cascade hypothesis. *Science*. 1992;256:184–185.
12. FDA approves new treatment for Alzheimer's disease: presence of beta amyloid must be confirmed before treatment. Society of Nuclear Medicine and Molecular Imaging website. www.snmmi.org/NewsPublications/NewsDetail.aspx?ItemNumber=42942. January 6, 2023. Accessed March 6, 2023.
13. U.S. Centers for Medicare & Medicaid Services. CMS statement on FDA accelerated approval of lecanemab. U.S. Centers for Medicare & Medicaid Services website. www.cms.gov/newsroom/press-releases/cms-statement-fda-accelerated-approval-lecanemab. Accessed March 6, 2023.
14. Johnson KA, Minoshima S, Bohnen NI, et al. Appropriate use criteria for amyloid PET: a report of the Amyloid Imaging Task Force, the Society of Nuclear Medicine and Molecular Imaging, and the Alzheimer's Association. *J Nucl Med*. 2013;54:476–490.

Nuclear Medicine from a Novel Perspective: Buvat and Weber Talk with OpenAI's ChatGPT

Irène Buvat, PhD¹, and Wolfgang Weber, MD, PhD²

¹Inserm Laboratory of Translational Imaging in Oncology, Institut Curie, Orsay, France; ²University Hospital, Technische Universität München, Munich, Germany

Irène Buvat, PhD, Centre National de la Recherche Scientifique director of research and head of the Inserm Laboratory of Translational Imaging in Oncology at the Institut Curie, Orsay (France), and Wolfgang Weber, MD, PhD, director of the Department of Nuclear Medicine at “Klinikum rechts der Isar” (University Hospital of the Technische Universität München, Germany) talked with ChatGPT, an artificial intelligence (AI) language model. ChatGPT was developed by OpenAI (San Francisco, CA), a research organization dedicated to advancing artificial intelligence (AI) in a safe and beneficial way. The bot was trained on a large dataset of text, including books, articles, and other sources of information, to develop language processing and understanding capabilities. It has been designed to be able to respond to a wide range of questions and provides information quickly and easily on a variety of topics. ChatGPT was launched on November 30, 2022, and, by January 2023, had reached more than 100 million users—a faster rate of adoption than Instagram or TikTok. By February, ChatGPT had been featured in 10 articles in the *New York Times* and been on the covers of *TIME* magazine and the *Economist*. Drs. Buvat and Weber asked ChatGPT about the current practice and future development of nuclear medicine.

Commentary, Drs. Buvat and Weber: ChatGPT no longer needs an introduction for most people, but, for those who have been hibernating for the last few months, it is a “bot,” a program that can interact with human users. The user types in a question in a natural language (with >90 available languages), and ChatGPT responds in natural language. The bot can be asked to adopt a specific style, such as Shakespearean or journalistic language. In conversations with users, ChatGPT always “pays attention” and remembers the thread of the dialogue. It is sometimes a bit stubborn but very polite and eager to help. Its knowledge is impressively broad, including aspects of medicine and medical imaging. When it cannot find an answer, it says so. Sound like the perfect personal assistant? Not quite. It is more like a trainee with impressive skills and knowledge. In January 2023 we challenged ChatGPT with a few questions relevant to nuclear medicine to illustrate the role it could play in our field. (**Note:** ChatGPT received no special preparation for this interview and responded entirely with information already in its extensive dataset. Bot responses to questions have not been edited to this journal's style; instead, they are reproduced exactly as they appeared to the interviewers.)

Published online Mar. 23, 2023.

COPYRIGHT © 2023 by the Society of Nuclear Medicine and Molecular Imaging.
DOI: 10.2967/jnumed.123.265636

Q1, Dr. Weber: Hello. Could you please write a PET/CT report for a patient with suspected lung cancer? The scan shows a hypermetabolic mass in the right upper lobe and hypermetabolic lymph nodes in the right hilar and left lower paratracheal region. Please include the TNM stage.

ChatGPT:

Patient: [Patient Name] Date of Exam: [Date].

Indication: Evaluation of suspected lung cancer.

Technique: Whole body PET/CT scan was performed with the administration of [dose] of FDG.

Findings:

1. Hypermetabolic mass is identified in the right upper lobe (SUV max 8.2) with an associated spiculated margin, consistent with a primary lung malignancy.
2. Hypermetabolic lymph nodes are identified in the right hilar (SUV max 6.5) and left lower paratracheal (SUV max 6.7) regions, consistent with nodal involvement by lung cancer.
3. CT scan of the chest also confirms the above-mentioned findings and also shows no evidence of distant metastasis.

TNM stage: T3N2M0 (The tumor is located in the right upper lobe, it is larger than 7cm and there is nodal involvement in the right hilar and left lower paratracheal region, no evidence of distant metastasis).

Impression: Hypermetabolic mass in the right upper lobe with associated spiculated margin and hypermetabolic lymph nodes in the right hilar and left lower paratracheal region consistent with lung cancer. Recommend further workup and histopathological correlation, including biopsy of the primary tumor and involved lymph nodes.

Commentary, Drs. Buvat and Weber: This quite impressive response was given within a few seconds! ChatGPT uses the typical language of radiology reports and provides SUV_{max} values that



Irène Buvat, PhD



Wolfgang Weber,
MD, PhD

are consistent with high metabolic activity. It also gets the TNM stage almost right. It interprets the left paratracheal nodes as “contralateral mediastinal nodes” and assigns the correct N2 stage. Interestingly, it uses the slightly outdated 7th edition of lung cancer TNM staging, which defines T3 as a tumor with a diameter of >7 cm. The current 8th edition defines T3 by a tumor diameter between 5 and 7 cm.

Commentary, Dr. Weber: Although ChatGPT should definitely not be used to write patient reports at this stage, one could envision that an AI could be trained specifically for writing radiology reports in the near future. Such a system could automatically generate structured reports and avoid all the common typographic and grammatical errors that plague current radiology reports. It also does not seem to be too far-fetched to combine an AI that analyzes images with AI that generates a human-readable, standardized report. Such a system could dramatically streamline radiology workflows if appropriately validated and would enable radiologists to report many more scans than currently possible.

Q2, Dr. Buvat: *Could you please explain what the Ki Patlak slope calculated from an FDG PET/CT scan represents?*

ChatGPT: The Ki Patlak slope from FDG PET/CT scan represents the rate of influx of the radiotracer (fluorodeoxyglucose, FDG) into tissues, which reflects the local tissue glucose metabolism. It is used to quantify the regional cerebral blood flow (rCBF) and can provide information about tissue perfusion and functional brain activity. The Ki Patlak method is a graphical analysis that plots the distribution volume of the tracer in tissue over time. The slope of this line

most accurate and specific measure of metabolic activity within a lesion.

Commentary, Dr. Buvat: Here we see the limits of ChatGPT’s knowledge. The sentences sound correct, but the content is mostly wrong. This illustrates one of the dangers of ChatGPT: its responses can sound very convincing even when they are simply wrong.

Q4, Dr. Buvat: *Based on current knowledge, what do you think are the 3 most promising radiotracers in oncology for routine use in the future?*

ChatGPT: There is ongoing research and development in the field of molecular imaging and radiotracers, and several promising radiotracers are being studied for their potential use in oncology. Here are three radiotracers that are considered to be among the most promising for routine use in the future:

PSMA-PET: PSMA is a protein that is highly expressed in prostate cancer, and PSMA-PET imaging using radiolabeled PSMA ligands has shown high sensitivity and specificity for detecting prostate cancer, even in its early stages.

68Ga-DOTA-peptides: 68Ga-DOTA-peptides are a group of radiotracers that bind to specific receptors or antigens on cancer cells and are used for imaging and staging of various types of cancer, including neuroendocrine tumors, gastrointestinal tumors, and others.

18F-FDG: 18F-FDG is a widely used radiotracer that has been validated for the evaluation of malignant lesions, including various types of cancer such as lymphoma, lung cancer, and others. The high glucose uptake in malignant cells makes 18F-FDG a useful tool for detecting and staging cancer.

“[O]ne of the dangers of ChatGPT: its responses can sound very convincing even when they are simply wrong.”

represents the rate of tracer uptake, with a steeper slope indicating a faster uptake rate and thus higher tissue metabolism. This method is commonly used in the assessment of neurological and oncological disorders, among other applications.

Commentary, Dr. Buvat: An almost correct answer. ChatGPT mixes up cerebral blood flow and cerebral metabolic rate in 1 sentence. The information is probably more comprehensive than a Google search about Patlak analysis. It is remarkable that ChatGPT can answer this question, because Patlak analysis is used only in nuclear medicine research, which constitutes only a very small part of the overall information found on the Internet.

Q3, Dr. Buvat: *In a tumor seen on an FDG PET/CT image, would you recommend reporting SUV_{peak} or SUV_{max} in the medical report?*

ChatGPT: In a medical report for an FDG PET/CT scan, both the SUV_{peak} and the SUV_{max} can be reported as measures of tumor metabolic activity. However, the SUV_{peak} is typically used as the standard measure in clinical practice.

SUV_{peak} refers to the maximum standard uptake value (SUV) within a region of interest (ROI) that is used to define a specific lesion, whereas the SUV_{max} refers to the highest SUV within the entire image. The SUV_{peak} provides a more accurate representation of the metabolic activity within a lesion, as it takes into account only the highest SUV within that lesion, rather than including the background or normal physiological activity.

Therefore, it is generally recommended to report the SUV_{peak} in the medical report for an FDG PET/CT scan, as it provides the

It is important to note that the use of these and other radiotracers is dependent on ongoing research, regulatory approval, and clinical validation, and the most promising radiotracers for routine use may change over time as new information becomes available.

Commentary, Dr. Weber: A nicely worded answer to what has literally become a “billion-dollar question.” ChatGPT cannot see into the future but summarizes nicely what has been said about the 3 most commonly used classes of tracers. It doesn’t really answer the question, because all these agents are already in clinical use. But, of course, their use may increase in the coming years, and, therefore, the answer is not incorrect. A human “expert” would probably have mentioned agents that are not yet FDA approved and are undergoing clinical testing, e.g. fibroblast-activation protein ligands or gastrin-releasing peptide-receptor ligands.

Q5, Dr. Buvat: *Do you think I can trust AI-based segmentation tools for segmenting head and neck tumors from PET/CT in the context of radiation therapy planning?*

ChatGPT: AI-based segmentation tools for head and neck tumor segmentation from PET/CT scans have shown promise and have the potential to improve the accuracy and efficiency of radiation therapy planning. However, their reliability and accuracy depend on the quality of the training data used to develop the AI algorithms, as well as the complexity and heterogeneity of the tumors being segmented.

Currently, AI-based segmentation tools are often used as a tool to support human interpretation and decision-making, rather than as a replacement for human expertise. It is important to validate the results

of AI-based segmentation tools against established clinical criteria and to assess their performance in a robust and systematic manner.

In conclusion, AI-based segmentation tools have the potential to be a valuable tool in radiation therapy planning, but they should be used in conjunction with human expertise and with appropriate validation to ensure the reliability and accuracy of the results.

Commentary, Dr. Buvat: This answer is again quite impressive; there is little a human expert could add. The key challenges are described (i.e., heterogeneity of the tissue, need for sufficient training sets, etc.).

Q6, Dr. Buvat: *Which such tool would you recommend?*

ChatGPT: As a language model developed by OpenAI, I don't have personal opinions or biases, and I do not endorse any specific product or brand. The choice of an AI-based segmentation tool for head and neck tumor segmentation from PET/CT scans depends on several factors, including the clinical and technical requirements of the specific case, the available resources, and the preferences and experience of the clinician.

When selecting an AI-based segmentation tool, it is important to consider the following factors:

- Validation and reliability: The tool should have been validated against established clinical criteria and should have a demonstrated track record of reliability and accuracy.
- User-friendliness: The tool should be easy to use and should provide results in a timely and efficient manner.
- Technical support and customer service: The vendor should provide robust technical support and customer service to assist with any questions or problems that may arise during use.
- Integration with other software and systems: The tool should be compatible with the other software and systems used in the clinical environment, such as the radiation therapy planning system, and should provide seamless integration.

Ultimately, the choice of an AI-based segmentation tool should be based on a thorough evaluation of the specific requirements and resources of the clinical environment, and should be made in consultation with relevant experts and stakeholders.

Commentary, Dr. Weber: A very useful answer that avoids giving a concrete recommendation. All the factors ChatGPT lists are relevant when deciding which computer system to purchase. It would be difficult for a human expert to list all these items as quickly as ChatGPT did. This illustrates how ChatGPT can be helpful for collecting relevant information before making a purchase decision.

Q7, Dr. Buvat: *Do you think it is the right time to build a theranostic center for molecular radiation therapy?*

ChatGPT: The development of a theranostic center for molecular radiation therapy is a complex and multi-disciplinary effort that requires significant resources and expertise. Whether it is the "right time" to build such a center depends on several factors, including the local demand for advanced cancer treatment options, the availability of expertise and resources, and the regulatory and reimbursement landscape.

In general, the field of molecular radiation therapy is rapidly evolving and has shown significant promise in improving the outcomes of cancer treatment. There is increasing demand for these advanced treatment options, particularly among patients with complex or advanced-stage cancers.

However, the development of a theranostic center is a significant investment and requires a commitment to long-term sustainability, as well as a comprehensive understanding of the regulatory, reimbursement, and economic factors that impact the delivery of these treatments.

In conclusion, the "right time" to build a theranostic center for molecular radiation therapy will depend on the specific circumstances and resources of the local environment. It is important to carefully assess the feasibility and sustainability of such a project, and to consult with relevant experts and stakeholders before proceeding.

Commentary, Dr. Weber: ChatGPT does very well with this timely question. It describes the potential of a theranostic center but also mentions the important regulatory and economic hurdles that physicians will face when setting up such centers. A human expert might have added that the current interest in theranostics almost exclusively stems from 2 diseases: neuroendocrine tumors (NETs) and prostate cancer. Alternative therapies for prostate cancer or NETs that are more effective, have less side effects, or are less expensive could significantly lessen the clinical relevance of theranostics. It is also largely unclear how quickly theranostic targets for other diseases can be identified that would broaden the spectrum of a theranostic center and decrease its dependence on only 2 therapeutic targets.

Summary commentary, Drs. Buvat and Weber: Overall, these chats illustrate the strengths and weaknesses of current bots. They can certainly help in time-consuming tasks, such as writing medical reports (Q1) or creating cover letters when submitting articles or simplified summaries for the public based on scientific abstracts. They can answer specific technical questions well and be used for educational purposes (Q2), but answers should always be verified, because they can look authoritative but be wrong (Q3: the definition of SUV_{peak} is approximate and the definition of SUV_{max} is not quite correct). ChatGPT has learned from data collected through 2021 and is clearly not aware of the latest advances in our field (Q4, fibroblast-activation protein is missing from the list) and does not fully understand the question (Q4: FDG is not a promising radiotracer). The bot is very cautious about giving recommendations (Q5) and does not promote a solution (Q6), as a colleague might do. It offers a synthetic view on current issues in only a few seconds (Q7) and avoids taking a firm position (Q3, Q7). Thanks to fierce competition among the GAFAM (Google, Apple, Facebook, Amazon, Microsoft), chatbots will evolve very quickly and will become more and more reliable as personal assistants. Thanks to continuous learning techniques, they will expand their knowledge and improve the accuracy of their answers. They should not be feared but rather considered promising allies who will help us cope with ever-increasing workloads, freeing up time to devote to patients and colleagues and to expend more energy on tasks that require unique and advanced expertise. A final note: ChatGPT is often quite busy and not always available. Sound familiar?

Functional Imaging of Chemobrain: Usefulness of Nuclear Medicine in the Fog Coming After Cancer

Agostino Chiaravalloti*^{1,2}, Luca Filippi*³, Marco Pagani^{†4,5}, and Orazio Schillaci^{†1}

¹Department of Biomedicine and Prevention, University of Rome Tor Vergata, Rome, Italy; ²IRCCS Neuromed, Pozzilli, Italy;

³Nuclear Medicine Section, Santa Maria Goretti Hospital, Latina, Italy; ⁴Institute of Cognitive Sciences and Technologies, Consiglio Nazionale Delle Ricerche, Rome, Italy; and ⁵Department of Medical Radiation Physics and Nuclear Medicine, Karolinska Hospital, Stockholm, Sweden

The impact of chemotherapy on brain functionality has been widely investigated from a clinical perspective, and there is a consensus on a significant impairment of multiple cognitive domains affecting cancer patients after treatment. Nuclear medicine offers a variety of biomarkers for evaluating possible effects of chemotherapy on the brain and for depicting brain changes after chemotherapy. This review summarizes the most relevant findings on brain imaging in patients undergoing chemotherapy for the most common oncologic diseases. The literature published to date offers exciting results on several radiolabeled compounds, from the more common imaging of glucose metabolism to neuroinflammation. This review also provides a general overview of the literature concerning clinical features and the physiopathologic basis of chemotherapy-related cognitive impairment.

Key Words: chemobrain; functional imaging; PET; FDG; DAT; neuroinflammation

J Nucl Med 2023; 64:508–514

DOI: 10.2967/jnumed.121.263294

Chemotherapy is associated with debilitating side effects that affect quality of life (1,2). The term *chemotherapy-related cognitive impairment* (CRCI) describes a clinical condition characterized by memory and concentration impairment, difficulties in information processing and executive functions, and mood and anxiety disorders (3,4), with a highly variable prevalence estimated to range from 17% to 75% (5). There is evidence that chemotherapy drugs such as cisplatin, carboplatin, paclitaxel, cyclophosphamide, vincristine, and lenalidomide are neurotoxic (6): at a molecular level, cytokine dysregulation and oxygen radical production are suspected to be responsible for CRCI (7). Despite several studies on CRCI, there is no consensus on whether specific brain areas are implicated (8). In recent years, molecular neuroimaging techniques have revealed interesting aspects of the underlying mechanisms of CRCI. This review highlights the contribution of neuroimaging to this field, underlining findings and information from the most important studies.

Received May 14, 2022; revision accepted Jan. 26, 2023.
For correspondence or reprints, contact Agostino Chiaravalloti (agostino.chiaravalloti@uniroma2.it).

*Contributed equally to this work.

†Contributed equally to this work.

Published online Feb. 2, 2023.

COPYRIGHT © 2023 by the Society of Nuclear Medicine and Molecular Imaging.

CLINICAL FEATURES OF CRCI

Recognition of an association between cancer-related treatment and cognitive changes in long-term survivors is not something new, with the first reports on this topic dating to the 1980s and 1990s (9). CRCI may have a wide spectrum of symptoms, ranging from problems with attention, concentration, and working memory to problems with executive function (Table 1) (10).

According to longitudinal neuropsychological studies, up to 35% of patients are affected by cognitive impairment months or years after completion of oncologic therapy (11). However, CRCI can affect distinct populations of cancer patients differently according to the differences in tumor histology, biologic behavior, location, and growth rate (12).

There is no consensus on the preferred tools for diagnosing and measuring cognitive impairment in cancer patients who have undergone chemotherapy. However, according to the existing literature, the 2 main methods of assessment in addition to neuroimaging are neuropsychological testing and self-reports of cognitive impairment. Regarding the former method, a wide range of neuropsychological batteries has been recommended (i.e., the Hopkins Verbal Learning Test, Revised; the Trail Making Test; the testing recommendations of the International Cognition and Cancer Task Force; and the Controlled Oral Word Association [part of the Multilingual Aphasia Examination]). The latter method is based mainly on a patient's subjective perception as measured through tools such as the European Organization for Research and Treatment of Cancer core quality-of-life questionnaire (QLQ-C30) or the Functional Assessment of Cancer Therapy–Cognitive Function Questionnaire.

CRCI PHYSIOPATHOLOGIC BASIS

Cognitive impairment may affect up to 50% of patients undergoing chemotherapy (13). Chemotherapy may lead to encephalopathy with highly complex and heterogeneous molecular mechanisms. The damage induced by chemotherapy affects neurons and microglia. Drug-induced damage to neurons elicits a cascade of events culminating in activation of microglia and astrocytes and disruption of the normal homeostatic relationship between myelinating cells (oligodendrocytes) and oligodendrocyte precursor cells (13). In addition, there is an increase of proinflammatory cytokines that, together with activation of astrocytes, promotes the release of paracrine factors, significantly hampering the maturation of oligodendrocytes (13). Direct involvement of chemotherapy in the release of cytokines needs to be further investigated. Instead of a local increase, it is more probable that circulating cytokines induced by chemotherapy penetrate the blood–brain barrier to directly act on the central nervous system,

TABLE 1
Cognitive Domains and Abilities More Commonly Involved in CRCI

Domain or ability	Description
Memory	
Working	Transient storage and elaboration of information
Episodic	Mental reexperience of context-dependent events
Remote	Retrieval of events from past
Executive function	Mental skills (e.g., flexible thinking and self-control) to learn, work, and manage self
Processing speed	Efficiency and speed in elaborating information to finalize specific task
Attention	Capacity to focus on certain topic by leaving out coexisting data and stimuli
Reaction time	Time needed to react to certain stimulus
Motor speed	Precision and speed with which simple motor task can be completed

activating microglia and astrocytes to secrete further cytokines (14). Chemotherapy may affect brain tissue by modifying the shape of neurons, neurotransmitter release, and blood–brain barrier integrity (1) and may slow neurotransmitter uptake and release into neurons (15–17). These findings may partially explain some of the clinical features of CRCI, particularly those related to alteration in emotion, learning, and memory.

SEARCH STRATEGY

Two separate literature searches of the PubMed/Medline databases were performed according to the PRISMA guidelines (Preferred Reporting Items for Systematic Reviews and Metaanalyses). The first assessed the effects of the most commonly used chemotherapeutic drugs on cognitive function, and the second assessed the results of available SPECT and PET examinations of the field of interest.

For search 1, the terms used were a combination of the most commonly used chemotherapeutic agents (i.e., cisplatin, carboplatin, oxaliplatin, cyclophosphamide, methotrexate, fluorouracil, doxorubicin, etoposide, irinotecan, taxanes) AND “chemotherapy-related cognitive impairment” OR “chemobrain.” The following types of studies were considered: head-to-head comparative series, matched-pair studies, clinical trials, case series, prospective studies, and retrospective cohorts. Case reports, conference proceedings, editorial commentaries, interesting images, and letters to the editor were excluded. We selected only studies published from 2012 to June 2022, limited to humans and in the English language, with a cohort of at least 20 enrolled patients (Supplemental Fig. 1; supplemental materials are available at <http://jnm.snmjournals.org>).

NOTEWORTHY

- Brain ¹⁸F-FDG PET imaging shows a reduction of glucose metabolism in CRCI.
- Chemotherapy may affect DAT receptor expression in the brain.
- Imaging of TSPO is a promising tool for the investigation of CRCI.

For search 2, we used a combination of the following terms: “PET” OR “PET/CT” OR “single photon emission tomography” OR “SPECT” OR “translocator protein” OR “dopamine transporter imaging” AND “chemotherapy-related cognitive impairment.” Studies were selected in the same way as for search 1; nevertheless, because of a shortage of published studies on this topic, we decided not to apply any temporal filter and to include studies with at least 10 patients (Supplemental Fig. 2).

Two reviewers conducted the literature search and independently appraised each study using a standard protocol and data extraction. The reference lists of the selected studies were carefully checked to identify any additional relevant literature.

For search 1 (chemotherapeutic agents and CRCI), the extracted data were type of study (e.g., prospective or retrospective), year and location of study, sample size, tumor, type of chemotherapy, and timing of CRCI assessment with regard to chemotherapy completion. For search 2 (PET and SPECT imaging), the extracted data were type (e.g., prospective or retrospective), year and location of the study, sample size, radiopharmaceuticals, device (SPECT or PET only or hybrid devices), modality of image assessment (qualitative or quantitative), type of chemotherapeutic agent, and the eventually performed neuropsychological tests.

Studies with incomplete technical or clinical data were considered ineligible. If studies were by the same group of researchers, only the study with the highest number of enrolled patients was considered. We resolved any discrepancy by discussion. As this was not a metaanalysis, no statistical analysis was performed.

RESULTS

In total, 142 nonduplicate studies were retrieved from the database for search 1 and 30 for search 2. After removal of duplicate records and screening based on title and abstract, the remaining studies underwent full-text eligibility assessment, which identified 22 relevant studies (search 1, *n* = 14; search 2, *n* = 8). The main findings of the selected studies for searches 1 and 2 are summarized in Supplemental Table 1 and Table 2, respectively.

Chemotherapeutic Agents and CRCI

Fourteen studies, encompassing 2,390 patients, on the effects of various chemotherapeutic agents on cognitive function were selected (18–31). Great heterogeneity in study design was registered, since only 4 of the 14 studies (28.5%) were prospective and 1 (7.1%) was a randomized trial, whereas the remaining 9 (71.4%) were retrospective observational studies. Great variability in timing and modality of CRCI assessment was also noted. Additionally, the time point of CRCI assessment meaningfully varied among selected studies, ranging from interim assessment during chemotherapy cycles to 20 y after therapy completion.

The majority of the selected studies were on breast cancer (53.3%), most probably because of the relevant advances in prevention, diagnosis, and therapy in this field and the relatively good prognosis of this type of cancer in comparison to other types, with 80% of women with primary breast cancer surviving for at least 10 y after mastectomy or breast-conserving surgery (32).

In 5 cases (35.7%), taxanes were used alone or in combination with other chemotherapeutic agents, whereas in 4 cases (28.5%), patients underwent platin-based therapies. Except for 1 study that analyzed the potential impact of treatment with rituximab, cyclophosphamide, hydroxydaunomycin, vincristine sulfate, and

TABLE 2
Studies on PET and SPECT in CRCI

Study	Year	Location	Study design	Cancer type	Chemotherapeutic drugs	Sample	Radiopharmaceutical	Imaging target	Device	Image assessment	Neuropsychiatric assessment	Comments
Véra et al. (42)	1999	France	Prospective	Acute myeloid/lymphoid leukemia	Cytarabine	12	^{99m} Tc-HMPAO	Cerebral blood flow	SPECT	Qual	Performed at baseline	^{99m} Tc-HMPAO SPECT detection of cerebral blood flow abnormalities associated with chemotherapy toxicity
Sorokin et al. (36)	2014	United States	Retrospective	Hodgkin disease	ABVD scheme	21	¹⁸ F-FDG	Metabolism	PET/CT	Qual + quant (VOI analysis)	NP	Reduced metabolism in whole gray matter
Ponto et al. (37)	2015	United States	Retrospective	Breast	Cyclophosphamide, methotrexate, and 5-fluorouracil or anthracycline	10	¹⁸ F-FDG	Metabolism	PET/CT	Qual + quant (VOI analysis)	NP	Reduced metabolism bilaterally in orbital frontal regions as compared with healthy subjects
Chiaravalloti et al. (40)	2015	Italy	Prospective	Hodgkin disease	ABVD scheme	74	¹⁸ F-FDG	Metabolism	PET/CT	Qual + quant (SPM)	NP	Significantly higher metabolic activity after first cycles in right angular gyrus; metabolic reduction in Brodmann areas 10, 11, and 32 bilaterally
Shrot et al. (52)	2019	Israel	Observational	Non-Hodgkin lymphoma	LMB-group B, Euro-LB-02, or ALCL-99 scheme	14	¹⁸ F-FDG	Metabolism	PET/CT	Qual + quant (ROI analysis)	NP	Reduced metabolism in deep gray matter nuclei and in brain stem
Tauty et al. (41)	2019	France	Retrospective	Hodgkin disease	ABVD or BEACOPP scheme	20	¹⁸ F-FDG	Metabolism	PET/CT	Qual + quant (SPM)	NP	Reduced metabolism in frontal, cingulate, and temporoinsular regions after 2 cycles, with less extent than in adults
Vitor et al. (35)	2019	Brazil	Prospective	Breast	Doxorubicin, cyclophosphamide	28	^{99m} Tc-TRODAT	DAT	SPECT	Qual + quant (DaTQUANT)	FACT-Cog Mini Mental	Cognitive impairment associated with reduced DAT density in striatum
Schroyen et al. (39)	2021	Belgium	Prospective	Breast	Epirubicin, cyclophosphamide, paclitaxel	19	¹⁸ F-DPA714	TSPO	PET/CT	Qual + quant (VOI analysis)	Questionnaires to derive cognitive failure score	PET-detected neuroinflammation in parietal and occipital brain in chemotherapy patients

HMPAO = ^{99m}Tc-hexamethyl-propylene-amine oxime; qual = qualitative; ABVD = doxorubicin, bleomycin, vinblastine, and dacarbazine; quant = quantitative; VOI = volume of interest; NP = not performed; SPM = statistical parametric map; ROI = region of interest; BEACOPP = bleomycin, etoposide, doxorubicin, cyclophosphamide, vincristine, procarbazine, and prednisone; TRODAT = 2-[2-[[[(1R,2R,3S,5S)-3-(4-chlorophenyl)-8-methyl-8-azabicyclo[3.2.1]octan-2-yl]methyl-(2-sulphidoethyl)amino]ethylazaniidyl]ethanethiolate; oxygen(2-); technetium(5+); FACT-Cog = Functional Assessment of Cancer Therapy-Cognitive Function.

prednisone on cognitive function (21), none of the analyzed studies was on recently implemented immunotherapeutic regimens, either those in which monoclonal antibodies targeted tumor-associated biomarkers or those aimed at removing negative immune regulation (33).

All but 1 selected study reported a decline in cognitive function after chemotherapy: in particular, 4 studies (28.5%) (20,23,26,27,29,31,34) reported a more relevant impairment of executive functions, 3 studies (21.4%) (27) documented self-reported or self-perceived cognitive impairment or mood changes (anxiety, trouble sleeping), and 1 study (7.1%) (24) reported reduced social attainment and poor quality of life in cancer survivors (Supplemental Fig. 3).

PET and SPECT Imaging of CRCI

We selected 8 studies concerning the application of SPECT or PET in CRCI and including 198 patients overall. Only 3 tumor types were evaluated: lymphoma (4 studies, 50%), breast cancer (3 studies, 37.5%), and acute myeloid/lymphoid leukemia (1 study, 12.5%); SPECT was used in 2 studies (24,35), whereas PET/CT was used in the remaining 6 studies. As expected because of its availability and its capacity to give accurate insight into brain metabolism, ¹⁸F-FDG was the most commonly used radiopharmaceutical (6 studies, 75%). A meaningful heterogeneity in PET evaluation was noted since authors used, aside from qualitative evaluation, quantitative analysis by volume of interest in 4 studies (36–39) and a statistical parametric map in 2 studies (40,41). As regards SPECT studies, one used visual image evaluation (42) and another used quantitative analysis of dopamine transporter (DAT) density (35).

Finally, only a minority (3 studies, 37.5%) (35,39,42) reported a correlation between imaging findings and neuropsychological assessment. Selected studies focusing on PET or SPECT imaging are discussed here.

SPECT Tracers for CRCI Imaging

Cerebral Blood Flow Measurement. Chemotherapy-induced microvascular damage in the brain is thought to be a causative factor of CRCI (43). SPECT with ^{99m}Tc-hexamethyl-propylene-amine oxime has been used to assess changes in cerebral blood flow (44), despite its well-known limitations in terms of spatial resolution and quantitation accuracy.

In a cohort of 12 pediatric patients, treated with high-dose cytarabine for acute myeloid leukemia ($n = 11$) or acute lymphoid leukemia ($n = 1$), Véra et al. investigated changes in cerebral blood flow through ^{99m}Tc-hexamethyl-propylene-amine oxime SPECT after the induction phase, immediately after the first intensification, and during follow-up (42). SPECT results were correlated with neuropsychological assessment and serial brain MRI. At the induction phase, brain SPECT was performed in 8 patients, with slightly heterogeneous findings in 4 and normal findings in the remaining 4, whereas in all 8 examined patients brain MRI findings were normal. At the high-dose consolidation phase, 5 patients had chemotherapy-related neurotoxicity: in such cases, MRI findings were normal in 4 of 5 patients, whereas SPECT findings were diffusely heterogeneous in 4 of 5 patients and slightly heterogeneous in 1 patient. Follow-up was available for 4 patients with neurotoxicity ($n = 5$); all regressed over time. One patient had particularly prolonged (60 mo) neurologic symptoms associated with persistent abnormalities on SPECT and brain MRI.

DAT Imaging. Molecular imaging of DATs through SPECT has been extensively applied in clinical practice to diagnose and monitor Parkinson disease and other extrapyramidal syndromes

(45,46). SPECT with ^{99m}Tc-TRODAT-1 (2-[2-[[[(1R,2R,3S,5S)-3-(4-chlorophenyl)-8-methyl-8-azabicyclo[3.2.1]octan-2-yl]methyl-(2-sulfinylethyl)amino]ethylazaniidyl]ethanethiolate; oxygen(2-); technetium(5+)) was performed by Vitor et al. to investigate DAT integrity in 28 women reporting cognitive impairment related to chemotherapy for breast cancer and in 22 healthy female controls matched for age and level of instruction (35). Calculation of tracer concentration in the striatum by dedicated software (DaTQUANT; GE Healthcare) showed significantly less striatal uptake (both at the analysis of the overall striatum and at the separate analysis of the caudate and putamen) in breast cancer patients experiencing CRCI than in healthy controls, indicating that toxic damage to the basal ganglia may be involved in the complex mechanisms leading to CRCI. Patients developing parkinsonism after chemotherapy are generally characterized by strong responsiveness to levodopa and tend to improve over time (Supplemental Fig. 4) (47).

¹⁸F-FDG PET Imaging in CRCI

When approaching PET imaging of the brain using ¹⁸F-FDG, one should consider that under normal conditions brain uses glucose as its sole source of energy (48), that hypometabolism may not correspond to areas with the greatest changes in routine neuropathology (49), that hypometabolism is not directly affected by intracellular or extracellular inclusions (50), and that glucose metabolism primarily reflects synaptic activity (51).

Few studies have investigated the potential role of ¹⁸F-FDG in patients with CRCI. One of the first was in 2015, on 49 patients with Hodgkin disease (40), who were evaluated at diagnosis and during treatment. Surprisingly, the authors reported a significantly higher metabolic activity after the first cycles in the right angular gyrus (Brodmann area 39) whereas a significant metabolic reduction was found in Brodmann areas 10, 11, and 32 bilaterally. All these changes disappeared at the end of the therapy course (40). The authors concluded that the results are consistent with a transient and limited impact of chemotherapy on brain metabolism in Hodgkin lymphoma. In agreement with the previous report (40), Shrot et al. found increased ¹⁸F-FDG uptake in the parietal and cingulate cortices in 14 pediatric patients diagnosed with lymphoma; decreased ¹⁸F-FDG uptake was found in deep gray matter nuclei and the brain stem (52). Tauty et al. and Goldfarb et al. found reduced metabolism bilaterally in the anterior cingulate cortex and left inferior frontal and insular cortex soon after 2 cycles of chemotherapy and hypometabolic areas in the left anterior cingulate cortex, in the left inferior frontal and insular cortex, and finally in the left temporal lobe after 6 cycles (53,54). A reduction of glucose metabolism was found in the frontal, cingulate, and temporoinsular regions after 2 cycles of chemotherapy (53). The differences from other studies cited previously may be partially explained by differences in the chemotherapy agents used. In non-Hodgkin lymphoma, a general reduction of around 20% in overall cerebral cortical metabolism was found after chemotherapy (36). These findings suggest a diffuse and severe impairment of brain functionality after chemotherapy in these patients (36). In a population of 10 patients with breast cancer, Ponto et al. found reduced metabolism bilaterally in orbital frontal regions as compared with healthy subjects (37). Interestingly, this finding is consistent with cognition and executive function impairment found by neuropsychological assessment (37).

PET with Tracers Other Than ¹⁸F-FDG: Translocator Protein (TSPO) Ligands for CRCI Imaging

In recent years, TSPO, an 18-kDa protein expressed mainly on the outer mitochondrial membrane of several cells of the central nervous system (microglia, astrocytes, and endothelial cells), has emerged as a target for molecular imaging of neuroinflammation, since its expression is minimal in the healthy brain but strong when microglia are activated in response to injury (55). The development of positron-emitting ligands selectively binding to TSPO has allowed in vivo assessment of neuroinflammation through PET/CT or PET/MRI technology (56,57). Notably, binding of second-generation tracers to TSPO is strongly influenced by a single polymorphism (rs6971) in exon 4 of the TSPO gene (58), according to which patients can be stratified into 3 categories: high-, mixed-, and low-affinity binders.

Schroyen et al. have recently investigated the potential of TSPO PET for in vivo imaging of neuroinflammation in breast cancer patients undergoing chemotherapy, also through correlation of PET findings, neuropsychological tests, and inflammatory markers (59). The authors prospectively enrolled patients distributed into 3 different cohorts: breast cancer patients undergoing chemotherapy, breast cancer patients not scheduled for chemotherapy, and a control group of healthy women. The chemotherapy cohort exhibited higher ¹⁸F-DPA714 (*N,N*-diethyl-2-[4-(2-fluoroethoxy)phenyl]-5,7-dimethylpyrazolo[1,5-*a*]pyrimidine-3-acetamide) uptake in the occipital and parietal lobes than did chemotherapy-naïve and healthy controls. Furthermore, patients undergoing chemotherapy showed altered neuropsychological test scores and increased inflammatory markers compared with the other 2 cohorts. Among inflammatory biomarkers, neurofilament light-chain protein, an axonal damage indicator, was particularly increased in chemotherapy patients and strongly correlated with TSPO PET findings. Despite ¹⁸F-DPA714 incorporation, patients undergoing chemotherapy did not show relevant alterations of micro- or macrostructure in white matter on MRI, as determined through pixel-based analysis of diffusion-weighted images.

CONCLUSIONS AND FUTURE OUTLOOK

Nuclear medicine techniques are not commonly considered in the work-up of patients with CRCI-related manifestations, despite their high potential to investigate different physiopathologic phenomena (i.e., cortical metabolism, DAT integrity, and neuroinflammation) through specific imaging probes (60). From careful analysis of the selected studies, some observations can be made on the role of functional neuroimaging in CRCI.

First, few studies have explored the usefulness of ¹⁸F-FDG PET/CT for imaging of CRCI, and even fewer studies have used statistical parametric mapping to assess changes in cortical metabolism before and after chemotherapy. We therefore suggest to implement statistical parametric mapping in future clinical trials on the use of ¹⁸F-FDG for CRCI imaging. This parametric analysis entails voxel-level statistical parametric mapping at the whole-brain level, comparing each patient with a reference group using a 2-sample *t* test, thus generating a contrast *t*-map for areas of relative hypometabolism in the study group compared with the controls (61). In this respect, technologic innovations may be of great value to further improve the imaging approach to CRCI: hybrid PET/MRI, as an example, is a still-underexplored tool for correlating eventual changes in T1- or T2-weighted images with metabolic abnormalities detected by ¹⁸F-FDG. In addition, the emergence of

artificial intelligence and radiomics may find interesting applications to extract potentially useful data, undetectable by visual evaluation, from ¹⁸F-FDG PET image texture analysis (62). PET tracers other than ¹⁸F-FDG, such as TSPO ligands, can provide an interesting opportunity to investigate in vivo, at a molecular level, the inflammatory landscape associated with CRCI, but their widespread use is still hampered by high cost, a lack of authorized compounds, and the dependence of image quality on genetic polymorphism.

Another issue is when and how to assess CRCI after therapy completion. An objective determination of chemotherapy effects on cognitive abilities is hampered by the multifaceted nature of CRCI, since underlying depression or anxiety disorders can also be responsible for some symptoms and are often classified as CRCI. The concept of cancer-related posttraumatic stress disorder, a complex set of symptoms affecting patients' psychosocial and physical well-being during cancer treatment and into survivorship (63), has been gaining ground and should be considered in future clinical trials aimed at applying functional imaging to CRCI investigation.

The impact of chemotherapy on brain has been assessed by a few imaging studies. Moreover, the methodology used in the studies, the most relevant of which are cited in this review, is characterized by a huge heterogeneity in imaging modalities, clinical evaluations, chemotherapies, and types of tumor. Moreover, there is a lack of longitudinal studies to investigate the possible reversible effect of neuronal impairment induced by chemotherapy.

Nuclear medicine offers several instruments for the detailed evaluation of physiopathologic processes underlying CRCI. The research performed for this review indicates that the major constraint on discoveries will be due not to the available techniques of functional imaging, which are constantly improving, but rather to the precision of our hypotheses and the creativity of our methods for testing them. In particular, longitudinal and standardized studies are needed to investigate the impact of each chemotherapy drug on the brain (considering, in particular, the same dose) or combinations of these drugs. Moreover, correlation with a standardized neuropsychological assessment is mandatory to exclude the possible contribution of stress and emotions, especially for functional studies.

DISCLOSURE

No potential conflict of interest relevant to this article was reported.

REFERENCES

1. Nguyen LD, Ehrlich BE. DISCLOSURE No potential conflict of interest relevant to this article was reported. *EMBO Mol Med*. 2020;12:e12075.
2. El-Agamy SE, Abdel-Aziz AK, Esmat A, Azab SS. Chemotherapy and cognition: comprehensive review on doxorubicin-induced chemobrain. *Cancer Chemother Pharmacol*. 2019;84:1–14.
3. Walczak P, Janowski M. Chemobrain as a product of growing success in chemotherapy: focus on glia as both a victim and a cure. *Neuropsychiatry (London)*. 2019;9:2207–2216.
4. Bou Khalil R. “Emotional chemobrain”: a new concept for chemotherapy adverse drug effect? *Encephale*. 2021;47:613–615.
5. Correa DD, Ahles TA. Cognitive adverse effects of chemotherapy in breast cancer patients. *Curr Opin Support Palliat Care*. 2007;1:57–62.
6. Markman M, Kennedy A, Webster K, Kulp B, Peterson G, Belinson J. Neurotoxicity associated with a regimen of carboplatin (AUC 5-6) and paclitaxel (175 mg/m² over 3 h) employed in the treatment of gynecologic malignancies. *J Cancer Res Clin Oncol*. 2001;127:55–58.

7. Gregg RW, Molepo JM, Monpetit VJ, et al. Cisplatin neurotoxicity: the relationship between dosage, time, and platinum concentration in neurologic tissues, and morphologic evidence of toxicity. *J Clin Oncol.* 1992;10:795–803.
8. Bernstein LJ, Edelstein K, Sharma A, Alain C. Chemo-brain: an activation likelihood estimation meta-analysis of functional magnetic resonance imaging studies. *Neurosci Biobehav Rev.* 2021;130:314–325.
9. Oxman TE, Silberfarb PM. Serial cognitive testing in cancer patients receiving chemotherapy. *Am J Psychiatry.* 1980;137:1263–1265.
10. Ahles TA, Saykin AJ. Candidate mechanisms for chemotherapy-induced cognitive changes. *Nat Rev Cancer.* 2007;7:192–201.
11. Janelins MC, Kohli S, Mohile SG, Usuki K, Ahles TA, Morrow GR. An update on cancer- and chemotherapy-related cognitive dysfunction: current status. *Semin Oncol.* 2011;38:431–438.
12. Gehring K, Aaronson NK, Taphoorn MJ, Sitskoorn MM. Interventions for cognitive deficits in patients with a brain tumor: an update. *Expert Rev Anticancer Ther.* 2010;10:1779–1795.
13. Dietrich J, Han R, Yang Y, Mayer-Pröschel M, Noble M. CNS progenitor cells and oligodendrocytes are targets of chemotherapeutic agents in vitro and in vivo. *J Biol.* 2006;5:22.
14. Seigers R, Timmermans J, van der Horn HJ, et al. Methotrexate reduces hippocampal blood vessel density and activates microglia in rats but does not elevate central cytokine release. *Behav Brain Res.* 2010;207:265–272.
15. Jarmolowicz DP, Gehringer R, Lemley SM, Sofis MJ, Kaplan S, Johnson MA. 5-fluorouracil impairs attention and dopamine release in rats. *Behav Brain Res.* 2019;362:319–322.
16. Kaplan SV, Limbocker RA, Gehringer RC, et al. Impaired brain dopamine and serotonin release and uptake in Wistar rats following treatment with carboplatin. *ACS Chem Neurosci.* 2016;7:689–699.
17. Thomas TC, Beitchman JA, Pomerleau F, et al. Acute treatment with doxorubicin affects glutamate neurotransmission in the mouse frontal cortex and hippocampus. *Brain Res.* 2017;1672:10–17.
18. Amidi A, Hosseini SMH, Leemans A, et al. Changes in brain structural networks and cognitive functions in testicular cancer patients receiving cisplatin-based chemotherapy. *J Natl Cancer Inst.* 2017;109(12).
19. Andreis F, Ferri M, Mazzocchi M, et al. Lack of a chemobrain effect for adjuvant FOLFOX chemotherapy in colon cancer patients. A pilot study. *Support Care Cancer.* 2013;21:583–590.
20. Cerulla N, Arcusa A, Navarro JB, et al. Role of taxanes in chemotherapy-related cognitive impairment: a prospective longitudinal study. *Breast Cancer Res Treat.* 2017;164:179–187.
21. Khan MA, Garg K, Bhurani D, Agarwal NB. Early manifestation of mild cognitive impairment in B-cell non-Hodgkin's lymphoma patients receiving CHOP and rituximab-CHOP chemotherapy. *Naunyn-Schmiedeberg's Arch Pharmacol.* 2016;389:1253–1265.
22. Lange M, Heutte N, Rigal O, et al. Decline in cognitive function in older adults with early-stage breast cancer after adjuvant treatment. *Oncologist.* 2016;21:1337–1348.
23. Miao H, Li J, Hu S, et al. Long-term cognitive impairment of breast cancer patients after chemotherapy: a functional MRI study. *Eur J Radiol.* 2016;85:1053–1057.
24. Ehrhardt MJ, Mulrooney DA, Li C, et al. Neurocognitive, psychosocial, and quality-of-life outcomes in adult survivors of childhood non-Hodgkin lymphoma. *Cancer.* 2018;124:417–425.
25. Sales MVC, Suemoto CK, Apolinario D, et al. Effects of adjuvant chemotherapy on cognitive function of patients with early-stage colorectal cancer. *Clin Colorectal Cancer.* 2019;18:19–27.
26. Beesley VL, Ross TL, King MT, et al. Evaluating patient-reported symptoms and late adverse effects following completion of first-line chemotherapy for ovarian cancer using the MOST (Measure of Ovarian Symptoms and Treatment concerns). *Gynecol Oncol.* 2022;164:437–445.
27. Durán-Gómez N, López-Jurado CF, Nadal-Delgado M, Pérez-Civantos D, Guerrero-Martín J, Cáceres MC. Chemotherapy-related cognitive impairment in patients with breast cancer based on functional assessment and NIRS analysis. *J Clin Med.* 2022;11:2363.
28. Keetile NM, Osuch E, Lento AG. Chemotherapy-related subjective cognitive impairment in breast cancer patients in semi-rural South Africa. *Health SA.* 2021;26:1605.
29. Phillips NS, Kesler SR, Scoggins MA, et al. Connectivity of the cerebello-thalamo-cortical pathway in survivors of childhood leukemia treated with chemotherapy only. *JAMA Netw Open.* 2020;3:e2025839.
30. van der Willik KD, Koppelmans V, Hauptmann M, Compter A, Ikram MA, Schaagen SB. Inflammation markers and cognitive performance in breast cancer survivors 20 years after completion of chemotherapy: a cohort study. *Breast Cancer Res.* 2018;20:135.
31. Wagner LI, Gray RJ, Sparano JA, et al. Patient-reported cognitive impairment among women with early breast cancer randomly assigned to endocrine therapy alone versus chemoendocrine therapy: results from TAILORx. *J Clin Oncol.* 2020;38:1875–1886.
32. Kontani K, Hashimoto S, Murazawa C, et al. Factors responsible for long-term survival in metastatic breast cancer. *World J Surg Oncol.* 2014;12:344.
33. Esfahani K, Roudaia L, Buhlaiga N, Del Rincon SV, Papneja N, Miller WH Jr. A review of cancer immunotherapy: from the past, to the present, to the future. *Curr Oncol.* 2020;27(suppl 2):S87–S97.
34. Cerulla N, Arcusa A, Navarro JB, et al. Cognitive impairment following chemotherapy for breast cancer: the impact of practice effect on results. *J Clin Exp Neuropsychol.* 2019;41:290–299.
35. Vitor T, Kozasa EH, Bressan RA, et al. Impaired brain dopamine transporter in chemobrain patients submitted to brain SPECT imaging using the technetium-99m labeled tracer TRODAT-1. *Ann Nucl Med.* 2019;33:269–279.
36. Sorokin J, Saboury B, Ahn JA, Moghbel M, Basu S, Alavi A. Adverse functional effects of chemotherapy on whole-brain metabolism: a PET/CT quantitative analysis of FDG metabolic pattern of the “chemo-brain.” *Clin Nucl Med.* 2014;39:e35–e39.
37. Ponto LL, Menda Y, Magnotta VA, Yamada TH, Denburg NL, Schultz SK. Frontal hypometabolism in elderly breast cancer survivors determined by [¹⁸F]fluorodeoxyglucose (FDG) positron emission tomography (PET): a pilot study. *Int J Geriatr Psychiatry.* 2015;30:587–594.
38. Ulitzur S, Kuhn J. The transcription of bacterial luminescence is regulated by sigma 32. *J Biolumin Chemilumin.* 1988;2:81–93.
39. Schroyen G, Blommaert J, van Weehaeghe D, et al. Neuroinflammation and its association with cognition, neuronal markers and peripheral inflammation after chemotherapy for breast cancer. *Cancers (Basel).* 2021;13:4198.
40. Chiaravalloti A, Pagani M, Cantonetti M, et al. Brain metabolic changes in Hodgkin disease patients following diagnosis and during the disease course: An ¹⁸F-FDG PET/CT study. *Oncol Lett.* 2015;9:685–690.
41. Tauty A, Noblet V, Paillard C, Fornecker LM, Namer IJ, Bund C. Evaluation of the effects of chemotherapy on brain glucose metabolism in children with Hodgkin's lymphoma. *Ann Nucl Med.* 2019;33:564–569.
42. Véra P, Rohrllich P, Stiévenart JL, et al. Contribution of single-photon emission computed tomography in the diagnosis and follow-up of CNS toxicity of a cytarabine-containing regimen in pediatric leukemia. *J Clin Oncol.* 1999;17:2804–2810.
43. Carlson BW, Craft MA, Carlson JR, Razaq W, Deardeuff KK, Benbrook DM. Accelerated vascular aging and persistent cognitive impairment in older female breast cancer survivors. *Geroscience.* 2018;40:325–336.
44. Prosser AMJ, Tossici-Bolt L, Kipps CM. The impact of regional ^{99m}Tc-HMPAO single-photon-emission computed tomography (SPECT) imaging on clinician diagnostic confidence in a mixed cognitive impairment sample. *Clin Radiol.* 2020;75:714.e7–714.e14.
45. Booi J, Tissingh G, Boer GJ, et al. [¹²³I]FP-CIT SPECT shows a pronounced decline of striatal dopamine transporter labelling in early and advanced Parkinson's disease. *J Neurol Neurosurg Psychiatry.* 1997;62:133–140.
46. Filippi L, Manni C, Pierantozzi M, et al. ¹²³I-FP-CIT semi-quantitative SPECT detects preclinical bilateral dopaminergic deficit in early Parkinson's disease with unilateral symptoms. *Nucl Med Commun.* 2005;26:421–426.
47. Chuang C, Constantino A, Balmaceda C, Eidelberg D, Frucht SJ. Chemotherapy-induced parkinsonism responsive to levodopa: an underrecognized entity. *Mov Disord.* 2003;18:328–331.
48. Mergenthaler P, Lindauer U, Dienel GA, Meisel A. Sugar for the brain: the role of glucose in physiological and pathological brain function. *Trends Neurosci.* 2013;36:587–597.
49. Grothe MJ, Teipel SJ; Alzheimer's Disease Neuroimaging Initiative. Spatial patterns of atrophy, hypometabolism, and amyloid deposition in Alzheimer's disease correspond to dissociable functional brain networks. *Hum Brain Mapp.* 2016;37:35–53.
50. Tönnies E, Trushina E. Oxidative stress, synaptic dysfunction, and Alzheimer's disease. *J Alzheimers Dis.* 2017;57:1105–1121.
51. Jueptner M, Weiller C. Review: does measurement of regional cerebral blood flow reflect synaptic activity? Implications for PET and fMRI. *Neuroimage.* 1995;2:148–156.
52. Shrot S, Abebe-Campino G, Toren A, Ben-Haim S, Hoffmann C, Davidson T. Fluorodeoxyglucose detected changes in brain metabolism after chemotherapy in pediatric non-Hodgkin lymphoma. *Pediatr Neurol.* 2019;92:37–42.
53. Tauty A, Noblet V, Paillard C, Fornecker LM, Namer IJ, Bund C. Evaluation of the effects of chemotherapy on brain glucose metabolism in children with Hodgkin's lymphoma. *Ann Nucl Med.* 2019;33:564–569.
54. Goldfarb L, Hubel F, Noblet V, Fornecker LM, Namer IJ. Effects of chemotherapy on brain metabolism in patients with Hodgkin's lymphoma: a pilot study in 37 patients. *Med Nucl (Paris).* 2017;41:93–98.
55. Filippi L, Schillaci O, Palumbo B. Neuroimaging with PET/CT in chronic traumatic encephalopathy: what nuclear medicine can do to move the field forward. *Expert Rev Mol Diagn.* 2022;22:149–156.

56. Coughlin JM, Yang T, Rebman AW, et al. Imaging glial activation in patients with post-treatment Lyme disease symptoms: a pilot study using [¹¹C]DPA-713 PET. *J Neuroinflammation*. 2018;15:346.
57. Coughlin JM, Wang Y, Ambinder EB, et al. In vivo markers of inflammatory response in recent-onset schizophrenia: a combined study using [¹¹C]DPA-713 PET and analysis of CSF and plasma. *Transl Psychiatry*. 2016;6:e777.
58. Owen DR, Yeo AJ, Gunn RN, et al. An 18-kDa translocator protein (TSPO) polymorphism explains differences in binding affinity of the PET radioligand PBR28. *J Cereb Blood Flow Metab*. 2012;32:1–5.
59. Schroyen G, Blommaert J, van Weehaeghe D, et al. Neuroinflammation and its association with cognition, neuronal markers and peripheral inflammation after chemotherapy for breast cancer. *Cancers (Basel)*. 2021;13:4198.
60. Alcantara A, Berenji GR, Scherling CS, Durcanova B, Diaz-Aguilar D, Silverman DHS. Long-term clinical and neuronuclear imaging sequelae of cancer therapy, trauma, and brain injury. *J Nucl Med*. 2019;60:1682–1690.
61. Perani D, Della Rosa PA, Cerami C, et al. Validation of an optimized SPM procedure for FDG-PET in dementia diagnosis in a clinical setting. *Neuroimage Clin*. 2014;6:445–454.
62. Yang F, Jiang J, Alberts I, et al. Combining PET with MRI to improve predictions of progression from mild cognitive impairment to Alzheimer's disease: an exploratory radiomic analysis study. *Ann Transl Med*. 2022;10:513.
63. Leano A, Korman MB, Goldberg L, Ellis J. Are we missing PTSD in our patients with cancer? Part I. *Can Oncol Nurs J*. 2019;29:141–146.

Role of ^{18}F -FDG PET/CT in Large Vessel Vasculitis and Polymyalgia Rheumatica

Riemer H.J.A. Slart^{1,2}, Pieter H. Nienhuis^{1,3}, Andor W.J.M. Glaudemans¹, Elisabeth Brouwer³, Olivier Gheysens⁴, and Kornelis S.M. van der Geest³

¹Medical Imaging Center, Department of Nuclear Medicine and Molecular Imaging, University Medical Center Groningen, University of Groningen, The Netherlands; ²Department of Biomedical Photonic Imaging, Faculty of Science and Technology, University of Twente, Enschede, The Netherlands; ³Department of Rheumatology and Clinical Immunology, University Medical Center Groningen, University of Groningen, The Netherlands; and ⁴Department of Nuclear Medicine, Cliniques Universitaires Saint-Luc and Institute of Clinical and Experimental Research, Université Catholique de Louvain, Brussels, Belgium

Learning Objectives: On successful completion of this activity, participants should be able to (1) understand the role of ^{18}F -FDG PET/CT for diagnosis and therapy monitoring of LVV and PMR; (2) learn about the strengths and limitations of ^{18}F -FDG PET/CT in LVV and PMR, including the pitfalls; (3) know the PET procedures around LVV and PMR; and (4) realize the potential of more specific PET tracers in LVV and PMR, particularly in monitoring disease activity.

Financial Disclosure: Kornelis van der Geest received a speaker fee from Roche and research support from AbbVie. In accordance with ACCME Revised Standards for Commercial Support and SNMMI Conflict-of-Interest Policy, the authors have indicated no other relevant relationships that could be perceived as a real or apparent conflict of interest. Disclosure of a relationship is not intended to suggest or to condone bias but is made to provide participants with information that might be of potential importance to their evaluation of the activity.

CME Credit: SNMMI is accredited by the Accreditation Council for Continuing Medical Education (ACCME) to sponsor continuing education for physicians. SNMMI designates each *JNM* continuing education article for a maximum of 2.0 AMA PRA Category 1 Credits. Physicians should claim only credit commensurate with the extent of their participation in the activity. For CE credit, SAM, and other credit types, participants can access this activity through the SNMMI website (<http://www.snmlearningcenter.org>) through April 2026.

Systemic vasculitides comprise a group of autoimmune diseases affecting blood vessels, including large vessel vasculitis (LVV) and medium-sized vessel vasculitis such as giant cell arteritis (GCA) and Takayasu arteritis (TAK). GCA frequently overlaps with polymyalgia rheumatica (PMR), a rheumatic inflammatory condition affecting bursae, tendons or tendon sheaths, and joints. ^{18}F -FDG PET/CT plays an important role in the diagnostic work-up of GCA, PMR, and TAK and is increasingly used to monitor treatment response. This continuing education article provides up-to-date guidance on the role of ^{18}F -FDG PET/CT in patients with LVV, medium-sized vessel vasculitis, and PMR. It provides a general introduction on the clinical presentation and challenges in the diagnostic work-up of LVV and medium-sized vessel vasculitis, with a focus on the 2 major LVV subtypes: GCA, including PMR, and TAK. Next, practice points to perform and interpret the results of ^{18}F -FDG PET/CT are described in line with the published procedure recommendations. Furthermore, the diagnostic performance and its role for treatment monitoring are discussed, taking into account recent international recommendations for the use of imaging in LVV and medium-sized vessel vasculitis in clinical practice. This is illustrated by several clinically representative PET/CT scan examples. Lastly, knowledge of limitations and pitfalls is essential to understand the role of ^{18}F -FDG PET/CT in LVV, medium-sized vessel vasculitis, and PMR. Challenges and opportunities, as well as future research and conclusions, are highlighted. Learning objectives provide up-to-date guidance for the role of ^{18}F -FDG PET/CT in patients with suspected LVV, medium-sized vessel vasculitis, and PMR.

Key Words: large vessel vasculitis; cranial GCA; PMR; ^{18}F -FDG PET/CT; procedures

J Nucl Med 2023; 64:515–521

DOI: 10.2967/jnumed.122.265016

The autoimmune vasculitides encompass a heterogeneous group of diseases characterized by inflammation of blood vessels. Classification is based on the size and the type of vessels that are preferentially affected by the specific type of vasculitis (1). The main forms of large vessel vasculitis (LVV) include giant cell arteritis (GCA) and Takayasu arteritis (TAK). GCA is the most common form of vasculitis in European populations, with the highest lifetime risk (i.e., 0.5%–1%) among people of Northern European descent (Figs. 1 and 2) (2). In contrast, TAK is more common in Asian populations (Fig. 3) (3). GCA and TAK more often affect women. One important distinction between GCA and TAK is the age of disease onset. TAK primarily occurs before the age of 40, whereas GCA affects individuals after the age of 50, with a mean age between 70–75 y (Fig. 4). Furthermore, GCA frequently overlaps with polymyalgia rheumatica (PMR), a rheumatic inflammatory condition affecting bursae, tendons or tendon sheaths, and joints (Fig. 5) (4–6). PMR may also occur in the absence of GCA and is the most common rheumatic inflammatory condition in the elderly, with an age distribution similar to that of GCA (2).

Historically, involvement of cranial arteries was thought to be a hallmark of GCA. This is reflected in one of the earlier names of the disease, temporal arteritis, and the American College of Rheumatology 1990 criteria for the classification of GCA, which focused on cranial symptoms and signs and biopsy proof of temporal artery inflammation. This cranial GCA (C-GCA) may give rise to classic symptoms such as headache, jaw claudication, and ischemic visual loss (7), the latter reflecting infarction of the optic nerve related to inflammation of the posterior ciliary arteries (8). With the emerging role of imaging, it has been recognized that

Received Dec. 21, 2022; revision accepted Feb. 2, 2023.

For correspondence or reprints, contact Riemer H.J.A. Slart (r.h.j.a.slart@umcg.nl).

COPYRIGHT © 2023 by the Society of Nuclear Medicine and Molecular Imaging.

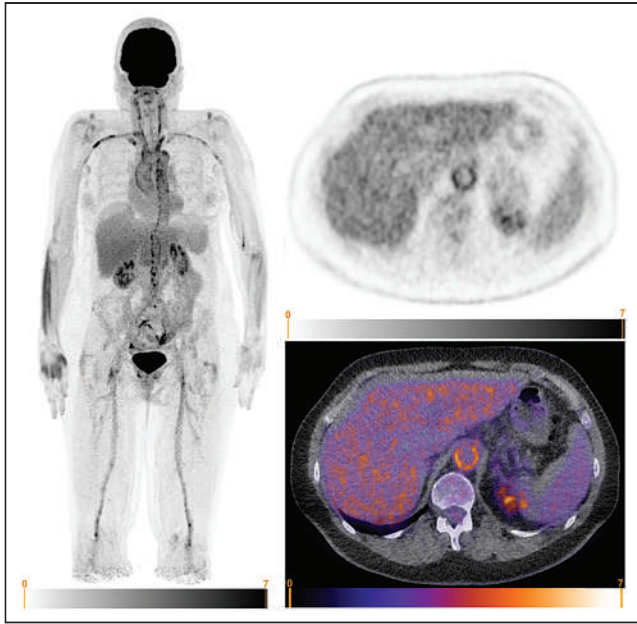


FIGURE 1. Digital ^{18}F -FDG PET/CT of 64-y-old female with suspected GCA. Patient presented with fatigue and claudication of arms. Measurements of systolic blood pressure in brachial arteries varied significantly. Measurements lower than 100 mm Hg and higher than 120 mm Hg were sequentially registered. Duplex ultrasonography showed bilateral stenosis of subclavian and axillary arteries. Patient also complained of morning stiffness and pain in neck, shoulders, and hips. (Left) Maximum-intensity-projection ^{18}F -FDG PET image showing significantly increased uptake (higher than liver) in aorta, carotid, subclavian, and axillary arteries. Increased uptake (similar to liver) may also be seen in femoral and popliteal arteries, as well as around hips and shoulders. (Right bottom) Axial fused ^{18}F -FDG PET/CT images showing significantly increased uptake in suprarenal abdominal aorta. Diffuse and circular uptake is highly suggestive of LVV.

many patients with GCA may also have inflammation of the aorta and its major branches and that this large vessel involvement can occur in the absence of cranial artery involvement (9). Consequently, clinicians now classify C-GCA and large vessel GCA (LV-GCA) according to symptoms or affected arteries on imaging (10).

In general, TAK can affect the same vasculature as LV-GCA, although some differences exist. For instance, carotid, mesenteric, and renal artery involvement is more common in TAK. In contrast, temporal artery involvement is less common in TAK, and involvement of the ocular arterial system is rare (11). Patients with LV-GCA or TAK may present with fever of unknown origin, but more specific symptoms such as arm claudication and carotidynia can occur (7,11). Aortitis is an all-encompassing term ascribed to inflammation solely of the aorta (Fig. 6). It includes “true” aortitis limited to the vascular wall and periaortitis and involving the adventitial layer and potentially surrounding fat and other soft tissues. Periaortitis may also present as an inflammatory aneurysm or retroperitoneal fibrosis.

In all vasculitides, laboratory testing usually shows raised inflammatory markers in the blood. C-GCA can be further demonstrated by temporal artery biopsy, color Doppler ultrasonography (CDUS) of the superficial vessels, and MR angiography (MRA), with recent clinical guidelines suggesting a prominent role of CDUS as a first-line test in suspected C-GCA (12). MRA, CT angiography (CTA), and CDUS can be used for detection of vascular inflammation in LV-GCA and TAK (12). Ultrasonography and MRI of the shoulder

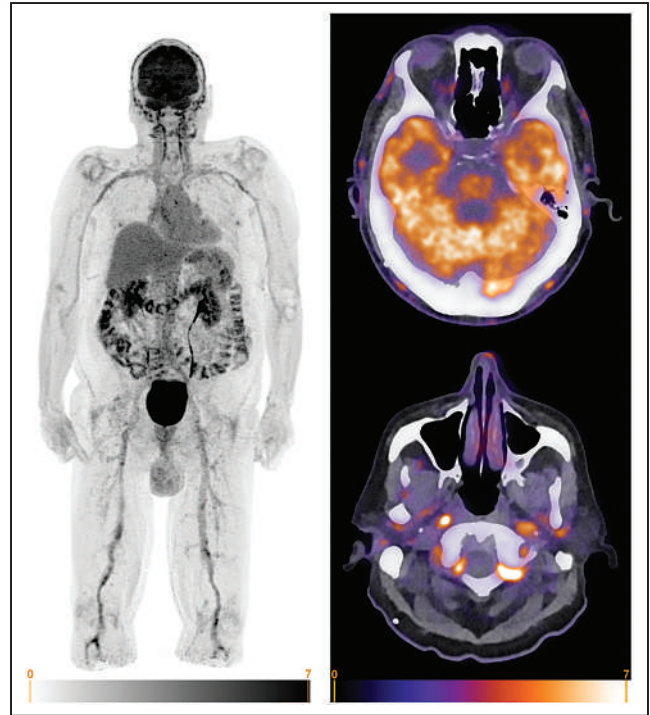


FIGURE 2. Digital ^{18}F -FDG PET/CT of 80-y-old male with suspected GCA. Patient’s main symptom consisted of both-sided temporal headache, which was accompanied by fatigue. Laboratory investigation showed C-reactive protein of 120 mg/L. (Left) Maximum-intensity-projection ^{18}F -FDG PET image showing strongly elevated uptake (significantly higher than background) in cranial arteries, most notably in superficial temporal and carotid arteries. Elevated uptake (similar to liver uptake) can be seen in subclavian, axillary, femoral, and popliteal arteries. These findings are highly suggestive of C-GCA and LV-GCA. In addition, moderate uptake can be seen around shoulders and hips, suspected for PMR activity. (Right) Axial ^{18}F -FDG PET/CT fusion images of head. (Right top) Elevated uptake in frontal and parietal branches of superficial temporal artery, left posterior auricular artery, and occipital arteries. (Right bottom) Significantly increased uptake in internal carotid and vertebral arteries. Elevated uptake can also be seen at junction of external carotid artery and common superficial temporal artery, as well as maxillary arteries and right posterior deep temporal artery.

and hip girdle may demonstrate inflammation of bursae, tendons or tendon sheaths, and joints in patients with PMR (13–15). In addition, ^{18}F -FDG PET/CT is considered an important tool to demonstrate inflammation in GCA, PMR, and TAK.

Glucocorticoid (GC) treatment is the cornerstone in GCA, PMR, and TAK. High initial GC doses are used in GCA and TAK: typically 40–60 mg of prednisone daily, with 500- to 1,000-mg methylprednisolone pulse therapy on 3 consecutive days reserved for patients with severe ischemic manifestations (e.g., visual loss) (16). In TAK, the clinical guidelines indicate that GC treatment should be combined with other immunosuppressive agents early in the disease. First-line treatment of TAK may consist of conventional synthetic disease-modifying antirheumatic drugs, such as methotrexate and azathioprine (16,17). Anti-TNF and anti-IL-6 receptor therapy may serve as second-line immunosuppressive therapy in refractory and relapsing cases. Treatment guidelines for GCA by the American College of Rheumatology suggest early initiation of anti-IL-6 receptor therapy in all newly diagnosed patients (18), whereas European League Against Rheumatism recommendations advocate the addition of anti-IL-6R



FIGURE 3. ^{18}F -FDG PET/CT of 16-y-old female with suspected TAK. Patient had been experiencing generalized malaise. Laboratory investigations showed C-reactive protein of 98 mg/L and ESR of 119 mm/h. Maximum-intensity-projection ^{18}F -FDG PET image shows elevated uptake in thoracic aorta and part of abdominal aorta. ESR = erythrocyte sedimentation rate.

therapy in cases of relative contraindications for GC treatment or a relapsing disease course (16). Methotrexate is considered a reasonable alternative for anti-IL-6 receptor therapy, according to American College of Rheumatology guidelines and European League Against Rheumatism recommendations. Patients with PMR are typically started on medium GC doses (15 mg of prednisone) daily (19). GC-sparing immunosuppressants such as methotrexate are usually added when patients with PMR suffer from GC side effects or disease relapse.

ROLE OF ^{18}F -FDG PET/CT ANGIOGRAPHY (PET/CT[A]) IN DIAGNOSING LJV AND PMR

Ultrasonography and MRA are mainly used to detect C-GCA, whereas CTA, MRA, and ^{18}F -FDG PET/CT are useful

for detecting LV-GCA in patients presenting with general symptoms (12). However, the new-generation PET/CT scanners, providing superior sensitivity and better spatial resolution, also allows visualization of the cranial arteries by ^{18}F -FDG PET/CT (20,21). ^{18}F -FDG PET/CT can be used in patients with clinical symptoms of C-GCA, LV-GCA, and TAK to visualize which vessels are involved, disease extent and activity, and coexistence of PMR. ^{18}F -FDG PET/CT can also be used in patients without typical clinical symptoms but with persisting fever or inflammation of unknown origin. Vasculitis or PMR can be one of the diseases causing this inflammation or fever.

Normally, low-dose CT is performed in PET imaging for attenuation correction and anatomic localization. However, performing contrast-enhanced CT is also possible according to local practice or guidelines, and newer PET/CT camera systems offer the possibility to perform a CTA directly after the PET acquisition and with the same quality as performed on a single CT camera system. Therefore, PET/CTA combines the unique characteristics of the PET part in visualizing the metabolic activity of the vessel walls and the CTA characteristics of visualizing anatomic changes or stenoses of the vessels in a single imaging modality.

In GCA, a prospective study of ^{18}F -FDG PET imaging in patients with GCA showed vascular ^{18}F -FDG uptake in 83% of patients, particularly at the subclavian arteries (74%) but also in the thoracic and abdominal aorta (>50%) and the femoral arteries (37%) (22). A metaanalysis of 6 studies evaluating ^{18}F -FDG PET for the diagnosis of GCA reported an overall sensitivity of 80% and specificity of 89%. Moreover, the negative predictive value of a ^{18}F -FDG PET scan for GCA was excellent (88%) (23).

^{18}F -FDG PET/CT is also widely used for the diagnosis of TAK (24). One metaanalysis, including patients with TAK, reported a sensitivity of 81% and specificity of 74% for ^{18}F -FDG PET/CT (25). For diagnosing C-GCA, a binary visual ^{18}F -FDG uptake score has been proposed that yields a sensitivity of 73%–83% and specificity of 75%–100% (20,21,26).

^{18}F -FDG PET/CT is an accurate imaging method for distinguishing between aortitis and periaortitis, which is important for identifying the underlying cause (e.g., infectious and noninfectious conditions) (27,28). Mild and heterogeneous metabolic activity of the aortic wall is frequently noticed in the absence of vasculitis, especially in atherosclerotic aneurysms (29). Periaortitis is characterized by a periaortic soft-tissue mass surrounding the aorta and eccentric to the calcifications of the media, visible on radiographic imaging and ultrasound. ^{18}F -FDG uptake is an important indicator of active disease, potentially enabling (treatment) follow-up (30).

^{18}F -FDG PET/CT can also show inflammation of periarticular and articular synovial structures in overlapping PMR or in isolated PMR. Van der Geest et al. (31) demonstrated in a systematic review that

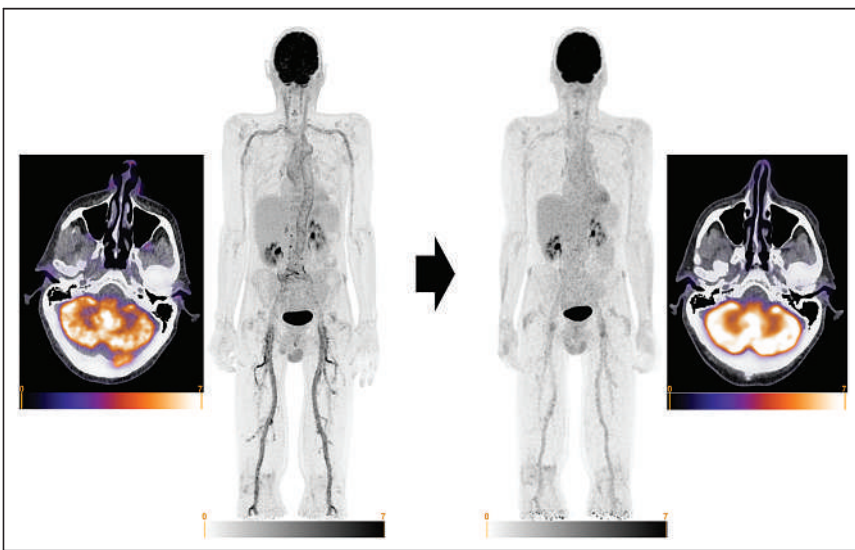


FIGURE 4. ^{18}F -FDG PET/CT imaging at time of diagnosis (before treatment) and after 1 y of treatment in 67-y-old male GCA patient. At time of diagnosis, patient presented with complaints of PMR, accompanied by C-reactive protein (CRP) of 121 mg/L and ESR of 106 mm/h. Patient had been treated with prednisolone and subsequently with methotrexate. At 1 y, CRP remained elevated despite methotrexate treatment. Patient did not experience GCA-related symptoms at that time but had some symptoms of PMR. (Left) Axial ^{18}F -FDG PET/CT fusion image of head and whole-body maximum-intensity-projection (MIP) image at time of diagnosis. Moderately increased uptake (higher than background) can be seen in maxillary arteries. Significantly increased uptake (higher than liver) can also be found in aorta and carotid, subclavian, axillary, iliac, and femoral arteries (PETVAS = 27). In addition, moderately increased uptake (similar to liver) can be observed surrounding shoulders and hips. (Right) Whole-body MIP image and axial ^{18}F -FDG PET/CT fusion of head after 1 y of treatment. Slightly increased uptake (similar to liver) can be observed in aorta and carotid, subclavian, axillary, iliac, and femoral arteries (PETVAS = 13). No uptake was found in maxillary arteries. Moderately increased uptake was found surrounding hip joints. ESR = erythrocyte sedimentation rate.

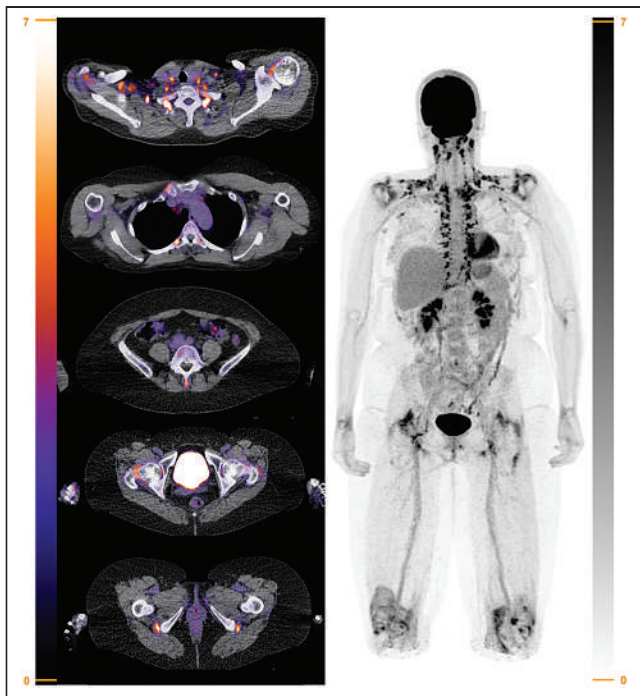


FIGURE 5. Digital ^{18}F -FDG PET/CT in 59-y-old female patient suspected of having PMR. Patient presented at rheumatology outpatient clinic with pain in neck, shoulders, and hips. She also experienced morning stiffness of 2 h, and her blood inflammatory markers were increased (C-reactive protein, 63 mg/L; ESR, 72 mm/h). (Left) Axial ^{18}F -FDG PET/CT fusion images showing significantly increased uptake (higher than liver) in shoulders, right sternoclavicular joint, lumbar interspinous bursa, hips, and ischial tuberosities. (Right) Whole-body maximum-intensity-projection image showing significantly increased ^{18}F -FDG uptake in shoulders, sternoclavicular joints, lumbar interspinous bursa, hips, ischial tuberosities, and knees. Slightly elevated ^{18}F -FDG uptake may be seen in wrists. Increased ^{18}F -FDG uptake due to brown fat activation can also be seen in neck and paravertebral at thoracic spine (Leuven score = 23, Groningen/Leuven score = 14) (Supplemental Table 1). ESR = erythrocyte sedimentation rate.

^{18}F -FDG uptake at multiple anatomic sites in the shoulder and hip girdle and spinal column is informative for a diagnosis of PMR.

ROLE OF ^{18}F -FDG PET/CT(A) IN THERAPY MONITORING OF LVV AND PMR

Therapeutic monitoring can be challenging in patients with LVV and PMR, because signs and symptoms and laboratory tests are not specific for these conditions. In addition, inflammatory markers in the blood are often lower during relapse than at diagnosis (32). Imaging tools could thus be of interest for monitoring disease activity during treatment.

Currently, ^{18}F -FDG PET/CT is not routinely recommended for treatment monitoring in GCA and PMR in clinical routine (33). Even though high-dose GC treatment has substantial effects on ^{18}F -FDG uptake after 10 d of treatment (34), it seems that some arterial wall ^{18}F -FDG uptake may persist during treatment-induced remission later in the disease course (35). Nevertheless, most studies show that the extent and intensity of ^{18}F -FDG uptake decrease during treatment. Hence, a metaanalysis suggested that ^{18}F -FDG PET/CT has a moderate sensitivity of 78% and specificity of 71% for distinguishing active from quiescent LV-GCA during treatment (24). A comparable diagnostic accuracy was

noted in a recent study with 100 consecutive LV-GCA patients (36). The treatment effect on arterial wall uptake is not restricted to GC treatment, but a similar decrease has been observed in GCA patients treated with methotrexate and anti-IL-6 receptor therapy (37).

Few studies have examined the potential role of ^{18}F -FDG PET/CT for treatment monitoring of PMR, because response to treatment is usually based on a clinical evaluation (38,39). Comparable to arterial wall ^{18}F -FDG uptake in LVV, studies in PMR patients have shown that ^{18}F -FDG uptake at the shoulder and pelvic girdle and interspinous bursae decreases, but not necessarily normalizes, during treatment-induced remission (31).

PET PROCEDURES

Patient Preparation and Scan Acquisition

Optimal patient preparation is crucial (Table 1). Patients must be fasting for at least 6 h and avoid strenuous activity for 24 h before ^{18}F -FDG injection. Blood glucose levels are preferably less than 7 mmol/L. ^{18}F -FDG PET should be performed before GC treatment (unless there is a risk of ischemic complications) or within the first 3 d of treatment. For PET/CT acquisition, low-dose, non-contrast-enhanced CT (for attenuation correction and anatomic reference) is performed from the vertex to the feet (or at least including the knees) 60 min after ^{18}F -FDG injection, with the patient in a supine position with the arms next to the body. It is described that a time interval of 2 h may be even more optimal for PET activity detection in GCA (40). Injected activities, scan duration, or diagnostic contrast-enhanced CT may be performed according to applicable local protocols and guidelines (33).

Scan Interpretation and ^{18}F -FDG PET/CT Scores

Several ^{18}F -FDG PET interpretation criteria, both visual and semi-quantitative, have been proposed, and there is insufficient evidence that semiquantitative parameters may outperform a visual grading scale to diagnose LVV in routine clinical practice (41). A standardized 4-point visual grading scale (arterial to liver uptake) is recommended with grade 0, no uptake; grade 1, uptake lower than liver; grade 2, uptake similar to liver; and grade 3, uptake higher than liver. Grade 3 is considered positive for LVV, whereas grade 2 may be indicative of LVV (33). In addition, a quantitative composite score, based on the visual grading scale of several individual arterial segments (typically between 7 and 15 segments), could be applied that is known as the total vascular score or PET vascular activity score (PETVAS) (33,42,43). This composite score provides an overall assessment of disease burden, has proven robust with little interobserver variability, and may be preferred for evaluating treatment response. ^{18}F -FDG uptake in cranial arteries are scored as 3-point visual grading (0–2), with grade 0 representing uptake not above the surrounding tissue, grade 1 representing uptake just above the surrounding tissue, and grade 2 representing uptake significantly above the surrounding tissue (21).

In PMR, various ^{18}F -FDG PET scores have been reported. The Leuven score is the best validated one, providing a pooled sensitivity of 89.6% and specificity of 93.3% (Supplemental Table 1) (supplemental materials are available at <http://jnm.snmjournals.org>) (44–46). The Leuven score is the summed score of visual ^{18}F -FDG uptake at the cervical and lumbar interspinous bursae, sternoclavicular joints, ischial tuberosities, greater trochanters, hips, and shoulders (44). ^{18}F -FDG uptake is graded according to a standardized 3-point visual ^{18}F -FDG grading scale: grade 0, no uptake; grade 1, uptake lower than liver; and grade 2, uptake similar to or higher

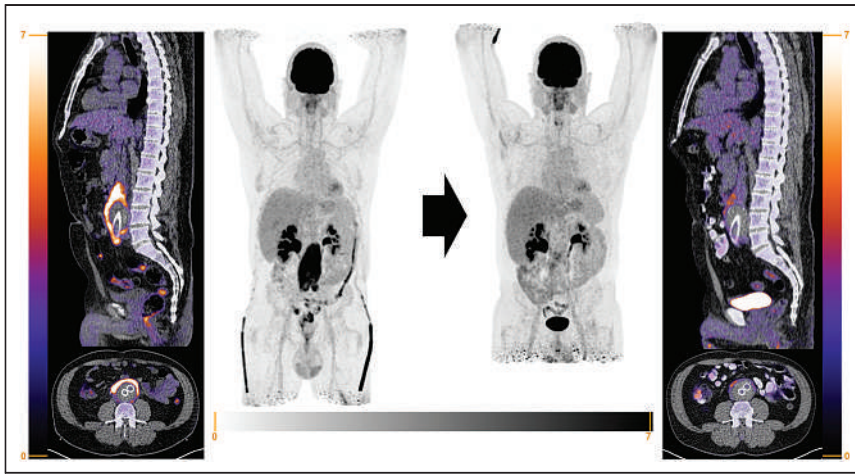


FIGURE 6. ^{18}F -FDG PET/CT of 52-y-old man with history of idiopathic inflammatory abdominal aortic aneurysm for which he underwent prosthetic vascular graft surgery. Patient presented 1 y after surgery with increased C-reactive protein (231 mg/L) and decreased kidney function based on post-renal obstruction. Patient was diagnosed with recurrence of inflammatory aneurysm and received therapy with high-dose GCs and azathioprine. Ureteric obstruction was treated with temporary nephrostomy catheters. Immunosuppressive therapy was tapered in following 2 y. No clinical or biochemical signs of active (peri-)aortitis recurred. (Left) Sagittal and axial ^{18}F -FDG PET/CT fusion images and whole-body maximum-intensity-projection (MIP) image of patient at time of diagnosis (before starting immunosuppressive treatment). Markedly increased, diffuse, and circular ^{18}F -FDG uptake is seen in dilated aortic wall. There is no evidence of inflammatory activity in other locations, including prosthetic graft itself. Right: whole-body MIP image and sagittal and axial ^{18}F -FDG PET/CT fusion images of patient 2 y later after withdrawal of GC therapy. ^{18}F -FDG uptake was significantly decreased compared with time of diagnosis but had not completely normalized.

than liver. A concise version, the Leuven/Groningen score, appears to be at least equally informative for a diagnosis of PMR, only requiring visual assessment of ^{18}F -FDG uptake at the sternoclavicular joints, hips, ischial tuberosities, and lumbar interspinous bursa (45,46). The Leuven and Leuven/Groningen scores also provide excellent interrater agreement (46).

Pitfalls

Blood glucose levels should be as low as possible (preferably <7 mmol/L). Even though hyperglycemia may not have a significant impact on the false-negative rate of ^{18}F -FDG PET for detecting inflammatory lesions (in contrast to oncologic indications), a negative correlation has been observed between blood glucose levels and ^{18}F -FDG arterial wall uptake (47,48).

rather reflects a chronic, low-grade, nonspecific reaction to the graft material (51).

CHALLENGES FOR THE FUTURE AND CONCLUSIONS

Although ^{18}F -FDG PET/CT has become an important diagnostic test in the evaluation of LVV and PMR, various questions regarding its use in LVV and PMR warrant further research. Standardization of ^{18}F -FDG PET/CT scans is crucial, including the complete PET procedure, patient preparation, scan acquisition, scan reconstruction, and image analysis, and standards should be followed and adapted when needed (33). Development of scoring methods for PMR activity on PET is ongoing, and these methods need to be validated in large, prospective cohort studies. Developments in PET/CT camera

Oral GC therapy for at least 10 d decreases the sensitivity of ^{18}F -FDG PET for diagnosing LVV, but its sensitivity is not affected when performed within 3 d after oral GC initiation (34). There are no prospective data available on the 3- to 10-d window, and adherence to the 3-d window is recommended to date. In addition, GCs may increase liver uptake, thereby affecting the visual scoring of vascular ^{18}F -FDG uptake (49).

Atherosclerotic vascular uptake, especially in the elderly and at the iliofemoral arteries, may reduce the specificity of ^{18}F -FDG PET for diagnosing LVV (50). Despite the possible overlap between entities, ^{18}F -FDG uptake patterns and the presence of calcifications on CT are helpful to hint toward one or the other: LVV appears as a linear, diffuse, and circumferential uptake, whereas atherosclerosis is characterized by a typical patchy uptake pattern with generally low intensity.

Arterial graft-associated ^{18}F -FDG uptake might raise concerns regarding the diagnosis or disease activity assessment in patients with LVV because the ^{18}F -FDG uptake pattern is similar. However, significant ^{18}F -FDG uptake confined to the arterial graft does not equate to active vasculitis but

TABLE 1
Patient Preparation and ^{18}F -FDG PET/CT Acquisition

Preparation	Acquisition
Dietary preparation	Fast for ≥ 6 h before ^{18}F -FDG administration
Blood glucose level	Preferably <7 mmol/L; <11 mmol/L for diabetic patients
GC interference	Delay therapy until after PET (unless risk of ischemic complications) Optional: PET within 3 d after start of GCs
PET acquisition	Positioning: supine, arms next to body Range: vertex down to feet (or at least including knees) Incubation time: standard, 60 min; optional, 120 min PET/CT: low-dose, non-contrast-enhanced CT for attenuation correction and anatomic reference Optional: diagnostic contrast-enhanced CT(A) according to local protocols and guidelines Optional: 5 min per bed position for skull only

systems, such as digital or total-body systems, may enhance sensitivity and spatial resolution with a better signal-to-noise (i.e., vessel wall vs. lumen) ratio, including the possibility to scan at later time points while retaining adequate image quality. Furthermore, these new-generation PET/CT scanners allow administration of lower tracer activities to patients while achieving similar or even better image quality than conventional scanners. These systems, including the new-generation PET/MRI scanners, may also visualize pathologic uptake in the smaller cranial vessels (e.g., temporal and vertebral arteries) (20,52). PET/MRI will further reduce the radiation dose, because CT lacks comparable accuracy in GCA diagnosis (53), and it has the advantage of tissue characterization of GCA and PMR, which is of particular value in younger individuals and in (repetitive) monitoring of disease activity (54,55).

Combining total-body systems with more specific immuno-PET tracers for vasculitis would allow more thorough insight into how specific cell subpopulations are involved and behave in the pathogenesis of specific types of vasculitis. Moreover, multiorgan changes regarding kinetic uptake of specific PET tracers after appropriate treatment of vasculitis could be assessed with total-body systems, something that was not possible before the development of this type of scanner (56).

Immuno-PET tracers, binding to specific immune cell subsets, could potentially be more accurate than conventional ¹⁸F-FDG for treatment monitoring of patients with LV-GCA (57,58). However, further understanding regarding immune cell subsets in vasculitic lesions is needed for better selection of tracers and targets for tracer development.

Future studies are also needed to investigate the role of ¹⁸F-FDG PET/CT in treatment monitoring and as a prognostic factor for LVV and PMR. For instance, studies have suggested that aortic ¹⁸F-FDG uptake at diagnosis is associated with an enhanced risk for development of aortic aneurysms many years thereafter (59). Decision-making is always needed in the clinical context. When more specific immuno-PET tracers become available, the question may arise whether therapy should or can be modified based solely on imaging results and whether distinct immunosuppressive treatments have an equal effect on vascular uptake in patients with LVV.

In conclusion, ¹⁸F-FDG PET/CT is an important diagnostic tool for detecting inflammation of large- and medium-sized vessels in patients with systemic vasculitides and in PMR. ¹⁸F-FDG PET/CT can provide complementary information to other conventional imaging techniques. Furthermore, ¹⁸F-FDG PET/CT may have a role in therapeutic monitoring of patients with vasculitis and PMR, but it remains challenging to differentiate remission from smoldering disease activity. A new generation of total-body PET scanners can limit radiation exposure while providing excellent sensitivity. The introduction of immune-cell targeted radiotracers will potentially allow direct visualization of inflammatory cell infiltrates in the vasculature of patients with vasculitis.

REFERENCES

1. Jennette JC, Falk RJ, Bacon PA, et al. 2012 Revised International Chapel Hill Consensus Conference Nomenclature of Vasculitides. *Arthritis Rheum.* 2013;65:1–11.
2. Crowson CS, Matteson EL, Myasoedova E, et al. The lifetime risk of adult-onset rheumatoid arthritis and other inflammatory autoimmune rheumatic diseases. *Arthritis Rheum.* 2011;63:633–639.
3. Watts RA, Robson J. Introduction, epidemiology and classification of vasculitis. *Best Pract Res Clin Rheumatol.* 2018;32:3–20.
4. van der Geest KSM, Sandovici M, van Sleen Y, et al. Review: what is the current evidence for disease subsets in giant cell arteritis? *Arthritis Rheumatol.* 2018;70:1366–1376.

5. Mackie SL, Koduri G, Hill CL, et al. Accuracy of musculoskeletal imaging for the diagnosis of polymyalgia rheumatica: systematic review. *RMD Open.* 2015;1:e000100.
6. Jiemy WF, Zhang A, Boots AMH, et al. Expression of interleukin-6 in synovial tissue of patients with polymyalgia rheumatica. *Ann Rheum Dis.* 2023;82:440–442.
7. van der Geest KSM, Sandovici M, Brouwer E, Mackie SL. Diagnostic accuracy of symptoms, physical signs, and laboratory tests for giant cell arteritis: a systematic review and meta-analysis. *JAMA Intern Med.* 2020;180:1295–1304.
8. Soriano A, Muratore F, Pipitone N, Boiardi L, Cimino L, Salvarani C. Visual loss and other cranial ischaemic complications in giant cell arteritis. *Nat Rev Rheumatol.* 2017;13:476–484.
9. Nielsen BD, Hansen IT, Keller KK, Therkildsen P, Gormsen LC, Hauge E-M. Diagnostic accuracy of ultrasound for detecting large-vessel giant cell arteritis using FDG PET/CT as the reference. *Rheumatology.* 2020;59:2062–2073.
10. Ponte C, Grayson PC, Robson JC, et al. 2022 American College of Rheumatology/EULAR classification criteria for giant cell arteritis. *Ann Rheum Dis.* 2022;81:1647–1653.
11. Koster MJ, Warrington KJ. Classification of large vessel vasculitis: can we separate giant cell arteritis from Takayasu arteritis? *Presse Med.* 2017;46:e205–e213.
12. DeJaco C, Ramiro S, Duftner C, et al. EULAR recommendations for the use of imaging in large vessel vasculitis in clinical practice. *Ann Rheum Dis.* 2018;77:636–643.
13. Fruth M, Seggewiss A, Kozik J, Martin-Seidel P, Baraliakos X, Braun J. Diagnostic capability of contrast-enhanced pelvic girdle magnetic resonance imaging in polymyalgia rheumatica. *Rheumatology.* 2020;59:2864–2871.
14. Mackie SL, Pease CT, Fukuba E, et al. Whole-body MRI of patients with polymyalgia rheumatica identifies a distinct subset with complete patient-reported response to glucocorticoids. *Ann Rheum Dis.* 2015;74:2188–2192.
15. Dasgupta B, Cimmino MA, Kremers HM, et al. 2012 international classification criteria for polymyalgia rheumatica: a European League Against Rheumatism/American College of Rheumatology collaborative initiative. *Arthritis Rheum.* 2012;64:943–954.
16. Hellmich B, Agueda A, Monti S, et al. 2018 update of the EULAR recommendations for the management of large vessel vasculitis. *Ann Rheum Dis.* 2020;79:19–30.
17. Barra L, Yang G, Pagnoux C. Non-glucocorticoid drugs for the treatment of Takayasu's arteritis: a systematic review and meta-analysis. *Autoimmun Rev.* 2018;17:683–693.
18. Maz M, Chung SA, Abril A, et al. 2021 American College of Rheumatology/Vasculitis Foundation guideline for the management of giant cell arteritis and Takayasu arteritis. *Arthritis Rheumatol.* 2021;73:1349–1365.
19. DeJaco C, Singh YP, Perel P, et al. Current evidence for therapeutic interventions and prognostic factors in polymyalgia rheumatica: a systematic literature review informing the 2015 European League Against Rheumatism/American College of Rheumatology recommendations for the management of polymyalgia rheumatica. *Ann Rheum Dis.* 2015;74:1808–1817.
20. Nienhuis PH, Sandovici M, Glaudemans AW, Slart RH, Brouwer E. Visual and semiquantitative assessment of cranial artery inflammation with FDG-PET/CT in giant cell arteritis. *Semin Arthritis Rheum.* 2020;50:616–623.
21. Nielsen BD, Hansen IT, Kramer S, et al. Simple dichotomous assessment of cranial artery inflammation by conventional ¹⁸F-FDG PET/CT shows high accuracy for the diagnosis of giant cell arteritis: a case-control study. *Eur J Nucl Med Mol Imaging.* 2019;46:184–193.
22. Blockmans D, Bley T, Schmidt W. Imaging for large-vessel vasculitis. *Curr Opin Rheumatol.* 2009;21:19–28.
23. Besson FL, Parienti J-J, Bienvenu B, et al. Diagnostic performance of ¹⁸F-fluorodeoxyglucose positron emission tomography in giant cell arteritis: a systematic review and meta-analysis. *Eur J Nucl Med Mol Imaging.* 2011;38:1764–1772.
24. van der Geest KSM, Treglia G, Glaudemans AJWJ, et al. Diagnostic value of [¹⁸F]FDG-PET/CT for treatment monitoring in large vessel vasculitis: a systematic review and meta-analysis. *Eur J Nucl Med Mol Imaging.* 2021;48:3886–3902.
25. Barra L, Kanji T, Malette J, Pagnoux C. Imaging modalities for the diagnosis and disease activity assessment of Takayasu's arteritis: a systematic review and meta-analysis. *Autoimmun Rev.* 2018;17:175–187.
26. Thibault T, Durand-Bailloud B, Soudry-Faure A, et al. PET/CT of cranial arteries for a sensitive diagnosis of giant cell arteritis. *Rheumatology.* July 22, 2022 [Epub ahead of print].
27. Espitia O, Blonz G, Urbanski G, et al. Symptomatic aortitis at giant cell arteritis diagnosis: a prognostic factor of aortic event. *Arthritis Res Ther.* 2021;23:14.
28. Yabusaki S, Oyama-Manabe N, Manabe O, et al. Characteristics of immunoglobulin G4-related aortitis/periarteritis and periarteritis on fluorodeoxyglucose positron emission tomography/computed tomography co-registered with contrast-enhanced computed tomography. *EJNMMI Res.* 2017;7:20.
29. Barwick TD, Lyons OTA, Mikhael NG, Waltham M, O'Doherty MJ. ¹⁸F-FDG PET-CT uptake is a feature of both normal diameter and aneurysmal aortic wall and is not related to aneurysm size. *Eur J Nucl Med Mol Imaging.* 2014;41:2310–2318.

30. Treglia G, Stefanelli A, Mattoli MV, Leccisotti L, Muoio B, Bertagna F. Usefulness of ¹⁸F-FDG PET/CT in evaluating disease activity at different times in a patient with chronic periaortitis. *Nucl Med Mol Imaging*. 2013;47:69–71.
31. van der Geest KSM, Treglia G, Glaudemans AWJM, et al. Diagnostic value of [¹⁸F]FDG-PET/CT in polymyalgia rheumatica: a systematic review and meta-analysis. *Eur J Nucl Med Mol Imaging*. 2021;48:1876–1889.
32. Kermani TA, Warrington KJ, Cuthbertson D, et al. Disease relapses among patients with giant cell arteritis: a prospective, longitudinal cohort study. *J Rheumatol*. 2015;42:1213–1217.
33. Slart RHJA, Slart RHJA, Glaudemans AWJM, et al. FDG-PET/CT(A) imaging in large vessel vasculitis and polymyalgia rheumatica: joint procedural recommendation of the EANM, SNMMI, and the PET Interest Group (PIG), and endorsed by the ASNC. *Eur J Nucl Med Mol Imaging*. 2018;45:1250–1269.
34. Nielsen BD, Gormsen LC, Hansen IT, Keller KK, Therkildsen P, Hauge E-M. Three days of high-dose glucocorticoid treatment attenuates large-vessel ¹⁸F-FDG uptake in large-vessel giant cell arteritis but with a limited impact on diagnostic accuracy. *Eur J Nucl Med Mol Imaging*. 2018;45:1119–1128.
35. Quinn KA, Ahlman MA, Malayeri AA, et al. Comparison of magnetic resonance angiography and ¹⁸F-fluorodeoxyglucose positron emission tomography in large-vessel vasculitis. *Ann Rheum Dis*. 2018;77:1165–1171.
36. Galli E, Muratore F, Mancuso P, et al. The role of PET/CT in disease activity assessment in patients with large vessel vasculitis. *Rheumatology*. 2022;61:4809–4816.
37. Schönau V, Roth J, Tascilar K, et al. Resolution of vascular inflammation in patients with new-onset giant cell arteritis: data from the RIGA study. *Rheumatology*. 2021;60:3851–3861.
38. Charpentier A, Verhoeven F, Sondag M, Guillot X, Prati C, Wendling D. Therapeutic response to prednisone in relation to age in polymyalgia rheumatica: a comparison study. *Clin Rheumatol*. 2018;37:819–823.
39. Palard-Novello X, Querellou S, Gouillou M, et al. Value of (18)F-FDG PET/CT for therapeutic assessment of patients with polymyalgia rheumatica receiving tocilizumab as first-line treatment. *Eur J Nucl Med Mol Imaging*. 2016;43:773–779.
40. Quinn KA, Rosenblum JS, Rimland CA, Gribbons KB, Ahlman MA, Grayson PC. Imaging acquisition technique influences interpretation of positron emission tomography vascular activity in large-vessel vasculitis. *Semin Arthritis Rheum*. 2020;50:71–76.
41. Gheysens O, Jamar F, Glaudemans AWJM, Yildiz H, van der Geest KSM. Semi-quantitative and quantitative [¹⁸F]FDG-PET/CT indices for diagnosing large vessel vasculitis: a critical review. *Diagnostics (Basel)*. 2021;11:2355.
42. Grayson PC, Alehashemi S, Bagheri AA, et al. 18 F-fluorodeoxyglucose-positron emission tomography as an imaging biomarker in a prospective, longitudinal cohort of patients with large vessel vasculitis. *Arthritis Rheumatol*. 2018;70:439–449.
43. Prieto Peña D, Martínez-Rodríguez I, Atienza-Mateo B, et al. Evidence for uncoupling of clinical and 18-FDG activity of PET/CT scan improvement in tocilizumab-treated patients with large-vessel giant cell arteritis. *Clin Exp Rheumatol*. 2021;39(suppl 129):S69–S75.
44. Henckaerts L, Gheysens O, Vanderschueren S, Goffin K, Blockmans D. Use of ¹⁸F-fluorodeoxyglucose positron emission tomography in the diagnosis of polymyalgia rheumatica: a prospective study of 99 patients. *Rheumatology*. 2018;57:1908–1916.
45. van der Geest KSM, van Sleen Y, Nienhuis P, et al. Comparison and validation of FDG-PET/CT scores for polymyalgia rheumatica. *Rheumatology*. 2022;61:1072–1082.
46. Moreel L, Boeckxstaens L, Betrains A, et al. Diagnostic accuracy and validation of ¹⁸F-fluorodeoxyglucose positron emission tomography scores in a large cohort of patients with polymyalgia rheumatica. *Front Med*. 2022;9:1026944.
47. Rabkin Z, Israel O, Keidar Z. Do hyperglycemia and diabetes affect the incidence of false-negative ¹⁸F-FDG PET/CT studies in patients evaluated for infection or inflammation and cancer? A comparative analysis. *J Nucl Med*. 2010;51:1015–1020.
48. Buceri J, Mani V, Moncrieff C, et al. Optimizing ¹⁸F-FDG PET/CT imaging of vessel wall inflammation: the impact of ¹⁸F-FDG circulation time, injected dose, uptake parameters, and fasting blood glucose levels. *Eur J Nucl Med Mol Imaging*. 2014;41:369–383.
49. Stellingwerff MD, Brouwer E, Lensen K-JDF, et al. Different scoring methods of FDG PET/CT in giant cell arteritis: need for standardization. *Medicine (Baltimore)*. 2015;94:e1542.
50. Nienhuis PH, van Praagh GD, Glaudemans AWJM, Brouwer E, Slart RHJA. A review on the value of imaging in differentiating between large vessel vasculitis and atherosclerosis. *J Pers Med*. 2021;11:236.
51. Youngstein T, Tombetti E, Mukherjee J, et al. FDG uptake by prosthetic arterial grafts in large vessel vasculitis is not specific for active disease. *JACC Cardiovasc Imaging*. 2017;10:1042–1052.
52. Nienhuis PH, van Sluis J, van Snick JH, et al. A case of clinical uncertainty solved: giant cell arteritis with polymyalgia rheumatica swiftly diagnosed with long axial field of view PET. *Diagnostics (Basel)*. 2022;12:2694.
53. Einspieler I, Thürmel K, Pyka T, et al. Imaging large vessel vasculitis with fully integrated PET/MRI: a pilot study. *Eur J Nucl Med Mol Imaging*. 2015;42:1012–1024.
54. Young V, Khalsa U, Balboni I, Nadel H. PET/MR findings in large vessel vasculitis in children. *J Nucl Med*. 2020;61(suppl 1):1584.
55. Clemente G, de Souza AW, Leão Filho H, et al. Does [¹⁸F]F-FDG-PET/MRI add metabolic information to magnetic resonance image in childhood-onset Takayasu's arteritis patients? A multicenter case series. *Adv Rheumatol*. 2022;62:28.
56. Slart RHJA, Tsoumpas C, Glaudemans AWJM, et al. Long axial field of view PET scanners: a road map to implementation and new possibilities. *Eur J Nucl Med Mol Imaging*. 2021;48:4236–4245.
57. van der Geest KSM, Sandovici M, Nienhuis PH, et al. Novel PET imaging of inflammatory targets and cells for the diagnosis and monitoring of giant cell arteritis and polymyalgia rheumatica. *Front Med (Lausanne)*. 2022;9:902155.
58. Jiemy WF, Heeringa P, Kamps JAAM, van der Laken CJ, Slart RHJA, Brouwer E. Positron emission tomography (PET) and single photon emission computed tomography (SPECT) imaging of macrophages in large vessel vasculitis: current status and future prospects. *Autoimmun Rev*. 2018;17:715–726.
59. Tomelleri A, van der Geest KSM, Sebastian A, et al. Disease stratification in giant cell arteritis to reduce relapses and prevent long-term vascular damage. *Lancet Rheumatol*. 2021;3:e886–e895.

The Latest Advances in Peptide Receptor Radionuclide Therapy for Gastroenteropancreatic Neuroendocrine Tumors

Elif Hindié¹, Eric Baudin², Rodney J. Hicks³, and David Taïeb⁴

¹Department of Nuclear Medicine, CHU de Bordeaux, University of Bordeaux, Bordeaux, France; ²Department of Endocrine Oncology and Imaging, Gustave Roussy Cancer Campus, Villejuif, France; ³Department of Medicine, St. Vincent's Hospital Medical School, University of Melbourne, Melbourne, Victoria, Australia; and ⁴Department of Nuclear Medicine, La Timone Hospital, Aix-Marseille University, Marseille, France

We would like to draw attention to the latest advances in the field of peptide receptor radionuclide therapy (PRRT) of neuroendocrine tumors (NETs) of gastroenteropancreatic origin. The term *NET* refers to well-differentiated tumors that can be grade 1 (Ki-67 index, <3), 2 (Ki-67, 3–20), or 3 (Ki-67, >20); it excludes poorly differentiated grade 3 neuroendocrine carcinomas.

The seminal NETTER-1 trial has positioned PRRT with ¹⁷⁷Lu-DOTATATE at the forefront of oncologic treatments in patients with midgut NETs that have progressed on somatostatin analogs; the treatment has shown a major improvement in progression-free survival (PFS) and a positive impact on time to deterioration of quality of life. At long-term follow-up, improvement in overall survival was nonsignificant. Late serious adverse events were rare; myelodysplasia occurred in 2 of 111 (2%) ¹⁷⁷Lu-DOTATATE-treated patients, with 1 death (1). The disease in most patients ultimately progresses. Retreatment is not standardized, but some trials are ongoing (NCT04954820).

NETTER-1, however, did not include pancreatic NETs; also, in some countries PRRT is not reimbursed for this specific indication. Therefore, the results of the OCLURANDOM trial, recently presented at the European Society of Medical Oncology 2022 meeting, are important (2). On the other hand, multiple options are being actively investigated to increase the objective response rate over that obtained in NETTER-1 (18%) and further improve outcomes with PRRT.

PANCREATIC NETS

In the prospective randomized noncomparative phase II study OCLURANDOM (2), patients with somatostatin receptor (SSTR) imaging-positive advanced pancreatic NETs with progressive disease were randomized 1:1 to ¹⁷⁷Lu-DOTATATE, 7.4 GBq every 8 wk for 4 cycles (¹⁷⁷Lu-octreotate arm, *n* = 41), or the antiangiogenic agent sunitinib, 37.5 mg/d (sunitinib arm, *n* = 43). Among the included patients, 81% had grade 2 or 3, 37% had a Ki-67 of more than 10%, 42% had more than 25% liver involvement, 43% had received 2 or more prior systemic lines, and 57% had received prior chemotherapy. The primary endpoint was met, with a 12-mo PFS rate of 80% in the ¹⁷⁷Lu-octreotate arm and 42% in the sunitinib arm.

Median PFS was 20.7 mo in the ¹⁷⁷Lu-octreotate arm and 11 mo in the sunitinib arm. Grade 3 or higher adverse events occurred less frequently in the ¹⁷⁷Lu-octreotate arm (44%) than in the sunitinib arm (60%). Other important results are expected with final trial analysis.

Some ongoing phase III trials enrolled both pancreatic NET patients and gastroenteric NET patients. COMPETE (NCT03049189) is comparing ¹⁷⁷Lu-DOTATOC with the mammalian-target-of-rapamycin inhibitor everolimus in grade 1 or 2 gastroenteropancreatic NETs, with 309 enrolled patients. Substudies within this trial are investigating the role of dosimetry. NETTER-2 (NCT03972488) and COMPOSE (NCT04919226) are exploring the role of PRRT in gastroenteropancreatic NET patients with high grade 2 or 3 tumors (Ki-67 range, 10%–55%).

SSTR ANTAGONISTS

Somatostatin antagonist analogs are not internalized but display higher occupancy and more prolonged binding to SSTR than do agonists. In a phase I study of ¹⁷⁷Lu-satoreotide tetraxetan (also called ¹⁷⁷Lu-IPN01072, ¹⁷⁷Lu-OPS201, and ¹⁷⁷Lu-DOTA-JR11) in 20 NET patients, the maximum activity was 7.4 GBq/cycle (3). Although response rates were encouraging, 4 of 7 patients (57%) experienced grade 4 hematologic toxicity after cycle 2, hence leading to a modification in the protocol. A phase I/II trial (NCT02592707) with ¹⁷⁷Lu-satoreotide has now completed its recruitment. Part A enrolled 15 patients who received 3 cycles of ¹⁷⁷Lu-satoreotide tetraxetan with 4.5 GBq (peptide mass, 300 µg)/cycle. Part B enrolled 25 patients who completed 1–5 cycles at different administered activities (4.5 or 6.0 GBq/cycle) and peptide masses (300, 700, or 1,300 µg/cycle). Preliminary reporting at the European Society of Medical Oncology 2020 meeting described safety and early efficacy data (4). The major toxicities were hematologic, the objective response rate was 21%, and for the 20 patients with adequate follow-up, the disease control rate at 12 mo was 90%.

¹⁷⁷Lu-DOTA-LM3 is another SSTR antagonist, recently evaluated in 51 metastatic NET patients (5). ⁶⁸Ga-NODAGA-LM3 PET/CT was used for patient selection. Therapy cycles ranged between 1 (half the patients) and 4, with a median of 6.1 GBq/cycle. Partial response was obtained in 36.2%. Grade 3 thrombocytopenia occurred in 5.9% of patients.

α-THERAPY AND OTHER PROMISING RADIONUCLIDES

Initial results with α-emitting radioligands are also promising. A phase 1 dose-escalation trial evaluated ²¹²Pb-DOTAMTATE in

Received Nov. 5, 2022; revision accepted Jan. 4, 2023.

For correspondence or reprints, contact Elif Hindié (elif.hindie@chu-bordeaux.fr).

Published online Jan. 5, 2023.

COPYRIGHT © 2023 by the Society of Nuclear Medicine and Molecular Imaging.

DOI: 10.2967/jnumed.122.264422

PRRT-naïve NET patients (6). In the absence of dose-limiting toxicity, the recommended phase 2 dose was established at the highest activity tested, defined as a 2.50 MBq/kg dose of ²¹²Pb-DOTAMTATE administered 4 times at 8-wk intervals. For the first 10 subjects treated at this recommended activity, the objective response rate was 80%. There were 2 cases of transient renal toxicity and 1 case of renal toxicity that did not recover, but that patient had several confounding factors. A phase II study of ²¹²Pb-DOTAMTATE (NCT05153772) is ongoing.

In a single-center study, 91 patients received ²²⁵Ac-DOTATATE (100–120 kBq/kg of body weight) at 8-wk intervals (median, 4 cycles; range, 1–10). All patients received concomitant capecitabine therapy (7). Fifty-seven had received prior ¹⁷⁷Lu-DOTATATE therapy, with 33 being considered to have progressive disease or disease refractory to ¹⁷⁷Lu-PRRT. Treatment-related toxicities were deemed minimal. Among 79 patients with assessable disease, the objective response rate was 51%. The 24-mo PFS was 67.5%. Prior ¹⁷⁷Lu-PRRT–refractory disease was associated with poorer PFS. A prospective phase 1b/3 trial (NCT05477576) of ²²⁵Ac-DOTATATE in gastroenteropancreatic NET patients who experienced progression after ¹⁷⁷Lu-somatostatin analog therapy is ongoing.

From preclinical studies, the combined β- and Auger-emitter ¹⁶¹Tb also appears promising, especially when coupled to an SSTR antagonist, probably leading to substantial damage to tumor cell membranes (8).

⁶⁷Cu-SARTATE PRRT can be paired with ⁶⁴Cu-SARTATE with the potential for dosimetry planning (9). The chelator MeCOSar (5-(8-methyl-3,6,10,13,16,19-hexaaza-bicyclo[6.6.6]icosan-1-ylamino)-5-oxopentanoic acid) offers improved retention of copper compared with previous chelators. ⁶⁷Cu-SARTATE has entered clinical trials, albeit in neuroblastoma (NCT04023331).

LIVER-DOMINANT DISEASE

A subtle way to increase the uptake of radioligands in liver metastases could be the use of intraarterial PRRT after selective catheterization of the hepatic artery. A non–head-to-head comparison of intraarterial PRRT (15 patients) versus the standard intravenous route (14 other patients) found that intraarterial PRRT was associated with a higher concentration and absorbed dose in liver metastases (10). Whether a higher response rate was achieved was not reported. Prospective studies are needed since earlier reports were not uniformly positive. Trials with intraarterial ¹⁷⁷Lu-DOTATATE are ongoing (NCT03590119, NCT04837885).

COMBINATION THERAPY

Many studies have investigated PRRT combined with chemotherapy, notably in higher-grade tumors or ¹⁸F-FDG–avid metastatic disease, as it is associated with a poorer prognosis (11). A phase II study evaluated ¹⁷⁷Lu-DOTATATE (5 cycles of 5.5 GBq each) plus oral capecitabine in the intercycle in patients with ¹⁸F-FDG–positive advanced gastroenteropancreatic NETs (12). Of 37 enrolled patients, 68% had G2 or G3 NETs and 68% had pancreatic NETs. Grade 3 or 4 adverse events included hematologic toxicity (16.2%), diarrhea (5.4%), and asthenia (5.4%). Five patients (13%) discontinued the protocol. No renal toxicity was observed. A partial response 3 mo after the end of the 5 cycles was obtained in 10 of 33 evaluable patients (30%). The median PFS was 31.4 mo but still was difficult to interpret in the absence of randomization. The phase II CONTROL NET trial presented at 2022 meeting of the American

Society of Clinical Oncology evaluated the combination of PRRT (¹⁷⁷Lu-DOTATATE) and capecitabine plus temozolomide (CAPTEM) in 75 patients with advanced progressive NETs (45 midgut NETs and 27 pancreatic NETs) (13). Patients with midgut NETs were randomized 2 to 1 to PRRT + CAPTEM (*n* = 33) or PRRT alone (*n* = 14), and those with pancreatic NETs were randomized 2 to 1 to PRRT + CAPTEM (*n* = 19) or CAPTEM alone (*n* = 9). A nonsignificant trend for better PFS (hazard ratio, 0.41; *P* = 0.08) with PRRT + CAPTEM was observed for pancreatic NET patients, suggesting continuing investigations in this subgroup of NET patients only (13). The risk of long-term hematologic toxicity should be considered (14).

There is also a lot of exciting preclinical work and ongoing trials in NET patients on the combination of PRRT with immune checkpoint inhibitors, such as pembrolizumab (NCT03457948) or nivolumab (NCT04525638), or with DNA-damage response-modifying agents, such as the poly(adenosine diphosphate-ribose) polymerase inhibitors olaparib (NCT04086485, NCT04375267) and talazoparib (NCT05053854), the DNA-dependent protein kinase inhibitor peposertib (NCT04750954), or the ribonucleotide reductase inhibitor 3-aminopyridine-2-carboxaldehyde thiosemicarbazone (Triapine; Nanoshift, LLC) (NCT04234568).

The mentioned clinical trials, and others investigating the role of dosimetry and predictive imaging and blood biomarkers to improve patient selection and precision medicine approaches to personalized treatment, will no doubt further reinforce the role of PRRT in gastroenteropancreatic NET patients in the years to come.

DISCLOSURE

¹⁷⁷Lu-DOTATATE for the academic OCLURANDOM trial was supplied by AAA/Novartis. Eric Baudin and David Taieb are advisors for AAA/Novartis. Rodney Hicks is a shareholder of Telix Pharmaceuticals. No other potential conflict of interest relevant to this article was reported.

REFERENCES

1. Strosberg JR, Caplin ME, Kunz PL, et al. ¹⁷⁷Lu-Dotatate plus long-acting octreotide versus high-dose long-acting octreotide in patients with midgut neuroendocrine tumours (NETTER-1): final overall survival and long-term safety results from an open-label, randomised, controlled, phase 3 trial. *Lancet Oncol*. 2021;22:1752–1763.
2. Baudin E, Walter TA, Beron A, et al. First multicentric randomized phase II trial investigating the antitumor efficacy of peptide receptor radionuclide therapy with ¹⁷⁷lutetium-octreotate (OCLU) in unresectable progressive neuroendocrine pancreatic tumor: results of the OCLURANDOM trial [abstract]. *Ann Oncol*. 2022;33(suppl 7):S954.
3. Reidy-Lagunes D, Pandit-Taskar N, O'Donoghue JA, et al. Phase I trial of well-differentiated neuroendocrine tumors (NETs) with radiolabeled somatostatin antagonist ¹⁷⁷Lu-satoreotide tetraxetan. *Clin Cancer Res*. 2019;25:6939–6947.
4. Nicolas GP, Ansquer C, Lenzo NP, et al. An international open-label study on safety and efficacy of ¹⁷⁷Lu-satoreotide tetraxetan in somatostatin receptor positive neuroendocrine tumours (NETs): an interim analysis [abstract]. *Ann Oncol*. 2020;31(suppl 4):S771.
5. Baum RP, Zhang J, Schuchardt C, Muller D, Macke H. First-in-humans study of the SSTR antagonist ¹⁷⁷Lu-DOTA-LM3 for peptide receptor radionuclide therapy in patients with metastatic neuroendocrine neoplasms: dosimetry, safety, and efficacy. *J Nucl Med*. 2021;62:1571–1581.
6. Delpassand ES, Tworowska I, Esfandiari R, et al. Targeted α-emitter therapy with ²¹²Pb-DOTAMTATE for the treatment of metastatic SSTR-expressing neuroendocrine tumors: first-in-humans dose-escalation clinical trial. *J Nucl Med*. 2022;63:1326–1333.
7. Ballal S, Yadav MP, Tripathi M, Sahoo RK, Bal C. Survival outcomes in metastatic gastroenteropancreatic neuroendocrine tumor patients receiving concomitant

- ²²⁵Ac-DOTATATE targeted alpha therapy and capecitabine: a real-world scenario management based long-term outcome study. *J Nucl Med*. July 21, 2022 [Epub ahead of print].
8. Borgna F, Haller S, Rodriguez JMM, et al. Combination of terbium-161 with somatostatin receptor antagonists: a potential paradigm shift for the treatment of neuroendocrine neoplasms. *Eur J Nucl Med Mol Imaging*. 2022;49:1113–1126.
 9. Hicks RJ, Jackson P, Kong G, et al. ⁶⁴Cu-SARTATE PET imaging of patients with neuroendocrine tumors demonstrates high tumor uptake and retention, potentially allowing prospective dosimetry for peptide receptor radionuclide therapy. *J Nucl Med*. 2019;60:777–785.
 10. Thakral P, Sen I, Das SS, Manda D, Cb V, Malik D. Dosimetric analyses of intra-arterial versus standard intravenous administration of ¹⁷⁷Lu-DOTATATE in patients of well differentiated neuroendocrine tumor with liver-dominant metastatic disease. *Br J Radiol*. 2021;94:20210403.
 11. Binderup T, Knigge U, Johnbeck CB, et al. ¹⁸F-FDG PET is superior to WHO grading as a prognostic tool in neuroendocrine neoplasms and useful in guiding PRRT: a prospective 10-year follow-up study. *J Nucl Med*. 2021;62:808–815.
 12. Nicolini S, Bodei L, Bongiovanni A, et al. Combined use of ¹⁷⁷Lu-DOTATATE and metronomic capecitabine (Lu-X) in FDG-positive gastro-entero-pancreatic neuroendocrine tumors. *Eur J Nucl Med Mol Imaging*. 2021;48:3260–3267.
 13. Pavlakis N, Ransom DT, Wyld D. Australasian gastrointestinal trials group (AGITG) CONTROL NET study: ¹⁷⁷Lu-DOTATATE peptide receptor radionuclide therapy (PRRT) and capecitabine plus temozolomide (CAPTEM) for pancreas and midgut neuroendocrine tumours (pNETS, mNETS)—final results [abstract]. *J Clin Oncol*. 2022;40(suppl):4122.
 14. Kesavan M, Grover P, Lam WS, Claringbold PG, Turner JH. Long-term hematologic toxicity of ¹⁷⁷Lu-octreotate-capecitabine-temozolomide therapy of GEPNET. *Endocr Relat Cancer*. 2021;28:521–527.

Summary: Appropriate Use Criteria for Lymphoscintigraphy in Sentinel Node Mapping and Lymphedema/Lipedema

Kevin J. Donohoe¹, Brett J. Carroll², David K. V. Chung³, Elizabeth H. Dibble^{1,4}, Emilia Diego⁵, Francesco Giammarile⁶, Frederick D. Grant¹, Stephen Y. Lai⁷, Hannah Linden⁸, Megan E. Miller⁹, Neeta Pandit-Taskar^{1,10}, Nicholas E. Tawa, Jr.¹¹, and Sergi Vidal-Sicart⁶

¹Society of Nuclear Medicine and Molecular Imaging, Reston, Virginia; ²Society for Vascular Medicine, East Dundee, Illinois; ³Australia and New Zealand Society of Nuclear Medicine, Vermont South, Australia; ⁴American College of Radiology, Reston, Virginia; ⁵Society of Surgical Oncology, Rosemont, Illinois; ⁶European Association of Nuclear Medicine, Vienna, Austria; ⁷American Head and Neck Society, Los Angeles, California; ⁸American Society of Clinical Oncology, Alexandria, Virginia; ⁹American Society of Breast Surgeons, Columbia, Maryland; ¹⁰American College of Nuclear Medicine, Reston, Virginia; and ¹¹American College of Surgeons, Chicago, Illinois

Expert representatives from 11 professional societies, as part of an autonomous work group, researched and developed appropriate use criteria (AUC) for lymphoscintigraphy in sentinel lymph node mapping and lymphedema. The complete findings and discussions of the work group, including example clinical scenarios, were published on October 8, 2022, and are available at <https://www.snmmi.org/ClinicalPractice/content.aspx?ItemNumber=42021>. The complete AUC document includes clinical scenarios for scintigraphy in patients with breast, cutaneous, and other cancers, as well as for mapping lymphatic flow in lymphedema. Pediatric considerations are addressed. These AUC are intended to assist health care practitioners considering lymphoscintigraphy. Presented here is a brief overview of the AUC, including the rationale and methodology behind development of the document. For detailed findings of the work group, the reader should refer to the complete AUC document online.

Key Words: lymphoscintigraphy; lymphedema/lipedema; appropriate use; sentinel node mapping

J Nucl Med 2023; 64:525–528
DOI: 10.2967/jnumed.123.265560

Since the introduction of the “sentinel lymph node” (SLN) concept more than 40 y ago the use of lymphoscintigraphy for mapping the lymphatic system and localizing sentinel nodes has evolved with improvements in imaging technology and in the expanding clinical use of lymphatic mapping. To better define current recommendations for the use of lymphoscintigraphy, expert representatives from 11 professional societies, as part of an autonomous work group, researched and developed appropriate use criteria (AUC) to describe the use of lymphoscintigraphy in SLN mapping and lymphedema. This process was performed in accordance with the Protecting Access to Medicare Act of 2014, which requires that all referring physicians consult AUC by using a

clinical decision support mechanism before ordering advanced diagnostic imaging services. The result of the literature review and workgroup discussions was published on the Society of Nuclear Medicine and Molecular Imaging (SNMMI) website on October 8, 2022, and is available at <https://www.snmmi.org/ClinicalPractice/content.aspx?ItemNumber=42021>. Here we present a brief report on and summary of these AUC.

The full AUC include several possible clinical scenarios for which lymphoscintigraphy may be considered. Once these clinical scenarios were collected, the expert panel considered and graded them for appropriateness based on available literature as well as expert opinion. The most common current clinical use of lymphoscintigraphy is for SLN detection of breast and cutaneous malignancies; therefore, these indications are covered in more detail. However, the value of lymphoscintigraphy is recognized for SLN detection in other malignancies, as well as for mapping lymphatic flow in lymphedema. The work group prepared the AUC to assist health care practitioners who may be considering lymphoscintigraphy for their patients. Because each patient is unique, the appropriateness recommendations should not replace clinical judgment.

Mapping of sentinel node location should be performed for each patient undergoing SLN sampling. SLN mapping can be done with optical agents, such as isosulfan or methylene blue, as well as with radiotracers and fluorescent tracers or a combination of techniques. SLN localization with these techniques in individual patients has allowed a more accurate localization of nodes draining a primary tumor site. Histopathologic evaluation of the sentinel node allows patients to avoid the risk of the morbidity and mortality associated with complete node bed dissection if there is no evidence of metastatic disease in the sentinel node. The full AUC document discusses the challenges with the variety of lymphoscintigraphy tracers in use around the world. In the United States, only 2 tracers are generally available for clinical use: ^{99m}Tc-sulfur colloid and ^{99m}Tc-tilmanocept. Those tracers were the primary radiopharmaceuticals considered in the writing of the AUC document.

METHODOLOGY

Expert Work Group

Experts in this AUC work group were convened by SNMMI to represent a multidisciplinary panel of health care providers with substantive knowledge about the use of nuclear medicine in

Received Feb. 3, 2023; revision accepted Feb. 3, 2023.
For correspondence or reprints, contact Kevin J. Donohoe (kjd@bidmc.harvard.edu).
Published online Mar. 23, 2023.
COPYRIGHT © 2023 by the Society of Nuclear Medicine and Molecular Imaging.

lymphoscintigraphy. In addition to SNMMI members, representatives from the Society for Vascular Medicine, Australia and New Zealand Society of Nuclear Medicine, American College of Radiology, Society of Surgical Radiology, European Association of Nuclear Medicine, American Head and Neck Society, American Society of Clinical Oncology, American Society of Breast Surgeons, American College of Nuclear Medicine, and American College of Surgeons were included in the work group. Thirteen physician members were ultimately selected to participate and contribute to the AUC. A complete list of work group participants and external reviewers can be found in Appendix A in the online version of the AUC, where additional appendices provide term definitions and acronyms, author disclosures, and the process used to engage public commentary. Also included are qualifying statements and evidence limitations.

AUC Development

The process for AUC development was modeled after the RAND/UCLA Appropriateness Method and included identification of relevant clinical scenarios in which lymphoscintigraphy may be used, a systematic review of evidence related to these clinical scenarios, and a systematic synthesis of available evidence, followed by grading of each of the clinical scenarios using a modified Delphi process. In addition, the work group followed Institute of Medicine standards for developing trustworthy clinical guidance. The final document was drafted based on group ratings and discussions. A total of 32 relevant clinical scenarios were identified, with resulting AUC based on evidence and expert opinion regarding diagnostic accuracy and effects on clinical outcomes and clinical decision making. Other factors affecting the AUC recommendations were potential harm (including long-term harm, which may be difficult to

capture), costs, availability, and patient preferences. An extensive systematic review of the relevant literature was conducted by the Pacific Northwest Evidence-Based Practice Center at the Oregon Health and Science University under the direction of Roger Chou, MD, guided by key questions from the work group about lymphoscintigraphy in nodal staging and lymphatic dysfunction. Inclusion criteria, search parameters, and databases searched are included in the full AUC document, as well as data extraction, evidence weighting, rating, and scoring procedures. The work group met several times online via audiovisual conference to analyze results and contribute clinical expertise to derive final consensus scores for each clinical indication/scenario. Final appropriate use ratings were summarized in a format similar to the RAND/UCLA Appropriateness Method. Each clinical scenario was scored on a scale from 1 to 9; a score of 7–9 indicates that the procedure is appropriate for the specific clinical indication and is generally considered acceptable; a score of 4–6 indicates that the procedure may be appropriate for the specific indication and may imply that more evidence is needed to definitively classify the indication; and a score of 1–3 indicates that the procedure is rarely appropriate for the specific indication. Division of scores into 3 general levels of appropriateness is partially arbitrary, and numeric designations should be viewed as a continuum. When work group members could not agree on a common score, those indications were given “may be appropriate” ratings to indicate a lack of definitive literature and lack of work group consensus, indicating the need for additional research.

SUMMARY RECOMMENDATIONS FROM THE WORK GROUP

Breast Cancer (Table 1)

The use of radiopharmaceuticals for SLN mapping in breast cancer is appropriate for patients <70 y old after initial diagnosis

TABLE 1
Appropriateness Ratings for Clinical Scenarios for Lymphoscintigraphy in Breast Cancer

Scenario no.	Description	Appropriateness	Score
1	Invasive breast cancer of any histologic type without evidence of axillary or distant metastases and without evidence of skin or chest wall invasion	Appropriate	9
2	Invasive breast cancer of any histologic type with pathologic evidence of axillary metastases and no evidence of skin or local chest wall invasion or distant metastases	May be appropriate	5
3	Invasive breast cancer of any histologic type with evidence of distant metastases	May be appropriate	5
4	Ductal carcinoma in situ (DCIS) without suspicious features and DCIS or pleomorphic lobular carcinoma in situ (LCIS) without planned mastectomy or other surgery affecting lymphatic drainage	Rarely appropriate	2
5	DCIS with suspicious features and DCIS or pleomorphic LCIS with planned mastectomy or other surgery affecting lymphatic drainage	Appropriate	8
6	Planned reduction mammoplasty or risk-reducing mastectomy in patients without a known breast cancer diagnosis	Rarely appropriate	1
7	In-breast recurrence or de novo ipsilateral breast cancer without evidence of axillary or distant metastases and without evidence of skin or chest wall invasion	Appropriate	9
8	Inflammatory breast cancer or breast cancer with evidence of skin or local chest wall invasion	Rarely appropriate	1
9	Phyllodes tumor	Rarely appropriate	1
10	Paget disease of the breast, cancer not identified before surgery	May be appropriate	6

TABLE 2
Appropriateness Ratings for Clinical Scenarios for Lymphoscintigraphy in Skin Cancer

Scenario no.	Description	Appropriateness	Score
11	Primary cutaneous melanoma of appropriate stage without clinical evidence of metastasis	Appropriate	9
12	Cutaneous melanoma after a local-regional recurrence	May be appropriate	6
13	Pigmented lesions of uncertain metastatic potential	May be appropriate	6
14	Primary melanoma of the anus or vagina without clinical evidence of metastasis	Appropriate	7
15	Cutaneous and mucosal (penile, vulvar) squamous cell carcinoma (SCC) or basal cell carcinoma without clinical evidence of metastasis	Appropriate	8
16	Merkel cell carcinoma without clinical evidence of metastasis	Appropriate	9
17	Malignant adnexal cutaneous tumors (eccrine, sweat gland, SCC with eccrine dedifferentiation) without clinical evidence of metastasis	May be appropriate	6
18	Selected sarcoma subtypes (synovial, epithelioid, rhabdomyosarcoma, angiosarcoma, clear cell sarcoma) without evidence of metastasis	May be appropriate	6

of invasive breast cancer of any histologic type if there is no clinical or imaging-based evidence of axillary or distant metastasis, either in the de novo setting or in the setting of an in-breast recurrence. In patients with evidence of local or distant metastatic disease, however, the benefit of SLN mapping is less apparent.

SLN biopsy (SLNB) may be appropriate in patients ≥ 70 -y-old if the results will impact adjuvant treatment. SLN mapping may also be considered appropriate in patients with ductal carcinoma in situ or pleomorphic lobular carcinoma in situ for whom a mastectomy is planned or in the setting of breast-conserving surgery where the procedure may affect the option for future lymphatic mapping or where suspicion for invasive disease is present.

SLN mapping is rarely appropriate in patients diagnosed with an inflammatory breast cancer or breast cancer with evidence of skin or local chest wall invasion, with Paget disease of the breast without evidence of an underlying invasive cancer identified before surgery, with Phyllodes tumors, or in the setting of a prophylactic mastectomy or reduction mammoplasty in women without a history of breast cancer.

Skin Cancer (Table 2)

SLNB has been shown to be helpful in the management of patients with melanoma and Merkel cell carcinoma. Preliminary evidence of SLNB with other cutaneous lesions suggests there may be some utility; however, more controlled studies are needed. At present, SLNB in rare tumors may be performed when the nodal status will affect management, when the possibility of nodal metastasis is believed to be significant, or when there is no other evidence of metastatic disease. As therapy for some cutaneous malignancies improves, the need for SLNB will change, particularly when sentinel node status no longer changes management or prognosis.

Cancers at Other Sites (Table 3)

The success of sentinel node localization in melanoma and breast cancer has led to the application of sentinel node scintigraphy to several other diseases, including gynecologic, gastrointestinal, urologic, bladder and renal, and thyroid cancers. Other than for cervical cancer and oral cavity cancers, the effectiveness of SLNB using radiotracers in these other malignancies is still under investigation.

TABLE 3
Appropriateness Ratings for Clinical Scenarios for Lymphoscintigraphy in Cancers at Other Sites

Scenario no.	Description	Appropriateness	Score
19	Prostate cancer (initial stage)	Appropriate	7
20	Cervical cancer (initial stage)	Appropriate	7
21	Endometrial cancer, low-risk patient	May be appropriate	5
22	Endometrial cancer, high-risk patient	May be appropriate	6
23	Ovarian cancer	Rarely appropriate	3
24	Vaginal squamous cell cancer	May be appropriate	6
25	Primary malignancy of the gastrointestinal tract without clinical evidence of metastasis	May be appropriate	5
26	Oral cavity cancer	Appropriate	9
27	Oropharyngeal cancer	May be appropriate	6

TABLE 4
 Appropriateness Ratings for Clinical Scenarios for Lymphoscintigraphy in Lymphedema and Lipedema

Scenario no.	Description	Appropriateness	Score
28	Clinical suspicion for primary lymphedema of the extremities	Appropriate	8
29	Clinical suspicion for secondary lymphedema of the extremities	Appropriate	7
30	Clinical suspicion for breast lymphedema	May be appropriate	4
31	Lipedema of the extremities	May be appropriate	6
32	Limb edema of unclear etiology	Appropriate	8

Lymphedema (Table 4)

Lymphoscintigraphy is an appropriate test for evaluation of primary lymphedema or limb edema of unclear etiology. Lymphoscintigraphy can also be appropriate for patients with suspicion for secondary lymphedema, particularly if the clinical history or exam is not definitive for the diagnosis of lymphedema. Lymphoscintigraphy can be helpful to confirm lymphatic dysfunction before lymphatic surgery. Lymphoscintigraphy may be appropriate in select patients with lipedema or breast lymphedema, although the value of lymphoscintigraphy in these populations is not widely published.

Pediatric Considerations

The pediatric indications for lymphoscintigraphy and SLNB are similar to those in adults, although the differing incidences and causes of lymphatic diseases in children should be considered.

It is uncommon for studies of the clinical utility of lymphoscintigraphy to focus solely on children, yet many published reports include children in their study populations. Lymphoscintigraphy has been reported to have a role in guiding the management and treatment of some pediatric cancers and in evaluation of lymphedema in children. The complete AUC document includes statements on lymphoscintigraphy in pediatric breast and skin cancers, as well as pediatric sarcoma and lymphedema.

SUMMARY

This report is a summary of the complete Appropriate Use Criteria for Lymphoscintigraphy in Sentinel Node Mapping and Lymphedema/Lipedema, available at <https://www.snmni.org/ClinicalPractice/content.aspx?ItemNumber=42021>.

Real-Life Experience in the Treatment of Intrahepatic Cholangiocarcinoma by ⁹⁰Y Radioembolization: A Multicenter Retrospective Study

Benedikt M. Schaarschmidt¹, Roman Kloeckner², Thomas Dertnig¹, Aydin Demircioglu¹, Lukas Müller², Timo Alexander Auer^{3,4}, Daniel Pinto dos Santos^{5,6}, Verena Steinle⁷, Matthias Miederer⁸, Bernhard Gebauer³, Sonia Radunz⁹, Stefan Kasper¹⁰, Manuel Weber¹¹, and Jens Theysohn¹

¹Institute of Diagnostic and Interventional Radiology and Neuroradiology, University Hospital Essen, Essen, Germany; ²Department of Diagnostic and Interventional Radiology, University Medical Center of the Johannes Gutenberg University Mainz, Mainz, Germany; ³Department of Radiology, Charité–Universitätsmedizin Berlin, Corporate Member of Freie Universität Berlin and Humboldt Universität zu Berlin, Berlin, Germany; ⁴Berlin Institute of Health, Berlin, Germany; ⁵Department of Diagnostic and Interventional Radiology, Faculty of Medicine and University Hospital Cologne, University of Cologne, Cologne, Germany; ⁶Department of Diagnostic and Interventional Radiology, University Hospital Frankfurt, Frankfurt, Germany; ⁷Department of Diagnostic and Interventional Radiology, University Hospital of Heidelberg, Heidelberg, Germany; ⁸Clinic of Nuclear Medicine, University Medical Center of the Johannes Gutenberg University Mainz, Mainz, Germany; ⁹Department of General, Visceral, and Transplant Surgery, University Hospital Essen, Essen, Germany; ¹⁰Department of Medical Oncology, West German Cancer Center, University Hospital Essen, Essen, Germany; and ¹¹Clinic of Nuclear Medicine, University Hospital Essen, Essen, Germany

Limited treatment options in patients with intrahepatic cholangiocarcinoma (iCCA) demand the introduction of new, catheter-based treatment options. Especially, ⁹⁰Y radioembolization may expand therapeutic abilities beyond surgery or chemotherapy. Therefore, the purpose of this study was to identify factors associated with an improved median overall survival (mOS) in iCCA patients receiving radioembolization in a retrospective study at 5 major tertiary-care centers. **Methods:** In total, 138 radioembolizations in 128 patients with iCCA (female, 47.7%; male, 52.3%; mean age ± SD, 61.1 ± 13.4 y) were analyzed. Clinical data, imaging characteristics, and radioembolization reports, as well as data from RECIST, version 1.1, analysis performed 3, 6, and 12 mo after radioembolization, were collected. mOS was compared among different subgroups using Kaplan–Meier curves and the log-rank test. **Results:** Radioembolization was performed as first-line treatment in 25.4%, as second-line treatment in 38.4%, and as salvage treatment in 36.2%. In patients receiving first-line, second-line, and salvage radioembolization, the disease control rate was 68.6%, 52.8%, and 54.0% after 3 mo; 31.4%, 15.1%, and 12.0% after 6 mo; and 17.1%, 5.7%, and 6.0% after 1 y, respectively. In patients receiving radioembolization as first-line, second-line, and salvage treatment, mOS was 12.0 mo (95% CI, 7.6–23.4 mo), 11.8 mo (95% CI, 9.1–16.6 mo), and 8.4 mo (95% CI, 6.3–12.7 mo), respectively. No significant differences among the 3 groups were observed ($P = 0.15$). Hepatic tumor burden did not significantly influence mOS ($P = 0.12$). **Conclusion:** Especially in advanced iCCA, second-line and salvage radioembolization may be important treatment options. In addition to ongoing studies investigating the role of radioembolization as first-line treatment, the role of radioembolization in the later treatment stages of the disease demands further attention.

Key Words: cholangiocarcinoma; CCA; radioembolization; TARE; SIRT

Received Jun. 30, 2022; revision accepted Oct. 27, 2022.
For correspondence or reprints, contact Benedikt M. Schaarschmidt (benedikt.schaarschmidt@uk-essen.de).
Published online Nov. 3, 2022.
COPYRIGHT © 2023 by the Society of Nuclear Medicine and Molecular Imaging.

J Nucl Med 2023; 64:529–535
DOI: 10.2967/jnumed.122.264598

Cholangiocarcinoma is a rare, aggressive malignancy that accounts for approximately 3% of all gastrointestinal tumors and is associated with low median overall survival (mOS) rates (1,2). Surgery remains the most promising approach, although recurrence rates are high (2–6). In patients who have recurrent or metastatic disease or are ineligible for resection, therapeutic options are limited. In such cases, cytotoxic chemotherapy with modest response rates is the standard of care (4,6). Because other treatment options such as radiotherapy or thermal ablation are confined to small, localized tumors, various catheter-based treatment options have been proposed to overcome this troubling situation, most notably for intrahepatic cholangiocarcinoma (iCCA) (4,5,7). For this use, hepatic artery infusion, transarterial chemoembolization (TACE), and radioembolization have gained particular considerable attention.

In hepatic artery infusion, a high hepatic dose of a chemotherapeutic agent is achieved by local administration of a chemotherapeutic agent in the hepatic artery. Vascular access can be achieved either by surgical placement of a hepatic arterial infusion pump or by interventional catheter placement via the femoral artery. mOS of up to 25.0 mo has been reported (8,9).

TACE, on the other hand, relies on the combined effect of vessel occlusion at a capillary level and local administration of a chemotherapeutic agent. Promising results have been reported in recent meta-analyses, indicating an mOS of up to 15.9 mo in a selected patient cohort (10–12). In addition to conventional TACE, other embolic agents such as degradable starch microspheres or drug-eluting beads have been proposed. Because of small patient cohorts, however, a generalized recommendation on these new embolic agents cannot be derived from the available data (13–15).

Radioembolization uses the increased vasculature of intrahepatic tumors in comparison to hepatic tissue (16,17). Radioactive microspheres that have been previously injected into the hepatic artery accumulate predominantly in the capillary bed of tumors. The short range of β^- -radiation emitted by ^{90}Y ensures highly effective control of the local tumor, whereas the surrounding tissue is spared. Before radioembolization, pretherapeutic angiography followed by local injection of $^{99\text{m}}\text{Tc}$ -labeled macroaggregated albumin is mandatory to exclude extrahepatic shunting. With an mOS of up to 14.3 mo, the results are comparable to those for TACE (10–12,18,19).

Because of the lack of prospective, comparative studies, the overall evidence for each of these treatment regimens is low. Current recommendations are derived mostly from metaanalyses that are based on a variety of prospective and retrospective datasets with low patient numbers (10,11). In the advent of prospective studies focusing on early radioembolization, it is crucial to identify other potential applications for radioembolization in larger cohorts (20). Therefore, the aim of this multicenter retrospective study was to analyze the impact of clinical and tumor-associated factors on mOS. Such research will facilitate patient selection for radioembolization in the future and further the applications for this promising technique in iCCA patients beyond early radioembolization.

MATERIALS AND METHODS

Retrospectively, we collected data on patients with cholangiocarcinoma who underwent radioembolization at any of 5 major tertiary-care centers in Germany during the 14 y from May 2007 to May 2021. To be included, the patients had to have histopathologically proven iCCA and had to have undergone radioembolization. Exclusion criteria were extrahepatic cholangiocarcinomas such as Klatskin tumors or gallbladder carcinomas.

At each center, a standardized questionnaire was used to obtain all necessary data (supplemental data, section 1; supplemental materials are available at <http://jnm.snmjournals.org>). Tumor response was assessed according to RECIST, version 1.1, at the corresponding centers to obtain the disease control rate (DCR) after radioembolization (21). Then, data from each center were anonymized and merged into a single database for further statistical analysis. The institutional ethic committee of the

University Duisburg–Essen approved the study (application 20-9747-BO) on June 7, 2021. Because the analysis was retrospective, the need for informed consent was waived.

Statistical Analysis

OS was the primary endpoint of this study. Kaplan–Meier curves, including log-rank tests, were used to investigate the impact of tumor type, hepatic tumor burden, and tumor vascularization pattern; the presence of extrahepatic metastases and tumor-accompanying ailments such as ascites and cirrhosis; the administered microsphere type; and the line of therapy (first-line, second-line, or salvage therapy). Additionally,

TABLE 1
Baseline Characteristics of All Radioembolizations

Characteristic	%	<i>n</i>
Initial UICC tumor stage		
I	1.4	2
II	21	29
IIIa	14.5	20
IIIb	38.5	53
IV	20.3	28
Unknown	4.3	6
Tumor type		
Mass-forming	58.7	81
Diffuse intrahepatic	39.9	55
Unknown	1.4	2
Tumor vascularization		
Hypervascularized	34.8	48
Hypovascularized	36.2	50
Mixed appearance	22.5	31
Unknown	6.5	9
Hepatic tumor burden		
<25%	52.2	72
25%–50%	25.4	35
>50%	15.2	21
Unknown	7.2	10
Distant metastases at time of radioembolization		
Yes	43.5	60
Lymph nodes	10.1	14
Peritoneum	7.2	10
Pancreas	0.7	1
Lung	10.9	15
Bone	5.1	7
Brain	2.2	3
No	56.5	78
Liver cirrhosis at time of radioembolization		
Yes	15.9	22
No	83.4	115
Unknown	0.7	1
Ascites at time of radioembolization		
Yes	23.9	33
No	76.1	105

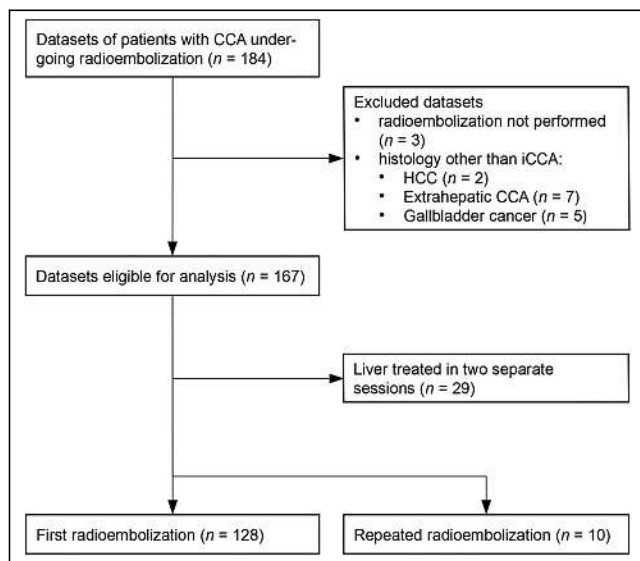


FIGURE 1. Flowchart of analyzed patients. CCA = cholangiocarcinoma; HCC = hepatocellular carcinoma.

a multivariable Cox regression analysis was performed (supplemental data, section 2).

A *P* value of less than 0.05 indicated statistical significance. Because the study was explorative, no α -error correction was performed. SPSS Statistics (version 27; IBM) and R (version 4.2.0; R Core Team, 2022) were used for statistical analysis.

RESULTS

Baseline Characteristics

Data on 184 radioembolizations in 142 patients were collected from all 5 centers. Seventeen cases did not match the inclusion criteria and were excluded from further analysis (Fig. 1). In 29 cases, the liver was treated in 2 separate sessions, which were considered as 1 treatment. Therefore, 138 radioembolizations in 128 patients were eligible for further analysis (female, 47.7% [61/128]; male, 52.3% [67/128]; mean height [\pm SD], 172.1 \pm 9.5 cm; mean weight, 75.3 \pm 17.1 kg; mean age, 61.1 \pm 13.4 y). In 10 cases, radioembolization was repeated because of relapse (Table 1; supplemental data, section 3).

Before radioembolization, other treatments had been conducted on 84.6% (103/138). In total, 25.4% (35/138) received first-line radioembolization without any prior therapy, 38.4% (53/138) received second-line radioembolization, and 36.2% (50/138) received salvage radioembolization after multiple prior therapies (Table 2). Section 4 of the supplemental data provides further information on baseline characteristics, preinterventional imaging, and radioembolization.

Follow-up Examinations

For the entire cohort, follow-up examinations were performed after 3 mo (mean, 86 \pm 49 d), 6 mo (mean, 166 \pm 78 d), and 1 y (mean, 346 \pm 81 d). DCR for the entire cohort was 57.2% (79/138) after 3 mo, 18.1% (25/138) after 6 mo, and 6.5% (9/138) after 1 y. In patients receiving first-line radioembolization, DCR was 68.6% (24/35) after 3 mo, 31.4% (11/35) after 6 mo, and 17.1% (6/35) after

1 y. In patients receiving second-line radioembolization, DCR was 52.8% (28/53) after 3 mo, 15.1% (8/53) after 6 mo, and 5.7% (3/53) after 1 y. In patients receiving radioembolization as a salvage treatment, however, DCR was 54.0% (27/50) after 3 mo, 12.0% (6/53) after 6 mo, and 6.0% (3/50) after 1 y.

Survival Analysis

mOS in the entire cohort was 10.7 mo (95% CI, 8.4–12.7 mo). One-year OS was 45.3% (95% CI, 37.2–55.2 mo), and 2-y OS was 16.7% (95% CI, 10.8–25.9 mo). At the time of the analysis, 75.4% (104/138) were deceased, 10.9% (15/138) were alive, and 13.7% (19/138) were lost to follow-up.

To identify potential differences among different subgroups, a further analysis was performed with a focus on the following tumor

TABLE 2
Treatments Before Radioembolization

Treatment	%	<i>n</i>
Prior therapy		
Yes	84.6	103
Hepatic surgery	31.9	44
Extrahepatic surgery	3.6	5
Radiation	2.9	4
Radioembolization	7.2	10
TACE/TAE/HAI	5.1	7
Local ablation (MWA/RFA)	5.8	8
Chemotherapy	62.3	86
Tyrosine kinase inhibitor therapy	2.2	3
No	25.4	35
First-line radioembolization	25.4	35
Second-line radioembolization	38.4	53
Salvage radioembolization	36.2	50

HAI = hepatic artery infusion; MWA = microwave ablation; RFA = radiofrequency ablation.

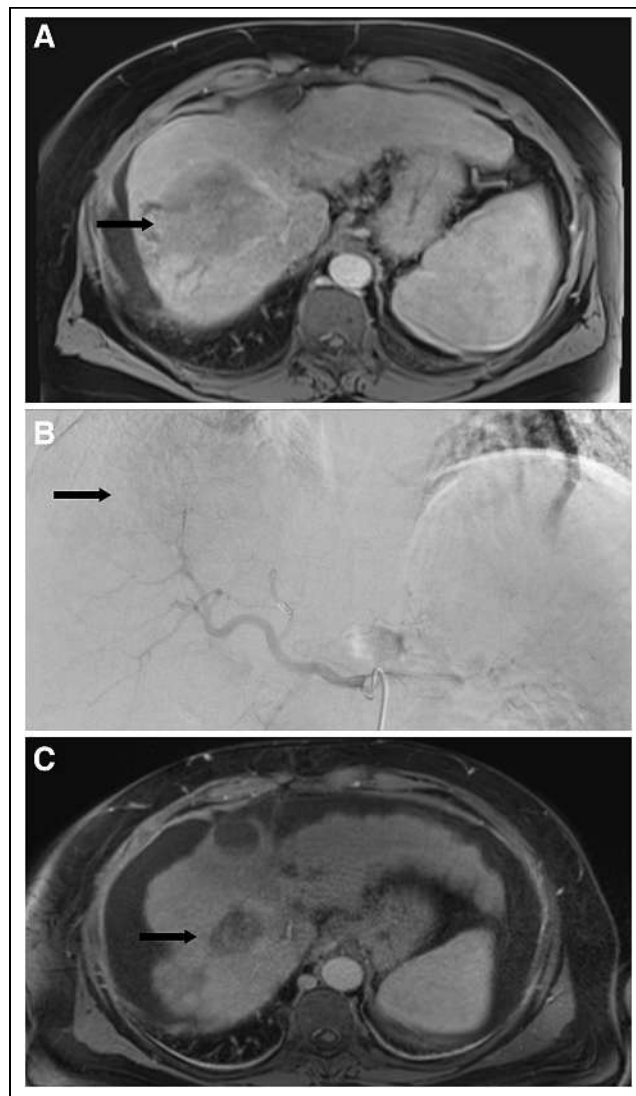


FIGURE 2. A 64-y-old man with stage 4 ICCA with lymph node metastases. (A and B) Initial MRI shows hypovascularized tumor in right liver lobe (A, arrow), with faint contrast agent uptake in preinterventional angiography with subsequent ^{99m}Tc -macroaggregated albumin injection (B, arrow). Radioembolization of right hepatic artery with 4.64 GBq was performed 27 d after ^{99m}Tc -macroaggregated albumin injection. (C) Postinterventional MRI 126 d after radioembolization showed partial tumor response (arrow). Patient died after 176 d.

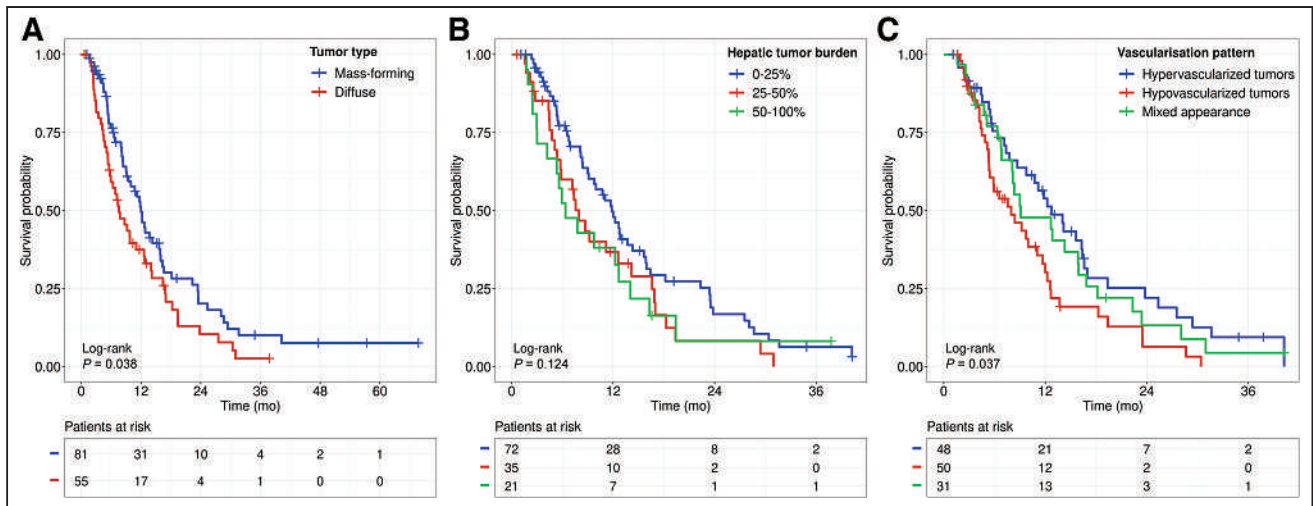


FIGURE 3. Kaplan–Meier survival curves for different tumor characteristics in analyzed cohort: tumor type (A), hepatic tumor burden (B), and tumor vascularization pattern (C).

characteristics: tumor type (diffuse vs. mass-forming), hepatic tumor burden, and tumor vascularization pattern. Mass-forming tumors had a significantly longer survival than tumors with a diffuse growth pattern (mass-forming, 12.0 mo [95% CI, 9.5–15.9 mo]; diffuse growth pattern, 7.6 mo [95% CI, 5.8–12.7 mo], $\chi^2_1 [n = 136] = 4.3, P = 0.038$, Fig. 2A). A lower hepatic tumor burden tended to be associated with an increased mOS (<25%, 11.8 mo [95% CI, 9.1–15.6 mo]; 25%–50%, 8.0 mo [95% CI, 5.8–16.6 mo]; >50%, 6.4 mo [95% CI, 4.2–16.3 mo]). However, no statistical differences among the subgroups were detected by the log-rank test ($\chi^2_2 [n = 128] = 4.2, P = 0.12$, Fig. 2B). mOS was 12.7 mo (95% CI, 9.8–17.0 mo) for hypervascularized tumors, 8.0 mo (95% CI, 5.4–12.0 mo) for hypovascularized tumors, and 9.1 mo (95% CI, 8.1–16.9) for tumors with a mixed appearance. According to the log-rank test, a slight significant difference in OS existed among the 3 subgroups ($\chi^2_1 [n = 129] = 6.6, P = 0.037$; Fig. 3).

Patients with extrahepatic metastases had a significantly shorter mOS than patients without distant metastases (extrahepatic metastases,

8.1 mo [95% CI, 6.4–12.2 mo]; no extrahepatic metastases, 12.7 mo [95% CI, 9.2–18.2 mo], $\chi^2_1 [n = 138] = 8.3, P = 0.004$). However, mOS was significantly influenced neither by the presence of liver cirrhosis (present, 11.7 mo [95% CI, 6.8–23.5 mo]; absent, 11.0 mo [95% CI, 8.4–13.7 mo]; $\chi^2_1 [n = 137] = 0.9, P = 0.34$) nor by the presence of ascites (present, 8.0 mo [95% CI, 6.3–19.4 mo]; absent, 11.0 mo [95% CI, 9.0–13.7 mo]; $\chi^2_1 [n = 138] = 0.2, P = 0.66$) (Fig. 4).

In the analyzed cohort, radioembolization was characterized as first-line (no prior therapy), second-line (only one kind of prior therapy), or salvage treatment (at least 2 prior therapies). In patients receiving radioembolization as first- and second-line treatment, mOS was 12.0 mo (95% CI, 7.6–23.4 mo) and 11.8 mo (95% CI, 9.1–16.6 mo), respectively. In patients receiving radioembolization as salvage therapy, mOS was 8.4 mo (95% CI, 6.3–12.7 mo). No significant differences among the 3 groups were detected by the log-rank test ($\chi^2_2 [n = 138] = 3.7, P = 0.15$; Fig. 5; supplemental data, section 4).

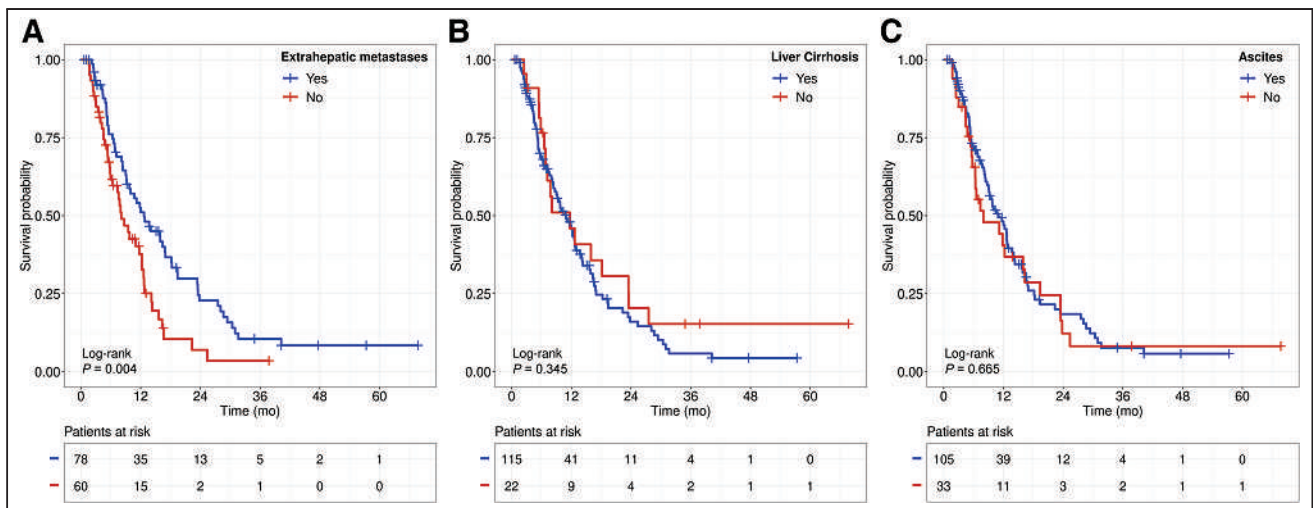


FIGURE 4. Kaplan–Meier survival curves for different baseline characteristics in analyzed cohort: extrahepatic metastases (A), liver cirrhosis (B), and ascites (C).

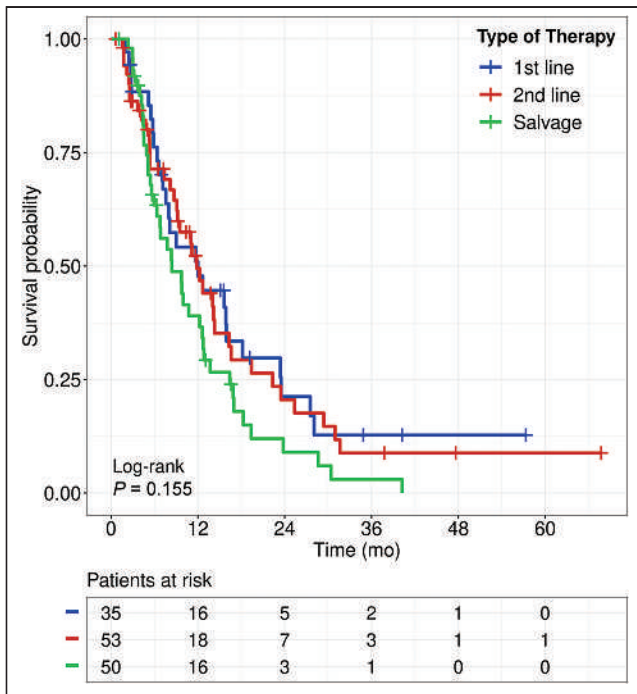


FIGURE 5. Kaplan–Meier survival curves for different treatment lines in analyzed cohort.

Cox Regression

The assumption of proportional hazards of the Cox model was met globally ($P = 0.55$) and by all variables ($P > 0.05$). The analysis revealed that the presence of extrahepatic metastases (hazard ratio [HR], 1.99 [95% CI, 1.25–3.2]; $P = 0.004$) and vascularization patterns other than hypervascularization (hypovascularization: HR, 2.27 [95% CI, 1.35–3.8]; $P = 0.002$) (mixed: HR 2.21 [95% CI, 1.15–4.2]; $P = 0.017$) were statistically significant predictors of a worse mOS (Fig. 6). Although higher HRs were observed for a higher hepatic tumor burden, no significant differences could be observed (25%–50%: HR, 1.46 [95% CI, 0.82–2.6]; $P = 0.197$) (>50%: HR, 1.60 [95% CI, 0.77–3.3]; $P = 0.209$).

DISCUSSION

To aid in making clinical decisions on iCCA patients, it is key to have a large retrospective study that identifies factors favoring radioembolization. Four main factors were identified in our multicenter study, comprising, to our knowledge, the largest cohort of iCCA patients treated with radioembolization to date. First, second-line or salvage radioembolization of iCCA patients is a viable option, with promising DCRs, and might have a favorable effect on mOS. Second, mOS is significantly longer in iCCA patients with hypervascularized tumors than in iCCA patients with other tumor types. Third, even a high tumor burden does not lead to significant changes in mOS. Fourth,

extrahepatic metastases have a significant impact on mOS in iCCA patients.

Despite relevant advances in oncology, treatment of iCCA remains challenging. At the moment, surgical treatment has to be considered the most favorable option. If complete tumor removal can be achieved, an mOS of up to 45.1 mo can be achieved in iCCA patients in general (6). In patients with resected iCCA, 5-y survival rates of up to 63% have been published (22,23). Despite the introduction of adjuvant radio- or chemotherapy, R0 resection remains a prerequisite for such a favorable outcome. However, because of the necessary extent of tumor removal, R0 resection can be achieved in approximately only 36% of cases. Chemotherapeutic regimens for iCCA are scarce (4,5). Hence, the lack of further therapeutic options leads to a relevant decrease in mOS if chemotherapy fails or patients are ineligible for medical therapy: although active palliative treatment still has an mOS of 10.6 mo, an mOS of only 4.0 mo for best supportive care was reported in the recent analysis of the European Network for the Study of Cholangiocarcinoma (ENSCCA) registry by Izquierdo-Sanchez et al. (6).

Therefore, expanding therapeutic options is of the utmost importance. Especially in liver-dominant disease, minimally invasive, catheter-based therapies such as hepatic artery infusion, TACE, or radioembolization might be important adjuncts to the contemporary arsenal (8–12). Although a comparative study between TACE and radioembolization has been started by Kloeckner et al., the results have not been published yet (24). As a result, no comparative studies between these options are available to date and no relevant differences between them have been reported in the available metaanalyses (11,12). However, distinct advantages of radioembolization are a favorable safety profile and excellent patient comfort (25). In comparison to TACE, postinterventional infections after radioembolization are exceptionally rare, and the short-term toxicity caused by postembolization syndrome can be

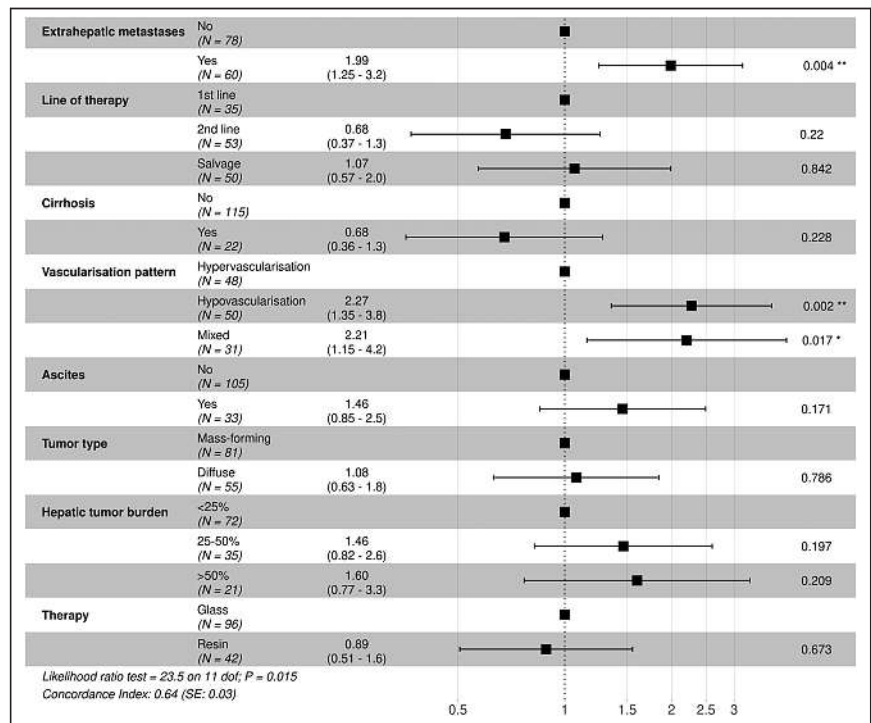


FIGURE 6. Forest plot for multivariable Cox regression analysis. dof = degrees of freedom.

drastically reduced (26,27). Our data confirm the potential of radioembolization as second-line treatment and in a salvage setting. Even in heavily pretreated patients, mOS after radioembolization was 8.4 mo, which is considerably higher than the mOS of patients receiving best supportive care in the ENSCCA registry (6). Furthermore, mOS in patients receiving salvage radioembolization did not differ significantly from that in patients receiving second-line radioembolization in our cohort and showed no relevant aberrations from previously published data on second-line radioembolization (25,28).

In this cohort, a significantly higher mOS was seen in patients with mass-forming and hypervascularized tumors. This observation is most likely associated with an increased accumulation of microspheres in the vasculature of the tumor—an accumulation that is far more distinct than in hypovascular masses or tumors with a diffuse growth pattern. These findings are interesting additions to those of Willowson et al., who found that a high total lesion glycolysis at baseline and a low tumor heterogeneity in ¹⁸F-FDG uptake were considered as predictors of treatment response (29). In recent studies, Bourien et al. and Manceau et al. found that tumor doses higher than 158 and 260 Gy, respectively, were predictive of tumor response in patients treated with and without concomitant chemotherapy and radioembolization (30,31). Henceforth, these findings may provide the basis for further inquiries into the role of personalized dosimetry in patients with iCCA. However, we did not find high hepatic tumor burden to have a negative impact on mOS as previously described by Paprottka et al. (25), thus confirming the preliminary results of Köhler et al. (20). Additionally, as previously reported, neither the presence of ascites nor liver cirrhosis seems to influence mOS after radioembolization (20,25).

In contrast to the study by Köhler et al., the presence of extrahepatic metastases had a significant impact on mOS in our cohort. Thus, our results are in accordance with a study by Jia et al., who observed, in a univariable Cox regression model, that the presence of lymph node metastases was significantly associated with survival (28). The most probable explanation for this finding is the notably larger patient cohort in the present study (20). Although this finding might be interpreted as an exclusion criterion for radioembolization, even in patients with liver-dominant disease, the lack of other treatment options could still lead to considerable gains in OS in comparison to best supportive care in this scenario.

At first sight, the results of first-line radioembolization have to be considered sobering. The observed mOS of 12.0 mo after first-line radioembolization is considerably lower than found in previously published surgical studies or the ENSCCA registry (6,22,23). Additionally, other retrospective studies on first-line radioembolization, such as a recent study by Buettner et al., reported an mOS of 16 mo (26). However, it is highly probable that radioembolization was reserved for patients ineligible for surgery or chemotherapy in our cohort, resulting in a potential selection bias. Still, as a minimally invasive procedure with limited side effects, first-line radioembolization may be a valuable option in patients who can neither undergo surgery nor receive chemotherapy. Because the literature on early radioembolization is limited (32), the final verdict on early radioembolization will depend on the overdue results of prospective studies such as the SIRRCA trial (NCT02807181).

The limitations of the study are caused mainly by its retrospective nature. In particular, retrospective data on iCCA patients treated with first-line radioembolization in the current clinical setting have to be

interpreted with extreme caution. As first-line radioembolization is not incorporated in the current guidelines, it is possible that mainly patients with comorbidities underwent this procedure in our cohort, which might result in a considerable selection bias. Further comparative studies are necessary before the value of first-line radioembolization can be judged appropriately. Additionally, differences in patient selection cannot be circumvented in the setting of the current study, stressing the need for further prospective investigations.

Low enrollment rates per year might have led to worse outcomes due to lack of user experience. However, all centers performed radioembolizations regularly for other tumors, such as hepatocellular carcinoma, leading to a high level of expertise at each participating center.

CT was the main imaging modality used in our cohort, albeit MRI is considered far more sensitive in evaluating local tumor spread in iCCA (4). Hence, an underestimation of tumor extent before radioembolization may be possible in the present cohort and may impact mOS analysis. As this analysis focused solely on radioembolization, and other treatment modalities were not investigated, a distinct recommendation between hepatic artery infusion, TACE, and radioembolization cannot be derived from the present dataset. However, the findings of this analysis may provide an important basis for the design of forthcoming studies. Furthermore, the retrospective nature of this study thwarted the analysis of personalized dosimetry. On the basis of the SPECT/CT scan after ^{99m}Tc-macroaggregated albumin injection, the injected ⁹⁰Y activity can be adapted to ensure a preferably high radiation dose without damaging adjacent, nontumorous liver tissue. This concept may be of considerable value in tumors such as iCCA that are notoriously difficult to treat.

CONCLUSION

Second-line and salvage radioembolization may be an important option in advanced iCCA, independent of the hepatic tumor burden or the presence of tumor-accompanying ailments such as ascites or liver cirrhosis. In the onset of studies investigating the role of first-line radioembolization, the potential benefits of radioembolization in the later treatment stages of the disease should not be underestimated. Here, further investigation in prospective studies is necessary.

DISCLOSURE

Benedikt Schaarschmidt and Jens Theysohn received a research grant from PharmaCept for an ongoing investigator-initiated study not related to this paper. Roman Kloeckner is a consultant for Boston Scientific, Bristol-Myers Squibb, Guerbet, and SIRTEX and received lecture fees from AstraZeneca, BTG, Guerbet, Ipsen, SIRTEX, and MSD—Merck Sharp & Dohme. Daniel Pinto dos Santos is a consultant for Cook Medical and received lecture fees from Bayer. Manuel Weber is a consultant for Boston Scientific, Terumo, Advanced Accelerator Applications, and Eli Lilly. Jens Theysohn is a consultant for Boston Scientific, PharmaCept, Guerbet, and Roche. No other potential conflict of interest relevant to this article was reported.

ACKNOWLEDGMENTS

This publication contains parts of the doctoral thesis of Thomas Dertnig and is therefore in partial fulfillment of the requirements for an MD thesis at the Medical Faculty of the University Duisburg—Essen. Helin Durnus assisted with data collection at the Department of Diagnostic and Interventional Radiology, University of Cologne.

KEY POINTS

QUESTION: What are beneficial scenarios for radioembolization in cholangiocarcinoma patients?

PERTINENT FINDINGS: In this multicenter retrospective study, we showed that second-line or salvage radioembolization were viable options, with promising DCRs and a possibly favorable effect on mOS. In particular, hypervascularized tumors showed a statistically significant longer mOS than other tumor types.

IMPLICATIONS FOR PATIENT CARE: Second-line and salvage radioembolization may be important treatment options in advanced cholangiocarcinoma, independent of hepatic tumor burden, ascites, or liver cirrhosis. In addition to studies investigating the role of first-line radioembolization, the potential benefits of radioembolization in later treatment stages should be investigated in prospective studies.

REFERENCES

- Rizvi S, Gores GJ. Pathogenesis, Diagnosis, and Management of Cholangiocarcinoma. *Gastroenterology*. 2013;145:1215–1229.
- Razumilava N, Gores GJ. Cholangiocarcinoma. *Lancet*. 2014;383:2168–2179.
- Bridgewater J, Galle PR, Khan SA, et al. Guidelines for the diagnosis and management of intrahepatic cholangiocarcinoma. *J Hepatol*. 2014;60:1268–1289.
- Valle JW, Borbath I, Khan SA, et al. Biliary cancer: ESMO clinical practice guidelines for diagnosis, treatment and follow-up. *Ann Oncol*. 2016;27(suppl 5):v28–v37.
- Cholangiocarcinoma Working Group. Italian clinical practice guidelines on cholangiocarcinoma—part II: treatment. *Dig Liver Dis*. 2020;52:1430–1442.
- Izquierdo-Sanchez L, Lamarca A, La Casta A, et al. Cholangiocarcinoma landscape in Europe: diagnostic, prognostic and therapeutic insights from the ENSCCA registry. *J Hepatol*. 2022;76:1109–1121.
- Sommer CM, Kauczor HU, Pereira PL. Locoregional therapies of cholangiocarcinoma. *Visc Med*. 2016;32:414–420.
- Cercek A, Boerner T, Tan BR, et al. Assessment of hepatic arterial infusion of floxuridine in combination with systemic gemcitabine and oxaliplatin in patients with unresectable intrahepatic cholangiocarcinoma. *JAMA Oncol*. 2020;6:60–67.
- Wang X, Hu J, Cao G, et al. Phase II study of hepatic arterial infusion chemotherapy with oxaliplatin and 5-fluorouracil for advanced perihilar cholangiocarcinoma. *Radiology*. 2017;283:580–589.
- Boehm LM, Jayakrishnan TT, Miura JT, et al. Comparative effectiveness of hepatic artery based therapies for unresectable intrahepatic cholangiocarcinoma. *J Surg Oncol*. 2015;111:213–220.
- Mosconi C, Solaini L, Vara G, et al. Transarterial chemoembolization and radioembolization for unresectable intrahepatic cholangiocarcinoma: a systemic review and meta-analysis. *Cardiovasc Intervent Radiol*. 2021;44:728–738.
- Edeline J, Lamarca A, McNamara MG, et al. Locoregional therapies in patients with intrahepatic cholangiocarcinoma: a systematic review and pooled analysis. *Cancer Treat Rev*. 2021;99:102258.
- Goerg F, Zimmermann M, Bruners P, Neumann U, Luedde T, Kuhl C. Chemoembolization with degradable starch microspheres for treatment of patients with primary or recurrent unresectable, locally advanced intrahepatic cholangiocarcinoma: a pilot study. *Cardiovasc Intervent Radiol*. 2019;42:1709–1717.
- Schicho A, Pereira PL, Pützler M, et al. Degradable starch microspheres transcatheter arterial chemoembolization (DSM-TACE) in intrahepatic cholangiocellular carcinoma (ICC): results from a national multi-center study on safety and efficacy. *Med Sci Monit*. 2017;23:796–800.
- Aliberti C, Carandina R, Sarti D, et al. Chemoembolization with drug-eluting microspheres loaded with doxorubicin for the treatment of cholangiocarcinoma. *Anticancer Res*. 2017;37:1859–1863.
- Helmberger T, Golfieri R, Pech M, et al. Clinical application of trans-arterial radioembolization in hepatic malignancies in Europe: first results from the prospective multicentre observational study CIRSE registry for SIR-Spheres therapy (CIRT). *Cardiovasc Intervent Radiol*. 2021;44:21–35.
- Schaarschmidt BM, Wildgruber M, Kloeckner R, et al. ⁹⁰Y radioembolization in the treatment of neuroendocrine neoplasms: results of an international multicenter retrospective study. *J Nucl Med*. 2022;63:679–685.
- Zhen Y, Liu B, Chang Z, Ren H, Liu Z, Zheng J. A pooled analysis of transarterial radioembolization with yttrium-90 microspheres for the treatment of unresectable intrahepatic cholangiocarcinoma. *Onco Targets Ther*. 2019;12:4489–4498.
- Badar W, Van Ha T, Zangan S, et al. Yttrium-90 radioembolization therapy for combined hepatocellular and cholangiocarcinoma. *Gastrointest Tumors*. 2020;7:144–150.
- Köhler M, Harders F, Lohöfer F, et al. Prognostic factors for overall survival in advanced intrahepatic cholangiocarcinoma treated with yttrium-90 radioembolization. *J Clin Med*. 2019;9:56.
- Eisenhauer EA, Therasse P, Bogaerts J, et al. New response evaluation criteria in solid tumours: revised RECIST guideline (version 1.1). *Eur J Cancer*. 2009;45:228–247.
- Ma KW, Cheung TT, She WH, et al. The effect of wide resection margin in patients with intrahepatic cholangiocarcinoma: a single-center experience. *Medicine (Baltimore)*. 2016;95:e4133.
- DeOliveira ML, Cunningham SC, Cameron JL, et al. Cholangiocarcinoma: thirty-one-year experience with 564 patients at a single institution. *Ann Surg*. 2007;245:755–762.
- Kloeckner R, Ruckes C, Kronfeld K, et al. Selective internal radiotherapy (SIRT) versus transarterial chemoembolization (TACE) for the treatment of intrahepatic cholangiocellular carcinoma (CCC): study protocol for a randomized controlled trial. *Trials*. 2014;15:311.
- Paprottka KJ, Galiè F, Ingrisch M, et al. Outcome and safety after 103 radioembolizations with yttrium-90 resin microspheres in 73 patients with unresectable intrahepatic cholangiocarcinoma: an evaluation of predictors. *Cancers (Basel)*. 2021;13:5399.
- Buettner S, Braat AJAT, Margonis GA, et al. Yttrium-90 radioembolization in intrahepatic cholangiocarcinoma: a multicenter retrospective analysis. *J Vasc Interv Radiol*. 2020;31:1035–1043.e2.
- Currie BM, Soulen MC. Decision making: intra-arterial therapies for cholangiocarcinoma—TACE and TARE. *Semin Intervent Radiol*. 2017;34:92–100.
- Jia Z, Paz-Fumagalli R, Frey G, Sella DM, McKinney JM, Wang W. Resin-based yttrium-90 microspheres for unresectable and failed first-line chemotherapy intrahepatic cholangiocarcinoma: preliminary results. *J Cancer Res Clin Oncol*. 2017;143:481–489.
- Willowson KP, Eslick EM, Bailey DL. Individualised dosimetry and safety of SIRT for intrahepatic cholangiocarcinoma. *EJNMMI Phys*. 2021;8:65.
- Bourien H, Palard X, Rolland Y, et al. Yttrium-90 glass microspheres radioembolization (RE) for biliary tract cancer: a large single-center experience. *Eur J Nucl Med Mol Imaging*. 2019;46:669–676.
- Manceau V, Palard X, Rolland Y, et al. A MAA-based dosimetric study in patients with intrahepatic cholangiocarcinoma treated with a combination of chemotherapy and ⁹⁰Y-loaded glass microsphere selective internal radiation therapy. *Eur J Nucl Med Mol Imaging*. 2018;45:1731–1741.
- Edeline J, Toucheffeu Y, Guiu B, et al. Radioembolization plus chemotherapy for first-line treatment of locally advanced intrahepatic cholangiocarcinoma. *JAMA Oncol*. 2020;6:51–59.

Prognostic Value of ^{18}F -FDG PET/CT in Diffuse Large B-Cell Lymphoma Treated with a Risk-Adapted Immunochemotherapy Regimen

Laure Michaud*¹, Kurt Bantilan*², Audrey Mauguen³, Craig H. Moskowitz⁴, Andrew D. Zelenetz², and Heiko Schöder¹

¹Department of Radiology, Memorial Sloan Kettering Cancer Center, New York, New York; ²Department of Medicine, Memorial Sloan Kettering Cancer Center, New York, New York; ³Department of Epidemiology and Biostatistics, Memorial Sloan Kettering Cancer Center, New York, New York; and ⁴Department of Medicine, University of Miami Health System, Miami, Florida

Early identification of patients with diffuse large B-cell lymphoma (DLBCL) who are likely to experience disease recurrence or refractory disease after rituximab plus cyclophosphamide, doxorubicin, vincristine, and prednisone (R-CHOP) would be useful for improving risk-adapted treatment strategies. We aimed to assess the prognostic value of ^{18}F -FDG PET/CT parameters at baseline, interim, and end of treatment (EOT). **Methods:** We analyzed the prognostic impact of ^{18}F -FDG PET/CT in 166 patients with DLBCL treated with a risk-adapted immunochemotherapy regimen. Scans were obtained at baseline, after 4 cycles of R-CHOP or 3 cycles of RR-CHOP (double dose of R) and 1 cycle of CHOP alone (interim) and 6 wk after completing therapy (EOT). Progression-free survival (PFS) and overall survival (OS) were estimated using Kaplan–Meier and the impact of clinical/PET factors assessed with Cox models. We also assessed the predictive ability of the recently proposed International Metabolic Prognostic Index (IMPI). **Results:** The median follow-up was 7.9 y. International Prognostic Index (IPI), baseline metabolic tumor volume (MTV), and change in maximum SUV ($\Delta\text{SUV}_{\text{max}}$) at interim scans were statistically significant predictors for OS. Baseline MTV, interim $\Delta\text{SUV}_{\text{max}}$, and EOT Deauville score were statistically significant predictors of PFS. Combining interim PET parameters demonstrated that patients with Deauville 4–5 and positive $\Delta\text{SUV}_{\text{max}} \leq 70\%$ at restaging ($\sim 10\%$ of the cohort) had extremely poor prognosis. The IMPI had limited discrimination and slightly overestimated the event rate in our cohort. **Conclusion:** Baseline MTV and interim $\Delta\text{SUV}_{\text{max}}$ predicted both PFS and OS with this sequential immunochemotherapy program. Combining interim Deauville score with interim $\Delta\text{SUV}_{\text{max}}$ may identify an extremely high-risk DLBCL population.

Key Words: ^{18}F -FDG PET/CT; diffuse large B-cell lymphoma; metabolic tumor volume; δ -SUV_{max}; Deauville score

J Nucl Med 2023; 64:536–541
DOI: 10.2967/jnumed.122.264740

Diffuse large B-cell lymphoma (DLBCL) is a common and aggressive lymphoma subtype. The treatment regimen of rituximab plus cyclophosphamide, doxorubicin, vincristine, and prednisone (R-CHOP) is considered the standard first-line DLBCL

treatment, with a long-term remission rate of 60%–70% (1). However, patients who do not respond to R-CHOP have a poor prognosis, and pretreatment prognostic models such as the International Prognostic Index (IPI) that are used to predict survival (2) fail to identify these high-risk patients. Several studies have evaluated more aggressive first-line treatments using risk-adapted strategies for patients with good versus poor prognosis (3,4). Hence, early identification of patients who are likely to experience disease recurrence or refractory disease after R-CHOP is important for improving stratification to modified and innovative regimens.

^{18}F -FDG PET/CT scans at baseline have proven to be highly sensitive in determining sites of disease for DLBCL (5,6). Furthermore, PET/CT scans at the end of treatment (EOT) have demonstrated high prognostic value for assessing long-term remission (6). However, there is still no consensus on the predictive value of interim PET/CT scans in the management of patients with DLBCL. Evidence that changing treatment strategy based on interim PET/CT scans improves outcome remains to be confirmed (4,6,7).

Imaging biomarkers have often been evaluated separately. Parameters calculated from PET/CT, such as metabolic tumor volume (MTV) at baseline and change in maximum SUV between baseline and interim scans ($\Delta\text{SUV}_{\text{max}}$), were demonstrated to be prognostic in DLBCL (1,3,7–12) and may prove useful for risk stratification. Recently, a simple prognostic model, the International Metabolic Prognostic Index (IMPI), which combines baseline MTV, age, and stage, was shown to predict outcomes in DLBCL with higher accuracy than the IPI (13). Against this background, we aimed to assess the prognostic value of baseline, interim, and EOT ^{18}F -FDG PET/CT scans and validate IMPI in patients with DLBCL who were uniformly treated with a risk-adapted immunochemotherapy regimen.

MATERIALS AND METHODS

Study Population

Two risk-adapted studies treating patients with advanced-stage large cell lymphomas were approved by Memorial Sloan Kettering Cancer Center (MSK)'s institutional review board. From March 2002 to November 2006, 98 patients were enrolled onto protocol 01-142 (NCT00039195) and from July 2008 to May 2013, 99 patients were enrolled onto 08-026 (NCT00712582). All patients provided written informed consent. From November 2006 through September 2010, 26 patients were treated at MSK with a non-cross-reactive chemotherapeutic program consistent with that of 01-142 but performed off-protocol since 01-142 was closed at the time.

Patients were treated with R-CHOP $\times 4$ or RR-CHOP (double dose of R) $\times 3$ + CHOP $\times 1$ induction, and either 3 cycles of ifosfamide, carboplatin, and etoposide (ICE), ICE $\times 2$ + rituximab-ICE (R-ICE) $\times 1$,

Received Jul. 29, 2022; revision accepted Oct. 4, 2022.
For correspondence or reprints, contact Heiko Schöder (schoderh@mskcc.org).
*Contributed equally to this work.
Published online Dec. 22, 2022.
COPYRIGHT © 2023 by the Society of Nuclear Medicine and Molecular Imaging.

or augmented R-ICE ×2 consolidation chemotherapy. Those with both an interim ¹⁸F-FDG PET-positive result and confirmatory positive biopsy of the ¹⁸F-FDG-positive site went on to receive high-dose therapy and autologous stem cell rescue.

The 223 patients had similar pretreatment characteristics and similar outcome after a median follow-up of 7.7 y (95% CI, 7.0–8.7), which justified combining the 3 cohorts. From the total cohort of 223 patients, 166 patients with baseline, interim, or EOT PET/CT scans available in MSK’s PACS were included in this analysis. A consort diagram of evaluable patients is shown in Supplemental Figure 1 (supplemental materials are available at <http://jnm.snmjournals.org>). No clinical (Supplemental Table 1) or follow-up (Supplemental Figure 2) differences were observed between the 166 patients in the PET/CT cohort analyzed in this paper and the 57 patients who were excluded. Only a sex difference was observed (Supplemental Table 1).

¹⁸F-FDG PET/CT Imaging and Analysis

¹⁸F-FDG PET/CT scans were obtained at baseline, after 4 cycles of R-CHOP (interim), and 6 wk after completing immunochemotherapy (EOT). Patients fasted for 6 h before injection of 444 ± 44 MBq of ¹⁸F-FDG. PET/CT scans from midskull to upper thighs were obtained on Discovery scanners (GE Healthcare) after a standardized uptake time of approximately 60 min.

Baseline, interim, and EOT PET/CT scans were interpreted by an experienced nuclear medicine physician masked to patient outcome. Mediastinal blood pool and normal liver were used as reference regions for background activity. Sites of abnormal ¹⁸F-FDG uptake, defined as intensity greater than surrounding local background, were recorded. The intensity of ¹⁸F-FDG uptake was measured using the SUV_{max}, defined as the highest SUV recorded among all lesions for each scan. Focal bone uptake corresponded to bone metastasis. Diffuse marrow uptake was defined visually and may represent lymphoma involvement or reactive hyperplasia. The SUV_{max} of diffuse uptake was not recorded.

All measurable lesions were identified at baseline. Volumetric regions of interest were placed over all sites of abnormal uptake in lymph nodes, soft-tissue organs, or focal bone lesions. Metabolic tumor volume (MTV) was measured using the semiautomatic software Beth Israel plugin for Fiji and applying a 41% SUV_{max} threshold (14). Total MTV was obtained by summing the metabolic volumes of all measurable lesions. Furthermore, focal bone involvement and diffuse marrow uptake were recorded. The IMPI score, which represents the probability of being progression free at 36 mo, was calculated for each patient on the basis of age, stage, and baseline MTV as described by Mikhael et al. (13).

The visual Deauville/Lugano 5-point scale was applied to the interim and EOT scans, with scores of 1–3 (indicating uptake ≤ that of the liver) considered negative and scores 4–5 (indicating uptake > the liver) considered positive. To measure metabolic change after induction therapy, ΔSUV_{max} was assessed using the most intense tumor in any region or organ at the interim scan—even if the location differed from the original tumor at baseline—calculated as follows: ΔSUV_{max} = (baseline SUV_{max} – interim SUV_{max})/baseline SUV_{max} (15). Patients with ΔSUV_{max} ≤ 70% were considered positive and patients with ΔSUV_{max} > 70% were considered negative. The 70% threshold was chosen for this series based on the previously identified optimal cutoff to predict progression or death for ΔSUV_{max} after 4 cycles in the LNH2007-3B trial (16). As outlined by Meignan et al. based on the PETAL trial (NCT00554164), LNH2007-3B (NCT00498043), and International validation studies (17), patients with low baseline SUV_{max} (<10) or high interim SUV_{max} (>5) were deemed unsuitable for ΔSUV_{max} calculations. Visual assessment was used for these patients.

Statistical Analysis

Progression-free survival (PFS) and overall survival (OS) were used to evaluate the prognostic value of clinical and PET/CT parameters.

PFS was defined as the time from the start of treatment to the date of disease progression/relapse or death from any cause. Patients without progression/relapse or death were censored at their last follow-up. OS was defined as the time from the start of treatment to the date of death from any cause. Surviving patients were censored at their last follow-up. To assess the prognostic value of parameters measured at interim or EOT, landmark analyses were used where PFS and OS were defined

TABLE 1
Patient Characteristics (n = 166)

Clinical characteristic	n
Median age (y)	50 (range, 20–71)
Ann Arbor stage	
II	34 (20%)
III–IV	132 (80%)
Median LDH	332 (range, 130–1,925)
KPS	
≤70	49 (30%)
>70	117 (70%)
Standard IPI score	
0	33 (20%)
1	39 (23%)
2	53 (32%)
3	41 (25%)
Baseline PET	166
Focal bone uptake	55 (33%)
Diffuse marrow uptake	20 (12%)
Median liver SUV _{max}	2.42 (range, 0.81–7.20)
Unknown	2
Median SUV _{max}	24.35 (range, 6.30–60.36)
Median TMTV	297.82 (range, 6–5,145.85)
≤510 mL	117 (70%)
>510 mL	49 (30%)
Interim PET	157
ΔSUV _{max}	
Median	0.90 (range, –0.33–0.98)
Negative	140 (89%)
Positive	17 (11%)
Deauville score	
1–3	118 (75%)
4	36 (23%)
5	3 (2%)
EOT PET	151
Deauville score	
1–3	124 (82%)
4	19 (13%)
5	8 (5%)

LDH = lactate dehydrogenase; KPS = Karnofsky performance scale; TMTV = total metabolic tumor volume; ΔSUV_{max} = change in SUV_{max}; EOT = end of treatment.

TABLE 2
Univariable Cox Regression Analyses

Clinical characteristic	OS			PFS		
	HR	95% CI	<i>P</i>	HR	95% CI	<i>P</i>
Standard IPI score			0.015			0.13
0	—	—		—	—	
1	0.91	0.23, 3.65		0.71	0.26, 1.97	
2	1.12	0.33, 3.82		1.00	0.42, 2.39	
3	3.35	1.12, 10.0		1.81	0.79, 4.14	
Baseline PET						
Focal bone uptake	0.88	0.42, 1.88	0.75	0.73	0.39, 1.36	0.31
Diffuse marrow uptake	1.52	0.58, 3.98	0.41	1.12	0.47, 2.64	0.81
SUV _{max} (per 5 units)	1.07	0.88, 1.30	0.53	0.92	0.79, 1.09	0.34
TMTV (dichotomized)			0.011			0.004
≤510 mL	—	—		—	—	
>510 mL	2.54	1.25, 5.13		2.33	1.32, 4.12	
Interim PET (landmark)						
ΔSUV _{max} (continuous)	0.03	0.01, 0.14	<0.001	0.08	0.02, 0.32	0.007
ΔSUV _{max} (dichotomized)			0.007			0.015
Negative	—	—		—	—	
Positive	3.75	1.60, 8.80		2.91	1.35, 6.29	
Deauville score			0.15			0.21
1–3	—	—		—	—	
4–5	1.79	0.83, 3.84		1.54	0.80, 2.95	
EOT PET (landmark)						
Deauville score			0.092			0.010
1–3	—	—		—	—	
4–5	2.24	0.93, 5.41		2.72	1.34, 5.51	

HR = hazard ratio; TMTV = total metabolic tumor volume; ΔSUV_{max} = change in SUV_{max}; EOT = end of treatment.

from the interim or EOT, respectively. Patients with the events of interest before the landmark time or without the corresponding PET/CT scans were excluded.

IPI, baseline PET/CT parameters (SUV_{max}, MTV, focal bone uptake, diffuse marrow uptake), interim PET/CT parameters (ΔSUV_{max} [positive vs. negative or continuous], Deauville scores [1–3 vs. 4–5]), and EOT PET/CT parameters (Deauville scores [1–3 vs. 4–5]) were evaluated as prognostic factors. We used 510 mL as the optimal cutoff for MTV as proposed by Meignan et al. (18), which we validated for PFS and OS in our cohort (Supplemental Fig. 3). PFS and OS rates were estimated using a Kaplan–Meier estimator. The impact of candidate factors on survival were assessed using univariable and multivariable Cox proportional hazards models. The median follow-up was estimated using the reverse Kaplan–Meier method. The comparison between the patients included and excluded from the cohorts was done using the Wilcoxon rank-sum test for continuous variables and the Fisher exact test for categorical variables. A 2-sided *P* value < 0.05 was considered statistically significant.

To assess the predictive ability of IMPI (probability of being progression free at 36 mo), its complement, cIMPI (probability of a progression event by 36 mo), was analyzed using 3 methods: measures of discrimination (Harrell's c-index), prediction error (Brier score), and calibration

(calibration plot). Analyses were performed using R (version 4.1.0; R Foundation).

RESULTS

The median follow-up for the 166 patients included in this analysis was 7.9 y (95% CI, 6.7–8.8). Clinical characteristics and quantitative PET parameters are summarized in Table 1. Of the total, 48 patients experienced a progression event and 31 died (2 of these deaths were unrelated to cancer). The 5-y PFS and OS rates were 76% and 85%, respectively. The 10-y rates were 69% and 80%, respectively.

All 166 patients underwent baseline PET/CT scans. The median SUV_{max} was 24.35 (range, 6.30–60.36). Median MTV was 297.82 mL (range, 6.45–5,145.85 mL) and average MTV was 522.32 mL. Fifty-five patients had ¹⁸F-FDG-positive focal bone lesions, and 20 patients had diffuse marrow uptake; among these, 5 patients had mixed focal bone lesions and diffuse uptake. Of the total, 157 patients underwent interim PET/CT after R-CHOP. For the remaining 9 patients, interim PET/CT was either not performed or not available (Supplemental Fig. 5). One patient progressed before interim scanning and was

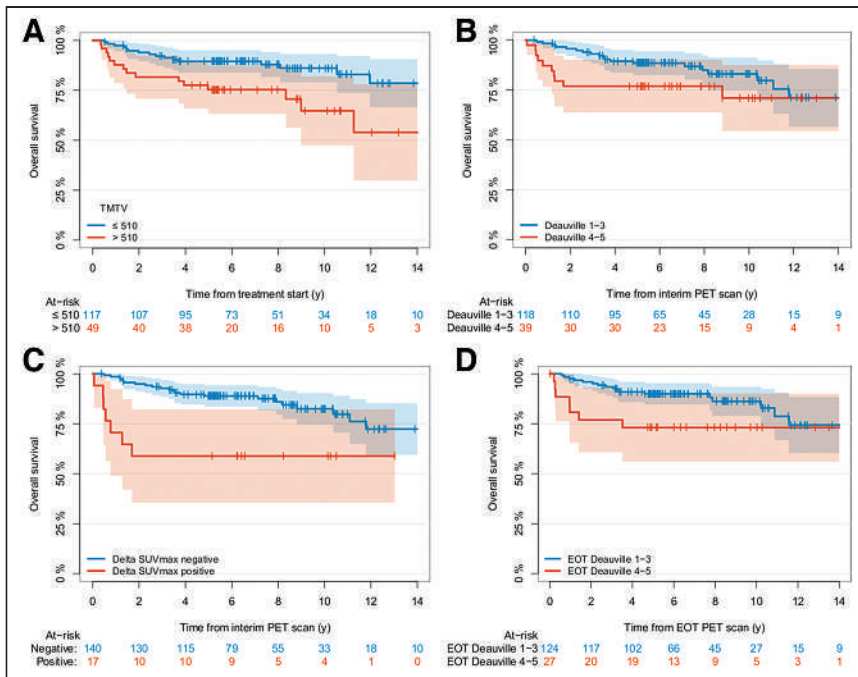


FIGURE 1. OS stratified by baseline total metabolic tumor volume (TMTV) (A), interim Deauville score (B), interim $\Delta\text{SUV}_{\text{max}}$ (C), and end-of-treatment (EOT) Deauville score (D).

excluded in PFS landmark analysis. By visual Deauville/Lugano classification, there were 39 interim PET/CT-positive patients (25%) and 118 interim PET/CT-negative patients (75%). The median $\Delta\text{SUV}_{\text{max}}$ was 0.90% (−0.33%–0.98%). When $\Delta\text{SUV}_{\text{max}}$ criteria was used, 17

patients were classified as positive (11%) and 140 patients were classified as negative (89%) at interim. Among them, 23 had initial $\text{SUV}_{\text{max}} < 10$ (6 patients) or interim $\text{SUV}_{\text{max}} > 5$ (17 patients); Deauville scores were used to classify them as positive or negative. All but 15 patients, for whom imaging was not performed or not available, were analyzed for EOT PET/CT (Supplemental Fig. 5). Three patients progressed before or on the day of EOT scan and were excluded in PFS landmark analysis. Visual Deauville/Lugano assessment was positive for 27 patients (17 of 27 also had a positive interim PET/CT result per Deauville/Lugano response criteria) and 124 were considered negative at EOT.

IPI, baseline MTV, and interim $\Delta\text{SUV}_{\text{max}}$ were statistically significant predictors of OS (Table 2; Fig. 1). IPI ($P = 0.059$) and baseline MTV ($P = 0.066$) were independent prognostic factors of OS in a multivariable model with borderline significance. Baseline MTV, interim $\Delta\text{SUV}_{\text{max}}$, and EOT Deauville score were statistically significant predictors of PFS (Table 2; Fig. 2). Casanovas et al. showed that combining visual (International Harmonization Project criteria) and quantitative ($\Delta\text{SUV}_{\text{max}}$) PET assessments after 4 cycles of induction treatment identified patients at extremely high risk of induction failure or early relapse (16). We performed a similar analysis looking at the prognostic relevance of interim PET parameters (Deauville score and $\Delta\text{SUV}_{\text{max}}$) to outcome by combining these 2 interim response criteria. This Kaplan–Meier analysis demonstrated that patients with Deauville of 4–5 and positive $\Delta\text{SUV}_{\text{max}}$ at restaging (~10% of the cohort) had extremely poor prognosis (Fig. 3). Among these, 9 patients also had high initial MTV.

The IMPI was calculated for all patients as a probability of being progression free at 36 mo. The predicted event rate was compared with the actual event rate (Supplemental Fig. 4), and we found that the IMPI overestimated the event rate.

DISCUSSION

Early prediction of poor prognosis during the course of DLBCL therapy would be helpful for improving long-term outcome. Although assessing early response to treatment using PET/CT scans has identified potential prognostic factors, there is currently no consensus on how to adapt treatment strategies based on molecular imaging parameters. For example, studies with large DLBCL cohorts have identified baseline MTV as a significant predictor for PFS and OS (9,12,19). Other studies showed $\Delta\text{SUV}_{\text{max}}$ on interim PET to be associated with both PFS and OS (3,10,20).

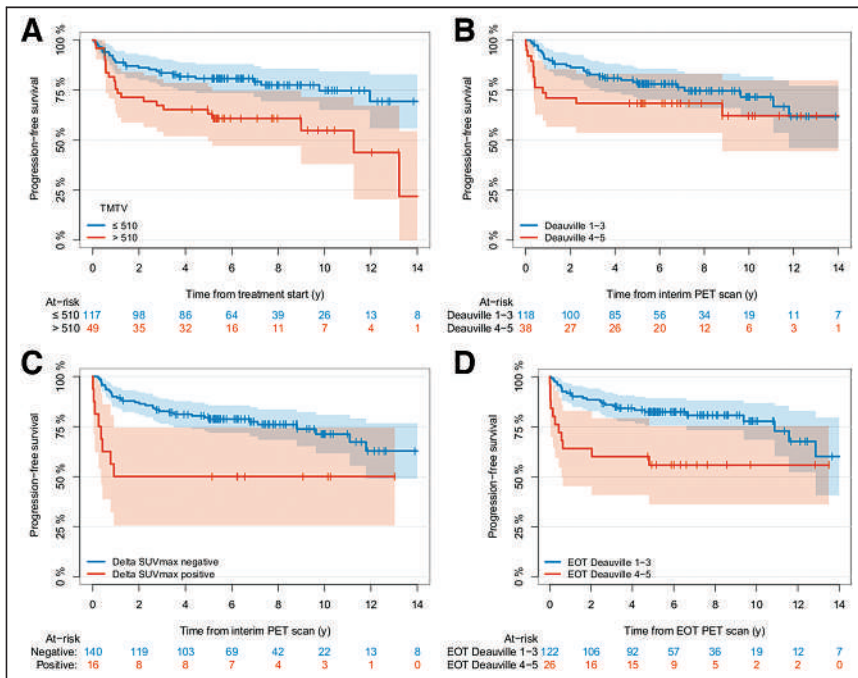


FIGURE 2. PFS stratified by baseline total metabolic tumor volume (TMTV) (A), interim Deauville score (B), interim $\Delta\text{SUV}_{\text{max}}$ (C), and end-of-treatment (EOT) Deauville score (D). One patient progressed before interim scan and was excluded from landmark analysis (B and C), 3 patients progressed before or on the day of EOT scan and were excluded from landmark analysis (D).

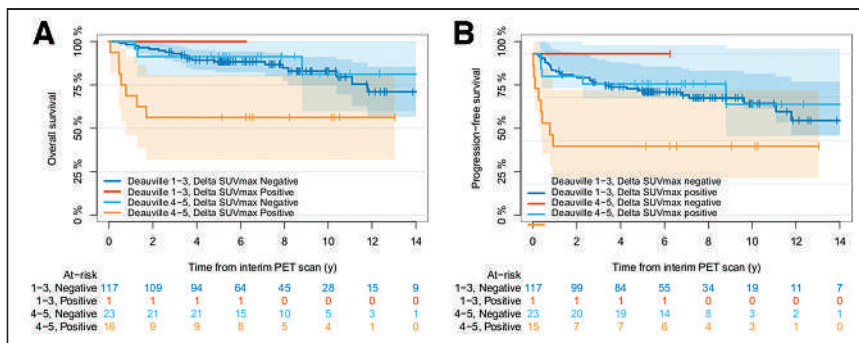


FIGURE 3. OS (A) and PFS (B) stratified by combination of interim Deauville score and interim $\Delta\text{SUV}_{\text{max}}$. 1 patient progressed before interim scan and was excluded from landmark analysis (B).

Data reported by Casasnovas et al. also suggest that interim $\Delta\text{SUV}_{\text{max}}$ is more discriminant of outcome after 4 cycles of treatment than after 2 cycles (3). However, another large prospective trial reported interim PET/CT having limited prognostic relevance. Mamot et al. demonstrated that when interim PET/CT after 2 cycles was already positive, PET scans after 4 cycles of chemotherapy provided no additional predictive value compared with 2 cycles, and that only scans at EOT identified a significant difference in outcome (7).

To explore the prognostic value of PET/CT in DLBCL, we looked at the prognostic value of several PET/CT parameters in a group of 166 patients uniformly treated with a risk-adapted immunochemotherapy regimen. Our results showed that baseline MTV and interim $\Delta\text{SUV}_{\text{max}}$ were significant predictors of PFS and OS. We also found that EOT Deauville score was prognostic for PFS. To note, EOT PET demonstrated less prognostic value in our study than what was reported by Mamot et al. (7). This difference may be because of the risk-adapted treatment regimen as well as the longer follow-up in our series.

The recently proposed IMPI (13), which combines baseline MTV and age as continuous variables to predict patient outcome in DLBCL, is potentially useful for identifying patients with worse prognosis who might benefit from more aggressive or investigational treatment. We sought to validate this model in our cohort. In our series, the IMPI predictions overestimated the event rate. There are several potential explanations for the lower predictive accuracy in our population. Our patients were treated with R-CHOP followed by ICE/RICE, whereas Mikhael et al. used clinical data from patients treated with R-CHOP alone. Second, baseline MTV was calculated using different software. Finally, MTV was measured by including tumor with different SUV cutoffs (current analysis used the 41% SUV_{max} threshold method, whereas Mikhael et al. used $\text{SUV}_{\text{max}} \geq 4.0$). Nevertheless, the median MTV in the current study was similar to theirs (298 vs. 308 mL).

In our series, combining interim PET parameters Deauville score and $\Delta\text{SUV}_{\text{max}}$ demonstrated that patients with Deauville scores of 4-5 and positive $\Delta\text{SUV}_{\text{max}}$ (10% of the cohort) had extremely poor prognosis. These results combining visual and quantitative assessments are similar to those previously reported in an independent cohort after 4 cycles of induction treatment (16). Thus, it appears that adding $\Delta\text{SUV}_{\text{max}}$ to visual analysis may be a robust and reproducible tool for identifying high-risk patients with DLBCL. Combining the 2 interim PET parameters identifies patients who have a poor outcome with standard chemoimmunotherapy and may help define a cohort of patients for evaluation of alternative therapeutic

approaches, such as CAR T-cell therapy. ZUMA-12 attempted to identify patients with a poor prognosis for early intervention with axicabtagene ciloleucel (21); however, that trial has been criticized for the means of selecting the poor risk cohort. The interim PET evaluation described herein could potentially identify a more uniform group of patients with a poor outcome. A prospective trial could randomize these high-risk patients to CAR T-cell versus second-line therapy followed by high-dose therapy and autologous stem cell rescue, similar to the ZUMA-7 (22) and TRANSFORM (23) clinical trials. Other studies evaluating the role of PET/CT metrics for treatment guidance

in DLBCL have reported other parameter combinations to be relevant. Cottreau et al. demonstrated that baseline MTV and standardized D_{max} (the largest distance between 2 lesions) complement each other in characterizing tumor burden and disease spread (11), whereas Vercellino et al. combined baseline MTV with the Eastern Cooperative Oncology Group performance status to identify a very-high-risk DLBCL subgroup (12). Recently, Eertink et al., on behalf of PETRA investigators, demonstrated in 217 patients that MTV, $\text{D}_{\text{max}_{\text{bulk}}}$, SUV_{peak} , World Health Organization performance score, and age identify patients at risk of relapse at baseline (24).

To determine the optimal combination of PET/CT parameters and prognostic indices to improve the prediction of outcome in clinical practice, standardized methods of measurement are needed across all PET/CT centers internationally. Some examples include whether interim PET/CT scans should be acquired after 2 versus 4 cycles, standardized definitions of $\Delta\text{SUV}_{\text{max}}$, and methods for determination of MTV (25). Once a robust set of parameters or score is determined, multiple large studies would need to validate the results for a consensus to be reached. Standardization is potentially complicated by different initial regimens. For the results to be applicable across studies, the parameters would ideally be independent of treatment. To move from being a prognostic tool to a predictive tool, well-designed clinical trials need to evaluate new treatment strategies for the high-risk DLBCL patient and show improved outcome.

CONCLUSION

Our study confirmed the prognostic value of baseline MTV and interim $\Delta\text{SUV}_{\text{max}}$ in DLBCL. Combining interim Deauville score with interim $\Delta\text{SUV}_{\text{max}}$ could improve risk stratification for patients with extremely poor prognosis. These results warrant large multicenter studies to develop standardized practices and refine existing prognostic indices in DLBCL.

DISCLOSURE

This work was supported in part by the NIH/NCI Cancer Center Support grant P30 CA008748. Andrew D. Zelenetz serves or has served as a consultant to Genentech/Roche, Gilead/Kite, BMS/Celgene/Juno, Janssen, Novartis, Adaptive Biotechnology, MorphoSys, Abbvie, AstraZeneca, MEI Pharma, and BeiGene; has collaborated on research with MEI Pharmaceuticals, Genentech/Roche, and BeiGene; and has served as a DMC member for BMS/Celgene/Juno. No other potential conflict of interest relevant to this article was reported.

KEY POINTS

QUESTION: Do baseline MTV, alone or in combination with Δ SUV, and the recently proposed IMPI score predict outcome in patients with DLBCL treated with the RCHOP-ICE drug regimen?

PERTINENT FINDINGS: Baseline MTV and Δ SUV_{max} at interim predict OS. Patients with Deauville scores of 4–5 and positive Δ SUV_{max} \leq 70% at interim (~10% of the cohort) had extremely poor prognosis. The new IMPI score had limited discrimination and slightly overestimated the event rate in our cohort.

IMPLICATIONS FOR PATIENT CARE: Combining interim Deauville scores with interim Δ SUV_{max} could improve risk stratification for DLBCL patients with extremely poor prognosis.

REFERENCES

- Dührsen U, Muller S, Hertenstein B, et al. Positron Emission Tomography-Guided Therapy of Aggressive Non-Hodgkin Lymphomas (PETAL): a multicenter, randomized phase iii trial. *J Clin Oncol.* 2018;36:2024–2034.
- International Non-Hodgkin's Lymphoma Prognostic Factors Project. A predictive model for aggressive non-Hodgkin's lymphoma. *N Engl J Med.* 1993;329:987–994.
- Casasnovas RO, Ysebaert L, Thieblemont C, et al. FDG-PET-driven consolidation strategy in diffuse large B-cell lymphoma: final results of a randomized phase 2 study. *Blood.* 2017;130:1315–1326.
- Moskowitz CH, Schoder H, Teruya-Feldstein J, et al. Risk-adapted dose-dense immunochemotherapy determined by interim FDG-PET in advanced-stage diffuse large B-cell lymphoma. *J Clin Oncol.* 2010;28:1896–1903.
- Juweid ME, Stroobants S, Hoekstra OS, et al. Use of positron emission tomography for response assessment of lymphoma: consensus of the Imaging Subcommittee of International Harmonization Project in Lymphoma. *J Clin Oncol.* 2007;25:571–578.
- Barrington SF, Mikhaeel NG, Kostakoglu L, et al. Role of imaging in the staging and response assessment of lymphoma: consensus of the International Conference on Malignant Lymphomas Imaging Working Group. *J Clin Oncol.* 2014;32:3048–3058.
- Mamot C, Klingbiel D, Hitz F, et al. Final results of a prospective evaluation of the predictive value of interim positron emission tomography in patients with diffuse large B-cell lymphoma treated with R-CHOP-14 (SAKK 38/07). *J Clin Oncol.* 2015;33:2523–2529.
- Zhao P, Yu T, Pan Z. Prognostic value of the baseline ¹⁸F-FDG PET/CT metabolic tumour volume (MTV) and further stratification in low-intermediate (L-I) and high-intermediate (H-I) risk NCCNPI subgroup by MTV in DLBCL MTV predict prognosis in DLBCL. *Ann Nucl Med.* 2021;35:24–30.
- Mikhaeel NG, Smith D, Dunn JT, et al. Combination of baseline metabolic tumour volume and early response on PET/CT improves progression-free survival prediction in DLBCL. *Eur J Nucl Med Mol Imaging.* 2016;43:1209–1219.
- Schöder H, Polley MC, Knopp MV, et al. Prognostic value of interim FDG-PET in diffuse large cell lymphoma: results from the CALGB 50303 clinical trial. *Blood.* 2020;135:2224–2234.
- Cottreau AS, Meignan M, Nioche C, et al. Risk stratification in diffuse large B-cell lymphoma using lesion dissemination and metabolic tumor burden calculated from baseline PET/CT(dagger). *Ann Oncol.* 2021;32:404–411.
- Vercellino L, Cottreau AS, Casasnovas O, et al. High total metabolic tumor volume at baseline predicts survival independent of response to therapy. *Blood.* 2020;135:1396–1405.
- Mikhaeel NG, Heymans MW, Eertink JJ, et al. Proposed new dynamic prognostic index for diffuse large B-cell lymphoma: international metabolic prognostic index. *J Clin Oncol.* 2022;40:2352–2360.
- Kanoun S, Tal I, Berriolo-Riedinger A, et al. Influence of software tool and methodological aspects of total metabolic tumor volume calculation on baseline [¹⁸F]FDG PET to predict survival in Hodgkin lymphoma. *PLoS One.* 2015;10:e0140830.
- Itti E, Lin C, Dupuis J, et al. Prognostic value of interim ¹⁸F-FDG PET in patients with diffuse large B-cell lymphoma: SUV-based assessment at 4 cycles of chemotherapy. *J Nucl Med.* 2009;50:527–533.
- Casasnovas RO, Meignan M, Berriolo-Riedinger A, et al. SUVmax reduction improves early prognosis value of interim positron emission tomography scans in diffuse large B-cell lymphoma. *Blood.* 2011;118:37–43.
- Meignan M, Gallamini A, Itti E, Barrington S, Haioun C, Polliack A. Report on the Third International Workshop on Interim Positron Emission Tomography in Lymphoma held in Menton, France, 26–27 September 2011 and Menton 2011 consensus. *Leuk Lymphoma.* 2012;53:1876–1881.
- Meignan M, Cottreau AS, Versari A, et al. Baseline metabolic tumor volume predicts outcome in high-tumor-burden follicular lymphoma: a pooled analysis of three multicenter studies. *J Clin Oncol.* 2016;34:3618–3626.
- Kostakoglu L, Mattiello F, Martelli M, et al. Total metabolic tumor volume as a survival predictor for patients with diffuse large B-cell lymphoma in the GOYA study. *Haematologica.* 2022;107:1633–1642.
- Burggraaff CN, Eertink JJ, Lugtenburg PJ, et al; HOVON Imaging Working Group and the HOVON Lymphoma Working Group. ¹⁸F-FDG PET improves baseline clinical predictors of response in diffuse large B-cell lymphoma: The HOVON-84 study. *J Nucl Med.* 2022;63:1001–1007.
- Neelapu SS, Dickinson M, Munoz J, et al. Axicabtagene ciloleucel as first-line therapy in high-risk large B-cell lymphoma: the phase 2 ZUMA-12 trial. *Nat Med.* 2022;28:735–742.
- Elsawy M, Chavez JC, Avivi I, et al. Patient-reported outcomes in ZUMA-7, a phase 3 study of axicabtagene ciloleucel in second-line large B-cell lymphoma. *Blood.* 2022;140:2248–2260.
- Kamdar M, Solomon SR, Arnason J, et al. Lisocabtagene maraleucel versus standard of care with salvage chemotherapy followed by autologous stem cell transplantation as second-line treatment in patients with relapsed or refractory large B-cell lymphoma (TRANSFORM): results from an interim analysis of an open-label, randomised, phase 3 trial. *Lancet.* 2022;399:2294–2308.
- Eertink JJ, van de Brug T, Wieggers SE, et al. ¹⁸F-FDG PET baseline radiomics features improve the prediction of treatment outcome in diffuse large B-cell lymphoma. *Eur J Nucl Med Mol Imaging.* 2022;49:932–942.
- Ilyas H, Mikhaeel NG, Dunn JT, et al. Defining the optimal method for measuring baseline metabolic tumour volume in diffuse large B cell lymphoma. *Eur J Nucl Med Mol Imaging.* 2018;45:1142–1154.

Cure of Disseminated Human Lymphoma with [¹⁷⁷Lu]Lu-Ofatumumab in a Preclinical Model

Kyuhwan Shim*¹, Mark S. Longtine*¹, Diane S. Abou¹, Mark J. Hoegger¹, Richard S. Laforest¹, Daniel L.J. Thorek^{1,2}, and Richard L. Wahl^{1,3}

¹Mallinckrodt Institute of Radiology, Washington University School of Medicine, St. Louis, Missouri; ²Department of Biomedical Engineering, Washington University, St. Louis, Missouri; and ³Department of Radiation Oncology, Washington University, St. Louis, Missouri

Although immunotherapies that target CD20 on most non-Hodgkin lymphoma (NHL) cells have improved patient outcomes, current therapies are inadequate because many cases are, or become, refractory or undergo relapse. Here, we labelled the third-generation human anti-CD20 antibody ofatumumab with ¹⁷⁷Lu, determined the in vitro characteristics of [¹⁷⁷Lu]Lu-ofatumumab, estimated human dosimetry, and assayed tumor targeting and therapeutic efficacy in a murine model of disseminated NHL. **Methods:** CHX-A''-diethylenetriaminepentaacetic acid-[¹⁷⁷Lu]Lu-ofatumumab was prepared. We evaluated radiochemical yield, purity, in vitro immunoreactivity, stability, ($n = 7$), affinity, and killing of CD20-expressing Raji cells ($n = 3$). Human dosimetry was estimated from biodistribution studies as percentage injected activity per gram using C57BL/6N mice. Tissue and organ biodistribution was determined in R2G2 immunodeficient mice with subcutaneous Raji-cell tumors. Therapy studies used R2G2 mice with disseminated human Raji-luc tumor cells ($n = 10$ mice/group). Four days after cell injection, the mice were left untreated or were treated with ofatumumab, 8.51 MBq of [¹⁷⁷Lu]Lu-IgG, or 0.74 or 8.51 MBq of [¹⁷⁷Lu]Lu-ofatumumab. Survival, weight, and bioluminescence were tracked. **Results:** Radiochemical yield was $93\% \pm 2\%$, radiochemical purity was $99\% \pm 1\%$, and specific activity was 401 ± 17 MBq/mg. Immunoreactivity was substantially preserved, and more than 75% of ¹⁷⁷Lu remained chelated after 7 d in serum. [¹⁷⁷Lu]Lu-ofatumumab specifically killed Raji-luc cells in vitro ($P < 0.05$). Dosimetry estimated that an effective dose for human administration is 0.36 mSv/MBq and that marrow may be the dose-limiting organ. Biodistribution in subcutaneous tumors 1, 3, and 7 d after [¹⁷⁷Lu]Lu-ofatumumab injection was 11, 15, and 14 percentage injected activity per gram, respectively. In the therapy study, median survival of untreated mice was 19 d, not statistically different from mice treated with 8.51 MBq of [¹⁷⁷Lu]Lu-IgG (25 d). Unlabeled ofatumumab increased survival to 46 d, similar to 0.74 MBq of [¹⁷⁷Lu]Lu-ofatumumab (59 d), with both being superior to no treatment ($P < 0.0003$). Weight loss and increased tumor burden preceded death or killing of the animal for cause. In contrast, treatment with 8.51 MBq of [¹⁷⁷Lu]Lu-ofatumumab dramatically increased median survival (>221 d), permitted weight gain, eliminated detectable tumors, and was curative in 9 of 10 mice. **Conclusion:** [¹⁷⁷Lu]Lu-ofatumumab shows favorable in vitro characteristics, localizes to tumor, and

demonstrates curative therapeutic efficacy in a disseminated lymphoma model, showing potential for clinical translation to treat NHL.

Key Words: CD20; lymphoma; targeted β -particle therapy; radioimmunotherapy; lutetium

J Nucl Med 2023; 64:542–548

DOI: 10.2967/jnumed.122.264816

Non-Hodgkin lymphoma (NHL) is a common hematologic malignancy, with over 80,000 new cases and 20,000 deaths estimated for the United States in 2022 (1). The standard of care for many cases of NHL involves chemotherapy and immunotherapy targeting the CD20 protein, which is highly expressed on most NHL cells, with murine/human chimeric rituximab used most commonly. Although this chemotherapy-with-immunotherapy combination is usually initially effective, many cases are refractory or undergo relapse, indicating the need for improved therapies.

Radioimmunotherapy joined clinical practice 2 decades ago with Food and Drug Administration approval of 2 anti-CD20 radioimmunotherapies for lymphoma: Zevalin (⁹⁰Y-ibritumomab tiuxetan; Acrotech Biopharma, Inc.) and Bexxar (tositumomab and ¹³¹I-tositumomab; GlaxoSmithKline), which use murine-derived antibodies radiolabeled with β -particle-emitting radioisotopes. Because of potential immune reactions, these antibodies were approved for only a single therapeutic dose. ⁹⁰Y (half-life [$t_{1/2}$], 2.7 d) emits high-energy β -particles (average, 934 keV), whereas ¹³¹I emits lower-energy β -particles (average, 187 keV), with average ranges in tissue of 3,800 μ m and 360 μ m, respectively (2), enabling killing over many cell diameters. Thus, in addition to working against individual tumor cells, β -particles may work against larger tumors, tumor-cell aggregates with imperfect antibody access, and heterogeneous tumors, although with potential off-target damage. Despite long-term safety and clinical effectiveness, Bexxar has been discontinued in the United States and Zevalin is applied infrequently (3), in part because of economic and logistic concerns that were present when they were introduced and because of competing nonradioactive therapies (4).

Some concerns that limited the use of Bexxar and Zevalin have been overcome with greater integration of radiopharmaceutical therapy into medicine (5), as exemplified by the Food and Drug Administration approval of ¹⁷⁷Lu-labeled agents for prostate cancer treatment (Pluvicto; Advanced Accelerator Applications (6)) and neuroendocrine tumors (Lutathera; Advanced Accelerator Applications (7)). ¹⁷⁷Lu ($t_{1/2}$, 6.6 d) emits β -particles of 149 keV

Received Aug. 22, 2022; revision accepted Oct. 25, 2022.

For correspondence or reprints, contact Richard L. Wahl (rwahl@wustl.edu).

*Contributed equally to this work.

Published online Nov. 10, 2022.

Immediate Open Access: Creative Commons Attribution 4.0 International License (CC BY) allows users to share and adapt with attribution, excluding materials credited to previous publications. License: <https://creativecommons.org/licenses/by/4.0/>. Details: <http://jnm.snmjournals.org/site/misc/permission.xhtml>.

COPYRIGHT © 2023 by the Society of Nuclear Medicine and Molecular Imaging.

on average, with an average tissue range of 220 μm . Emission of low-abundance γ -particles by ^{177}Lu permits imaging by SPECT.

Recently, ofatumumab, a third-generation anti-CD20 fully human antibody, was developed. Ofatumumab is a type I antibody that is internalized after CD20 binding (8). We showed by biodistribution and PET imaging studies that [^{89}Zr]Zr-DFO-ofatumumab targets CD20-positive subcutaneous xenograft tumors as well as [^{89}Zr]Zr-DFO-rituximab (9).

Here, we describe the synthesis and evaluation of [^{177}Lu]Lu-ofatumumab. We present in vitro characteristics, dosimetry estimation, and subcutaneous tumor targeting. We also show that [^{177}Lu]Lu-ofatumumab therapy results in long-term survival and elimination of tumor cells in a murine model of disseminated human lymphoma.

MATERIALS AND METHODS

Reagents and Cell Culture

Ofatumumab (IgG1 κ ; Novartis) was purchased from the Washington University clinical pharmacy, and human IgG1 κ was purchased from BioXcel. Raji cells and Raji-luc cells stably expressing luciferase (10) were cultured as previously described (9). SCN-CHX-A''-DTPA ({{[(R)-2-amino-3-(4 isothiocyanatophenyl)propyl]-trans-(S,S)-cyclohexane-1,2-diamine-pentaacetic acid]}}) was from Macrocytics, size-exclusion chromatography columns from Fisher Scientific, and D-luciferin from GoldBio. Sigma provided human serum, sodium acetate, diethylenetriamine pentaacetate, tetramethylammonium acetate, and L-sodium ascorbate. ^{177}Lu from the University of Missouri was dissolved in 0.2 M HCl. Silica gel thin-layer chromatography paper was from Agilent, and the 3-(4,5-dimethylthiazol-2-yl)-5-(3-carboxymethoxyphenyl)-2-(4-sulfophenyl)-2H-tetrazolium (MTS) salt assay was from Promega.

Antibody Conjugation, Radiolabeling, Thin-Layer Chromatography, Mass Spectrometry, and Fast-Performance Liquid Chromatography

Antibody was incubated with SCN-CHX-A''-DTPA in 0.1 M sodium carbonate, pH 9.0, at a chelator-to-antibody molar ratio of 8:1 for 1 h at 37°C and purified by size-exclusion chromatography into 0.5 M NH_4OAc , pH 7.0. A 477-MBq quantity of ^{177}Lu was added to 400 μg of CHX-A''-DTPA-antibody with 20 mM NH_4OAc , pH 7.0. After 2 h at 37°C, DTPA was added to 5 mM final concentration, followed by size-exclusion chromatography purification into saline and the addition of a 10 mg/mL concentration of L-sodium ascorbate. Thin-layer chromatography and fast-performance liquid chromatography were done as previously described (9). Radiochemical yield was assayed with a CRC55-tW dose calibrator. Chelate number was determined using a Fisher Scientific Exactive Plus EMR mass spectrometer operating at a mass (m)-to-charge (z) range from 800 to 12,000 and a resolving power of 8,750 or 17,500 at 300 m/z . Data were analyzed using Protein Metric Intact software.

Serum Stability, Immunoreactivity, In Vitro Stability, Affinity, and Cell Killing Assays

To assay stability, 14.8 MBq of [^{177}Lu]Lu-ofatumumab or ^{177}Lu were added to 10% human serum in 20 mM NaOAc 150 mM NaCl pH 7.0 with 10 mg/mL L-SA and incubated at 37°C. Another aliquot of [^{177}Lu]Lu-ofatumumab was incubated at 4°C in buffer without serum and with 10 mg/mL L-SA. Aliquots were analyzed by thin-layer chromatography at 0, 1, 5, and 7 d. Immunoreactivity was assayed as previously described (9). To assay affinity, 2.5×10^6 Raji cells without or with 10 μg of ofatumumab were incubated with [^{177}Lu]Lu-ofatumumab, washed after 4 h at 23°C, and γ -counted. To assay cell killing, 2×10^6 Raji-luc cells in 1 mL of RPMI medium with 10% heat-treated fetal bovine serum were exposed to no treatment, ofatumumab, [^{177}Lu]Lu-IgG, or [^{177}Lu]Lu-ofatumumab, with cognate unlabeled antibody added to 20 μg total. After 14 h at 37°C, the cells were

washed and 20% were resuspended in fresh medium for an additional 168 h followed by MTS assay.

Biodistribution of [^{177}Lu]Lu-Ofatumumab in Mice with Subcutaneous Raji Tumors

The Washington University in St. Louis Animal Care and Use Committee approved the animal studies. Biodistribution with tumor-bearing mice used female 6- to 8-wk-old immunodeficient Rag2-IL2rg (R2G2, B6;129-Rag2^{tm1Fwa}IL2rg^{tm1Rsky}/DwlHsd) mice (Envigo) injected subcutaneously with 5×10^6 Raji-luc cells. Mice with palpable tumors were injected intravenously with 10–20 μg of [^{177}Lu]Lu-ofatumumab and killed 1, 3, or 7 d later. Distribution was calculated as decay-corrected percentage injected activity per gram (%IA/g) using a Beckman 8000 γ -counter and a 1- to 500-keV window.

Dosimetry Estimation

Naïve 5- to 6-wk-old C57Bl6/N mice injected intravenously with 370 kBq (10 μg) of [^{177}Lu]Lu-ofatumumab were killed 4 h, 1 d, 2 d, 5 d, or 11 d later, and tissue and organs were γ -counted. Bone was counted after marrow separation. Urine and feces were collected at 4 h, 1 d, and 2 d. Organ residence times were calculated by analytic integration of single or multiexponential fits of the time-activity curve and scaled to human

TABLE 1
Human Radiation Dose Estimates for [^{177}Lu]Lu-Ofatumumab Extrapolated to Adult Female Model

Organ	mSv/MBq	rad/mCi
Adrenals	0.39	1.44
Brain	0.05	0.19
Breasts	0.25	0.91
Esophagus	0.26	0.96
Eyes	0.25	0.91
Gallbladder wall	0.28	1.02
Left colon	0.36	1.34
Small intestine	0.41	1.50
Stomach wall	0.29	1.09
Right colon	0.29	1.08
Rectum	0.26	0.97
Heart wall	1.02	3.77
Kidneys	0.43	1.60
Liver	0.36	1.32
Lungs	0.53	1.96
Ovaries	0.39	1.44
Pancreas	0.21	0.77
Salivary glands	0.25	0.92
Red marrow	0.54	2.01
Osteogenic cells	0.82	3.02
Spleen	0.48	1.76
Thymus	0.26	0.96
Thyroid	0.80	2.97
Urinary bladder wall	0.34	1.27
Uterus	0.54	2.00
Total body	0.31	1.14
Effective dose (mGy/MBq; rem/mCi)	0.36	1.34

organ weight by relative organ mass scaling (11), which was not applied to the gastrointestinal tract organs. To estimate human radiation dose, residence times were entered into OLINDA, version 2.2, using the MIRD adult-female model and organ weights from International Commission on Radiological Protection publication 106 (12). The calculated radiation dose includes contributions from β - and γ -rays from ^{177}Lu within the organ, neighboring organs, and remainder of the body.

Therapeutic Studies, Mouse Weight, and Bioluminescent Imaging

R2G2 mice (10 per group) injected intravenously with 1×10^6 Raji-luc cells and either left untreated or injected 4 d later with ofatumumab, [^{177}Lu]Lu-IgG, or [^{177}Lu]Lu-ofatumumab. When used, 20 μg of antibody were injected per mouse. Bioluminescent images were acquired as previously described (13). Mice were killed if they experienced hind-limb paralysis, lost more than 20% of their body weight, or had other signs of morbidity.

Statistics

Statistical analyses used Prism software (version 9.0; GraphPad).

RESULTS

Synthesis of [^{177}Lu]Lu-Ofatumumab and Radiochemical Yield, Purity, and Immunoreactivity

SCN-CHX-A''-DTPA was conjugated to ofatumumab and purified. Mass spectrometry indicated an average of 3.2 chelators per antibody. After ^{177}Lu radiolabeling, [^{177}Lu]Lu-ofatumumab was purified ($n = 7$). Radiochemical purity was more than $99\% \pm 1\%$, radiochemical yield was $93\% \pm 2\%$, and specific activity was $401 \pm 17 \text{ MBq/mg}$. Immunoreactivity was $49\% \pm 3\%$ and $2\% \pm 1\%$ after blocking with unlabeled ofatumumab.

Serum Stability, In Vitro Cell Killing, and Affinity of [^{177}Lu]Lu-Ofatumumab

After 7 d, over 90% of ^{177}Lu remained chelated in buffer at 4°C , and over 75% remained chelated in human serum at 37°C (Supplemental Fig. 1A; supplemental materials are available at <http://jnm.snmjournals.org>). Targeting and killing of CD20-expressing cells were assayed (Supplemental Fig. 1B) by adding either no antibody or [^{177}Lu]Lu-ofatumumab or [^{177}Lu]Lu-IgG (0.74–11.10 MBq/mL) to Raji-luc cells; incubating for 14 h; changing the medium; and, 168 h later, determining cell viability. Compared with no antibody, [^{177}Lu]Lu-IgG showed no cell killing at any dose. [^{177}Lu]Lu-ofatumumab at 3.7 MBq/mL or higher showed dose-dependent killing compared with no antibody and [^{177}Lu]Lu-IgG ($P < 0.05$, $n = 3$). [^{177}Lu]Lu-ofatumumab showed a 4.3 nM dissociation constant for CD20 (Supplemental Fig. 1C), consistent with that noted previously (as described for 2F2 by Teeling et al. (14)).

Biodistribution of [^{177}Lu]Lu-Ofatumumab in C57Bl6/N Mice and Estimation of Human Dosimetry

[^{177}Lu]Lu-ofatumumab biodistribution was determined in C57Bl6/N mice 4 h, 1 d, 2 d, 7 d, and 11 d after injection (Supplemental Table 1) as %IA/g. Blood %IA/g was 38% at 4 h and 19% after 11 d. Bone distribution

was less than 4%, indicating stable chelation because free ^{177}Lu is a bone-seeking radionuclide (15). Liver was 9 %IA at 4 h and 5 %IA/g at 11 d, and marrow was 14 %IA at 4 h and 9 %IA/g at 11 d. Spleen was 8–9 %IA/g. Approximately 13% of the injected activity was excreted.

To estimate human dosimetry, integrated time–activity curves for [^{177}Lu]Lu-ofatumumab were calculated (Supplemental Table 2). The longest (59.7 h) was in the blood, with extended time–activity curves seen in the blood-rich heart cavity, lung, and liver. Because of its large mass, muscle had the second longest time–activity curve, at 39 h. The adult human female model (Table 1) showed estimated dosimetry of 0.2–0.5 mSv/MBq in most organs, with the largest dose being to the heart wall (1.02 mSv/MBq) and lesser doses found for liver, spleen, and kidney (0.36, 0.48, and 0.43 mSv/MBq, respectively). Estimated doses to the osteogenic cells (bone surfaces) and red marrow were 0.82 and 0.54 mSv/MBq, respectively. The estimated effective dose was 0.36 mSv/MBq.

Biodistribution of [^{177}Lu]Lu-Ofatumumab in Mice with Subcutaneous Raji-Cell Tumors

Biodistribution was investigated in R2G2 mice with subcutaneous Raji-cell tumors (Fig. 1). These mice are proficient in double-strand DNA-break repair and are less likely to show artifactual radiation toxicity than are repair-deficient *Prkdc^{SCID}* mice (16). [^{177}Lu]Lu-ofatumumab was injected at a low activity (370–444 kBq) to limit therapeutic effect, and biodistribution was determined 1, 3, and 7 d later (3–16 mice per time point). Blood decreased from about 13 to 6 %IA/g, with a similar splenic distribution. Liver levels were about 5%, and marrow was 10 %IA at 1 d and 5 %IA/g at 7 d. Bone distribution was 2–3 %IA/g. Tumor targeting was 11, 15, and 14 %IA/g at 1, 3, and 7 d, respectively.

Murine Therapy Study

To evaluate [^{177}Lu]Lu-ofatumumab therapeutic efficacy, R2G2 mice were injected intravenously with Raji-luc cells, and tumor

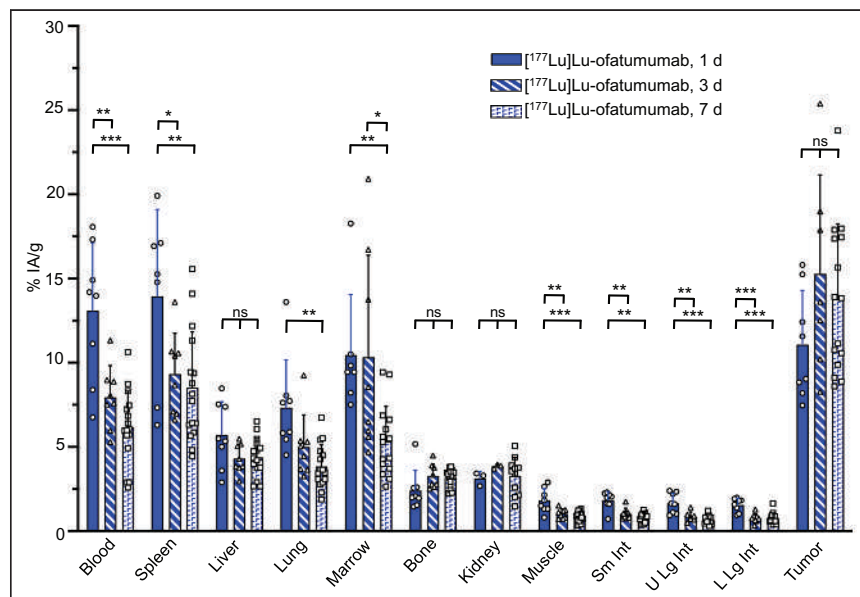


FIGURE 1. [^{177}Lu]Lu-ofatumumab biodistribution in R2G2 mice with subcutaneous Raji tumors. Biodistribution was assayed 1, 3, or 7 d after radiopharmaceutical injection (3–16 mice per time point), with data presented as mean \pm SD. One-way ANOVA compares distribution in organ or tissue at each time point. * $P < 0.05$. ** $P < 0.001$. *** $P < 0.0001$. Sm Int = small intestine; U Lg Int = upper large intestine; L Lg Int = lower large intestine.

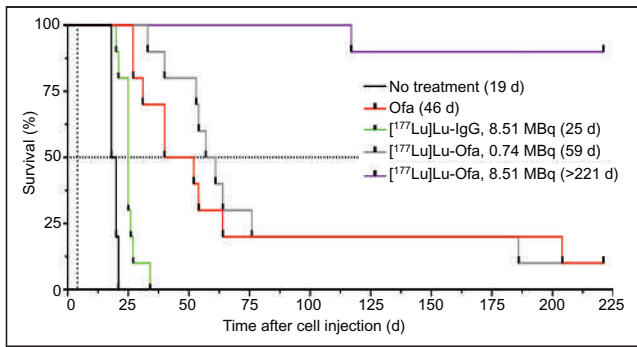


FIGURE 2. Survival analysis of mice with disseminated Raji-luc cells with therapy initiated 4 d after cell injection. Kaplan-Meier graph shows median survival, in days. Ofa = ofatumumab.

cells were quantified by bioluminescent imaging (13). After injection, these cells disseminate to many organs (10,13,17,18), with hind-limb paralysis being a typical cause for killing of the animal due to growth in and around the spine.

Four days after cell injection, the mice either were left untreated or were treated with native ofatumumab, 8.51 MBq of [¹⁷⁷Lu]Lu-human IgG1 (345 ± 27 MBq/kg), 0.74 MBq (30 ± 2.2 MBq/kg) of [¹⁷⁷Lu]Lu-ofatumumab, or 8.51 MBq (345 ± 25.1 MBq/kg) of [¹⁷⁷Lu]Lu-ofatumumab (10 mice per group). Survival (Fig. 2), weight (Supplemental Fig. 2), and bioluminescence (Fig. 3A) were tracked for 221 d. Representative bioluminescent images at selected time points are shown in Figure 3B, and images of all mice just before they died or were killed for cause or study termination are shown in Figure 4.

The median survival of untreated mice was 19 d, with none surviving beyond 22 d. Unlabeled ofatumumab yielded a median survival of 46 d, superior to untreated mice (Mantel-Cox, *P* < 0.0001), with 1 mouse surviving without weight loss or increased bioluminescence. An 8.51-MBq dose of [¹⁷⁷Lu]Lu-IgG yielded 0 of 10 surviving mice and a median survival of 25 d, which was not different from that of untreated mice. For all 3 groups, increased bioluminescence and weight loss occurred before death or killing for cause.

A 0.74-MB dose of [¹⁷⁷Lu]Lu-ofatumumab yielded median survival of 59 d (9/10 mice not surviving), with increased bioluminescence and weight loss before death or killing for cause. This survival was superior to that of untreated mice (Mantel-Cox, *P* < 0.0001) but not to that of mice receiving treatment with unlabeled ofatumumab. Hind-limb paralysis was frequently associated with death or killing for cause (Supplemental Table 3).

Notable therapeutic efficacy resulted from treatment with 8.51 MBq of [¹⁷⁷Lu]Lu-ofatumumab, with 9 of 10 mice surviving with

continuous low bioluminescence (Figs. 3 and 4). This survival was greater than that of untreated mice and of mice treated with unlabeled ofatumumab, 8.51 MBq of [¹⁷⁷Lu]Lu-IgG, or 0.74 MBq of [¹⁷⁷Lu]Lu-ofatumumab (Mantel-Cox, *P* < 0.0003 for all comparisons). One mouse succumbed at 117 d, but this death appeared unrelated to tumor burden or therapy as no weight loss or increased bioluminescence occurred. Surviving mice displayed weight loss from 10 to 35 d after cell injection but recovered and gained weight.

To determine how quickly therapy affected tumor cells, bioluminescence slopes from 1 to 18 d after initiation of therapy were compared (Fig. 5; Supplemental Fig. 3). Compared with no treatment, ofatumumab, 8.51 MBq of [¹⁷⁷Lu]Lu-IgG, and 0.74 MBq of [¹⁷⁷Lu]Lu-ofatumumab slowed, but did not eliminate, tumor-cell proliferation. In contrast, 8.51 MBq of [¹⁷⁷Lu]Lu-ofatumumab quickly eliminated tumor cells, a finding that was significant compared with no treatment, treatment with unlabeled ofatumumab, treatment with 8.51 MBq of [¹⁷⁷Lu]Lu-IgG, or treatment with 0.75 MBq of [¹⁷⁷Lu]Lu-ofatumumab (*P* < 0.05).

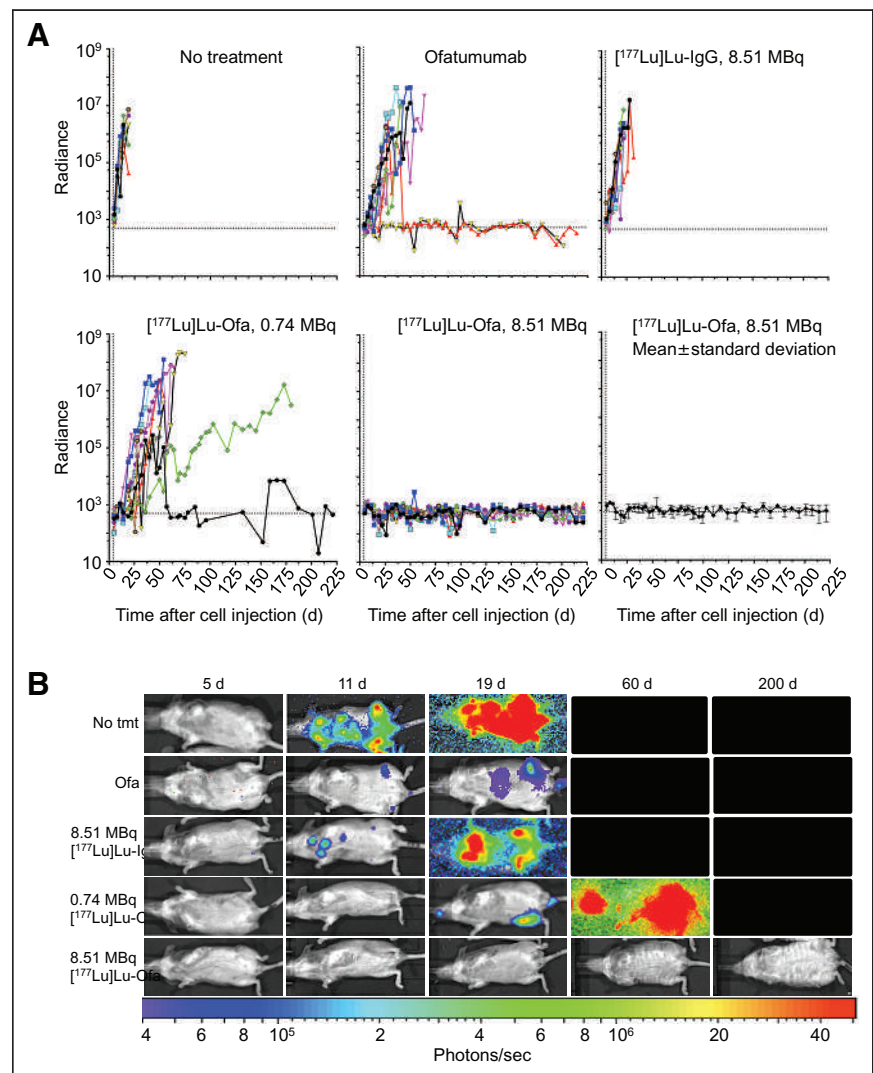


FIGURE 3. Tumor burden of mice with disseminated Raji-luc cells with therapy initiated 4 d after cell injection. (A) Bioluminescence (10 mice per group). (B) Representative bioluminescence images at indicated days after cell injection. Radiance is photons/s/cm²/steradian. Ofa = ofatumumab.

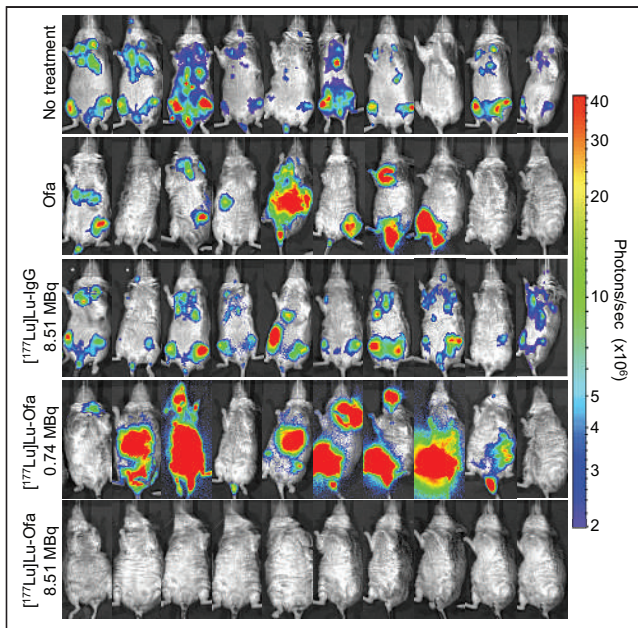


FIGURE 4. Bioluminescence images of untreated or treated mice with disseminated Raji-luc cells on final imaging event before mice were killed for cause or study termination. Ofa = ofatumumab.

DISCUSSION

Our preclinical studies add to prior work demonstrating the potential of radiolabeled anti-CD20 antibodies to treat NHL. We show that [¹⁷⁷Lu]Lu-ofatumumab can be produced with high radiochemical yield and purity, excellent affinity, good stability and immunoreactivity, and potent cell killing. Additional advances include using a fully human anti-CD20 and ¹⁷⁷Lu, which have broad applicability in radiotherapy of cancer. In a model of rapidly progressing disease, we evaluated [¹⁷⁷Lu]Lu-ofatumumab therapy using dose-response studies and bioluminescence monitoring of tumor-cell burden. A single 8.51-MBq dose of [¹⁷⁷Lu]Lu-ofatumumab displayed curative efficacy.

Human dosimetry estimates predict that the highest dose from [¹⁷⁷Lu]Lu-ofatumumab (1.02 mSv/MBq) will be to the heart wall. The relatively radiation-resistant liver and spleen showed 0.36 and

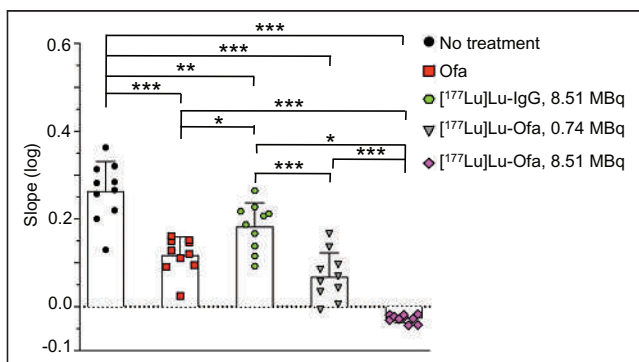


FIGURE 5. Tumor-cell growth in mice 1–18 d after initiation of therapy. Log of slopes of radiance (photons/s/cm²/steradian) over this time are shown as mean ± SD and were analyzed by ANOVA, comparing all samples with each other (10 mice per group). **P* < 0.05. ***P* < 0.005. ****P* < 0.0001. Ofa = ofatumumab.

0.48 mSv/MBq, respectively. The predicted dose to red marrow is 0.54 mSv/MBq, and hematologic toxicity likely will be dose limiting in clinical use, as was found with Bexxar, Zevalin, [¹⁷⁷Lu]Lu-J591 (19), [¹⁷⁷Lu]Lu-G250 anti-CAIX (20), and [¹⁷⁷Lu]Lu-rituximab (21). As 2 Sv is a typical maximal dose for acceptable hematologic toxicity without stem cell support, delivering this radiation to the marrow would be tolerable. As there may be patient-to-patient variability with [¹⁷⁷Lu]Lu-ofatumumab due to cross reactivity with normal CD20-positive cells, our dosimetry data provide guidance for activity administration to humans. Dosimetric estimation could also potentially be obtained using a PET imaging surrogate, such as [⁸⁹Zr]Zr-ofatumumab (9,22).

The stable in vivo chelation of ¹⁷⁷Lu by CHX-A''-DTPA-ofatumumab agrees with the results of others using this chelator–radionuclide combination (23,24). Although it has been suggested that, for stable ¹⁷⁷Lu chelation, macrocyclic DOTA requires high temperatures incompatible with maintaining antibody function (24,25), experiments show that this is not the case (26,27). Thus, CHX-A''-DTPA and DOTA both appear practical for chelation of ¹⁷⁷Lu to antibodies and antibody fragments.

Others have used [¹⁷⁷Lu]Lu-anti-CD20 intact antibodies or ¹⁷⁷Lu-labeled antibody-based radiopharmaceuticals for preclinical and clinical therapy. Ertveld et al. (23), using a single-domain anti-CD20 antibody in immunocompetent mice with CD20-expressing subcutaneous tumors, found a modest therapeutic effect at 140 MBq/mouse; 50 MBq/mouse induced expression of proinflammatory genes, whereas 140 MBq/mouse increased the percentage in the tumor of PD-L1–positive myeloid cells and alternatively activated macrophages. Krasniqi et al. (28) compared a single-domain anti-CD20 antibody with unlabeled rituximab and [¹⁷⁷Lu]Lu-CHX-A''-DTPA-rituximab in mice with CD20-expressing subcutaneous tumors. All treatments increased survival over no treatment, but [¹⁷⁷Lu]Lu-CHX-A''-DTPA-rituximab was only slightly better than rituximab. In a phase I/II study of [¹⁷⁷Lu]Lu-DOTA-rituximab in 31 patients with relapsed or refractory CD20-positive lymphoma, mainly hematologic toxicity was observed, with frequent tumor responses and 8 of 11 patients with follicular lymphoma alive after an 84-mo median follow-up (29).

A major finding of the current study is the high therapeutic efficacy of [¹⁷⁷Lu]Lu-ofatumumab in a murine model of disseminated lymphoma. Therapy was initiated 4 d after intravenous cell injection, when tumor cells are present individually or as small groups, comparable to micrometastatic or minimal residual disease in humans. An 8.51-MBq dose of [¹⁷⁷Lu]Lu-ofatumumab reduced tumor burden within about 2 d and eliminated bioluminescence-detectable tumors, with 9 of 10 mice still alive 221 d later. This response was dose-dependent and specific, as 0.74 MBq of [¹⁷⁷Lu]Lu-ofatumumab and 8.51 MBq of [¹⁷⁷Lu]Lu-IgG did not extend survival or prevent tumor-cell proliferation. Although attenuation from tissue, skin, and fur means that bioluminescent imaging may not detect a low tumor-cell burden (13), the durability of the response suggests complete elimination of tumor cells by 8.51 MBq of [¹⁷⁷Lu]Lu-ofatumumab. After initial weight loss, these mice gained weight, suggesting no or low whole-body toxicity. The internalization of ofatumumab after CD20 binding (30) and the residualization of ¹⁷⁷Lu within the cell may contribute to its therapeutic efficacy. Moreover, the lack of murine sequences in [¹⁷⁷Lu]Lu-ofatumumab suggests a potential for fractionated therapy or repeated treatments. In an interesting approach, with relatively small subcutaneous tumors of rituximab-resistant Raji cells, Malenge et al. (26) combined [¹⁷⁷Lu]Lu-lilotomab (anti-CD37) and unlabeled rituximab, with good therapeutic results.

α -particle therapy is another potential approach to treating lymphoma. Using a murine Raji-cell disseminated lymphoma model, [^{213}Bi]Bi-rituximab ($t_{1/2}$, 45.6 min) was typically curative when tumor burden was low (4 d after cell injection) but not when it was higher (18), perhaps because of lack of time to target larger tumor masses before decay. Similarly, [^{149}Tb]Tb-rituximab ($t_{1/2}$, 4.2 h) therapy initiated 2 d after Daudi-cell intravenous injection increased survival (31). A 1F5 anti-CD20 antibody with chelated ^{211}At ($t_{1/2}$, 7.2 h) was 80% curative when injected 6 d after intravenous cell injection with supporting stem-cell transplantation but only slowly reduced the growth of subcutaneous tumors (32). On the basis of these results and on the multiday tumor-targeting pharmacokinetics of intact antibodies, radioimmunotherapy of larger tumor masses with intact antibodies will likely be most successful using radioisotopes that permit tumor localization before decay, including ^{177}Lu or α -particle-emitting ^{225}Ac with its 10-d half-life.

Our studies add to the literature demonstrating the effectiveness of ^{177}Lu -radiopharmaceuticals in cancer therapy. We found remarkable effectiveness in micrometastatic disease, and the 6.6-d half-life and multiple-cell-diameter killing range of ^{177}Lu suggests that [^{177}Lu]Lu-ofatumumab may be effective against larger tumors.

Although initial anti-CD20 radioimmunotherapies showed limited commercial success for several reasons, we suggest that a re-evaluation of next-generation β - and α -particle therapies is in order. [^{177}Lu]Lu-ofatumumab CD20-targeted radioimmunotherapy may be an effective approach for therapy of NHL or other CD20-expressing diseases.

CONCLUSION

Chx-A''-DTPA-ofatumumab stably chelates ^{177}Lu in vitro and in vivo, and [^{177}Lu]Lu-Chx-A''-ofatumumab effectively targets CD20-expressing tumor xenografts. In a mouse model of disseminated human lymphoma, therapy with [^{177}Lu]Lu-ofatumumab showed curative therapeutic efficacy.

DISCLOSURE

This study was supported in part by the National Institutes of Health (R01CA240711, R01CA229893, and R01CA201035 to Daniel Thorek), the Children's Discovery Institute (MC-II-2021-961 to Diane Abou), and the NIGMS (9995P41GM103422 to the Washington University Biomedical Mass Spectrometry Resource). Richard Wahl is on the scientific advisory board of Clarity Pharmaceuticals, Voximetry, and Seno Medical; has stock options in Clarity Pharmaceutical and Voximetry; receives honoraria from Bristol Myers Squibb, Actinium Pharmaceuticals, Jubilant Draximage, and ITM; and receives research support from Actinium Pharmaceuticals, BMS, Bayer, Siemens, and White Rabbit AI. Diane Abou and Daniel Thorek have an advisory board role for, and own stock in, Diaprost AB and Pharma15. Richard Laforest is a consultant to Curium Pharmaceuticals. No other potential conflict of interest relevant to this article was reported.

ACKNOWLEDGMENTS

We appreciate the assistance of the Washington University Small Animal Imaging Core, cyclotron facilities, and the Biomedical Mass Spectrometry Resource in the Department of Chemistry.

KEY POINTS

QUESTION: Can [^{177}Lu]Lu-anti-CD20 ofatumumab be produced and effectively treat disseminated human NHL in a murine model?

PERTINENT FINDINGS: [^{177}Lu]Lu-ofatumumab specifically killed lymphoma cells in vitro, was cytotoxic in vivo as assessed by bioluminescence imaging, and was curative of disseminated human lymphoma in the murine model. Dosimetry estimates support the feasibility of human translation.

IMPLICATIONS FOR PATIENT CARE: [^{177}Lu]Lu-ofatumumab has exceptional potential for CD20-targeted radioimmunotherapy of patients with NHL.

REFERENCES

1. Siegel RL, Miller KD, Fuchs HE, Jemal A. Cancer statistics, 2022. *CA Cancer J Clin.* 2022;72:7–33.
2. Frost SH, Frayo SL, Miller BW, et al. Comparative efficacy of ^{177}Lu and ^{90}Y for anti-CD20 pretargeted radioimmunotherapy in murine lymphoma xenograft models. *PLoS One.* 2015;10:e0120561.
3. Shadman M, Li H, Rimsza L, et al. Continued excellent outcomes in previously untreated patients with follicular lymphoma after treatment with CHOP plus rituximab or CHOP plus ^{131}I -tositumomab: long-term follow-up of phase III randomized study SWOG-S0016. *J Clin Oncol.* 2018;36:697–703.
4. Sarbisheh EK, Price E. The radiopharmaceutical chemistry of the radioisotopes of lutetium and yttrium. In: Lewis JS, Windhorst AD, Zeglis BM, eds. *Radiopharmaceutical Chemistry.* Springer; 2019:359–370.
5. Wahl RL, Chareonthitawee P, Clarke B, et al. Mars shot for nuclear medicine, molecular imaging, and molecularly targeted radiopharmaceutical therapy. *J Nucl Med.* 2021;62:6–14.
6. Henrich U, Kopka K. Lutathera[®]: The first FDA- and EMA-approved radiopharmaceutical for peptide receptor radionuclide therapy. *Pharmaceuticals (Basel).* 2019;12:E114.
7. Keam SJ. Lutetium Lu 177 vipivotide tetraxetan: first approval. *Mol Diagn Ther.* 2022;26:467–475.
8. Klein C, Lammens A, Schafer W, et al. Epitope interactions of monoclonal antibodies targeting CD20 and their relationship to functional properties. *MAbs.* 2013;5:22–33.
9. Yoon JT, Longtine MS, Marquez-Nostra BV, Wahl RL. Evaluation of next-generation anti-CD20 antibodies labeled with ^{89}Zr in human lymphoma xenografts. *J Nucl Med.* 2018;59:1219–1224.
10. Chao MP, Alizadeh AA, Tang C, et al. Anti-CD47 antibody synergizes with rituximab to promote phagocytosis and eradicate non-Hodgkin lymphoma. *Cell.* 2010;142:699–713.
11. Stabin M. *Fundamentals of Nuclear Medicine Dosimetry.* Springer; 2008:77–119.
12. Radiation dose to patients from radiopharmaceuticals. Addendum 3 to ICRP publication 53. ICRP publication 106. Approved by the Commission in October 2007. *Ann ICRP.* 2008;38:1–197.
13. Hoegger MJ, Longtine MS, Shim K, Wahl RL. Bioluminescent tumor signal is mouse strain and pelt color dependent: experience in a disseminated lymphoma model. *Mol Imaging Biol.* 2021;23:697–702.
14. Teeling JL, French RR, Cragg MS, et al. Characterization of new human CD20 monoclonal antibodies with potent cytolytic activity against non-Hodgkin lymphomas. *Blood.* 2004;104:1793–1800.
15. Repetto-Llamazares AH, Larsen RH, Mollatt C, Lassmann M, Dahle J. Biodistribution and dosimetry of ^{177}Lu -tetulomab, a new radioimmunoconjugate for treatment of non-Hodgkin lymphoma. *Curr Radiopharm.* 2013;6:20–27.
16. A comparative analysis of Rag2/Il2rg (R2G2) and NSG radiosensitivity. ENVIGO website. <https://insights.envigo.com/r2g2-radiation-study-data-a-comparative-analysis-of-r2g2-and-nsg-radiosensitivity>. Published 2017. Accessed December 13, 2022.
17. Ghetie MA, Richardson J, Tucker T, Jones D, Uhr JW, Vitetta ES. Disseminated or localized growth of a human B-cell tumor (Daudi) in SCID mice. *Int J Cancer.* 1990;45:481–485.
18. Havlena GT, Kapadia NS, Huang P, et al. Cure of micrometastatic B-cell lymphoma in a SCID mouse model using ^{213}Bi anti-CD20 monoclonal antibody. *J Nucl Med.* August 18, 2022 [Epub ahead of print].
19. Bander NH, Milowsky MI, Nanus DM, Kostakoglu L, Vallabhajosula S, Goldsmith SJ. Phase I trial of ^{177}Lu -labeled J591, a monoclonal antibody to

- prostate-specific membrane antigen, in patients with androgen-independent prostate cancer. *J Clin Oncol*. 2005;23:4591–4601.
20. Stillebroer AB, Boerman OC, Desar IM, et al. Phase 1 radioimmunotherapy study with lutetium 177-labeled anti-carbonic anhydrase IX monoclonal antibody girentuximab in patients with advanced renal cell carcinoma. *Eur Urol*. 2013;64:478–485.
 21. Yadav MP, Singla S, Thakral P, Ballal S, Bal C. Dosimetric analysis of ¹⁷⁷Lu-DOTA-rituximab in patients with relapsed/refractory non-Hodgkin's lymphoma. *Nucl Med Commun*. 2016;37:735–742.
 22. Giesen D, Lub de Hooge MN, Nijland M, et al. ⁸⁹Zr-PET imaging to predict tumor uptake of ¹⁷⁷Lu-NNV003 anti-CD37 radioimmunotherapy in mouse models of B cell lymphoma. *Sci Rep*. 2022;12:6286.
 23. Ertveldt T, De Beck L, De Ridder K, et al. Targeted radionuclide therapy with low and high-dose lutetium-177-labeled single domain antibodies induces distinct immune signatures in a mouse melanoma model. *Mol Cancer Ther*. 2022;21:1136–1148.
 24. Tully KM, Tendler S, Carter LM, et al. Radioimmunotherapy targeting Delta-like ligand 3 in small cell lung cancer exhibits antitumor efficacy with low toxicity. *Clin Cancer Res*. 2022;28:1391–1401.
 25. Kostelnik TI, Orvig C. Radioactive main group and rare earth metals for imaging and therapy. *Chem Rev*. 2019;119:902–956.
 26. Malenge MM, Patzke S, Ree AH, et al. ¹⁷⁷Lu-lilotomab satetraxetan has the potential to counteract resistance to rituximab in non-Hodgkin's lymphoma. *J Nucl Med*. 2020;61:1468–1475.
 27. Repetto-Llamazares AHV, Malenge MM, O'Shea A, et al. Combination of ¹⁷⁷Lu-lilotomab with rituximab significantly improves the therapeutic outcome in preclinical models of non-Hodgkin's lymphoma. *Eur J Haematol*. 2018;101:522–531.
 28. Krasniqi A, D'Huyvetter M, Xavier C, et al. Theranostic radiolabeled anti-CD20 sdAb for targeted radionuclide therapy of non-Hodgkin lymphoma. *Mol Cancer Ther*. 2017;16:2828–2839.
 29. Forrer F, Oechslein-Oberholzer C, Campana B, et al. Radioimmunotherapy with ¹⁷⁷Lu-DOTA-rituximab: final results of a phase I/II study in 31 patients with relapsing follicular, mantle cell, and other indolent B-cell lymphomas. *J Nucl Med*. 2013;54:1045–1052.
 30. Kumar A, Planchais C, Fronzes R, Mouquet H, Reyes N. Binding mechanisms of therapeutic antibodies to human CD20. *Science*. 2020;369:793–799.
 31. Beyer G-J, Miederer M, Vranješ-Đurić S, et al. Targeted alpha therapy in vivo: direct evidence for single cancer cell kill using ¹⁴⁹Tb-rituximab. *Eur J Nucl Med Mol Imaging*. 2004;31:547–554.
 32. Green DJ, Shadman M, Jones JC, et al. Astatine-211 conjugated to an anti-CD20 monoclonal antibody eradicates disseminated B-cell lymphoma in a mouse model. *Blood*. 2015;125:2111–2119.

²²⁵Ac-MACROPATATE: A Novel α -Particle Peptide Receptor Radionuclide Therapy for Neuroendocrine Tumors

A. Paden King*¹, Nicholas T. Gutsche*¹, Natarajan Raju², Stanley Fayn¹, Kwamena E. Baidoo¹, Meghan M. Bell¹, Colleen S. Olkowski¹, Rolf E. Swenson², Frank I. Lin¹, Samira M. Sadowski³, Stephen S. Adler⁴, Nikki A. Thiele⁵, Justin J. Wilson⁶, Peter L. Choyke¹, and Freddy E. Escorcía^{1,7}

¹Molecular Imaging Branch, Center for Cancer Research, National Cancer Institute, National Institutes of Health, Bethesda, Maryland; ²Chemical and Synthesis Center, National Heart, Lung, and Blood Institute, National Institutes of Health, Bethesda, Maryland; ³Surgical Oncology Program, Center for Cancer Research, National Cancer Institute, National Institutes of Health, Bethesda, Maryland; ⁴Clinical Research Directorate, Frederick National Laboratory for Cancer Research, Frederick, Maryland; ⁵Chemical Sciences Division, Oak Ridge National Laboratory, Oak Ridge, Tennessee; ⁶Department of Chemistry and Chemical Biology, Baker Laboratory, Cornell University, Ithaca, New York; and ⁷Radiation Oncology Branch, Center for Cancer Research, National Cancer Institute, National Institutes of Health, Bethesda, Maryland

Neuroendocrine tumors (NETs) express somatostatin receptors (SSTRs) 2 and 5. Modified variants of somatostatin, the cognate ligand for SSTR2 and SSTR5, are used in treatment for metastatic and locoregional disease. Peptide receptor radionuclide therapy with ¹⁷⁷Lu-DOTATATE (DOTA-octreotate), a β -particle-emitting somatostatin derivative, has demonstrated survival benefit in patients with SSTR-positive NETs. Despite excellent results, a subset of patients has tumors that are resistant to treatment, and alternative agents are needed. Targeted α -particle therapy has been shown to kill tumors that are resistant to targeted β -particle therapy, suggesting that targeted α -particle therapy may offer a promising treatment option for patients with ¹⁷⁷Lu-DOTATATE-resistant disease. Although DOTATATE can chelate the clinically relevant α -particle-emitting radionuclide ²²⁵Ac, the labeling reaction requires high temperatures, and the resulting radioconjugate has suboptimal stability. **Methods:** We designed and synthesized MACROPATATE (MACROPA-octreotate), a novel radioconjugate capable of chelating ²²⁵Ac at room temperature, and assessed its in vitro and in vivo performance. **Results:** MACROPATATE demonstrated comparable affinity to DOTATATE (dissociation constant, 21 nM) in U2-OS-SSTR2, a SSTR2-positive transfected cell line. ²²⁵Ac-MACROPATATE demonstrated superior serum stability at 37°C over time compared with ²²⁵Ac-DOTATATE. Biodistribution studies demonstrated higher tumor uptake of ²²⁵Ac-MACROPATATE than of ²²⁵Ac-DOTATATE in mice engrafted with subcutaneous H69 NETs. Therapy studies showed that ²²⁵Ac-MACROPATATE exhibits significant antitumor and survival benefit compared with saline control in mice engrafted with SSTR-positive tumors. However, the increased accumulation of ²²⁵Ac-MACROPATATE in liver and kidneys and subsequent toxicity to these organs decreased its therapeutic index compared with ²²⁵Ac-DOTATATE. **Conclusion:** ²²⁵Ac-MACROPATATE and ²²⁵Ac-DOTATATE exhibit favorable therapeutic efficacy in animal models. Because of elevated liver and kidney accumulation and lower administered activity for dose-limiting toxicity of ²²⁵Ac-MACROPATATE, ²²⁵Ac-DOTATATE

was deemed the superior agent for targeted α -particle peptide receptor radionuclide therapy.

Key Words: oncology; actinium; targeted α -therapy; neuroendocrine tumors; octreotate; somatostatin

J Nucl Med 2023; 64:549–554

DOI: 10.2967/jnumed.122.264707

Neuroendocrine tumors (NETs) are a heterogeneous family of neoplasms originating in cells within the endocrine and nervous systems that reside in the gastrointestinal tract, lungs, pancreas, thyroid, and gonads (1,2). Many NETs overexpress somatostatin receptors (SSTRs) (3). This high receptor expression offers a targetable vulnerability in NETs, which has long been exploited for therapy.

Somatostatin-like derivatives have been used as drugs themselves or as scaffolds to deliver radioisotopes for peptide receptor radionuclide therapy (PRRT). One of the most successful of these is the pairing of Tyr³-octreotate with the chelator DOTA, yielding DOTATATE (4,5). Radiolabeled DOTATATE has been successfully used for both PET imaging (6) (⁶⁸Ga, ⁶⁴Cu) and therapeutic (¹⁷⁷Lu) purposes. The phase 3 randomized controlled clinical trial NETTER-1 showed that patients with treatment-refractory NETs who received ¹⁷⁷Lu-DOTATATE had significantly better progression-free survival than patients receiving somatostatin analogs (7). The results of this trial led to FDA approval of ¹⁷⁷Lu-DOTATATE (Lutathera; Advanced Accelerator Applications) in January 2018 for the treatment of SSTR-positive gastroenteropancreatic NETs (8).

Although these results made PRRT a first-in-class treatment option for patients with NETs, many are *ab initio* resistant to, or develop resistance after treatment with, β -particle-emitting ¹⁷⁷Lu-DOTATATE. α -particle-emitting radionuclides are an attractive alternative to β -particle-emitting radionuclides because of their short range, which can mitigate off-target effects, and the high energy deposited by these particles over that short range (also known as high linear energy transfer, or LET) (9,10). The α -particle-emitting nuclide ²²⁵Ac has been coupled to prostate-specific membrane antigen (PSMA)-targeting ligands to successfully treat prostate cancers refractory to treatments with androgen deprivation, taxanes, and ¹⁷⁷Lu-PSMA-617 (Pluvicto; Advanced Accelerator Applications),

Received Jul. 22, 2022; revision accepted Nov. 3, 2022.

For correspondence or reprints, contact Freddy E. Escorcía (freddy.escorcía@nih.gov).

*Contributed equally to this work.

Published online Nov. 17, 2022.

Immediate Open Access: Creative Commons Attribution 4.0 International License (CC BY) allows users to share and adapt with attribution, excluding materials credited to previous publications. License: <https://creativecommons.org/licenses/by/4.0/>. Details: <http://jnm.snmjournals.org/site/misc/permission.xhtml>.

COPYRIGHT © 2023 by the Society of Nuclear Medicine and Molecular Imaging.

which is approved for treatment of patients with PSMA-positive metastatic castration-resistant prostate cancer in the United States (11–14). Recently, a phase I clinical trial of patients with gastroenteropancreatic NETs previously treated with ^{177}Lu -DOTATATE and receiving ^{225}Ac -DOTATATE therapy showed stable disease or a partial response in 82% of patients (15). Similarly, another study with ^{225}Ac -DOTATATE found it to have efficacy in patients with SSTR-positive paraganglioma (16). α -emitting PRRT with ^{213}Bi (half-life, 45 min) and ^{212}Pb (half-life, 10.6 h) have shown promising clinical results as well (17,18).

DOTA and its derivatives are used to chelate ^{225}Ac and many of the previously mentioned radionuclides. However, to chelate ^{225}Ac with DOTA to yield high-specific-activity radioconjugates, temperatures above 70°C are typically required. Even if these temperatures are used, the resulting complex's thermodynamic stability (19) and labeling kinetics are suboptimal (20). Thiele *et al.* showed that MACROPA, an 18-membered macrocycle, is capable of chelating ^{225}Ac at room temperature more quickly and at lower concentrations than DOTA (21). The ^{225}Ac -MACROPA complex showed comparable stability (8 d) to ^{225}Ac -DOTA in human serum and in C57BL6 mice. Further preclinical studies have demonstrated the suitability of ^{225}Ac -labeled MACROPA-containing radioconjugates for targeted α -therapy with both small-molecule and antibody conjugates (22,23).

In this work, we synthesized and characterized MACROPATATE, consisting of MACROPA coupled to Tyr³-octreotate, and compared its performance with that of DOTATATE with respect to ^{225}Ac labeling efficiency, serum stability, target engagement, and therapeutic efficacy. We found that MACROPATATE exhibits improved stability over DOTATATE when complexed to ^{225}Ac , maintains high SSTR binding affinity, demonstrates favorable *in vivo* target localization, and has significant antitumor activity.

MATERIALS AND METHODS

Synthesis and Radiolabeling of MACROPATATE and DOTATATE

MACROPATATE and DOTATATE were prepared by conjugating isothiocyanate-activated MACROPA and DO3A-tri-tert-butyl ester, respectively, to immobilized octreotate (21,24,25). After synthesis and deprotection, the products were characterized for purity and identity by high-performance liquid chromatography and liquid chromatography–mass spectrometry, respectively. Full synthetic details for both conjugates are reported in Supplemental Figure 1 (supplemental materials are available at <http://jnm.snmjournals.org>). Radiolabeling of MACROPATATE and DOTATATE with ^{225}Ac was performed at room temperature or 70°C , respectively, in NH_4OAc (pH 5.5), and the products were characterized using instant thin-layer chromatography (ITLC). Full radiolabeling and characterization details are provided in the supplemental information.

Cell Culture and In Vitro Assays

A panel of SSTR2- and SSTR5-expressing cell lines were cultured, and their SSTR2 and SSTR5 expression levels were evaluated using flow cytometry. The highly positive U2OS-SSTR2 cell line was used to confirm the binding affinity of radiolabeled ^{225}Ac -MACROPATATE in a saturation binding assay. Full cell culture details and experimental procedures for flow cytometry and saturation assays are reported in the supplemental information.

Serum Stability Studies

^{225}Ac -MACROPATATE and ^{225}Ac -DOTATATE were evaluated for stability in human serum (EMD Millipore) at 37°C and pH 7.4. Radiochelate was diluted to 370 kBq in 1 mL of human serum and placed on an Eppendorf ThermoMixer set to 37°C . At fixed intervals, aliquots were removed from the reactions and analyzed by ITLC as described in the supplemental information.

Murine Subcutaneous Xenograft Models

All procedures and animal studies followed a protocol approved by the National Institutes of Health Institutional Animal Care and Use Committee (protocol ROB104). Female athymic homozygous nude mice (NCI Athymic NCr-nu/nu strain 553; Charles River Laboratories), 8–10 wk old, were subcutaneously engrafted with 8×10^6 H69 cells in 200 μL of ice-cold phosphate-buffered saline. Treatment of tumors with radiotracers for biodistribution or therapy studies was performed once palpable tumors developed, approximately 1 mo after inoculation. The biodistributions of both ^{225}Ac -MACROPATATE and ^{225}Ac -DOTATATE were evaluated in H69 subcutaneous tumor models, both with and without D-lysine pretreatment (26). Full experimental details for the biodistribution experiments are reported in the supplemental information.

Dose-Finding Study for ^{225}Ac -MACROPATATE

To evaluate the therapeutic potential of ^{225}Ac -MACROPATATE, we performed a dose-finding study on mice. Mice ($n \geq 3$) bearing H69 tumor xenografts were first injected with D-lysine hydrochloride (35 mg/mouse) and then treated with 148, 93.3, 46.3, or 23.1 kBq of ^{225}Ac -MACROPATATE; their body weights and tumor growth were monitored over several weeks. The highest tested dose of ^{225}Ac -MACROPATATE was based on a recent report of therapy using ^{225}Ac -DOTATATE, which found that 148 kBq was well tolerated in mice (27).

Head-to-Head Therapy Study with ^{225}Ac -MACROPATATE or ^{225}Ac -DOTATATE

For our therapy study, we wished to identify the highest administered activities that exhibited acceptable toxicity as measured by mouse weight loss and survival, and we found 46.3 kBq of ^{225}Ac -MACROPATATE and 148 kBq of ^{225}Ac -DOTATATE to be suitable. Animals engrafted with H69 cells were treated with either of the 2 radioconjugates or saline ($n = 8$ –10, each). Local control and survival were the primary outcomes. All groups were tracked for humane endpoints including, but not limited to, tumors larger than 2,000 mm^3 and weight loss greater than 20%.

Statistical Analysis

Statistical analysis was performed using Prism (version 9.0; GraphPad Software). Statistical analysis of survival curves was performed using the log-rank test. Comparisons of organ uptake, tumor volume, and stability were performed using the Student *t* test.

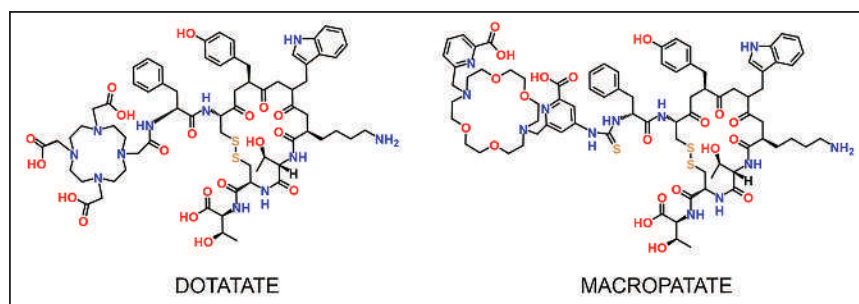


FIGURE 1. Structures of DOTATATE and MACROPATATE.

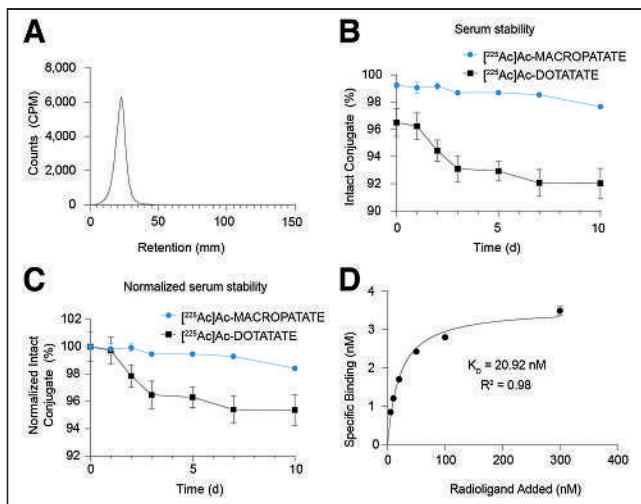


FIGURE 2. MACROPATATE stably chelates ^{225}Ac and binds to SSTR. (A) Representative ITLC chromatogram of ^{225}Ac -MACROPATATE. (B) Intact conjugate remaining over time of ^{225}Ac -MACROPATATE and ^{225}Ac -DOTATATE in human serum incubated at 37°C , as measured by ITLC. (C) Percentage of initial intact conjugate remaining over time, normalized to starting amount, after incubation in human serum at 37°C . (D) Assessment of SSTR2 binding affinity of ^{225}Ac -MACROPATATE in U2-OS SSTR2 cells using saturation binding assay.

RESULTS

MACROPATATE Forms Stable Complex with ^{225}Ac at Room Temperature

We successfully synthesized DOTATATE and MACROPATATE with good yields and high purity, characterizing the identity and purity of both molecules via high-performance liquid chromatography and mass spectrometry (Fig. 1; Supplemental Fig. 1). After synthesis, we labeled both DOTATATE and MACROPATATE with ^{225}Ac . Radiolabeling was conducted in mildly acidic (pH 5.5) NH_4OAc buffer (0.1 M). We found that MACROPATATE could be radiolabeled quantitatively after 1 h of incubation at room temperature ($18\text{--}20^\circ\text{C}$), whereas DOTATATE required heating at 70°C for 1 h to achieve comparable purity and yield. Typical specific activities for both radioconjugates were approximately 185 GBq/mmol. A representative instant thin-layer chromatogram of ^{225}Ac -MACROPATATE is shown in Figure 2A and Supplemental Figure 2, and an instant thin-layer chromatogram of ^{225}Ac -DOTATATE is shown in Supplemental Figure 3.

We evaluated the stability of both molecules in human serum at 37°C using ITLC (Figs. 2B and 2C; Supplemental Figs. 4–7). ^{225}Ac -MACROPATATE and ^{225}Ac -DOTATATE were stable to 10 d. Stability experiments conducted in human serum indicated that ^{225}Ac -MACROPATATE has significantly greater stability than ^{225}Ac -DOTATATE (98% vs. 95%, $P = 0.0097$), and our results compared well with a recent stability investigation of ^{225}Ac -DOTATATE reported by others, which found 90% intact ^{225}Ac -DOTATATE after 10 d (27). Thus, ^{225}Ac -MACROPATATE exhibited a modest yet significant stability advantage over ^{225}Ac -DOTATATE.

^{225}Ac -MACROPATATE Retains Affinity for SSTR

After evaluating the purity and stability of the ^{225}Ac -MACROPATATE conjugate, we sought to confirm its binding affinity using SSTR2-expressing cells *in vitro* (28–30). Saturation binding assays showed a binding affinity of 21 nM (Fig. 2D), comparable to that reported for Eu-DOTATATE (22 nM), which has been used as a surrogate for ^{225}Ac -labeled DOTATATE (27). This value is also in a similar range to other studies examining radiolabeled somatostatin derivatives (31,32). These results confirmed that MACROPA conjugation to octreotate does not adversely affect SSTR binding.

Cell Lines Were Selected for *In Vivo* Studies

To find a suitable model for our murine subcutaneous xenograft models, we assessed SSTR2 and SSTR5 expression by flow cytometry in several cell lines (U2-OS, U2-OS-SSTR2, AR42J, H69, Bon-1, and U937) (Fig. 3). U2-OS exhibited low to negligible levels of both SSTR2 and SSTR5. All other cell lines were SSTR2-positive, with expression decreasing in the order U2OS-SSTR2 > H69 > AR42J > U937 > Bon-1. The cell lines H69, AR42J, and U937 also displayed moderate expression of SSTR5. The H69 cell line was chosen for *in vivo* experiments because of its high expression of SSTR2 and SSTR5 and its established history as a model system for investigating SSTR-targeting radioconjugates (33,34).

^{225}Ac -MACROPATATE Demonstrates Target Engagement *In Vivo*

After confirming the stability and SSTR binding of ^{225}Ac -MACROPATATE *in vitro*, we evaluated its biodistribution and compared it with that of ^{225}Ac -DOTATATE in mice bearing SSTR-positive H69 tumor xenografts. Both tracers showed favorable tumor uptake, with percentage injected activity per gram of tissue of 9% and 5% at 2 h and 4% and 2% at 24 h for ^{225}Ac -MACROPATATE and ^{225}Ac -DOTATATE, respectively (Figs. 4A and 4B; Supplemental Figs. 8–11). Although both tracers displayed excellent tumor-to-muscle ratios of more than 50:1 at 4 h (Fig. 4C), they also had high renal uptake, as is typical of SSTR-targeting peptides (35,36). ^{225}Ac -MACROPATATE displayed significantly higher tumor accumulation at 2 and 24 h than did ^{225}Ac -DOTATATE ($P < 0.05$). However, the liver and kidney uptake of ^{225}Ac -MACROPATATE were also higher, possibly because the higher hydrophobicity of the conjugate could slow clearance, leading to increased liver uptake. The liver accumulation

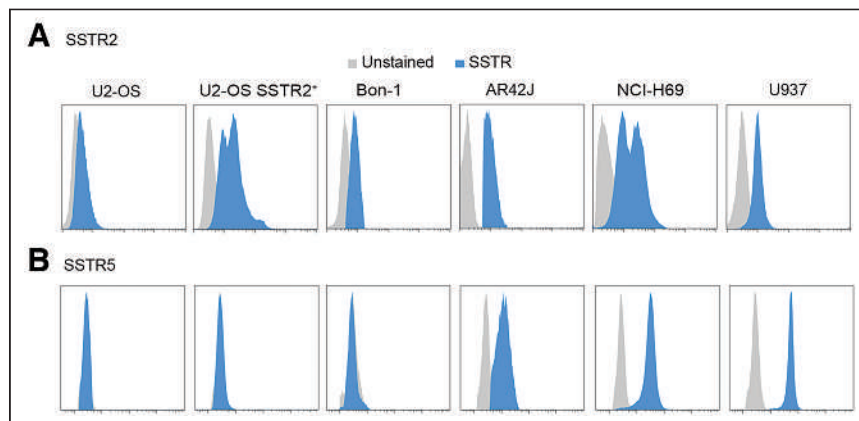


FIGURE 3. Flow cytometry assessment of SSTR2 (A) and SSTR5 (B) in panel of SSTR-expressing cell lines.

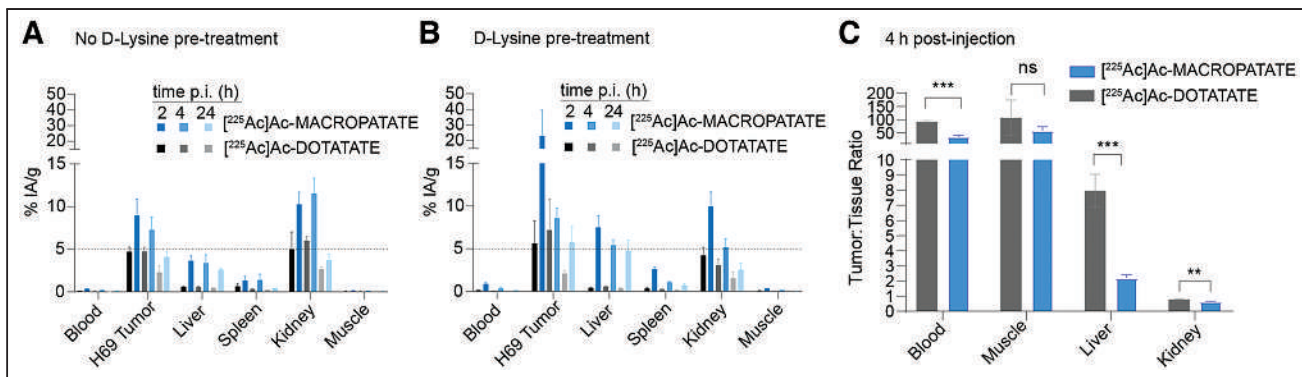


FIGURE 4. ^{225}Ac -labeled MACROPATATE and DOTATATE bind to SSTR-positive tumors. (A and B) Selected-organ biodistribution ($n = 3$) of ^{225}Ac -MACROPATATE and ^{225}Ac -DOTATATE (37 kBq) without (A) or with (B) preadministration of D-lysine (35 mg/mouse). (C) Corresponding tumor-to-tissue ratios for selected organs with lysine pretreatment. Full 12-organ biodistribution data are reported in Supplemental Figures 8–11. Error bars represent SD. *** $P < 0.005$. * $P < 0.01$. %IA/g = percentage injected activity per gram of tissue.

of ^{225}Ac -MACROPATATE was 2–3 times higher than that of ^{225}Ac -DOTATATE at all time points investigated.

The high kidney accumulation of peptide radioconjugates is routinely lowered by preadministration of D-lysine (26). Accordingly, we observed a lower kidney percentage injected activity per gram of tissue for both ^{225}Ac -MACROPATATE and ^{225}Ac -DOTATATE after D-lysine administration than in kidneys of animals not receiving D-lysine. This lowered kidney accumulation of the radiotracers was most pronounced at 4 h after injection, with the kidney signal for ^{225}Ac -MACROPATATE changing from 11.5% to 5.2% ($P = 0.0057$) and ^{225}Ac -DOTATATE decreasing from 6.0% to 3.1% ($P = 0.0039$).

^{225}Ac -MACROPATATE and ^{225}Ac -DOTATATE Delay Tumor Growth and Improve Survival of Mice Bearing NET Xenografts

The promising biodistribution profile of ^{225}Ac -MACROPATATE led us to investigate its therapeutic efficacy. As a preliminary investigation, we evaluated a series of treatment activities of ^{225}Ac -MACROPATATE ranging from 23.1 to 148 kBq in mice bearing H69 tumor xenografts. All mice in the 148-kBq treatment group (10/10) and 1 of 3 mice in the 92.3-kBq group were euthanized within 10 d of treatment because of substantial weight loss (>20%). All other mice displayed minimal weight loss, and a clear dose-dependent reduction in tumor volume was evident (Supplemental Figs. 12–14). On the basis of these results, 46.3 kBq of ^{225}Ac -MACROPATATE was selected as the appropriate dose for further investigation.

Animals treated with ^{225}Ac -MACROPATATE and ^{225}Ac -DOTATATE demonstrated a significant tumor growth delay and improvements in survival compared with saline-treated controls (Figs. 5A–5C; Supplemental Figs. 15–17). Mice treated with ^{225}Ac -MACROPATATE exhibited an initial reduction in tumor volume lasting approximately 3 wk after treatment. However,

the tumors subsequently relapsed in most mice (7 of 8). Conversely, ^{225}Ac -DOTATATE treatment resulted in complete, durable tumor remission for all mice. However, 2 mice in the ^{225}Ac -DOTATATE treatment group were euthanized because of weight loss. Although mice in the MACROPATATE treatment group also displayed some weight loss immediately after treatment, their weights stabilized within 2 wk (Fig. 5D). ^{225}Ac -MACROPATATE significantly improved median survival relative to the vehicle control (55 d vs. 26 d; log rank, $P = 0.0006$), whereas 8 of 10 mice (80%) treated with ^{225}Ac -DOTATATE survived the full 100-d duration of the study.

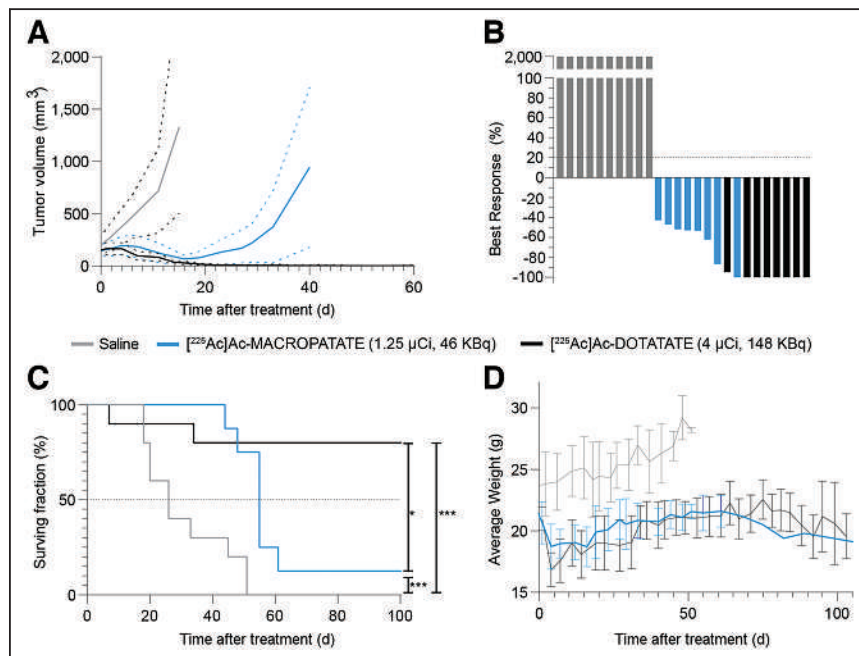


FIGURE 5. Therapeutic response of mice bearing H69 lung NET xenografts treated with ^{225}Ac -MACROPATATE (46 kBq), ^{225}Ac -DOTATATE (148 kBq), or vehicle control shows that targeted α -therapy with ^{225}Ac -MACROPATATE and ^{225}Ac -DOTATATE is effective. (A) Tumor volume measurements over time. Solid lines represent average volume, and dashed lines represent 95% CI. Plots for each dataset are discontinued after first mouse death due to excessive tumor volume. Full tumor volume measurements for study duration for each mouse are reported in Supplemental Figures 15–17. (B) Maximal response to treatment (tumor volume growth percentage) of individual mice. Nonresponding mice are represented as full tumor growth (2,000% increase). (C) Mouse survival over time. Endpoint was defined as tumor volume > 2,000 mm^3 or weight loss over 20% of starting weight. (D) Average mouse body weights over time for each treatment group. Error bars represent SD. *** $P < 0.005$. * $P < 0.05$.

Overall, ^{225}Ac -MACROPATATE exhibited favorable local control and a survival benefit over saline-treated animals. However, mice treated with ^{225}Ac -DOTATATE showed significantly better local control and overall survival ($P < 0.02$).

DISCUSSION

PRRT with ^{177}Lu -DOTATATE represents a significant advance for patients with SSTR-expressing NETs. Nevertheless, treatment options for tumors refractory to ^{177}Lu -based PRRT are needed. By exploiting the unique properties of α -particles, namely high energy deposition over a short path, we may be able to overcome resistance to ^{177}Lu -based PRRT (16,27,37,38). However, the DOTA chelator used in these and other studies is suboptimal for chelation of the large Ac^{3+} ion (19). With the goal of achieving a more stable SSTR-targeting radioconjugate for ^{225}Ac targeted α -particle therapy, we designed, synthesized, and characterized the conjugate MACROPATATE, wherein we replace the DOTA of DOTATATE with the expanded macrocyclic chelator MACROPA, which has been shown to more stably chelate $^{225}\text{Ac}^{3+}$ than DOTA can (21).

We confirmed that ^{225}Ac -MACROPATATE displayed a high tumor accumulation, tumor growth delay, and survival benefit in xenograft models of NETs. However, our radioconjugate also exhibited a narrow therapeutic index as evinced by toxicity at lower injected activities than is the case with ^{225}Ac -DOTATATE. As such, the head-to-head therapy study was performed with a 3-fold higher injected activity in animals receiving ^{225}Ac -DOTATATE than in those receiving ^{225}Ac -MACROPATATE. Biodistribution studies indicated a relatively high liver accumulation for ^{225}Ac -MACROPATATE. Notably, unlike most other organs, this liver signal did not appear to diminish over time. This persistent accumulation of ^{225}Ac may arise from metabolism of the radioconjugate and may be responsible for the observed higher toxicity of ^{225}Ac -MACROPATATE. Previous investigations of ^{177}Lu -DOTATATE have indicated significant degradation of the targeting octreotate portion of the tracer, likely because of metabolism (39). Such metabolism may significantly impact the biodistribution of the ^{225}Ac radioconjugates explored in this work. Thus, the disparate off-target uptake of ^{225}Ac -MACROPATATE and ^{225}Ac -DOTATATE despite their similar tumor accumulation may also reflect accumulation of fragmented species in nontarget organs. Although ^{225}Ac -MACROPATATE demonstrates significant antitumor activity in SSTR-expressing models of NET, ^{225}Ac -MACROPATATE remains inferior to ^{225}Ac -DOTATATE *in vivo*. Therefore, ^{225}Ac -MACROPATATE requires significant optimization to decrease off-target accumulation and associated toxicity. For instance, variation of the specific activity or molar amount of ^{225}Ac -MACROPATATE injected may provide decreased background accumulation while preserving tumor uptake, for such optimization has been shown to greatly improve the pharmacokinetic profile of ^{177}Lu -DOTATATE (40).

Targeted α -particle therapy agents directed at NETs, such as ^{225}Ac -DOTATATE, have demonstrated promising results in small clinical studies and warrant further investigation. Other α -particle-emitting radionuclides being investigated include ^{213}Bi and ^{212}Pb . Recently, a phase I study with the α -particle-emitting PRRT agent ^{212}Pb -DOTAMTATE, which has a lead-optimized chelator, has shown good tolerability and overall response rates of 80% in patients naïve to PRRT (18). The phase II study (NCT05153772) is open and recruiting. These studies indicate that the intrinsic properties of α -emitters can elicit responses in tumors otherwise refractory to β -emitting PRRT (41,42).

More broadly, several strategies aiming to improve the efficacy of ^{177}Lu -PRRT in NETs are being investigated and may apply to targeted α -particle therapy PRRT as well. For instance, deploying epigenetic modulators has been shown to increase the membrane expression of SSTR and subsequent accumulation of PRRT agent (43–46). Combinatorial approaches exploiting inhibitors of DNA damage repair are also being explored (NCT04086485, NCT04375267, and NCT03958045).

CONCLUSION

We have successfully synthesized MACROPATATE, a novel SSTR2- and SSTR5-targeting PRRT agent tailored to deliver ^{225}Ac to NETs. Importantly, we showed that MACROPATATE is able to chelate ^{225}Ac at room temperature and that this complex has 4-fold lower susceptibility to degradation than ^{225}Ac -DOTATATE in human serum. Both ^{225}Ac -MACROPATATE and ^{225}Ac -DOTATATE demonstrated excellent *in vivo* target engagement in NET xenografts and exhibited local control and survival superior to saline. However, although ^{225}Ac -MACROPATATE had *in vitro* stability superior to ^{225}Ac -DOTATATE, it underperformed compared with ^{225}Ac -DOTATATE *in vivo*. Optimization is therefore needed before further translation.

DISCLOSURE

This work was supported in part by the National Institutes of Biomedical Imaging and Bioengineering of the National Institutes of Health (awards R21EB027282 and R01EB029259), as well as by the National Cancer Institute from Intramural Research Program funds ZIA BC 011800 and ZIA BC 010891. This project was funded in whole or in part by the National Cancer Institute, National Institutes of Health, under contract 75N91019D00024. The content of this publication does not necessarily reflect the views or policies of the Department of Health and Human Services, nor does mention of trade names, commercial products, or organizations imply endorsement by the U.S. government. Justin Wilson and Nikki Thiele are authors of a patent for the use of MACROPA as a chelator for ^{225}Ac chelation. No other potential conflict of interest relevant to this article was reported.

ACKNOWLEDGMENTS

We thank Dr. Julie Nonnekens for providing the U2OS-SSTR2 cell line and Dr. Mark Hellmitch for providing the Bon-1 cell line. The graphical abstract figure was created using BioRender.com.

KEY POINTS

QUESTION: Can chemical conjugation of the MACROPA chelator to SSTR-targeting octreotate result in an SSTR-targeting radioconjugate for targeted α -therapy superior to DOTATATE?

PERTINENT FINDINGS: ^{225}Ac -MACROPATATE demonstrated *in vitro* SSTR2 affinity comparable to that of the standard ^{225}Ac -DOTATATE, as well as higher *in vivo* uptake in SSTR-positive xenografts. However, its efficacy is limited by a poor therapeutic index, highlighting a need for further optimization before translation.

IMPLICATIONS FOR PATIENT CARE: We confirm that targeted α -therapies for NETs demonstrate high efficacy in preclinical studies. Such agents warrant further clinical investigation to offer a therapeutic option for patients with disease refractory to β -particle PRRT.

REFERENCES

- Oronsky B, Ma PC, Morgensztern D, Carter CA. Nothing but NET: a review of neuroendocrine tumors and carcinomas. *Neoplasia*. 2017;19:991–1002.
- Chauhan A, Yu Q, Ray N, et al. Global burden of neuroendocrine tumors and changing incidence in Kentucky. *Oncotarget*. 2018;9:19245–19254.
- Alonso-Gordoa T, Capdevila J, Grande E. GEP-NETs update: biotherapy for neuroendocrine tumours. *Eur J Endocrinol*. 2015;172:R31–R46.
- Pauwels E, Cleeren F, Bormans G, Deroose CM. Somatostatin receptor PET ligands: the next generation for clinical practice. *Am J Nucl Med Mol Imaging*. 2018;8:311–331.
- Reubi JC, Schar JC, Waser B, et al. Affinity profiles for human somatostatin receptor subtypes SST1–SST5 of somatostatin radiotracers selected for scintigraphic and radiotherapeutic use. *Eur J Nucl Med*. 2000;27:273–282.
- Wild D, Bomanji JB, Benkert P, et al. Comparison of ⁶⁸Ga-DOTANOC and ⁶⁸Ga-DOTATATE PET/CT within patients with gastroenteropancreatic neuroendocrine tumors. *J Nucl Med*. 2013;54:364–372.
- Strosberg J, El-Haddad G, Wolin E, et al. Phase 3 trial of ¹⁷⁷Lu-Dotatate for mid-gut neuroendocrine tumors. *N Engl J Med*. 2017;376:125–135.
- Mitra ES. Neuroendocrine tumor therapy: ¹⁷⁷Lu-DOTATATE. *AJR*. 2018;211:278–285.
- Wild D, Frischknecht M, Zhang H, et al. Alpha- versus beta-particle radiolabeled therapy in a human prostate cancer model (²¹³Bi-DOTA-PESIN and ²¹³Bi-AMBA versus ¹⁷⁷Lu-DOTA-PESIN). *Cancer Res*. 2011;71:1009–1018.
- King AP, Lin FI, Escorcia FE. Why bother with alpha particles? *Eur J Nucl Med Mol Imaging*. 2021;49:7–17.
- Kojima S, Cuttler JM, Shimura N, Koga H, Murata A, Kawashima A. Present and future prospects of radiation therapy using alpha-emitting nuclides. *Dose Response*. 2018;16:1559325817747387.
- Kratochwil C, Bruchertseifer F, Rathke H, et al. Targeted alpha-therapy of metastatic castration-resistant prostate cancer with ²²⁵Ac-PSMA-617: swimmer-plot analysis suggests efficacy regarding duration of tumor control. *J Nucl Med*. 2018;59:795–802.
- Sathekge M, Bruchertseifer F, Knoesen O, et al. ²²⁵Ac-PSMA-617 in chemotherapy-naïve patients with advanced prostate cancer: a pilot study. *Eur J Nucl Med Mol Imaging*. 2019;46:129–138.
- Sartor O, de Bono J, Chi KN, et al. Lutetium-177-PSMA-617 for metastatic castration-resistant prostate cancer. *N Engl J Med*. 2021;385:1091–1103.
- Ballal S, Yadav MP, Bal C, Sahoo RK, Tripathi M. Broadening horizons with ²²⁵Ac-DOTATATE targeted alpha therapy for gastroenteropancreatic neuroendocrine tumour patients stable or refractory to ¹⁷⁷Lu-DOTATATE PRRT: first clinical experience on the efficacy and safety. *Eur J Nucl Med Mol Imaging*. 2020;47:934–946.
- Yadav MP, Ballal S, Sahoo RK, Bal C. Efficacy and safety of ²²⁵Ac-DOTATATE targeted alpha therapy in metastatic paragangliomas: a pilot study. *Eur J Nucl Med Mol Imaging*. 2022;49:1595–1606.
- Kratochwil C, Giesel FL, Bruchertseifer F, et al. ²¹³Bi-DOTATOC receptor-targeted alpha-radiation therapy induces remission in neuroendocrine tumours refractory to beta radiation: a first-in-human experience. *Eur J Nucl Med Mol Imaging*. 2014;41:2106–2119.
- Delpassand ES, Tworowska I, Esfandiari R, et al. Targeted alpha-emitter therapy with ²¹²Pb-DOTAMTATE for the treatment of metastatic SSTR-expressing neuroendocrine tumors: first-in-human, dose-escalation clinical trial. *J Nucl Med*. 2022;63:1326–1333.
- Deal KA, Davis IA, Mirzadeh S, Kennel SJ, Brechbiel MW. Improved in vivo stability of actinium-225 macrocyclic complexes. *J Med Chem*. 1999;42:2988–2992.
- Yang H, Wilson JJ, Orvig C, et al. Harnessing alpha-emitting radionuclides for therapy: radiolabeling method review. *J Nucl Med*. 2022;63:5–13.
- Thiele NA, Brown V, Kelly JM, et al. An eighteen-membered macrocyclic ligand for actinium-225 targeted alpha therapy. *Angew Chem Int Ed Engl*. 2017;56:14712–14717.
- Kelly JM, Amor-Coarasa A, Ponnala S, et al. A single dose of ²²⁵Ac-RPS-074 induces a complete tumor response in an LNCaP xenograft model. *J Nucl Med*. 2019;60:649–655.
- Bell MM, Gutsche NT, King AP, et al. Glypican-3-targeted alpha particle therapy for hepatocellular carcinoma. *Molecules*. 2020;26:4.
- Axelsson O, Olsson A, inventors; GE Healthcare AS, assignee. Synthesis of cyclen derivatives. U.S. patent 8,138,332 (B2). March 20, 2012.
- Haug AR, Auernhammer CJ, Wangler B, et al. ⁶⁸Ga-DOTATATE PET/CT for the early prediction of response to somatostatin receptor-mediated radionuclide therapy in patients with well-differentiated neuroendocrine tumors. *J Nucl Med*. 2010;51:1349–1356.
- Behr TM, Sharkey RM, Sgouros G, et al. Overcoming the nephrotoxicity of radiometal-labeled immunoconjugates: improved cancer therapy administered to a nude mouse model in relation to the internal radiation dosimetry. *Cancer*. 1997;80:2591–2610.
- Tafreshi NK, Pandya DN, Tichacek CJ, et al. Preclinical evaluation of [²²⁵Ac]Ac-DOTA-TATE for treatment of lung neuroendocrine neoplasms. *Eur J Nucl Med Mol Imaging*. 2021;48:3408–3421.
- Lin M, Welch MJ, Lapi SE. Effects of chelator modifications on ⁶⁸Ga-labeled [Tyr³]octreotide conjugates. *Mol Imaging Biol*. 2013;15:606–613.
- Fani M, Del Pozzo L, Abiraj K, et al. PET of somatostatin receptor-positive tumors using ⁶⁴Cu- and ⁶⁸Ga-somatostatin antagonists: the chelate makes the difference. *J Nucl Med*. 2011;52:1110–1118.
- Fani M, Braun F, Waser B, et al. Unexpected sensitivity of sst2 antagonists to N-terminal radiometal modifications. *J Nucl Med*. 2012;53:1481–1489.
- Stallons TAR, Saidi A, Tworowska I, Delpassand ES, Torgue JJ. Preclinical investigation of ²¹²Pb-DOTAMTATE for peptide receptor radionuclide therapy in a neuroendocrine tumor model. *Mol Cancer Ther*. 2019;18:1012–1021.
- Ullrich M, Bergmann R, Peitzsch M, et al. Multimodal somatostatin receptor therapeutics using [⁶⁴Cu]-[¹⁷⁷Lu]-DOTA-(Tyr³)octreotate and AN-238 in a mouse pheochromocytoma model. *Theranostics*. 2016;6:650–665.
- Bogden AE, Taylor JE, Moreau JP, Coy DH, LePage DJ. Response of human lung tumor xenografts to treatment with a somatostatin analogue (Somatuline). *Cancer Res*. 1990;50:4360–4365.
- Isobe T, Onn A, Morgensztern D, et al. Evaluation of novel orthotopic nude mouse models for human small-cell lung cancer. *J Thorac Oncol*. 2013;8:140–146.
- Geenen L, Nonnekens J, Konijnenberg M, Baatout S, De Jong M, Aerts A. Overcoming nephrotoxicity in peptide receptor radionuclide therapy using [¹⁷⁷Lu]-DOTA-TATE for the treatment of neuroendocrine tumours. *Nucl Med Biol*. 2021;102–103:1–11.
- Vegt E, de Jong M, Wetzels JF, et al. Renal toxicity of radiolabeled peptides and antibody fragments: mechanisms, impact on radionuclide therapy, and strategies for prevention. *J Nucl Med*. 2010;51:1049–1058.
- Bal C, Yadav M, Ballal S, Tripathi M. Safety and therapeutic efficacy of ²²⁵Ac-DOTATATE targeted alpha therapy in metastatic gastroenteropancreatic neuroendocrine tumors stable or refractory to ¹⁷⁷Lu-DOTATATE PRRT [abstract]. *J Nucl Med*. 2020;61(suppl 1):416.
- Miederer M, Henriksen G, Alke A, et al. Preclinical evaluation of the alpha-particle generator nuclide ²²⁵Ac for somatostatin receptor radiotherapy of neuroendocrine tumors. *Clin Cancer Res*. 2008;14:3555–3561.
- Lubberink M, Wilking H, Ost A, et al. In vivo instability of ¹⁷⁷Lu-DOTATATE during peptide receptor radionuclide therapy. *J Nucl Med*. 2020;61:1337–1340.
- Nicolas GP, Mansi R, McDougall L, et al. Biodistribution, pharmacokinetics, and dosimetry of ¹⁷⁷Lu-, ⁹⁰Y-, and ¹¹¹In-labeled somatostatin receptor antagonist OPS201 in comparison to the agonist ¹⁷⁷Lu-DOTATATE: the mass effect. *J Nucl Med*. 2017;58:1435–1441.
- Yadav MP, Ballal S, Sahoo RK, Tripathi M, Seth A, Bal C. Efficacy and safety of ²²⁵Ac-PSMA-617 targeted alpha therapy in metastatic castration-resistant prostate cancer patients. *Theranostics*. 2020;10:9364–9377.
- Kratochwil C, Bruchertseifer F, Giesel FL, et al. ²²⁵Ac-PSMA-617 for PSMA-targeted α -radiation therapy of metastatic castration-resistant prostate cancer. *J Nucl Med*. 2016;57:1941–1944.
- Sharma R, Earla B, Baidoo K, et al. Upregulation of somatostatin receptor type 2 in a receptor-deficient *in vivo* pancreatic neuroendocrine tumor model improves tumor response to targeted ¹⁷⁷Lu-DOTATATE. bioRxiv website. <https://www.biorxiv.org/content/10.1101/2022.04.25.489401v1>. Published April 26, 2022. Accessed December 28, 2022.
- Taelman VF, Radojewski P, Marinček N, et al. Upregulation of key molecules for targeted imaging and therapy. *J Nucl Med*. 2016;57:1805–1810.
- Guenther R, Aweda T, Carmona Matos DM, et al. Overexpression of somatostatin receptor type 2 in neuroendocrine tumors for improved Ga68-DOTATATE imaging and treatment. *Surgery*. 2020;167:189–196.
- Shah RG, Meriin MA, Adant S, Zine-Eddine F, Beauregard JM, Shah GM. Chemotherapy-induced upregulation of somatostatin receptor-2 increases the uptake and efficacy of ¹⁷⁷Lu-DOTA-octreotate in neuroendocrine tumor cells. *Cancers (Basel)*. 2021;13:232.

Preclinical Evaluation of ⁸⁹Zr-Desferrioxamine-Bexmarilimab, a Humanized Antibody Against Common Lymphatic Endothelial and Vascular Endothelial Receptor-1, in a Rabbit Model of Renal Fibrosis

Olli Moisio¹, Jenni Virta¹, Emrah Yatkin², Heidi Liljenbäck^{1,3}, Senthil Palani¹, Riikka Viitanen¹, Maxwell W.G. Miner¹, Vesa Oikonen¹, Tuula Tolvanen^{4,5}, Danielle J. Vugts⁶, Pekka Taimen^{7,8}, Xiang-Guo Li^{1,8,9}, Maija Hollmén^{8,10}, Sirpa Jalkanen^{8,10}, and Anne Roivainen^{1,3,4,8}

¹Turku PET Centre, University of Turku, Turku, Finland; ²Central Animal Laboratory, University of Turku, Turku, Finland; ³Turku Center for Disease Modeling, University of Turku, Turku, Finland; ⁴Turku PET Centre, Turku University Hospital, Turku, Finland; ⁵Department of Medical Physics, Turku University Hospital, Turku, Finland; ⁶Department of Radiology and Nuclear Medicine, Amsterdam UMC, VU University, Amsterdam, The Netherlands; ⁷Institute of Biomedicine, University of Turku, and Department of Pathology, Turku University Hospital, Turku, Finland; ⁸InFLAMES Research Flagship Center, University of Turku, Turku, Finland; ⁹Department of Chemistry, University of Turku, Turku, Finland; and ¹⁰MediCity Research Laboratory, University of Turku, Turku, Finland

Bexmarilimab is a new humanized monoclonal antibody against common lymphatic endothelial and vascular endothelial receptor-1 (CLEVER-1) and is in clinical trials for macrophage-guided cancer immunotherapy. In addition being associated with cancer, CLEVER-1 is also associated with fibrosis. To facilitate prospective human PET studies, we preclinically evaluated ⁸⁹Zr-labeled bexmarilimab in rabbits. **Methods:** Bexmarilimab was conjugated with desferrioxamine (DFO) and radiolabeled with ⁸⁹Zr. Retained immunoreactivity was confirmed by flow cytometry. The distribution kinetics of intravenously administered ⁸⁹Zr-DFO-bexmarilimab (0.1 mg/kg) were determined for up to 7 d in a rabbit model of renal fibrosis mediated by unilateral ureteric obstruction. The *in vivo* stability of ⁸⁹Zr-DFO-bexmarilimab was evaluated by sodium dodecyl sulfate-polyacrylamide gel electrophoresis in combination with autoradiography. Additionally, we estimated the human radiation dose from data obtained in healthy rabbits. **Results:** ⁸⁹Zr-DFO-bexmarilimab cleared rapidly from the blood circulation and distributed to the liver and spleen. At 24 h after injection, PET/CT, *ex vivo* γ -counting, and autoradiography demonstrated that there was significantly higher ⁸⁹Zr-DFO-bexmarilimab uptake in unilateral ureteric obstruction-operated fibrotic renal cortex, characterized by abundant CLEVER-1-positive cells, than in contralateral or healthy kidneys. The estimated effective dose for a 70-kg human was 0.70 mSv/MBq. **Conclusion:** The characteristics of ⁸⁹Zr-DFO-bexmarilimab support future human PET studies to, for example, stratify patients for bexmarilimab treatment, evaluate the efficacy of treatment, or monitor disease progression.

Key Words: bexmarilimab; CLEVER-1; PET/CT; renal fibrosis; whole-body distribution; ⁸⁹Zr

J Nucl Med 2023; 64:555–560
DOI: 10.2967/jnumed.122.264725

Received Aug. 16, 2022; revision accepted Oct. 19, 2022.
For correspondence or reprints, contact Anne Roivainen (anne.roivainen@utu.fi).
Published online Oct. 27, 2022.
Immediate Open Access: Creative Commons Attribution 4.0 International License (CC BY) allows users to share and adapt with attribution, excluding materials credited to previous publications. License: <https://creativecommons.org/licenses/by/4.0/>. Details: <http://jnm.snmjournals.org/site/misc/permission.xhtml>.
COPYRIGHT © 2023 by the Society of Nuclear Medicine and Molecular Imaging.

Common lymphatic endothelial and vascular endothelial receptor-1 (CLEVER-1, also known as stabilin-1 and FEEL-1 [fasciadin, EGF-like, laminin type EGF-like, and link domain containing scavenger receptor 1]) is a multifunctional scavenger receptor expressed on antiinflammatory, alternatively activated M2 macrophages (1,2). In addition, the molecule is present, as the name suggests, in the lymphatic and vascular endothelium. In human tissues, CLEVER-1 is specifically expressed in the noncontinuous endothelial cells of the spleen, liver, adrenal cortex, and lymph nodes (3–5).

The humanized anti-CLEVER-1 antibody bexmarilimab (dissociation constant, 0.75×10^9 M to human CLEVER-1) has been developed for immunotherapy and has recently shown promising results in clinical trials (6). Although the main research focus of studies investigating CLEVER-1 has been its effects on tumor-associated macrophages and cancer (7), CLEVER-1 mediates tissue homeostasis and prevents fibrosis in liver injury. In this context, CLEVER-1 protects against excessive fibrosis in response to oxidative stress by clearing modified low-density lipoproteins. The uptake of modified low-density lipoproteins reduces profibrogenic chemokine (C-C motif) ligand 3 secretion, resulting in reduced fibrosis and promotion of healing (8).

Therefore, we propose that CLEVER-1 may also be a relevant marker of tissue repair and the healing response in inflammatory diseases, and we present the preclinical evaluation of ⁸⁹Zr-labeled desferrioxamine (DFO)-conjugated bexmarilimab in a rabbit model of renal fibrosis. Notably, the parental antihuman CLEVER-1 antibody 3-372 can also recognize rabbit CLEVER-1 (9). To obtain a detailed assessment of the whole-body distribution kinetics of intravenously administered bexmarilimab and its CLEVER-1-targeting ability, we radiolabeled bexmarilimab and preclinically evaluated the effects of ⁸⁹Zr-DFO-bexmarilimab in healthy rabbits and rabbits with renal fibrosis induced by unilateral ureteric obstruction (UUO).

MATERIALS AND METHODS

Supplemental materials and methods are available at <http://jnm.snmjournals.org> (10).

Study Design

The study protocol is presented in Figure 1. The UUO model of renal fibrosis in rabbits was used as the animal model. The left ureter was ligated in 7 female New Zealand White rabbits 7 d before ^{89}Zr -DFO-bexmarilimab injection. Six healthy rabbits were studied as controls.

The whole-body distribution kinetics of intravenously administered ^{89}Zr -DFO-bexmarilimab were studied in rabbits ($n = 13$; weight, 2.12 ± 0.19 kg) using in vivo PET/CT imaging for up to 7 d, as well as ex vivo γ -counting of excised tissues and digital autoradiography of kidney cryosections. Histologic and immunohistochemistry results supported the ex vivo autoradiographic results. Renal perfusion was determined by ^{15}O -radiowater PET/CT before ^{89}Zr -DFO-bexmarilimab injection, and the kidney volume was determined by CT. Human radiation dose estimates for ^{89}Zr -DFO-bexmarilimab were extrapolated from healthy rabbit data.

All animal experiments were approved by the national project authorization board in Finland (license numbers ESAVI/856/04.10.07/2017 and ESAVI/5882/2020) and were performed in compliance with European Union directive 2010/EU/63 on the protection of animals used for scientific purposes.

Preparation of ^{89}Zr -DFO-Bexmarilimab

Bexmarilimab (IgG4, ~ 150 kDa, in a 25 mg/mL stock solution containing 10 mM L-histidine/HCl [pH 6.0], 20 mM L-methionine, 280 mM trehalose, and 0.02% polysorbate 20) was obtained from Faron Pharmaceuticals (11). The DFO conjugation and radiolabeling of bexmarilimab with ^{89}Zr were performed using a previously published protocol with slight modifications (12). To attach the hexadentate chelator DFO, bexmarilimab stock was reconstituted to a concentration of 3 mg/mL in sodium bicarbonate buffer (1.0 M, 1 mL, pH 9.0) by ultrafiltration (Amicon Ultra 60 kDa; Millipore). Subsequently, to 1 mL of the rebuffered antibody, isothiocyanatobenzyl-DFO (p-DFO-Bz-NCS, 10 μL , 3.5 mM in dimethyl sulfoxide, 2 equivalents) was added and the solution was incubated at 37°C for 30 min while being mixed. Then, the reaction mixture was transferred onto a PD-10 size-exclusion column (Cytiva) and DFO-bexmarilimab was eluted in 1.5 mL of formulation buffer containing 10 mM L-histidine, 20 mM methionine, 280 mM sucrose, and 0.02% polysorbate 20 in water at pH 6.0 (adjusted with HCl).

The radiolabeling was performed by mixing 40–45 MBq of ^{89}Zr (100 μL , 1.0 M oxalic acid; Cyclotron VU), Na_2CO_3 (45 μL , 2.0 M), 4-(2-hydroxyethyl)-1-piperazineethanesulfonic acid buffer (500 μL , 0.5 M, pH 7.2), and DFO-bexmarilimab (355 μL , 1.3 mg/mL). The mixture was incubated at room temperature for 60 min while being

mixed. The crude product mixture was transferred onto a PD-10 size-exclusion column, and ^{89}Zr -DFO-bexmarilimab was eluted in 1.5 mL of formulation buffer.

The radiochemical quality of ^{89}Zr -DFO-bexmarilimab was analyzed with 2 methods: ultrafiltration and sodium dodecyl sulfate–polyacrylamide gel electrophoresis (SDS-PAGE). For the ultrafiltration method, 5 μL of the product were added to a Microcon spin filter (60-kDa cutoff; Millipore) containing 95 μL of 5% dimethyl sulfoxide in phosphate-buffered saline. The product was centrifuged at $14,000g$ for 6 min followed by 2 washes with 100 μL of 5% dimethyl sulfoxide in phosphate-buffered saline. The radioactivity remaining in the filter and filtrate was then separately measured with a γ -counter (Wizard 1480; PerkinElmer). The radiochemical purity of ^{89}Zr -DFO-bexmarilimab was determined as the amount of radioactivity on the filter divided by the total amount of radioactivity multiplied by 100%. The measurements were performed in triplicate. SDS-PAGE was performed to detect possible aggregates and larger fragments of antibodies. The assay was run on a Miniprotein electrophoresis system using precast 4%–20% nondenaturing Tris-glycine polyacrylamide gels (Bio-Rad). Subsequently, the gel was rinsed in water, placed on a phosphor imaging plate (Fujifilm), and after exposure scanned on a BAS-5000 scanner (Fujifilm). The resulting images were analyzed with an AIDA image analyzer (Raytest) to determine the percentage of intact ^{89}Zr -DFO-bexmarilimab.

The immunoreactivity and CLEVER-1 binding of DFO-bexmarilimab and ^{89}Zr -DFO-bexmarilimab after radioactive decay were confirmed by flow cytometry using unmodified bexmarilimab (clone CP-12; Abzena) as a reference molecule. Briefly, peripheral blood mononuclear cells (Finnish Red Cross) enriched with CD14-microbeads (Miltenyi) or the CLEVER-1^{high} acute myelogenous leukemia cell line KG-1 (CCL-246; ATCC) was used. KG-1 cells were cultured in Iscove modified Dulbecco medium supplemented with 20% fetal bovine serum and penicillin/streptomycin. The cells (0.5×10^6 /well) were plated in a round-bottom 96-well plate (Sarstedt) and stained with varying concentrations ($\mu\text{g}/\text{mL}$) of bexmarilimab, DFO-bexmarilimab, and ^{89}Zr -DFO-bexmarilimab. An irrelevant isotype IgG4 control antibody, (S241/L248E)-Alexa Fluor 647 (Abzena), was used to normalize the signal. The cells were stained with mouse anti-human IgG4-Alexa Fluor 488 (catalog no. 9200-30; Southern Biotech). Fixed samples were subjected to flow cytometry on an LSRFortessa cell analyzer (Becton Dickinson) and analyzed with FlowJo10 (TreeStar Ashland) software.

Radiosynthesis of ^{15}O -Radiowater

^{15}O -radiowater was synthesized as previously described (13).

PET/CT Imaging

A Discovery-690 PET/CT (GE Healthcare) device was used for imaging studies.

Rabbits were sedated and anesthetized with a subcutaneous injection of a mixture of medetomidine (Cepetor Vet, 1 mg/mL, 0.1 mg/kg; CP-Pharma), ketamine (Ketaminol, 50 mg/kg, 2 mg/kg; Intervet Oy), and midazolam (5 mg/mL, 0.1 mg/kg; Hameln Pharma). For scanning on day 1, 2 cannulas were inserted, one in the left ear vein for injecting tracers and the other in the right ear vein or artery for blood sampling. For scans on day 2 onward, only one ear vein was cannulated for blood sampling.

For measurement of renal perfusion, 20 ± 0 MBq of ^{15}O -radiowater were injected intravenously and the rabbits were imaged for 6 min (time frames: $15 \times 4\text{ s}$, $4 \times 10\text{ s}$, $4 \times 20\text{ s}$, and $3 \times 60\text{ s}$).

^{89}Zr -DFO-bexmarilimab (7.2 ± 2.5 MBq [mean \pm SD]; range, 4.4–10.2 MBq; 3.5 ± 1.3 MBq/kg; 0.1 mg/kg) was injected on the

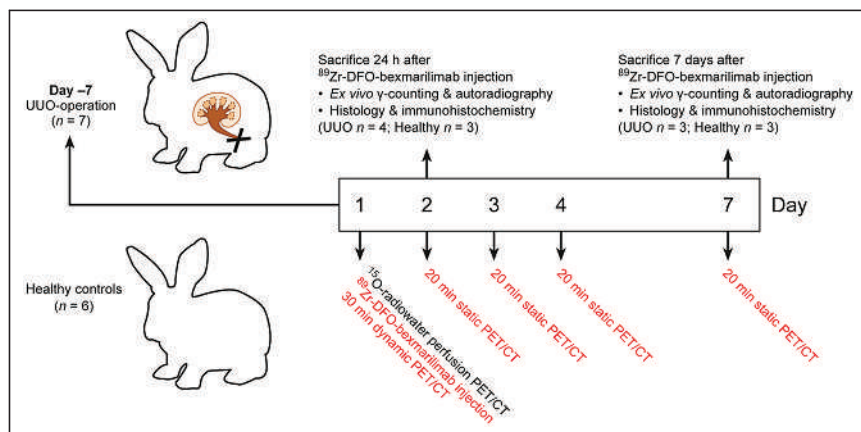


FIGURE 1. Study design for 6 healthy and 7 UUO New Zealand White rabbits. UUO surgery was performed 7 d before start of study, which began on day 1. Rabbits first were examined for renal perfusion using ^{15}O -radiowater PET/CT. They then were intravenously injected with ^{89}Zr -DFO-bexmarilimab for sequential PET/CT imaging for up to 7 d after injection and were killed for postmortem studies either 24 h or 7 d after injection.

first scanning day, and dynamic whole-body PET/CT scanning was performed for 30 min immediately after the injection. Static whole-body scans were then obtained at 24 h, 2 d, 3 d, and 7 d after injection. Dynamic emission scans of 12 time frames (4×30 s, 4×60 s, 2×120 s, and 2×600 s) were acquired by serial imaging of the body in 2 contiguous segments. Three bed positions were required for static whole-body PET, with a 6-min acquisition time for each position.

PET/CT images were analyzed using Carimas software (www.turkupetcentre.fi/carimas/). Regions of interest were defined for the whole kidney (parenchyma), kidney cortex, kidney medulla, left ventricle cavity (representing blood), liver, lungs, muscle, myocardium, and spleen on the PET/CT images; the CT scan was used to provide an anatomic reference. The suprarenal abdominal aorta was used as the region of interest representing blood in ^{15}O -radiowater analyses. Kidney volumes were determined from CT images. Results are expressed as SUVs and time-activity curves.

Renal perfusion was estimated by fitting a single-tissue compartmental model to the regional radioactivity concentration curves. An image-derived arterial blood curve was used as the model input function. The nonlinear sum-of-least-squares method was used to estimate perfusion ($\text{mL}_{\text{blood}}/\text{mL}_{\text{tissue}} \times \text{min}$).

In Vivo Stability of ^{89}Zr -DFO-Bexmarilimab

Blood samples (100–1,500 μL) were collected into heparinized tubes at 1 min, 5 min, 10 min, 30 min, 1 h, 2 h, 3 h, 4 h, 24 h, 2 d, 3 d, and 7 d after ^{89}Zr -DFO-bexmarilimab injection. The radioactivity of the whole-blood samples was measured with a Wizard γ -counter. Plasma was subsequently separated by centrifugation (2,100g for 5 min at 4°C), and radioactivity was measured using the γ -counter.

To determine the amount of intact ^{89}Zr -DFO-bexmarilimab, aliquots of plasma were applied to native SDS-PAGE as described above. Briefly, a small volume of plasma (up to 10 μL) was added to 10 μL of 4 \times Laemmli sample buffer (Bio-Rad), filled to a volume of 40 μL with H_2O , and applied on the gel. For high-radioactivity samples (0–4 h after injection), plasma was diluted with physiologic saline before preparation of the sample. ^{89}Zr -DFO-bexmarilimab in formulation buffer (stored at 4°C) was used as a reference.

Ex Vivo Biodistribution and Digital Autoradiography

Rabbits were euthanized either at 24 h (4 UUO, 3 healthy) or at 7 d (3 UUO, 3 healthy) after ^{89}Zr -DFO-bexmarilimab injection. After the last PET/CT examination, the rabbits were euthanized under deep ketamine–medetomidine–midazolam anesthesia by cardiac puncture and an overdose of pentobarbital (Mebunat; Orion Pharma). Tissues and organs were immediately dissected, weighed, and assayed for radioactivity with a Wizard γ -counter. The radioactive decay of ^{89}Zr (half-life, 3.3 d) was corrected for the time of injection. The uptake of radioactivity is expressed as SUV.

Samples of kidneys were embedded and frozen in Tissue-Tek (Sakura) and cut into 8- μm and 20- μm slices. The 20- μm cryosections were thaw-mounted onto microscope slides and immediately exposed to a phosphor imaging plate (Fujifilm). After an exposure time of approximately 3 d, the imaging plates were scanned with a BAS-5000 scanner. After scanning, sections were stained with hematoxylin–eosin and scanned with a digital slide scanner (Pannoramic 250 Flash; 3DHistec). The 8- μm sections were stored at -70°C and used for CLEVER-1 immunohistochemical staining.

The accumulation of ^{89}Zr -DFO-bexmarilimab in the renal cortex and medulla was analyzed on superimposed autoradiographs and hematoxylin–eosin images using Carimas software. Results were decay-corrected for injection and exposure time, normalized to the injected radioactivity

dose, and expressed as the photostimulated luminescence per square millimeter.

The 8- μm cryosections of the kidneys and spleen were stained with anti-CLEVER-1 (clone 3-372; InVivo Biotech) peroxidase. Briefly, the slides were acetone-fixed, blocked with horse serum, and incubated overnight at 4°C in a humidified chamber with a 10 $\mu\text{g}/\text{mL}$ concentration of clone 3-372 or mouse IgG1 control antibody. The signal was detected using a Vectastain Elite ABC kit (Vector Laboratories) and liquid chromogen 3,3'-diaminobenzidine substrate (DAKO). The slides were counterstained with hematoxylin and imaged with the Pannoramic 250 Flash digital slide scanner. Endogenous peroxidase activity was not blocked before staining because this procedure reduces the staining quality.

Additional formalin-fixed, paraffin-embedded 7- μm kidney sections were stained with picrosirius red to evaluate kidney damage and the development of renal fibrosis.

Statistical Analysis

Results are expressed as the mean \pm SD. Differences between groups were determined with the independent-samples *t* test using Excel (Microsoft). *P* values of less than 0.05 were considered statistically significant.

RESULTS

Characterization of the UUO Rabbit Model

Visual and histologic inspection of the left kidney demonstrated obvious damage (swollen, enlarged kidney) due to blockage of urine flow to the bladder (Supplemental Fig. 1). The contralateral kidney appeared healthy, with no obvious damage.

The renal perfusion parameters in rabbits 7 d after the UUO operation are presented in Figure 2A and Supplemental Table 1. The ^{15}O -radiowater PET analysis revealed that renal perfusion was significantly lower in the UUO renal cortex ($2.00 \pm 0.95 \text{ mL}_{\text{blood}}/\text{mL}_{\text{tissue}}/\text{min}$) than in the contralateral ($5.57 \pm 1.96 \text{ mL}_{\text{blood}}/\text{mL}_{\text{tissue}}/\text{min}$, $P = 0.001$) or healthy ($5.25 \pm 0.55 \text{ mL}_{\text{blood}}/\text{mL}_{\text{tissue}}/\text{min}$, $P < 0.001$) renal cortex.

On the basis of in vivo CT results, the volume of UUO-operated kidneys was enlarged, whereas the contralateral kidneys were similar in size to the kidneys from healthy rabbits (Fig. 2B).

The histopathologic analysis showed dilation of renal tubules, focal injury of tubular epithelial cells, and varying levels of inflammation in UUO kidneys. Additionally, picrosirius red staining showed tubulointerstitial fibrosis of the renal cortex in UUO kidneys. There were no histologic abnormalities in the contralateral kidneys from UUO rabbits or kidneys from healthy control rabbits (Fig. 2C). Anti-CLEVER-1 staining of UUO kidneys showed specific immunoreactivity on recruited macrophages in the tubulointerstitium. The contralateral kidneys or the kidneys from healthy rabbits did not show this pattern of immunoreactivity (Fig. 2C). No significant differences in staining were observed between the 7- and 14-d samples.

Anti-CLEVER-1 staining of spleen and kidney sections, as well as hematoxylin–eosin and picrosirius red staining of kidney sections obtained 7 d and 14 d after surgery, are presented in Supplemental Figures 2 and 3.

Preparation of ^{89}Zr -DFO-Bexmarilimab and Immunoreactivity

The DFO-NCS conjugation and labeling method enabled us to obtain a final formulation of ^{89}Zr -DFO-bexmarilimab (Supplemental Fig. 4A) that was of excellent quality and without antibody aggregates or fragments, as measured by SDS-PAGE. The retained immunoreactivity of DFO-bexmarilimab was $87.5\% \pm 2.2\%$ ($n = 4$), indicating that the modification with a chelator did not substantially alter antibody binding to CLEVER-1. Using 4 radiolabeled batches ($n = 4$), we determined that ^{89}Zr -DFO-bexmarilimab had a radiochemical

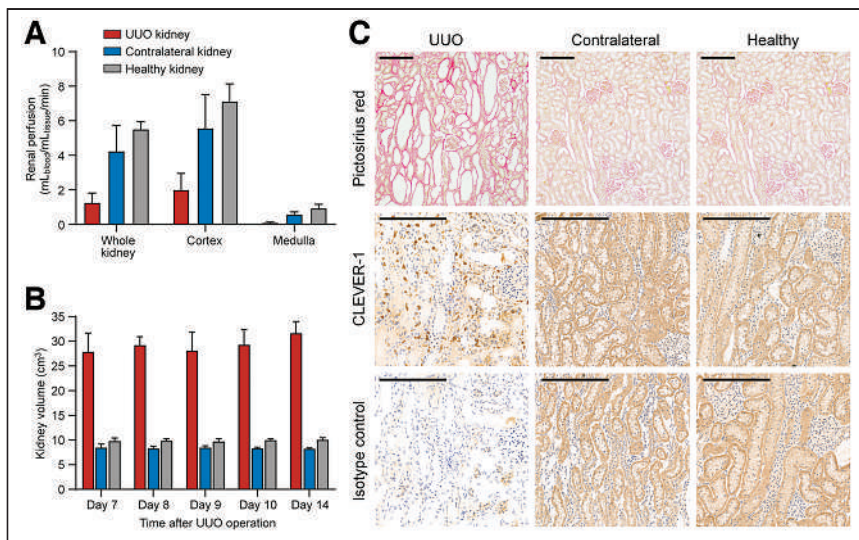


FIGURE 2. Characterization of rabbit UUO model. (A) Renal perfusion determined using ^{15}O -radio-water PET/CT 7 d after UUO operation (UUO and contralateral, $n = 6$; healthy, $n = 5$). (B) Kidney volumes of UUO and healthy rabbits based on CT imaging ($n = 3$). (C) Picrosirius red staining shows dilation of renal tubules and tubulointerstitial fibrosis of renal cortex in UUO kidneys, whereas histologic findings are normal in contralateral kidney from same animal and in healthy control rabbits. Anti-CLEVER-1 immunohistochemical staining shows specific immunoreactivity in tissue macrophages in UUO kidney. Light brown unspecific background staining from urine flow can be observed in area of contralateral and healthy kidney tissue but not in UUO tissue. Scale bar is 200 μm .

yield of $78.2\% \pm 4.2\%$, specific radioactivity of 76.1 ± 5.1 MBq/mg, and radioactivity concentration of 14.9 ± 4.4 MBq/mL. The radiochemical purity was $99.1\% \pm 0.3\%$ when measured by ultrafiltration and 100% when measured by SDS-PAGE autoradiography (Supplemental Fig. 4B). When measured in a single batch, the immunoreactivity of ^{89}Zr -DFO-bexmarilimab after radioactive decay (~ 4 wk after radiolabeling, stored at -20°C) was similar to that of DFO-bexmarilimab (Supplemental Fig. 4C).

^{89}Zr -DFO-Bexmarilimab PET/CT Imaging and Biodistribution

In UUO and healthy rabbits, in vivo PET/CT clearly visualized the liver and spleen and showed that there was some uptake of ^{89}Zr -DFO-bexmarilimab in bone, bone marrow, and intestines (Fig. 3A). The highest radioactivity concentration after intravenous injection of ^{89}Zr -DFO-bexmarilimab was in the liver, but the concentration decreased over time (Supplemental Figs. 5 and 6). The radioactivity concentration was always higher in the renal cortex than in the medulla, and the UUO kidney cortex was clearly visualized (Fig. 3A).

Uptake of ^{89}Zr -DFO-bexmarilimab at 24 h after injection was significantly higher in the UUO renal cortex than in the contralateral or healthy renal cortex and was even more pronounced when normalized to the level of renal perfusion (Figs. 3B and 3C). Decay-corrected time-activity curves revealed that uptake of ^{89}Zr -DFO-bexmarilimab in the

UUO renal cortex remained constant after 24 h but increased over time in the contralateral renal cortex (Fig. 3D).

Supplemental Table 2 shows the ex vivo biodistribution of ^{89}Zr -DFO-bexmarilimab in rabbits at 24 h and 7 d after injection. The organs with the highest radioactivity concentration were the liver, spleen, and bone or bone marrow; this result confirmed the in vivo PET/CT findings. Uptake was lowest in the brain.

In Vivo Stability and Plasma Pharmacokinetics of ^{89}Zr -DFO-Bexmarilimab

The SDS-PAGE analysis of serial plasma samples from UUO rabbits showed that the proportion of intact ^{89}Zr -DFO-bexmarilimab decreased from $97.0\% \pm 1.2\%$ of total plasma radioactivity at 4 h after tracer injection to $78.2\% \pm 13.1\%$, $51.2\% \pm 9.8\%$, and $33.2\% \pm 3.4\%$ at 24 h, 2 d, and 3 d, respectively. In healthy rabbits, the proportion of intact ^{89}Zr -DFO-bexmarilimab was $96.2\% \pm 0.1\%$, $51.1\% \pm 8.5\%$, $24.9\% \pm 6.6\%$, and $15.6\% \pm 4.3\%$ at 4 h, 24 h, 2 d, and 3 d, respectively, after tracer injection (Figs. 4A and 4B). Representative

autoradiographs of SDS-PAGE are shown in Supplemental Figure 7. The blood-to-plasma ratio of radioactivity was about 0.6 and did not change appreciably over the 7-d PET study (Supplemental

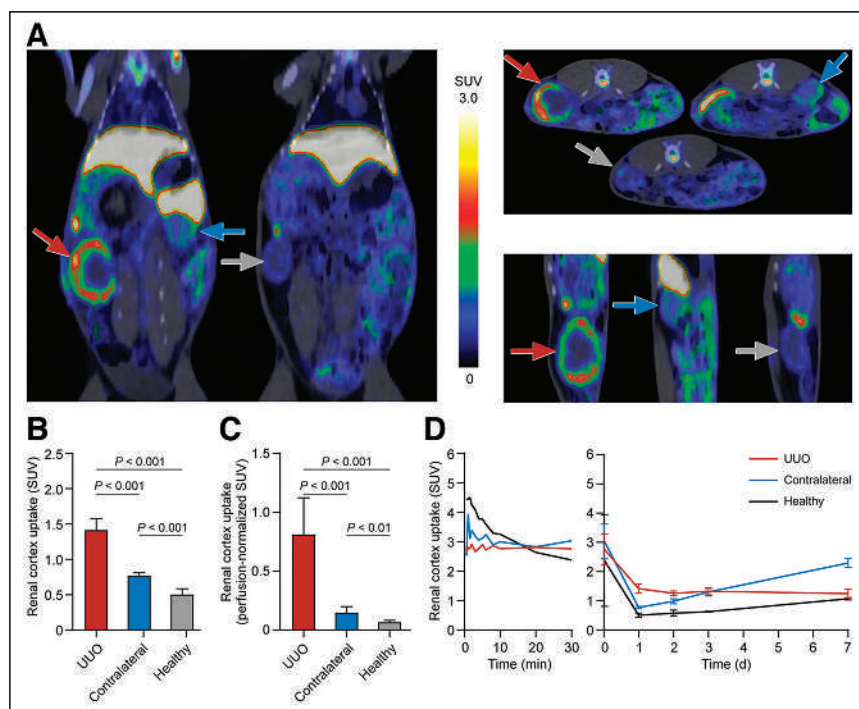


FIGURE 3. (A) Representative PET/CT images of 2 rabbits 24 h after single intravenous injection of ^{89}Zr -DFO-bexmarilimab. Red arrows denote UUO kidneys; blue arrows, contralateral kidneys; and gray arrows, healthy kidneys. (B and C) Radioactivity concentration in renal cortex without perfusion correction (B) and with ^{15}O -radio-water-based perfusion correction (C). (D) Time-activity curves for ^{89}Zr -DFO-bexmarilimab uptake in renal cortex.

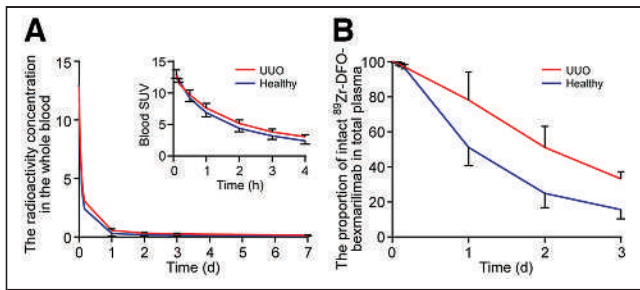


FIGURE 4. Distribution of ⁸⁹Zr-DFO-bexmarilimab in rabbit blood circulation. (A) Radioactivity concentration in whole blood. (B) Proportion of intact ⁸⁹Zr-DFO-bexmarilimab in total plasma. Lines represent mean values and bars are SDs of experiments.

Fig. 8). The plasma pharmacokinetic parameters are summarized in Supplemental Table 3. ⁸⁹Zr-DFO-bexmarilimab had a relatively fast clearance from the blood circulation, with total clearance of 10.4 ± 2.1 mL/h ($n = 3$) in UUO rabbits and 17 ± 2.1 mL/h ($n = 3$) in healthy rabbits ($P = 0.030$).

Digital Autoradiography

Digital autoradiography of rabbit kidney cryosections combined with hematoxylin–eosin staining confirmed that ⁸⁹Zr-DFO-bexmarilimab was retained in the renal cortex (Fig. 5). Despite impaired renal perfusion in the UUO kidney, uptake 24 h after injection was higher in the UUO renal cortex and medulla than in the contralateral and healthy kidneys ($P < 0.05$). At 7 d after injection, uptake was highest in the contralateral renal cortex; this finding is consistent with the results of PET/CT studies and ex vivo γ -counting.

Radiation Dose Estimates

The human residence times (the normalized numbers of disintegrations) for the various source organs and the remainder of the

body extrapolated from healthy rabbit data are listed in Supplemental Table 4. Supplemental Figure 9 shows the time–activity curves of the organs on which the dosimetry calculation using OLINDA/EXM 2.1 was based. The estimates of the organ doses given in Supplemental Table 5 were calculated for a 70-kg man. The organs with the highest doses were the liver (5.860 ± 1.100 mGy/MBq), gallbladder wall (2.580 ± 0.420 mGy/MBq), and adrenal glands (1.777 ± 0.240 mGy/MBq). The mean effective dose (ICRP 103 (14)) was calculated as 0.702 ± 0.051 mSv/MBq. For example, a 37-MBq dose of ⁸⁹Zr-DFO-bexmarilimab would likely result in an effective dose of 26 mSv.

DISCUSSION

Bexmarilimab is a new humanized anti-CLEVER-1 antibody currently in clinical immunotherapy trials. In addition to its potential use as an immunotherapeutic, we are interested in determining whether the antibody is suitable for immuno-PET imaging. The information presented from this study increases our understanding of its pharmacokinetics and in vivo biodistribution and provides estimates for the human radiation dose, which will support future clinical translation of ⁸⁹Zr-DFO-bexmarilimab immuno-PET.

To enable ⁸⁹Zr-radiolabeling, bexmarilimab was successfully conjugated with a DFO chelator without compromising immunoreactivity, that is, 87.5% of the immunoreactivity was retained. Subsequent radiolabeling resulted in the formation of ⁸⁹Zr-DFO-bexmarilimab that had a high radiochemical yield and high radiochemical purity. SDS-PAGE was a particularly suitable method to evaluate purity because it enabled all radioactive substances with different molecular sizes, whether free ⁸⁹Zr or antibody aggregates, to be separated from the intact tracer in the same assay. Most importantly, conjugating bexmarilimab with ⁸⁹Zr and DFO did not lead to loss of immunoreactivity. This finding is important, since ⁸⁹Zr-DFO-bexmarilimab is intended for use in clinical PET applications.

CLEVER-1, as observed by anti-CLEVER-1 immunohistochemistry, was clearly expressed on macrophages residing in the UUO kidney, which were not present in the contralateral and healthy kidneys. PET/CT imaging, ex vivo γ -counting, and autoradiography analysis similarly showed significant differences in the uptake of ⁸⁹Zr-DFO-bexmarilimab into UUO kidneys compared with the contralateral and healthy kidneys at 24 h after injection. ⁸⁹Zr-DFO-bexmarilimab showed a surprisingly fast clearance coupled with fast initial uptake in the target tissues.

Although the kidneys show uptake of ⁸⁹Zr-DFO-bexmarilimab at 24 h after injection, they are also a likely route of excretion of radiometabolites and fragments. We hypothesize that the increased uptake of tracer in the contralateral and healthy kidneys 7 d after injection, as shown by PET/CT and ex vivo results, is due to uptake of radiometabolites, given that the level of radiometabolites in the bloodstream increases in the days after the injection of ⁸⁹Zr-DFO-bexmarilimab. In UUO and healthy rabbits, radiometabolites consisted of, on average,

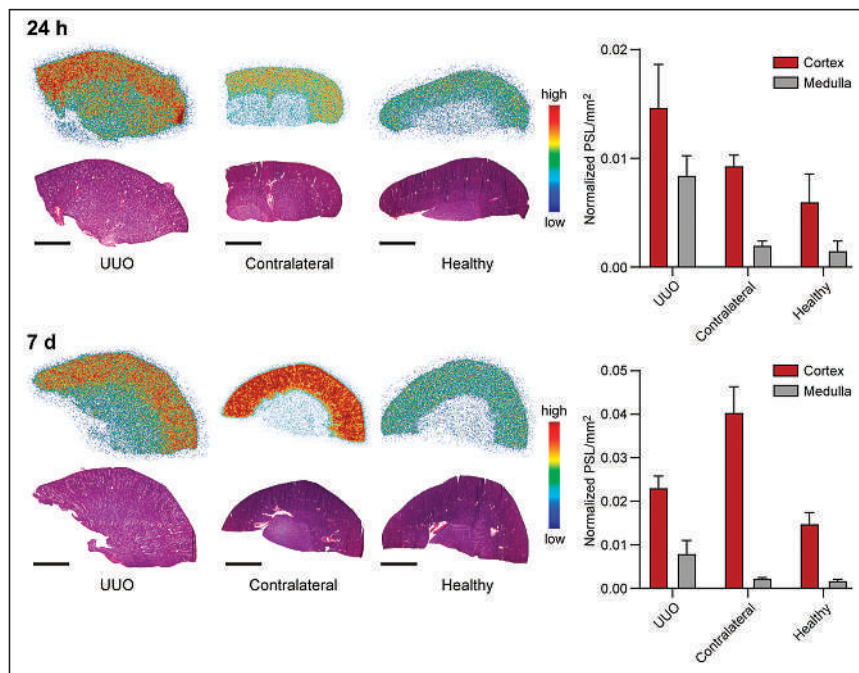


FIGURE 5. Representative ex vivo digital autoradiographs and hematoxylin–eosin staining of 20- μ m kidney cryosections and quantification data 24 h and 7 d after ⁸⁹Zr-DFO-bexmarilimab injection. Scale bar is 5 mm.

84% and 67%, respectively, of the total plasma radioactivity on day 3 after injection. Almost no intact ^{89}Zr -DFO-bexmarilimab was detected on day 7, although the total plasma radioactivity at that time was too low for accurate detection. An approximate doubling of radioactivity uptake in the contralateral kidney compared with the healthy kidney on day 7 would support this hypothesis, as the contralateral kidney compensates for the loss of UO kidney function. A likely source of circulating metabolites may be the liver, as a decrease in liver radioactivity was observed after the 24- and 48-h time points (Supplemental Fig. 6).

The fast uptake and clearance of ^{89}Zr -DFO-bexmarilimab highlight the importance of determining the optimal time window for PET studies in achieving meaningful results. In this study, the optimal time window was clearly at 24 h, when tracer accumulation in the UO kidney had stabilized, blood radioactivity had diminished, and radiometabolites had not yet begun to accumulate in the healthy and contralateral kidneys.

In general, the uptake of ^{89}Zr -DFO-bexmarilimab in the liver and spleen corresponded to previously reported CLEVER-1 expression in human tissues (3–5). However, although we confirmed CLEVER-1 expression by immunohistochemical staining in the spleen and UO kidneys, we did not analyze the liver and other tissues that possibly express CLEVER-1.

The estimated human radiation burden due to a single intravenous ^{89}Zr -DFO-bexmarilimab injection is comparable to that of other ^{89}Zr -labeled monoclonal antibodies (15–17) and is suitable for clinical studies. In this study, scaling between rabbit and human data was performed using organ and whole-body masses of rabbits and humans. Despite similarities between species, the accuracy of extrapolation of biokinetic data from laboratory animals to humans is uncertain, particularly for the liver because of qualitative differences between species in the handling of many elements by this organ.

CONCLUSION

On the basis of the preclinical results of this study, including the estimated human radiation burden, ^{89}Zr -DFO-bexmarilimab is suitable for future clinical PET studies.

DISCLOSURE

Maija Hollmén and Sirpa Jalkanen own stock in Faron Pharmaceuticals. The study was financially supported by grants from Business Finland, the Jane and Aatos Erkko Foundation, the Academy of Finland (#350117), and the Finnish Cultural Foundation. Olli Moisio is a PhD student partially supported by the Drug Research Doctoral Program of the University of Turku Graduate School and the doctoral module of the InFLAMES Flagship. No other potential conflict of interest relevant to this article was reported.

ACKNOWLEDGMENTS

Timothy Johnson and Toby Holmes (Sheffield University, U.K.) are thanked for their advice and help regarding the UO rabbit model. Professional assistance from Aake Honkaniemi (Turku PET Centre), Sari Mäki (MediCity Research Laboratory), and Marja-Riitta Kajaala and Erika Nyman (the University of Turku Histocore Facility) is greatly appreciated. The personnel of the University of Turku Central Animal Laboratory are thanked for expert animal care. We thank Timo Kattelus for preparing the figures.

KEY POINTS

QUESTION: Are the characteristics of CLEVER-1-targeted ^{89}Zr -DFO-bexmarilimab suitable for prospective human PET studies?

PERTINENT FINDINGS: This preclinical rabbit study revealed that intravenously administered ^{89}Zr -DFO-bexmarilimab was able to detect fibrosis associated with abundant CLEVER-1-positive cells. The estimated human effective dose was within the safe limits for potential human use.

IMPLICATIONS FOR PATIENT CARE: Clinical studies to determine whether ^{89}Zr -DFO-bexmarilimab-PET is suitable for, for example, stratifying patients for bexmarilimab treatment, evaluating treatment efficacy, and monitoring disease progression, may be justified.

REFERENCES

1. Kzhyshkowska J, Gratchev A, Goerd S. Stabilin-1, a homeostatic scavenger receptor with multiple functions. *J Cell Mol Med*. 2006;10:635–649.
2. Palani S, Maksimov M, Miiluniemi M, Auvinen K, Jalkanen S, Salmi M. Stabilin-1/CLEVER-1, a type 2 macrophage marker, is an adhesion and scavenging molecule on human placental macrophages. *Eur J Immunol*. 2011;41:2052–2063.
3. Goerd S, Walsh LJ, Murphy GF, Pober JS. Identification of a novel high molecular weight protein preferentially expressed by sinusoidal endothelial cells in normal human tissues. *J Cell Biol*. 1991;113:1425–1437.
4. Hansen B, Longati P, Elvevold K, et al. Stabilin-1 and stabilin-2 are both directed into the early endocytic pathway in hepatic sinusoidal endothelium via interactions with clathrin/AP-2, independent of ligand binding. *Exp Cell Res*. 2005;303:160–173.
5. Martens JH, Kzhyshkowska J, Falkowski-Hansen M, et al. Differential expression of a gene signature for scavenger/lectin receptors by endothelial cells and macrophages in human lymph node sinuses, the primary sites of regional metastasis. *J Pathol*. 2006;208:574–589.
6. Virtakoivu R, Rannikko JH, Viitala M, et al. Systemic blockade of Clever-1 elicits lymphocyte activation alongside checkpoint molecule downregulation in patients with solid tumors: results from a phase I/II clinical trial. *Clin Cancer Res*. 2021;27:4205–4220.
7. Hollmén M, Figueiredo CR, Jalkanen S. New tools to prevent cancer growth and spread: a ‘CLEVER’ approach. *Br J Cancer*. 2020;123:501–509.
8. Rantakari P, Patten DA, Valtonen J, et al. Stabilin-1 expression defines a subset of macrophages that mediate tissue homeostasis and prevent fibrosis in chronic liver injury. *Proc Natl Acad Sci USA*. 2016;113:9298–9303.
9. Irjala H, Elima K, Johansson EL, et al. The same endothelial receptor controls lymphocyte traffic both in vascular and lymphatic vessels. *Eur J Immunol*. 2003;33:815–824.
10. Stabin MG, Siegel JA. RADAR dose estimate report: a compendium of radiopharmaceutical dose estimates based on OLINDA/EXM version 2.0. *J Nucl Med*. 2018;59:154–160.
11. Hollmén M, Maksimov M, Rannikko JH, et al. Nonclinical characterization of bexmarilimab, a Clever-1-targeting antibody for supporting immune defense against cancers. *Mol Cancer Ther*. 2022;21:1207–1218.
12. Vosjan MJ, Perk L, Visser G, et al. Conjugation and radiolabeling of monoclonal antibodies with zirconium-89 for PET imaging using the bifunctional chelate p-isothiocyanatobenzyl-desferrioxamine. *Nat Protoc*. 2010;5:739–743.
13. Sipilä HT, Clark JC, Peltola O, Teräs M. An automatic [^{15}O]H $_2$ O production system for heart and brain studies. *J Labelled Comp Radiopharm*. 2001;44(suppl):S1066–S1068.
14. ICRP publication 103: the 2007 recommendations of the International Commission on Radiological Protection. *Ann ICRP*. 2007;37:1–333.
15. Börjesson PK, Jauw YW, de Bree R, et al. Radiation dosimetry of ^{89}Zr -labeled chimeric monoclonal antibody U36 as used for immuno-PET in head and neck cancer patients. *J Nucl Med*. 2009;50:1828–1836.
16. Laforest R, Lapi SE, Oyama R, et al. [^{89}Zr]trastuzumab: evaluation of radiation dosimetry, safety, and optimal imaging parameters in women with HER2-positive breast cancer. *Mol Imaging Biol*. 2016;18:952–959.
17. O’Donoghue JA, Lewis JS, Pandit-Taskar N, et al. Pharmacokinetics, biodistribution, and radiation dosimetry for ^{89}Zr -trastuzumab in patients with esophagogastric cancer. *J Nucl Med*. 2018;59:161–166.

Radioiodine Ablation of Thyroid Remnants in Patients with Graves' Orbitopathy

Michael Oeverhaus¹, Jana Koenen², Nikolaos Bechrakis¹, Mareile Stöhr¹, Ken Herrmann², Wolfgang P. Fendler², Anja Eckstein¹, and Manuel Weber²

¹Department of Ophthalmology, University Hospital Essen, Essen, Germany; and ²Department of Nuclear Medicine, University Hospital Essen, Essen, Germany

Our purpose was to assess response after ablation of thyroid remnants (ATR) with radioactive iodine therapy in patients with unstable Graves' orbitopathy (GO) after subtotal thyroidectomy. **Methods:** Thirty patients with mild ($n = 4$, 13%), moderate-to-severe ($n = 25$, 83%), or very severe GO ($n = 1$, 3%) were analyzed in this retrospective study. The primary endpoint was the improvement of GO-related symptoms as assessed by clinical activity scores, NOSPECS, and soft-tissue inflammation scores at 3 and 12 mo after ATR. Ablation success was defined by a decrease in ^{99m}Tc uptake on thyroid scintigraphy, remnant volume, and thyrotropin receptor antibody levels at 3 mo after ATR. **Results:** Twelve months after ATR, clinical activity scores, NOSPECS, and soft-tissue inflammation scores showed a significant decrease from 3.4 to 1.3 ($P < 0.0001$), 5.9 to 4.9 ($P = 0.007$), and 4.7 to 2.1 ($P = 0.0001$), respectively. The GO was inactive in 27 of the 30 (90%) patients after 3 mo and in 29 (97%) after 12 mo. No new activation of GO occurred. Remnant volume (1.4 vs. 0.4 cm³, $P = <0.0001$), mean thyrotropin receptor antibody level titer (19.02 vs. 13.37 IU/L, $P < 0.0001$), and ^{99m}Tc uptake (0.5% vs. 0.1%; $n = 12$; $P = 0.04$) decreased significantly until 3 mo after ATR. **Discussion:** Radioactive iodine therapy after thyroidectomy can successfully ablate residual thyroid remnants, leading to an improvement in GO, a reduction in inflammatory activity, and stabilization of thyroid function. Thus, scintigraphy should be considered for patients with unstable GO after thyroidectomy to rule out thyroid remnants.

Key Words: thyroid eye disease; radioactive iodine therapy; RAIT; total thyroid ablation; GO; TED

J Nucl Med 2023; 64:561–566
DOI: 10.2967/jnumed.122.264660

Graves' orbitopathy (GO), the most common extrathyroidal manifestation of Graves' disease, is a disorder of autoimmune origin. Typically, patients show symptoms of inflammation of the orbital soft tissues, inflammation-triggered fibrosis of the ocular muscles, and adipogenesis (1–3). Autoantibodies against the thyroid-stimulating hormone (TSH) receptor mediate these changes, which stimulate the receptors on orbital fibroblasts. In conjunction with the induction of crosstalk with insulinlike growth factor 1 receptors, this stimulation leads to a cascade of inflammatory conditions (4). Antibodies and autoimmune T cells stimulate orbital fibroblasts to release inflammatory

cytokines to produce hyaluronic acid and to differentiate into adipocytes and myofibroblasts (5–9). Consequently, patients experience signs of inflammation (pain, swelling), diplopia (due to fibrosis of the extraocular muscles), and proptosis (due to adipogenesis), which have a serious impact on quality of life (10,11). Most severely afflicted GO patients can have vision loss due to optic nerve compression (12). Despite recent advances in targeted therapy, there is none available in Europe yet. Therefore, current treatment can often reduce symptoms but not prevent the need for rehabilitative surgery (13–16). Management of GO comprises 2 main therapeutic principles: antiinflammatory treatment and reduction of risk factors for deterioration. According to the EUGOGO (European Group on Graves' Orbitopathy) 2021 guideline, patients with moderate-to-severe GO are treated with immunosuppression by intravenous glucocorticoids alone or in combination with mycophenolate sodium (17). The aim of this antiinflammatory therapy is to temper inflammation and prevent further deterioration. Poor control of thyroid function and high TSH receptor antibody levels can lead to development of new GO or worsening of preexisting GO (18–21). Consequently, rapid achievement of euthyroidism is crucial (8,17,20–22). Hyperthyroidism is treated primarily with anti-thyroid drugs. Definitive treatment with radioactive iodine ablation or thyroidectomy is performed in cases of relapse or poor thyroid control despite antithyroid drug treatment (13,17,23). The status of GO has an impact on the choice of procedure; thyroidectomy is recommended in the presence of active GO stages, though radioactive iodine might be used with sufficient corticosteroid prophylaxis (17,23,24). Near-total thyroidectomy is performed on patients with Graves' disease in some cases, even minimally invasively with video assistance (25). Small remnants are left to preserve the recurrent laryngeal nerve. Scintigraphy is not always performed (26). Therefore, ectopic thyroid tissue is sometimes left behind. There is evidence that larger thyroid residues are associated with poorer control of thyroid function, ongoing GO activity, and persistent thyrotropin receptor antibody (TRAb) levels (27,28). In accordance, several studies have shown a higher rate of stable GO and inactivated GO if thyroidectomy is combined with postoperative radioactive iodine therapy (total ablation) (29–31). This beneficial role might be due to complete thyroid-antigen removal, which is associated with a reduction in antigenic stimulation, a drop in antibody levels and cell-mediated immunoreactivity to TSH receptor, and improvement in GO (31,32). To evaluate the benefit of ablation of a significant thyroid remnant in patients with unstable GO and persistent unstable thyroid function in terms of GO activity and severity, we performed an interdisciplinary retrospective study at our tertiary GO referral center.

Received Jul. 14, 2022; revision accepted Oct. 8, 2022.
For correspondence or reprints, contact Manuel Weber (manuel.weber@uk-essen.de).
Published online Nov. 23, 2022.
COPYRIGHT © 2023 by the Society of Nuclear Medicine and Molecular Imaging.

MATERIALS AND METHODS

Study Population

We searched the institutional database of our EUGOGO tertiary referral center from January 2005 until October 2020 ($n = 4,641$) for patients who underwent ablation of thyroid remnants (ATR) for persistent or worsening GO and thyroid dysfunction after subtotal thyroidectomy. Only patients with active GO at baseline, comprehensive eye and thyroid examinations before ATR and 3 and 12 mo afterward, elevated TRAb, and significant uptake on baseline thyroid scintigraphy were included. This retrospective study was performed in accordance with the Declaration of Helsinki and was approved by the Ethics Commission of the University of Essen (reference number 17-7542-BO).

Outcome Measures

Primary outcome measures were an improvement in GO-related symptoms as assessed by clinical activity score (CAS), modified NOSPECS score (where N = no symptoms or signs, O = only signs, S = soft-tissue involvement, P = proptosis, E = extraocular muscle involvement, C = corneal involvement, and S = sight loss due to optic nerve compression) (33), and soft-tissue score at 3 and 12 mo after ATR (17).

For this study, a successful ablation was defined as decreases in TRAb, ^{99m}Tc uptake, and ultrasound-derived thyroid volume, as well as an increase in levothyroxine dose at 3 mo after ATR.

Clinical Assessment

Eye examinations were performed using a modified EUGOGO case record form and color atlas in a standardized manner (34). All patients were evaluated by a highly trained orthoptist and by 1 of 2 specialized ophthalmologists. Follow-up examinations were done by the same ophthalmologist at 3 and 12 mo after ATR to ensure homogeneity and reproducibility. GO was diagnosed by the presence of typical clinical signs on examination, including slit-lamp biomicroscopy, applanation tonometry, funduscopy, Hertel exophthalmometry, assessment of subjective diplopia, and objective measurement of deviation using the prism cover test and measurement of monocular excursions. GO activity was evaluated using the CAS classification system established by Mourits et al. (35,36). By analysis of personal photos of the patients and patient history concerning double vision and visual acuity, we determined the dynamic of the disease and scored CAS on a scale of up to 10 points at baseline. GO was classified as active if the CAS value was at least 4/10 points. Additionally, the severity of GO (modified NOSPECS) was classified according to the proposed criteria of the EUGOGO, as previously described (33,37). A maximum of 14 NOSPECS points was possible, with no signs of GO classified as 0 points. In addition, we scored the soft-tissue inflammation signs derived from CAS more gradually as follows: spontaneous retrobulbar pain (0–1), upper lid edema (0–2), lower lid edema (0–2), conjunctival injection (0–1), chemosis (0–1), lid redness (0–1), and swelling of the caruncle or plica (0–1). The sum builds the clinical soft-tissue score.

Thyroid examinations were performed or supervised by a board-certified nuclear medicine physician at baseline and 3 mo after radioactive iodine therapy. The examinations included patient history, ultrasound, and a thyroid panel including thyroid hormones and TRAb in all patients. Follow-up ^{99m}Tc -pertechnetate thyroid scintigraphy of residual thyroid gland tissue was performed for a subgroup ($n = 12$).

Radioiodine ATR

The ^{131}I activity was determined with the aim of delivering an absorbed dose of 500 Gy to the thyroid remnants. To this end, 2 different methodologies were used.

In 17 of the 30 patients, a radioactive iodine uptake (RAIU) test was performed, and the treatment activity was calculated using the formula of Musholt et al. (38). If the target dose could be achieved only by use of excessive administered activity (i.e., considerably higher than

500 MBq), 0.09 mg of recombinant human TSH (rhTSH) were administered on each of the 2 d leading up to ATR. This was the case in 8 of 17 patients with an RAIU deemed insufficient (median, 192 h; uptake, 1.6% vs. 7.4% in those who did not receive rhTSH). This approach was favored in mainly later years and in patients with larger thyroid remnants.

In 13 of the 30 patients, rhTSH was administered as described above, and ^{99m}Tc -pertechnetate thyroid scintigraphy performed on the day of the second injection. If the ^{99m}Tc uptake was deemed sufficient by the treating physician, the administered dose was calculated as follows, estimating an RAIU of 10%:

$$A [\text{MBq}] = 3.27 \times \frac{\text{dose} [\text{Gy}] \times \text{volume} [\text{cm}^3]}{\text{uptake} [\%]}$$

The second approach was used mainly in earlier years and in patients with small thyroid remnants, for which the reliability of an RAIU test was considered questionable. Levothyroxine treatment was not withdrawn. ATR was performed with an average activity of 452 MBq of ^{131}I , and measurements of intratherapeutic RAIU were performed twice daily for a minimum of 5 total measurements. These measurements were used to calculate the thyroid remnant doses reached following the MIRD approach. Additionally, 25 patients received oral glucocorticoid therapy with 30 mg of prednisolone for 4 wk. In 5 patients with highly active GO, intravenous glucocorticoid therapy was necessary. After ATR, thyroid parameters were closely monitored, and medication was adapted to ensure normal TSH levels.

Statistical Evaluation

For metric data, median (\bar{x}) and range or mean \pm SD were calculated, and differences between groups were evaluated with the Student t test (2-tailed) if the D'Agostino–Pearson omnibus normality test showed a normal distribution or with the Wilcoxon test if the distribution was not normal. The Fisher exact test was used to evaluate group distributions of binary variables. The level of statistical significance

TABLE 1
Characteristics of Study Population

Characteristic	Data
Subjects	100% (30)
Age (y)	52.1 \pm 9.9
Female	90% (27)
Duration of thyroid disease (y)	2.7 (1–16)
Duration from primary thyroid treatment to ATR (mo)	17.5 (1–256)
^{99m}Tc uptake (%)	0.2 (0.01–1.7)
Lobus pyramidalis present at baseline	50% (15)
ATR	
Oral steroids during ATR	83% (25)
Intravenous steroids during ATR	17% (5)
GO status at baseline	
Mild	13% (4)
Moderate-to-severe	83% (25)
Very severe	3% (1)
Previous steroid therapy	83% (25)
Subsequent steroid therapy	20% (6)

Qualitative data are percentage and number; continuous data are mean \pm SD or median and range.

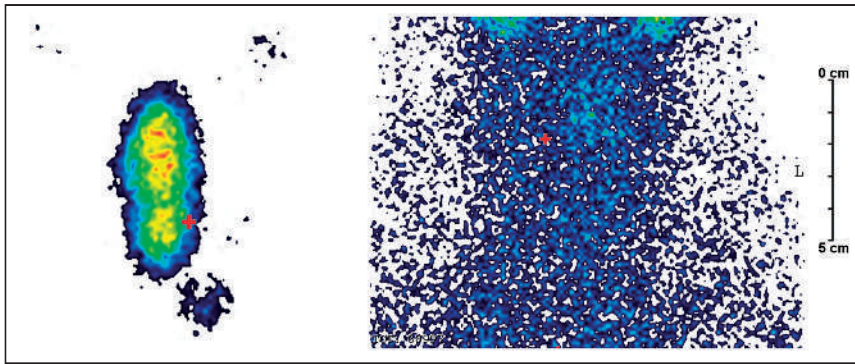


FIGURE 1. Patient example of remaining active thyroid tissue seen on ^{99m}Tc -pertechnetate scintigraphy (left) and no uptake 3 mo after ATR (right).

was defined as a 2-tailed 2α value of less than 0.05. All calculations were performed with SPSS (version 22.0.0; IBM) and Prism (version 9.0.0; GraphPad) for Windows (Microsoft). P values are given descriptively without α -adjustment for multiple testing.

RESULTS

Study Population

Thirty patients who met all inclusion and exclusion criteria were identified and analyzed. Four showed mild (13%), 25 moderate-to-severe (83%), and 1 sight-threatening (3%) GO. Of these, 27 were female and 3 male; the mean age was 52.1 y (range, 29–80 y) (an overview of baseline characteristics is provided in Table 1). All patients showed unstable GO and fluctuating thyroid parameters. To increase radioiodine uptake, 21 patients received rhTSH before ATR.

Changes in Thyroid Parameters

Half the patients ($n = 15$) showed a remaining pyramidal lobe on pre-ATR ^{99m}Tc -pertechnetate thyroid scintigraphy. Because scintigraphy was not routinely included in follow-up examinations, only 6 of 15 patients with a pyramidal lobe received a second analysis after ATR. In all 6 of these patients, the pyramidal lobe was not visible on repeat thyroid scintigraphy 6 mo after ATR (Fig. 1).

Mean ^{99m}Tc uptake in all patients with pre- and post-ATR ^{99m}Tc -pertechnetate thyroid scintigraphy decreased from 0.5% to 0.1% at 3 mo after ATR ($n = 12$, $P = 0.04$; Fig. 2).

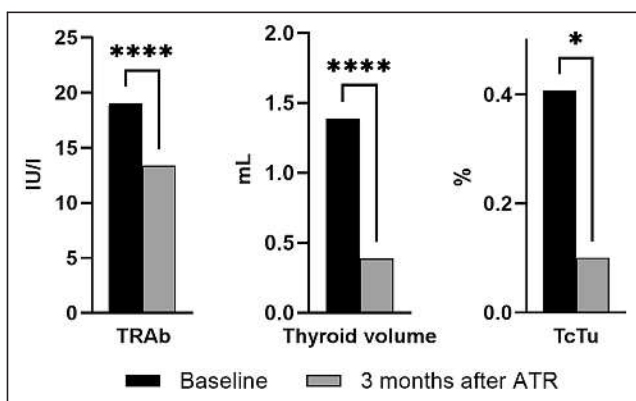


FIGURE 2. Significant decrease in TRAb level, thyroid volume, and uptake on ^{99m}Tc -pertechnetate scintigraphy at 3-mo follow-up compared with baseline, indicating successful ATR. $*P \leq 0.05$. $****P \leq 0.0001$. TcTu = ^{99m}Tc uptake.

The average thyroid volume ($n = 28$) shrank from 1.4 to 0.4 cm^3 from baseline to 3 mo after ATR. The mean TRAb titer ($n = 21$) decreased from 19.02 to 13.37 IU/L. Both changes were highly statistically significant ($P < 0.0001$). All patients showed a positive TRAb titer at baseline. In no case could a complete regression in antibodies be measured after ATR.

Compared with baseline, average TSH increased from 1.3 to 1.42 mU/L ($P = 0.75$), despite increasing levothyroxine therapy (81.5 vs. 101.3 μg after 3 mo [$P = 0.002$] and vs. 108 μg after 12 mo [$P = 0.006$]), emphasizing the loss of functional thyroid tissue and the success of ATR. An overview

of the assessed thyroid parameters before and after ATR is provided in Table 2, and an overview of the radioactive iodine therapy parameter is provided in Table 3.

Ophthalmologic Assessment

Three months after ATR, CAS decreased significantly from an average of 3.4 to 1.9 ($P = 0.0003$; Fig. 3). The rate of active forms decreased to 10%. To reach an inactive status, 3 patients needed glucocorticoids in addition to the glucocorticoids all patients received during ablation. After 12 mo, 96% of patients had an inactive status. CAS further improved significantly to an average of 1.3 ($P < 0.0001$). Worsening of CAS was observed in only 1 patient (4%), who was a heavy smoker and showed unstable thyroid function and high levels of TRAb before ATR.

The soft-tissue score decreased at 3 mo after ATR to an average of 3.4 ($P = 0.002$). After 12 mo, there was a highly significant improvement to an average score of 2.1 ($P = 0.0001$).

NOSPECS was reduced from 5.9 at baseline to 5.2 at 3 mo ($P = 0.013$; Fig. 3). A significant reduction in NOSPECS was also observed at the evaluation 12 mo after ATR (4.9, $P = 0.007$). Worsening of NOSPECS at 3 and 12 mo was observed only in the aforementioned high-risk patient.

For the proptosis analysis, we excluded all patients who underwent orbital decompression surgery during the follow-up period and included only patients with clinically significant exophthalmos of at least 20 mm or side differences of at least 2 mm. This left, at baseline, 8 (27%) patients. Three months after ATR, 3 of these 8 patients improved to a clinically significant extent (reduction ≥ 2 mm), 4 patients were stable, and the condition of 1 patient had deteriorated

TABLE 2
Thyroid Status

Parameter	Baseline	3 mo after TTA	12 mo after TTA
LT4 dose (μg)	81.5 \pm 42.5	101 \pm 26.9	108 \pm 25.8
TRAb (IU/L)	18.4 (1.4–>40)	13.4 (0.58–>40)	
Thyroid volume (cm^3)	0.95 (0–5.5)	0.05 (0–2)	

Data are mean \pm SD or median and range. $N = 30$ subjects.

TABLE 3
Radioactive Iodine Therapy Parameters

Parameter	Data
Target volume (cm ³)	0.95 (0–5.5)
Activity (MBq of ¹³¹ I)	411 (100–1,036)
Thyroid remnant dose (Gy)	488 (63–2,153)
24-h radioiodine uptake (%)	13.4 ± 7
Effective half-life (d)	2.8 ± 1.5

Data are mean ± SD or median and range. *N* = 30 subjects.

(increase ≥ 1 mm). This was the same at the 12-mo follow-up. All patients whose proptosis was inconspicuous at baseline (*n* = 16) underwent no changes in proptosis during follow-up.

An improvement or worsening of ocular motility was defined by an increase of reduction in total motility by no less than 8°. Patients who underwent orbital decompression or eye muscle surgery during the follow-up period were excluded, leaving 19 patients for analysis (63%). At the 3-mo follow-up visit, 26% of these patients had improved motility, 74% had stable motility, and 2 patients had decreased motility. Changes in ophthalmologic parameters are shown in Table 4.

DISCUSSION

The results of this retrospective study show a clinical benefit of ATR in patients with unstable GO after prior thyroidectomy. Because of the complicated anatomic location, small remnants of thyroid tissue can persist after surgery and subsequently trigger hyperthyroidism and GO (39,40). Our results encourage the use of ATR in these patients with unstable thyroid function and, consequently, unstable GO. This practice is in concordance with the therapeutic principle of aiming for stable euthyroidism in GO (11,41).

Ophthalmologic Assessment

Corresponding to the improvement in thyroid parameters, an early response assessment at 3 mo after ATR already showed significant reductions in CAS, NOSPECS, and soft-tissue scores,

with further improvements occurring until the 12-mo follow-up. Worsening can mostly be prevented with concomitant glucocorticoid treatment (oral or intravenous, depending on the activity and severity of GO before ATR). Only 1 patient showed worsening of CAS and NOSPECS during the follow-up trial. This individual was a heavy smoker (30 cigarettes per day), which might be the reason for the insufficient treatment response. The significant reduction in inflammatory activity is less likely due to the corticosteroid treatment that patients received during ATR because of the brevity of the treatment (4–6 wk) and previous unsuccessful attempts to stabilize the GO with corticosteroids. However, a beneficial effect cannot be ruled out and should be investigated.

Our findings are in line with the results of prior studies. A retrospective analysis of 55 GO patients who underwent thyroidectomy showed that the prevalence of inactive GO was significantly higher in the fraction of patients treated with additional adjuvant ATR. This has been confirmed in subsequently performed randomized control trials comparing the effects of thyroidectomy versus thyroidectomy plus ATR on GO improvement (29,30). Different results have been reported from a longitudinal study on 60 patients with mild to moderate GO undergoing thyroidectomy, thyroidectomy plus radioactive iodine therapy, or treatment with antithyroid drugs, without statistically significant differences between the thyroidectomy group and the thyroidectomy-plus-radioactive iodine group. Still, both groups showed significantly better outcomes than the group treated with antithyroid drugs (42). The differing results might indicate that not all patients benefit from ATR after thyroidectomy. At our center, therefore, ATR was performed not immediately after thyroidectomy but in cases of unstable GO after surgery, which entails a negative preselector. Our findings therefore indicate a potential role for ATR in this setting as well. In contrast to Menconi et al. (29) and De Bellis et al. (42), we also included patients with severe GO, and in contrast to Moleti et al. (30), intravenous glucocorticoids were administered to only 5 patients.

Despite the large number of GO patients in our tertiary referral center, only relatively few patients could be included in this trial. There were multiple reasons, such as the high number of mild-GO cases and the many externally performed ATR due to the tertiary referral status of our center and the long journeys to it. Furthermore, further treatment after thyroidectomy was only deemed necessary in a small fraction of patients, suggesting that surgery alone may be sufficient in most cases.

Most patients in our analysis showed a moderate-to-severe GO, probably because patients with mild cases are less often referred to a university eye hospital. The higher number of referred cases of more severe GO may also indicate that mild forms need extensive thyroid treatment less frequently. However, this possibility cannot be extrapolated from our data and should be investigated in a larger study. Our cohort had only 1 patient with sight-threatening disease; such patients are rare even in a tertiary referral center.

The less beneficial effect on proptosis and motility was not unexpected, since fibrotic changes in the extraocular muscles and proptosis due to adipogenesis react less to inactivation of GO, as demonstrated in clinical trials of antiinflammatory agents (16,17).

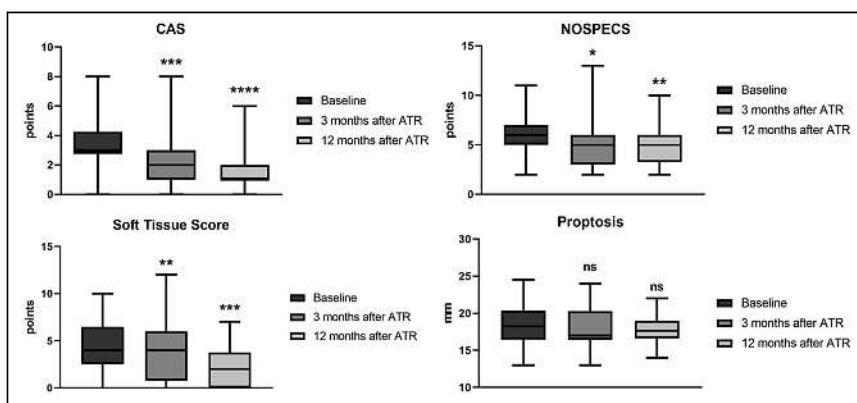


FIGURE 3. Significant decrease in disease activity as assessed with soft-tissue score and CAS at 3 and 12 mo after ATR, compared with baseline. NOSPECS also showed significant decrease (*P* = 0.013) at both time points. Proptosis was mostly stable, with no significant improvement. **P* ≤ 0.05. ***P* ≤ 0.01. ****P* ≤ 0.001. *****P* ≤ 0.0001; ns = not statistically significant.

TABLE 4
Ophthalmic Status

Parameter	Baseline	3 mo after TTA	12 mo after TTA
CAS	3.4 ± 1.8	1.9 ± 1.6	1.3 ± 1.2
NOSPECS	5.9 ± 1.9	5.1 ± 2.6	4.9 ± 2
Soft-tissue score	4.7 ± 2.6	3.4 ± 2.9	2.1 ± 2.1
Proptosis (mm)	18.4 (13–24.5)	18.1 (13–24)	17.9 (14–22)
Motility (°)	296.8 (157–350)	302.2 (215–350)	298.6 (180–350)

Data are mean ± SD or median and range. *N* = 30 subjects.

Changes in Thyroid Parameters

In line with prior observations, ATR showed a good safety profile, and the administration of rhTSH was not associated with any severe ophthalmologic side effects (30). Follow-up examinations after 3 and 12 mo showed reductions in TRAb titer, thyroid volume, and ^{99m}Tc uptake, implicating successful irradiation of thyroid remnant tissue. We also observed increases in levothyroxine requirements, which may be interpreted as an additional marker of successful ablation but may also be attributable to other causes, such as weight gain, which is commonly observed in patients treated with corticosteroids.

The therapeutic effect of ATR affirms prior observations that even small thyroid remnants can play a role in mediating GO and that its irradiation reduces autoimmune activity (43,44). Of note, half our patients displayed a prominent pyramidal lobe on pretreatment ^{99m}Tc scintigraphy, suggesting that its nonresection may play a role in the course of postthyroidectomy hyperthyroidism and GO. However, since ^{99m}Tc scintigraphy is not performed as a routine follow-up examination after thyroidectomy, it remains unknown how many patients with residual pyramidal lobes may experience no complications.

Regarding TRAb, most patients (93%) showed levels above 2 IU/L (median, 18.4 IU/L) at baseline 2 y after the beginning of the thyroid disease. This finding agrees with previous studies showing that patients with severe, progressive GO have a persistent TRAb level of at least 2–6 IU/L even 2 y after the onset of Graves' disease. In contrast, less severely afflicted patients already showed negative TRAb levels at this time point (8,21). Our patient cohort confirms these findings and represents an at-risk cohort regarding the progression of GO. Still, ATR was able to reduce TRAb levels from a median of 18.4 to 13.4 IU/L after 3 mo. Furthermore, the fact that 96% of patients showed inactivation after ATR, even in this at-risk group regarding TRAb levels, underlines the effectiveness of ATR.

Lastly, a wide range of thyroid remnant doses was reached in our cohort. Interestingly, for all patients in whom the thyroid remnant dose of 500 Gy was exceeded by 20% or more, the activity calculation was performed using the pretherapeutic ^{99m}Tc-pertechnetate thyroid scintigraphy or rhTSH was administered after the RAIU test, meaning that the conditions during TRAb and RAIU testing were not comparable.

Patients in whom the target thyroid remnant dose was undershot by 20% or more (*n* = 10) had a lower RAIU during TRAb testing than in the previously performed RAIU test (*n* = 7) or than the assumed RAIU of 10% in the patients for whom no RAIU test was performed (*n* = 3).

Limitations

Limitations of this study include its retrospective design and the lack of a control group in which the course of GO without additional

ATR could be observed. Additionally, follow-up thyroid scintigraphy was missing in a subgroup of patients. Furthermore, the treatment protocol within the collective was variable, with some patients being treated after an RAIU test whereas in others an RAIU of 10% was assumed if the ^{99m}Tc uptake was rated sufficient by visual assessment. On the basis of the small sample size, caution is warranted in comparing these 2 approaches. Yet, insufficient thyroid remnant doses were more commonly observed in the cohort that underwent a pretherapeutic RAIU test (7/17 vs. 3/13), implying that a clear benefit of an RAIU test cannot be stated.

CONCLUSION

Our data indicate that radioiodine ATR is a viable treatment option in patients with unstable GO and persistence of thyroid dysfunction after thyroidectomy. Therefore, scintigraphy should be considered for patients with unstable GO after thyroidectomy and fluctuating thyroid parameters, and additional ablation should be performed if there is a significant thyroid remnant. Persistence of the pyramidal lobe after surgery may play a pivotal role in the pathogenesis. Further randomized, controlled studies are needed to determine the standalone impact of ATR.

DISCLOSURE

No potential conflict of interest relevant to this article was reported.

ACKNOWLEDGMENT

We would like to pay tribute to our colleague Ina Binse, who contributed to the study design and supervised data collection and analysis but who sadly died before the study was finished.

KEY POINTS

QUESTION: How does thyroid remnant ablation by use of radioactive iodine impact the course of disease in patients with persistent or worsening GO after prior thyroidectomy?

PERTINENT FINDINGS: Ophthalmologic assessment revealed clinical improvement at 3 and 12 mo after thyroid remnant ablation in 29 of 30 patients. Furthermore, ultrasound, thyroid scintigraphy, and TRAb levels indicated successful ablation.

IMPLICATIONS FOR PATIENT CARE: Thyroid remnant ablation is well tolerated and may improve the treatment outcome in GO patients.

REFERENCES

- Shan SJ, Douglas RS. The pathophysiology of thyroid eye disease. *J Neuroophthalmol*. 2014;34:177–185.
- Bahn RS. Current insights into the pathogenesis of Graves' ophthalmopathy. *Horm Metab Res*. 2015;47:773–778.
- Davies TF, Andersen S, Latif R, et al. Graves' disease. *Nat Rev Dis Primers*. 2020; 6:52.
- Krieger CC, Place RF, Bevilacqua C, et al. TSH/IGF-1 receptor cross talk in Graves' ophthalmopathy pathogenesis. *J Clin Endocrinol Metab*. 2016;101:2340–2347.
- Morshed SA, Davies TF. Graves' disease mechanisms: the role of stimulating, blocking, and cleavage region TSH receptor antibodies. *Horm Metab Res*. 2015; 47:727–734.
- Tsui S, Naik V, Hoa N, et al. Evidence for an association between thyroid-stimulating hormone and insulin-like growth factor 1 receptors: a tale of two antigens implicated in Graves' disease. *J Immunol*. 2008;181:4397–4405.
- Krieger CC, Neumann S, Place RF, Marcus-Samuels B, Gershengorn MC. Bidirectional TSH and IGF-1 receptor cross talk mediates stimulation of hyaluronan secretion by Graves' disease immunoglobulins. *J Clin Endocrinol Metab*. 2015;100: 1071–1077.
- Stöhr M, Oeverhaus M, Lytton SD, et al. Predicting the course of Graves' orbitopathy using serially measured TSH-receptor autoantibodies by automated binding immunoassays and the functional bioassay. *Horm Metab Res*. 2021;53:435–443.
- Plöhn S, Edelmann B, Japtok L, et al. CD40 enhances sphingolipids in orbital fibroblasts: potential role of sphingosine-1-phosphate in inflammatory T-cell migration in Graves' orbitopathy. *Invest Ophthalmol Vis Sci*. 2018;59:5391–5397.
- Gerding MN, Terwee CB, Dekker FW, Koornneef L, Prummel MF, Wiersinga WM. Quality of life in patients with Graves' ophthalmopathy is markedly decreased: measurement by the medical outcomes study instrument. *Thyroid*. 1997;7:885–889.
- Burch HB, Wartofsky L. Graves' ophthalmopathy: current concepts regarding pathogenesis and management. *Endocr Rev*. 1993;14:747–793.
- Dunne JW, Edis RH. Optic nerve involvement in Graves' ophthalmopathy: a case report and review. *Aust N Z J Med*. 1985;15:258–261.
- Bartalena L, Baldeschi L, Boboridis K, et al. The 2016 European Thyroid Association/European Group on Graves' Orbitopathy guidelines for the management of Graves' orbitopathy. *Eur Thyroid J*. 2016;5:9–26.
- Oeverhaus M, Wittler T, Lax H, Esser J, Fuhrer D, Eckstein A. Combination therapy of intravenous steroids and orbital irradiation is more effective than intravenous steroids alone in patients with Graves' orbitopathy. *Horm Metab Res*. 2017; 49:739–747.
- Eckstein A, Esser J, Oeverhaus M, Saeed P, Jellema HM. Surgical treatment of diplopia in Graves orbitopathy patients. *Ophthalm Plast Reconstr Surg*. 2018;34(suppl 1): S75–S84.
- Oeverhaus M, Stohr M, Moller L, Fuhrer D, Eckstein A. Graves' orbitopathy: current concepts for medical treatment. *Klin Monatsbl Augenheilkd*. 2021;238:24–32.
- Bartalena L, Kahaly GJ, Baldeschi L, et al. The 2021 European Group on Graves' Orbitopathy (EUGOGO) clinical practice guidelines for the medical management of Graves' orbitopathy. *Eur J Endocrinol*. 2021;185:G43–G67.
- Prummel MF, Wiersinga WM, Mourits MP, Koornneef L, Berghout A, van der Gaag R. Effect of abnormal thyroid function on the severity of Graves' ophthalmopathy. *Arch Intern Med*. 1990;150:1098–1101.
- Karlsson F, Westermark K, Dahlberg PA, Jansson R, Enoksson P. Ophthalmopathy and thyroid stimulation. *Lancet*. 1989;2:691.
- Wiersinga W, Zarkovic M, Bartalena L, et al. Predictive score for the development or progression of Graves' orbitopathy in patients with newly diagnosed Graves' hyperthyroidism. *Eur J Endocrinol*. 2018;178:635–643.
- Eckstein AK, Plicht M, Lax H, et al. Thyrotropin receptor autoantibodies are independent risk factors for Graves' ophthalmopathy and help to predict severity and outcome of the disease. *J Clin Endocrinol Metab*. 2006;91:3464–3470.
- Burch HB. Graves' ophthalmopathy: current concepts regarding pathogenesis and management. *Endocr Rev*. 1993;14:747–793.
- Kahaly GJ, Bartalena L, Hegedus L, Leenhardt L, Poppe K, Pearce SH. 2018 European Thyroid Association Guideline for the management of Graves' hyperthyroidism. *Eur Thyroid J*. 2018;7:167–186.
- Bartalena L, Marocci C, Bogazzi F, Panicucci M, Lepri A, Pinchera A. Use of corticosteroids to prevent progression of Graves' ophthalmopathy after radioiodine therapy for hyperthyroidism. *N Engl J Med*. 1989;321:1349–1352.
- Alesina PF, Singaporewalla RM, Eckstein A, Lahner H, Walz MK. Is minimally invasive, video-assisted thyroidectomy feasible in Graves' disease? *Surgery*. 2011; 149:556–560.
- Musholt TJ, Bockisch A, Clerici T, et al. Update of the S2k guidelines: surgical treatment of benign thyroid diseases [in German]. *Chirurg*. 2018;89:699–709.
- Wilhelm SM, McHenry CR. Total thyroidectomy is superior to subtotal thyroidectomy for management of Graves' disease in the United States. *World J Surg*. 2010; 34:1261–1264.
- Dralle H, Sekulla C. Morbidity after subtotal and total thyroidectomy in patients with Graves' disease: the basis for decision-making regarding surgical indication and extent of resection [in German]. *Z Arztl Fortbild Qualitatssich*. 2004;98(suppl 5): 45–53.
- Menconi F, Marino M, Pinchera A, et al. Effects of total thyroid ablation versus near-total thyroidectomy alone on mild to moderate Graves' orbitopathy treated with intravenous glucocorticoids. *J Clin Endocrinol Metab*. 2007;92:1653–1658.
- Moleti M, Violi MA, Montanini D, et al. Radioiodine ablation of postsurgical thyroid remnants after treatment with recombinant human TSH (rhTSH) in patients with moderate-to-severe Graves' orbitopathy (GO): a prospective, randomized, single-blind clinical trial. *J Clin Endocrinol Metab*. 2014;99:1783–1789.
- Menconi F, Leo M, Vitti P, Marocci C, Marino M. Total thyroid ablation in Graves' orbitopathy. *J Endocrinol Invest*. 2015;38:809–815.
- Meyer Zu Horste M, Pateronis K, Walz MK, et al. The effect of early thyroidectomy on the course of active Graves' orbitopathy (GO): a retrospective case study. *Horm Metab Res*. 2016;48:433–439.
- Eckstein AK, Plicht M, Lax H, et al. Clinical results of anti-inflammatory therapy in Graves' ophthalmopathy and association with thyroidal autoantibodies. *Clin Endocrinol (Oxf)*. 2004;61:612–618.
- Dickinson AJ, Perros P. Controversies in the clinical evaluation of active thyroid-associated orbitopathy: use of a detailed protocol with comparative photographs for objective assessment. *Clin Endocrinol (Oxf)*. 2001;55:283–303.
- Mourits MP, Koornneef L, Wiersinga WM, Prummel MF, Berghout A, van der Gaag R. Clinical criteria for the assessment of disease activity in Graves' ophthalmopathy: a novel approach. *Br J Ophthalmol*. 1989;73:639–644.
- Mourits MP, Prummel MF, Wiersinga WM, Koornneef L. Clinical activity score as a guide in the management of patients with Graves' ophthalmopathy. *Clin Endocrinol (Oxf)*. 1997;47:9–14.
- Prummel MF, Bakker A, Wiersinga WM, et al. Multi-center study on the characteristics and treatment strategies of patients with Graves' orbitopathy: the first European Group on Graves' Orbitopathy experience. *Eur J Endocrinol*. 2003;148:491–495.
- Hammes J, van Heek L, Hohberg M, et al. Impact of different approaches to calculation of treatment activities on achieved doses in radioiodine therapy of benign thyroid diseases. *EJNMMI Phys*. 2018;5:32.
- DeGroot LJ, Benjasuratwong Y. Evaluation of thyroid ablative therapy for ophthalmopathy of Graves' disease. *Orbit*. 1996;15:187–196.
- Dietlein M. *Differenziertes Schilddrüsenkarzinom: Behandlungskorridore und Interdisziplinäre Konzepte*. Thieme; 2013/2014:R1–R32.
- Bartalena L, Baldeschi L, Dickinson AJ, et al. Consensus statement of the European Group on Graves' Orbitopathy (EUGOGO) on management of Graves' orbitopathy. *Thyroid*. 2008;18:333–346.
- De Bellis A, Conzo G, Cennamo G, et al. Time course of Graves' ophthalmopathy after total thyroidectomy alone or followed by radioiodine therapy: a 2-year longitudinal study. *Endocrine*. 2012;41:320–326.
- Marocci C, Bartalena L, Bogazzi F, Bruno-Bossio G, Pinchera A. Relationship between Graves' ophthalmopathy and type of treatment of Graves' hyperthyroidism. *Thyroid*. 1992;2:171–178.
- Tallstedt L, Lundell G. Radioiodine treatment, ablation, and ophthalmopathy: a balanced perspective. *Thyroid*. 1997;7:241–245.

Interim Analysis of a Prospective Validation of 2 Blood-Based Genomic Assessments (PPQ and NETest) to Determine the Clinical Efficacy of ^{177}Lu -DOTATATE in Neuroendocrine Tumors

Lisa Bodei^{1,2}, Nitya Raj³, Richard K. Do^{1,2}, Audrey Mauguen⁴, Simone Krebs^{1,2}, Diane Reidy-Lagunes³, and Heiko Schöder^{1,2}

¹Department of Radiology, Memorial Sloan Kettering Cancer Center, New York, New York; ²Department of Radiology, Weill Cornell Medical College, New York, New York; ³Department of Medicine, Memorial Sloan Kettering Cancer Center, New York, New York; and ⁴Department of Epidemiology and Biostatistics, Memorial Sloan Kettering Cancer Center, New York, New York

Reliable biomarkers for neuroendocrine tumor (NET) management during peptide receptor radionuclide therapy (PRRT) are lacking. We validated the role of 2 circulating biomarkers: the PRRT prediction quotient (PPQ) as a predictive marker for response and the NETest as a monitoring biomarker. Furthermore, we evaluated whether tissue-based genetic alterations are effective in predicting progression-free survival (PFS). **Methods:** Data were prospectively collected on patients at the Memorial Sloan Kettering Cancer Center with ^{177}Lu -DOTATATE-treated somatostatin receptor (SSTR)-positive gastroenteropancreatic and lung NETs ($n = 67$; median age, 66 y; 52% female; 42% pancreatic, 39% small-bowel; 78% grade 1 or 2). All cases were metastatic (89% liver) and had received 1–8 prior treatments (median, 3), including somatostatin analogs (91%), surgery (55%), or chemotherapy (49%). Treatment response included PFS. According to RECIST, version 1.1, responders had stable disease or a partial response (disease-control rate) and nonresponders had progression. Blood was collected before each cycle and at follow-up. Samples were deidentified and assayed and underwent masked analyses. The gene expression assays included RNA isolation, real-time quantitative polymerase chain reaction, and multialgorithm analyses. The PPQ (positive predicts a responder; negative predicts a nonresponder) at baseline was determined. The NETest (0–100 score) was performed. Statistics were analyzed using Mann–Whitney U testing (2-tailed) or Kaplan–Meier survival testing (PFS). In patients with archival tumor tissue, next-generation sequencing was performed through an institutional platform (Memorial Sloan Kettering–Integrated Mutation Profiling of Actionable Cancer Targets). **Results:** Forty-one patients (61%) were responders. PPQ accurately predicted 96% (64/67). The hazard ratio for prediction was 24.4 (95% CI, 8.2–72.5). Twelve-month disease control was 97% for PPQ-positive patients versus 26% for PPQ-negative patients ($P < 0.0001$). Median progression-free survival was not reached in those predicted to respond (PPQ-positive, $n = 40$) but was 8 mo in those predicted not to respond (PPQ-negative, $n = 27$). The NETest result in responders was 67 ± 25 at baseline and significantly ($P < 0.05$) decreased ($-37 \pm 44\%$) at follow-up. The NETest result in nonresponders was 44 ± 23 at baseline and significantly ($P < 0.05$) increased ($+76\% \pm 56\%$) at progression. Overall, the NETest changes (increases or decreases) were 90% accurate. Thirty patients underwent next-generation sequencing. Tumors were microsatellite-stable, and the median mutational burden was 1.8. Alterations involved mainly the

mTOR/PTEN/TSC pathway (30%). No relationship was associated with PRRT response. **Conclusion:** Our interim analysis confirmed that PPQ is an accurate predictor of ^{177}Lu -DOTATATE responsiveness (radiosensitivity) and that NETest changes accurately correlated with treatment response. Tissue-based molecular genetic information had little value in PRRT prediction. Blood-based gene signatures may improve the management of patients undergoing ^{177}Lu -DOTATATE by providing information on tumor radiosensitivity and disease course, thus allowing individualized strategies.

Key Words: NETest; PPQ; PRRT; NET

J Nucl Med 2023; 64:567–573

DOI: 10.2967/jnumed.122.264363

Peptide receptor radionuclide therapy (PRRT) is an established treatment for metastatic or nonresectable neuroendocrine tumors (NETs) that involves systemic administration of radiolabeled octreotide derivatives targeting overexpressed somatostatin receptors (SSTRs) on NETs. There are no objective means to predict therapeutic efficacy (1). Effective treatment is defined as disease stabilization and partial or complete response on structural imaging (CT or MRI). ^{68}Ga -labeled somatostatin analog PET/CT (^{68}Ga -SSA PET) is used to amplify diagnostic information, although response criteria remain to be defined (2–4). Treatment is effective in about 60% of cases (5); about 15%–30% of patients will exhibit disease progression during therapy, and 10%–15% will progress within 6–12 mo after treatment (2,3,5,6).

A precise, objective methodology for predicting therapeutic efficacy remains elusive (7). Primary tumor site, histopathologic grading, and SSTR imaging (particularly octreotide scanning) have limited accuracy in the prediction of responsiveness, at 60% for tumors with the highest uptake (3). In the NETTER-1 study, no difference in response was seen between patients with grade 4 uptake and those with lower uptake, such as grade 2 or 3 (5). Tumor burden, histologic grading, and the presence or intensity of ^{18}F -FDG uptake provide prognostic information but cannot specifically predict response to PRRT (3,5). It is probable that the determinants of therapeutic efficacy are intrinsic and reflect the molecular biologic and genomic characteristics of a specific tumor. The efficacy of PRRT therefore depends on biologic parameters that determine tumor sensitivity to radionuclide therapy.

Received May 2, 2022; revision accepted Nov. 1, 2022.

For correspondence or reprints, contact Lisa Bodei (bodeil@mskcc.org).

Published online Nov. 17, 2022.

COPYRIGHT © 2023 by the Society of Nuclear Medicine and Molecular Imaging.

Currently, there are no specific molecular features (e.g., proliferation, mutation status, or chromosomal abnormalities) that can predict radiosensitivity (1). In other settings (e.g., breast or head-and-neck cancer), tissue transcriptomic-based or gene expression assays predicted response to external-beam radiotherapy (8–10). Such approaches require tumor tissue for evaluation, which can be obtained only by surgery or biopsy (1). Similar information from a blood-based assay would be desirable.

In 2018, we reported a circulating transcript assay (the PRRT prediction quotient [PPQ]) predicting PRRT response in gastroenteropancreatic and bronchopulmonary NETs as about 95% accurate (11,12). This study included 2 comparator cohorts: an SSA cohort and a wait-and-watch cohort. The PPQ could not predict outcome in either the SSA cohort or the wait-and-watch cohort, consistent with the proposal that the PPQ is a predictive marker specifically for PRRT. This blood-based assay comprises expression of 8 genes and captures both growth factor and metabolomic expression specifically related to oxidative stress, metabolism, and hypoxic signaling (12).

A different blood-based transcriptomic assay, the NETest, evaluates 51 NET-specific genes (13–15). This test functions as a surrogate biomarker, and changes in score, compared with before treatment (e.g., SSAs or surgery), strongly correlated with tumor progression measured with CT or MRI (16,17). Quarterly blood sampling provides a real-time evaluation of tumor status (18). A recent report on 3 independent, prospective European cohorts demonstrated the NETest to be effective (98%) in monitoring response to PRRT. NETest levels decreased in RECIST responders to treatment and remained elevated in those who progressed despite therapy (19). At the conclusion of therapy, NETest levels significantly correlated with progression-free survival (PFS).

Currently, PRRT response is evaluated with morphologic and, when possible, molecular imaging. This has well-recognized limitations, including difficulties in assessing small-volume or coalescent disease when differentiating disease stabilization from pseudoprogression (4,20–22). There is thus a need to introduce and validate alternative companion biomarkers of treatment response to define therapeutic efficacy.

In this larger prospective study, we validated the role of the PPQ as a predictive marker for PRRT efficacy in gastroenteropancreatic and bronchopulmonary NETs. The PPQ output is binary (PPQ-positive [PPQ+] and PPQ-negative [PPQ–]) and identifies those who are predicted to respond (PPQ+) versus those predicted not to respond (PPQ–) (12). We evaluated the accuracy of this output in our patient cohort to assess its utility. Thereafter, we examined the value of the NETest as a clinical monitoring biomarker for PRRT efficacy. We compared pre-PRRT levels with follow-up levels. In addition, we evaluated whether changes in NETest levels were concordant with RECIST 1.1–based status. Lastly, we evaluated whether tissue-based molecular genetic alterations (Memorial Sloan Kettering–Integrated Mutation Profiling of Actionable Cancer Targets [MSK-IMPACT]) (23) were effective in PFS prediction and compared this result with the blood-based PPQ in a subset for which tissue was available. Herein we report our interim analysis.

MATERIALS AND METHODS

Ethics Approval

The study was approved by the Institutional Ethics Committee at Memorial Sloan Kettering Cancer Center (approval 19-022; January 18, 2019; NCT01775072). Informed written consent was obtained

from participants. All data were collected prospectively (February 2019 to May 2021).

Therapeutic Response Assessment

Response was assessed by an independent radiologist per RECIST, version 1.1. CT (or MRI) was performed at baseline (≤ 3 mo before PRRT) and about 2–12 mo after PRRT per the protocol (11). Forty-one of 67 (61%) patients were considered responders. Response was defined as disease control (partial or complete response to therapy or stable disease). Progression (treatment failure) was confirmation of radiologic progression, at the first scan after PRRT or earlier, if symptomatic. The latter included all who completed at least 1 PRRT cycle. Overall survival (OS) and PFS were defined as the time from PRRT commencement to death or progression, respectively. Patients alive, or alive without progression, were censored at their date of last follow-up.

Blood Sampling

Samples of blood were collected before PRRT and thereafter before each PRRT cycle (administered at intervals of ~ 2 mo [2–4 cycles]) and then at follow-up (first time point, 2–3 mo after PRRT completion; second time point, from 6–9 mo to 31 mo after the last PRRT cycle). At baseline, whole blood (5 mL) was collected in EDTA-K2 tubes that included RNA-stabilization buffer and were snap-frozen. The tubes were anonymously coded and stored at -80°C within 2 h of collection (24). Randomly selected, coded blood samples were sent deidentified to Wren Laboratories (CAP8640840, CL-0704, CLIA 07D2081388) for blinded measurement.

PPQ. PPQ analysis was performed on baseline blood. Details of the PPQ, a blood-based predictive classifier, have been described (24). In brief, circulating messenger RNA involved in growth factor biology and metabolism are amplified by PCR, and expression levels are integrated with tumor grade to generate a prediction classifier summated using a logistic regression model. Samples are scored as either biomarker “positive” or “negative.” PPQ+ identifies those predicted to respond (disease stabilization or partial/complete response). PPQ– are predicted not to respond.

NETest. Details of the methodology, mathematic analysis, and validation of the NETest have been published (18,24). Briefly, it comprises a 2-step protocol (RNA isolation/cDNA production and quantitative polymerase chain reaction) from whole blood. Samples were assayed at a clinically certified laboratory (Wren Laboratories). The results are expressed as an activity index (NETest score) from 0 to 100 (11,24). The upper limit of normality is 20 (16).

Statistical Analysis

Prism (version 9.0; GraphPad Software) for Microsoft Windows and MedCalc Statistical Software (version 20.009; MedCalc Software) were used (11,24). The efficacy of PRRT was defined per the RECIST 1.1 evaluation of best response as either disease control rate (partial response + complete response + stable disease) or progression, as previously described (11,24). The accuracy of PPQ was assessed by evaluating the concordance between PPQ prediction and outcomes, including response and OS. The accuracy of NETest changes (increase or decrease) was evaluated comparing baseline with follow-up levels. Intergroup analyses were undertaken using 2-tailed nonparametric tests (Mann–Whitney *U* test or Wilcoxon signed-rank test) as applicable. The Fisher exact test was used to compare proportions, such as response rates and pretreatment groups. Survival rates (PFS and OS) were estimated using a Kaplan–Meier estimator. Log-rank tests were used to compare survival curves, whereas hazard ratios (HRs) were calculated in a Cox model to assess the impact of candidate factors on survival. The association between PFS and OS was measured using the Pearson *r*. Statistical significance was defined as a *P* value of less than 0.05

TABLE 1
Demographics

Evaluable patients	Total cohort	PPQ+	PPQ-
Total patients (n)	67	40	27
Age (y)	66 (26–88)	62 (26–86)	72 (30–88)*
Sex			
Male	32	19	13
Female	35	21	14
Time since diagnosis (mo)	65 (5–213) (mean ± SD, 68 ± 50)	74 (5–213) (mean ± SD, 75 ± 48)	39 (7–185) (mean ± SD, 56 ± 53)
Time from start of PRRT to final assessment (mo)	14 (1–31)	24 (5–30)	8 (0–31)*
NET origin			
Bronchopulmonary	3 (5%)	1	2
Typical carcinoids	2	1	1
Atypical carcinoids	0		
Carcinoids not otherwise specified	0		
High-grade (mixed adenocarcinoma and small cell lung carcinoma)	1		1
Gastroenteropancreatic	61 (91%)	38 (95%)	23 (85%)
Pancreas	28	19	9
Small intestine	26	17	9
Appendix	1	0	1
Rectum	6	2	4
Cancer of unknown primary	1	0	1
Renal	2	1	1
Gastroenteropancreatic NETs, tumor grade			
1 (Ki-67, 0%–2%)	17 (28%)	11	6
2 (Ki-67, 3%–20%)	35 (57%)	22	13
3 (Ki-67, >20%)	8 (13%)	4	4
Nonspecified (well-differentiated)	1 (2%)	1	0
Clinical stage IV at enrollment	67(100%)	40 (100%)	27 (100%)
Liver	58	32	26
Lymph nodes	51	27	24
Bone	37	18	19 [†]
Peritoneum	21	10	11
Lung	11	5	6
Other sites (e.g., adrenal, pleura, pericardium)	23	12	11
Previous therapy			
Surgery	37 (55%)	26 (65%)	11 (41%)
Somatostatin analogs	61 (91%)	37 (93%)	24 (89%)
Pharmacotherapy	57 (85%)	31 (77%)	26 (96%)
Capecitabine and temozolomide	21	12	9
Chemotherapy (platinum/dacarbazine)	12	8	4
Everolimus	15	7	8
Sunitinib	3	1	2
Others (axitinib, cabozatinib, denosumab, zoledronic acid, and levatinib)	6	3	3
Other therapies	38 (57%)	21 (53%)	17 (63%)
PRRT	8 [‡]	4 (3) [§]	4 (3) [§]
Radiotherapy	6	1	5
Liver-directed therapies	24	16	8

* $P < 0.05$ vs. PPQ+ (Mann–Whitney U test).

[†] $P < 0.05$ (χ^2).

[‡]Six previously treated with JR-11.

[§]Treated with JR-11.

^{||}Including chemoembolization, radioembolization, and selective internal radiation therapy. Qualitative data are number and percentage; continuous data are median and range.

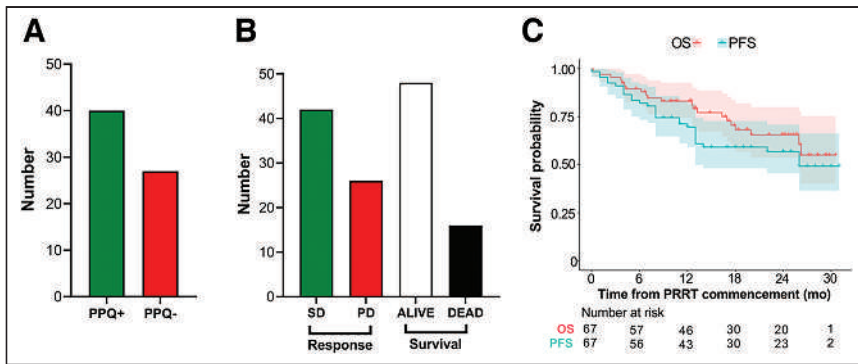


FIGURE 1. Response and baseline characteristics. (A) PPQ status before treatment. (B) Absolute response and survival in cohort. (C) Data showing that mPFS and mOS were not reached. Shading represents 95% CI for each survival curve. mOS = median overall survival; PD = progressive disease; SD = stable disease.

(2-sided). Data are presented as mean \pm SD. Ninety-five percent CIs are included when appropriate.

RESULTS

Patients

The cohort (including gastroenteropancreatic and bronchopulmonary NETs) included 100 patients recruited to date, 67 of whom had completed the PRRT treatment evaluations and are reported here. Clinical characteristics are in Table 1. Median age was 66 y (range, 26–88 y), 52% were female, 42% had pancreatic and 39% small-bowel NETs, and 78% had grade 1 or 2 disease. All had metastatic disease (100%) and had received 1–8 prior treatments (median, 3), including somatostatin analogs (SSAs, 91%), surgery (55%), or chemotherapy (49%, capecitabine and temozolomide or platinum-based therapy). Twenty-six were categorized as heavily pretreated. Forty-one were categorized as having received standard pretreatments. Heavy pretreatments (median, 4; range, 2–8) included chemotherapy, ^{177}Lu -DOTATATE ($n = 2$), and a somatostatin antagonist (^{177}Lu -satoreotide, $n = 6$) (25). Standard pretreatments (median, 2; range, 1–4) typically comprised surgery and SSAs, or SSAs and liver-directed therapy. Table 1 includes a breakdown of the PPQ+ and PPQ- cohorts. No significant differences were identified except that the PPQ- cohort was significantly older (median age, 72 y [range, 30–88] vs. 62 y [range, 26–86 y]; $P = 0.01$) and had more bone involvement (70% vs. 45%, $P = 0.048$).

Thirty (16 heavily pretreated, 14 with standard pretreatments) had next-generation tumor sequencing per MSK-IMPACT. This tool identifies actionable alterations in 341 key cancer genes and separately detects chromosomal abnormalities, such as 18q loss (23,26).

Forty (60%) were PPQ+ (predicted to respond to PRRT) (Fig. 1A). Treatment response (disease control rate) occurred in 41 (61%) of the 67 individuals, and 46 were alive at the time of evaluation (Fig. 1B). The median PFS (mPFS) was 26 mo and median OS was not reached (Fig. 1C). The 12-mo survival rates were 70% (PFS) and 83% (OS), respectively. The median pre-PRRT NETest score was 53 (range, 20–100).

PPQ

Forty were PPQ+. Thirty-nine (98%) responded to PRRT (Fig. 2A). Twenty-seven were PPQ-. Twenty-five (93%) progressed despite PRRT. The overall predictive accuracy was 96% (64/67).

4 exhibited stable disease. Three were PPQ+; the 2 progressors were both PPQ-.

NETest and PRRT Response. The NETest was elevated in all before therapy (58 ± 27). In responders, baseline NETest levels were 67 ± 25 (Fig. 3A). At follow-up, levels were significantly decreased by $-37\% \pm 44\%$ ($P = 0.0002$, Fig. 3B). This is consistent with the assay measuring a response to therapy (decrease in tumor activity). The waterfall plot indicates that 90% ($n = 35$) exhibited a stabilization or decrease in the NETest with PRRT (Fig. 3C). In nonresponders, baseline levels were 44 ± 23 (Fig. 4A). This was significantly ($P = 0.0005$) lower than baseline scores in responders. At follow-up, levels were significantly increased ($+76\% \pm 56\%$, $P = 0.0002$; Fig. 4B). The waterfall plot analysis (Fig. 4C) indicated that 89% ($n = 17$ of 19 evaluable) exhibited an increase.

A subanalysis showed similar response rates in those with fewer prior treatments (26/41, 63%) and those heavily pretreated (15/26, 58%; $P = 0.80$, Fisher test). Moreover, there were no differences in PFS ($P = 0.66$, log-rank test). The 12-mo OS was 80% in the heavily pretreated cohort and 85% in patients with fewer prior treatments ($P = 0.42$, log-rank test). Pretreatment NETest scores were similar in both groups (57 ± 27 in patients with fewer prior treatments

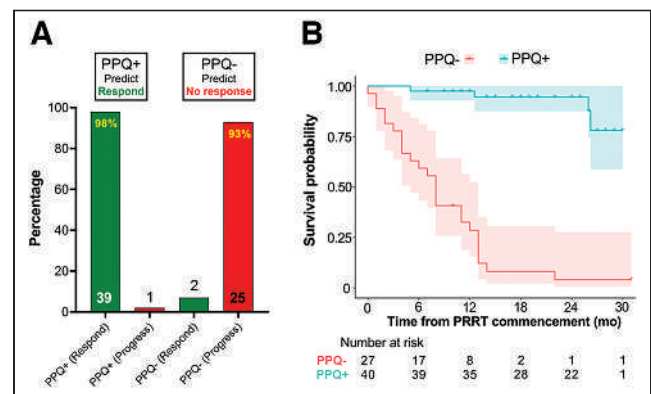


FIGURE 2. Relationship between PPQ and response. (A) Thirty-nine PPQ+ patients responded, whereas 1 patient progressed. Twenty-five PPQ- patients developed disease progression despite PRRT; 2 PPQ- patients responded to therapy. (B) mPFS was not reached for PPQ+ patients but was 8 mo for PPQ- patients. Difference was statistically significant (log-rank test, $P < 0.0001$). HR for the biomarker was 24. Shading represents 95% CI for each survival curve.

Patients who were PPQ- had a risk of progression or death 24 times higher than patients who were PPQ+ (HR, 24.4; 95% CI, 8.2–72.5).

The mPFS in PPQ+ was not reached (Fig. 2B). At 12 mo, 98% of PPQ+ patients were progression-free. The mPFS in the PPQ- cohort was 8 mo. At 12 mo, 29% were progression-free. All but 1 of 7 who were stable at 12 mo eventually developed progressive disease (by 23 mo).

The OS rate at 12 mo was 83%. OS (12 mo) was higher in PPQ+ (98%) than in PPQ- individuals (60%, $P < 0.0001$, log-rank test). Separately, 54% of heavily pretreated patients were PPQ+, compared with 63% of those with few prior treatments. Of the 6 previously treated with PRRT,

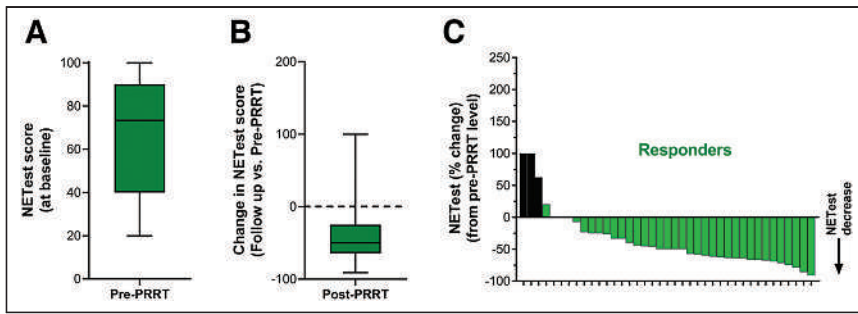


FIGURE 3. NETest in responders. (A) Baseline (pre-PRRT) NETest levels were 67 ± 25 . (B) NETest levels decreased by $-37\% \pm 44\%$ after PRRT ($P = 0.0002$). (C) Waterfall plot demonstrates decrease in NETest from baseline in individual responders. Black bars identify changes in score that were associated with posttreatment NETest levels > 40 .

vs. 60 ± 27 in the heavily pretreated patients; $P = 0.77$, Mann-Whitney test). In heavily pretreated patients, the decrease in NETest scores ($-9\% \pm 71\%$) was similar to that in patients with fewer prior treatments ($+5\% \pm 73\%$; $P = 0.34$, Mann-Whitney test). In patients who received prior PRRT ($n = 8$), responders exhibited a median NETest change of -66.5 ; in those with progression, the change was $+56\%$.

Molecular Genetic Evaluation (MSK-IMPACT) and Response

Thirty patients (45%) had tumor tissue molecular genetic testing; 16 were heavily pretreated, and 14 were not. All were microsatellite-stable. Tumor mutational burden was low (median, 1.8 mutations; range, 0–29.8). Overall, 11 (37%) had 0–1 mutations whereas 19 exhibited multiple mutations (63%). The most common alterations were in the mTOR/PTEN/TSC pathway ($n = 9$) and *MEN-1* ($n = 8$). Six (75%) with *MEN-1* mutations also had alterations in the mTOR/PTEN/TSC pathway. Separately, *DAXX* was mutated in 3 different patients, whereas *ATRX* was mutated in 1. Chromosomal losses were noted in 7 (23%). These included 11q losses in 2 (grade 3 renal NET and mixed adenocarcinoma and small cell lung carcinoma) and 18q losses in 5 (3 small-bowel NETs, 2 rectal NETs). Thirteen (81%) of 16 with heavy pretreatment and 11 of 14 (79%) with standard pretreatment exhibited a tumor mutational burden below the detection cutoff. The average number of mutations or chromosomal abnormalities was also similar in both (3.5 alterations per patient vs. 8.4 for the heavy pretreatment vs. the standard pretreatment, respectively). No apparent relationship was identified between mutations (burden or number) and the number of prior treatments.

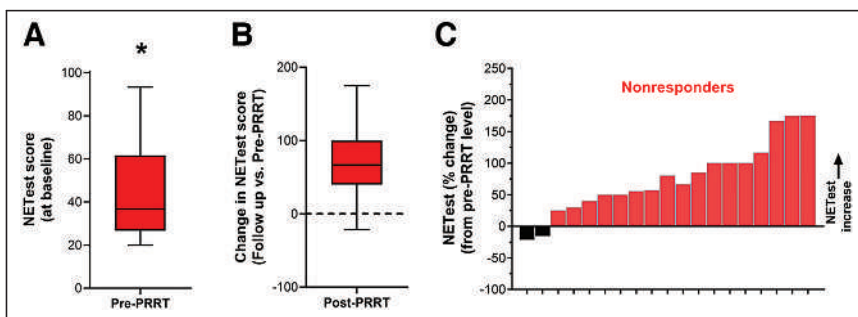


FIGURE 4. NETest in nonresponders. (A) Baseline (pre-PRRT) NETest levels were 44 ± 23 . (B) NETest levels increased by $+76\% \pm 56\%$ after PRRT ($P = 0.0002$). (C) Waterfall plot demonstrates increase in NETest from baseline in individual nonresponders. Black bars identify changes in score that were associated with posttreatment NETest levels > 40 . $*P = 0.0005$ vs. responders.

The relationship between PPQ, genetic abnormalities, and outcome (12-mo PFS) are summarized in Table 2. First, no relationship was identified between tumor mutational burden and response (45% response in those with 0–1 mutations vs. 58% response in those with > 1 mutation; $P = 0.71$, Fisher test). The PPQ biomarker was similarly distributed (PPQ+ in 5/11 or 45% of patients with 0–1 mutations vs. 10–19 or 53% of those with > 1 mutation; $P > 0.99$, Fisher test) in these groups.

Likewise, no relationship with response was noted between those with *MEN-1* mutations and those with no *MEN-1* (63% vs. 50%; $P = 0.69$, Fisher test) or mTOR pathway mutations (67% vs. 48%; $P = 0.44$, Fisher test). Similar proportions of those with *MEN-1* mutations or alterations in the mTOR pathway were PPQ+ (63% and 67%, respectively). All *DAXX* were PPQ+ and responded. The patient with an *ATRX* mutation was PPQ– and did not respond.

Chromosomal loss, in contrast, was associated with a poorer 12-mo PFS (43% vs. 74%; $P = 0.03$, log-rank test). All 5 with a Chr18q loss were PPQ–. None responded; the mPFS was 11 mo. Of note, 4 (80%) also perished, suggesting Chr18q loss to be a marker of poor prognosis.

DISCUSSION

The current study evaluated 2 blood-derived signatures as predictors and monitors of PRRT efficacy. The study, an independent, prospective U.S. study, validated the PPQ as a predictor of PRRT response and the NETest as an effective treatment monitor. Both tools were clinically valuable irrespective of previous treatments incurred, such as platinum-based chemotherapy or prior PRRT. Abnormalities, either common cancer-associated mutations or NET chromosomal abnormalities, as measured in tumor tissue (MSK-IMPACT) exhibited little value as predictors and did not consistently correlate with the PPQ-predictive output except, potentially, Chr18q loss. We are not, however, able to identify a causal relationship since none of the 8 genes that define the PPQ signature are encoded on Chr18q. At this point, we are of the opinion that any relationship between PPQ, Chr18q loss, and outcome may reflect a correlation between PFS and OS. Indeed, 18 of 26 (69%) subjects undergoing progression ultimately died within 20 mo of follow-up. Our assessment also identified no confounding variables that might be linked to PPQ, but we note that the PPQ– cohort was older than the PPQ+ cohort and had more bone involvement.

A critical unmet need in PRRT is to predict who will benefit so as to provide personalized, effective, and economically viable therapy. Prior studies have focused on clinical parameters such as staging, or biomarkers such as chromogranin A, to predict outcome. All provided limited information. Grading of SSTR expression by imaging has some value but cannot predict more than 60% of responses for lesions with a Krenning score of 4 (uptake greater than in the spleen or kidneys) by

TABLE 2
MSK-IMPACT, PPQ, and Outcomes

Category	<i>n</i>	Responder	Nonresponder	mPFS (mo)	12-mo PFS	PPQ+	PPQ–
0–1 mutations	11	5	6	11	46%	5	6
>1 mutation	19	11	8	26	79%	10	9*
No chromosomal losses	23	15	8	Not reached	74%	14	9 [†]
Chromosomal losses [‡]	7	1	6	11	43%	1	6
<i>mTOR/PTEN/TSC</i> mutations	9	6	3	26	78%	6	3
<i>MEN-1</i> mutations	8	5	3	26	75%	5	3

*One patient responded but was PPQ–. Patient had 6 mutations, including *PSM1*, *PMS2*, *BC2L11*, *INPP4A*, *NFE2L2*, and *PPP2R1A*.
[†]This is same patient as above.
[‡]11q (*n* = 2) or 18q (*n* = 5) losses.

octreotide scanning. For SSTR PET, higher uptake (mean SUV_{max} and tumor SUV_{max}/liver SUV_{average}) correlated with the therapy response, but not all patients with intense uptake respond to treatment (3,7,27).

Our study had several strengths. It was an independent, prospective study undertaken at a U.S. center of excellence. We report our analysis of the first 67 subjects. This cohort is large and includes heavily pretreated individuals. The study is ongoing, and our final target recruitment is 150 patients. A weakness of the study is that only 45% of patients have tissue molecular data. This reflects the difficulties engendered by the coronavirus disease 2019 pandemic, which significantly impacted how we treat and manage our cancer patients (hospital visits). Nevertheless, despite the inherent difficulties in follow-up and tissue acquisition during the pandemic, our study results are highly significant and provide a clear evaluation of how these 2 blood biomarkers might manage PRRT.

A previous European consortium that included 3 centers—Erasmus University, IEO Milan, and Bad Berka—examined the predictive utility of PPQ (11). This study included 2 comparator cohorts: an SSA cohort and a wait-and-watch cohort. The PPQ could not predict outcome in either of these cohorts. This finding is consistent with the proposal that the PPQ is a predictive marker specifically for PRRT. Although this study comprises a single treatment arm, future studies (e.g., NCT05247905) will evaluate whether the PPQ can predict outcomes after PRRT versus treatment with capecitabine and temozolomide.

The biomarker was initially developed in an Italian cohort. In 2 separate follow-up cohorts, from 2 ENETS centers of excellence, the PPQ was 95% accurate. The overall median PFS was not reached in PPQ+ versus PPQ– patients (10–14 mo; HR, 18–77; *P* < 0.0001). In the current study, the overall PPQ-predictive accuracy was 96% in the Memorial Sloan Kettering Cancer Center cohort. Prior treatment had no impact on the utility of PPQ as a predictive marker. The mPFS of those detected as PPQ– was 12 mo but was not reached for those who were PPQ+. The HR of 24.4 (95% CI, 8.2–72.5) confirmed the impact of this biomarker. PPQ accurately predicted response, irrespective of prior PRRT or heavy pretreatment, and provided utility as a stratification marker for PRRT.

We also evaluated the NETest to monitor treatment efficacy. We focused on pretreatment and follow-up blood results. The NETest was 90% accurate for determining PRRT response (stabilization or a decrease in PRRT responders vs. an increase in nonresponders). This confirms an earlier study showing a 90.2% accuracy in the

3 European cohorts (19). In the European studies, the NETest score had an average $-29\% \pm 26\%$ decrease in responders and a $+73\% \pm 11\%$ increase in nonresponders (pre-NETest to follow-up scores). Our results were similar: a $-37\% \pm 44\%$ decrease in responders and a $+76\% \pm 56\%$ increase in nonresponders. Our study validates the NETest as an accurate monitor of treatment response. Although a small proportion (<10%) will not exhibit clinically actionable changes, the NETest provides real-time clinical value for most. Moreover, this biomarker may add valuable information to current imaging protocols for response evaluation. Imaging accuracy is problematic because of frequent pseudoprogression or slow response. Of further interest is our observation that patients who responded to PRRT exhibited higher pretreatment NETest levels. The basis for this finding requires further investigation, but the finding indicates an intriguing potential utility for this biomarker in treatment stratification. An elevated NETest may identify the molecular hallmarks of treatment responsiveness.

To our knowledge, this is the first study to assess the relationship between genetic alterations and PRRT. A recent review identified the absence of any such peer-reviewed data and highlighted the importance of determining whether such relationships exist (1). In our study, 30 patients (45%) had tissue blocks available for MSK-IMPACT evaluation. All were microsatellite-stable and had few mutational or chromosomal abnormalities, as expected in NETs (28,29). No relationship between mutations, regardless of type (*mTOR/MEN-1*), and outcome (PFS/OS) was identified, suggesting that these have little predictive value in PRRT. This is supported by the absence of a relationship between mutations and PPQ; the latter is predictive in 96% of cases, compared with less than 50% for mutations. Of note, chromosomal losses (Chr 11q/18q) were associated with a poorer outcome. Individuals with such abnormalities failed to respond to PRRT, and a large proportion (70%) died during follow-up. This is consistent with a prognostic rather than predictive value; 18q loss is associated with metastatic spread and poorer outcomes (30).

In summary, this interim analysis confirmed the PPQ as an effective, accurate (96%) predictor of ¹⁷⁷Lu-DOTATATE-PRRT, unaffected by prior PRRT or chemotherapy, and consistent with a role as a radiation-responsive multigenomic blood biomarker. This study confirmed that NETest scores decreased in ¹⁷⁷Lu-DOTATATE responders. In contrast, in nonresponders, scores increased. Blood-based gene signatures may enhance the management of patients undergoing ¹⁷⁷Lu-DOTATATE therapy by providing

information on tumor radiosensitivity and early disease course, thus allowing individualized strategies.

CONCLUSION

We have independently validated 2 blood-based gene signatures and found them to be effective, noninvasive tools that can enhance the management of patients who undergo ¹⁷⁷Lu-DOTATATE therapy.

DISCLOSURE

PPQ/NETest measurements were provided pro bono by Wren Laboratories. This study was supported in part by NIH/NCI Cancer Center support grant P30 CA008748. Lisa Bodei is a nonremunerated consultant for AAA, ITM, Clovis Oncology, Curium, and Iba and receives research funding from AAA. Nitya Raj is on the advisory boards for Ipsen Pharma, HRA Pharma, Progenics Pharmaceuticals, and AAA. Simone Krebs is supported in part by the NIH/NCI Paul Calabresi Career Development Award for Clinical Oncology (K12 CA184746). Diane Reidy-Lagunes receives research funding from Merck, Ipsen, and Novartis and is a consultant for Novartis, Lexicon, and AAA. No other potential conflict of interest relevant to this article was reported.

KEY POINTS

QUESTION: Are validated liquid biopsies that can predict or monitor PRRT a critical unmet need in NET management?

PERTINENT FINDINGS: Two blood-based biomarkers were evaluated in a prospective study ($n = 67$). The PPQ was an accurate (96%) predictor of ¹⁷⁷Lu-DOTATATE response, and NETest changes correctly (90%) correlated with treatment response.

IMPLICATIONS FOR PATIENT CARE: Blood-based gene signatures may enhance the management of patients undergoing ¹⁷⁷Lu-DOTATATE by providing information on tumor radiosensitivity and disease course, thus allowing individualized strategies.

REFERENCES

- Bodei L, Schöder H, Baum RP, et al. Molecular profiling of neuroendocrine tumours to predict response and toxicity to peptide receptor radionuclide therapy. *Lancet Oncol*. 2020;21:e431–e443.
- Kwekkeboom DJ, de Herder WW, Kam BL, et al. Treatment with the radiolabeled somatostatin analog [¹⁷⁷Lu-DOTA⁰,Tyr³]octreotate: toxicity, efficacy, and survival. *J Clin Oncol*. 2008;26:2124–2130.
- Kwekkeboom DJ, Kam BL, van Essen M, et al. Somatostatin-receptor-based imaging and therapy of gastroenteropancreatic neuroendocrine tumors. *Endocr Relat Cancer*. 2010;17:R53–R73.
- Liberini V, Huellner MW, Grimaldi S, et al. The challenge of evaluating response to peptide receptor radionuclide therapy in gastroenteropancreatic neuroendocrine tumors: the present and the future. *Diagnostics (Basel)*. 2020;10:1083.
- Strosberg J, El-Haddad G, Wolin E, et al. Phase 3 trial of ¹⁷⁷Lu-Dotatate for mid-gut neuroendocrine tumors. *N Engl J Med*. 2017;376:125–135.
- Baum RP, Kulkarni HR, Singh A, et al. Results and adverse events of personalized peptide receptor radionuclide therapy with ⁹⁰yttrium and ¹⁷⁷lutetium in 1048 patients with neuroendocrine neoplasms. *Oncotarget*. 2018;9:16932–16950.
- Albertelli M, Dotto A, Di Dato C, et al. PRRT: identikit of the perfect patient. *Rev Endocr Metab Disord*. 2021;22:563–579.
- Eschrich SA, Fulp WJ, Pawitan Y, et al. Validation of a radiosensitivity molecular signature in breast cancer. *Clin Cancer Res*. 2012;18:5134–5143.
- Eschrich SA, Pramana J, Zhang H, et al. A gene expression model of intrinsic tumor radiosensitivity: prediction of response and prognosis after chemoradiation. *Int J Radiat Oncol Biol Phys*. 2009;75:489–496.
- Kim HS, Kim SC, Kim SJ, et al. Identification of a radiosensitivity signature using integrative metaanalysis of published microarray data for NCI-60 cancer cells. *BMC Genomics*. 2012;13:348.
- Bodei L, Kidd MS, Singh A, et al. PRRT genomic signature in blood for prediction of ¹⁷⁷Lu-octreotate efficacy. *Eur J Nucl Med Mol Imaging*. 2018;45:1155–1169.
- Kidd M, Modlin IM. Therapy: the role of liquid biopsies to manage and predict PRRT for NETs. *Nat Rev Gastroenterol Hepatol*. 2017;14:331–332.
- Modlin I, Drozdov I, Kidd M. The identification of gut neuroendocrine tumor disease by multiple synchronous transcript analysis in blood. *PLoS One*. 2013;8:e63364.
- Chen F, Zhang Y, Gibbons DL, et al. Pan-cancer molecular classes transcending tumor lineage across 32 cancer types, multiple data platforms, and over 10,000 cases. *Clin Cancer Res*. 2018;24:2182–2193.
- Pacak K, Kidd M, Meuter L, Modlin IM. A novel liquid biopsy (NETest) identifies paragangliomas and pheochromocytomas with high accuracy. *Endocr Relat Cancer*. 2021;28:731–744.
- Liu E, Paulson S, Gulati A, et al. Assessment of NETest clinical utility in a US registry-based study. *Oncologist*. 2019;24:783–790.
- Öberg K, Califano A, Strosberg JR, et al. A meta-analysis of the accuracy of a neuroendocrine tumor mRNA genomic biomarker (NETest) in blood. *Ann Oncol*. 2020;31:202–212.
- Kidd M, Drozdov I, Modlin I. Blood and tissue neuroendocrine tumor gene cluster analysis correlate, define hallmarks and predict disease status. *Endocr Relat Cancer*. 2015;22:561–575.
- Bodei L, Kidd MS, Singh A, et al. PRRT neuroendocrine tumor response monitored using circulating transcript analysis: the NETest. *Eur J Nucl Med Mol Imaging*. 2020;47:895–906.
- Bodei L, Sundin A, Kidd M, Prasad V, Modlin IM. The status of neuroendocrine tumor imaging: from darkness to light? *Neuroendocrinology*. 2015;101:1–17.
- Choi H, Chamsangavej C, Faria SC, et al. Correlation of computed tomography and positron emission tomography in patients with metastatic gastrointestinal stromal tumor treated at a single institution with imatinib mesylate: proposal of new computed tomography response criteria. *J Clin Oncol*. 2007;25:1753–1759.
- Brabander T, van der Zwan WA, Teunissen JJM, et al. Pitfalls in the response evaluation after peptide receptor radionuclide therapy with [¹⁷⁷Lu-DOTA⁰,Tyr³]octreotate. *Endocr Relat Cancer*. 2017;24:243–251.
- Cheng DT, Prasad M, Chekaluk Y, et al. Comprehensive detection of germline variants by MSK-IMPACT, a clinical diagnostic platform for solid tumor molecular oncology and concurrent cancer predisposition testing. *BMC Med Genomics*. 2017;10:33.
- Bodei L, Kidd M, Modlin IM, et al. Measurement of circulating transcripts and gene cluster analysis predicts and defines therapeutic efficacy of peptide receptor radionuclide therapy (PRRT) in neuroendocrine tumors. *Eur J Nucl Med Mol Imaging*. 2016;43:839–851.
- Reidy-Lagunes D, Pandit-Taskar N, O'Donoghue JA, et al. Phase I trial of well-differentiated neuroendocrine tumors (NETs) with radiolabeled somatostatin antagonist ¹⁷⁷Lu-satoreotide tetraxetan. *Clin Cancer Res*. 2019;25:6939–6947.
- Cheng DT, Mitchell TN, Zehir A, et al. Memorial Sloan Kettering-Integrated Mutation Profiling of Actionable Cancer Targets (MSK-IMPACT): a hybridization capture-based next-generation sequencing clinical assay for solid tumor molecular oncology. *J Mol Diagn*. 2015;17:251–264.
- Ortega C, Wong RKS, Schaefferkoetter J, et al. Quantitative ⁶⁸Ga-DOTATATE PET/CT parameters for the prediction of therapy response in patients with progressive metastatic neuroendocrine tumors treated with ¹⁷⁷Lu-DOTATATE. *J Nucl Med*. 2021;62:1406–1414.
- Simbolo M, Vicentini C, Mafficini A, et al. Mutational and copy number asset of primary sporadic neuroendocrine tumors of the small intestine. *Virchows Arch*. 2018;473:709–717.
- Scarpa A, Chang DK, Nones K, et al. Whole-genome landscape of pancreatic neuroendocrine tumours. *Nature*. 2017;543:65–71.
- Hofving T, Elias E, Rehammar A, et al. SMAD4 haploinsufficiency in small intestinal neuroendocrine tumors. *BMC Cancer*. 2021;21:101.

Safety and Survival Outcomes of ^{177}Lu -Prostate-Specific Membrane Antigen Therapy in Patients with Metastatic Castration-Resistant Prostate Cancer with Prior ^{223}Ra treatment: The RALU Study

Kambiz Rahbar¹, Markus Essler², Kim M. Pabst³, Matthias Eiber⁴, Christian la Fougère⁵, Vikas Prasad^{6,7}, Philipp Rassek¹, Ergela Hasa⁴, Helmut Dittmann⁵, Ralph A. Bundschuh⁸, Wolfgang P. Fendler³, Milena Kurtinecz⁹, Anja Schmall¹⁰, Frank Verhohlen¹⁰, and Oliver Sartor¹¹

¹Department of Nuclear Medicine, University of Münster Medical Center, Münster, Germany; ²Department of Nuclear Medicine, University Hospital Bonn, Bonn, Germany; ³Department of Nuclear Medicine, German Cancer Consortium (DKTK) University Hospital Essen, Essen, Germany; ⁴Department of Nuclear Medicine, Technical University of Munich, Munich, Germany; ⁵Department of Nuclear Medicine and Clinical Molecular Imaging, University Hospital Tübingen, Tübingen, Germany; ⁶Department of Nuclear Medicine, University of Ulm, Ulm, Germany; ⁷International Centers for Precision Oncology Foundation, Ravensburg, Germany; ⁸Department of Nuclear Medicine, Medical Faculty, University of Augsburg, Augsburg, Germany; ⁹Bayer HealthCare Pharmaceuticals, Whippany, New Jersey; ¹⁰Bayer Consumer Care, Basel, Switzerland; and ¹¹Tulane Cancer Center, Tulane Medical School, New Orleans, Louisiana

The radium lutetium (RALU) study evaluated the feasibility of sequential α - and β -emitter use in patients with bone-predominant metastatic castration-resistant prostate cancer. **Methods:** This preplanned interim retrospective analysis investigated safety and survival outcomes with ^{177}Lu -PSMA in patients treated with prior ^{223}Ra . **Results:** Forty-nine patients were evaluated. Patients received a median of 6 ^{223}Ra injections; 59% of patients received at least 4 ^{177}Lu -PSMA cycles. Most (69%) patients received at least 4 life-prolonging therapies before ^{177}Lu -PSMA. Common Terminology Criteria for Adverse Events grade 3–4 treatment-emergent adverse events during ^{177}Lu -PSMA therapy and a 30-d follow-up period included anemia (18%) and thrombocytopenia (2%). Median overall survival was 12.6 mo (95% CI, 8.8–16.1 mo) and 31.4 mo (95% CI, 25.7–37.6 mo) from starting ^{177}Lu -PSMA or ^{223}Ra , respectively. **Conclusion:** ^{177}Lu -PSMA treatment was well tolerated in patients who had received prior ^{223}Ra . ^{223}Ra use before ^{177}Lu -PSMA is feasible and can be considered for future assessment of the optimal treatment sequence.

Key Words: targeted α -therapy; ^{223}Ra ; ^{177}Lu -PSMA; metastatic castration-resistant prostate cancer; real-world practice

J Nucl Med 2023; 64:574–578

DOI: 10.2967/jnumed.122.264456

Overall survival and quality of life in patients with bone-predominant metastatic castration-resistant prostate cancer (mCRPC)

was improved by ^{223}Ra -dichloride, a targeted α -therapy with a good safety profile (1). ^{223}Ra therapy results in low myelosuppression rates, and recent preclinical data demonstrated its transient effect on the bone marrow without long-term effects (1,2). Therefore, earlier incorporation of ^{223}Ra in the treatment sequence may facilitate optimal build-in of life-prolonging therapies to improve survival outcomes.

The VISION study investigated a β -emitter, ^{177}Lu -PSMA-617, targeting PSMA-expressing cells and found prolonged overall survival and acceptable safety in heavily pretreated patients with mCRPC (3). Another ^{177}Lu -PSMA radioligand (^{177}Lu -PSMA-I&T) was also well tolerated, with few hematologic adverse events (AEs) of grade 3 or higher (4).

^{223}Ra and ^{177}Lu -PSMA regulatory approval (in some countries) for patients with mCRPC, albeit in different patient populations, prompted us to investigate the safety and survival outcomes of sequential ^{223}Ra and ^{177}Lu -PSMA. In VISION, 17.4% of patients received ^{223}Ra therapy before ^{177}Lu -PSMA without adversely affecting efficacy, but safety has not been reported for this subgroup (5). However, retrospective studies have shown that using ^{223}Ra before ^{177}Lu -PSMA is feasible, with acceptable safety (6,7). Moreover, ^{177}Lu -PSMA-617 initiation at no more than 8 wk after ^{223}Ra in patients with progressive bone-metastatic disease was effective, with acceptable safety (8). We analyzed interim data from the observational radium lutetium (RALU) study to further evaluate safety and survival for sequential ^{223}Ra and ^{177}Lu -PSMA therapy in patients with mCRPC.

MATERIALS AND METHODS

The RALU study was a retrospective, multicenter medical chart review investigating the safety of ^{177}Lu -PSMA in patients with mCRPC previously treated with ^{223}Ra . This analysis includes patients treated in Germany. Patients were at least 18 y old with mCRPC and received at least 1 ^{223}Ra injection and subsequently at least 1 ^{177}Lu -PSMA cycle.

Received Jul. 1, 2022; revision accepted Oct. 12, 2022.
For correspondence or reprints, contact Kambiz Rahbar (kambiz.rahbar@ukmuenster.de).

Published online Oct. 27, 2022.

Immediate Open Access: Creative Commons Attribution 4.0 International License (CC BY) allows users to share and adapt with attribution, excluding materials credited to previous publications. License: <https://creativecommons.org/licenses/by/4.0/>. Details: <http://jnm.snmjournals.org/site/misc/permission.xhtml>.

COPYRIGHT © 2023 by the Society of Nuclear Medicine and Molecular Imaging.

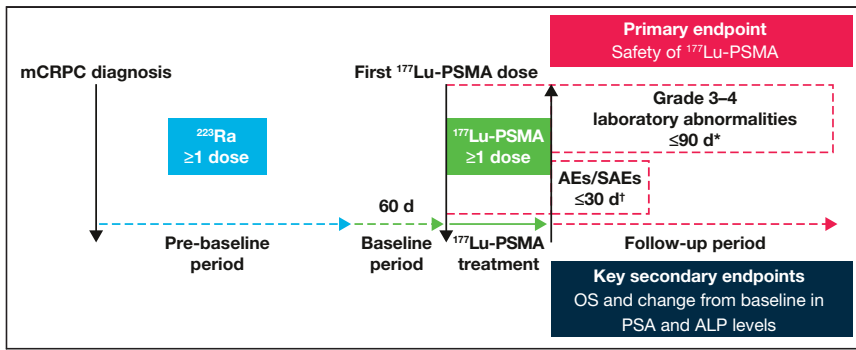


FIGURE 1. RALU study design. *From $^{177}\text{Lu-PSMA}$ start to 90 d after last dose. †From $^{177}\text{Lu-PSMA}$ start to 30 d after last dose. ALP = alkaline phosphatase; OS = overall survival; PSA = prostate-specific antigen; SAEs = serious AEs.

The retrospective observation period started at mCRPC diagnosis and ended either at the last available visit or death, whichever occurred first. Prebaseline, baseline, and follow-up period definitions are shown in Figure 1.

The primary endpoint was the safety of $^{177}\text{Lu-PSMA}$ after ^{223}Ra therapy. AEs used Common Terminology Criteria for Adverse Events grading. Secondary endpoints included OS, time to next treatment, and change from baseline in serum prostate-specific antigen and alkaline phosphatase levels. AEs and grade 3–4 laboratory abnormalities were recorded as per Figure 1.

The study was conducted in accordance with relevant guidelines and regulations (supplemental methods).

TABLE 1
Baseline Characteristics Before Starting $^{177}\text{Lu-PSMA}$

Characteristic	Data
Total patients	49 (100)
Age (y)	72 (57–83)
Eastern Cooperative Oncology Group performance status (baseline)	
0	0 (0)
1	36 (73)
2	13 (27)
3–4	0 (0)
Prostate-specific antigen (ng/mL)	287.0 (20–12,229)
Alkaline phosphatase (U/L)	142.5 (48–730)
Visceral metastatic disease	15 (31)
≥4 life-prolonging therapies*	30 (61)
Novel antiandrogen therapies	
Abiraterone	39 (80)
Enzalutamide	33 (67)
Abiraterone and enzalutamide	33 (67)
Number of any taxane-based chemotherapy lines†	
0	4 (8)
1	35 (71)
≥2	10 (20)
Docetaxel	45 (92)
Number of docetaxel cycles‡	
1–4	10 (20)
≥5	26 (53)
Cabazitaxel	9 (18)
Number of cabazitaxel cycles‡	
1–4 cycles	0 (0)
≥5 cycles	5 (10)
Taxane-based chemotherapy between ^{223}Ra and $^{177}\text{Lu-PSMA}$ §	25 (51)

*Docetaxel, cabazitaxel, abiraterone, enzalutamide, and ^{223}Ra .
†Chemotherapies with same start date \pm 15 d are counted as 1 line.
‡Not available for some patients.
§After last ^{223}Ra dose and 60 d before $^{177}\text{Lu-PSMA}$.
Qualitative data are number and percentage; continuous data are median and range.

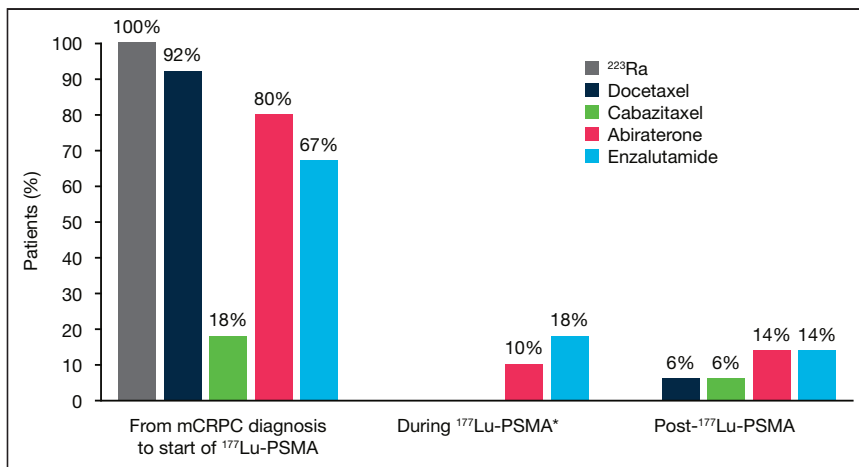


FIGURE 2. Use of life-prolonging therapies. *Chemotherapy was not used concomitantly with ¹⁷⁷Lu-PSMA.

RESULTS

This preplanned interim analysis included medical records from 49 patients (data cutoff, January 31, 2022) (Table 1). Before ¹⁷⁷Lu-PSMA initiation, 31% (15/49) of patients had visceral metastases, and median prostate-specific antigen and alkaline phosphatase values were 287.0 ng/mL and 142.5 U/L, respectively (Table 1). At least 1 line of taxane-based chemotherapy was received by 92% (45/49) of patients before ¹⁷⁷Lu-PSMA initiation, with 51% (25/49) receiving taxane-based chemotherapy between ²²³Ra and ¹⁷⁷Lu-PSMA (Table 1). Before starting ¹⁷⁷Lu-PSMA, 63% (30/49) of patients received at least 4 life-prolonging therapies (docetaxel, cabazitaxel, abiraterone, enzalutamide, and ²²³Ra; Table 1; Fig. 2). Most patients received chemotherapy before ¹⁷⁷Lu-PSMA; 92% received docetaxel, and 18% received cabazitaxel (Fig. 2).

The median time from the first ²²³Ra and ¹⁷⁷Lu-PSMA dose to the end of observation was 28.0 mo (range, 11.0–68.2 mo) and 8.9 mo (range, 1.4–63.9 mo), respectively. A median of 6 ²²³Ra injections was administered, and 71% (35/49) of patients received 5–6 ²²³Ra injections. The median ²²³Ra therapy duration was 4.7 mo (range, 1.0–7.0 mo). All patients received ¹⁷⁷Lu-PSMA (¹⁷⁷Lu-PSMA-617 [67%] or ¹⁷⁷Lu-PSMA-I&T [33%]), and 59% (29/49) received at least 4 ¹⁷⁷Lu-PSMA cycles. The median

TABLE 2

Incidence of Grade 3–4 Laboratory Abnormalities Measured from ¹⁷⁷Lu-PSMA Start to 90 Days After Last Dose

Abnormality	Patients (n)	Incidence (n)
Hemoglobin	49	17 (35%)
Platelet count	47	6 (13%)*
Neutrophils	49	1 (2%)
Aspartate aminotransferase	49	2 (4%)

*Four of 6 had low platelets at baseline, with further reductions at follow-up (1 had chemotherapy before ¹⁷⁷Lu-PSMA); 1 of 6 had normal platelets at baseline, with reductions seen after chemotherapy and at follow-up; 1 of 6 had normal platelets at baseline, with reduction at follow-up.

¹⁷⁷Lu-PSMA therapy duration was 4.9 mo (range, 0–57.1 mo). The median time from the last ²²³Ra injection to the first ¹⁷⁷Lu-PSMA dose was 9.3 mo (range, 0.9–41.9 mo). Overall, 51% (25/49) of patients received taxane-based chemotherapy during or after ²²³Ra and until 60 d before ¹⁷⁷Lu-PSMA.

During ¹⁷⁷Lu-PSMA, 92% (45/49) of patients experienced any grade of treatment-emergent AEs and 41% (20/49) experienced grade 3–4 (Supplemental Table 1). Grade 3–4 anemia and thrombocytopenia occurred in 18% (9/49) and 2% (1/49) of patients, respectively. Grade 1–2 dry mouth occurred in 27% (13/49) of patients; none had grade 3–4 dry mouth. One patient (2%) had grade 1–2 dry eye. The incidence of grade 3–4 laboratory abnormalities was highest for anemia (35% [17/49]) and thrombocytopenia (13% [6/49]) (Table 2). No grade 5 toxicities occurred.

Median overall survival was 12.6 mo (95% CI, 8.8–16.1 mo) and 31.4 mo (95% CI, 25.7–37.6 mo) from the first dose of ¹⁷⁷Lu-PSMA and ²²³Ra, respectively (Fig. 3). During ¹⁷⁷Lu-PSMA, 39% and 29% of patients had at least a 30% or 50% decline in prostate-specific antigen (best response), respectively; corresponding alkaline phosphatase declines were 6% and 4%.

DISCUSSION

Randomized trials have demonstrated low myelosuppression rates in patients with mCRPC receiving ²²³Ra or ¹⁷⁷Lu-PSMA (1,3,9). However, chemotherapy and advanced disease affecting bone marrow function can increase myelosuppression rates in this setting (10–12). Therefore, in real-world practice, radiopharmaceutical therapy after prior chemotherapy may result in more serious hematologic AEs.

¹⁷⁷Lu-PSMA after ²²³Ra treatment had an acceptable safety profile. Notably, this was despite the heavy pretreatment of the patient population, with more than 90% of patients having received chemotherapy in addition to ²²³Ra and ¹⁷⁷Lu-PSMA. Grade 3–4 anemia and thrombocytopenia incidences were 18% and 2%, respectively, consistent with the retrospective analysis of patients receiving the ²²³Ra and ¹⁷⁷Lu-PSMA sequence in the real-world REASSURE study (15% and 4%, respectively) (6). When ¹⁷⁷Lu-PSMA was given within 8 wk of ²²³Ra, the incidence of anemia of at least grade 3 was similar (18%), but the rates of leukopenia and thrombocytopenia of at least grade 3 were higher than reported here (14% vs. 0 and 21% vs. 2%, respectively) (8).

The median overall survival from the start of ¹⁷⁷Lu-PSMA or ²²³Ra therapy (12.6 and 31.4 mo, respectively) corresponded to that reported in REASSURE (13.2 and 28.0 mo, respectively) (6). In patients with mCRPC who underwent ¹⁷⁷Lu-PSMA therapy in the WARMTH study, overall survival was longer in patients with bone metastases receiving prior ²²³Ra than in those who did not (16 vs. 12 mo in patients with 6–20 bone lesions, $P = 0.038$, and 11 vs. 7 mo in patients with diffuse involvement, $P = 0.034$) (12).

This study's strength is underlined by broad inclusion criteria and high-quality data with few missing datapoints. Accordingly, we could effectively evaluate ¹⁷⁷Lu-PSMA safety in patients with a history of ²²³Ra therapy who received chemotherapy, before or after ²²³Ra treatment. Nevertheless, a retrospective study design may have contributed to a patient selection bias due to the preset

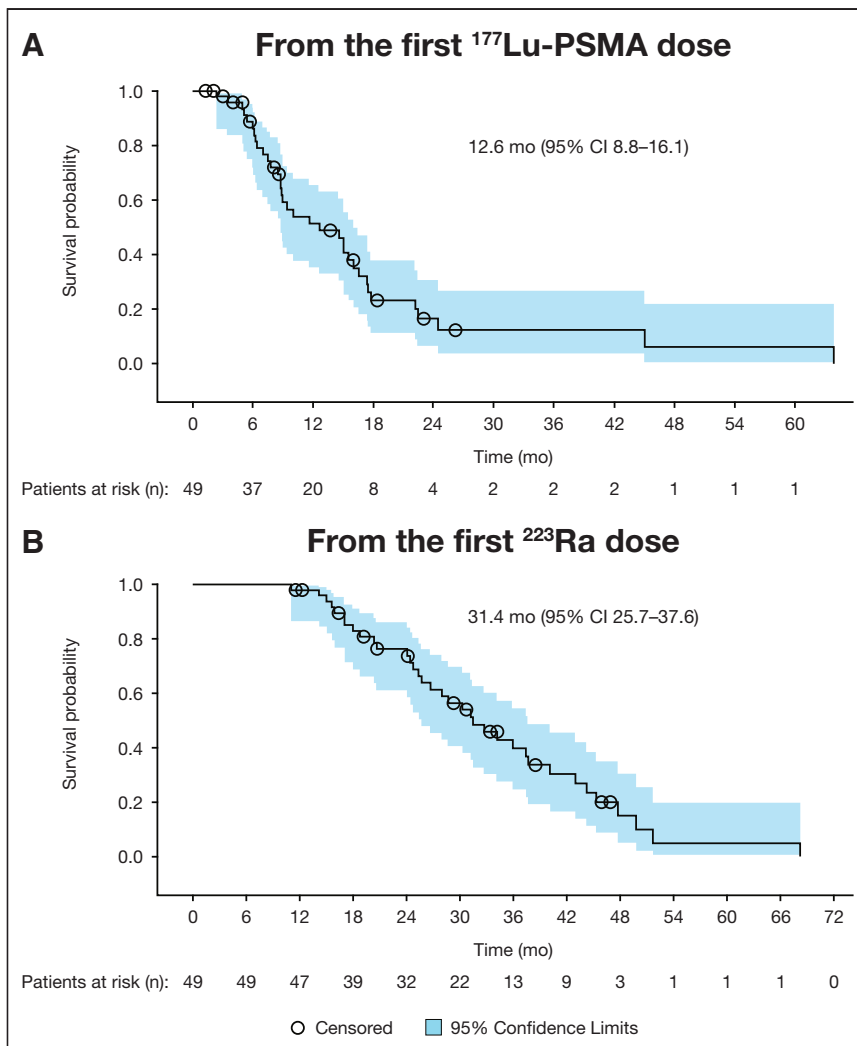


FIGURE 3. Kaplan–Meier plots for overall survival calculated from first ¹⁷⁷Lu-PSMA (A) and ²²³Ra (B) dose.

outcomes of interest. Other limitations include retrospective AE grading, lack of ascertainment of ¹⁷⁷Lu-PSMA doses and schedules, and a lack of comparison to patients who were not pretreated with ²²³Ra. Despite small patient numbers, patients were managed and treated in high-volume German nuclear medicine centers with extensive ²²³Ra and ¹⁷⁷Lu-PSMA experience.

CONCLUSION

This retrospective cohort study demonstrated that, for patients with bone-predominant mCRPC who were receiving ²²³Ra in routine care, subsequent ¹⁷⁷Lu-PSMA treatment was clinically feasible and well tolerated, with limited myelosuppression. Survival outcomes reflected those of previous reports. Therefore, in patients with bone-predominant mCRPC, ²²³Ra use before ¹⁷⁷Lu-PSMA can be considered in future assessments of the optimal sequence for life-prolonging therapies.

DISCLOSURE

Cancer Communications and Consultancy Ltd., Cheshire, U.K., provided medical writing assistance (funded by Bayer). Dr. Lila

Adnane (Bayer) provided editorial assistance. Kambiz Rahbar receives honoraria from Advanced Accelerator Applications (AAA) and Bayer and has a consultancy/advisory role with ABX GmbH, ABX-CRO, Bayer, and AAA. Markus Essler has a consultancy/advisory role with Bayer, AAA, and Ipsen and receives travel funds from Ipsen. Matthias Eiber owns stocks or has other ownership interests in Novartis and Telix Pharmaceuticals; has a consultancy/advisory role with Blue Earth Diagnostics, ABX Advanced Biochemical Compounds, Janssen Oncology, Telix Pharmaceuticals, and Novartis; receives research funding from Siemens, ABX Advanced Biochemical Compounds, Blue Earth Diagnostics, and Bayer; has a patent application for rhPSMA; and receives travel funds from Bayer Schering Pharma. Christian la Fougère has a consultancy/advisory role with Novartis, EUSA-Pharma, Ipsen, Oncodesign, and Sirtex Medical and receives research funding from Oncovision. Vikas Prasad receives honoraria from AAA; has a consultancy/advisory role with Bayer; and receives research funding from Ipsen. Wolfgang Fendler receives honoraria from Parexel and AAA; has a consultancy/advisory role with Janssen, Calyx, and Bayer; and receives research funding from SOFIE. Philipp Rassek is an employee of Porterhouse Group AG Paracelsus Kliniken. Helmut Dittmann has a consultancy/advisory role with Bayer, Ipsen, and Eisai AG. Ralph Bundschuh receives honoraria from Eisai AG and has a consultancy/advisory role with Bayer. Kim Pabst receives a Junior Clinician Scientist Stipend from the University Medicine Essen Clinician Scientist Academy (sponsor:

Faculty of Medicine and Deutsche Forschungsgemeinschaft) and research funding from Bayer. Milena Kurtinecz, and Frank Verholen are employees of Bayer. Oliver Sartor has a consultancy/advisory role with Bayer, Sanofi, AstraZeneca, Dendreon, Constellation Pharmaceuticals, AAA, Pfizer, Bristol-Myers Squibb, Bavarian Nordic, EMD Serono, Astellas Pharma, Progenics, Blue Earth Diagnostics, Myovant Sciences, Myriad Genetics, Novartis, Clarity Pharmaceuticals, Fusion Pharmaceuticals, Isotopen Technologien, Janssen, Noxopharm, Clovis Oncology, Noria Therapeutics, Point Biopharma, TeneoBio, Telix Pharmaceuticals, and Theragnostics; receives travel funds from Bayer, Johnson & Johnson, Sanofi, AstraZeneca, and Progenics; provides expert testimony for Sanofi; owns stocks or has other ownership interests in Lilly, GlaxoSmithKline, Abbvie, Cardinal Health, United Health Group, PSMA Therapeutics, Clarity Pharmaceuticals, Noria Therapeutics, and Clovis Oncology; and receives research funding from Bayer, Sanofi, Endocyte, Merck, InVitae, Constellation Pharmaceuticals, AAA, AstraZeneca, Dendreon, SOTIO, Janssen, and Progenics. No other potential conflict of interest relevant to this article was reported.

KEY POINTS

QUESTION: Is it safe to use ^{177}Lu -PSMA to treat patients with mCRPC if they have previously received ^{223}Ra ?

PERTINENT FINDINGS: Low rates of overall and hematologic AEs indicated an acceptable safety profile for this treatment sequence. Median OS was 12.6 and 31.4 mo from the first dose of ^{177}Lu -PSMA and ^{223}Ra , respectively, and 39% of patients had at least a 30% decline in prostate-specific antigen.

IMPLICATIONS FOR PATIENT CARE: Introduction of ^{223}Ra early in the treatment sequence in patients with bone-predominant mCRPC and subsequent treatment with ^{177}Lu -PSMA is feasible, well tolerated, and effective.

REFERENCES

1. Parker C, Nilsson S, Heinrich D, et al. Alpha emitter radium-223 and survival in metastatic prostate cancer. *N Engl J Med*. 2013;369:213–223.
2. Parker CC, Coleman RE, Sartor O, et al. Three-year safety of radium-223 dichloride in patients with castration-resistant prostate cancer and symptomatic bone metastases from phase 3 randomized alphasradin in symptomatic prostate cancer trial. *Eur Urol*. 2018;73:427–435.
3. Sartor O, de Bono J, Chi KN, et al. Lutetium-177-PSMA-617 for metastatic castration-resistant prostate cancer. *N Engl J Med*. 2021;385:1091–1103.
4. Heck MM, Tauber R, Schwaiger S, et al. Treatment outcome, toxicity, and predictive factors for radioligand therapy with ^{177}Lu -PSMA-I&T in metastatic castration-resistant prostate cancer. *Eur Urol*. 2019;75:920–926.
5. Vaishampayan N, Morris MJ, Krause BJ, et al. [^{177}Lu]Lu-PSMA-617 in PSMA-positive metastatic castration-resistant prostate cancer: prior and concomitant treatment subgroup analyses of the VISION trial. *J Clin Oncol*. 2022;40(16_Suppl):5001.
6. Sartor O, la Fougere C, Essler M, et al. Lutetium-177-prostate-specific membrane antigen ligand after radium-223 treatment in men with bone-metastatic castration-resistant prostate cancer: real-world clinical experience. *J Nucl Med*. 2021;63:410–414.
7. Ahmadzadehfar H, Zimbelmann S, Yordanova A, et al. Radioligand therapy of metastatic prostate cancer using ^{177}Lu -PSMA-617 after radiation exposure to ^{223}Ra -dichloride. *Oncotarget*. 2017;8:55567–55574.
8. Baumgarten J, Groener D, Nguyen Ngoc C, et al. Safety and efficacy of ^{177}Lu -PSMA-617 radioligand therapy shortly after failing ^{223}Ra -dichloride. *Cancers (Basel)*. 2022;14:557.
9. Hofman MS, Emmett L, Sandhu S, et al. [^{177}Lu]Lu-PSMA-617 versus cabazitaxel in patients with metastatic castration-resistant prostate cancer (TheraP): a randomised, open-label, phase 2 trial. *Lancet*. 2021;397:797–804.
10. Tannock IF, de Wit R, Berry WR, et al. Docetaxel plus prednisone or mitoxantrone plus prednisone for advanced prostate cancer. *N Engl J Med*. 2004;351:1502–1512.
11. de Bono JS, Oudard S, Ozguroglu M, et al. Prednisone plus cabazitaxel or mitoxantrone for metastatic castration-resistant prostate cancer progressing after docetaxel treatment: a randomised open-label trial. *Lancet*. 2010;376:1147–1154.
12. Ahmadzadehfar H, Matern R, Baum RP, et al. The impact of the extent of the bone involvement on overall survival and toxicity in mCRPC patients receiving [^{177}Lu]Lu-PSMA-617: a WARMTH multicentre study. *Eur J Nucl Med Mol Imaging*. 2021;48:4067–4076.

Phase III Study of ¹⁸F-PSMA-1007 Versus ¹⁸F-Fluorocholine PET/CT for Localization of Prostate Cancer Biochemical Recurrence: A Prospective, Randomized, Crossover Multicenter Study

Pierre Olivier¹, Anne-Laure Giraudet², Andrea Skanjeti^{3,4}, Charles Merlin⁵, Pierre Weinmann⁶, Ines Rudolph⁷, Alexander Hoepping⁷, and Mathieu Gauthé⁸

¹Nuclear Medicine and Nancyclotep Molecular Imaging Platform, CHRU-Nancy, Université de Lorraine, Nancy, France;

²Nuclear Medicine, LUMEN, Centre Leon Berard, Lyon, France; ³Nuclear Medicine, HCL, Claude Bernard University-Lyon-1, Lyon, France; ⁴Nuclear Medicine, Centre Hospitalier Sud Francilien, Corbeil Essonne, France; ⁵Department of Nuclear Medicine, Centre Jean Perrin, Clermont-Ferrand, France; ⁶HEGP-AP-HP, Nuclear Medicine, Université de Paris, Paris, France; ⁷ABX Advanced Biochemical Compounds, Radeberg, Germany; and ⁸Hôpital Tenon-AP-HP, Sorbonne Université, Paris, France

The objective of this study was to compare ¹⁸F-PSMA-1007 PET/CT and ¹⁸F-fluorocholine PET/CT for the localization of prostate cancer (PCa) biochemical recurrence. **Methods:** This prospective, open-label, randomized, crossover multicenter study included PCa patients with prior definitive therapy and suspected PCa recurrence. All men underwent both ¹⁸F-PSMA-1007 PET/CT and ¹⁸F-fluorocholine PET/CT (102 received ¹⁸F-PSMA-1007 PET/CT first and 88 received ¹⁸F-fluorocholine PET/CT first). All images were assessed independently by 3 readers masked to all clinical information using a 3-point qualitative scale (0 = no recurrence, 1 = undetermined, and 2 = recurrence). Patients were monitored for approximately 6 mo. An independent panel with a urologist, radiologist, and nuclear physician reviewed all clinical data, including imaging and response to therapy, but were masked regarding PET/CT information; acting in consensus, they determined a patient-based and region-based composite standard of truth for PCa lesions. The “correct detection rates” for PCa lesions on a patient basis for each radiopharmaceutical were compared for the 3 readers individually and for the “average reader.” Secondary objectives included determining whether PET/CT findings affected diagnostic thinking (impact of a test result on posttest vs. pretest probability of a correct diagnosis), therapeutic decision making (description and quantification of impact of diagnostic information gained with both radiopharmaceuticals on patient management), and adequacy of management changes. **Results:** A total of 190 patients were included. The primary endpoint was met. The overall correct detection rates were 0.82 for ¹⁸F-PSMA-1007 and 0.65 for ¹⁸F-fluorocholine ($P < 0.0001$) when undetermined findings were considered positive for malignancy and 0.77 and 0.57, respectively ($P < 0.0001$), when undetermined findings were considered negative for malignancy. A change in diagnostic thinking due to PET/CT was reported in 149 patients; ¹⁸F-PSMA-1007 contributed more than ¹⁸F-fluorocholine in 93 of these patients. In 122 patients, PET/CT led to an adequate diagnosis that benefited the patient; ¹⁸F-PSMA-1007 contributed

more than ¹⁸F-fluorocholine in 88 of these patients. **Conclusion:** ¹⁸F-PSMA-1007 PET/CT is superior to ¹⁸F-fluorocholine PET/CT for the localization of PCa recurrence. Decision making was more beneficial when based on ¹⁸F-PSMA-1007 PET/CT results.

Key Words: PET/CT; prostatic neoplasms; prostate-specific antigen; decision making

J Nucl Med 2023; 64:579–585

DOI: 10.2967/jnumed.122.264743

Prostate cancer (PCa) is the most prevalent cancer in men, with approximately 473,000 new diagnoses and more than 108,000 deaths in Europe in 2020 (1). Although long-term outcomes are good for most men, recurrence after definitive therapy is common. One study found that 37% of patients with radical prostatectomy and 48% of patients with radiation therapy had biochemical recurrence within 15 y of the initial definitive treatment; for both, most relapses occurred within the first 5 y (2). The diagnosis of PCa recurrence after prior definitive therapy is based on an increase in serum prostate-specific antigen (PSA); the threshold level varies by treatment, being higher for patients treated with radiation than for those treated by radical prostatectomy (3). PET/CT imaging is the recommended modality for the localization of PCa recurrence (3). ¹⁸F-fluorocholine has been recommended for PET/CT imaging of PCa recurrence since a marketing authorization was granted in France in 2010. The development of radiopharmaceuticals that directly target the extracellular domain of the prostate-specific membrane antigen (PSMA) resulted in an improvement in the detection of PCa lesions, and this approach is now recommended for PET/CT imaging of PCa recurrence.

A recent metaanalysis evaluated the diagnostic efficacy of all PSMA-directed PET agents and reported an overall detection rate of 74.1% with no notable differences among the various tracers (4). The authors concluded that PSMA-directed PET agents were preferable to choline PET, particularly in patients with a serum PSA level of less than 1 ng/mL (4). However, to date, only single-center studies with a limited number of patients have compared ¹⁸F-fluorocholine with a radiolabeled PSMA ligand for PET/CT

Received Jul. 30, 2022; revision accepted Oct. 27, 2022.

For correspondence or reprints, contact Mathieu Gauthé (mathieugauthé@yahoo.fr).

Published online Nov. 23, 2022.

Immediate Open Access: Creative Commons Attribution 4.0 International License (CC BY) allows users to share and adapt with attribution, excluding materials credited to previous publications. License: <https://creativecommons.org/licenses/by/4.0/>. Details: <http://jnm.snmjournals.org/site/misc/permission.xhtml>.

COPYRIGHT © 2023 by the Society of Nuclear Medicine and Molecular Imaging.

imaging of PCa recurrence localization, and large randomized controlled trials are lacking (5).

¹⁸F-PSMA-1007 was developed by Cardinale et al. (6) and Giesel et al. (7) in Heidelberg in 2016 as a PSMA-targeting ligand with low urinary excretion. The compound showed a high detection rate at low PSA values and high sensitivity and specificity in both biochemical recurrence and primary staging (8,9). In some patients, nonspecific bone uptake may be a confounding factor (10).

The ABX-CT-301 study (NCT04102553) aimed to compare ¹⁸F-PSMA-1007 PET/CT and ¹⁸F-fluorocholine PET/CT for the detection of PCa lesions in patients with biochemical recurrence. Secondary objectives were to compare the detection rates of the clinical investigators for both radiopharmaceuticals in a patient-based analysis; to assess the diagnostic performance of both radiotracers for PCa lesions in a region-based analysis; to assess the impact on diagnostic thinking, therapeutic decision making, and adequacy of therapy changes for both radiotracers; and to assess the safety profile of ¹⁸F-PSMA-1007.

MATERIALS AND METHODS

Population

This study was a prospective, open-label, randomized, 2-armed crossover study conducted in 6 study centers in France. Men who were at least 18 y old, who were diagnosed with PCa, and who had prior definitive therapy were considered for enrollment. Eligible patients presented with suspected PCa recurrence, defined as 3 consecutive PSA increases or a PSA rise of greater than or equal to 2.0 ng/mL above the nadir after radiotherapy (external-beam radiation therapy or brachytherapy) or cryotherapy or a PSA rise of greater than or equal to 0.2 ng/mL after prostatectomy. The main exclusion criteria were participation in another therapeutic clinical trial within 5 d of enrollment in the present study and a life expectancy of less than 6 mo.

The study protocol was approved by a national ethics committee certified by the French Ministry of Health (Institutional Review Board: IORG0009855). All patients gave written informed consent before randomization.

Intervention

All men underwent both ¹⁸F-PSMA-1007 PET/CT and ¹⁸F-fluorocholine PET/CT using a standardized imaging protocol (supplemental materials, available at <http://jnm.snmjournals.org>). Patients were randomized using a computer-generated block-randomized sequence, stratified by center, to receive either ¹⁸F-PSMA-1007 PET/CT or ¹⁸F-fluorocholine PET/CT first. Patients underwent both PET/CT examinations within a minimum of 24 h and a maximum of 240 h; depending on the individual site preferences, either low-dose or diagnostic CT could be used, but the use of contrast agents was not permitted. At each PET/CT visit, vital signs were recorded before and after injection of the study drug and again at the end of the PET/CT examination. Samples for laboratory tests, including serum PSA levels, were obtained before the administration of each study drug. Patients were monitored for adverse events for 24 h after the second PET/CT examination (supplemental materials). Then we collected all data related to the treatments, additional diagnostic methods (including biopsy confirmation of detected foci, if feasible) and PSA values obtained in the 6 months during which the patients were followed.

Image Reading and Standard of Truth

PET images were read on-site on the day of acquisition by investigators who were not masked regarding clinical data and were transferred to a core imaging laboratory where they were evaluated by 3 independent masked readers (supplemental materials). ¹⁸F-PSMA-1007 and ¹⁸F-fluorocholine images were read on separate days, at least 1 wk apart.

The results of an “average reader” were determined statistically from the 3 independent reader results and not by a consensus read.

The composite standard of truth (recurrence, no recurrence, or undetermined) at the time of imaging was determined by an independent expert panel that considered all available clinical patient data from before inclusion to the end of the follow-up period, excluding all information from PET/CT (supplemental materials). The expert panel consisted of a urologist, a radiologist, and a nuclear physician; they reached their conclusions by consensus.

Outcomes

The primary objective was to compare ¹⁸F-PSMA-1007 with ¹⁸F-fluorocholine with regard to the “correct detection rate” for recurrent PCa lesions on a patient basis, as determined by 3 independent readers and confirmed by an independent expert panel on the basis of a composite standard of truth (supplemental materials).

Secondary objectives were to compare the correct detection rates of the clinical investigators; to assess the correct detection rates of both radiotracers for PCa lesions in a region-based analysis; to report the impact on diagnostic thinking (impact of PET/CT result on posttest vs. pretest probability of a correct diagnosis), therapeutic decision making (impact on the comprehensive process by which physicians make decisions about the PCa response), and adequacy of management changes by the Investigators at 3 time points (before PET, immediately after both PET studies, and at the end of follow-up) and by the expert panel (only at the end of follow-up), using 3 dedicated forms (supplemental materials); to compare the masked intra- and interreader agreements; and to assess the safety profile of ¹⁸F-PSMA-1007.

Statistical Analysis

Analysis was performed using SAS 9.4 or higher (SAS Institute), detailed in the supplemental materials. A *P* value of less than or equal to 0.05 was considered statistically significant. Descriptive statistics were calculated for quantitative variables; frequency counts by category were given for qualitative variables. Ninety-five percent CIs or interquartile ranges were given when appropriate. The intention-to-treat (ITT) population was the primary population for the analyses of efficacy endpoints and all baseline characteristics. The correct detection rate was determined for each reader individually. Generalized estimation equations were used to account for the correlations between readers' assessments and to summarize the overall reader results (average reader). Patients for whom the expert panel could assess the true disease state on a patient level but for whom the affected region could not be identified by the expert panel were included as correct assessments on a patient basis. If, on a region basis, there was no region with a correct detection of recurrence compared with the standard of truth, then the patient was regarded as having a false-negative result. If at least in 1 region the reader and the expert panel detected a recurrence, independent of the other regions, then this result was classified as a true-positive result. Subgroup analyses were performed on the basis of the PSA level at baseline: less than 0.5 ng/mL, 0.5 ng/mL to less than 1.0 ng/mL, greater than or equal to 1.0 ng/mL to less than 2.0 ng/mL, and greater than or equal to 2.0 ng/mL. For the primary analysis on a patient level, 2 distinct analyses were performed by considering undetermined results as positive or negative for PCa recurrence. For subgroup and secondary analyses, undetermined results were considered negative for PCa recurrence. Intra- and interreader agreements were evaluated using pairwise and multiple Cohen κ -statistics. Each masked reader read 10% of the images twice (on separate occasions). Interreader agreement was assessed pairwise and across all 3 readers. The degree of agreement was defined as described by Landis and Koch (11). The sample size was selected to provide a power of at least 80% to detect a 10% difference in correct detection rates between the 2 products.

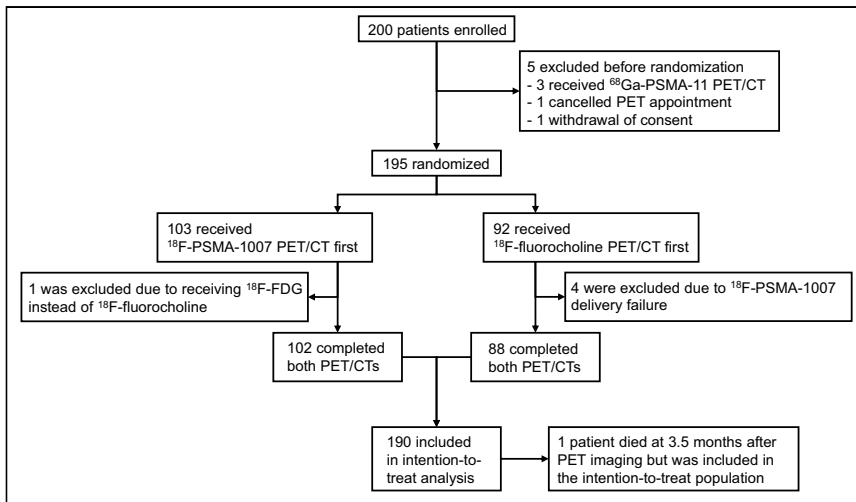


FIGURE 1. Trial chart.

RESULTS

Population

From March 5, 2019, to October 8, 2020, 200 patients consented to this study; 195 were randomized, and 189 completed all follow-up assessments (Fig. 1). One patient ended study participation prematurely because he died 3.5 mo after PET imaging but

was included in the ITT population. Most of the patients had previously undergone prostatectomy, and the median serum PSA level was 1.7 ng/mL. Study population characteristics are summarized in Table 1.

The median follow-up period for the ITT population was 8.3 mo (range, 2.9–16.1 mo), as its duration was extended because of the COVID-19 pandemic.

Primary Objective

Per-patient and per-region PET findings are detailed in the supplemental materials. At the patient level, the masked readers found evidence for PCa recurrence in 145–162 patients (76.3%–85.3%) with ¹⁸F-PSMA-1007 and 99–128 patients (52.1%–67.4%) with ¹⁸F-fluorocholine. Findings remained undetermined in 6–12 patients (3.2%–6.3%) with ¹⁸F-PSMA-1007 and 10–21 patients

(5.3%–11.1%) with ¹⁸F-fluorocholine (supplemental materials). The expert panel confirmed PCa recurrence according to the standard of truth in 179 of 190 cases (94%).

The overall proportion of patients with correct detection rates for PCa lesions with ¹⁸F-PSMA-1007 was 0.82 (95% CI, 0.78–0.86) or 0.77 (95% CI, 0.72–0.82) when undetermined results were

TABLE 1
Patient Characteristics (Intention-to-Treat Population)

Characteristic	All patients (n = 190)	¹⁸ F-PSMA-1007 first (n = 102)	¹⁸ F-fluorocholine first (n = 88)
Median age (y)*	69 (49–84)	68 (49–81)	70 (51–84)
Initial ISUP group grade at PCa diagnosis [†]			
1	29 (15.3)	12 (11.8)	17 (19.3)
2	64 (33.7)	32 (31.4)	32 (36.4)
3	55 (29.0)	33 (32.4)	22 (25)
4	14 (7.4)	8 (7.8)	6 (6.8)
5	21 (11.1)	13 (12.8)	8 (9.1)
Unknown	7 (3.7)	4 (3.9)	3 (3.4)
Prior prostatectomy [†]	154 (81)	80 (78)	74 (84)
With pelvic lymph node dissection (no. of patients)	93	51	42
Serum PSA levels, in ng/mL, before first PET examination [‡]			
Overall	1.7 (0.6–4.2)	2.0 (0.9–5.5)	1.3 (0.6–3.1)
In patients with prior prostatectomy	1.3 (0.5–3.2)	1.7 (0.6–3.5)	0.9 (0.4–2.5)
In patients without prior prostatectomy	4.5 (2.3–9.9)	6.3 (2.8–10.9)	3.0 (2.1–9.0)
Serum PSA doubling time, in mo, before first PET examination [‡]			
PSA doubling time ≤ 6 mo (% of patients)	49	47	51
PSA doubling time ≤ 12 mo (% of patients)	74	76	70

*Values in parentheses are ranges.

[†]Reported as numbers of patients, with percentages in parentheses.

[‡]Reported as medians, with interquartile ranges in parentheses.

ISUP = International Society of Urological Pathology.

TABLE 2

Patient-Level Overall Proportion of Patients With Correct Rate of Detection of Recurrent PCa According to Standard of Truth and Positive Predictive Value (ITT Population) (*n* = 190)

Parameter	¹⁸ F-PSMA-1007*	¹⁸ F-fluorocholine*	<i>P</i>
Undetermined lesions considered positive for PCa recurrence in analysis			
Proportion	0.82 (0.78–0.86)	0.65 (0.60–0.71)	
Difference in proportion	0.16 (0.11–0.22)		<0.0001
Odds ratio	2.40 (1.79–3.21)		<0.0001
Positive predictive value	0.96 (0.93–0.99)	0.96 (0.93–0.99)	
Difference in positive predictive value	0.002 (0.031–0.035)		0.90
Odds ratio	0.95 (0.42–2.15)		0.90
Undetermined lesions considered negative for PCa recurrence in analysis			
Proportion	0.77 (0.72–0.82)	0.57 (0.51–0.62)	
Difference in proportion	0.21 (0.15–0.26)		<0.0001
Odds ratio	2.61 (1.97–3.46)		<0.0001
Positive predictive value	0.95 (0.92–0.99)	0.97 (0.95–1.00)	
Difference in positive predictive value	0.02 (0.01–0.05)		0.25
Odds ratio	0.58 (0.22–1.55)		0.27

*Values in parentheses are 95% CIs.

considered positive or negative for malignancy, respectively; these values were statistically superior to the value 0.65 (95% CI, 0.60–0.71) or 0.57 (95% CI, 0.51–0.62) obtained with ¹⁸F-fluorocholine when undetermined results were considered positive or

negative for PCa, respectively (*P* < 0.0001) (Table 2). Thus, the primary endpoint was reached.

For both study drugs, the correct detection rate for PCa recurrence was higher for patients with higher PSA levels. For all

TABLE 3

Patient-Level Proportion of Patients With Correct Rate of Detection of PCa Lesions by PSA Level at Baseline (ITT Population) (*n* = 190)

Parameter	¹⁸ F-PSMA-1007*	¹⁸ F-fluorocholine*	<i>P</i>
PSA < 0.5 ng/mL			
No. of patients with recurrence detected by SOT = 43			
Proportion	0.57 (0.45–0.68)	0.39 (0.28–0.50)	
Odds ratio	2.10 (1.13–3.89)		0.002
0.5 ng/mL ≤ PSA < 1.0 ng/mL			
No. of patients with recurrence detected by SOT = 25			
Proportion	0.83 (0.72–0.93)	0.43 (0.28–0.58)	
Odds ratio	6.88 (3.35–14.13)		<0.0001
1.0 ng/mL ≤ PSA < 2.0 ng/mL			
No. of patients with recurrence detected by SOT = 33			
Proportion	0.81 (0.72–0.89)	0.50 (0.37–0.62)	
Odds ratio	4.31 (2.26–8.24)		<0.0001
PSA ≥ 2.0 ng/mL			
No. of patients with recurrence detected by SOT = 78			
Proportion	0.85 (0.79–0.91)	0.74 (0.66–0.82)	
Odds ratio	2.01 (1.27–3.19)		0.003

*Values in parentheses are 95% CIs.
SOT = standard of truth.

TABLE 4
Change in Diagnostic Thinking After Both PET/CT Scans (ITT Population) (*n* = 190)*

Change in diagnostic thinking	¹⁸ F-fluorocholine examination contributed more	¹⁸ F-PSMA-1007 examination contributed more	Both PET examinations contributed equally	Missing
Yes				
PET identified site of recurrence that was not known before	3 (1.6)	80 (42.1)	29 (15.3)	3 (1.6)
PET confirmed site of recurrence that was suspected before	1 (0.5)	6 (3.2)	3 (1.6)	
Other		4 (2.1)	15 (7.9)	
Missing		3 (1.6)	2 (1.1)	
No				
Missing		38 (20)		3 (1.6)

*Data are reported as numbers of patients, with percentages in parentheses.

examined PSA-level subgroups, the correct detection rate was statistically higher for ¹⁸F-PSMA-1007 (Table 3).

Masked intra- and interreader agreements for the detection of metastases (patient level) ranged from 0.24 to 0.73 and from 0.30 to 0.36 for ¹⁸F-PSMA-1007 and from 0.48 to 0.72 and 0.34 to 0.40 for ¹⁸F-fluorocholine, respectively (supplemental materials).

Secondary Objectives

Comparison of Patient-Based Correct Detection Rates According to Investigator Findings. On the basis of the clinical investigators' overall findings, the correct detection rates were 0.80 (95% CI, 0.74–0.86) for ¹⁸F-PSMA-1007 and 0.50 (95% CI, 0.42–0.57) for ¹⁸F-fluorocholine (*P* < 0.0001).

TABLE 5
Change in Diagnostic Thinking After Both PET Scans and Influence at End of Follow-up (ITT Population) (*n* = 190)*

Category	Influence was:			Missing
	To benefit of patient	Not to benefit of patient	Neither to benefit nor disadvantage of patient	
¹⁸F-fluorocholine examination contributed more				
More accurate diagnosis	6 (3.2)	0	0	0
Diagnostic thinking was misled by PET	0	0	0	0
PET had no influence	0	1 (0.5)	1 (0.5)	0
Missing	0	0	0	0
¹⁸F-PSMA-1007 examination contributed more				
More accurate diagnosis	88 (46.3)	2 (1.1)	10 (5.3)	2 (1.1)
Diagnostic thinking was misled by PET	1 (0.5)	1 (0.5)	2 (1.1)	0
PET had no influence	0	0	1 (0.5)	0
Missing	0	0	0	0
Both PET examinations contributed equally				
More accurate diagnosis	27 (14.2)	0	13 (6.8)	0
Diagnostic thinking was misled by PET	0	5 (2.6)	1 (0.5)	0
PET had no influence	5 (2.6)	2 (1.1)	16 (8.4)	0
Missing	0	0	1 (0.5)	0
Missing				
More accurate diagnosis	1 (0.5)	0	0	0
Diagnostic thinking was misled by PET	0	0	0	0
PET had no influence	0	0	0	0
Missing	0	0	0	4 (2.1)

*Data are reported as numbers of patients, with percentages in parentheses.

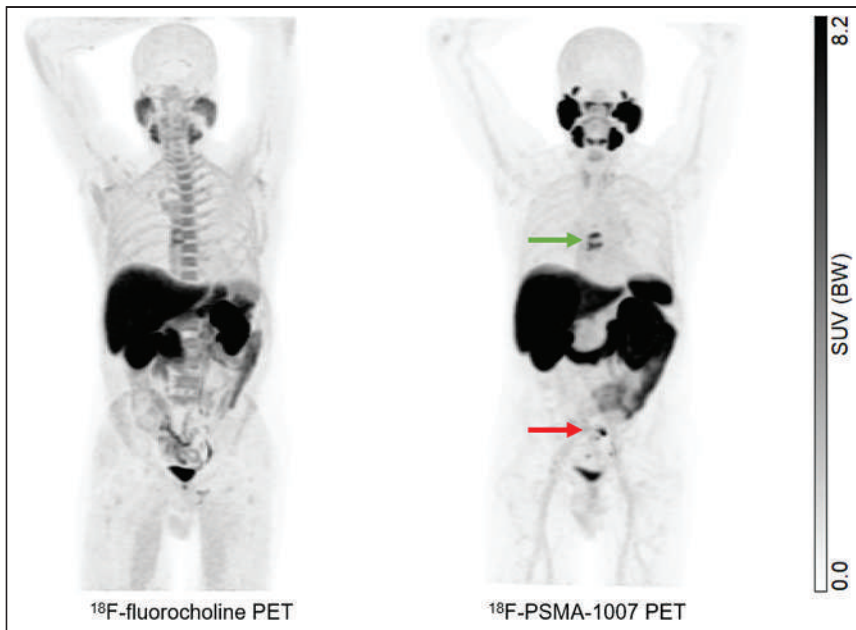


FIGURE 2. 62-y-old patient with history of PCa (International Society of Urological Pathology grade 3; PSA level of 5.7 ng/mL), initially treated with prostatectomy (pT3N0R0), prostate bed radiation therapy, and 6 mo of androgen deprivation therapy (ADT), presenting with PSA recurrence (0.72 ng/mL). ^{18}F -PSMA-1007 PET/CT detected pelvic lymph nodes (red arrow) and bone metastases (green arrow) that were not detected by ^{18}F -fluorocholine PET/CT. Therapeutic management changed from targeted radiation therapy before PET to ADT after PET, leading to drop in PSA level to 0.1 ng/mL at 6 mo. BW = body weight.

Comparison of Region-Based Correct Detection Rates According to Masked Readers' Findings. In the 72 patients for whom 1 or more regions could be assessed by the expert panel, there were 78 regions with confirmed PCa lesions. The most common sites for PCa lesions were the pelvis (59 patients) and the spine (6 patients) (supplemental materials). In the patients considered to have a positive PET result, more suggestive lesions were detected with ^{18}F -PSMA-1007 than with ^{18}F -fluorocholine, especially in patients with 3 or more lesions.

Overall composite region-level sensitivities were 0.77 (95% CI, 0.69–0.84) for ^{18}F -PSMA-1007 PET and 0.57 (95% CI, 0.48–0.67) for ^{18}F -fluorocholine PET ($P < 0.0001$).

Impact on Diagnostic Thinking, Therapeutic Decision Making, and Adequacy of Therapy Changes. The investigator assessments of the changes in diagnostic thinking after both PET/CT examinations and at the end of follow-up are summarized in Tables 4 and 5 and the supplemental materials. Treatment plans before and after PET/CT examinations were available in 187 patients. Treatment plans were changed in 100 patients; 89 of the changes were major (supplemental materials). Changes in diagnostic thinking due to PET/CT were reported in 149 patients. Diagnostic thinking was unchanged in 41 patients (including 3 with no reported answer in the questionnaire). In the 149 patients for whom there were changes in diagnostic thinking, ^{18}F -PSMA-1007 contributed more in 93 patients (62%), both tracers contributed equally in 49 patients (33%), and ^{18}F -fluorocholine contributed more in 4 patients (3%).

In 122 patients, PET/CT led to a more accurate diagnosis that benefited them. In 11 patients, PET/CT was not to the benefit of the patient, and in 45 patients, PET/CT did not exert a positive or negative influence. In the 122 patients with a more accurate diagnosis after PET/CT that benefited them, ^{18}F -PSMA-1007 contributed

more in 88 patients, ^{18}F -fluorocholine contributed more in only 6 patients, and both contributed equally in 27 patients.

Safety Profile of ^{18}F -PSMA-1007. There were no serious adverse events. No patient discontinued study participation because of an adverse event. Four patients had 4 events (toothache, diarrhea, chest discomfort, and arterial hypertension) after the administration of ^{18}F -PSMA-1007, and 1 patient had 1 event (shoulder pain) after the administration of ^{18}F -fluorocholine. None of the adverse events was considered to be attributable to the study drug.

DISCUSSION

To our knowledge, the present study is the first multicenter, crossover randomized study to compare ^{18}F -PSMA-1007 and ^{18}F -fluorocholine for the localization of biochemical recurrence of PCa. The correct detection rate was significantly higher with ^{18}F -PSMA-1007 PET/CT than with ^{18}F -fluorocholine PET/CT. Results were similar for the population as a whole and for the 72 patients for whom individual lesions could be verified, either by biopsy or response to local treatment. The difference was especially pronounced in patients with lower

serum PSA levels, allowing earlier, targeted salvage treatment. Our results for ^{18}F -PSMA-1007 are in agreement with those reported in the literature for ^{68}Ga -PSMA-11 (4,12–18). In a metaanalysis, Treglia et al. (19) also found similar results when comparing a PSMA tracer (^{68}Ga -PSMA-11 or ^{64}Cu -PSMA-617) and radiocholine. Because the results obtained with the various PSMA ligands are generally similar, it is generally accepted that the PSMA ligands are interchangeable for this indication. PSMA ligands radiolabeled with ^{18}F have wider accessibility than those radiolabeled with ^{68}Ga .

The investigator assessments after PET/CT and at the end of follow-up demonstrated the superiority of ^{18}F -PSMA-1007 over ^{18}F -fluorocholine in identifying sites of recurrence. The impact of ^{18}F -PSMA-1007 was to benefit the patient in most cases. These results are likely linked to the higher correct detection rate for ^{18}F -PSMA-1007. In previous studies with ^{18}F -fluorocholine (13,20) and ^{68}Ga -PSMA-11 (5,21), rates of impact on patient management of 39%–58% were reported. Our study is consistent with published data on ^{18}F -fluorocholine and demonstrates a higher impact of ^{18}F -PSMA-1007 on patient management.

The strengths of our study are its prospective, multicenter, randomized crossover design. Limitations include the lack of histopathology for most lesions. Because obtaining histopathology is often ethically questionable or medically impractical, our standard of truth was a composite based on biopsy, response to local therapy, imaging, and changes in serum PSA levels during 6 mo of follow-up, as established by an independent panel of experts. The use of the independent panel removed potential bias in determining “truth” while modeling what is done in “real-life” practice.

In this work, we found that ^{18}F -PSMA-1007 had an impact on diagnostic thinking and therapeutic decision making and that therapy changes were more beneficial when based on ^{18}F -PSMA-1007

PET/CT findings than when based on ^{18}F -fluorocholine PET/CT findings (Fig. 2). However, we did not make a statistical comparison of these data because the study was not powered for this purpose.

CONCLUSION

This prospective, multicenter, open-label, crossover randomized study demonstrated that ^{18}F -PSMA-1007 PET/CT localizes PCa recurrence in significantly more patients than ^{18}F -fluorocholine PET/CT, especially in patients with low PSA serum levels. ^{18}F -PSMA-1007 PET/CT also had a higher impact on diagnostic thinking, therapeutic decision making, and therapy changes than ^{18}F -fluorocholine PET/CT.

DISCLOSURE

This study was funded and supported by ABX Advanced Biochemical Compounds, Radeberg, Germany. Ines Rudolph and Alexander Hoepfing work for ABX Advanced Biochemical Compounds. Charles Merlin has received personal fees and nonfinancial support from Curium Pharma and Novartis. Mathieu Gauthé has received personal fees and nonfinancial support from Astellas, Curium Pharma, and Novartis. The manuscript was edited for English language by Dr. Jay R Wiggins, PhD, and Dr. Kelsey L. Pomykala, MD, supported by ABX Advanced Biochemical Compounds. The ABX-CT-301 ClinicalTrials.gov number is NCT04102553. No other potential conflict of interest relevant to this article was reported.

ACKNOWLEDGMENTS

We thank the following institutions and people for participating in this study: Hôpital Tenon—F. Montravers, C. Aveline, J.N. Talbot, T. Rusu, B. Mugnier, and N. Cailleux; HEGP—B. Clara, M. Bernardini, C. Smadja, H. Slimani, B. Truffault, and M. Homo Seban; CHRU Nancy—G. Karcher, P. Eschwege, M. Claudin, and D. Peiffert; Centre Léon Bérard—P. Pommier, C. Carrie, C. Laude, A. Serre, J.N. Badel, T. Mognetti, A. Lauret, and O. Osman; HCL—I. Morelec, A. Dhomp, J. Tordo, P. Got, C. Darcissac, F. Hallouard, P. Bonazza, and H. Belhouli; and Centre Jean Perrin—C. Bouvet, B. Barres, E. Villeneuve, C. Valla, M. Tempier, G. Loos, M. Chanchou, A. Kelly, J. Amat, P. Bouyon, L. Viala, F. Luzuy, J. Miroir, and F. Cachin.

KEY POINTS

QUESTION: Is ^{18}F -PSMA-1007 superior to ^{18}F -fluorocholine PET/CT for the localization of biochemical recurrence in PCa patients?

PERTINENT FINDINGS: In this prospective, open-label, randomized, crossover multicenter study that included 190 patients with PCa biochemical recurrence, we demonstrated that ^{18}F -PSMA-1007 PET/CT localizes significantly more PCa lesions than ^{18}F -fluorocholine PET/CT, especially when serum PSA levels are low.

IMPLICATIONS FOR PATIENT CARE: More accurate staging of recurrent PCa might lead to more beneficial decision making and patient management; a theranostic use of PSMA radioligands should be considered in recurrent PCa.

REFERENCES

1. Dyba T, Randi G, Bray F, et al. The European cancer burden in 2020: incidence and mortality estimates for 40 countries and 25 major cancers. *Eur J Cancer*. 2021; 157:308–347.
2. Uchio EM, Aslan M, Wells CK, Calderone J, Concato J. Impact of biochemical recurrence in prostate cancer among US veterans. *Arch Intern Med*. 2010;170: 1390–1395.
3. European Association of Urology. EAU guidelines: oncology guidelines. <https://uroweb.org/individual-guidelines/oncology-guidelines/>. Accessed January 9, 2023.
4. Crocero F, Marchioni M, Novara G, et al. Detection rate of prostate specific membrane antigen tracers for positron emission tomography/computerized tomography in prostate cancer biochemical recurrence: a systematic review and network meta-analysis. *J Urol*. 2021;205:356–369.
5. Morigi JJ, Stricker PD, van Leeuwen PJ, et al. Prospective comparison of ^{18}F -fluoromethylcholine versus ^{68}Ga -PSMA PET/CT in prostate cancer patients who have rising prostate-specific antigen after curative treatment and are being considered for targeted therapy. *J Nucl Med*. 2015;56:1185–1190.
6. Cardinale J, Schäfer M, Benešová M, et al. Preclinical evaluation of ^{18}F -PSMA-1007, a new prostate-specific membrane antigen ligand for prostate cancer imaging. *J Nucl Med*. 2017;58:425–431.
7. Giesel FL, Hadaschik B, Cardinale J, et al. F-18 labelled PSMA-1007: biodistribution, radiation dosimetry and histopathological validation of tumor lesions in prostate cancer patients. *Eur J Nucl Med Mol Imaging*. 2017;44:678–688.
8. Giesel FL, Knorr K, Spohn F, et al. Detection efficacy of ^{18}F -PSMA-1007 PET/CT in 251 patients with biochemical recurrence of prostate cancer after radical prostatectomy. *J Nucl Med*. 2019;60:362–368.
9. Sprute K, Kramer V, Koerber SA, et al. Diagnostic accuracy of ^{18}F -PSMA-1007 PET/CT imaging for lymph node staging of prostate carcinoma in primary and biochemical recurrence. *J Nucl Med*. 2021;62:208–213.
10. Grünig H, Maurer A, Thali Y, et al. Focal unspecific bone uptake on [^{18}F]-PSMA-1007 PET: a multicenter retrospective evaluation of the distribution, frequency, and quantitative parameters of a potential pitfall in prostate cancer imaging. *Eur J Nucl Med Mol Imaging*. 2021;48:4483–4494.
11. Landis JR, Koch GG. The measurement of observer agreement for categorical data. *Biometrics*. 1977;33:159–174.
12. Marzola MC, Chondrogiannis S, Ferretti A, et al. Role of ^{18}F -choline PET/CT in biochemically relapsed prostate cancer after radical prostatectomy: correlation with trigger PSA, PSA velocity, PSA doubling time, and metastatic distribution. *Clin Nucl Med*. 2013;38:e26–e32.
13. Gillebert Q, Huchet V, Rousseau C, et al. ^{18}F -fluorocholine PET/CT in patients with occult biochemical recurrence of prostate cancer: detection rate, impact on management and adequacy of impact—a prospective multicentre study. *PLoS One*. 2018;13:e0191487.
14. Perera M, Papa N, Roberts M, et al. Gallium-68 prostate-specific membrane antigen positron emission tomography in advanced prostate cancer: updated diagnostic utility, sensitivity, specificity, and distribution of prostate-specific membrane antigen-avid lesions—a systematic review and meta-analysis. *Eur Urol*. 2020;77: 403–417.
15. Mapelli P, Incerti E, Ceci F, Castellucci P, Fanti S, Picchio M. ^{11}C - or ^{18}F -choline PET/CT for imaging evaluation of biochemical recurrence of prostate cancer. *J Nucl Med*. 2016;57(suppl):43S–48S.
16. Mingels C, Bohn KP, Rominger A, Afshar-Oromieh A, Alberts I. Diagnostic accuracy of [^{18}F]PSMA-1007 PET/CT in biochemical recurrence of prostate cancer. *Eur J Nucl Med Mol Imaging*. 2022;49:2436–2444.
17. Lecouvet FE, Oprea-Lager DE, Liu Y, et al. Use of modern imaging methods to facilitate trials of metastasis-directed therapy for oligometastatic disease in prostate cancer: a consensus recommendation from the EORTC Imaging Group. *Lancet Oncol*. 2018;19:e534–e545.
18. Chevalme Y-M, Boudali L, Gauthé M, et al. Survey by the French Medicine Agency (ANSM) of the imaging protocol, detection rate, and safety of ^{68}Ga -PSMA-11 PET/CT in the biochemical recurrence of prostate cancer in case of negative or equivocal ^{18}F -fluorocholine PET/CT: 1084 examinations. *Eur J Nucl Med Mol Imaging*. 2021;48:2935–2950.
19. Treglia G, Pereira Mestre R, Ferrari M, et al. Radiolabelled choline versus PSMA PET/CT in prostate cancer restaging: a meta-analysis. *Am J Nucl Med Mol Imaging*. 2019;9:127–139.
20. Soyka JD, Muster MA, Schmid DT, et al. Clinical impact of ^{18}F -choline PET/CT in patients with recurrent prostate cancer. *Eur J Nucl Med Mol Imaging*. 2012;39: 936–943.
21. Han S, Woo S, Kim YJ, Suh CH. Impact of ^{68}Ga -PSMA PET on the management of patients with prostate cancer: a systematic review and meta-analysis. *Eur Urol*. 2018;74:179–190.

Differences in Failure-Free Survival After Salvage Radiotherapy Guided by Conventional Imaging Versus ¹⁸F-Fluciclovine PET/CT in Postprostatectomy Patients: A Post Hoc Substratification Analysis of the EMPIRE-1 Trial

Ismaheel O. Lawal^{1,2}, Ashesh B. Jani³, Omotayo A. Adediran¹, Subir Goyal⁴, Olayinka A. Abiodun-Ojo¹, Vishal R. Dhere³, Charles V. Marcus¹, Shreyas S. Joshi⁵, Viraj A. Master⁵, Pretesh R. Patel³, Mark Goodman¹, Joseph W. Shelton³, Omer Kucuk⁶, Bruce Hershatter³, Bridget Fielder¹, Raghuveer K. Halkar¹, and David M. Schuster¹

¹Department of Radiology and Imaging Sciences, Emory University, Atlanta, Georgia; ²Department of Nuclear Medicine, University of Pretoria, Pretoria, South Africa; ³Department of Radiation Oncology, Winship Cancer Institute of Emory University, Atlanta, Georgia; ⁴Biostatistics Shared Resource, Winship Cancer Institute of Emory University, Atlanta, Georgia; ⁵Department of Urology, Emory University, Atlanta, Georgia; and ⁶Department of Medical Oncology, Winship Cancer Institute of Emory University, Atlanta, Georgia

The EMPIRE-1 (Emory Molecular Prostate Imaging for Radiotherapy Enhancement 1) trial reported a survival advantage in recurrent prostate cancer salvage radiotherapy (SRT) guided by ¹⁸F-fluciclovine PET/CT versus conventional imaging. We performed a post hoc analysis of the EMPIRE-1 cohort stratified by protocol-specified criteria, comparing failure-free survival (FFS) between study arms. **Methods:** EMPIRE-1 randomized patients to SRT planning via either conventional imaging only (bone scanning plus abdominopelvic CT or MRI) (arm A) or conventional imaging plus ¹⁸F-fluciclovine PET/CT (arm B). Randomization was stratified by prostate-specific antigen (PSA) level (<2.0 vs. ≥ 2.0 ng/mL), adverse pathology, and androgen-deprivation therapy (ADT) intent. We subdivided patients in each arm using the randomization stratification criteria and compared FFS between patient subgroups across study arms. **Results:** Eighty-one and 76 patients received per-protocol SRT in study arms A and B, respectively. The median follow-up was 3.5 y (95% CI, 3.0–4.0). FFS was 63.0% and 51.2% at 36 and 48 mo, respectively, in arm A and 75.5% at both 36 and 48 mo in arm B. Among patients with a PSA of less than 2 ng/mL (mean, 0.42 ± 0.42 ng/mL), significantly higher FFS was seen in arm B than arm A at 36 mo (83.2% [95% CI, 70.0–91.0] vs. 66.5% [95% CI, 51.6–77.8], *P* < 0.001) and 48 mo (83.2% [95% CI, 70.0–91.0] vs. 56.2% [95% CI, 40.5–69.2], *P* < 0.001). No significant difference in FFS between study arms in patients with a PSA of at least 2 ng/mL was observed. Among patients with adverse pathology, significantly higher FFS was seen in arm B than arm A at 48 mo (68.9% [95% CI, 52.1–80.8] vs. 42.8% [95% CI, 26.2–58.3], *P* < 0.001) though not at the 36-mo follow-up. FFS was higher in patients without adverse pathology in arm B versus arm A (90.2% [95% CI, 65.9–97.5] vs. 73.1% [95% CI, 42.9–89.0], *P* = 0.006) at both 36 and 48 mo. Patients in whom ADT was intended in arm B had higher FFS than those in arm A, with the difference reaching statistical significance at 48 mo (65.2% [95% CI, 40.3–81.7] vs. 29.1% [95% CI, 6.5–57.2], *P* < 0.001). Patients without ADT intent in arm B had significantly higher FFS than patients in arm A at 36 mo (80.7% [95% CI, 64.9–90.0] vs. 68.0% [95% CI, 51.1–80.2]) and 48 mo (80.7% [95% CI, 64.9–90.0] vs. 58.6% [95% CI, 41.0–72.6]). **Conclusion:** The survival advantage

due to the addition of ¹⁸F-fluciclovine PET/CT to SRT planning is maintained regardless of the presence of adverse pathology or ADT intent. Including ¹⁸F-fluciclovine PET/CT to SRT leads to survival benefits in patients with a PSA of less than 2 ng/mL but not in patients with a PSA of 2 ng/mL or higher.

Key Words: ¹⁸F-fluciclovine PET/CT; salvage radiotherapy; EMPIRE-1 trial; prostate cancer; adverse pathology; prostate-specific antigen

J Nucl Med 2023; 64:586–591
DOI: 10.2967/jnumed.122.264832

Radical prostatectomy (RP) is one of the treatment choices offered to patients with localized prostate cancer (PCa) (1). After RP, recurrence manifests as a rising level of serum prostate-specific antigen (PSA) (2). Early detection of recurrence followed by salvage therapy is crucial for a favorable outcome (3). Salvage radiotherapy (SRT) with or without androgen-deprivation therapy (ADT) is recommended for biochemical recurrence of PCa (4). SRT can be curative if the irradiation volume encompasses all the sites of PCa recurrence (5). Imaging for lesion localization, therefore, plays a critical role in SRT planning.

Conventional imaging with MRI, CT, and radionuclide bone scintigraphy has traditionally been used for restaging and SRT planning. The performance of these conventional imaging modalities is heterogeneous across studies, with low lesion detection rates at a PSA level of less than 2.0 ng/mL, a level at which SRT may be curative (5,6). Several radionuclide probes targeting different epitopes in the PCa cells were subsequently developed to address the limited diagnostic performance of conventional imaging at low PSA levels and improve the lesion detection rate in biochemical recurrence of PCa before SRT. ¹⁸F-fluciclovine is a radiofluorinated synthetic amino acid transported into PCa cells (7,8). One of the strengths of ¹⁸F-fluciclovine PET imaging of PCa recurrence is its lack of significant early bladder excretion, allowing for detection of recurrence in the prostate bed (9,10). Our group and others have shown the high diagnostic performance of ¹⁸F-fluciclovine PET/CT, even at low PSA levels (11–13). We have also reported a high impact of ¹⁸F-fluciclovine PET/CT on therapy decisions during SRT planning (14).

Received Aug. 23, 2022; revision accepted Oct. 27, 2022.
For correspondence or reprints, contact Ismaheel O. Lawal (ilawal@emory.edu).
*Contributed equally to this work.
Published online Nov. 3, 2022.
COPYRIGHT © 2023 by the Society of Nuclear Medicine and Molecular Imaging.

The ability of SRT to lead to a decline in serum PSA level to below detectable limits and maintain disease control is the ultimate measure of the correctness of treatment decisions during radiotherapy planning. Unfortunately, most studies have focused on lesion detection rate and management change rather than the outcome of such decisions. Recently, the EMPIRE-1 (Emory Molecular Prostate Imaging for Radiotherapy Enhancement 1) study, a phase 2/3 trial that randomized patients with detectable serum PSA after RP to either conventional imaging only or conventional imaging plus ^{18}F -fluciclovine PET/CT to guide SRT, reported a significantly longer time to failure (failure-free survival, or FFS) for conventional imaging plus ^{18}F -fluciclovine PET/CT than for imaging only (15). The difference in the time to failure between arms was the primary aim for which the study was prospectively powered. Yet, the EMPIRE-1 trial also stratified patients using 3 criteria (serum PSA level < 2 ng/mL vs. ≥ 2 ng/mL; presence or absence of adverse pathologic features, including extracapsular extension, seminal vesicle invasion, and presence of lymph node metastases at RP; and ADT intent) that are known to influence SRT outcomes in patients with PCa recurrence (16,17). This stratified randomization afforded the opportunity to evaluate the impact of these characteristics known to affect SRT outcomes in post-SRT patients with PCa. We therefore performed a secondary analysis of the EMPIRE-1 trial cohort stratified by protocol-specified criteria and compared FFS between study arms.

MATERIALS AND METHODS

This is a secondary analysis of data from the EMPIRE-1 trial (NCT01666808). EMPIRE-1 is a phase 2/3 controlled trial that randomized patients with detectable serum PSA after RP to SRT guided by conventional imaging only or conventional imaging plus abdominopelvic ^{18}F -fluciclovine PET/CT. Details on the inclusion and exclusion criteria, randomization and masking, protocols for conventional imaging and ^{18}F -fluciclovine PET/CT, and outcome assessment have been published previously (15). Briefly, patients with detectable serum PSA after RP for adenocarcinoma of the prostate gland without evidence of systemic metastases on conventional imaging were randomized to undergo no additional imaging (arm A) versus additional ^{18}F -fluciclovine PET/CT for guiding the SRT decision. Systemic metastasis was defined as any site of metastasis outside the pelvic field of SRT. Conventional imaging included whole-body planar bone scintigraphy and abdominopelvic CT or MRI. Exclusion criteria were a history of previous pelvic radiotherapy, a European Cooperative Oncology Group performance status of at least 3, the presence of contraindications to radiotherapy, a previous invasive malignancy within the 3 y preceding enrollment, and severe concurrent illness. All trial subjects gave written informed consent. The institutional review board of Emory University approved the study.

Randomization

Randomization into the study arms was in a ratio of 1:1 and was stratified by serum PSA level (<2.0 vs. ≥ 2.0 ng/mL), presence of adverse pathology at RP (extracapsular extension, seminal vesicle invasion, and lymph node metastasis: none vs. any), and ADT intent (yes vs. no).

Image Analysis

Conventional images and ^{18}F -fluciclovine PET/CT images were interpreted by 2 experienced readers independently. They read the ^{18}F -fluciclovine PET/CT images on a MIMVista Workstation (MIM Software Inc.) without knowing the findings of conventional imaging

or the clinicopathologic history of the patients. Disagreements between the readers were resolved by consensus.

Treatment

In the conventional imaging-only arm, SRT decisions were based on the standard-of-care practice and were guided by the presurgical disease features, pathologic features of the RP specimen, and PSA trajectory. In the arm using conventional imaging plus ^{18}F -fluciclovine PET/CT, SRT decisions were guided by ^{18}F -fluciclovine PET/CT findings. No on-trial radiotherapy was given to patients with extrapelvic findings. Patients with pelvic findings received 64.8–70.2 Gy in 1.8-Gy fractions to the prostate bed and 45.0–50.4 Gy in 1.8-Gy fractions to the pelvis. Patients with prostate-only findings and those with negative ^{18}F -fluciclovine PET/CT findings received 64.8–70.2 Gy in 1.8-Gy fractions to the prostate bed only.

Follow-up and Outcome Determination

After SRT, all patients were followed up at 1 mo, 6 mo, and every 6 mo thereafter for 36 mo after SRT. Longer follow-up was permitted for patients who had not experienced treatment failure at 36 mo after SRT. During each follow-up visit, treatment failure was evaluated clinically with physical examination and biochemically with serum PSA level determination. We defined treatment failure as a rise in serum PSA by 0.2 ng/mL above the nadir achieved after SRT, followed by another rise in a subsequent measurement; failure to achieve a decline in serum PSA after SRT; failure based on imaging or clinical examination (including digital rectal examination) findings; or the initiation of systemic therapy (18). We defined FFS as the duration from the completion of SRT to the date that failure was confirmed.

Statistical Analysis

For the primary endpoint of the RCT, a sample of 146 patients, including 73 in each arm, was calculated to detect a 20% difference in 3-y FFS between the arms at a 0.05 level of confidence with 80% power. We set an overall enrollment target of 162 participants, assuming a 10% dropout rate. We used the z test to compare FFS between arms (15).

For the current investigation, we subsequently stratified patients in the 2 arms by the protocol-specified stratification criteria (PSA < 2.0 vs. ≥ 2.0 ng/mL, presence vs. absence of any adverse pathology at RP, and yes vs. no to ADT intent) and compared FFS between study arms at 3 and 4 y using the z test (19). In addition to dichotomizing each study arm by a PSA cutoff of 2 ng/mL for comparison, we performed exploratory comparisons between study arms using the z test at different PSA levels (<0.5 , <1.0 , and <2.0 ng/mL). We set statistical significance at a P value of less than 0.05. We performed statistical analysis using SAS, version 9.4 (SAS Institute, Inc.).

RESULTS

In total, 167 patients without systemic metastasis on conventional imaging were screened for inclusion. Two patients failed screening, and 165 patients were randomized, with 82 being allocated to arm A (conventional imaging only) and 83 to arm B (conventional imaging plus ^{18}F -fluciclovine PET/CT). One patient in arm A and 3 in arm B withdrew from the study after randomization. The remaining 81 patients in arm A received SRT without additional imaging. Of the remaining 80 patients in arm B, 79 had additional ^{18}F -fluciclovine PET/CT, whereas PET/CT could not be performed in 1 patient because of technical issues. Four patients in arm B had extrapelvic sites of metastasis and were excluded from undergoing SRT. Finally, 81 patients in arm A and 76 in arm B received SRT, and their data are presented in this work (Fig. 1).

Table 1 compares the patients in both arms according to the baseline clinicopathologic characteristics and the criteria applied

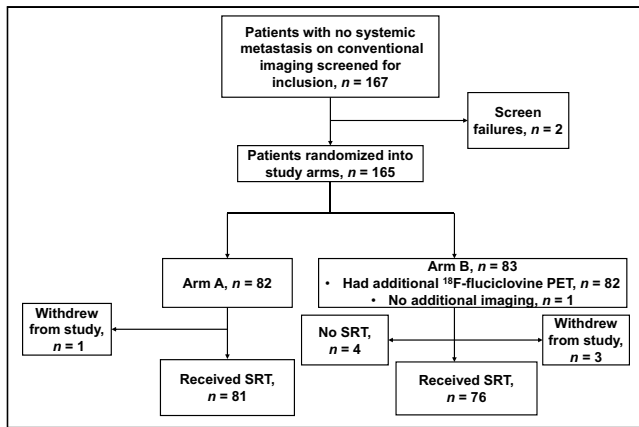


FIGURE 1. Flowchart showing patient recruitment and randomization into study arms.

in stratifying patients to study arms. Baseline PSA, presence of any adverse pathology, and ADT intent were stratification criteria and, hence, were similar between arms. Age and Gleason scores at RP were also similar between groups.

In arm A, 56 patients (69.1%) received radiation to the prostate bed alone, whereas 25 (30.9%) received radiation to the prostate bed and pelvis. Among patients in arm B whose SRT decision was guided by findings on ¹⁸F-fluciclovine PET/CT, 41 (53.9%) received radiation to the prostate bed alone, whereas 35 (46.1%) received radiation to the prostate bed and the pelvis.

The median follow-up was 3.5 y (95% CI, 3.0–4.0 y). At the 36-mo follow-up, 22 and 15 patients had experienced treatment failure in arms A and B, respectively. In arm A, FFS was 63.0% and 51.2% at the 36- and 48-mo follow-ups, respectively, whereas in arm B, FFS was 75.5% at both the 36- and the 48-mo follow-ups.

Among patients with a PSA level of less than 2 ng/mL, 66.5% and 83.2% in arms A and B, respectively, were failure-free at the 36-mo

follow-up ($P < 0.001$), whereas 56.2% and 83.2%, respectively, were failure-free at the 48-mo follow-up (Table 2). Among patients with a PSA level of 2 ng/mL or higher, 40.4% and 26.3% in arms A and B, respectively were failure-free at 36-mo follow-up, whereas 0% and 26.3%, respectively, were failure-free at 48 mo after SRT.

In our exploratory comparison of FFS at different PSA thresholds, we found significant differences between study arms (Table 3). At a PSA level of less than 0.5 ng/mL, there was no significant difference in FFS between arms A and B at the 36-mo follow-up (79.3% vs. 85.3%, $P = 0.184$). At 48 mo, however, FFS was significantly higher in arm B than arm A (85.3% vs. 63.2%, $P < 0.001$). Among patients with a PSA level of less than 1 ng/mL, FFS was significantly higher in arm B than arm A at 36 mo (84.7% vs. 72.8%, $P = 0.005$) and 48 mo (84.7% vs. 60.5%, $P < 0.001$).

Dichotomization of patients in each arm was based on the presence of any extracapsular extension, seminal vesicle invasion, or lymph node metastasis in the surgical specimen at pathologic evaluation after RP. Among patients with any of the adverse pathologic features, 59.9% and 68.9% of patients were failure-free at the 36-mo follow-up in arms A and B, respectively ($P = 0.085$), and at 48 mo, FFS remained significantly higher in arm B than arm A (68.9% vs. 42.8%, $P < 0.001$). Among patients without any of these adverse pathologic features, FFS was also significantly higher in arm B than arm A at both 36 and 48 mo (Table 2).

On the basis of their disease-associated risk, there was ADT intent for 28 and 27 patients in arms A and B, respectively. At the 36-mo follow-up, FFS did not significantly differ between study arms (52.3% for arm A vs. 65.2% for arm B, $P = 0.113$). At the 48-mo follow-up, FFS was significantly higher in arm B (65.2%) than arm A (29.1%) ($P < 0.001$). In the cohorts of patients without ADT intent, FFS was significantly higher in arm B than arm A at 36 mo (80.7 vs. 68.0, $P = 0.008$) and 48 mo (80.7 vs. 58.6, $P < 0.001$).

DISCUSSION

The EMPIRE-1 trial, which stratified patients into study arms on the basis of pre-SRT serum PSA level, presence or absence of adverse pathologic features, and the intent to add ADT in management, reported that SRT decisions guided by findings on ¹⁸F-fluciclovine PET/CT result in a favorable FFS (15). The benefit of ¹⁸F-fluciclovine PET/CT on FFS reported in the EMPIRE-1 study was at a group level. In the current study, we performed a substratification post hoc analysis of the EMPIRE-1 data to determine whether the FFS advantage conferred by adding ¹⁸F-fluciclovine PET/CT to SRT planning is maintained across different patient strata. In this study, FFS was significantly higher in patients with a serum PSA of less than 2 ng/mL who underwent additional ¹⁸F-fluciclovine PET/CT (arm B) for SRT planning than in patients whose SRT planning was based on conventional imaging only. At a PSA level of more than 2 ng/mL, we found no significant difference in FFS between study arms. This finding may be related to the limited number of patients with this PSA level (22 patients) in the EMPIRE-1 cohort but requires further study before definitive conclusions can be made.

SRT has been recommended at low serum PSA levels (<0.5 ng/mL) (20) because of the decrease in its benefits as PSA rises (21). Given this, we performed an explorative analysis to see whether the FFS benefit conferred by ¹⁸F-fluciclovine PET/CT is retained at lower PSA levels. Indeed, FFS remained significantly higher in arm B than arm A at a PSA level of less than 1 ng/mL at both the 36- and the 48-mo follow-ups. Among patients with a PSA level of less than 0.5 ng/mL, FFS was significantly higher in arm B than arm A, with

TABLE 1
Baseline Characteristics of Patients Randomized into Study Arms

Characteristic	Arm A (n = 81)	Arm B (n = 76)
Age (y)	61 (55–68)	61 (57–68)
Baseline PSA (ng/mL)	0.34 (0.13–0.95)	0.34 (0.18–1.10)
<2	69 (85.2)	66 (86.8)
≥2	12 (14.8)	10 (13.2)
Any adverse pathology		
Present	61 (75.3)	53 (69.7)
Absent	20 (24.7)	23 (30.3)
ADT intent		
Yes	28 (34.6)	27 (35.5)
No	53 (65.4)	49 (64.5)
Gleason score		
<8	52 (64.2)	53 (69.7)
≥8	29 (35.8)	23 (30.3)

Qualitative data are number and percentage; continuous data are median and interquartile range.

TABLE 2
Comparison of FFS Rates Between Arms Stratified According to PSA, Adverse Pathology, and ADT Intent

Stratification criterion	Follow-up time (mo)	Arm A (%)	Arm B (%)	<i>P</i>
PSA				
<2 ng/mL	36	66.5 (51.6–77.8)	83.2 (70.0–91.0)	<0.001*
	48	56.2 (40.5–69.2)	83.2 (70.0–91.0)	<0.001*
≥2 ng/mL	36	40.4 (9.8–70.2)	26.3 (4.0–57.5)	0.231
	48	0.0 (NA–NA)	26.3 (4.0–57.5)	NA
Adverse pathology				
Present	36	59.9 (43.7–72.8)	68.9 (52.1–80.8)	0.085
	48	42.8 (26.2–58.3)	68.9 (52.1–80.8)	<0.001*
Absent	36	73.1 (42.9–89.0)	90.2 (65.9–97.5)	0.006*
	48	73.1 (42.9–89.0)	90.2 (65.9–97.5)	0.006*
ADT intent				
Yes	36	52.3 (27.7–72.1)	65.2 (40.3–81.7)	0.113
	48	29.1 (6.5–57.2)	65.2 (40.3–81.7)	<0.001*
No	36	68.0 (51.1–80.2)	80.7 (64.9–90.0)	0.008
	48	58.6 (41.0–72.6)	80.7 (64.9–90.0)	<0.001*

**P* < 0.005.

NA = not applicable.

Data in parentheses are 95% CIs. Adverse pathology considered was extraprostatic extension, seminal vesicle invasion, and presence of nodal metastases in pathology specimen obtained during RP.

the difference reaching statistical significance at the 48-mo follow-up. This finding suggests that although the use of ¹⁸F-fluciclovine PET/CT for SRT planning is beneficial in patients with a PSA of more than 0.5 ng/mL, this benefit reaches significance in the long

term, and this finding may be related to the more sustained disease control seen in patients who had ¹⁸F-fluciclovine PET/CT as part of SRT planning compared with the progressive increase in failure rate over time in patients who did not.

TABLE 3
Differences in FFS Between Arms A and B for SRT Planning

Parameter	Arm A (%)	Arm B (%)	<i>P</i>
PSA < 0.5 ng/mL			
<i>n</i>	48	51	
Mean ± SD	0.19 ± 0.13	0.23 ± 0.12	
FFS at 36 mo	79.3 (61.3–89.6)	85.3 (69.7–93.2)	0.184
FFS at 48 mo	63.2 (42.8–78.1)	85.3 (69.7–93.2)	<0.001*
PSA < 1 ng/mL			
<i>n</i>	61	57	
Mean ± SD	0.29 ± 0.24	0.29 ± 0.20	
FFS at 36 mo	72.8 (56.8–83.6)	84.7 (70.3–92.5)	0.005*
FFS at 48 mo	60.5 (43.2–74.0)	84.7 (70.3–92.5)	<0.001*
PSA < 2 ng/mL			
<i>n</i>	69	66	
Mean ± SD	0.41 ± 0.41	0.43 ± 0.43	
FFS at 36 mo	66.5 (51.6–77.8)	83.2 (70.0–91.0)	<0.001*
FFS at 48 mo	56.2 (40.5–69.2)	83.2 (70.0–91.0)	<0.001*

**P* < 0.05.

Data in parentheses are 95% CIs.

Adverse pathologic features such as extraprostatic extension, seminal vesicle invasion, and the presence of nodal metastases in the pathology specimen obtained during RP are suggestive of advanced disease (17). The EMPIRE-1 trial therefore stratified patients during randomization into study arms according to the presence or absence of these adverse pathologic features. The FFS benefit conferred by incorporating ¹⁸F-fluciclovine PET/CT into SRT planning was maintained in patients with and without adverse pathologic features at the 36- and 48-mo follow-ups. In patients with adverse pathology present, the higher FFS rate seen in arm B than arm A at the 36-mo follow-up showed a trend toward statistical significance, whereas significance was clearly seen at the 48-mo follow-up, again highlighting the long-term tumor control afforded by SRT decisions guided by ¹⁸F-fluciclovine PET/CT.

Adding ADT to SRT improves progression-free survival, especially in patients with high-risk disease phenotypes (16,22). To remove the confounding effect of additional ADT on SRT outcome, ADT intent was balanced between study arms. Among patients with no ADT intent, FFS was significantly higher at the 36- and 48-mo follow-ups in arm B than arm A. Among patients for whom additional ADT was planned, there was a higher FFS in arm B than arm A at the 36-mo follow-up, with the difference reaching statistical significance at the 48-mo follow-up. The improvement in FFS due to SRT conferred by ¹⁸F-fluciclovine PET/CT was more prominent at the 48-mo follow-up than at the 36-mo follow-up, a finding that was consistently seen across different patient strata. Fifteen patients experienced SRT failure in arm B, all of which occurred within 36 mo of SRT. There was no further event during the 36- to 48-mo follow-up interval. Conversely, in arm A, 22 events occurred within 36 mo of SRT and a further 5 events occurred between the 36- and 48-mo follow-ups. It is notable and expected that, regardless of arm, patients with higher PSA levels, adverse histology, and ADT intent generally have lower FFS than those with lower PSA levels, no adverse histology, and no ADT intent.

Among patients randomized to arm B, 4 did not receive SRT because of detection of extrapelvic metastases on ¹⁸F-fluciclovine PET/CT. In these patients, ¹⁸F-fluciclovine PET/CT prevented futile SRT. In arm A, 30.9% of patients received pelvic radiotherapy in addition to radiotherapy to the prostate bed. This rate is lower than the 46.1% of patients in arm B who had pelvic radiotherapy in addition to radiotherapy to the prostate bed, a decision guided by the findings on ¹⁸F-fluciclovine PET/CT. Put together, the higher FFS brought about by the incorporation of ¹⁸F-fluciclovine PET/CT during SRT decision making is a result of a combination of better patient selection and more accurate radiotherapy target delineation. We previously reported that ¹⁸F-fluciclovine PET/CT had a greater impact on SRT management decisions than conventional imaging in the EMPIRE-1 cohort (14). A more favorable survival outcome in patients undergoing additional ¹⁸F-fluciclovine PET/CT, compared with patients whose SRT was guided by conventional imaging alone, suggests that the change in management decision brought about by ¹⁸F-fluciclovine PET/CT led to a favorable treatment outcome.

The detection of additional lesions on ¹⁸F-fluciclovine PET/CT compared with conventional imaging is often associated with an increase in the pretreatment defined target volume (23). The higher rate of radiotherapy to the pelvis in the ¹⁸F-fluciclovine PET/CT arm in the current study, therefore, has the potential to expose such patients to radiotherapy-induced toxicities. A recent report that evaluated provider- and patient-reported SRT-induced toxicities in the EMPIRE-1 cohort did not find significant differences in the incidence of treatment-induced toxicities between study arms despite a significant increase in target volumes due to the incorporation of ¹⁸F-fluciclovine

PET/CT into SRT planning (24). This finding confirms that the improvement in lesion detection, SRT management decisions, and favorable SRT outcomes brought about by the incorporation of ¹⁸F-fluciclovine PET/CT into SRT planning occurs without exposing the patients to a higher rate or severity of treatment-induced toxicities.

Several studies have reported the diagnostic performance of ¹⁸F-fluciclovine PET/CT in patients with PCa recurrence (25–28). These studies have primarily evaluated the diagnostic performance of ¹⁸F-fluciclovine PET/CT or its effects on management decisions rather than the impact of imaging findings on patients' survival. Imaging studies that randomized patients into study arms and evaluated the impact of imaging findings on survival are rare. The strength of this study, therefore, lies in its design and the choice of FFS as the study endpoint. In the EMPIRE-1 trial design, power and sample size calculations were performed for the primary aim (i.e., to detect a 20% difference in 3-y FFS between study arms). The current subgroup investigation is purely exploratory. Despite not being powered to detect differences between study arms stratified according to protocol-specified criteria, we found that the survival benefit from adding ¹⁸F-fluciclovine PET/CT was maintained across most of the strata evaluated.

Of note, though there has been a recent expansion in the use of ⁶⁸Ga-PSMA PET/CT, with a few prospective single-arm trials reporting the time to failure as a study endpoint in patients whose SRT was guided by this novel imaging modality (29,30), there have been no randomized controlled trials of PSMA versus conventional imaging reported as yet in this postprostatectomy radiotherapy space. An ongoing phase III trial at the University of California Los Angeles (NCT03582774), when completed, will fill this void (31). We have an ongoing phase III trial at our institution comparing ⁶⁸Ga-PSMA PET/CT versus ¹⁸F-fluciclovine PET/CT (R01CA226992, NCT03762759) for guiding SRT of PCa recurrence. The results from this trial may provide further insights on the comparative benefits of these 2 approved imaging modalities for PCa recurrence in guiding SRT management decisions.

CONCLUSION

The addition of ¹⁸F-fluciclovine PET/CT to conventional imaging in SRT management planning reduces the occurrence of treatment failure. This benefit is seen across different PSA levels below 2 ng/mL. This benefit is also maintained regardless of the presence versus absence of adverse pathologic features or the intention to add ADT to SRT, or not, in the treatment of PCa recurrence after RP.

DISCLOSURE

This study received funding from the National Institutes of Health (R01 CA169188) and Blue Earth Diagnostics (fluciclovine synthesis cassettes to Emory University). Research reported in this publication was supported partly by the Biostatistics Shared Resource of Winship Cancer Institute of Emory University and National Institutes of Health/National Cancer Institute under award P30CA138292. Ashesh Jani reports personal fees from Blue Earth Diagnostics for advisory board services outside the submitted work. Mark Goodman is entitled to a royalty derived from sale of products related to the research described in this report. The terms of this arrangement have been reviewed and approved by Emory University in accordance with its conflict-of-interest policies. The research consent forms state that he is entitled to a share of sales royalty received by Emory University from Nihon MediPhysics under that agreement. The terms of this arrangement have been reviewed and approved by Emory University

in accordance with its conflict-of-interest policies. David Schuster participates through the Emory University Office of Sponsored Projects in sponsored grants including those funded or partially funded by Blue Earth Diagnostics, Nihon MediPhysics, Telix Pharmaceuticals (U.S.), Advanced Accelerator Applications, FUJIFILM Pharmaceuticals USA, and Amgen and reports consultant fees outside the submitted work from Syncona, AIM Specialty Health, Global Medical Solutions Taiwan, and Progenics Pharmaceuticals. No other potential conflict of interest relevant to this article was reported.

ACKNOWLEDGMENTS

We thank the following individuals at Emory University for their support and assistance: Walter J. Curran, Mark McDonald, Sherric Cooper, and the entire radiation oncology clinical trials team; the entire imaging team; Ronald J. Crowe and the entire cyclotron and synthesis team from Emory University Center for Systems Imaging; and Martin Sanda, Mehrdad Alemozaffar, and the entire urology clinical enterprise and clinical trials team. We thank all participating patients.

KEY POINTS

QUESTION: Is the survival advantage from adding ^{18}F -fluciclovine PET/CT to SRT planning for PCa recurrence, as reported in the EMPIRE-1 trial, maintained in different patient subpopulations?

PERTINENT FINDINGS: The incorporation of ^{18}F -fluciclovine PET/CT in SRT management decisions improved FFS across different PSA strata below 2 ng/mL. The survival benefit was retained regardless of whether adverse pathologic features were present or whether concomitant ADT was planned with SRT.

IMPLICATIONS FOR PATIENT CARE: The addition of ^{18}F -fluciclovine PET/CT SRT planning improves FFS in patients with disease recurrence after RP, and the benefit is retained across different patient categories.

REFERENCES

- Eastham JA, Auffenberg GB, Barocas DA, et al. Clinically localized prostate cancer: AUA/ASTRO guideline, part I: introduction, risk assessment, staging, and risk-based management. *J Urol*. 2022;208:10–18.
- Kupelian P, Katcher J, Levin H, Zippe C, Klein E. Correlation of clinical and pathologic factors with rising prostate-specific antigen profiles after radical prostatectomy alone for clinically localized prostate cancer. *Urology*. 1996;48:249–260.
- Tilki D, Preisser F, Graefen M, Huland H, Pompe RS. External validation of the European Association of Urology biochemical recurrence risk groups to predict metastasis and mortality after radical prostatectomy in a European cohort. *Eur Urol*. 2019;75:896–900.
- Pisansky TM, Thompson IM, Valicenti RK, D'Amico AV, Selvarajah S. Adjuvant and salvage radiation therapy after prostatectomy: ASTRO/AUA guideline amendment, executive summary 2018. *Pract Radiat Oncol*. 2019;9:208–213.
- Zaorsky NG, Calais J, Fanti S, et al. Salvage therapy for prostate cancer after radical prostatectomy. *Nat Rev Urol*. 2021;18:643–668.
- Kane CJ, Amling CL, Johnstone PA, et al. Limited value of bone scintigraphy and computed tomography in assessing biochemical failure after radical prostatectomy. *Urology*. 2003;61:607–611.
- Oka S, Okudaira H, Yoshida Y, Schuster DM, Goodman MM, Shirakami Y. Transport mechanisms of trans-1-amino-3-fluoro[^{14}C]cyclobutanecarboxylic acid in prostate cancer cells. *Nucl Med Biol*. 2012;39:109–119.
- Ono M, Oka S, Okudaira H, et al. [^{14}C]fluciclovine (alias anti- ^{14}C]FACBC) uptake and ASCT2 expression in castration-resistant prostate cancer cells. *Nucl Med Biol*. 2015;42:887–892.
- Schuster DM, Nanni C, Fanti S, et al. Anti-1-amino-3- ^{18}F -fluorocyclobutane-1-carboxylic acid: physiologic uptake patterns, incidental findings, and variants that may simulate disease. *J Nucl Med*. 2014;55:1986–1992.
- Nye JA, Schuster DM, Yu W, Camp VM, Goodman MM, Votaw JR. Biodistribution and radiation dosimetry of the synthetic nonmetabolized amino acid analogue anti- ^{18}F -FACBC in humans. *J Nucl Med*. 2007;48:1017–1020.
- Marcus C, Abiodun-Ojo OA, Jani AB, Schuster DM. Clinical utility of ^{18}F -fluciclovine PET/CT in recurrent prostate cancer with very low (≤ 0.3 ng/mL) prostate-specific antigen levels. *Am J Nucl Med Mol Imaging*. 2021;11:406–414.
- Bulbul JE, Grybowski D, Lovrec P, et al. Positivity rate of [^{18}F]fluciclovine PET/CT in patients with suspected prostate cancer recurrence at PSA levels below 1 ng/mL. *Mol Imaging Biol*. 2022;24:42–49.
- Salavati A, Gencturk M, Koksels Y, et al. A bicentric retrospective analysis of clinical utility of ^{18}F -fluciclovine PET in biochemically recurrent prostate cancer following primary radiation therapy: is it helpful in patients with a PSA rise less than the Phoenix criteria? *Eur J Nucl Med Mol Imaging*. 2021;48:4463–4471.
- Abiodun-Ojo OA, Jani AB, Akintayo AA, et al. Salvage radiotherapy management decisions in postprostatectomy patients with recurrent prostate cancer based on ^{18}F -fluciclovine PET/CT guidance. *J Nucl Med*. 2021;62:1089–1096.
- Jani AB, Schreiber E, Goyal S, et al. ^{18}F -fluciclovine-PET/CT imaging versus conventional imaging alone to guide postprostatectomy salvage radiotherapy for prostate cancer (EMPIRE-1): a single centre, open-label, phase 2/3 randomised controlled trial. *Lancet*. 2021;397:1895–1904.
- Pollack A, Karrison TG, Balogh AG, et al. The addition of androgen deprivation therapy and pelvic lymph node treatment to prostate bed salvage radiotherapy (NRG Oncology/RTOG 0534 SPPORT): an international, multicentre, randomised phase 3 trial. *Lancet*. 2022;399:1886–1901.
- Pisansky TM, Agrawal S, Hamstra DA, et al. Salvage radiation therapy dose response for biochemical failure of prostate cancer after prostatectomy: a multi-institutional observational study. *Int J Radiat Oncol Biol Phys*. 2016;96:1046–1053.
- Tendulkar RD, Agrawal S, Gao T, et al. Contemporary update of a multi-institutional predictive nomogram for salvage radiotherapy after radical prostatectomy. *J Clin Oncol*. 2016;34:3648–3654.
- Klein JP, Moeschberger ML. *Survival Analysis: Techniques for Censored and Truncated Data*. Springer; 2003:234–237.
- Cornford P, Bellmunt J, Bolla M, et al. EAU-ESTRO-SIOG guidelines on prostate cancer. Part II: treatment of relapsing, metastatic, and castration-resistant prostate cancer. *Eur Urol*. 2017;71:630–642.
- King CR. The timing of salvage radiotherapy after radical prostatectomy: a systematic review. *Int J Radiat Oncol Biol Phys*. 2012;84:104–111.
- Carrie C, Hasbini A, de Laroche G, et al. Salvage radiotherapy with or without short-term hormone therapy for rising prostate-specific antigen concentration after radical prostatectomy (GETUG-AFU 16): a randomised, multicentre, open-label phase 3 trial. *Lancet Oncol*. 2016;17:747–756.
- Jani AB, Schreiber E, Rossi PJ, et al. Impact of ^{18}F -fluciclovine PET on target volume definition for postprostatectomy salvage radiotherapy: initial findings from a randomized trial. *J Nucl Med*. 2017;58:412–418.
- Dhere VR, Schuster DM, Goyal S, et al. Randomized trial of conventional versus conventional plus fluciclovine (^{18}F) positron emission tomography/computed tomography-guided postprostatectomy radiation therapy for prostate cancer: volumetric and patient-reported analyses of toxic effects. *Int J Radiat Oncol Biol Phys*. 2022;113:1003–1014.
- Odewole OA, Tade FI, Nieh PT, et al. Recurrent prostate cancer detection with anti-3- ^{18}F]FACBC PET/CT: comparison with CT. *Eur J Nucl Med Mol Imaging*. 2016;43:1773–1783.
- Solanki AA, Savir-Baruch B, Liauw SL, et al. ^{18}F -fluciclovine positron emission tomography in men with biochemical recurrence of prostate cancer after radical prostatectomy and planning to undergo salvage radiation therapy: results from LOCATE. *Pract Radiat Oncol*. 2020;10:354–362.
- Calais J, Ceci F, Eiber M, et al. ^{18}F -fluciclovine PET-CT and ^{68}Ga -PSMA-11 PET-CT in patients with early biochemical recurrence after prostatectomy: a prospective, single-centre, single-arm, comparative imaging trial. *Lancet Oncol*. 2019;20:1286–1294.
- Scarsbrook AF, Bottomley D, Teoh EJ, et al. Effect of ^{18}F -fluciclovine positron emission tomography on the management of patients with recurrence of prostate cancer: results from the FALCON trial. *Int J Radiat Oncol Biol Phys*. 2020;107:316–324.
- Ceci F, Rovera G, Iorio GC, et al. Event-free survival after ^{68}Ga -PSMA-11 PET/CT in recurrent hormone-sensitive prostate cancer (HSPC) patients eligible for salvage therapy. *Eur J Nucl Med Mol Imaging*. 2022;49:3257–3268.
- Emmett L, Tang R, Nandurkar R, et al. 3-year freedom from progression after ^{68}Ga -PSMA PET/CT-triaged management in men with biochemical recurrence after radical prostatectomy: results of a prospective multicenter trial. *J Nucl Med*. 2020;61:866–872.
- Calais J, Czernin J, Fendler WP, Elashoff D, Nickols NG. Randomized prospective phase III trial of ^{68}Ga -PSMA-11 PET/CT molecular imaging for prostate cancer salvage radiotherapy planning [PSMA-SRT]. *BMC Cancer*. 2019;19:97.

A Pilot Study of ^{68}Ga -PSMA11 and ^{68}Ga -RM2 PET/MRI for Evaluation of Prostate Cancer Response to High-Intensity Focused Ultrasound Therapy

Heying Duan¹, Pejman Ghanouni², Bruce Daniel², Jarrett Rosenberg¹, Guido A. Davidzon¹, Carina Mari Aparici¹, Christian Kunder³, Geoffrey A. Sonn^{2,4}, and Andrei Iagaru¹

¹Division of Nuclear Medicine and Molecular Imaging, Department of Radiology, Stanford University, Stanford, California; ²Division of Body MRI, Department of Radiology, Stanford University, Stanford, California; ³Department of Pathology, Stanford University, Stanford, California; and ⁴Department of Urology, Stanford University, Stanford, California

Focal therapy for localized prostate cancer (PC) using high-intensity focused ultrasound (HIFU) is gaining in popularity as it is noninvasive and associated with fewer side effects than standard whole-gland treatments. However, better methods to evaluate response to HIFU ablation are an unmet need. Prostate-specific membrane antigen (PSMA) and gastrin-releasing peptide receptors are both overexpressed in PC. In this study, we evaluated a novel approach of using both ^{68}Ga -RM2 and ^{68}Ga -PSMA11 PET/MRI in each patient before and after HIFU to assess the accuracy of target tumor localization and response to treatment. **Methods:** Fourteen men, 64.5 ± 8.0 y old (range, 48–78 y), with newly diagnosed PC were prospectively enrolled. Before HIFU, the patients underwent prostate biopsy, multiparametric MRI, ^{68}Ga -PSMA11, and ^{68}Ga -RM2 PET/MRI. Response to treatment was assessed at a minimum of 6 mo after HIFU with prostate biopsy ($n = 13$), as well as ^{68}Ga -PSMA11 and ^{68}Ga -RM2 PET/MRI ($n = 14$). The SUV_{max} and SUV_{peak} of known or suspected PC lesions were collected. **Results:** Pre-HIFU biopsy revealed 18 cancers, of which 14 were clinically significant (Gleason score $\geq 3 + 4$). Multiparametric MRI identified 18 lesions; 14 of them were at least score 4 in the Prostate Imaging–Reporting and Data System. ^{68}Ga -PSMA11 and ^{68}Ga -RM2 PET/MRI each showed 23 positive intraprostatic lesions; 21 were congruent in 13 patients, and 5 were incongruent in 5 patients. Before HIFU, ^{68}Ga -PSMA11 identified all target tumors, whereas ^{68}Ga -RM2 PET/MRI missed 2 tumors. After HIFU, ^{68}Ga -RM2 and ^{68}Ga -PSMA11 PET/MRI both identified clinically significant residual disease in 1 patient. Three significant ipsilateral recurrent lesions were identified, whereas 1 was missed by ^{68}Ga -PSMA11. The pretreatment level of prostate-specific antigen decreased significantly after HIFU, by 66%. Concordantly, the pretreatment SUV_{max} decreased significantly after HIFU for ^{68}Ga -PSMA11 ($P = 0.001$) and ^{68}Ga -RM2 ($P = 0.005$). **Conclusion:** This pilot study showed that ^{68}Ga -PSMA11 and ^{68}Ga -RM2 PET/MRI identified the target tumor for HIFU in 100% and 86% of cases, respectively, and accurately verified response to treatment. PET may be a useful tool in the guidance and monitoring of treatment success in patients receiving focal therapy for PC. These preliminary findings warrant larger studies for validation.

Key Words: ^{68}Ga -RM2; ^{68}Ga -PSMA11; PET; prostate cancer; HIFU

J Nucl Med 2023; 64:592–597

DOI: 10.2967/jnumed.122.264783

Received Aug. 9, 2022; revision accepted Oct. 27, 2022.

For correspondence or reprints, contact Andrei Iagaru (aiagaru@stanford.edu).

Published online Nov. 3, 2022.

COPYRIGHT © 2023 by the Society of Nuclear Medicine and Molecular Imaging.

Standard treatment options for localized prostate cancer (PC) include active surveillance, radical prostatectomy, radiation (with or without hormonal therapy), and local therapy. Focal ablation is particularly of interest as whole-gland treatment with surgery or radiation may cause adverse events such as incontinence, impotence, and bowel or bladder dysfunction. These side effects may adversely impact the patients' quality of life (1–4). High-intensity focused ultrasound (HIFU) is a noninvasive local treatment that uses thermal energy to ablate low-risk PC lesions. Recently published data from large multicenter studies reported minimal impact on quality of life, with preservation of continence in 98% and of sexual function in 90% (5), and a 7-y failure-free survival rate of 69% (6). However, there is a 20%–40% rate of residual disease or relapse, requiring repeat HIFU. Treatment evaluation is an unmet need as there are no noninvasive, validated methods to assess success or failure (7). Posttreatment serum prostate-specific antigen (PSA) is a poor measure as it falls to a variable nadir due to continued production by residual prostate. The Phoenix criterion for biochemical failures after radiation therapy is commonly used after HIFU; however, it has poor sensitivity and specificity of only 65% and 77%, respectively (8). The subsequently introduced Stuttgart definition is specific for patients treated with HIFU and defines biochemical failure as the PSA nadir plus 1.2 ng/mL (9). The use of multiparametric MRI (mpMRI) for HIFU treatment assessment is impeded by signal alteration due to scar tissue, focal hemorrhage, and central necrosis (10–13). Therefore, posttreatment prostate biopsy remains the most accurate tool to evaluate treatment outcome but is invasive and includes significant risks such as pain, bleeding, and infection (14,15).

PET combined with MRI using radiopharmaceuticals that target prostate-specific membrane antigen (PSMA) or gastrin-releasing peptide receptors (GRPR)—both are overexpressed on PC cells—have been evaluated for staging and biochemical recurrence of PC. It may also be a useful technique to evaluate treatment outcome after HIFU. The effect of HIFU on the expression of PSMA or GRPR has not been investigated yet. In this study, we evaluated a novel approach using both ^{68}Ga -RM2 and ^{68}Ga -PSMA11 PET/MRI in each PC patient before and at a minimum of 6 mo after HIFU to assess the accuracy of target tumor localization and response to treatment.

MATERIALS AND METHODS

Participants

Participants with newly diagnosed PC scheduled to undergo HIFU were prospectively enrolled and scanned with ^{68}Ga -PSMA11 followed

by ^{68}Ga -RM2 PET/MRI within 2 wk, or vice versa. The local institutional review board approved this Health Insurance Portability and Accountability Act-compliant study (NCT03949517). All patients gave written informed consent. The participants' clinical characteristics before treatment are shown in Table 1.

PET/MRI Protocol

Imaging was performed using a 3-T time-of-flight-enabled PET/MRI scanner (Signa; GE Healthcare), as previously described (16,17). The pre-HIFU image acquisition started at 46.50 ± 3.50 min (range, 44.00–57.00 min) after injection of 151.33 ± 44.80 MBq (range,

70.30–222.00 MBq) of ^{68}Ga -PSMA11 and at 45.50 ± 2.12 min (range, 43.00–52.00 min) after injection of 138.80 ± 4.61 MBq (range, 132.98–150.20 MBq) of ^{68}Ga -RM2. Simultaneous PET/MRI was acquired from vertex to mid thigh with an acquisition time of 4 min per bed position for an overall scan length of 49.00 ± 16.96 min (range, 30.00–83.00 min) for ^{68}Ga -PSMA11 and 47.00 ± 6.58 min (range, 36.00–60.00 min) for ^{68}Ga -RM2. The PET/MRI examinations included a dedicated 20-min pelvic acquisition. These images were acquired after a delay of 23.00 ± 9.19 min (range, 22.00–49.00 min) for ^{68}Ga -PSMA11 and 25.00 ± 5.54 min (range, 11.00–37.00 min) for ^{68}Ga -RM2. The PET/MRI scans were performed 5.50 ± 2.50 d (range, 2.00–9.00 d) apart. The syntheses of ^{68}Ga -PSMA11 and ^{68}Ga -RM2 were previously described (18). The post-HIFU ^{68}Ga -PSMA11 and ^{68}Ga -RM2 image acquisition details were similar to pretreatment imaging (Table 2).

TABLE 1
Patients' Characteristics Before HIFU Ablation

Characteristic	Data
<i>n</i>	14
Age (y)	64.50 ± 8.00 (48.00–78.00)
PSA (ng/mL)	8.41 ± 3.47 (1.22–15.90)
PSA density (ng/mL ²)	0.23 ± 0.09 (0.07–0.31)
mpMRI	18 lesions
PI-RADS 5	3 (17%)
PI-RADS 4	11 (61%)
PI-RADS 3	4 (22%)
Biopsy, Gleason grade	18 lesions
1	3 (17%)
2	5 (28%)
3	7 (39%)
4	2 (11%)
5	1 (5%)
Risk	
Intermediate	13
High	1
Clinical stage	
T1c	5
T2a	2
T2b	4
T2c	3
^{68}Ga -PSMA11	
Injected activity (MBq)	151.33 ± 44.80 (70.30–222.00)
Uptake time (min)	46.50 ± 3.50 (44.00–57.00)
Length of PET/MRI (min)	49.00 ± 16.96 (30.00–83.00)
Delay to pelvic PET/MRI (min)	23.00 ± 9.19 (22.00–49.00)
^{68}Ga -RM2	
Injected activity (MBq)	138.80 ± 4.61 (132.98–150.20)
Uptake time (min)	45.50 ± 2.12 (43.00–52.00)
Length of PET/MRI (min)	47.00 ± 6.58 (36.00–60.00)
Delay to pelvic PET/MRI (min)	25.00 ± 5.54 (11.00–37.00)
Time between scans (d)	5.50 ± 2.50 (2.00–9.00)

Qualitative data are number and percentage; continuous data are median \pm SD and range.

mpMRI Protocol

All mpMRI was performed as routine clinical scans before and 1 y after HIFU using a 3-T scanner (MR750; GE Healthcare) with an external 32-channel body array coil. The imaging protocol consisted

TABLE 2
Patients' Characteristics After HIFU Ablation

Characteristic	Data
<i>n</i>	14
PSA (ng/mL)	2.83 ± 1.65 (0.02–5.79)
PSA density (ng/mL ²)	0.07 ± 0.04 (0.00–0.17)
PSA nadir (ng/mL)	2.80 ± 1.48 (0.01–5.79)
Time to PSA nadir (mo)	6.55 ± 5.92 (2.90–24.83)
Biopsy (<i>n</i> = 13)	
Residual lesions	
Clinically significant	1
Clinically insignificant	3
Recurrent lesions	
Clinically significant	3
Clinically insignificant	6
^{68}Ga -PSMA11	
Injected activity (MBq)	145.60 ± 37.75 (82.51–221.26)
Uptake time (min)	47.50 ± 2.40 (41.00–49.00)
Length of PET/MRI (min)	45.50 ± 5.90 (33.00–62.00)
Delay to pelvic PET/MRI (min)	26.00 ± 6.53 (22.00–48.00)
^{68}Ga -RM2	
Injected activity (MBq)	139.77 ± 5.04 (133.32–149.67)
Uptake time (min)	46.00 ± 3.14 (39.00–52.00)
Length of PET/MRI (min)	51.50 ± 9.53 (41.00–73.00)
Delay to pelvic PET/MRI (min)	26.00 ± 6.22 (21.00–47.00)
Time between scans (d)	5.00 ± 40.66 (2.00–172.00)
Time between pre- and post-HIFU scans (mo)	7.43 ± 2.37 (5.93–12.60)

Qualitative data are number and percentage; continuous data are median \pm SD and range.

of T2-weighted, diffusion-weighted, and dynamic contrast-enhanced sequences. The acquisition parameters were previously described in detail (19). The target tumor for HIFU treatment was determined on mpMRI and defined as having a Prostate Imaging–Reporting and Data System (PI-RADS) score of at least 4 and clinically significant PC (csPC) on biopsy (Gleason score $\geq 3 + 4$).

Image Analysis

Two nuclear medicine physicians, experienced in interpreting PSMA- and GRPR-targeted molecular imaging, reviewed and analyzed the PET images independently, in random order, and masked to the clinical results. A consensus reading was performed for discordant findings. The framework from the PROMISE criteria was used for PSMA PET interpretation. Focal uptake of ^{68}Ga -RM2 or ^{68}Ga -PSMA11 above the adjacent prostate background and not associated with physiologic accumulation was recorded as suggestive of PC. A region of interest was drawn over suspected lesions to measure SUV_{max} and SUV_{peak} . SUV_{peak} is defined as the average SUV within a small, fixed-size region of interest (1 cm^3).

mpMRI was analyzed using the PI-RADS criteria, version 2 (20). Lesions with a PI-RADS score of at least 3 were recorded. A PI-RADS score of 3 was considered equivocal for PC, PI-RADS 4 likely for PC, and PI-RADS 5 highly likely for PC.

HIFU

Focal HIFU ablation of localized PC was performed with curative intent using the Sonablate device (Sonacare Medical). One target tumor was treated per patient. Treated areas included the MRI lesion with an 8- to 10-mm margin of normal surrounding tissue. The follow-up included PSA and follow-up visits every 3 mo and mpMRI and biopsy at 1 y.

Prostate Biopsy

Prostate biopsy was performed under local anesthesia using MRI–ultrasound fusion and included targeted sampling of the treated zone, any MRI lesions, and standard-template 12-core biopsy with 1 core through the apex, mid, and base regions, both medially and laterally, from the left and right prostate lobes (21,22).

Statistical Analysis

Statistical analysis was performed using Stata, version 16.1 (Stata-Corp LP), and R, version 4.1.1 (r-project.org). Continuous data are presented as median \pm SD, range, and interquartile range. Comparison between biopsy-positive and biopsy-negative regions of PI-RADS, ^{68}Ga -PSMA11, and ^{68}Ga -RM2 (SUV_{max}), and between SUV_{max} and

SUV_{peak} for whole-body and delayed pelvic imaging before and after HIFU ablation, was done by the Wilcoxon rank sum test, adjusted for clustering. A *P* value of less than 0.05 was considered significant. Sensitivity and specificity (adjusted for clustering) were calculated using a segment-based approach in which the prostate was divided into the same 12 segments as for systematic prostate biopsy. The segments were dichotomized according to the pathologic findings from biopsy. Values are given as percentages with 95% CIs.

RESULTS

Fourteen men 64.5 ± 8.0 y old (range, 48–78 y) with newly diagnosed PC and scheduled to undergo HIFU were prospectively enrolled. Tables 1 and 2 summarize pre- and post-HIFU patient characteristics, respectively.

PSA and PSA Density

PSA and PSA density before HIFU ablation were 8.41 ± 3.47 ng/mL (range, 1.22–15.90 ng/mL) and 0.23 ± 0.09 ng/mL² (range, 0.07–0.31 ng/mL²), respectively. At posttreatment PET imaging, 7.43 ± 2.37 mo (range, 5.93–12.60 mo) after HIFU, PSA and PSA density decreased by 66% to 2.83 ± 1.65 ng/mL (range, 0.02–5.79 ng/mL) (*P* = 0.001) and 0.07 ± 0.04 ng/mL² (range, 0.00–0.17 ng/mL²) (*P* = 0.001), respectively. A PSA nadir of 2.80 ± 1.48 ng/mL (range, 0.01–5.79 ng/mL) was found at 6.55 ± 5.92 mo (range, 2.90–24.83 mo) after treatment.

mpMRI

Routine clinical pre-HIFU mpMRI identified 18 lesions (3 PI-RADS 5, 11 PI-RADS 4, and 4 PI-RADS 3). The dominant csPC lesion was treated with HIFU. The sensitivity and specificity of pre-HIFU mpMRI were 43% and 98%, respectively. After treatment, routine mpMRI was available for 13 participants because 1 patient was lost to follow-up 1 y after HIFU: 9 of 13 patients were negative, and 4 of 13 patients had a PI-RADS 3 lesion. One of these 4 correlated to residual Gleason 4 + 4 disease (mpMRI also identified 2 pathologic lymph nodes), 2 correlated to Gleason 3 + 3 residual lesions (not identified on PET because of urinoma), and 1 was benign on post-HIFU biopsy. One PI-RADS 4 lesion in the same participant was benign on biopsy as well. Significant ipsilateral (*n* = 3) and contralateral (*n* = 6) recurrences were all missed by mpMRI (negative scan). A direct comparison of mpMRI, ^{68}Ga -PSMA11, and ^{68}Ga -RM2 PET/MRI is shown in Table 3.

TABLE 3
Direct Comparison of mpMRI, ^{68}Ga -PSMA11, and ^{68}Ga -RM2 PET/MRI Findings Before and After HIFU Ablation

Parameter	mpMRI		^{68}Ga -PSMA11		^{68}Ga -RM2	
	Before HIFU	After HIFU	Before HIFU	After HIFU	Before HIFU	After HIFU
All lesions (<i>n</i>)	18 (PI-RADS 3: 4; PI-RADS 4: 11; PI-RADS 5: 3)	5 (PI-RADS 3: 4; PI-RADS 4: 1)	23	9 (2 residual; 7 recurrent)	23	9 (1 residual; 8 recurrent)
Target lesions	14	9/13 patients: negative; 3/13 patients: PI-RADS 3 (1 csPC, 2 ncsPC)	14	2 residual (1 csPC; 2 ncsPC)	12	1 residual (1 csPC)
Sensitivity	43%		81%		70%	
Specificity	98%		89%		88%	

TABLE 4

SUV_{max} and SUV_{peak} of Target Lesions in Whole Body and Delayed Pelvic ⁶⁸Ga-PSMA11 and ⁶⁸Ga-RM2 PET/MRI Before and After HIFU Ablation

Parameter	⁶⁸ Ga-PSMA11		⁶⁸ Ga-RM2	
	Whole body	Delayed pelvic	Whole body	Delayed pelvic
Before HIFU, SUV _{max}	9.51 (6.63–18.50)	8.91 (6.66–18.94)	7.70 (5.67–11.05)	7.48 (4.97–11.51)
After HIFU				
SUV _{max}	2.27 (1.80–2.78)	2.03 (1.80–2.51)	2.55 (2.07–3.48)	2.61 (1.68–2.74)
<i>P</i>	0.001	0.001	0.005	0.006
Before HIFU, SUV _{peak}	5.04 (3.97–8.84)	5.16 (4.27–9.50)	5.22 (4.15–8.05)	4.96 (4.02–8.57)
After HIFU				
SUV _{peak}	1.96 (1.89–2.31)	2.11 (1.83–2.39)	3.06 (2.85–3.49)	2.81 (2.22–3.08)
<i>P</i>	0.012	0.068	0.026	0.084

Data are median and interquartile range.

Prostate Biopsy

Before HIFU, prostate biopsies showed 18 lesions, of which 14 were csPC with a Gleason score of at least 3 + 4 and were determined to be target tumors for HIFU ablation. After treatment, prostate biopsy was available for 13 participants: Residual disease was detected in 4 patients: 1 was csPC with Gleason 4 + 4 (identified on both ⁶⁸Ga-PSMA11 and ⁶⁸Ga-RM2 PET/MRI), and 3 were Gleason 3 + 3 cancers (2/3 not seen on PET because of urinoma, 1/3 identified with ⁶⁸Ga-PSMA11 but missed on ⁶⁸Ga-RM2 PET/MRI). Outside the treated area, 3 ipsilateral Gleason 4 + 3 recurrences were found in 3 patients (2/3 seen with both radiopharmaceuticals, 1/3 missed by ⁶⁸Ga-PSMA11 but positive on ⁶⁸Ga-RM2) and subsequently received HIFU. Nonaggressive recurrence contralaterally was detected in 6 patients (1 lesion each was missed by either radiopharmaceutical in 2 different patients, the rest were identified with both ⁶⁸Ga-PSMA11 and ⁶⁸Ga-RM2 PET/MRI); 3 of these 6 lesions were known from pre-HIFU biopsy.

⁶⁸Ga-PSMA11 PET/MRI

Pre-HIFU ⁶⁸Ga-PSMA11 PET/MRI showed 23 intraprostatic lesions; all 14 target tumors for HIFU were correctly identified. Other positive lesions correlated to non-clinically significant PC (ncsPC) (*n* = 4) or high-grade prostatic intraepithelial neoplasia (*n* = 3) from pre-HIFU prostate biopsy. The sensitivity and specificity of pre-HIFU ⁶⁸Ga-PSMA11 PET/MRI were 81% and 89%, respectively. After HIFU ablation, ⁶⁸Ga-PSMA11 PET/MRI identified 9 lesions, which correlated to residual csPC (*n* = 1) and ncsPC (*n* = 1) and recurrent ipsilateral csPC (*n* = 2) and contralateral ncsPC (*n* = 5). The SUV_{max} from whole-body and dedicated pelvic imaging decreased significantly after HIFU, whereas SUV_{peak} showed significance only in the whole-body images. Table 4 summarizes all SUVs.

⁶⁸Ga-RM2 PET/MRI

The pre-HIFU ⁶⁸Ga-RM2 PET/MRI also showed 23 intraprostatic lesions, of which 12 of 14 (85.7%) target tumors for HIFU were identified. Other positive lesions correlated to ncsPC (*n* = 4), high-grade prostatic intraepithelial neoplasia (*n* = 3), and atypical small acinar proliferation suggestive of but nondiagnostic for PC (*n* = 1) in pre-HIFU biopsies. The sensitivity and specificity of pre-HIFU ⁶⁸Ga-RM2 PET/MRI were 70% and 88%, respectively.

After HIFU, ⁶⁸Ga-RM2 PET/MRI also identified 9 lesions, which correlated to residual csPC (*n* = 1), recurrent ipsilateral csPC (*n* = 3), and contralateral ncsPC (*n* = 5). Concordant with ⁶⁸Ga-PSMA11 PET, the SUV_{max} from whole-body and dedicated pelvic images decreased significantly after HIFU, whereas SUV_{peak} was significant only for the whole-body images (Table 4).

Comparison Between ⁶⁸Ga-PSMA11 and ⁶⁸Ga-RM2

Before HIFU, ⁶⁸Ga-PSMA11 and ⁶⁸Ga-RM2 PET/MRI were concordant in 21 of 23 lesions in 14 patients and discordant in 5 lesions in 5 patients. Except for the 2 target tumors missed by ⁶⁸Ga-RM2 PET, all target tumors were congruent (Fig. 1). Incongruent lesions correlated to atypical small acinar proliferation (*n* = 1) and false-positive uptake (*n* = 2) in pre-HIFU biopsy. After HIFU, ⁶⁸Ga-PSMA11 and ⁶⁸Ga-RM2 PET/MRI showed concordant uptake in a Gleason 4 + 4 residual lesion. In this participant, pretreatment ⁶⁸Ga-PSMA11 identified a positive pelvic lymph node that was subsequently treated with stereotactic body radiation therapy. On the posttreatment ⁶⁸Ga-PSMA11 PET, this lymph node showed resolution, but 2 new pelvic lymph nodes were identified; all were all negative on ⁶⁸Ga-RM2 PET. ⁶⁸Ga-RM2 PET also missed 1 nonsignificant residual lesion seen on ⁶⁸Ga-PSMA11, whereas ⁶⁸Ga-PSMA11 missed 1 recurrent csPC lesion identified on ⁶⁸Ga-RM2 PET. Both radiopharmaceuticals showed congruent uptake in 2 ipsilateral recurrent csPC lesions, which were treated with HIFU. Nonsignificant contralateral recurrent disease showed congruency in 4 patients, of which 3 were already seen in the pre-HIFU biopsies and were positive on both pretreatment scans. ⁶⁸Ga-PSMA11 missed a nonaggressive recurrence, which was seen on ⁶⁸Ga-RM2 PET, and vice versa in another patient. Two nonsignificant residual lesions were missed by both radiopharmaceuticals because of an adjacent urinoma. There were no false-positive findings on post-HIFU PET.

DISCUSSION

In this era driven by precise, personalized medicine, interest is growing in noninvasive, targeted, focal treatment of csPC lesions using HIFU, and adoption is widening. We hypothesized that noninvasive PET/MRI assessment of response to HIFU may be a useful tool. The effect of HIFU on PSMA- and GRPR-overexpressing PC

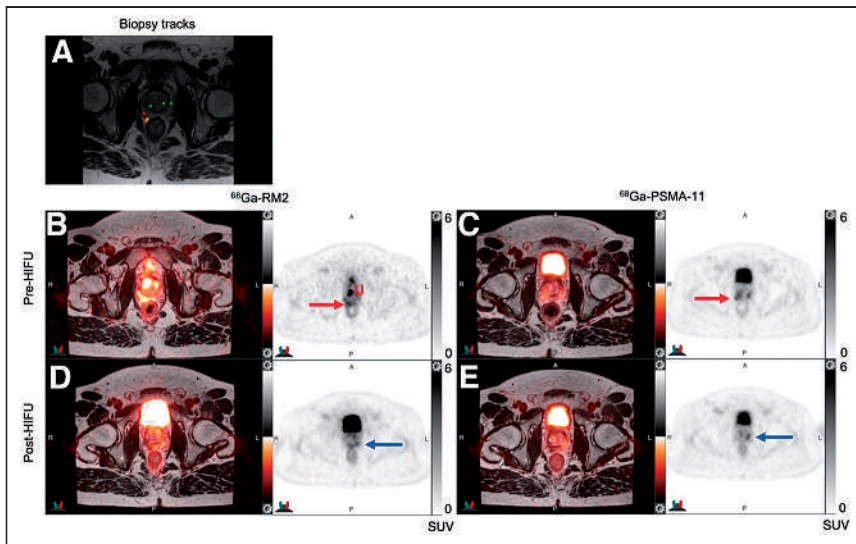


FIGURE 1. A 62-year-old man with Gleason 3 + 4 PC in right lateral base and Gleason 3 + 3 PC in right posterior base (A shows color-coded needle tracks from biopsy; green: benign, yellow: Gleason 3 + 3, red: Gleason \geq 3 + 4). He presented with PSA of 7.0 ng/mL and PSA density of 0.24 ng/mL². Pretherapy ⁶⁸Ga-RM2 (B) and ⁶⁸Ga-PSMA-11 (C) axial PET/MRI and PET, respectively, show focal uptake in right prostate lesion (red arrows). This was treated with HIFU, and 6 mo later, uptake resolved on ⁶⁸Ga-RM2 (D) and ⁶⁸Ga-PSMA11 (E) axial PET/MRI and PET, respectively. Focal uptake in left prostate (blue arrows) was subsequently biopsied and showed nonaggressive PC. U = urethra with excreted ⁶⁸Ga-RM2.

cells has not been investigated yet in a direct comparison. This prospective study showed that ⁶⁸Ga-RM2 and ⁶⁸Ga-PSMA11 PET/MRI are feasible for identification of the target lesion for HIFU, as well as for evaluation of treatment success. Therefore, repeated invasive prostate biopsies after HIFU may be avoided in some men.

Burger et al. were the first to evaluate a very specific subgroup of patients with residual csPC on biopsy but negative mpMRI results after HIFU with ⁶⁸Ga-PSMA11 PET/MRI (23). Six of the 10 patients were positive on ⁶⁸Ga-PSMA11, without any false-positives. The sensitivity, specificity, and positive and negative predictive values were 55%, 100%, 100%, and 85%, respectively. The authors concluded that ⁶⁸Ga-PSMA11 PET/MRI may be able to detect residual PC not seen on mpMRI after HIFU but acknowledged the risk of false-negative ⁶⁸Ga-PSMA11 PET results. In our study, both ⁶⁸Ga-PSMA11 and ⁶⁸Ga-RM2 accurately identified the only patient with residual csPC. ⁶⁸Ga-PSMA11 also detected 1 patient with non-aggressive residual disease, missed on ⁶⁸Ga-RM2. Because our patient cohort consisted mostly of those with negative mpMRI findings, and those negative for or with nonaggressive residual PC after HIFU, no direct comparison can be made between the studies. There are no other studies evaluating the use of ⁶⁸Ga-PSMA11 or ⁶⁸Ga-RM2 PET to guide or evaluate focal treatment of PC.

Before HIFU, ⁶⁸Ga-PSMA11 and ⁶⁸Ga-RM2 PET/MRI identified the target tumor in 100% and 86% of cases, respectively. These results are comparable to recently published detection rates of 98% and 95% for ⁶⁸Ga-PSMA11 and ⁶⁸Ga-RM2, respectively, in patients with newly diagnosed PC correlated with postprostatectomy pathologic findings (24). Most PET-positive lesions were concordant between the 2 radiopharmaceuticals. The discordant uptake pattern reflects the difference in expression pattern between PSMA and GRPR, which has previously been reported by our group (17,24,25) and is supported by immunohistochemistry

analyses (26), suggesting that PSMA- and GRPR-targeting radiopharmaceuticals may be complementary to each other. mpMRI was equivocal in 2 residual ncsPC lesions that PET missed, whereas the csPC residual and ipsilateral recurrent disease was missed by mpMRI. The only PI-RADS 4 lesion correlated to benign prostatic tissue in post-treatment biopsy. The post-HIFU mpMRI interpretation is impeded by signal alteration of the treated area, whereas ipsilateral recurrence is particularly difficult to read because of potential focal hemorrhage, edema, scar tissue, and central necrosis (10–13).

In the interpretation of post-HIFU ⁶⁸Ga-PSMA11 and ⁶⁸Ga-RM2 PET/MRI, we observed an intense PET signal correlating to or associated with a widened urethral lumen on the accompanying MRI, which could be “pulled” toward the treated area, most likely because of scar tissue formation after ablation. This has been previously described by Kirkham et al. as “capacious prostatic cavity continuous with the urethra” (11) and is similar to the change in prostate appearance after transurethral resection (27). This finding suggests that PET/MRI may be better suited to evaluate HIFU treatment outcome

than mpMRI and PET/CT because of high soft-tissue contrast and thus better delineation of structural changes and distinguishing of urinoma with excreted radiotracer from true residual tumor or ipsilateral recurrence.

The patients with Gleason 4 + 3 recurrence subsequently underwent HIFU ablation. This additional finding suggests that ⁶⁸Ga-PSMA11 and ⁶⁸Ga-RM2 PET/MRI may also play a role in delineating recurrent lesions for HIFU retreatment and therefore in guiding patient management after HIFU.

PSA decreased significantly after HIFU by 66% within 7 mo, and the PSA nadir occurred at 6.5 mo. These results are consistent with other studies reporting that the median time to the PSA nadir after HIFU varied from 3 to 12 mo, with a PSA reduction of between 53% and 84% (28–31).

Focal therapies aim to address patients who fall between active surveillance and radical whole-gland treatment. Finding a cutoff for when to treat with which modality remains difficult. No clear guidelines exist on optimal candidates for HIFU, as long-term results are still lacking. The most recent consensus, from 2017 (32), suggests HIFU for localized disease with low to intermediate risk; however, more recent trends favor active surveillance over treatment for low-risk cancers. One interesting finding in our study was the patient who showed metastatic disease before treatment but progression after HIFU. This suggests that HIFU is not suitable for metastasized-PC patients and supports the importance of molecular whole-body imaging.

Our study had 3 noteworthy limitations. The first was the small number of patients. This is common in pilot studies. Second, 1 participant lacked posttreatment biopsy and mpMRI, as he is still awaiting his 1-y follow-up. Delays in patient care due to the study’s being conducted during the coronavirus disease 2019 pandemic resulted in a wider time span of post-HIFU evaluations than originally planned. Third, the relatively short follow-up after HIFU

prevented us from investigating the correlation of signal loss on ^{68}Ga -RM2 and ^{68}Ga -PSMA11 PET with long-term outcome. However, the encouraging data presented here warrant larger studies investigating the role of ^{68}Ga -RM2 and ^{68}Ga -PSMA11 PET/MRI in focal-therapy patient selection, treatment planning, and follow-up evaluation.

CONCLUSION

In this pilot study, ^{68}Ga -PSMA11 and ^{68}Ga -RM2 PET/MRI identified the dominant lesion for HIFU ablation in 100% and 86% of cases, respectively, and accurately verified response to treatment. Clinically significant residual disease and ipsilateral recurrences were accurately identified by both radiopharmaceuticals. PET may be a useful tool in the guidance and monitoring of treatment success in patients receiving focal therapy. Further evaluation in larger cohorts is needed to validate these results.

DISCLOSURE

The study was partially supported by GE Healthcare. No other potential conflict of interest relevant to this article was reported.

KEY POINTS

QUESTION: Is the use of ^{68}Ga -PSMA11 and ^{68}Ga -RM2 PET/MRI feasible to identify the target tumor for HIFU and assess treatment success in patients with intermediate-risk PC?

PERTINENT FINDINGS: ^{68}Ga -PSMA11 and ^{68}Ga -RM2 PET/MRI identified the target tumor for HIFU ablation in 100% and 86% of cases, respectively. Clinically significant residual disease and ipsilateral recurrences were accurately identified by both radiopharmaceuticals. ^{68}Ga -PSMA11 additionally detected lymph node metastases, which ultimately changed patient management.

IMPLICATIONS FOR PATIENT CARE: Use of ^{68}Ga -PSMA11 and ^{68}Ga -RM2 PET/MRI was feasible for monitoring HIFU treatment success and may avoid repeated biopsies for treatment verification.

REFERENCES

1. Nepple KG, Stephenson AJ, Kallogjeri D, et al. Mortality after prostate cancer treatment with radical prostatectomy, external-beam radiation therapy, or brachytherapy in men without comorbidity. *Eur Urol*. 2013;64:372–378.
2. Handy FC, Donovan JL, Lane JA, et al. 10-year outcomes after monitoring, surgery, or radiotherapy for localized prostate cancer. *N Engl J Med*. 2016;375:1415–1424.
3. Barocas DA, Alvarez J, Resnick MJ, et al. Association between radiation therapy, surgery, or observation for localized prostate cancer and patient-reported outcomes after 3 years. *JAMA*. 2017;317:1126–1140.
4. Capogrosso P, Vertosick EA, Benfante NE, et al. Are we improving erectile function recovery after radical prostatectomy? analysis of patients treated over the last decade. *Eur Urol*. 2019;75:221–228.
5. Lovegrove CE, Peters M, Guillaumier S, et al. Evaluation of functional outcomes after a second focal high-intensity focused ultrasonography (HIFU) procedure in men with primary localized, non-metastatic prostate cancer: results from the HIFU Evaluation and Assessment of Treatment (HEAT) registry. *BJU Int*. 2020;125:853–860.
6. Reddy D, Peters M, Shah TT, et al. Cancer control outcomes following focal therapy using high-intensity focused ultrasound in 1379 men with nonmetastatic prostate cancer: a multi-institute 15-year experience. *Eur Urol*. 2022;81:407–413.
7. Barret E, Harvey-Bryan KA, Sanchez-Salas R, Rozet F, Galiano M, Cathelineau X. How to diagnose and treat focal therapy failure and recurrence? *Curr Opin Urol*. 2014;24:241–246.
8. Roach M III, Hanks G, Thames H Jr, et al. Defining biochemical failure following radiotherapy with or without hormonal therapy in men with clinically localized prostate cancer: recommendations of the RTOG-ASTRO Phoenix Consensus Conference. *Int J Radiat Oncol Biol Phys*. 2006;65:965–974.
9. Blana A, Brown SC, Chaussy C, et al. High-intensity focused ultrasound for prostate cancer: comparative definitions of biochemical failure. *BJU Int*. 2009;104:1058–1062.
10. Rouvière O, Lyonnet D, Raudrant A, et al. MRI appearance of prostate following transrectal HIFU ablation of localized cancer. *Eur Urol*. 2001;40:265–274.
11. Kirkham AP, Emberton M, Hoh IM, Illing RO, Freeman AA, Allen C. MR imaging of prostate after treatment with high-intensity focused ultrasound. *Radiology*. 2008;246:833–844.
12. Rosenkrantz AB, Taneja SS. Radiologist, be aware: ten pitfalls that confound the interpretation of multiparametric prostate MRI. *AJR*. 2014;202:109–120.
13. Rouvière O, Girouin N, Glas L, et al. Prostate cancer transrectal HIFU ablation: detection of local recurrences using T2-weighted and dynamic contrast-enhanced MRI. *Eur Radiol*. 2010;20:48–55.
14. Tay KJ, Amin MB, Ghai S, et al. Surveillance after prostate focal therapy. *World J Urol*. 2019;37:397–407.
15. Loeb S, Vellekoop A, Ahmed HU, et al. Systematic review of complications of prostate biopsy. *Eur Urol*. 2013;64:876–892.
16. Duan H, Baratto L, Hatami N, et al. Reduced acquisition time per bed position for PET/MRI using ^{68}Ga -RM2 or ^{68}Ga -PSMA-11 in patients with prostate cancer: a retrospective analysis. *AJR*. 2022;218:333–340.
17. Minamimoto R, Hancock S, Schneider B, et al. Pilot comparison of ^{68}Ga -RM2 PET and ^{68}Ga -PSMA-11 PET in patients with biochemically recurrent prostate cancer. *J Nucl Med*. 2016;57:557–562.
18. Minamimoto R, Sonni I, Hancock S, et al. Prospective evaluation of ^{68}Ga -RM2 PET/MRI in patients with biochemical recurrence of prostate cancer and negative findings on conventional imaging. *J Nucl Med*. 2018;59:803–808.
19. Sonn GA, Fan RE, Ghanouni P, et al. Prostate magnetic resonance imaging interpretation varies substantially across radiologists. *Eur Urol Focus*. 2019;5:592–599.
20. Weinreb JC, Barentsz JO, Choyke PL, et al. PI-RADS prostate imaging—reporting and data system: 2015, version 2. *Eur Urol*. 2016;69:16–40.
21. Heidenreich A, Bastian PJ, Bellmunt J, et al. EAU guidelines on prostate cancer. Part 1: screening, diagnosis, and local treatment with curative intent—update 2013. *Eur Urol*. 2014;65:124–137.
22. Wolf AM, Wender RC, Etzioni RB, et al. American Cancer Society guideline for the early detection of prostate cancer: update 2010. *CA Cancer J Clin*. 2010;60:70–98.
23. Burger IA, Muller J, Donati OF, et al. ^{68}Ga -PSMA-11 PET/MR detects local recurrence occult on mpMRI in prostate cancer patients after HIFU. *J Nucl Med*. 2019;60:1118–1123.
24. Duan H, Baratto L, Fan RE, et al. Correlation of ^{68}Ga -RM2 PET with postsurgery histopathology findings in patients with newly diagnosed intermediate- or high-risk prostate cancer. *J Nucl Med*. 2022;63:1829–1835.
25. Baratto L, Song H, Duan H, et al. PSMA- and GRPR-targeted PET: results from 50 patients with biochemically recurrent prostate cancer. *J Nucl Med*. 2021;62:1545–1549.
26. Touijer KA, Michaud L, Alvarez HAV, et al. Prospective study of the radiolabeled GRPR antagonist BAY86-7548 for positron emission tomography/computed tomography imaging of newly diagnosed prostate cancer. *Eur Urol Oncol*. 2019;2:166–173.
27. Sheu MH, Chiang H, Wang JH, Chang YH, Chang CY. Transurethral resection of the prostate-related changes in the prostate gland: correlation of MRI and histopathology. *J Comput Assist Tomogr*. 2000;24:596–599.
28. Dickinson L, Ahmed HU, Hindley RG, et al. Prostate-specific antigen vs. magnetic resonance imaging parameters for assessing oncological outcomes after high intensity-focused ultrasound focal therapy for localized prostate cancer. *Urol Oncol*. 2017;35:30.e9–30.e15.
29. Chapelon JY, Rouvière O, Crouzet S, Gelet A. Prostate focused ultrasound therapy. *Adv Exp Med Biol*. 2016;880:21–41.
30. Rischmann P, Gelet A, Riche B, et al. Focal high intensity focused ultrasound of unilateral localized prostate cancer: a prospective multicentric hemiablation study of 111 patients. *Eur Urol*. 2017;71:267–273.
31. Ahmed HU, Dickinson L, Charman S, et al. Focal ablation targeted to the index lesion in multifocal localised prostate cancer: a prospective development study. *Eur Urol*. 2015;68:927–936.
32. Tay KJ, Scheltema MJ, Ahmed HU, et al. Patient selection for prostate focal therapy in the era of active surveillance: an international Delphi consensus project. *Prostate Cancer Prostatic Dis*. 2017;20:294–299.

¹⁸F-PSMA Cerenkov Luminescence and Flexible Autoradiography Imaging in a Prostate Cancer Mouse Model and First Results of a Radical Prostatectomy Feasibility Study in Men

Pedro Fragoso Costa^{*1,2}, Lukas Püllen^{*2,3}, Claudia Kesch^{2,3}, Ulrich Krafft^{2,3}, Stephan Tschirdewahn^{2,3}, Alexandros Moraitis^{1,2}, Jan Philipp Radtke^{2,3}, Saskia Ting⁴, Michael Nader^{1,2}, Jasmin Wosniack^{1,2}, David Kersting^{1,2}, Katharina Lückerath^{1,2}, Ken Herrmann^{1,2}, Wolfgang Peter Fendler^{1,2}, Boris Alexander Hadaschik^{2,3}, and Christopher Darr^{2,3}

¹Department of Nuclear Medicine, University Hospital Essen, Essen, Germany; ²German Cancer Consortium–University Hospital Essen, Essen, Germany; ³Department of Urology, University Hospital Essen, Essen, Germany; and ⁴Institute of Pathology, University Duisburg–Essen, Essen, Germany

Intraoperative identification of positive resection margins (PRMs) in high-risk prostate cancer (PC) needs improvement. Cerenkov luminescence imaging (CLI) with ⁶⁸Ga-PSMA-11 is promising, although limited by low residual activity and artificial signals. Here, we aimed to assess the value of CLI and flexible autoradiography (FAR) with ¹⁸F-PSMA-1007. **Methods:** Mice bearing subcutaneous PSMA-avid RM1-PGLS tumors were administered ¹⁸F-PSMA-1007, and PET/CT was performed. After the animals had been killed, organs were excised and measured signals in CLI and FAR CLI were correlated with tracer activity concentrations (ACs) obtained from PET/CT. For clinical assessment, 7 high-risk PC patients underwent radical prostatectomy immediately after preoperative ¹⁸F-PSMA PET/CT. Contrast-to-noise ratios (CNRs) were calculated for both imaging modalities in intact specimens and after incision above the index lesion. **Results:** In the heterotopic in vivo mouse model ($n = 5$), CLI did not detect any lesion. FAR CLI detected a distinct signal in all mice, with a lowest AC of 7.25 kBq/mL (CNR, 5.48). After incision above the index lesion of the prostate specimen, no increased signal was observed at the cancer area in CLI. In contrast, using FAR CLI, a signal was detectable in 6 of 7 patients. The AC in the missed index lesion was 1.85 kBq/mL, resulting in a detection limit of at least 2.06 kBq/mL. Histopathology demonstrated 2 PRMs, neither of which was predicted by CLI or FAR CLI. **Conclusion:** ¹⁸F-PSMA FAR CLI was superior to CLI in tracer-related signal detectability. PC could be visualized in radical prostatectomy down to 2.06 kBq/mL. However, the detection of PRMs was limited. Direct anatomic correlation of FAR CLI is challenging because of the scintillator overlay.

Key Words: flexible autoradiography; Cerenkov luminescence imaging; prostate cancer; margin assessment

J Nucl Med 2023; 64:598–604
DOI: 10.2967/jnumed.122.264670

Negative resection margins are a key component of tumor surgery in curatively intended interventions. Radical prostatectomy (RP) is one of the treatment options, along with radiotherapy, in men with localized or locally advanced prostate cancer (PC) (1). Positive resection margins (PRMs) occur in 11%–38% of patients undergoing RP, resulting in a higher risk of recurrence and disease-related mortality by a factor of 3 (2,3).

Preoperative MRI and nomograms have become widely used for local staging and for prediction of extracapsular extension. Recently, PSMA PET/CT was also included in the primary diagnosis of high-risk PC in the guidelines (1). Besides this, the use of intraoperative frozen section analysis reduces PRMs to 15% for all stages (4–6). Consequently, there is a wish to accurately detect malignant areas in real time during RP to ensure complete removal of PC.

For margin assessment, there currently are several newly implemented technologies with promising results, but some lack the large clinical studies required for subsequent use in clinical routine. Intraoperative conditions affecting the signal, long imaging times, and comparison with histopathology results are the main challenges (7,8).

Previously developed γ -counters are well established with single-photon-emitting radionuclides (9). Maurer et al. demonstrated reliable identification of small or atypically localized lesions for ^{99m}Tc-PSMA-guided surgery. The procedure has proven to be valuable for the successful intraoperative detection and removal of metastatic lesions in PC patients scheduled for salvage surgery (10–13).

The same technique has been successfully applied to β^+ -emitters, giving way to potentially every radioligand in diagnostic PET/CT to be used in radioguided surgery (14). Other ex vivo imaging techniques, such as small-animal PET/CT for 3-dimensional analysis of lesions, which might provide volumetric information about the removed specimens, currently require further study-based investigation (15). In patients with biochemical recurrence, PSMA PET/CT demonstrates high accuracy, allowing surgical resection to be pursued for single lymph node metastases. Recently, the introduction of a so-called drop-in γ -probe has allowed for PSMA-guided surgery during minimally invasive robot-assisted surgery. Intraoperatively, γ -probes not only facilitate intraoperative in vivo guidance but also enable ex vivo measurements to confirm successful resection of

Received Jul. 14, 2022; revision accepted Oct. 27, 2022.
For correspondence or reprints, contact Christopher Darr (christopher.darr@uk-essen.de).
^{*}Contributed equally to this work.
Published online Nov. 10, 2022.
COPYRIGHT © 2023 by the Society of Nuclear Medicine and Molecular Imaging.

these metastatic PC lesions, with a specificity of more than 95% for ^{99m}Tc -PSMA-I&S (11).

Cerenkov luminescence imaging (CLI) is based on the detection of photons produced in a dielectric medium, when the medium interacts with β -particles traveling at a speed greater than the velocity of light. Cerenkov luminescence comprises predominantly ultraviolet and blue light, which is highly susceptible to attenuation in biologic tissue, therefore limiting CLI to the detection of signals emitted in superficial tissue layers (16,17). In the context of RP, the detected signals can accordingly be indicative of a PRM (13,14).

The feasibility and safety of ^{68}Ga -PSMA CLI have recently been demonstrated in RP. However, so far, only feasibility studies have been described, and larger multicenter randomized trials are pending. In addition, clinical application without intraoperative tracer injection is challenged by the short half-life of ^{68}Ga and the time required for prostate removal (18–20). ^{18}F -PSMA CLI would easily overcome this restriction with respect to the half-life. However, 1 limitation for ^{18}F may arise from having a theoretically 26-fold lower Cerenkov light yield compared with ^{68}Ga , which is caused by the lower β^+ -energy (21).

An alternative way of generating photons that can be detected by the same imaging system as in CLI may be introduced by adding a scintillator between the specimen and the detectors. In this novel approach, called flexible autoradiography (FAR), scintillations are produced by a micrometers-thick flexible scintillating film draped over an excised specimen (Supplemental Fig. 1; supplemental materials are available at <http://jnm.snmjournals.org>). The physical principle differs from CLI in that the high-energy β -particles from the radiotracer interact with the scintillator, which subsequently produces photons in the visible light spectrum. Since the Cerenkov photons are also detected, this is referred to as FAR CLI. The main advantage of a flexible scintillation film over conventional rigid autoradiography techniques is that the former conforms to the shape of the excised specimen. By maximizing the contact area, sectioning of the tissue can be eliminated and signal intensity increased. The thinness of a flexible scintillator makes it insensitive to the ^{18}F 511-keV γ -photons (22,23). FAR CLI in an in vitro preclinical application increased the signal for ^{18}F by a factor of 11, allowing for further development of ^{18}F tracers also in the context of intraoperative imaging (24). The behavior of ^{18}F -PSMA CLI and ^{18}F -PSMA-FAR CLI in human perfused tissue undergoing RP is unknown.

The primary objective of the study was to investigate the feasibility of both modalities in RP, with examination of the minimum detectable activity level as a secondary objective. We first investigated the applicability of both imaging modalities— ^{18}F -PSMA CLI and ^{18}F -PSMA-FAR CLI—in a mouse model that possesses optical characteristics similar to those of prostate tissue, and we then translated the findings to RP. To our knowledge, we are the first to perform CLI and FAR CLI using ^{18}F -PSMA in PC patients.

MATERIALS AND METHODS

To investigate the imaging behavior and minimum detectable activity concentration (AC) of ^{18}F -PSMA-1007 in CLI and FAR CLI, a 2-step approach was used (Fig. 1). First, multimodal PET/CT (β -Cube/X-Cube; Molecubes), as well as CLI and FAR CLI imaging with the LightPath system (Lightpoint Medical Ltd.), was performed on mice bearing subcutaneous PSMA-avid RM1-PGLS tumors (25). Subsequently, the findings were transferred and evaluated in RP. The studies were formally approved by the North Rhine–Westphalia State Agency for Nature, Environment, and Consumer (LANUV; Z.81-02.04.2018.A090) and the local Ethical Committee of the University of Duisburg–Essen (19-8749-BO). Additionally, a dilution series with ^{18}F -PSMA was prepared and used to measure CLI and FAR CLI in Eppendorf tubes and assess the device's performance with respect to linearity and minimum detectable AC in the absence of tissue.

Preclinical Setup: Mouse Model

RM1-PGLS cells were cultured in Rosewell Park Memorial Institute 1640 medium/10% fetal bovine serum at 37°C and 5% CO_2 . Contamination with *Mycoplasma* was excluded using the Venor GeM *Mycoplasma* detection kit (Sigma Aldrich).

Male C57BL/6 mice (5–12 wk old; Charles River) were bred and housed under pathogen-free conditions, with food and water ad libitum and a 12 h–12 h light–dark cycle. Eight days before intraperitoneal injection of 2.61 MBq (range, 2.02–3.06 MBq) of ^{18}F -PSMA-1007, RM1-PGLS (0.1×10^6 cells in 1:1 Matrigel [Corning]:phosphate-buffered saline) were injected subcutaneously into the shoulder region of 5 mice. Small-animal PET/CT was performed 2 h after injection, and reconstructed ACs were used to correlate the CLI and FAR CLI signals. Immediately after PET/CT, the mice were killed for CLI and FAR CLI. The first CLI/FAR CLI imaging set-up included the whole mouse to visualize both kidneys and the shoulder region in the LightPath system. The kidneys and tumor tissue were then excised and reexamined with the LightPath system. The main rationale

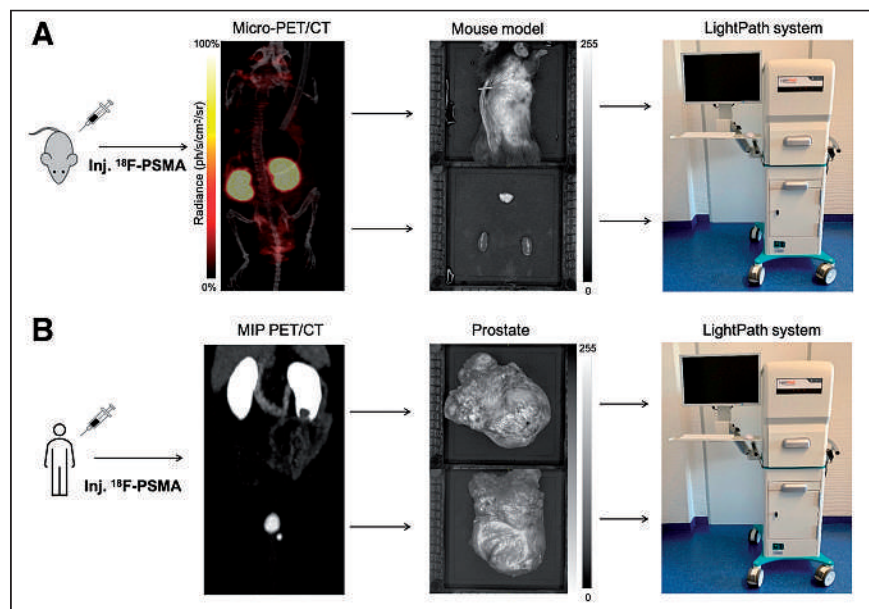


FIGURE 1. Study design. (A) Injection of ^{18}F -PSMA into tumor-bearing mice. Two hours afterward, small-animal PET/CT was performed. Next, CLI and FAR of whole mouse were acquired, followed by analysis of excised kidneys and PC tissue. (B) In second approach, prostate specimen in patients undergoing RP was examined, with direct preoperative ^{18}F -PSMA PET/CT. Removal of prostate was followed by immediate examination of intact prostate specimen and target lesion (after incision) by CLI and FAR. MIP = maximum-intensity projection.

for using mouse specimens was that, in principle, they should have optical characteristics similar to those of the prostate and therefore provide a more valid surrogate for sensitivity than Eppendorf tubes, for example (26).

Clinical Setup: RP

Patients with histologically confirmed PC without metastases on conventional staging were scheduled for RP. On the day of surgery, ^{18}F -PSMA-1007 was injected intravenously for routine PSMA PET staging before surgery (27). Approximately 60 min after injection, PET/CT was performed and assessed by dedicated specialists in nuclear medicine. In the case of high-volume metastatic disease on PET/CT, same-day surgery would have been cancelled. After PET/CT, RP was performed by 1 experienced surgeon ahead of extended pelvic lymph node dissection to minimize signal intensity reduction from radiotracer decay in the time between ^{18}F -PSMA injection and CLI/FAR CLI imaging. After retrieval of the prostate, it was rinsed twice to clear any potential radioactive contamination from blood or urine, followed by imaging of the entire specimen. Two or 3 images were necessary to capture all sides of the prostate. MRI-guided incision above the index lesion was then performed, followed by imaging (CLI and FAR CLI) of the lesion. This allowed direct examination of the tumor tissue with assessment of the present luminescence, corresponding to a PRM. On completion of the investigational imaging, the prostatectomy specimen was sent for postoperative histopathologic analysis. We recently demonstrated that a single injection of ^{68}Ga -PSMA as part of the PET/CT/CLI procedure is associated with acceptable occupational exposure (28). According to the model, the use of ^{18}F -PSMA would increase occupational exposure comparatively to ^{68}Ga -PSMA, allowing for 117 procedures before reaching the lower occupational yearly limit of 6 mSv. The exposed personnel are continuously monitored in accordance with the legal requirements. Because of the design of this feasibility study, the surgical course remained unaffected by the intraoperative imaging results, and no further tissue was resected if positive margins were suspected.

Imaging and Image Analysis

The LightPath system, an in vitro diagnostic device, was used to visualize the location of ^{18}F -PSMA for CLI and FAR CLI. This system was further described by Ciarocchi et al. (29). Both a luminescence image and a gray-scaled image of the specimen were captured through the system. Both CLI and FAR CLI were acquired in a standardized manner, with an acquisition time of 300 s, 8×8 binning, and no optical filter (29). The images had to be acquired in a light-tight chamber. The 12- μm -thick flexible scintillating film (Lightpoint Medical Ltd.) used in FAR CLI consisted of a multilayer sandwich construction as follows: 3 μm of mylar, 6 μm of P43 scintillating phosphor, and 3 μm of mylar (22).

Background signals and elevated signals of both imaging modalities were subsequently analyzed using PMOD (version 3.204; PMOD Technologies LLC). Mean radiance (photons/s/cm²/sr) was measured in regions of interest with a 50% threshold. Two-dimensional regions of interest were selected in areas showing increased signal intensity (tumor) or no increased signal (tissue background) to calculate contrast-to-noise ratios (CNRs):

$$\text{CNR} = \frac{\text{tumor average} - \text{background average}}{\text{background SD}}$$

In the absence of increased signal, the corresponding MRI-informed target lesion was contoured. In terms of detectability, foci were

considered sufficiently visible with a CNR of 5 or more, a condition also referred to as the Rose criterion (30).

Statistical Analysis

Numeric variables were summarized with median values and interquartile ranges, and categorical variables were summarized with proportions (%). To compare the medians of nonparametric data, the Mann-Whitney *U* test was used for 2 groups. The Spearman correlation coefficient was used for correlation, with significance set at a *P* value of less than 0.05. The CLI CNR values were plotted as a function of the measured PET mean AC (decay-corrected to the time of CLI), and a linear regression model (least-squares method) was applied, constraining the model to pass at the origin (i.e., the condition in which there is no tracer, when the CNR output should be close to zero). Statistical analysis was performed with SPSS Statistics, version 26 (IBM).

RESULTS

Preclinical Setup: Mouse Model

Our in vitro assay with ^{18}F -PSMA demonstrated activity levels in Eppendorf tubes of up to 5.46 kBq/mL for CLI and 1.60 kBq/mL for FAR CLI (Supplemental Fig. 2). Linear regression between AC and CNR revealed r^2 values of 0.91 and 0.85 (both $P < 0.0001$).

In small-animal PET/CT, the reconstructed median AC 2 h after tracer administration was 651.72, 608.56, and 52.99, for the left kidney, right kidney, and PC tissue, respectively. Linear regression between CLI CNR and the decay-corrected PET AC of the small-animal PET/CT images 2 h after injection demonstrated r^2 values of 0.92 ($P < 0.0001$) and 0.62 ($P < 0.0001$) for the excised organs and whole mouse, respectively (Fig. 2).

During examination of the whole mouse, visualization of the subcutaneous PC tissue was not possible on CLI in any of the 5 cases. In FAR CLI, 3 cases showed a weak signal with a minimum AC of 22.16 kBq/mL at a CNR of 7.07. Regarding the examination of excised PC tissue, on CLI no signal was detectable with a maximum AC of up to 15 kBq/mL. In contrast, ^{18}F -PSMA uptake could be visualized by FAR CLI in all 5 PC samples, with a lowest detected AC and CNR of 7.25 kBq/mL and 5.48, respectively (Fig. 3). Despite the different detection threshold, there was no statistical difference between FAR CLI and CLI ($P < 0.09$), and least-squares linear regression showed good agreement between the two modalities ($r^2 = 0.75$; $P = 0.05$). Direct examination of high ACs revealed a contiguous uptake region in the kidneys and PC tissue on FAR CLI. The signal from the PC tumors could be visualized reliably in the single examination (Supplemental Fig. 3). Consequently, the specimens were placed farther apart in the subsequent measurements.

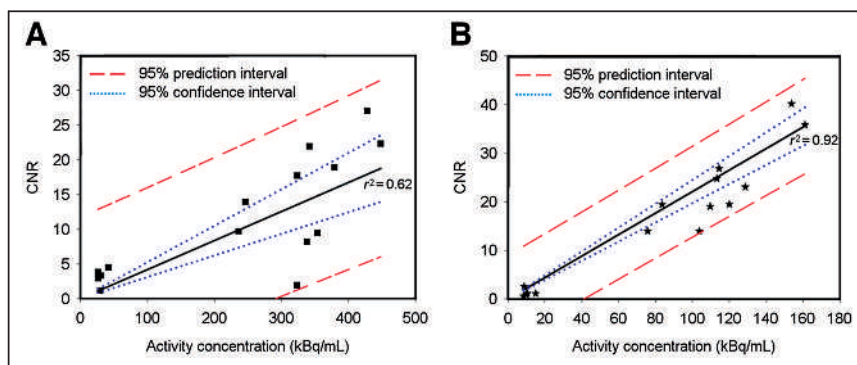


FIGURE 2. Linear regression of preclinical CLI with standardized imaging protocol. CNR is plotted against small-animal PET/CT AC. (A) PET vs. whole-mouse CLI comparison. (B) PET vs. excised kidneys and PC tissue comparison.

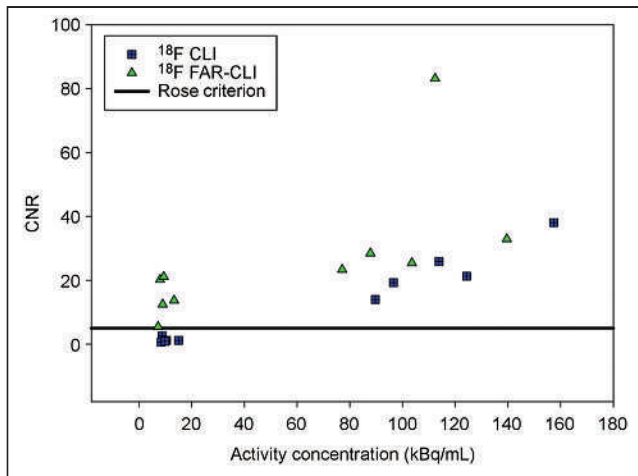


FIGURE 3. Visual detectability of excised kidneys and PC tissue. CNR is plotted against small-animal PET/CT AC. Highest AC region corresponds to signals from kidneys, whereas lowest cluster refers to PC signals. Foci with CNR ≥ 5 were considered detectable (Rose criterion).

At time of imaging, there was no significant difference in tracer AC between CLI and FAR CLI, but there was a significant increase in the CNR of visible foci (Supplemental Table 1). There was a strong correlation between a higher AC of the excised kidneys and PC tissue with a higher CNR, with a Spearman ρ of 0.783 ($P < 0.001$) for CLI and 0.712 ($P < 0.001$) for FAR CLI. Examination of the whole mouse also showed a strong correlation, with a Spearman ρ of 0.559 ($P < 0.001$) for CLI and 0.379 ($P = 0.01$) for FAR CLI.

Clinical Setup: RP

Seven patients were included in this feasibility study, among whom 6 had a high risk of progression according to the guidelines of the National Comprehensive Cancer Network (31). Imaging and patient characteristics are displayed in Table 1.

CLI detected a median of 2 lesions on the prostate surface, 1 of which was always at the bladder neck, with a median CNR of 33.96 (Table 2). In terms of CNR and number of lesions detected, there was a significant reduction using FAR CLI ($P = 0.02$) at comparable AC levels. Two patients showed PRMs after histopathologic evaluation. The PRMs consisted once of an International Society of Urological Pathology Gleason Grading Group (ISUP-GGG) of 4 with a diameter of 2 mm. Both CLI and FAR CLI showed no signal in the corresponding location. The second PRM, with an ISUP-GGG of 1 and a diameter of 1 mm, also showed no corresponding image morphologic correlate on CLI and FAR CLI. The PRM was histopathologically located at the right dorsal apex. CLI and FAR CLI showed a suggestive signal at the right lateral apex (Supplemental Fig. 4).

After incision over the MRI-informed index lesion, no luminescence on CLI was detectable, with a median CNR of 0.26. The mean gain in the sensitivity of FAR CLI in comparison to CLI was evaluated for Eppendorf tubes by calculating the fold increase in radiance normalized for AC. FAR CLI showed an approximately 2.1-fold radiance enhancement (Supplemental Fig. 5). Median AC at the time of incision was 3.06 kBq/mL. In contrast, a suggestive luminescence of PC was detectable in 6 of 7 patients on FAR CLI (Fig. 4). The AC of the 1 missed index lesion was 1.85 kBq/mL, resulting in a detection limit of at least 2.06 kBq/mL with a median

TABLE 1
Nuclear Medicine and Patient Characteristics

Characteristic	Data
Imaging	
Activity injected (MBq)	312 (280–332)
Tracer activity at PET/CT (kBq/mL)	17.71 (12.46–34)
Activity at CLI (kBq/mL)	3.54 (2.57–6.91)
Time from injection to CLI/FAR CLI (min)	329 (308–333)
CNR	
CLI	0.26 (0–1.5)
FAR CLI	9.13 (4.13–19.23)
Patient	
Age (y)	65.14 (63–67)
Initial PSA (ng/mL)	11 (5.1–22)
NCCN risk at biopsy	
High risk	6 (86%)
Intermediate risk	1 (14%)
NCCN risk score at final histopathology	
High risk	5 (71%)
Intermediate risk	2 (29%)
Resection status	
R1 resection	2 (29%)
R0 resection	5 (71%)

PSA = prostate-specific antigen; NCCN = National Comprehensive Cancer Network.

Qualitative data are number and percentage; continuous data are median and interquartile range.

CNR of 8.78. Direct anatomic correlation was challenging because of the scintillator overlay.

DISCUSSION

In mice with subcutaneous PSMA-avid PC, different levels of AC were evaluated in terms of visualization. Because of the difference in tracer uptake between kidneys and PC tissue, it was possible to generate a broad spectrum of signals over time. Previously, Olde Heuvel et al. described a detection limit of 3.42 kBq/mL for ^{18}F -CLI in vitro (32). Our in vitro assay demonstrated similar findings, with a detection limit in Eppendorf tubes of 5.46 kBq/mL for CLI and 1.60 kBq/mL for FAR CLI. Such a radiance enhancement was also reported by Pratt et al., who evaluated nanoparticles in the presence of β -emitters (33). In contrast, no significant CLI signal from PC tissue up to 15 kBq/mL was observed in our mouse model. The discrepancies between in vitro and mouse measurements can be explained by the absorption (e.g., by hemoglobin) and scattering in biologic tissues, severely limiting sensitivity (34). On the basis of our study design with preoperative tracer injection and an estimated time from injection to prostate examination of approximately 5 h, ACs above 15 kBq/mL are not expected. In contrast to CLI, FAR CLI visualized PC tissue up to an activity of 7.25 kBq/mL. A clear

TABLE 2
Cerenkov Luminescence and Autoradiography Imaging Measurements of Prostatectomy Specimen with Corresponding Activity Levels

Parameter	CLI	FAR CLI	P
Intact specimen (n = 7)			
Activity (kBq/mL)	3.53 (2.57–6.91)	3.95 (2.16–7.22)	NS
CNR	33.96 (15.71–43.29)	6.13 (4.07–21.43)	0.02
Lesions	2 (1–2)	1 (0.5–1)	0.02
Incised specimen (n = 7)			
Activity (kBq/mL)	3.06 (1.98–5.98)	2.8 (2.06–5.72)	NS
CNR	0.26 (0–1.5)	9.53 (4.13–19.23)	0.002

CNR = contrast-to-noise-ratio; NS = not significant.
Data are median and interquartile range. Significance is set at $P < 0.05$.

discrimination was possible, with a median CNR of 5.48, so that FAR CLI seems to be a promising modality for low AC levels. We were able to show that subcutaneous (at <1 mm depth) PC tumors could be visualized down to the lowest measured AC of 23.02 kBq/mL on FAR CLI.

Next, we tested FAR CLI in men undergoing RP. This first-in-men study investigated the feasibility of assessing tumor margin status and of evaluating minimum detection limits.

After incision, no increased signal on CLI was visible. CLI using an ^{18}F -PSMA did not provide any useful signals, only luminescence artifacts. In contrast, with the aid of the flexible scintillator, FAR CLI detected cancer foci. The minimum detectable AC was 2.06 kBq/mL, with a CNR of 10.84. On this basis, good detection of PRMs should be assumed. However, the use of FAR CLI for PRM assessment is challenging. PRMs were found in 2 patients. In 1 patient, histology demonstrated a 2-mm positive margin with an ISUP-GGG of 4 at the left seminal vesicle plateau, but even with FAR CLI, no signal was visible in this area. The second PRM, with

an ISUP-GGG of 1 and a length of 1 mm, also showed no corresponding correlate on FAR CLI.

Jurrius et al. also investigated the use of FAR to assess resection margins (23). In the context of breast-conserving surgery with ^{18}F -FDG, an overall accuracy of 80.5% was shown, with a sensitivity of 46.2%. Although a direct comparison between breast cancer and PC is difficult, our results do not show the same benefit for FAR CLI. On the one hand, this may be due to tumor biology; on the other hand, it may be related to the study design. A major difference is the timing between tracer injection and measurement of CLI or FAR CLI activity. In our study, measurements were taken about 2 h later than in the work of Jurrius et al.

In principle, every radioguided-surgery technique requires a high CNR, high sensitivity, and user friendliness to provide a net benefit for patients and surgeons in routine care. CLI provides good surface contrast but, as has been shown in this report, insufficient sensitivity at very low activities, mainly because of tissue light absorption. Although FAR CLI, is able to compensate for the

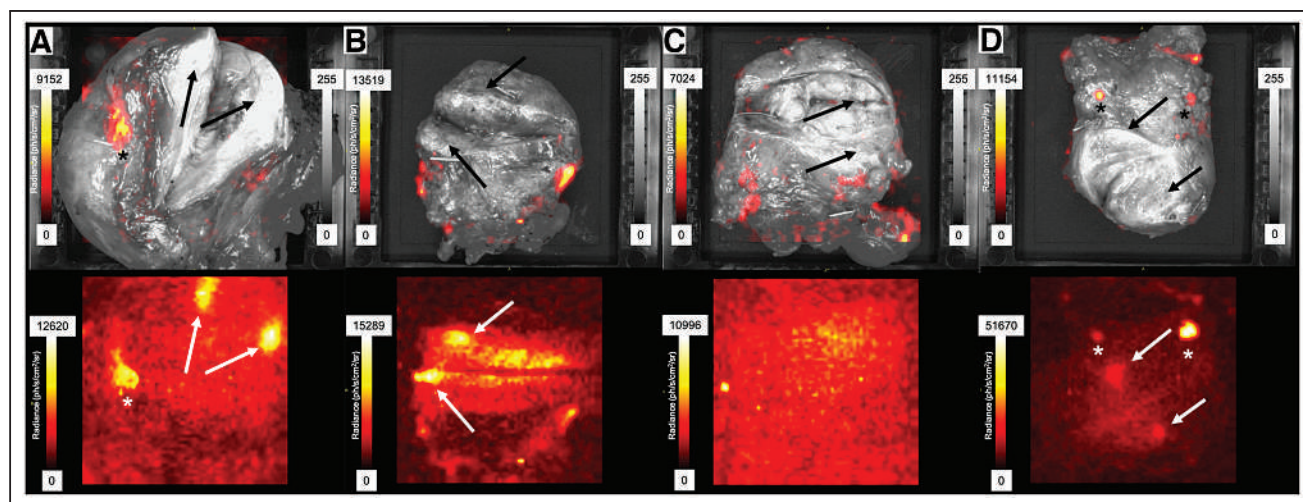


FIGURE 4. Images of incised prostate specimens: CLI with overlying gray-scale photographs (top) and FAR CLI (bottom). CLI shows no hot spots (arrows) in PC lesions seen on FAR CLI (arrows). Artificial signals in CLI and correlating FAR CLI signals are indicated (*). Histopathology proved absence of PC at surface. FAR CLI in A and B shows good signal, with CNRs of 9.13 and 23.03. FAR CLI in C shows no increased signal detectable in PC, with activity of 1.85 kBq/mL and corresponding CNR of 3.69. FAR CLI in D shows increased signal, with CNR of 10.84 at activity of 2.06 kBq/mL.

lack of sensitivity by increasing the net light output per emitted β -particle, the result is imaged foci that have a lower spatial resolution, making it difficult to discriminate closely adjacent regions of uptake. Furthermore, because CLI and FAR CLI are highly sensitive to ambient light, measurements can be made only in a light-tight chamber. This limitation must be considered when designing further implementations of the system. A possible improvement to the presented method might be achieved by topical application of nanoparticles. Pratt et al. described the advantages of Gd_2O_3 and Eu_2O_3 , which showed the greatest enhancement in radiance. The combination of Gd_2O_3 and Eu_2O_3 with ^{68}Ga and ^{18}F , respectively, produced distinct visible emission peaks (33).

Additional limitations of our work deserve further discussion. In our study setting, ^{18}F -PSMA represents a suboptimal tracer because of very low activity in the context of RP. Although, in contrast to other tracers, the half-life is prolonged, the emitted energy is lower. Adjustment of the current workflow is necessary to achieve higher activity levels at the time of RP through optimization of dosing and timing. However, radiation exposure of medical personnel and patients must be considered, as well as possible negative effects on specificity. The fact that, in most of the patients, a signal was detected on FAR CLI after incision demonstrated the feasibility of ^{18}F -PSMA-FAR CLI. When there are suggestive findings, CLI might subsequently be used for surface assessment. The extent to which this can be applied clinically remains to be investigated. The flexible scintillation film is semiopaque and thus obscures the white-light reference image of the sample, presenting a challenge for accurate correlation of the FAR CLI signal with the exact anatomic location on the sample.

CONCLUSION

Detection of PC using ^{18}F -PSMA-FAR CLI is possible—even at low activity levels down to 2.06 kBq/mL. However, anatomic correlation is difficult and detection of PRMs failed. ^{18}F -PSMA CLI had no value in this setup.

DISCLOSURE

Claudia Kesch reports consulting fees from Apogepha and research funding from Advanced Accelerator Applications (Novartis). Stephan Tschirdewahn reports personal and travel fees from Ipsen, Eisai, Bayer, Janssen, Novartis, Bristol-Myers-Squibb, and BrachySolutions and research funding from Ipsen. Jan Radtke reports personal and travel fees from Invivo Uronav, Bender Group, Beckelmann and Partners, and Saegeling Medizintechnik and research funding from Advanced Accelerator Applications and Novartis. Ken Herrmann reports personal fees from Bayer, Sofie Biosciences, SIRTEX, Adacap, Curium, Endocyte and BTG. Wolfgang Fendler reports fees from SOFIE Bioscience (research funding), Janssen (consultant, speakers' bureau), Calyx (consultant), Bayer (consultant, speakers' bureau, research funding), and Parexel (image review) outside the submitted work. Boris Hadaschik reports personal fees from ABX, Bayer, LightPoint Medical Inc., Janssen R&D, Bristol-Myers-Squibb, and Astellas; research funding from Profound Medical, German Cancer Aid, German Research Foundation, Janssen R&D, Bristol-Myers-Squibb, MSD, Pfizer, and Astellas; and travel fees from AstraZeneca, Janssen R&D, and Astellas. This work was supported by the Deutsche Forschungsgemeinschaft (project HA 5160/5-1). No other potential conflict of interest relevant to this article was reported.

KEY POINTS

QUESTION: Are CLI and FAR CLI useful for displaying PC cells close to or at the surface of prostatectomy specimens?

PERTINENT FINDINGS: In this feasibility study, 7 patients undergoing RP and an ^{18}F -PSMA PET/CT scan on the same day were analyzed for suggestive intensity levels. FAR CLI, in contrast to CLI, was able to clearly highlight PC cells from surrounding tissue after incision. However, detection of PC in PRMs was not possible by either modality.

IMPLICATIONS FOR PATIENT CARE: ^{18}F -CLI has no value for the detection of resection margins in a preoperative ^{18}F -PSMA administration protocol. ^{18}F -FAR CLI is possible, but without meaningful clinical benefit.

REFERENCES

1. Prostate cancer. European Association of Urology website. <https://uroweb.org/guidelines/prostate-cancer>. Published 2022. Accessed December 22, 2022.
2. Iczkowski KA, Lucia MS. Frequency of positive surgical margin at prostatectomy and its effect on patient outcome. *Prostate Cancer*. 2011;2011:673021.
3. Yossepowitch O, Briganti A, Eastham JA, et al. Positive surgical margins after radical prostatectomy: a systematic review and contemporary update. *Eur Urol*. 2014; 65:303–313.
4. Schlomm T, Tennstedt P, Huxhold C, et al. Neurovascular structure-adjacent frozen-section examination (NeuroSAFE) increases nerve-sparing frequency and reduces positive surgical margins in open and robot-assisted laparoscopic radical prostatectomy: experience after 11,069 consecutive patients. *Eur Urol*. 2012;62:333–340.
5. Nyarangi-Dix J, Wiesenfarth M, Bonekamp D, et al. Combined clinical parameters and multiparametric magnetic resonance imaging for the prediction of extraprostatic disease: a risk model for patient-tailored risk stratification when planning radical prostatectomy. *Eur Urol Focus*. 2020;6:1205–1212.
6. Petralia G, Musi G, Padhani AR, et al. Robot-assisted radical prostatectomy: multiparametric MR imaging-directed intraoperative frozen-section analysis to reduce the rate of positive surgical margins. *Radiology*. 2015;274:434–444.
7. Collamati F, van Oosterom MN, Hadaschik BA, Frago Costa P, Darr C. Beta radioguided surgery: towards routine implementation? *Q J Nucl Med Mol Imaging*. 2021;65:229–243.
8. Olde Heuvel J, de Wit-van der Veen BJ, Huizing DMV, et al. State-of-the-art intraoperative imaging technologies for prostate margin assessment: a systematic review. *Eur Urol Focus*. 2021;7:733–741.
9. Meershoek P, van Oosterom MN, Simon H, et al. Robot-assisted laparoscopic surgery using DROP-IN radioguidance: first-in-human translation. *Eur J Nucl Med Mol Imaging*. 2019;46:49–53.
10. Maurer T, Robu S, Schottelius M, et al. ^{99m}Tc -based prostate-specific membrane antigen-radioguided surgery in recurrent prostate cancer. *Eur Urol*. 2019;75:659–666.
11. Maurer T, Graefen M, van der Poel H, et al. Prostate-specific membrane antigen-radioguided surgery. *J Nucl Med*. 2020;61:6–12.
12. Knipper S, Mehdi Irai M, Simon R, et al. Cohort study of oligorecurrent prostate cancer patients: oncological outcomes of patients treated with salvage lymph node dissection via prostate-specific membrane antigen-radioguided surgery. *Eur Urol*. 2023;83:62–69.
13. Koehler D, Sauer M, Klutmann S, et al. Feasibility of ^{99m}Tc -MIP-1404 for SPECT/CT imaging and subsequent PSMA-radioguided surgery in early biochemical recurrent prostate cancer: a case series of 9 patients. *J Nucl Med*. July 14, 2022 [Epub ahead of print].
14. Collamati F, van Oosterom MN, De Simoni M, et al. A DROP-IN beta probe for robot-assisted ^{68}Ga -PSMA radioguided surgery: first ex vivo technology evaluation using prostate cancer specimens. *EJNMMI Res*. 2020;10:92.
15. Debacker JM, Schelfhout V, Brochez L, et al. High-resolution ^{18}F -FDG PET/CT for assessing three-dimensional intraoperative margins status in malignancies of the head and neck, a proof-of-concept. *J Clin Med*. 2021;10:3737.
16. Grootendorst MR, Cariati M, Pinder SE, et al. Intraoperative assessment of tumor resection margins in breast-conserving surgery using ^{18}F -FDG Cerenkov luminescence imaging: a first-in-human feasibility study. *J Nucl Med*. 2017;58:891–898.
17. Chin PT, Welling MM, Meskers SC, Valdes Olmos RA, Tanke H, van Leeuwen FW. Optical imaging as an expansion of nuclear medicine: Cerenkov-based luminescence vs fluorescence-based luminescence. *Eur J Nucl Med Mol Imaging*. 2013;40:1283–1291.

18. Darr C, Harke NN, Radtke JP, et al. Intraoperative ^{68}Ga -PSMA Cerenkov luminescence imaging for surgical margins in radical prostatectomy: a feasibility study. *J Nucl Med*. 2020;61:1500–1506.
19. Olde Heuvel J, de Wit-van der Veen BJ, van der Poel HG, et al. ^{68}Ga -PSMA Cerenkov luminescence imaging in primary prostate cancer: first-in-man series. *Eur J Nucl Med Mol Imaging*. 2020;47:2624–2632.
20. Darr C, Fragoso Costa P, Kesch C, et al. Prostate specific membrane antigen (PSMA)-radio guided surgery using Cerenkov luminescence imaging: utilization of a short-pass filter to reduce technical pitfalls. *Transl Androl Urol*. 2021;10:3972–3985.
21. Gill RK, Mitchell GS, Cherry SR. Computed Cerenkov luminescence yields for radionuclides used in biology and medicine. *Phys Med Biol*. 2015;60:4263–4280.
22. Vyas KN, Grootendorst M, Mertzaniou T, et al. Flexible scintillator autoradiography for tumor margin inspection using ^{18}F -FDG. In: *Proceedings Volume 10478, Molecular-Guided Surgery: Molecules, Devices, and Applications IV*. SPIE; 2018:1–12.
23. Jurrius P, Grootendorst MR, Krotewicz M, et al. Intraoperative [^{18}F]FDG flexible autoradiography for tumour margin assessment in breast-conserving surgery: a first-in-human multicentre feasibility study. *EJNMMI Res*. 2021;11:28.
24. Annual Congress of the European Association of Nuclear Medicine. October 13–17, 2018, Düsseldorf, Germany. *Eur J Nucl Med Mol Imaging*. 2018;45:1–844.
25. Lückereath K, Stuparu AD, Wei L, et al. Detection threshold and reproducibility of ^{68}Ga -PSMA11 PET/CT in a mouse model of prostate cancer. *J Nucl Med*. 2018;59:1392–1397.
26. olde Heuvel J, de Wit-van der Veen L, Tuch D, Vyas K, Stokkel M, Slump C. Performance evaluation of Cerenkov luminescence imaging: a comparison of ^{68}Ga with ^{18}F [abstract]. *J Nucl Med*. 2018;59(suppl 1):365.
27. Fendler WP, Eiber M, Beheshti M, et al. ^{68}Ga -PSMA PET/CT: joint EANM and SNMMI procedure guideline for prostate cancer imaging: version 1.0. *Eur J Nucl Med Mol Imaging*. 2017;44:1014–1024.
28. Costa PF, Fendler WP, Herrmann K, et al. Radiation protection and occupational exposure on ^{68}Ga -PSMA-11-based Cerenkov luminescence imaging procedures in robot-assisted prostatectomy. *J Nucl Med*. 2022;63:1349–1356.
29. Ciarrocchi E, Vanhove C, Descamps B, De Lombaerde S, Vandenberghe S, Belcari N. Performance evaluation of the LightPath imaging system for intra-operative Cerenkov luminescence imaging. *Phys Med*. 2018;52:122–128.
30. Bright DS, Newbury DE, Steel EB. Visibility of objects in computer simulations of noisy micrographs. *J Microsc*. 1998;189:25–42.
31. Prostate cancer (version 1.2023). National Comprehensive Cancer Network website. https://www.nccn.org/professionals/physician_gls/pdf/prostate.pdf. Published September 16, 2022. Accessed December 22, 2022.
32. Olde Heuvel J, de Wit-van der Veen BJ, Vyas KN, et al. Performance evaluation of Cerenkov luminescence imaging: a comparison of ^{68}Ga with ^{18}F . *EJNMMI Phys*. 2019;6:17.
33. Pratt EC, Shaffer TM, Zhang Q, Drain CM, Grimm J. Nanoparticles as multimodal photon transducers of ionizing radiation. *Nat Nanotechnol*. 2018;13:418–426.
34. Ciarrocchi E, Belcari N. Cerenkov luminescence imaging: physics principles and potential applications in biomedical sciences. *EJNMMI Phys*. 2017;4:14.

Prognostic Value of Tumor Volume Assessment on PSMA PET After ^{177}Lu -PSMA Radioligand Therapy Evaluated by PSMA PET/CT Consensus Statement and RECIP 1.0

Felix Kind¹, Ann-Christin Eder^{1,2}, Cordula A. Jilg³, Philipp E. Hartrampf⁴, Philipp T. Meyer^{1,5}, Juri Ruf^{1,5}, and Kerstin Michalski¹

¹Department of Nuclear Medicine, Medical Center, University of Freiburg, Freiburg, Germany; ²Radiopharmaceutical Development, German Cancer Consortium, Freiburg, Germany, and German Cancer Research Center, Heidelberg, Germany; ³Department of Urology, Medical Center, University of Freiburg, Freiburg, Germany; ⁴Department of Nuclear Medicine, University Hospital Würzburg, Würzburg, Germany; and ⁵German Cancer Consortium, Freiburg, Germany, and German Cancer Research Center, Heidelberg, Germany

Quantitative evaluation of prostate-specific membrane antigen (PSMA)-targeting PET/CT remains challenging but is urgently needed for the use of standardized PET-based response criteria, such as the PSMA PET/CT consensus statement or Response Evaluation Criteria in PSMA PET/CT (RECIP 1.0). A recent study evaluated the prognostic value of whole-body tumor volume using a semiautomatic method relying on a 50% threshold of lesion SUV_{max} (PSMA_{TV50}). In the present study, we analyzed the suitability of this approach comparing ^{18}F -PSMA-1007 with ^{68}Ga -PSMA-11 PET/CT scans and the potential of PSMA_{TV50} for the prediction of overall survival (OS) in patients before ^{177}Lu -PSMA radioligand therapy (RLT). Moreover, PSMA_{TV50} was integrated into the PSMA PET/CT consensus statement as well as RECIP 1.0, and the prognostic value of these response classification systems was compared. **Methods:** This retrospective study included 70 patients with metastatic castration-resistant prostate cancer undergoing PSMA RLT. Thirty-three patients were monitored by ^{68}Ga -PSMA-11 PET/CT, and 37 patients by ^{18}F -PSMA-1007 PET/CT. PET/CT scans before (baseline) and at the end of PSMA RLT after 2–4 cycles (follow-up) were separately analyzed by 2 readers. PSMA_{TV50} at baseline and its change at the time of follow-up ($\Delta\text{PSMA}_{\text{TV50}}$, expressed as a ratio) were correlated with OS using Cox proportional-hazards regression. The results of both subgroups were compared. The integration of $\Delta\text{PSMA}_{\text{TV50}}$ in existing response classification systems was evaluated. To assess and compare the discriminatory strength of these classification systems, Gönen and Heller concordance probability estimates were calculated. **Results:** PSMA_{TV50} determination was technically feasible in all examinations. A higher PSMA_{TV50} at baseline and a higher $\Delta\text{PSMA}_{\text{TV50}}$ were strongly associated with a shorter OS for both ^{68}Ga -PSMA-11 (PSMA_{TV50}: hazard ratio [HR] of 1.29 [95% CI, 1.05–1.55], $P = 0.009$; $\Delta\text{PSMA}_{\text{TV50}}$: HR of 1.83 [95% CI, 1.08–3.09], $P = 0.024$) and ^{18}F -PSMA-1007 (PSMA_{TV50}: HR of 1.84 [95% CI, 1.13–2.99], $P = 0.014$; $\Delta\text{PSMA}_{\text{TV50}}$: HR of 1.23 [95% CI, 1.04–1.51], $P = 0.03$). Response assessment provided high discriminatory power for OS for the PSMA PET/CT consensus statement (concordance probability estimate, 0.73) as well as RECIP 1.0 (concordance probability estimate, 0.74). **Conclusion:** PSMA_{TV50} and $\Delta\text{PSMA}_{\text{TV50}}$ proved to be predictive of OS not only for ^{68}Ga -PSMA-11 but also for ^{18}F -PSMA-1007 PET/CT scans. Subsequent integration of $\Delta\text{PSMA}_{\text{TV50}}$

into the PSMA PET/CT consensus statement and RECIP 1.0 provided equally high prognostic value for both classification systems.

Key Words: radioligand therapy; PSMA PET/CT; PSMA_{TV50}; response assessment; RECIP 1.0

J Nucl Med 2023; 64:605–610

DOI: 10.2967/jnumed.122.264489

Prostate-specific membrane antigen (PSMA)-targeting PET/CT has remarkably advanced the staging of patients with prostate cancer and has proven to be superior to conventional imaging (1). Additionally, PSMA PET/CT is also frequently used in the context of PSMA radioligand therapy (RLT) to assess sufficient PSMA expression of prostate cancer manifestations before treatment and to evaluate therapy response (2). However, systematic response evaluation of PSMA RLT is still based primarily on biochemical parameters, that is, serum prostate-specific antigen level (3) and nonstandardized qualitative PSMA PET/CT assessment. With the emerging clinical significance of PSMA RLT in the management of prostate cancer (4,5), particularly highlighted by the recently completed phase III study (6) and the recent approval of ^{177}Lu -PSMA-617 by the American Food and Drug Administration (7), an implementation of a reproducible and systematic evaluation system for PSMA PET/CT is of high interest.

Fanti et al. recently published PSMA PET progression criteria for general response assessment of prostate cancer treatments, integrating PSMA PET/CT with clinical and biochemical parameters (8). Although not yet clinically implemented, these response assessment criteria were validated for PSMA RLT as reproducible and highly predictive of overall survival (OS) in a retrospective analysis by our study group (9) and have been updated by a recently published PSMA PET/CT consensus statement (10). Therein, the definition of partial response (PR), stable disease, and progressive disease (PD) of patients with polymetastatic disease is based on a change in whole-body tumor volume on PSMA PET/CT. Another promising evaluation system is the recently suggested Response Evaluation Criteria in PSMA PET/CT (RECIP 1.0) (11), which showed the highest reproducibility and prognostic accuracy in a comparison of 5 different response criteria (including PSMA PET progression criteria) (12). Several quantification methods for the assessment of whole-body

Received Jun. 6, 2022; revision accepted Oct. 13, 2022.

For correspondence or reprints, contact Felix Kind (felix.kind@uniklinik-freiburg.de).

Published online Oct. 27, 2022.

COPYRIGHT © 2023 by the Society of Nuclear Medicine and Molecular Imaging.

tumor volume have been proposed, mainly using a liver-based threshold on ^{68}Ga -PSMA-11 PET/CT (13–17). However, this approach cannot be directly transferred to ^{18}F -PSMA-1007 PET/CT because of the hepatobiliary excretion of this tracer (18). In contrast, Seifert et al. (19) recently introduced a semiautomatic method using a 50% threshold of lesion SUV_{max} to assess the whole-body tumor volume ($\text{PSMA}_{\text{TV50}}$). As this threshold approach is independent of the different physiologic tracer uptake of PSMA-targeting radiopharmaceuticals, it could also be applicable to ^{18}F -PSMA-1007 PET/CT.

The primary objective of this retrospective analysis was to assess the feasibility and the prognostic value of $\text{PSMA}_{\text{TV50}}$ for OS in both ^{68}Ga -PSMA-11 PET/CT and ^{18}F -PSMA-1007 PET/CT in patients with advanced metastatic castration-resistant prostate cancer. In a second step, $\text{PSMA}_{\text{TV50}}$ was integrated into the PSMA PET/CT consensus statement and RECIP 1.0 criteria, and the secondary objective was to compare the prognostic value of these response classification systems.

MATERIALS AND METHODS

Patient Population

All patients treated with at least 1 cycle of PSMA RLT between July 2015 and October 2020 at our department were screened for eligibility. PSMA PET/CT scans were performed before PSMA RLT (baseline PSMA PET/CT) and at the end of therapy after either 2 or 4 cycles (follow-up PSMA PET/CT). For inclusion, both baseline and follow-up PET/CT had to be performed in-house with the same PSMA radioligand (^{68}Ga -PSMA-11 or ^{18}F -PSMA-1007) but not necessarily on the same PET/CT scanner. Another inclusion criterion was the availability of survival data. Patients without a follow-up PET/CT scan (i.e., in cases of clinical progression) were excluded from the analysis. The local institutional review board approved this study (approval 251/17), and all subjects gave written informed consent. PSMA RLT was performed on a compassionate-use basis according to individual tumor board recommendations (20,21).

Treatment and Imaging Protocol

PSMA RLT was performed according to current guidelines (20). The standard protocol consisted of infusion of 6.0 GBq of ^{177}Lu -PSMA-617 ($n = 59$) or ^{177}Lu -PSMA-I&T ($n = 11$) (which are of comparable efficacy (20,22)) at an interval of 6–8 wk, with treatment response assessed by PSMA PET/CT and laboratory data 6–8 wk after the second cycle. Depending on the response to therapy, PSMA RLT was either continued with 2 additional cycles, following the same protocol, or discontinued if there was a good response or clear progression (based on clinical decision). Whole-body PSMA PET scans were acquired after 1 h (^{68}Ga -PSMA-11) or 2 h (^{18}F -PSMA-1007) from mid thigh to skull, typically using a scan duration of 2 min per bed position. Contrast-enhanced diagnostic CT with dose modulation (120 kVp, 100–400 mAs) was performed. Scans were acquired on a Vereos digital PET/CT (Philips), a Gemini TF 64 PET/CT (Philips), or a Gemini TF 16 Big-Bore PET/CT (Philips) device. Images were reconstructed with a vendor-specific iterative reconstruction algorithm (blob ordered-subset time-of-flight) with 3 iterations and 9 subsets (relaxation parameter, 0.35) and a voxel size of $2 \times 2 \times 2$ mm (Vereos digital) or with 3 iterations and 33 subsets (relaxation parameter, 0.35) and a voxel size of $2 \times 2 \times 2$ mm (Gemini TF 64 and Gemini TF 16 Big-Bore). The spatial resolution of the reconstructed PET images was about 5 mm (Vereos) and 7 mm (both Gemini TF devices) in full width at half maximum, respectively. Prostate-specific antigen levels were assessed directly before administration of PSMA RLT and at follow-up PSMA PET/CT.

Semiautomatically Quantified Tumor Volume Assessment

^{68}Ga -PSMA-11 PET/CT and ^{18}F -PSMA-1007 PET/CT scans at baseline and follow-up were retrospectively analyzed by 2 readers with 2 and

4 y of PSMA PET/CT reader experience. Fiji (23) and the Beth Israel plugin (24) were used to calculate whole-body tumor volume. Autosegmentation was used for automatic delineation of PET-positive lesions, that is, regions of interest. Regions of interest comprising tissue with physiologic radioligand uptake were carefully removed manually, whereas regions of interest for pathologic lesions not detected by autosegmentation were added manually by the reader. In accordance with Seifert et al. (19), individual lesions were volumetrically assessed by applying a lesion-specific threshold of 50% of the local SUV_{max} to each region of interest. The summed volumes of all lesions correspond to the whole-body PSMA tumor volume ($\text{PSMA}_{\text{TV50}}$, measured in mL). The change in $\text{PSMA}_{\text{TV50}}$ at follow-up PSMA PET/CT compared with the baseline assessment ($\Delta\text{PSMA}_{\text{TV50}}$, expressed as a ratio) was calculated for all individuals.

Response Assessment Using the PSMA PET/CT Consensus Statement and RECIP 1.0

PET/CT images were retrospectively analyzed by the readers using the local PACS system DeepUnity Diagnost (Dedalus HealthCare). According to RECIP 1.0, the appearance of at least 1 new lesion was noted. After the assessment of interobserver agreement, a final consensus was reached and used for further comparisons in combination with $\Delta\text{PSMA}_{\text{TV50}}$. Since all patients in our cohort were polymetastatic, progression according to the PSMA PET/CT consensus statement was based solely on an increase in $\Delta\text{PSMA}_{\text{TV50}}$ of more than 30% and not on the appearance of new lesions as well, which is proposed for an early stage of disease. The definitions of disease progression for the respective criteria are summarized in Table 1.

Statistical Analysis

SPSS, version 24.0.0.0 (IBM), was used for statistical analyses. Data are presented as mean \pm SD and range. An unpaired t test was used to assess differences between the characteristics of the 2 subgroups (^{68}Ga -PSMA-11 PET/CT and ^{18}F -PSMA-1007 PET/CT). An OS landmark analysis was performed, monitoring the interval between the follow-up PSMA PET/CT and either death or last follow-up. OS is presented as median with the 95% CI. To assess interrater reliability for tumor volume assessment, intraclass correlation coefficient was used, using single measures, calculated with a 2-way mixed-effect model (intraclass correlation coefficient(3,1)) for absolute agreement. For qualitative response assessment, the Cohen κ was used to assess interrater reliability. The association of $\text{PSMA}_{\text{TV50}}$ and $\Delta\text{PSMA}_{\text{TV50}}$ with OS for each radiotracer, as well as for the sum of all patients, was analyzed by Cox proportional-hazards regression using hazard ratios (HRs). To assess and compare the discriminatory strength of response classification systems, Gönen and Heller concordance probability estimates excluding ties (25) were calculated using R, version 4.2.1, whereas the χ^2 test with Cramér V was used to assess their cross-table correlation. Corresponding Kaplan–Meier-curves were analyzed by log-rank tests. P values of less than 0.05 were considered statistically significant.

RESULTS

Between July 2015 and October 2020, 70 of 120 patients receiving PSMA RLT were included in this retrospective analysis. Mean age was 73.0 ± 8.3 y (range, 53–90 y). In total, 196 treatment cycles were administered, with 43 patients receiving only 2 cycles and 27 patients receiving 4 cycles. PSMA RLT was stopped after 2 cycles because of either a clear response (clinical, biochemical, or PET/CT; $n = 27$) or respective progression ($n = 16$). The mean and cumulative administered activity was 5.8 ± 0.8 GBq (range, 3.0–7.5 GBq) per cycle and 16.1 ± 6.0 GBq (6.1–24.6 GBq), respectively. Detailed patient characteristics are given in Table 2. Previous ^{223}Ra -dichloride therapy was significantly more prevalent among patients examined with the formerly used ^{68}Ga -PSMA-11

TABLE 1
Response Assessment According to PSMA PET/CT Consensus Statement (10) and RECIP 1.0

Response	PSMA PET/CT consensus statement	RECIP 1.0
PR	Decline in tumor volume > 30%	No new lesions* and decline in tumor volume > 30%
SD	Change in tumor volume ≤ ±30%	Change in tumor volume of -30% to +20%, or ≥1 new lesion* and decline in tumor volume ≥ 30%, or no new lesions* and increase in tumor volume ≥ 20%
PD	Polymetastatic prostate cancer: increase in tumor volume > 30%	≥1 new lesion* and increase in tumor volume > 20%

*On either PET or CT images

SD = stable disease.

Lesion and tumor volume assessed on PSMA PET.

($P = 0.007$), as this treatment has in large part been replaced by PSMA RLT. Apart from that, no significant differences in age, time since initial diagnosis, serum prostate-specific antigen level before PSMA RLT, Gleason score, or other previous treatments

were found for the 2 subgroups (^{68}Ga -PSMA-11 and ^{18}F -PSMA-1007; $P > 0.05$). The interval between baseline PSMA PET/CT and application of the first cycle was 45 ± 26 d (range, 2–126 d). The time from baseline PSMA PET/CT to the end of therapy and

TABLE 2
Patient Characteristics at Baseline ($n = 70$)

Characteristic	All patients ($n = 70$)	Patients with ^{68}Ga -PSMA-11 PET/CT ($n = 33$)	Patients with ^{18}F -PSMA-1007 PET/CT ($n = 37$)	P^*
Age (y)	73 (53–90)	72 (53–88)	74 (57–90)	0.383
Time since initial diagnosis (y)	9.0 (0.7–26.9)	9.4 (0.7–22.2)	8.3 (1.2–26.9)	0.609
Prostate-specific antigen (ng/mL)	338.3 (0.1–3,129)	416.1 (0.1–3,129)	269.0 (5.8–2,980)	0.348
Gleason score				0.695
<8	25 (36)	11 (44)	14 (56)	
≥8	45 (64)	22 (49)	23 (51)	
Previous treatment [†]				
Prostatectomy	38 (54)	22 (66)	16 (43)	0.059
Radiotherapy to prostate/prostate bed	50 (71)	26 (79)	24 (6)	0.449
Androgen deprivation therapy	70 (100)	33 (100)	37 (100)	0.935
Abiraterone	42 (60)	16 (48)	26 (70)	0.063
Enzalutamide	24 (34)	11 (33)	13 (35)	0.874
Docetaxel	40 (57)	18 (54)	22 (59)	0.678
Cabazitaxel	9 (13)	2 (6)	7 (19)	0.109
^{223}Ra -dichloride	9 (13)	8 (24)	1 (3)	0.007 [‡]
Sites of metastatic disease [†]				
Lymph node	56 (80)	30 (91)	26 (70)	0.062
Bone	61 (87)	30 (9)	31 (84)	0.374
Liver	2 (3)	1 (3)	1 (3)	0.935
Lung	15 (21)	9 (27)	6 (16)	0.26
Local recurrence	22 (31)	9 (27)	13 (35)	0.479
Other	13 (19)	3 (9)	10 (27)	0.054

*Difference between patients with ^{68}Ga -PSMA-11 PET/CT and ^{18}F -PSMA-1007 PET/CT according to independent t test or χ^2 test.

[†]Multiple namings possible.

[‡]Statistically significant.

Nominal data are presented as number and percentage; continuous data are presented as mean and range.

to follow-up PSMA PET/CT was 195 ± 66 d (range, 84–346 d) and 48 ± 9 d (range, 29–69 d), respectively. In 33 patients, PSMA RLT was monitored using ^{68}Ga -PSMA-11 PET/CT, and 37 patients were examined using ^{18}F -PSMA-1007 PET/CT. Mean prostate-specific antigen levels at follow-up PSMA PET/CT were 227.0 ng/mL (range, 0.1–1,111.0 ng/mL) for the ^{68}Ga -PSMA-11 group and 394.5 ng/mL (range, 0.15–5,000.0 ng/mL) for the ^{18}F -PSMA-1007 group.

Determination of $\text{PSMA}_{\text{TV50}}$ was technically feasible in all 140 examinations (Fig. 1). Interrater agreement for $\text{PSMA}_{\text{TV50}}$ at both baseline and follow-up PSMA PET/CT was high for both ^{68}Ga -PSMA-11 PET/CT (intraclass correlation coefficient(3,1), 0.92 [95% CI, 0.87–0.95]; $P < 0.001$) and ^{18}F -PSMA-1007 PET/CT (intraclass correlation coefficient(3,1), 0.82 [95% CI, 0.72–0.88]; $P < 0.001$). Detailed $\text{PSMA}_{\text{TV50}}$ and interrater data for both radiopharmaceuticals at all time points are given in Supplemental Table 1 (supplemental materials are available at <http://jnm.snmjournals.org>). Interrater agreement on response assessment was very high for both PSMA PET/CT consensus statement (98.6%; Cohen $\kappa = 0.97$, $P < 0.001$) and RECIP 1.0 (95.7%; Cohen $\kappa = 0.93$, $P < 0.001$).

Median follow-up (reverse Kaplan–Meier estimator) was 25.0 mo (95% CI, 12.7–37.3 mo) from follow-up PSMA PET/CT. Median OS was 9.0 mo (95% CI, 8.0–10.0 mo), with 24 patients (34%) being alive at the last follow-up. There were no therapy-related deaths documented.

Association of $\text{PSMA}_{\text{TV50}}$ and $\Delta\text{PSMA}_{\text{TV50}}$ with OS

A higher $\text{PSMA}_{\text{TV50}}$ at baseline PSMA PET/CT was significantly associated with a shorter OS for patients examined with ^{68}Ga -PSMA-11 PET/CT ($n = 33$; HR, 1.29 [95% CI, 1.05–1.55]; $P = 0.009$) and ^{18}F -PSMA-1007 PET/CT ($n = 37$; HR, 1.84 [95% CI, 1.13–2.99]; $P = 0.014$). An increase in $\text{PSMA}_{\text{TV50}}$ at the follow-up PSMA PET/CT, resulting in a higher ratio of $\Delta\text{PSMA}_{\text{TV50}}$ (>1.0), was strongly associated with a shorter OS for both ^{68}Ga -PSMA-11 PET/CT ($n = 33$; HR, 1.83 [95% CI, 1.08–3.09]; $P = 0.024$) and ^{18}F -PSMA-1007 PET/CT ($n = 37$; HR, 1.23 [95% CI, 1.04–1.51]; $P = 0.03$). Taking both radiopharmaceuticals together, the same

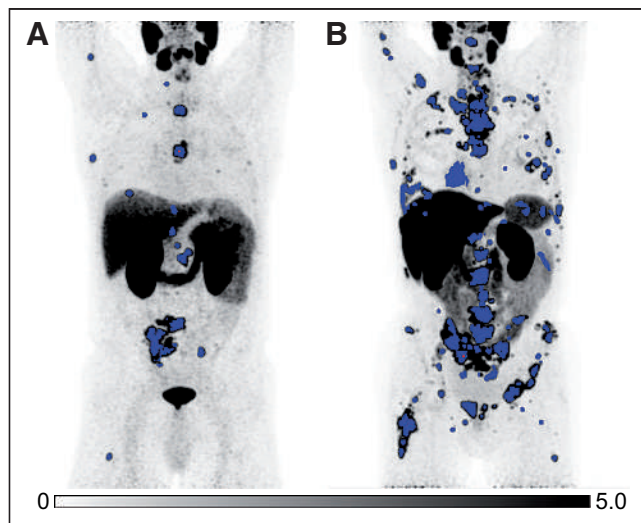


FIGURE 1. Maximum-intensity projections of ^{68}Ga -PSMA-11 (A) and ^{18}F -PSMA-1007 (B) PET scans of patients with metastasized prostate cancer before PSMA RLT. PSMA-positive prostate cancer lesions were delineated semiautomatically and highlighted in blue. Lesion-specific threshold of 50% was used. Intensity-scale bar is SUV.

association with OS was found for baseline $\text{PSMA}_{\text{TV50}}$ ($n = 70$; HR, 1.48 [95% CI, 1.16–1.90]; $P = 0.002$) and for $\Delta\text{PSMA}_{\text{TV50}}$ ($n = 70$; HR, 1.23 [95% CI, 1.02–1.49]; $P = 0.032$).

Integration of $\Delta\text{PSMA}_{\text{TV50}}$ into the PSMA PET/CT Consensus Statement and RECIP 1.0 Criteria

The PSMA PET/CT consensus statement classified 56% ($n = 39$) of patients as PD, 24% ($n = 17$) as stable disease, and 20% ($n = 14$) as PR. Kaplan–Meier analysis revealed a strong association between PD and shorter median OS compared with non-PD (PR and stable disease) in median OS (8.0 mo [95% CI, 6.7–9.3 mo] vs. 21.0 mo [95% CI, 17.9–40.2 mo], $P = 0.002$; Fig. 2A) and risk of death (HR, 2.65 [95% CI, 1.37–5.12]; $P = 0.004$). At least 2 new lesions appeared in 57% of patients ($n = 40$), but this parameter was not integrated into the response classification because all patients were in the polymetastatic stage of disease. New lesions were seen predominantly in patients classified as PD ($n = 31$, 78%), were less frequent in patients with stable disease ($n = 7$, 17%), and were seen in only 2 cases of PR (5%). According to RECIP 1.0, 53% ($n = 37$) of all patients were categorized as PD, whereas 31% ($n = 22$) and 16%

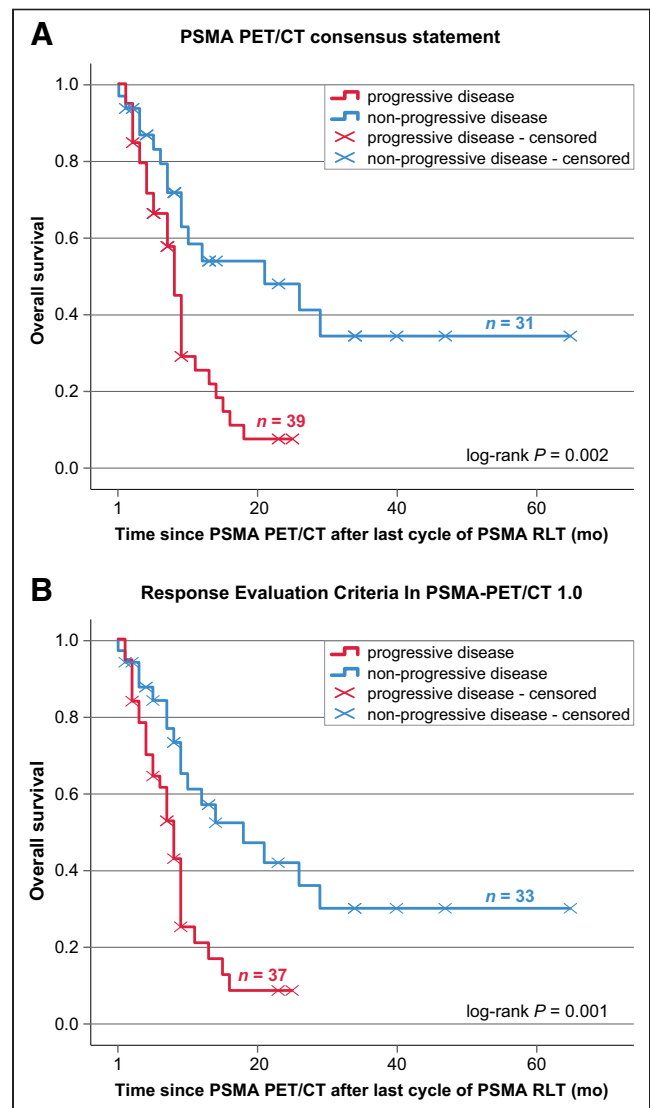


FIGURE 2. Kaplan–Meier curves of OS of all patients ($n = 70$) classified by PSMA PET/CT consensus statement (A) and RECIP 1.0 (B).

($n = 11$) were classified as stable disease and PR, respectively. Of the 48 patients with at least 1 new lesion on either PET or CT, 77% ($n = 37$) were classified as PD; the remaining 23% ($n = 11$) were classified as stable disease. Kaplan–Meier analysis again showed a large difference in median OS for patients with PD compared with non-PD (8.0 mo [95% CI, 6.2–9.8 mo] vs. 18.0 mo [95% CI, 6.1–19.9 mo], $P = 0.001$; Fig. 2B) and a significantly higher risk of death (HR, 2.69 [95% CI, 1.42–5.11]; $P = 0.002$). A Kaplan–Meier analysis comparing all 3 response groups for both classification systems is given in Supplemental Figure 1.

Correlation between both systems was very high ($\chi^2_4 = 90.3$, $P < 0.001$, Cramér $V = 0.80$). Correspondingly, concordance probability estimates were high for both the PSMA PET/CT consensus statement, at 0.73 (SE, 0.07), and RECIP 1.0, at 0.74 (SE, 0.06). A corresponding cross table comparison is shown in Table 3.

DISCUSSION

^{68}Ga -PSMA-11 PET/CT evaluation at baseline before PSMA RLT showed a significant association between an increase in $\text{PSMA}_{\text{TV50}}$ and shorter OS, which is in line with the findings of Seifert et al. (19), despite the use of a different software solution. For ^{18}F -PSMA-1007 PET/CT, $\text{PSMA}_{\text{TV50}}$ before PSMA RLT was also a prognostic biomarker for OS. $\text{PSMA}_{\text{TV50}}$ should be validated as a prognostic biomarker before other systemic treatment options (i.e., docetaxel or olaparib) and might serve as a decision support for treatment eligibility of patients. Furthermore, the change in $\text{PSMA}_{\text{TV50}}$ from baseline to follow-up PSMA PET/CT after the end of PSMA RLT was strongly associated with OS for both tracers. In summary, irrespective of the PSMA-targeting radiopharmaceutical used, $\text{PSMA}_{\text{TV50}}$ appears to be not only a suitable imaging-based biomarker for a response prediction before PSMA RLT but also a robust response assessment parameter after PSMA RLT, independent of the number of administered cycles. Thus, $\Delta\text{PSMA}_{\text{TV50}}$ could be integrated into existing response classifications and used for systematic, quantitative, and reproducible response assessment, comparable to, for example, RECIST (26) for CT, which is necessary for the use of PSMA PET/CT in clinical trials. In addition, a lesion-specific percentage threshold (and its whole-body summary) may be suitable for different PSMA-targeting radiopharmaceuticals established in clinical practice (e.g., ^{68}Ga -PSMA-11, ^{18}F -PSMA-1007, ^{18}F -DCFPyL PSMA, or ^{18}F -rh-PSMA-7) since it does not depend on the (slightly) different (27) physiologic distribution of the tracers (28).

$\Delta\text{PSMA}_{\text{TV50}}$ data of all patients were used to assess end-of-treatment response to PSMA RLT according to the PSMA PET/CT

consensus statement and RECIP 1.0. The correlation between the classification systems was high. Both provided strong discriminatory power for OS between progressive and nonprogressive disease. The exclusion of laboratory criteria and focus on PET data alone, as well as the emphasis on change in tumor volume shared by both classification systems, allow for a simple and highly predictive risk assessment. Interestingly, the appearance of a new PSMA PET–positive lesion, which is part of RECIP 1.0, was obviously without impact in this advanced, polymetastatic disease stage. Further research is necessary to compare these classification systems in an early stage of disease. Notably, 1 patient with a relatively short survival of 4 mo, who showed an overall decrease in tumor volume of more than 30% and 2 new PET-negative liver metastases at follow-up, was subsequently categorized as PR according to the PSMA PET/CT consensus statement. Although the overall shift in focus away from the occurrence of new lesions as a solitary criterion prevents overestimation of PD and appears beneficial (12), a solely PET-based definition of new lesions seems disadvantageous compared with RECIP 1.0 and should be reviewed.

The present analysis has some limitations. First, it is inherently limited by its retrospective design. Second, the number of treatment cycles varied between 2 and 4. However, for each individual patient, the end of therapy was not defined by a fixed number of cycles but rather was determined by either disease progression or the maximum achievable therapy response. Third, the comparison of the 2 subgroups (^{68}Ga -PSMA-11 PET/CT and ^{18}F -PSMA-1007 PET/CT) is not based on a matched-pair analysis. However, no significant differences in characteristics between the 2 subgroups were found, and the groups were thus considered comparable. Fourth, the software solution used for segmentation (23,24) was developed for ^{18}F -FDG PET and not for PSMA PET. Nevertheless, assessment of $\text{PSMA}_{\text{TV50}}$ by ^{68}Ga -PSMA-11 PET/CT before PSMA RLT was confirmed to be a prognostic imaging-based marker in line with the findings by Seifert et al. (19). In addition, $\text{PSMA}_{\text{TV50}}$ was found to be valid for ^{18}F -PSMA-1007 PET/CT. Last, despite the semiautomatic approach of $\text{PSMA}_{\text{TV50}}$ assessment, the present study still relied on manual deletion of physiologic tracer uptake, resulting in multiple manual adjustments, such as in the delineation of liver metastases (found in only 3% of patients). Broadly available software solutions based on, for example, user-independent deep-learning artificial intelligence could overcome this time-consuming process (~5–10 min per scan), achieve a high repeatability of tumor volume assessment (17), and facilitate clinical adaptability.

CONCLUSION

This study presents $\text{PSMA}_{\text{TV50}}$ as a prognostic biomarker for OS before PSMA RLT, as well as its potential as a quantitative end-of-treatment response marker for patients undergoing PSMA RLT. Applying a semiautomatic approach, we found that $\text{PSMA}_{\text{TV50}}$ and $\Delta\text{PSMA}_{\text{TV50}}$ were predictive of OS not only for ^{68}Ga -PSMA-11 but also for ^{18}F -PSMA-1007 PET/CT scans. Subsequent integration of $\Delta\text{PSMA}_{\text{TV50}}$ in the PSMA PET/CT consensus statement and RECIP 1.0 provided an equally high prognostic value for both classification systems. Further research is necessary to compare the strength of these classification systems in an early stage of disease.

DISCLOSURE

No potential conflict of interest relevant to this article was reported.

TABLE 3

Comparison of Response According to PSMA PET/CT Consensus Statement (10) and RECIP 1.0

RECIP 1.0	PSMA PET/CT consensus statement		
	PR	SD	PD
PR	11 (16)	0	0
SD	3 (4)	15 (21)	4 (6)
PD	0	2 (3)	35 (50)

SD = stable disease.

Data are number of patients, with percentage in parentheses.

ACKNOWLEDGMENT

We thank Dr. Lars Frings, Medical Center, University of Freiburg, for his statistical counsel and advice.

KEY POINTS

QUESTION: Is semiautomatic, percentage-threshold-based whole-body tumor volume assessment in PSMA PET/CT a feasible and meaningful parameter for systematic response assessment of PSMA RLT?

PERTINENT FINDINGS: For both ^{68}Ga -PSMA-11 or ^{18}F -PSMA-1007—individually as well as together—PSMA_{TV50} at baseline and its change at the end of PSMA RLT were significant prognostic markers for OS. Integration of PSMA_{TV50} in the PSMA PET/CT consensus statement and RECIP 1.0 provided high prognostic value for both classification systems.

IMPLICATIONS FOR PATIENT CARE: Response assessment using change in PSMA_{TV50} can complement and possibly enhance existing PSMA PET/CT response assessment criteria.

REFERENCES

- Hofman MS, Lawrentschuk N, Francis RJ, et al. Prostate-specific membrane antigen PET-CT in patients with high-risk prostate cancer before curative-intent surgery or radiotherapy (proPSMA): a prospective, randomised, multicentre study. *Lancet*. 2020;395:1208–1216.
- Emmett L, Crumbaker M, Ho B, et al. Results of a prospective phase 2 pilot trial of ^{177}Lu -PSMA-617 therapy for metastatic castration-resistant prostate cancer including imaging predictors of treatment response and patterns of progression. *Clin Genitourin Cancer*. 2019;17:15–22.
- Scher HI, Morris MJ, Stadler WM, et al. Trial design and objectives for castration-resistant prostate cancer: updated recommendations from the Prostate Cancer Clinical Trials Working Group 3. *J Clin Oncol*. 2016;34:1402–1418.
- Hofman MS, Violet J, Hicks RJ, et al. [^{177}Lu]-PSMA-617 radionuclide treatment in patients with metastatic castration-resistant prostate cancer (LuPSMA trial): a single-centre, single-arm, phase 2 study. *Lancet Oncol*. 2018;19:825–833.
- Hofman MS, Emmett L, Sandhu S, et al. [^{177}Lu]-PSMA-617 versus cabazitaxel in patients with metastatic castration-resistant prostate cancer (TheraP): a randomised, open-label, phase 2 trial. *Lancet*. 2021;397:797–804.
- Sartor O, de Bono J, Chi KN, et al. Lutetium-177-PSMA-617 for metastatic castration-resistant prostate cancer. *N Engl J Med*. 2021;385:1091–1103.
- FDA approves Pluvicto for metastatic castration-resistant prostate cancer. Food and Drug Administration website. <https://www.fda.gov/drugs/resources-information-approved-drugs/fda-approves-pluvicto-metastatic-castration-resistant-prostate-cancer>. Updated March 23, 2022. Accessed November 29, 2022.
- Fanti S, Hadaschik B, Herrmann K. Proposal for systemic-therapy response-assessment criteria at the time of PSMA PET/CT imaging: the PSMA PET progression criteria. *J Nucl Med*. 2020;61:678–682.
- Michalski K, Klein C, Brueggemann T, Meyer PT, Jilg CA, Ruf J. Assessing response to [^{177}Lu]PSMA radioligand therapy using modified PSMA PET progression criteria. *J Nucl Med*. 2021;62:1741–1746.
- Fanti S, Goffin K, Hadaschik BA, et al. Consensus statements on PSMA PET/CT response assessment criteria in prostate cancer. *Eur J Nucl Med Mol Imaging*. 2021;48:469–476.
- Gafita A, Rauscher I, Weber M, et al. Novel framework for treatment response evaluation using PSMA PET/CT in patients with metastatic castration-resistant prostate cancer (RECIP 1.0): an international multicenter study. *J Nucl Med*. 2022;63:1651–1658.
- Gafita A, Rauscher I, Fendler WP, et al. Measuring response in metastatic castration-resistant prostate cancer using PSMA PET/CT: comparison of RECIST 1.1, aPCWG3, aPERCIST, PPP, and RECIP 1.0 criteria. *Eur J Nucl Med Mol Imaging*. 2022;49:4271–4281.
- Schmuck S, von Klot CA, Henkenberens C, et al. Initial experience with volumetric ^{68}Ga -PSMA 1&T PET/CT for assessment of whole-body tumor burden as a quantitative imaging biomarker in patients with prostate cancer. *J Nucl Med*. 2017;58:1962–1968.
- Schmidkonz C, Cordes M, Schmidt D, et al. ^{68}Ga -PSMA-11 PET/CT-derived metabolic parameters for determination of whole-body tumor burden and treatment response in prostate cancer. *Eur J Nucl Med Mol Imaging*. 2018;45:1862–1872.
- Gafita A, Bieth M, Krönke M, et al. qPSMA: semiautomatic software for whole-body tumor burden assessment in prostate cancer using ^{68}Ga -PSMA11 PET/CT. *J Nucl Med*. 2019;60:1277–1283.
- Michalski K, Mix M, Meyer PT, Ruf J. Determination of whole-body tumour burden on [^{68}Ga]PSMA-11 PET/CT for response assessment of [^{177}Lu]PSMA-617 radioligand therapy: a retrospective analysis of serum PSA level and imaging derived parameters before and after two cycles of therapy. *Nuklearmedizin*. 2019;58:443–450.
- Jansen BHE, Cysouw MCF, Vis AN, et al. Repeatability of quantitative ^{18}F -DCFPyL PET/CT measurements in metastatic prostate cancer. *J Nucl Med*. 2020;61:1320–1325.
- Giesel FL, Hadaschik B, Cardinale J, et al. F-18 labelled PSMA-1007: biodistribution, radiation dosimetry and histopathological validation of tumor lesions in prostate cancer patients. *Eur J Nucl Med Mol Imaging*. 2017;44:678–688.
- Seifert R, Herrmann K, Kleesiek J, et al. Semiautomatically quantified tumor volume using ^{68}Ga -PSMA-11 PET as a biomarker for survival in patients with advanced prostate cancer. *J Nucl Med*. 2020;61:1786–1792.
- Kratochwil C, Fendler WP, Eiber M, et al. EANM procedure guidelines for radionuclide therapy with ^{177}Lu -labelled PSMA-ligands (^{177}Lu -PSMA-RLT). *Eur J Nucl Med Mol Imaging*. 2019;46:2536–2544.
- Fendler WP, Kratochwil C, Ahmadzadehfard H, et al. ^{177}Lu -PSMA-617 therapy, dosimetry and follow-up in patients with metastatic castration-resistant prostate cancer [in German]. *Nuklearmedizin*. 2016;55:123–128.
- Hartrampf PE, Weinzierl F-X, Buck AK, et al. Matched-pair analysis of [^{177}Lu]Lu-PSMA 1&T and [^{177}Lu]Lu-PSMA-617 in patients with metastatic castration-resistant prostate cancer. *Eur J Nucl Med Mol Imaging*. 2022;49:3269–3276.
- Schindelin J, Arganda-Carreras I, Frise E, et al. Fiji: an open source platform for biological image analysis. *Nat Methods*. 2012;9:676–682.
- Kanoun S, Tal I, Vrigneaud J-M, Cochet A. Beth Israel plugin for FIJI: free and open source software for scientific research [in French]. *Med Nucl (Paris)*. 2016;40:194.
- Heller G, Mo Q. Estimating the concordance probability in a survival analysis with a discrete number of risk groups. *Lifetime Data Anal*. 2016;22:263–279.
- Eisenhauer EA, Therasse P, Bogaerts J, et al. New response evaluation criteria in solid tumours: revised RECIST guideline (version 1.1). *Eur J Cancer*. 2009;45:228–247.
- Ferreira G, Iravani A, Hofman MS, Hicks RJ. Intra-individual comparison of ^{68}Ga -PSMA-11 and ^{18}F -DCFPyL normal-organ biodistribution. *Cancer Imaging*. 2019;19:23.
- Ceci F, Oprea-Lager DE, Emmett L, et al. E-PSMA: the EANM standardized reporting guidelines v1.0 for PSMA-PET. *Eur J Nucl Med Mol Imaging*. 2021;48:1626–1638.

A Single-Arm, Low-Dose, Prospective Study of ^{177}Lu -EB-PSMA Radioligand Therapy in Patients with Metastatic Castration-Resistant Prostate Cancer

Guochang Wang*¹, Jie Zang*², Yuanyuan Jiang*¹, Qingxing Liu¹, Huimin Sui¹, Rongxi Wang¹, Xinrong Fan^{†3}, Jingjing Zhang^{†4-6}, Zhaohui Zhu^{†1}, and Xiaoyuan Chen^{†4-7}

¹Department of Nuclear Medicine, State Key Laboratory of Complex Severe and Rare Diseases, Beijing Key Laboratory of Molecular Targeted Diagnosis and Therapy in Nuclear Medicine, Peking Union Medical College Hospital, Chinese Academy of Medical Sciences, Peking Union Medical College, Beijing, China; ²Department of Nuclear Medicine, First Affiliated Hospital, Fujian Medical University, Fuzhou, China; ³Department of Urology, Peking Union Medical College Hospital, Chinese Academy of Medical Sciences, Peking Union Medical College, Beijing, China; ⁴Departments of Diagnostic Radiology, Surgery, Chemical Engineering, Biomolecular Engineering, and Biomedical Engineering, Yong Loo Lin School of Medicine and College of Design and Engineering, National University of Singapore, Singapore, Singapore; ⁵Clinical Imaging Research Centre, Centre for Translational Medicine, Yong Loo Lin School of Medicine, National University of Singapore, Singapore, Singapore; ⁶Nanomedicine Translational Research Program, NUS Center for Nanomedicine, Yong Loo Lin School of Medicine, National University of Singapore, Singapore, Singapore; and ⁷Institute of Molecular and Cell Biology, Agency for Science, Technology, and Research (A*STAR), Proteos, Singapore, Singapore

We aimed to investigate the safety and therapeutic efficacy of radioligand therapy (RLT) of ^{177}Lu -EB-prostate-specific membrane antigen (PSMA) in patients with metastatic castration-resistant prostate cancer.

Methods: Thirty men with progressive metastatic castration-resistant prostate cancer previously treated with taxane-based chemotherapy and second-generation androgen deprivation therapy were enrolled. All patients received up to 3 cycles of approximately 2.0 GBq (55 mCi) of ^{177}Lu -EB-PSMA per cycle at 8-wk intervals. The primary endpoint was therapeutic safety, including changes in hematologic status, liver function, and renal function. An additional primary endpoint was therapeutic efficacy, including prostate-specific antigen (PSA) response and molecular imaging response. The secondary endpoints were PSA progression-free survival (PFS) and overall survival (OS). Another endpoint was patient-reported health-related quality of life. **Results:** From January 2019 to December 2021, 30, 22, and 11 patients received 1, 2, or 3 cycles of ^{177}Lu -EB-PSMA RLT, respectively. During the entire follow-up period, 33.3% of patients experienced grade 3 hematologic adverse events. Seventeen (56.7%) patients achieved a PSA reduction of at least 50%. The median PSA PFS was 4.6 mo (95% CI, 2.7–6.5 mo), and the median OS was 12.6 mo (95% CI, 8.1–17.1 mo). A higher whole-body PSMA SUV_{mean} correlated with a better PSA response, higher baseline alkaline phosphatase and larger total PSMA-positive tumor volume were associated with worse PSA PFS, and the existence of visceral metastases and higher PSA value at baseline were significant prognosticators of worse OS. Health-related quality-of-life outcomes improved significantly after ^{177}Lu -EB-PSMA RLT. **Conclusion:** RLT based on approximately 2.0 GBq of ^{177}Lu -EB-PSMA for up to 3 cycles may achieve a PSA response and hematologic toxicity comparable to those from 7.4-GBq doses of ^{177}Lu -PSMA-617 for up to 4–6 cycles. Further studies with more cycles of ^{177}Lu -EB-PSMA RLT are needed to evaluate the potential benefits in terms of PFS and OS.

Key Words: ^{177}Lu -EB-PSMA; radioligand therapy; metastatic castration-resistant prostate cancer (mCRPC); Evans blue; albumin binding

J Nucl Med 2023; 64:611–617

DOI: 10.2967/jnumed.122.264857

Treatment of metastatic castration-resistant prostate cancer (mCRPC) remains a huge challenge for urologists and oncologists. Radioligand therapy (RLT) targeting prostate-specific membrane antigen (PSMA) has attracted interest as a potential treatment modality for mCRPC. The phase 3 VISION trial demonstrated that RLT based on ^{177}Lu -PSMA-617 plus standard care significantly extended imaging-based progression-free survival (PFS) and overall survival (OS) versus standard care alone in patients with advanced PSMA-positive mCRPC (1). Additionally, some phase 2 trials revealed that ^{177}Lu -PSMA-617 therapy achieved a better serum prostate-specific antigen (PSA) response and fewer grade 3–4 adverse events in the treatment of mCRPC than cabazitaxel (2) and docetaxel (3). Given these remarkable results, PSMA-targeted radioligand therapy (PRLT) seems to be a promising treatment modality for mCRPC. On March 23, 2022, the U.S. Food and Drug Administration approved Pluvicto (^{177}Lu -PSMA-617; Novartis) to treat men with PSMA-positive mCRPC who have been treated with androgen receptor pathway inhibition and taxane-based chemotherapy (4), representing a significant advance in the theranostics of prostate cancer.

Currently, PRLT is based mainly on small-molecule inhibitors, such as PSMA-617 and PSMA I&T (5,6). Previous studies have reported no significant difference in safety and efficacy between ^{177}Lu -PSMA-617 and ^{177}Lu -PSMA I&T (7,8). However, radiolabeled small molecules targeting PSMA are cleared quickly from the blood (9). Therefore, PRLT based on both PSMA-617 and PSMA I&T requires high doses, which may cause obvious systemic toxicity, require more radiation protection, and lead to a

Received Aug. 30, 2022; revision accepted Oct. 19, 2022.

For correspondence or reprints, contact Xinrong Fan (pumcxfx@126.com) or Xiaoyuan Chen (chen.shawn@nus.edu.sg).

*Contributed equally to this work.

†Contributed equally to this work.

Published online Nov. 3, 2022.

COPYRIGHT © 2023 by the Society of Nuclear Medicine and Molecular Imaging.

large financial burden. We conjugated a truncated Evans blue (EB) molecule and DOTA chelator onto PSMA-617 and labeled it with ^{177}Lu to obtain a new radiopharmaceutical, ^{177}Lu -EB-PSMA (10). EB can bind to albumin to slow its plasma clearance rate, thereby increasing tumor accumulation and reducing the total dose of ^{177}Lu . Because of the limited supply of ^{177}Lu , ^{177}Lu -EB-PSMA may be an option to consider by which more patients may benefit. In a previous dosimetry study, Zang et al. demonstrated that the tumor-accumulated radioactivity of ^{177}Lu -EB-PSMA was about 3.02-fold higher than that of ^{177}Lu -PSMA-617, and a single low dose of ^{177}Lu -EB-PSMA RLT revealed that the tumor uptake of ^{68}Ga -PSMA-617 in patients was decreased more significantly than the same dose of ^{177}Lu -PSMA-617 RLT. However, the red bone marrow and kidneys also showed higher uptake for ^{177}Lu -EB-PSMA than for ^{177}Lu -PSMA-617 (9). Subsequently, Zang et al. conducted an escalating dose study, which revealed that 2.12 ± 0.19 GBq (57.3 ± 5.1 mCi) per dose of ^{177}Lu -EB-PSMA exhibited relatively high efficacy and acceptable side effects (11). All these studies suggested ^{177}Lu -EB-PSMA to be a promising alternative radiopharmaceutical in PRLT against mCRPC.

This prospective trial was designed to further assess the safety and therapeutic efficacy of low-dose ^{177}Lu -EB-PSMA, in doses of approximately 2.0 GBq (55 mCi) for up to 3 cycles, in patients with mCRPC.

MATERIALS AND METHODS

The study was approved by the Institutional Review Board of Peking Union Medical College Hospital, the Chinese Academy of Medical Sciences, and Peking Union Medical College (approval JS-2105) and was registered at ClinicalTrials.gov (NCT04996602).

Patients

Participants who met the inclusion criteria (as stated in the supplemental materials, available at <http://jnm.snmjournals.org>) underwent ^{68}Ga -PSMA-617 and ^{18}F -FDG PET/CT within 2 wk before PRLT to confirm high PSMA expression, which was defined as most tumors' ($\geq 80\%$) having a baseline SUV_{max} significantly (≥ 1.5 times) greater than the SUV_{mean} of the normal liver. Patients were excluded if they had an ^{18}F -FDG-positive tumor without corresponding PSMA uptake (3,12).

PET/CT Imaging

The ^{68}Ga -PSMA-617 and ^{18}F -FDG PET/CT acquisitions were performed as previously described (13).

The images were transferred to MIM software (version 7.1.4; MIM Software Inc.). The volume of interest for the tumor was segmented using PET Edge (MIM Software Inc.), a gradient-based segmentation algorithm with an SUV threshold of at least 3.0. For segmentation of liver metastases, a threshold of 1.5 times the SUV_{mean} of the normal liver tissue was used (14–16). Total lesion PSMA (TLP) was calculated through the summed product of total PSMA-positive tumor volume (PSMA-VOL) times the SUV_{mean} of all tumors. Whole-body PSMA SUV_{mean} was calculated through dividing TLP by PSMA-VOL.

Treatment Regimen and Follow-up

The median administered activity per cycle was 2.0 GBq (range, 1.9–2.2 GBq). The radiopharmaceutical was diluted into 100 mL of normal saline and slowly administered intravenously to the patient within 30–60 min. Before ^{177}Lu -EB-PSMA administration, all patients accepted intravenous hydration with normal saline for 30 min, and the salivary glands were cooled with an ice pack for 30 min to minimize dry mouth syndrome. Each patient received up to 3 cycles of ^{177}Lu -EB-PSMA RLT at 8-wk intervals.

Hematologic status was assessed every 2 wk after the injection of ^{177}Lu -EB-PSMA; liver function, renal function, and serum PSA values

were documented every 4 wk. Short-term follow-up ended at 10 wk after the last cycle of PRLT. Long-term follow-up with laboratory testing ended at the time of death from any cause, the start of another treatment modality, or the latest study visit. ^{68}Ga -PSMA-617 PET/CT reexaminations were performed 1 wk before the administration of ^{177}Lu -EB-PSMA and 8 wk after the last treatment cycle. In addition, patient-reported health-related quality of life was assessed using the European Organization for Research and Treatment of Cancer Quality-of-Life Questionnaire, which includes 30 items related to functioning and symptom scales, within 1 wk before each cycle of therapy and at the 8 wk after the final treatment session.

Outcomes

The first primary endpoint was adverse events, which were categorized according to the Common Toxicity Criteria for Adverse Events, version 5.0 (11). The second primary endpoint was best PSA response based on the Prostate Cancer Clinical Trials Working group 3 guidelines, which defined a PSA decrease of at least 50% from baseline as partial response (PR), a PSA increase of at least 25% as progressive disease (PD), and a PSA increase of less than 25% or a decrease of less than 50% as stable disease. The third primary endpoint was molecular imaging response according to the adapted PET Response Criteria in Solid Tumors (PERCIST), version 1.0, and Response Evaluation Criteria in PSMA PET/CT (RECIP), version 1.0. In the former, a complete response was defined as complete disappearance of TLP from target tumors on ^{68}Ga -PSMA-617 PET/CT compared with the baseline scan, a PR was defined as at least a 30% decrease in the TLP of target tumors without the appearance of new lesions, a PD was defined as at least a 30% increase in the TLP of target tumors or the appearance of new lesions, and stable disease was defined as a TLP increase of less than 30% or a TLP decrease of less than 30% and no appearance of new lesions (15,17). In RECIP, a complete response was defined as absence of any PSMA ligand uptake, PR was defined as at least a 30% decline in PSMA-VOL and no appearance of new lesions, PD was defined as at least a 20% increase in PSMA-VOL and the appearance of new lesions, and stable disease was defined as any condition but RECIP-PR or RECIP-PD (18).

The secondary endpoints were PSA PFS and OS. PSA PFS was defined as the interval from the date of patient enrollment to PSA progression, which was defined as an increase of at least 25% and at least 2 ng/mL after 12 wk (2,12,19). OS was defined as the interval from the date of patient enrollment to death from any cause or the last study visit (1,15). Another endpoint was health-related quality-of-life assessment (2).

RESULTS

Demographic and Clinical Characteristics

Thirty patients were enrolled. Data on PSA response rate and toxic side effects for the first 10 patients were previously published (11). The first cycle of PRLT was performed in January 2019, and the last ^{177}Lu -EB-PSMA therapy session was in December 2021. The date of the last follow-up was August 20, 2022. In total, 22 and 11 patients received 2 and 3 cycles of ^{177}Lu -EB-PSMA RLT, respectively. The reasons for not completing all 3 cycles as scheduled were non-tumor-related death for 1 patient (3.3%), disease progression for 5 patients (16.7%), severe side effects for 3 patients (10.0%), withdrawal from the study for 2 patients (6.6%), and quarantine measures during the novel coronavirus disease 2019 pandemic for 8 patients (26.7%). Detailed patient characteristics and flowcharts are shown in Supplemental Table 1 and Figure 1, respectively.

Safety

All patients tolerated approximately a 2.0-GBq (55 mCi) dose of ^{177}Lu -EB-PSMA well; there were no immediate adverse effects

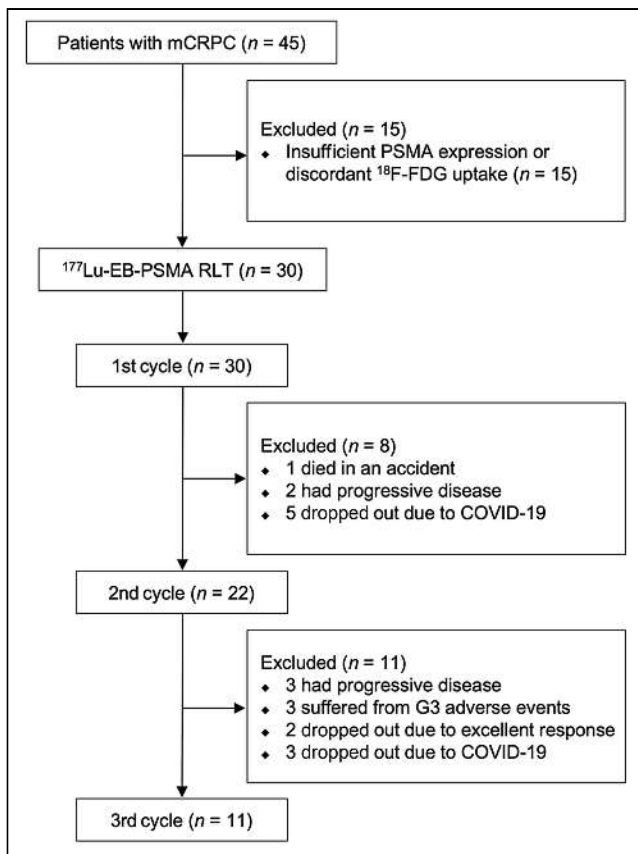


FIGURE 1. Flowchart of patient enrollment process and follow-up.

recorded during administration and no treatment-related deaths. One death occurred 7 wk after the first cycle of therapy because of non-treatment-related respiratory aspiration.

The most common toxic effects were fatigue, dry mouth, and nausea, which were recorded in 16 (53.3%), 12 (40.0%), and 12 (40.0%) patients, respectively. These adverse events, however, were classified as exclusively grade 1–2 and usually did not require additional interventions. In addition, 9 (30.0%) patients experienced temporary ostealgia, 3 (10.0%) patients developed mild diarrhea, and 2 (6.7%) patients reported temporary appetite loss. There were no noticeable fluctuations in liver function at any point during the entire follow-up for any enrolled patients. No patients had renal adverse events during short-term follow-up. During long-term follow-up, however, 1 patient had a grade 2 renal adverse event (increased serum creatinine) at 16 wk after the third cycle of $^{177}\text{Lu-EB-PSMA}$ PRLT, 1 patient had a grade 1 renal adverse event at 18 wk after the second cycle of PRLT, and 1 patient had a grade 1 renal adverse event at 24 wk after the third cycle of PRLT.

Hematologic toxicity was the most serious side effect and caused 3 (10.0%) patients to drop out of the clinical trial. During short-term follow-up, 24 (80.0%) patients developed grade 1–2 adverse events and 9 (30.0%) patients developed grade 3 adverse events at 4–6 wk after PRLT. During long-term follow-up, 1 patient had additional grade 3 thrombocytopenia at 16 wk after the third cycle of PRLT. No patients experienced grade 4 adverse events. Details are shown in Supplemental Table 2.

Therapeutic Response

The primary endpoint of a PSA reduction of 50% or more from baseline was achieved in 17 (56.7%; 95% CI, 37.8%–75.5%)

patients over all cycles of $^{177}\text{Lu-EB-PSMA}$ RLT, with 23 (76.7%; 95% CI, 60.6%–92.7%) patients showing any decline in PSA level. After the first cycle of $^{177}\text{Lu-EB-PSMA}$ RLT, 10 (33.3%; 95% CI, 15.4%–51.2%) patients demonstrated at least a 50% PSA decline, with 20 (66.6%; 95% CI, 48.8%–84.6%) patients showing any decline in PSA level. Supplemental Figure 1 shows the waterfall plots of the percentage change in PSA response compared with baseline after the first cycle of $^{177}\text{Lu-EB-PSMA}$ RLT and the best PSA response rate for all courses.

During the first, second, and third observation cycles of PRLT, 27, 18, and 10 patients, respectively, underwent $^{68}\text{Ga-PSMA}$ PET/CT on schedule. For adapted PERCIST, after the first cycle of treatment, 14 (51.9%) patients achieved PR, 7 (25.9%) patients had stable disease, and 6 (22.2%) patients had PD. After the second cycle of PRLT, 11 (61.1%), 4 (22.2%), and 3 (16.7%) patients had PR, stable disease, and PD, respectively. After the last cycle of PRLT, 6 (60.0%), 3 (30.0%), and 1 (10.0%) patients had PR, stable disease, and PD, respectively. Regarding RECIP, after the first cycle of PRLT, 13 (48.1%) patients achieved PR, 9 (33.3%) patients had stable disease, and 5 (18.5%) patients had PD. After the second cycle of PRLT, 10 (55.5%), 5 (27.8%), and 3 (16.7%) patients had PR, stable disease, and PD, respectively. After the third cycle of PRLT, 5 (50.0%), 4 (40.0%), and 1 (10.0%) patients had PR, stable disease, and PD, respectively.

The baseline TLP had a moderate correlation with baseline serum PSA level ($r = 0.578$, $P = 0.001$), and there was a strong association between change in (Δ) TLP and ΔPSA in patients during the matched cycle of PRLT ($r = 0.709$, $P < 0.001$). Similarly, the baseline PSMA-VOL also had a moderate correlation with baseline PSA ($r = 0.584$, $P = 0.001$), and there was a moderate association between $\Delta\text{PSMA-VOL}$ and ΔPSA in patients during the matched cycle of PRLT ($r = 0.587$, $P = 0.001$), as shown in Figures 2 and 3. A higher whole-body PSMA SUV_{mean} (odds ratio, 2.085 [95% CI, 1.131–3.843]; $P = 0.009$) and higher baseline TLP (odds ratio, 1.102 [95% CI, 1.008–1.205]; $P = 0.032$) were closely associated with the best PSA response. However, multivariable analysis revealed that only a higher whole-body PSMA SUV_{mean} (odds ratio, 1.977 [95% CI, 1.014–3.855]; $P = 0.043$) was predictive of the best PSA response.

PSA PFS and OS

At a median follow-up of 23.8 mo, PSA progression occurred in all 29 (96.7%) patients (except for 1 death), and 22 (73.3%) patients had died. The median PSA PFS was 4.6 mo (95% CI, 2.7–6.5 mo), and the median OS was 12.6 mo (95% CI, 8.1–17.1 mo), as shown in Figure 4.

Univariate analysis of potential predictive factors for PSA PFS showed that higher baseline alkaline phosphatase (ALP) (hazard ratio [HR], 1.005 [95% CI, 1.001–1.008]; $P = 0.006$) and higher baseline PSMA-VOL (HR, 1.026 [95% CI, 1.003–1.083]; $P = 0.015$) were closely associated with worse PSA PFS. Multivariable analysis revealed that baseline ALP (HR, 1.006 [95% CI, 1.001–1.011]; $P = 0.010$) and baseline PSMA-VOL (HR, 1.047 [95% CI, 0.972–1.092]; $P = 0.026$) also remained predictive of PSA PFS, as shown in Figure 5.

The presence of visceral disease (HR, 0.059 [95% CI, 0.011–0.317]; $P = 0.001$), higher baseline PSA (HR, 1.003 [95% CI, 1.001–1.004]; $P = 0.001$), and higher baseline TLP (HR, 1.078 [95% CI, 1.025–1.134]; $P = 0.023$) were closely associated with worse OS. Multivariable analysis revealed that the presence of visceral disease (HR, 0.101 [95% CI, 0.024–0.437]; $P = 0.002$) and baseline PSA (HR, 1.002 [95% CI, 1.000–1.003]; $P = 0.039$) were predictive factors for OS, as shown in Figure 5.

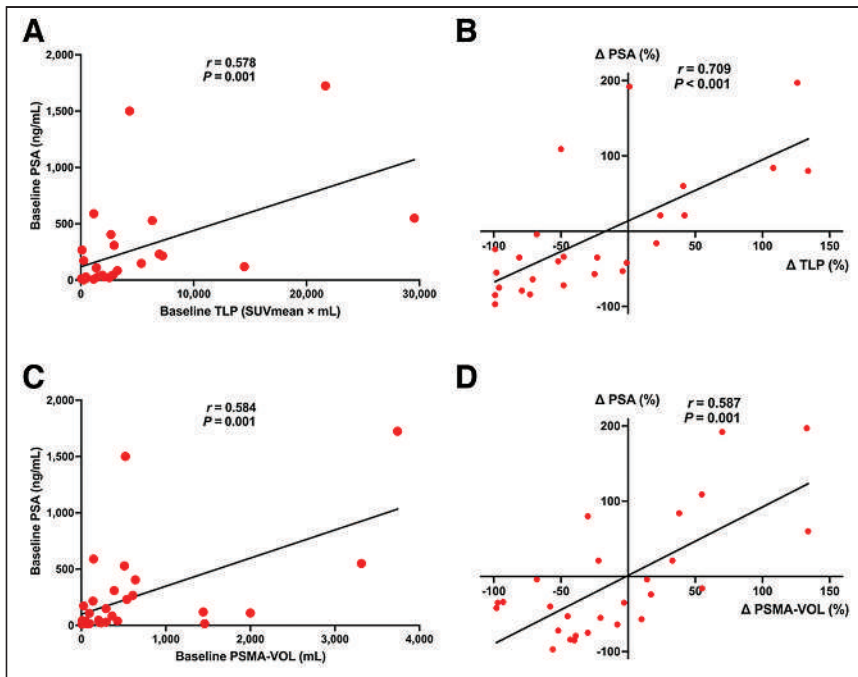


FIGURE 2. Correlations of baseline TLP with baseline PSA (A), Δ TLP and Δ PSA in patients during matched cycle of PRLT (B), baseline PSMA-VOL and baseline PSA (C), and Δ PSMA-VOL and Δ PSA in patients during matched cycle of PRLT (D).

Quality of Life

We summarized the health-related quality-of-life scores, as shown in Supplemental Table 3. The baseline assessment was completed by

all 30 participants. Subsequently, 29, 21, and 11 men completed the same assessments after 1, 2, and 3 cycles of ^{177}Lu -EB-PSMA RLT, respectively.

Overall, physical functioning and global health status improved significantly after 2 cycles of PRLT, and the mean pain severity score decreased from baseline. After the first cycle of ^{177}Lu -EB-PSMA RLT, there was a transient increase in fatigue and appetite loss scores, but no statistically significant difference was found between baseline and cycles 2 or 3.

DISCUSSION

We conducted a clinical study to verify the safety and therapeutic efficacy of ^{177}Lu -EB-PSMA at approximately 2.0 GBq (55 mCi) per cycle in a 30-person cohort with mCRPC. Our study exhibited a 50% or higher PSA decline from baseline in 56.7% of patients undergoing ^{177}Lu -EB-PSMA RLT, as well as exhibiting significantly improved health-related quality-of-life scores, whereas a high rate of hematologic toxicity was also observed.

Sartor et al. conducted a phase 3 trial to assess the efficacy and safety of ^{177}Lu -PSMA-617 RLT (7.4 GBq every 6 wk for 4–6 cycles) in patients with mCRPC and reported that adverse events of grade 3 or above occurred in 52.7% of patients (1). Another clinical trial (TheraP), conducted by Hofman et al., compared ^{177}Lu -PSMA-617 (6.0–8.5 GBq

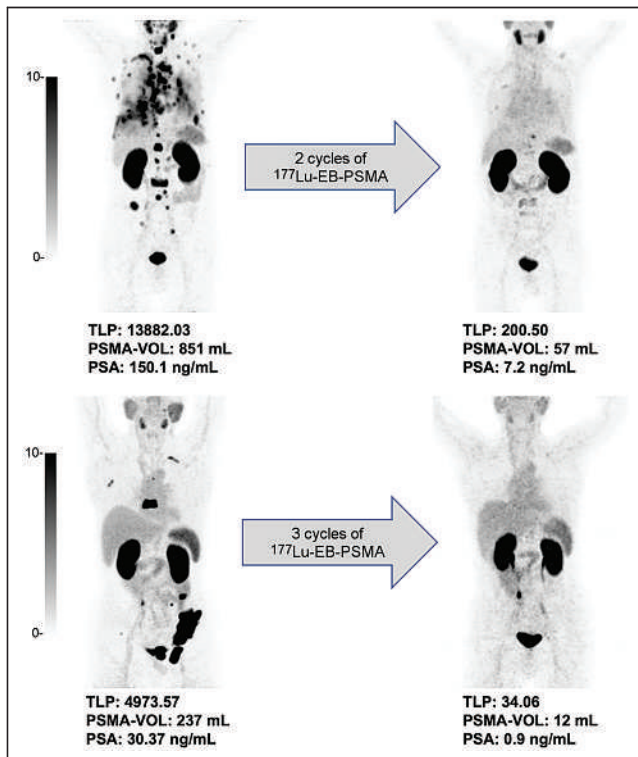


FIGURE 3. Representative molecular imaging and PSA responses in 2 patients before and 8 wk after ^{177}Lu -EB-PSMA therapy.

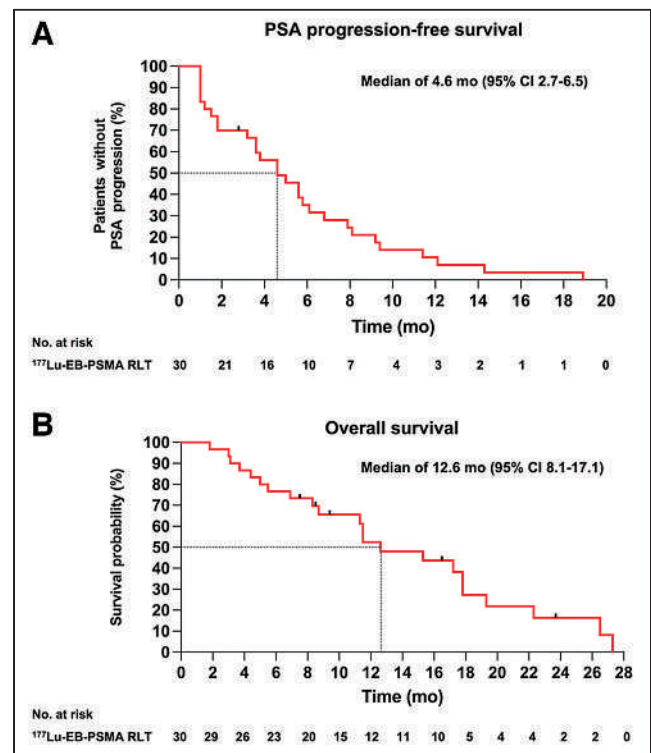


FIGURE 4. Kaplan–Meier curves of PSA PFS (A) and OS (B).

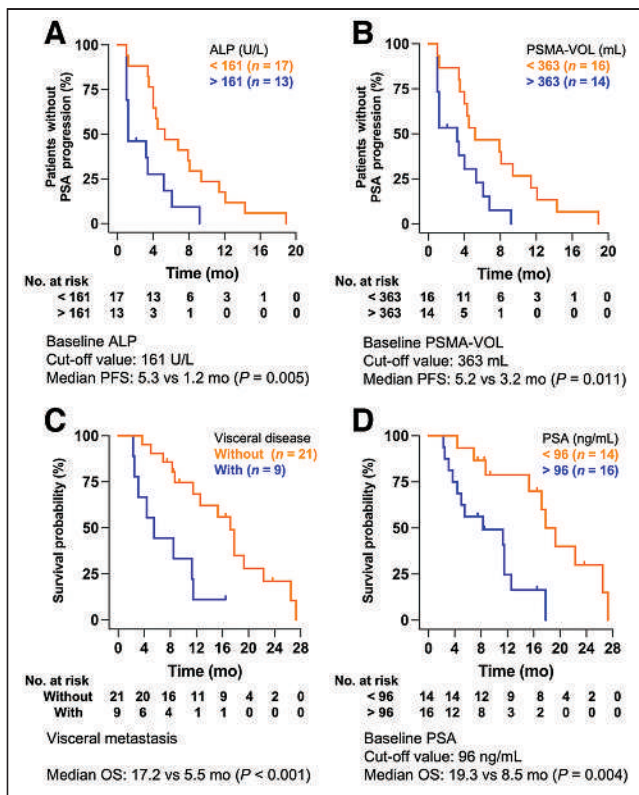


FIGURE 5. Kaplan-Meier curves of PSA PFS and OS using log-rank comparison. Patients with higher baseline ALP (A) and larger baseline PSMA-VOL (B) showed worse PSA PFS. Patients with visceral metastasis (C) and higher baseline PSA (D) showed worse OS.

every 6 wk for up to 6 cycles) with cabazitaxel in patients with mCRPC and showed that 32 of 98 (32.7%) patients had grade 3–4 adverse events in the ^{177}Lu -PSMA-617 group (2). Previous studies have confirmed that the kidney- and red bone marrow-accumulated radioactivities of ^{177}Lu -EB-PSMA were about 6.51-fold and 6.13-fold higher, respectively, than those of ^{177}Lu -PSMA-617. On the basis of the dosimetry of ^{177}Lu -EB-PSMA to red bone marrow and kidneys, as well as the respective maximum tolerated doses of 2 Gy and 23–29 Gy (9,20), respectively, similar mCRPC patients can accept up to 5–6 cycles of ^{177}Lu -EB-PSMA RLT with approximately 2.0 GBq (55 mCi) per cycle. In our study, no renal adverse event was observed during short-term follow-up, and 3 grade 1–2 adverse events occurred at long-term follow-up. Importantly, 33.3% of patients had grade 3 hematologic events within up to 3 cycles of PRLT, which was comparable to 7.4-GBq (200 mCi) doses of ^{177}Lu -PSMA-617 for up to 4–6 cycles; this result suggests that future studies with larger samples and more cycles (≥ 4) of treatment must be carefully performed.

Regarding PSA response, the clinical trial conducted by Sartor et al. reported a PSA decrease of at least 50% in 177 of 385 (46.0%) patients (1). A systematic review also reported that approximately 46.0% of mCRPC patients achieved a PSA decrease of at least 50% after at least 1 cycle of RLT (^{177}Lu -PSMA-617 or ^{177}Lu -PSMA-I&T) (21). It is encouraging that ^{177}Lu -EB-PSMA at a third or fourth of the dose of ^{177}Lu -PSMA-617 can achieve a comparable best PSA response rate (56.7%). A previous study reported that more PRLT cycles may be associated with a higher proportion of patients who

achieve the best PSA responses (21). In this study, we performed an average of only 2 cycles of PRLT, which may reduce the real therapeutic efficacy of ^{177}Lu -EB-PSMA. In addition, the median PSA PFS and OS in our study were 4.6 mo (95% CI, 2.7–6.5 mo) and 12.6 mo (95% CI, 8.1–17.1 mo), respectively. Hofman et al. (12) revealed a median PSA PFS of 7.6 mo (95% CI, 6.3–9.0 mo) and a median OS of 13.5 mo (95% CI, 10.4–22.7 mo) in their ^{177}Lu -PSMA trial (^{177}Lu -PSMA-617, 7.4 GBq every 6 wk for up to 4 cycles). Satapathy et al. compared ^{177}Lu -PSMA-617 (6.0–7.4 GBq every 8 wk for up to 4 cycles) with docetaxel in patients with mCRPC and reported a median PFS of 4.0 mo (95% CI, 1.8–6.2 mo) (3). In addition, Sartor et al. revealed a median OS of 15.3 mo (1). Quite a few studies confirmed that prior chemotherapy and visceral metastasis correlated with worse time-to-event outcomes after PRLT (22–24). In our study, all patients received chemotherapy before PRLT, and 30.0% of patients were diagnosed with visceral metastasis, which may partly contribute to relatively shorter PSA PFS and OS. Another important reason may be that some patients did not complete their established treatment plans because of the coronavirus disease 2019 pandemic. Of course, these speculations need to be further confirmed in subsequent studies.

We analyzed the possible predictors of treatment response and prognosis and found that whole-body PSMA SUV_{mean} was an independent predictor of the best PSA response, and this was confirmed by some previous studies (14,25,26). At present, most clinical trials on PRLT use PSMA PET/CT to screen participants, and the SUV_{max} of the tumor is the most common evaluation parameter. However, whole-body PSMA SUV_{mean} may be more suitable than SUV_{max} to assess the heterogeneity of PSMA expression in mCRPC patients. In addition, a previous dosimetry study demonstrated that whole-body PSMA SUV_{mean} was associated with the average absorbed radiation dose and therapeutic response (27). Hence, we suggest that whole-body PSMA SUV_{mean} may be a better biomarker for guiding enrollment screening in future studies. A higher baseline ALP and larger PSMA-VOL correlated with worse PSA PFS, as is consistent with other studies (14,28). A higher ALP and larger PSMA-VOL indicate a higher tumor burden, especially bone metastases. Therefore, it is biologically plausible that ALP and PSMA-VOL are significant prognosticators of PSA PFS. Finally, visceral metastasis and baseline PSA were negative predictive factors for OS, as also agrees with previous studies (22,29–32). All these findings are valuable in guiding future PRLT.

In this study, the molecular imaging response was assessed by ^{68}Ga -PSMA-617 PET/CT based on adapted PERCIST and RECIP. We observed that baseline TLP and PSMA-VOL had a moderate correlation with baseline PSA. In addition, we found a strong correlation between ΔTLP and ΔPSA and a moderate association between $\Delta\text{PSMA-VOL}$ and ΔPSA in patients during the matched cycle of PRLT. Recently, some researchers confirmed that evaluating PSMA response with PET had value even better than that of RECIST and the adapted Prostate Cancer Clinical Trials Working Group 3 Criteria (33–35). In our study, some parameters derived from PSMA PET, such as whole-body PSMA SUV_{mean} and PSMA-VOL, also correlated significantly with therapeutic response evaluation and PSA PFS. Hence, we believe that PSMA PET should be used not only for screening patients based on the inclusion criteria but also for restaging disease during the course of PRLT to standardize PSMA-driven response assessments in patients with mCRPC.

Our study had some limitations. The most notable issue was the limited number of participants and treatment cycles. In particular, more than half the patients did not complete the established 3 cycles of treatment for various reasons. The second limitation is the lack of a control group for standard RLT with ^{177}Lu -PSMA-617, as comparing the therapeutic value of ^{177}Lu -EB-PSMA with the published literature might lead to some bias. Larger studies are needed to validate these results.

Even so, this prospective study demonstrated the potential value of ^{177}Lu -EB-PSMA in the treatment of mCRPC. In other words, it is feasible to reduce the dose of each injection and optimize the use of ^{177}Lu by improving the internal pharmacokinetics of the therapeutic drug, although the resulting systemic toxicity should be closely monitored.

CONCLUSION

Our study demonstrated that ^{177}Lu -EB-PSMA may be an alternative radiopharmaceutical in the therapy of mCRPC. A low dose (~2.0 GBq) of ^{177}Lu -EB-PSMA for up to 3 cycles may reach a PSA response rate and hematologic toxicity comparable to those from 7.4 GBq per cycle of ^{177}Lu -PSMA-617 for up to 4–6 cycles. In our study, shorter PFS and OS may be attributed partly to fewer cycles of ^{177}Lu -EB-PSMA RLT. Further studies with increased numbers of patients and more cycles of treatment are warranted.

DISCLOSURE

This study was supported by the Chinese Academy of Medical Science Innovation Fund for Medical Sciences (2021-I2 M-1-016, 2022-I2 M-2-002), the Beijing Natural Science Foundation (M22035), the National Natural Science Foundation of China (81871392), the National University of Singapore Start-up Grant (NUHSRO/2020/133/Startup/08), and the National Research Foundation, Singapore, and National Medical Research Council, Singapore, under their NMRC Centre Grant Program (CG21APR1005). No other potential conflict of interest relevant to this article was reported.

KEY POINTS

QUESTION: Is RLT based on a low dose of ^{177}Lu -EB-PSMA safe and efficacious?

PERTINENT FINDINGS: A 2.0-GBq (55 mCi) dose of ^{177}Lu -EB-PSMA for up to 3 cycles achieved acceptable side effects and therapeutic response.

IMPLICATIONS FOR PATIENT CARE: RLT based on low-dose ^{177}Lu -EB-PSMA may be a promising therapeutic option for patients with mCRPC.

REFERENCES

- Sartor O, de Bono J, Chi KN, et al. Lutetium-177-PSMA-617 for metastatic castration-resistant prostate cancer. *N Engl J Med*. 2021;385:1091–1103.
- Hofman MS, Emmett L, Sandhu S, et al. [^{177}Lu]Lu-PSMA-617 versus cabazitaxel in patients with metastatic castration-resistant prostate cancer (TheraP): a randomised, open-label, phase 2 trial. *Lancet*. 2021;397:797–804.
- Satapathy S, Mittal BR, Sood A, et al. ^{177}Lu -PSMA-617 versus docetaxel in chemotherapy-naïve metastatic castration-resistant prostate cancer: a randomized, controlled, phase 2 non-inferiority trial. *Eur J Nucl Med Mol Imaging*. 2022;49:1754–1764.
- Mullard A. FDA approves first PSMA-targeted radiopharmaceutical. *Nat Rev Drug Discov*. 2022;21:327.
- Benešová M, Schafer M, Bauder-Wust U, et al. Preclinical evaluation of a tailor-made DOTA-conjugated PSMA inhibitor with optimized linker moiety for imaging and endoradiotherapy of prostate cancer. *J Nucl Med*. 2015;56:914–920.
- Weinisen M, Schottelius M, Simecek J, et al. ^{68}Ga - and ^{177}Lu -labeled PSMA I&T: optimization of a PSMA-targeted theranostic concept and first proof-of-concept human studies. *J Nucl Med*. 2015;56:1169–1176.
- Schuchardt C, Zhang J, Kulkarni HR, Chen X, Muller D, Baum RP. Prostate-specific membrane antigen radioligand therapy using ^{177}Lu -PSMA I&T and ^{177}Lu -PSMA-617 in patients with metastatic castration-resistant prostate cancer: comparison of safety, biodistribution, and dosimetry. *J Nucl Med*. 2022;63:1199–1207.
- Hartrampf PE, Weinzierl FX, Buck AK, et al. Matched-pair analysis of [^{177}Lu]Lu-PSMA I&T and [^{177}Lu]Lu-PSMA-617 in patients with metastatic castration-resistant prostate cancer. *Eur J Nucl Med Mol Imaging*. 2022;49:3269–3276.
- Zang J, Fan X, Wang H, et al. First-in-human study of ^{177}Lu -EB-PSMA-617 in patients with metastatic castration-resistant prostate cancer. *Eur J Nucl Med Mol Imaging*. 2019;46:148–158.
- Wang Z, Tian R, Niu G, et al. Single low-dose injection of Evans blue modified PSMA-617 radioligand therapy eliminates prostate-specific membrane antigen positive tumors. *Bioconjug Chem*. 2018;29:3213–3221.
- Zang J, Liu Q, Sui H, et al. ^{177}Lu -EB-PSMA radioligand therapy with escalating doses in patients with metastatic castration-resistant prostate cancer. *J Nucl Med*. 2020;61:1772–1778.
- Hofman MS, Violet J, Hicks RJ, et al. [^{177}Lu]PSMA-617 radionuclide treatment in patients with metastatic castration-resistant prostate cancer (LuPSMA trial): a single-centre, single-arm, phase 2 study. *Lancet Oncol*. 2018;19:825–833.
- Wang G, Zhou M, Zang J, et al. A pilot study of ^{68}Ga -PSMA-617 PET/CT imaging and ^{177}Lu -EB-PSMA-617 radioligand therapy in patients with adenoid cystic carcinoma. *EJNMMI Res*. 2022;12:52.
- Ferdinandus J, Violet J, Sandhu S, et al. Prognostic biomarkers in men with metastatic castration-resistant prostate cancer receiving [^{177}Lu]PSMA-617. *Eur J Nucl Med Mol Imaging*. 2020;47:2322–2327.
- Rosar F, Wenner F, Khreish F, et al. Early molecular imaging response assessment based on determination of total viable tumor burden in [^{68}Ga]Ga-PSMA-11 PET/CT independently predicts overall survival in [^{177}Lu]Lu-PSMA-617 radioligand therapy. *Eur J Nucl Med Mol Imaging*. 2022;49:1584–1594.
- Werner-Wasik M, Nelson AD, Choi W, et al. What is the best way to contour lung tumors on PET scans? Multiobserver validation of a gradient-based method using a NSCLC digital PET phantom. *Int J Radiat Oncol Biol Phys*. 2012;82:1164–1171.
- Wahl RL, Jacene H, Kasamon Y, Lodge MA. From RECIST to PERCIST: evolving considerations for PET response criteria in solid tumors. *J Nucl Med*. 2009;50(suppl 1):122S–150S.
- Gafita A, Rauscher I, Weber M, et al. Novel framework for treatment response evaluation using PSMA PET/CT in patients with metastatic castration-resistant prostate cancer (RECIP 1.0): an international multicenter study. *J Nucl Med*. 2022;63:1651–1658.
- Scher HI, Morris MJ, Stadler WM, et al. Trial design and objectives for castration-resistant prostate cancer: updated recommendations from the Prostate Cancer Clinical Trials Working Group 3. *J Clin Oncol*. 2016;34:1402–1418.
- Zhang J, Wang H, Jacobson O, et al. Safety, pharmacokinetics, and dosimetry of a long-acting radiolabeled somatostatin analog ^{177}Lu -DOTA-EB-TATE in patients with advanced metastatic neuroendocrine tumors. *J Nucl Med*. 2018;59:1699–1705.
- Sadaghiani MS, Sheikhbahaei S, Werner RA, et al. A systematic review and meta-analysis of the effectiveness and toxicities of lutetium-177-labeled prostate-specific membrane antigen-targeted radioligand therapy in metastatic castration-resistant prostate cancer. *Eur Urol*. 2021;80:82–94.
- Kessel K, Seifert R, Schafers M, et al. Second line chemotherapy and visceral metastases are associated with poor survival in patients with mCRPC receiving ^{177}Lu -PSMA-617. *Theranostics*. 2019;9:4841–4848.
- Ahmadzadehfah H, Matern R, Baum RP, et al. The impact of the extent of the bone involvement on overall survival and toxicity in mCRPC patients receiving [^{177}Lu]Lu-PSMA-617: a WARMTH multicentre study. *Eur J Nucl Med Mol Imaging*. 2021;48:4067–4076.
- Ahmadzadehfah H, Rahbar K, Baum RP, et al. Prior therapies as prognostic factors of overall survival in metastatic castration-resistant prostate cancer patients treated with [^{177}Lu]Lu-PSMA-617. A WARMTH multicenter study (the 617 trial). *Eur J Nucl Med Mol Imaging*. 2021;48:113–122.
- Pathmanandavel S, Crumbaker M, Yam AO, et al. ^{177}Lu -PSMA-617 and idronoxil in men with end-stage metastatic castration-resistant prostate cancer (LuPIN): patient

- outcomes and predictors of treatment response in a phase I/II trial. *J Nucl Med.* 2022;63:560–566.
26. Kuo P, Hesterman J, Rahbar K, et al. [⁶⁸Ga]Ga-PSMA-11 PET baseline imaging as a prognostic tool for clinical outcomes to [¹⁷⁷Lu]Lu-PSMA-617 in patients with mCRPC: a VISION substudy [abstract]. *J Clin Oncol.* 2022;40:5002.
 27. Violet J, Jackson P, Ferdinandus J, et al. Dosimetry of ¹⁷⁷Lu-PSMA-617 in metastatic castration-resistant prostate cancer: correlations between pretherapeutic imaging and whole-body tumor dosimetry with treatment outcomes. *J Nucl Med.* 2019;60:517–523.
 28. Fizazi K, Massard C, Smith M, et al. Bone-related parameters are the main prognostic factors for overall survival in men with bone metastases from castration-resistant prostate cancer. *Eur Urol.* 2015;68:42–50.
 29. Heck MM, Tauber R, Schwaiger S, et al. Treatment outcome, toxicity, and predictive factors for radioligand therapy with ¹⁷⁷Lu-PSMA-I&T in metastatic castration-resistant prostate cancer. *Eur Urol.* 2019;75:920–926.
 30. Barber TW, Singh A, Kulkarni HR, Niepsch K, Billah B, Baum RP. Clinical outcomes of ¹⁷⁷Lu-PSMA radioligand therapy in earlier and later phases of metastatic castration-resistant prostate cancer grouped by previous taxane chemotherapy. *J Nucl Med.* 2019;60:955–962.
 31. Seifert R, Kessel K, Schlack K, et al. PSMA PET total tumor volume predicts outcome of patients with advanced prostate cancer receiving [¹⁷⁷Lu]Lu-PSMA-617 radioligand therapy in a bicentric analysis. *Eur J Nucl Med Mol Imaging.* 2021;48:1200–1210.
 32. Seifert R, Herrmann K, Kleesiek J, et al. Semiautomatically quantified tumor volume using ⁶⁸Ga-PSMA-11 PET as a biomarker for survival in patients with advanced prostate cancer. *J Nucl Med.* 2020;61:1786–1792.
 33. Grubmüller B, Senn D, Kramer G, et al. Response assessment using ⁶⁸Ga-PSMA ligand PET in patients undergoing ¹⁷⁷Lu-PSMA radioligand therapy for metastatic castration-resistant prostate cancer. *Eur J Nucl Med Mol Imaging.* 2019;46:1063–1072.
 34. Michalski K, Klein C, Brueggemann T, Meyer PT, Jilg CA, Ruf J. Assessing response to [¹⁷⁷Lu]PSMA radioligand therapy using modified PSMA PET progression criteria. *J Nucl Med.* 2021;62:1741–1746.
 35. Gafita A, Rauscher I, Fendler WP, et al. Measuring response in metastatic castration-resistant prostate cancer using PSMA PET/CT: comparison of RECIST 1.1, aPCWG3, aPERCIST, PPP, and RECIP 1.0 criteria. *Eur J Nucl Med Mol Imaging.* 2022;49:4271–4281.

Three-Time-Point PET Analysis of ⁶⁸Ga-FAPI-46 in a Variety of Cancers

Mahnoosh Naeimi¹, Peter L. Choyke², Katharina Dendl¹, Yuriko Mori³, Fabian Staudinger¹, Tadashi Watabe⁴, Stefan A. Koerber⁵, Manuel Röhrich¹, Jürgen Debus⁵, Clemens Kratochwil¹, Uwe Haberkorn¹, and Frederik L. Giesel^{1,3,6}

¹Department of Nuclear Medicine, University Hospital Heidelberg, Heidelberg, Germany; ²Molecular Imaging Branch, Center for Cancer Research, National Cancer Institute, National Institutes of Health, Bethesda, Maryland; ³Department of Nuclear Medicine, Medical Faculty of Heinrich Heine University, University Hospital Düsseldorf, Düsseldorf, Germany; ⁴Department of Nuclear Medicine and Tracer Kinetics, Osaka University Graduate School of Medicine, Osaka, Japan; ⁵Department of Radiation Oncology, University Hospital Heidelberg, Heidelberg, Germany; and ⁶Institute of Radiation Science, Osaka University, Osaka, Japan

See an invited perspective on this article on page 623.

A growing family of ⁶⁸Ga-fibroblast activation protein inhibitor (FAPI) PET probes has shown promise in imaging a variety of medical conditions. ⁶⁸Ga-FAPI-46, in particular, has emerged as unique for both its diagnostic and its theranostic applications; however, the optimal timing of PET remains unclear. Therefore, we evaluated uptake at 3 time points after ⁶⁸Ga-FAPI-46 administration in a spectrum of tumor types.

Methods: The cohort consisted of 43 patients with diverse cancer diagnoses undergoing ⁶⁸Ga-FAPI-46 PET/CT at 3 time points (10 min, 1 h, and 3 h). We determined the tracer uptake based on SUV_{mean} and SUV_{max} and on tumor-to-background-ratios (TBRs) (SUV_{max}/SUV_{mean}). **Results:** There were 171 lesions in the 43 patients. Comparing all lesions at different time points, the mean SUV_{max} was maximal at 10 min (8.2) and declined slightly at 1 h (8.15) and 3 h (7.6) after tracer administration. Similarly, the mean SUV_{max} log still had a similar pattern in primary lesions at 10 min, 1 h, and 3 h ($n = 30$; 0.98, 1.01, and 0.98, respectively), lymph node metastases ($n = 37$; 0.82, 0.84, and 0.81, respectively), and distant metastases ($n = 104$; 0.81, 0.79, and 0.74, respectively). TBR also showed nonsignificant differences at the 3 times. **Conclusion:** ⁶⁸Ga-FAPI-46 PET/CT imaging revealed remarkably stable tumor and background uptake as determined by SUV metrics and maintained high TBRs within 3 h of injection. Thus, it may be possible to scan with ⁶⁸Ga-FAPI-46 within 10–20 min of injection, improving workflow and decreasing patient wait times. Confirmation of these findings in a larger cohort is under way.

Key Words: FAPI; fibroblast activation protein; PET; PET/CT; 3-time-point

J Nucl Med 2023; 64:618–622

DOI: 10.2967/jnumed.122.264941

Reliable staging tools are vital for oncologic management. Molecular imaging probes have been advancing rapidly and are capable of detecting cancer with high sensitivity. Fibroblast activation protein (FAP) is expressed by cancer-associated fibroblasts in many cancer types and is implicated in tumor cell migration, invasion, cell

Received Sep. 20, 2022; revision accepted Oct. 4, 2022.
For correspondence or reprints, contact Frederik L. Giesel (frederik.giesel@med.uni-duesseldorf.de).
Published online Nov. 10, 2022.
COPYRIGHT © 2023 by the Society of Nuclear Medicine and Molecular Imaging.

TABLE 1

Various Tumor Entities in 43 Patients

Tumor type	Patients (n)
Sarcoma	2
Anal cancer	4
Colorectal cancer	6
Lung cancer	11
Pancreatic cancer	5
Esophageal cancer	2
Head and neck cancer	3
Adrenocortical carcinoma	3
Breast cancer	2
Ovarian cancer	1
Bladder cancer	1
Lymphoma	1
Prostate cancer	1
Neuroblastoma	1

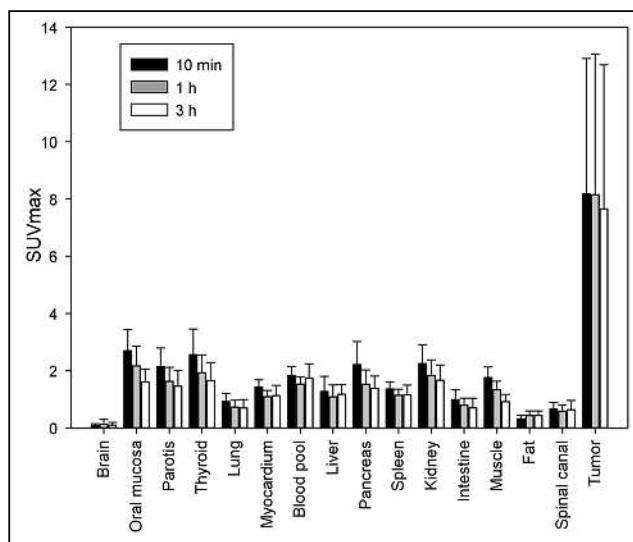


FIGURE 1. Biodistribution SUV_{max} of ⁶⁸Ga-FAPI-46 PET at 3 time points in normal organs vs. all tumor lesions.

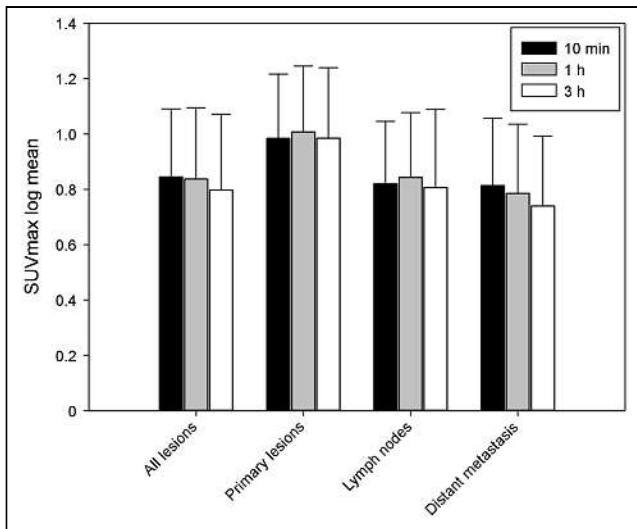


FIGURE 2. Tumor uptake (SUV_{max} log) through time points (10 min, 1 h, and 3 h) in all lesions ($n = 171$), primary lesions ($n = 30$), lymph node metastases ($n = 37$), and distant metastases ($n = 104$).

signaling, and tumor angiogenesis (1–3). FAP therefore represents an interesting target for new molecular imaging and therapeutic agents. The development of a quinoline-based FAP inhibitor (FAPI) with high affinity for FAP represents an opportunity to exploit this target for PET imaging (4). Such radiolabeled quinoline-based ligands have shown promising results in previous studies (5–7).

By convention, most molecular imaging agents are scanned 1 h after injection. Likewise, for FAP imaging, most of the previously published studies involved acquiring static PET images 1 h after injection (7). However, there are conflicting reports in the literature about optimal incubation times for FAPI agents, and no conclusive data have been published (8–12). In this investigation, we compared different incubation times of the agent ^{68}Ga -FAPI-46 in different cancers at 3 time points: 10 min, 1 h, and 3 h.

MATERIALS AND METHODS

Patient Cohort

This was a retrospective study of 43 patients with various malignancies who underwent ^{68}Ga -FAPI-46 PET/CT. The tumor types are summarized in Table 1. All imaging was performed at a single center, and all patients were referred by their attending oncologist or radiation oncologist for 1 of 3 reasons: to improve delineation of the target volume for

radiotherapy planning, to restage because of ambiguous findings on conventional imaging, or to follow up. All patients gave written informed consent to undergo ^{68}Ga -FAPI PET/CT on an individual-patient basis following national regulations and the declaration of Helsinki. The radiopharmaceutical was synthesized and labeled according to the German Pharmaceutical Act, §13(2b). The data were analyzed retrospectively with the approval of the local ethics committee (S016/2018).

Radiopharmaceuticals and ^{68}Ga -FAPI-46 PET/CT Imaging

^{68}Ga -FAPI-46 was synthesized and labeled as previously described (13). A non-contrast-enhanced low-dose CT scan (130 keV, 30 mAs, CareDose; reconstructed with a soft-tissue kernel to a slice thickness of 5 mm) and a Biograph mCT Flow scanner (Siemens) were used for imaging. All PET scans were acquired in 3-dimensional mode (matrix, 200×200). Each patient underwent PET/CT imaging at 3 time points after radiotracer injection: 10 min, 1 h, and 3 h. Patients were evaluated for adverse effects at several times during the examination, and vital signs were monitored until 30 min after the end of the examination.

Image Evaluation

Tracer uptake and biodistribution were quantified by SUV_{max} and SUV_{mean} at 10 min, 1 h, and 3 h after injection of ^{68}Ga -FAPI-46 (Fig. 1). For SUV calculation, e.soft software (Siemens) was used to manually draw circular volumes of interest around tumor lesions on transaxial slices at 1 h and were automatically transferred to the images obtained at 10 min and 3 h, using a 3-dimensional volume of interest at a 60% isocontour. Normal organs were evaluated with a 1-cm-diameter (for small organs: thyroid, parotid gland, myocardium, oral mucosa, spinal cord, and ovary) or 2-cm-diameter (brain, muscle, liver, pancreas, spleen, kidney, fat, aortic lumen content, lung, mammary gland, and endometrium) spheric region of interest (ROI) placed completely inside the organ parenchyma. For quantification of image contrast, tumor-to-background ratios (TBRs) were calculated. The formula was calculated using the geometric mean of the quotients of lesion tissue (SUV_{max}) to background tissue (SUV_{mean}). Liver tissue, oral mucosa, fat, and gluteal muscle were chosen as background tissue. The ^{68}Ga -FAPI PET/CT scans were analyzed in consensus by a board-certified radiologist, a board-certified radiation oncologist, and 2 board-certified nuclear medicine physicians.

Statistics

Descriptive analyses of patients and their tumors were performed. We determined SUVs using the median, arithmetic mean, SD and logarithm of SUVs to minimize potential mistakes during arithmetic mean calculations. The SUVs and SUV logs were distributed normally; therefore, a 2-sided t test with paired samples was used to compare ^{68}Ga -FAPI-46 SUVs in primary cancer, lymph node metastases, and distant metastases at the 3 time points. A P value of less than 0.05 was defined

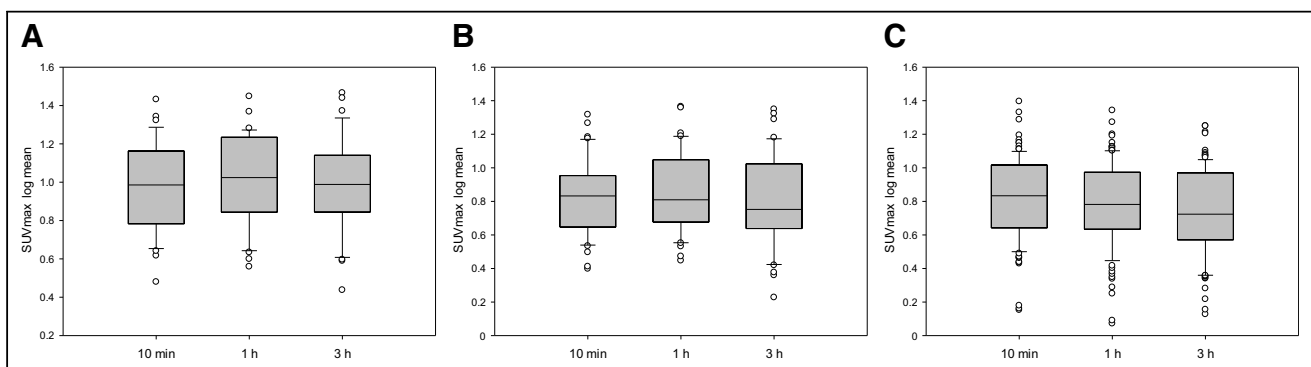


FIGURE 3. Box plot of ^{68}Ga -FAPI-46 PET distribution through time points (10 min, 1 h, and 3 h), with uptake (SUV_{max} log) by primary lesions (A), lymph node metastases (B), and distant metastases (C).

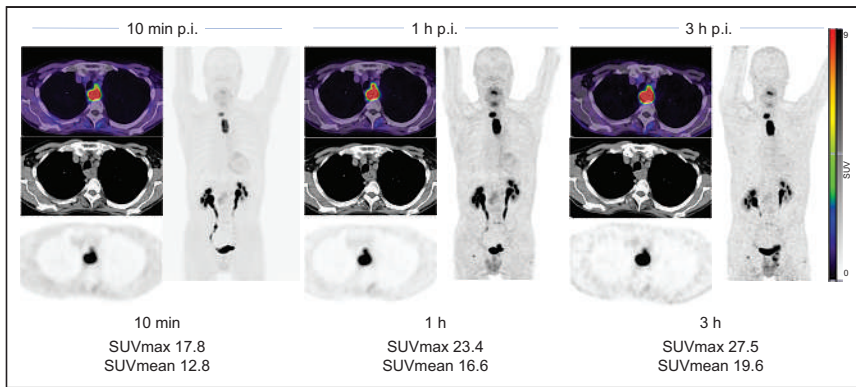


FIGURE 4. Case example of 63-y-old patient with esophageal cancer. ^{68}Ga -FAPI-46 PET/CT was performed for irradiation planning before definitive radiochemotherapy. ^{68}Ga -FAPI-46 PET was performed (10 min, 1 h, and 3 h) after injection (p.i.).

as statistically significant. All statistical analyses were performed using Excel (version 16.16; Microsoft) for Mac (Apple).

RESULTS

Study Population

Our data consisted of 43 patients with various malignancies, who are summarized in Table 1. Lesions consisted of primary cancers or tumor relapse ($n = 30$), lymphatic metastases ($n = 37$), and distant metastases ($n = 104$). The following tumor entities were included: lung cancer ($n = 11$); colorectal cancer ($n = 6$); pancreatic cancer ($n = 5$); anal cancer ($n = 4$); adrenocortical carcinoma ($n = 3$); head and neck cancer ($n = 3$); sarcoma, breast cancer, and ovarian cancer ($n = 2$); and bladder cancer, neuroblastoma, lymphoma, and prostate cancer ($n = 1$) (Table 1).

Biodistribution in Normal Organs

The biodistribution of ^{68}Ga -FAPI-46 in normal organs is shown in Figure 1, with stable low background activity; a mean SUV_{max} of 1.6, 1.3, and 1.2, at 10 min, 1 h, and 3 h, respectively; and a mean SUV_{mean} of 1.2, 1.0, 0.9, at 10 min, 1 h, and 3 h, respectively.

Biodistribution in normal organs decreased slightly from the 10-min to 3-h time points; however, no significant difference in SUV_{max} was observed among all normal organs (10 min vs. 3 h; $P = 5.5$, $n = 806$). The highest uptake in normal organs was always obtained on the first (10 min) scan, except for fat tissue. The overall

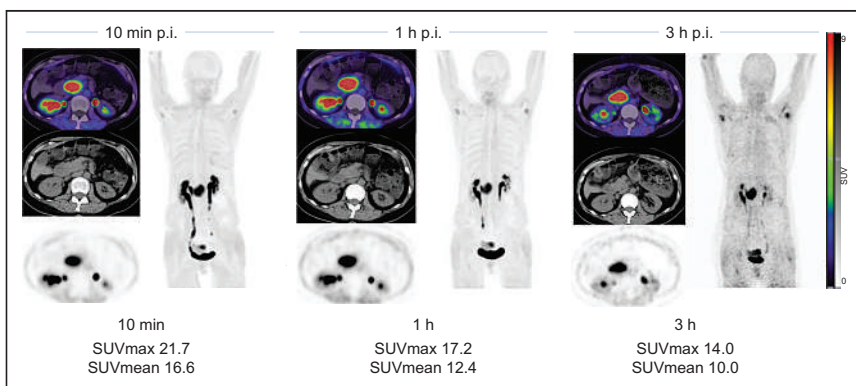


FIGURE 5. Case example of 60-y-old patient with pancreatic cancer. ^{68}Ga -FAPI-46 PET/CT was performed because of suspected recurrent mass in pancreatic head on ultrasound. ^{68}Ga -FAPI-46 PET was performed (10 min, 1 h, and 3 h) after injection (p.i.).

highest uptake was in the oral mucosa and thyroid tissue. Thus, within the oral mucosa, the mean SUV_{max} at 10 min, 1 h, and 3 h was 2.7, 2.2, and 1.6, respectively, whereas for thyroid tissue it was 2.6, 1.9, and 1.6, respectively. The lowest tracer uptake was in the brain, where mean SUV_{max} was 0.1, 0.1, and 0.1, respectively (Fig. 1).

Tumor Uptake

There were 171 lesions detected. All lesions were detected at all time points. At 10 min, 1 h, and 3 h, the mean SUV_{max} log was 0.98, 1.0, and 0.98, respectively, for primary lesions and local relapse ($n = 30$); 0.82, 0.84, and 0.80, respectively, for lymph node metastases ($n = 37$); and 0.81, 0.78, and 0.74, respectively, for distant metastases ($n = 104$). No significant difference was seen. The analysis of primary lesions or local relapse showed no significant difference in SUV_{max} at the 3 time points in 2-way comparisons (10 min vs. 1 h, $P = 0.2$; 10 min vs. 3 h, $P = 0.98$; and 1 h vs. 3 h, $P = 0.2$). The analysis of lymph node metastases ($n = 37$) showed increased tumor uptake at 1 h compared with the other 2 time points, with a significant difference for the comparison between 1 and 3 h ($P = 0.02$). There were no significant differences in SUV_{max} at other time points (10 min vs. 1 h, $P = 0.26$; 10 min vs. 3 h, $P = 0.66$). The analysis of distant metastases showed a significant decrease in tumor uptake through the time points. The highest tumor uptake was observed at 10 min (10 min vs. 1 h, $P = 0.02$; 10 min vs. 3 h, $P = 3.05E^{-5}$; 1 h vs. 3 h, $P = 1.27E^{-5}$) (Figs. 2 and 3). Two examples of patients with tumors with similar uptake on ^{68}Ga -FAPI-46 scans at the 3 time points are shown in Figures 4 and 5.

TBRs

Most background tissues showed a decrease in SUV_{max} and SUV_{mean} at longer incubation times, with the exception of fat tissue, which, at 10 min, 1 h, and 3 h, had a low SUV_{max} of 0.32, 0.44, and 0.44, respectively, and brain parenchyma, with an SUV_{max} of 0.09, 0.13, and 0.1, respectively. As expected, the primary and local relapse lesions demonstrated excellent contrast with normal tissue, and this contrast increased through the time points except for TBR versus fat tissue. Increased TBR could also be measured in lymph nodes and distant metastases except for tumor-to-fat ratios, which slightly decreased (Fig. 6). High TBRs were seen in primary and local relapse lesions versus fat tissue even after 3 h.

Quantifying ^{68}Ga -FAPI-46 Uptake in Different Types of Tumors

The highest average SUV_{max} (>20) in ^{68}Ga -FAPI-46 scans was in primary lesions. The highest SUV_{max} was in esophageal cancer (27.5; 3 h) and primary bladder cancer (29.2; 3 h). The highest SUV_{max} among all lymph node metastases was in esophageal lymph node metastases (19.5; 3 h). Among the distant metastases, breast cancer metastases demonstrated the highest SUV_{max} (15.7; 10 min) (Fig. 7).

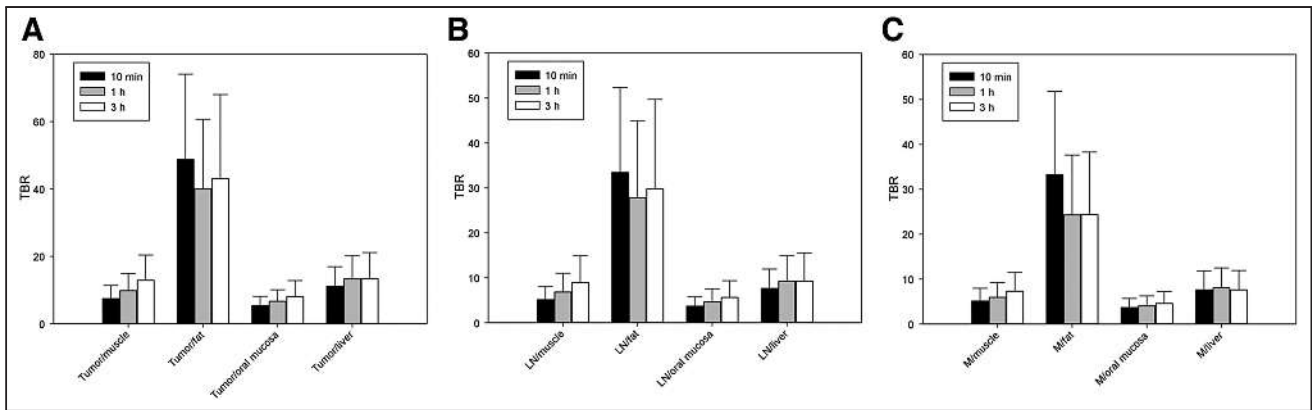


FIGURE 6. TBR through time points (10 min, 1 h, and 3 h) for tumor (primary/release; $n = 30$) (A), lymph node metastases ($n = 37$) (B), and distant metastases ($n = 104$) (C). LN = lymph node; M = distant metastases.

DISCUSSION

The aim of this study was to evaluate the optimal uptake time for ^{68}Ga -FAPI-46 based on time points between 10 min and 3 h after injection. The SUV_{max} for ^{68}Ga -FAPI-46 was remarkably stable at all 3 time points, although the 10-min time point generally had a slightly higher SUV_{max} . The detection rate of tumors was equal at all time points, implying that a diagnostic study can be achieved by 10 min after injection, which will have implications for patient throughput and decreased patient waiting times in the nuclear medicine department. Our study had findings similar to a previous analysis of ^{68}Ga -FAPI PET acquisitions at 5 time points earlier than 60 min regarding the best time for diagnostic imaging (14). However, because of the similar detection rate between 10 min and 1 h after injection and a slightly higher tumor uptake at the 10 min time point, we recommend 10–20 min after injection as the best time point for diagnostic imaging acquisition instead of 30–40 min after injection (14).

The steady uptake of ^{68}Ga -FAPI-46 also has implications for its use as a targeted theranostic agent for which high dose delivery will be achieved early and will be maintained over at least several hours (15). Meanwhile, background uptake, largely responsible for toxicity in targeted treatments, appears to clear rapidly over 3 h, resulting in high TBRs consistent with prior reports (4,13).

^{68}Ga -FAPI-46 is one of many FAPI derivatives but appears to have several desirable features, including high affinity for the target

and biologic stability (13,16). ^{68}Ga -FAPI-46 showed no significant washout between 10 min and 3 h, in comparison to other FAPI derivatives such as FAPI-02 and FAPI-04, which in a previous study showed 75% and 25% washout at 3 h after injection, respectively (17), making ^{68}Ga -FAPI-46 more valuable. Although that study (17) had a limited patient cohort, all 3 FAPI derivatives showed similar biodistributions and high TBRs between 10 min and 3 h.

^{68}Ga -FAPI-46 uptake was compared in primary lesions, lymph node metastases, and distant metastases in a spectrum of cancer types. The SUV_{max} log decreased over time in all stages of disease, and the TBR commensurately increased over the same period because of background washout. The findings were consistent regardless of the stage of the cancer lesion. These findings confirm prior studies showing similar results in a variety of cancers (8,11,18–20). It is expected that there will be minor differences in various single-institution studies because of differences in the composition of the patient cohort and types of tumor. Hu et al. found similar results using 2 related derivatives of FAPI: ^{18}F -FAPI-42 and ^{68}Ga -FAPI-04 (9).

The TBRs obtained in this study were based on various background tissues including muscle, oral mucosa, and liver. In each case, the TBR increased as expected through time. This finding is in line with similar previous studies (11,18). The highest TBR is seen with comparisons of the tumor to fat tissue, resulting in very high values even up to 3 h after injection. The highly favorable TBR obtained with

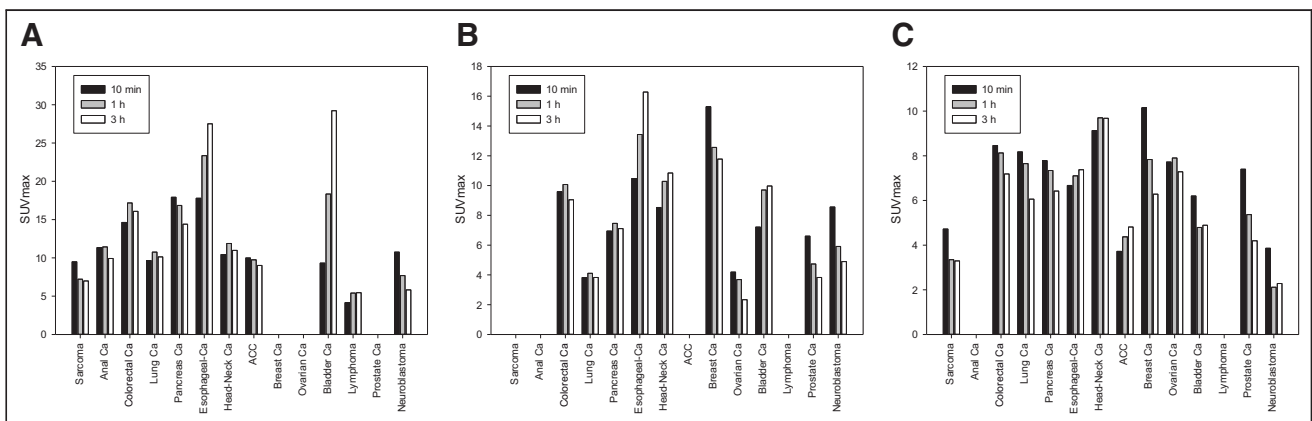


FIGURE 7. ^{68}Ga -FAPI-46 mean SUV_{max} in various tumor entities: primary/relapse tumors ($n = 30$) (A), lymph node metastases ($n = 37$) (B), and distant metastases ($n = 104$) (C). ACC = adrenocortical carcinoma; BC = bronchial carcinoma; CA = cancer; CRC = colorectal cancer; mama = mammary gland.

FAPi agents in general and ^{68}Ga -FAPi-46 specifically stands in contrast to the highly variable TBR obtained with ^{18}F -FDG PET scans.

This study had several limitations. Because of the limited number of patients, no reliable comparisons among tumor types was possible. False-positive findings in nontumorous lesions or inflammation, such as in the pancreas, could have influenced the results since histologic validation was not possible for all lesions. However, all patients were known to have extensive cancer based on conventional imaging, and it is highly likely that most lesions measured in this study were cancers.

CONCLUSION

We found that ^{68}Ga -FAPi-46 is a robust FAPi-targeting molecule that is highly reliable for diagnostic imaging as early as 10 min after injection. This result might have important implications for improving workflow and decreasing wait times in nuclear medicine departments, compared with more traditional PET agents such as ^{18}F -FDG PET. The results also suggest that ^{68}Ga -FAPi-46 might be an excellent theranostic agent, as it binds to its target soon after injection and maintains a high level of uptake over several hours while steadily decreasing background activity.

DISCLOSURE

Uwe Haberkorn, Clemens Kratochwil, and Frederik Giesel have filed a patent application for quinoline-based FAP-targeting agents for imaging and therapy in nuclear medicine and have shares in a consultancy group for iTheranostics. Frederik Giesel is an advisor to ABX, Telix Pharma, Alpha Fusion, and SOFIE Biosciences. No other potential conflict of interest relevant to this article was reported.

ACKNOWLEDGMENT

We highly appreciate the support of Patrick Päscht for data analysis.

KEY POINTS

QUESTION: What is the tumor residence of ^{68}Ga -FAPi-46 from 10 min to 3 h after injection in various cancers?

PERTINENT FINDINGS: ^{68}Ga -FAPi-46 is characterized by rapid and persistent tumor residence from 10 min to up to 3 h, enabling robust TBRs.

IMPLICATIONS FOR PATIENT CARE: ^{68}Ga -FAPi-46 has rapid uptake in different tumor entities and is retained in the tumor for 3 h after injection, findings that impact imaging procedures and also possible future theranostic applications of FAP ligands.

REFERENCES

1. LeBleu VS, Kalluri R. A peek into cancer-associated fibroblasts: origins, functions and translational impact. *Dis Model Mech*. 2018;11:dmm029447.
2. Kalluri R. The biology and function of fibroblasts in cancer. *Nat Rev Cancer*. 2016;16:582–598.
3. Sahai E, Astsaturov I, Cukierman E, et al. A framework for advancing our understanding of cancer-associated fibroblasts. *Nat Rev Cancer*. 2020;20:174–186.
4. Loktev A, Lindner T, Burger EM, et al. Development of fibroblast activation protein-targeted radiotracers with improved tumor retention. *J Nucl Med*. 2019;60:1421–1429.
5. Koerber SA, Staudinger F, Kratochwil C, et al. The role of ^{68}Ga -FAPi PET/CT for patients with malignancies of the lower gastrointestinal tract: first clinical experience. *J Nucl Med*. 2020;61:1331–1336.
6. Chen H, Pang Y, Wu J, et al. Comparison of [^{68}Ga]Ga-DOTA-FAPi-04 and [^{18}F] FDG PET/CT for the diagnosis of primary and metastatic lesions in patients with various types of cancer. *Eur J Nucl Med Mol Imaging*. 2020;47:1820–1832.
7. Kratochwil C, Flechsig P, Lindner T, et al. ^{68}Ga -FAPi PET/CT: tracer uptake in 28 different kinds of cancer. *J Nucl Med*. 2019;60:801–805.
8. Röhrich M, Leitz D, Glatting FM, et al. Fibroblast activation protein-specific PET/CT imaging in fibrotic interstitial lung diseases and lung cancer: a translational exploratory study. *J Nucl Med*. 2022;63:127–133.
9. Hu K, Wang L, Wu H, et al. [^{18}F]FAPi-42 PET imaging in cancer patients: optimal acquisition time, biodistribution, and comparison with [^{68}Ga]Ga-FAPi-04. *Eur J Nucl Med Mol Imaging*. 2022;49:2833–2843.
10. Wang S, Zhou X, Xu X, et al. Dynamic PET/CT imaging of ^{68}Ga -FAPi-04 in Chinese subjects. *Front Oncol*. 2021;11:651005.
11. Ferdinandus J, Kessler L, Hirmas N, et al. Equivalent tumor detection for early and late FAPi-46 PET acquisition. *Eur J Nucl Med Mol Imaging*. 2021;48:3221–3227.
12. Geist BK, Xing H, Wang J, et al. A methodological investigation of healthy tissue, hepatocellular carcinoma, and other lesions with dynamic ^{68}Ga -FAPi-04 PET/CT imaging. *EJNMMI Phys*. 2021;8:8.
13. Meyer C, Dahlborn M, Lindner T, et al. Radiation dosimetry and biodistribution of ^{68}Ga -FAPi-46 PET imaging in cancer patients. *J Nucl Med*. 2020;61:1171–1177.
14. Glatting FM, Hoppner J, Liew DP, et al. Repetitive early ^{68}Ga -FAPi PET acquisition comparing ^{68}Ga -FAPi-02, ^{68}Ga -FAPi-46, and ^{68}Ga -FAPi-74: methodologic and diagnostic implications for malignant, inflammatory/reactive, and degenerative lesions. *J Nucl Med*. 2022;63:1844–1851.
15. Giesel FL, Kratochwil C, Lindner T, et al. ^{68}Ga -FAPi PET/CT: biodistribution and preliminary dosimetry estimate of 2 DOTA-containing FAP-targeting agents in patients with various cancers. *J Nucl Med*. 2019;60:386–392.
16. Röhrich M, Naumann P, Giesel FL, et al. Impact of ^{68}Ga -FAPi PET/CT imaging on the therapeutic management of primary and recurrent pancreatic ductal adenocarcinomas. *J Nucl Med*. 2021;62:779–786.
17. Giesel FL, Kratochwil C, Schlittenhardt J, et al. Head-to-head intra-individual comparison of biodistribution and tumor uptake of ^{68}Ga -FAPi and ^{18}F -FDG PET/CT in cancer patients. *Eur J Nucl Med Mol Imaging*. 2021;48:4377–4385.
18. Mona CE, Benz MR, Hikmat F, et al. Correlation of ^{68}Ga -FAPi-46 PET biodistribution with FAP expression by immunohistochemistry in patients with solid cancers: interim analysis of a prospective translational exploratory study. *J Nucl Med*. 2022;63:1021–1026.
19. Ferdinandus J, Costa PF, Kessler L, et al. Initial clinical experience with ^{90}Y -FAPi-46 radioligand therapy for advanced-stage solid tumors: a case series of 9 patients. *J Nucl Med*. 2022;63:727–734.
20. Kratochwil C, Giesel FL, Rathke H, et al. [^{153}Sm]samarium-labeled FAPi-46 radioligand therapy in a patient with lung metastases of a sarcoma. *Eur J Nucl Med Mol Imaging*. 2021;48:3011–3013.

Could FAP-Targeted Molecular Imaging Replace ^{18}F -FDG for Standard-of-Care Oncologic PET?

Raghava Kashyap¹ and Aravind S. Ravi Kumar^{1,2}

¹Department of Cancer Imaging, Peter MacCallum Cancer Centre, Melbourne, Victoria, Australia; and ²Sir Peter MacCallum Department of Oncology, University of Melbourne, Parkville, Victoria, Australia

See the associated article on page 618.

The predominant radiotracer in oncologic PET is ^{18}F -FDG, to the point that many clinicians refer to ^{18}F -FDG PET scans simply as “PET scans.” Numerous other radiotracers have been studied but only somatostatin receptor–targeted agents and prostate-specific membrane antigen (PSMA) have been widely adopted, specific tracers largely used in neuroendocrine and prostate cancers, respectively.

^{18}F -FDG uptake is not simply a marker of tumor glucose metabolism but also reflects a complex interplay of metabolism in the stroma and immune infiltrate, hypoxic microenvironment, and other dysregulated metabolic pathways. Despite the complex and variable etiology of ^{18}F -FDG uptake, ^{18}F -FDG PET has a definite place in the staging, prognostication, and treatment response assessment in a broad range of malignancies. With precision medicine and molecularly targeted therapies, an unmet need exists for functional imaging techniques to provide biologic insights beyond glucose metabolism. Several malignancies have intrinsically low ^{18}F -FDG avidity or are poorly imaged with ^{18}F -FDG PET due to high background uptake, for example, in the brain.

Malignant tissues are complex and heterogeneous, consisting of neoplastic cells and tumor microenvironment comprising stroma (including several types of fibroblasts), neovasculature, and immunomodulatory cells. Tumor microenvironment may play a vital role in invasiveness, metastatic potential, and evading immune regulation. Imaging stromal components of tumors is very attractive, not only in overcoming some limitations of ^{18}F -FDG PET, but also in providing complementary or new biologic insights. Among targets that image tumor microenvironment, a particularly exciting one is fibroblast activation protein (FAP), a quinolone-based compound that is overexpressed in a subpopulation of cancer-associated fibroblasts (CAFs) in a wide range of malignancies (1).

There are several FAP inhibitor (FAPI) compounds available. A comparison among a few of these showed that FAPI-46 showed higher tumor-to-background ratio and higher uptake in malignant and inflammatory lesions (2). In the recent study, Naeimi et al. (3)

performed FAPI-46 PET in various tumor types and confirmed early uptake of FAPI-46. Uptake in malignant lesions occurred early but also demonstrated some heterogeneity, with no significant difference in the SUV_{max} log at 10 min and 3 h for uptake in primary but nodal uptake increased at 1 h, and uptake in the metastases was highest at 10 min. The rapid FAPI uptake in a variety of tumors with low background tissue uptake leads to the attractive possibility that FAPI PET may potentially complement or replace conventional ^{18}F -FDG PET in the future.

Another practical advantages to FAPI PET over conventional ^{18}F -FDG PET is lack of dietary requirements and uptake independent of blood glucose levels, a particular advantage for imaging of diabetic patients. The possibility of early imaging if combined with simultaneous whole-body PET technology is attractive for patient convenience and throughput with a favorable dosimetry (4).

FAPI may have a major complementary role in tumor types and anatomic sites at which ^{18}F -FDG is known to have reduced sensitivity, not least in the diagnostic setting in which lesion detection is of paramount importance. High FAPI radiopharmaceutical uptake has been demonstrated in certain tumors of the gastrointestinal tract (5,6), peritoneal disease (7), and biliary tract tumors (8) in contrast to ^{18}F -FDG. A significant strength of FAPI imaging is low physiologic uptake in most organs, leading to high target to background even if these lesions do not show absolute higher avidity for FAP than ^{18}F -FDG. This is especially true for cerebral lesions where physiologic uptake limits lesion detection with ^{18}F -FDG PET.

FAPI imaging is not without pitfalls. There is high uptake and similar retention of FAPI in inflammatory and malignant processes, leading to potential false-positive interpretations without careful attention to the clinical context and accompanying anatomic information of the CT component of the scan. With ^{18}F -FDG, this could be partly overcome with delayed imaging where inflammatory processes show washout and in general lower avidity. FAPI uptake in inflammatory lesions appears mostly stable over time (2). A crucial aspect that needs to be addressed is the extent and duration of FAPI uptake after surgery or radiation. Differentiation of viable tumor from inflammatory or fibrotic processes could be challenging when undertaking FAPI posttherapy assessments.

There is vast literature supporting ^{18}F -FDG PET, particularly in treatment response assessment and prognosis. There are early data on the prognostic value of FAPI avidity (9), but clearly larger studies in multiple tumor types are needed. Response assessment on ^{18}F -FDG PET is a major prognostic factor and guides adaptive management in many conditions such as lymphomas. There are a dearth of response assessment data with FAPI.

Received Nov. 2, 2022; revision accepted Jan. 26, 2023.
For correspondence or reprints, contact Aravind S. Ravi Kumar (aravind.ravikumar@petermac.org).
Published online Feb. 2, 2023.
COPYRIGHT © 2023 by the Society of Nuclear Medicine and Molecular Imaging.
DOI: 10.2967/jnumed.122.265003

Oncologic ^{18}F -FDG PET is broadly accepted in the clinical community and reimbursed by health-care providing agencies. It would be meaningful to generate evidence for FAP-targeted PET to better characterize tumor biology or in areas in which ^{18}F -FDG has shortcomings rather than replicating the entire volume of data available with ^{18}F -FDG. The economics of FAP-based tracers is bound to have an influence in its acceptance in routine practice. There is currently no literature on cost-benefit analysis of FAPI-based imaging.

Interestingly, FAP-targeted imaging is also being evaluated in nonmalignant cardiac, pulmonary, and rheumatologic conditions and early data appear promising.

Unlike ^{18}F -FDG, FAP-targeting radiopharmaceuticals have therapeutic potential. The newer cyclic peptide compound FAP-2286 has higher affinity, retention, and internalization than linear compound FAPI-46 (10). Interestingly, a study by Fendler et al. (11) shows that only a minority of tumors demonstrate high FAPI avidity ($\text{SUV}_{\text{max}} > 10$ in 18%) if this were considered as a predictor of dose delivered by radionuclide therapy. G3/4 hematologic toxicities, possibly related to the isotope, occurred in more than 30% with ^{90}Y -FAPI-mediated therapy partly attributable to the isotope (11,12). An early study with ^{177}Lu -FAP-2286 showed G3 toxicities in 3 of 11 patients and no G4 toxicity (13). The safety profile of ^{177}Lu -FAP-2286 is being evaluated further in clinical trials (14).

Simultaneous targeting of both tumor cells and CAFs (15), or delivering a cocktail of isotopes are areas for future research. Bispecific agents could offer simultaneous targeting of tumor and microenvironment. Clinical translation is awaited.

In conclusion, FAP-targeted imaging raises exciting opportunities with ease of patient preparation and favorable radiation dosimetry. Rapid uptake and high tumor-to-background ratio allow early imaging. Given the large volume of evidence with ^{18}F -FDG in diagnosis, prognostication, and response assessment, FAP-based imaging may be better approached, at least initially, as an agent complementary to ^{18}F -FDG, with specific applications. FAP-based therapy could substantially broaden the theranostics landscape.

DISCLOSURE

No potential conflict of interest relevant to this article was reported.

REFERENCES

1. Peltier A, Seban R-D, Buvat I, Bidard F-C, Mechta-Grigoriou F. Fibroblast heterogeneity in solid tumors: from single cell analysis to whole-body imaging. *Semin Cancer Biol.* 2022;86:262–272.
2. Glatting FM, Hoppner J, Liew DP, et al. Repetitive early FAPI-PET acquisition comparing FAPI-02, FAPI-46 and FAPI-74: methodological and diagnostic implications for malignant, inflammatory and degenerative lesions. *J Nucl Med.* 2022; 63:1844–1851.
3. Naeimi M, Choyke PL, Dendl K, et al. Three-time-point PET analysis of ^{68}Ga -FAPI-46 in a variety of cancers. *J Nucl Med.* 2023;64:618–622.
4. Meyer C, Dahlbom M, Lindner T, et al. Radiation dosimetry and biodistribution of ^{68}Ga -FAPI-46 PET imaging in cancer patients. *J Nucl Med.* 2020;61: 1171–1177.
5. Pang Y, Zhao L, Luo Z, et al. Comparison of ^{68}Ga -FAPI and ^{18}F -FDG uptake in gastric, duodenal, and colorectal cancers. *Radiology.* 2021;298:393–402.
6. Pang Y, Zhao L, Meng T, et al. PET imaging of fibroblast activation protein in various types of cancers by using ^{68}Ga -FAP-2286: comparison with ^{18}F -FDG and ^{68}Ga -FAPI-46 in a single-center, prospective study. *J Nucl Med.* September 2, 2022 [Epub ahead of print].
7. Lin R, Lin Z, Chen Z, et al. [^{68}Ga]Ga-DOTA-FAPI-04 PET/CT in the evaluation of gastric cancer: comparison with [^{18}F]FDG PET/CT. *Eur J Nucl Med Mol Imaging.* 2022;49:2960–2971.
8. Lan L, Zhang S, Xu T, et al. Prospective comparison of ^{68}Ga -FAPI versus ^{18}F -FDG PET/CT for tumor staging in biliary tract cancers. *Radiology.* 2022;304: 648–657.
9. Hu X, Zhou T, Ren J, et al. Response prediction using ^{18}F -FAPI-04 PET/CT in patients with esophageal squamous cell carcinoma treated with concurrent chemoradiotherapy. *J Nucl Med.* October 13, 2022 [Epub ahead of print].
10. Zboralski D, Hoehne A, Bredenbeck A, et al. Preclinical evaluation of FAP-2286 for fibroblast activation protein targeted radionuclide imaging and therapy. *Eur J Nucl Med Mol Imaging.* 2022;49:3651–3667.
11. Fendler WP, Pabst KM, Kessler L, et al. Safety and efficacy of ^{90}Y -FAPI-46 radioligand therapy in patients with advanced sarcoma and other cancer entities. *Clin Cancer Res.* 2022;28:4346–4353.
12. Ferdinandus J, Costa PF, Kessler L, et al. Initial clinical experience with ^{90}Y -FAPI-46 radioligand therapy for advanced-stage solid tumors: a case series of 9 patients. *J Nucl Med.* 2022;63:727–734.
13. Baum RP, Schuchardt C, Singh A, et al. Feasibility, biodistribution, and preliminary dosimetry in peptide-targeted radionuclide therapy of diverse adenocarcinomas using ^{177}Lu -FAP-2286: First-in-humans results. *J Nucl Med.* 2022;63: 415–423.
14. A study of ^{177}Lu -FAP-2286 in advanced solid tumors (LuMIERE). Clinicaltrials.gov website. <https://clinicaltrials.gov/ct2/show/NCT04939610>. Updated August 29, 2022. Accessed February 22, 2023.
15. Boinapally S, Lisok A, Lofland G, et al. Hetero-bivalent agents targeting FAP and PSMA. *Eur J Nucl Med Mol Imaging.* 2022;49:4369–4381.

Response Prediction Using ^{18}F -FAPI-04 PET/CT in Patients with Esophageal Squamous Cell Carcinoma Treated with Concurrent Chemoradiotherapy

Xinying Hu¹, Tao Zhou¹, Jiazhong Ren², Jinghao Duan¹, Hongbo Wu², Xiaoli Liu^{1,3}, Zhengshuai Mu⁴, Ning Liu¹, Yuchun Wei¹, and Shuanghu Yuan^{1,3}

¹Department of Radiology, Shandong Cancer Hospital and Institute, Shandong First Medical University, Shandong Academy of Medical Sciences, Jinan, China; ²PET/CT Center, Shandong Cancer Hospital and Institute, Shandong First Medical University and Shandong Academy of Medical Sciences, Jinan, China; ³Cheeloo College of Medicine, Shandong University, Jinan, China; and ⁴Department of Pathology, Shandong Cancer Hospital and Institute, Shandong First Medical University, Shandong Academy of Medical Sciences, Jinan, China

This prospective study examined whether imaging results obtained using the tracer ^{18}F -AIF-NOTA-fibroblast activation protein inhibitor (FAPI)-04 (denoted as ^{18}F -FAPI-04) in PET/CT can predict the short-term outcome in patients with locally advanced esophageal squamous cell carcinoma (LA-ESCC) treated with concurrent chemoradiotherapy (CCRT).

Methods: The 18 enrolled LA-ESCC patients underwent ^{18}F -FAPI-04 PET/CT scanning before CCRT. The SUV_{max} , SUV_{mean} , SUV_{peak} , metabolic tumor volume, and total lesion fibroblast activation protein expression of the primary tumor were recorded. Additionally, the SUV_{max} of the primary tumor and SUV_{mean} of normal tissue (muscle and blood) were measured, and their ratios were denoted as target-to-background ratios ($\text{TBR}_{\text{muscle}}$ and $\text{TBR}_{\text{blood}}$). Patients were classified as responders or non-responders according to RECIST (version 1.1), and variables were compared between the 2 groups. **Results:** The $\text{TBR}_{\text{blood}}$, $\text{TBR}_{\text{muscle}}$, and SUV_{mean} were significantly higher in nonresponders than in responders (all $P < 0.05$). Receiver-operating-characteristic curve analysis identified $\text{TBR}_{\text{blood}}$ (area under the curve [AUC], 0.883; $P = 0.008$), $\text{TBR}_{\text{muscle}}$ (AUC, 0.896; $P = 0.006$) and SUV_{mean} (AUC, 0.870; $P = 0.010$) as significant predictors of the response to CCRT, with cutoffs of 10.68, 10.95, and 6.88, respectively. The sensitivity, specificity, positive predictive value, negative predictive value, and accuracy were also determined for $\text{TBR}_{\text{blood}}$ (100.0%, 72.7%, 66.7%, 88.9%, and 77.8%, respectively), $\text{TBR}_{\text{muscle}}$ (100.0%, 72.7%, 66.7%, 88.9%, and 77.8%, respectively), and SUV_{mean} (85.7%, 81.8%, 75.0%, 90.0%, and 83.3%, respectively). On univariate logistic regression analysis, $\text{TBR}_{\text{blood}}$ ($P = 0.026$), $\text{TBR}_{\text{muscle}}$ ($P = 0.036$), SUV_{mean} ($P = 0.045$), and tumor site ($P = 0.032$) were significantly correlated with the short-term outcome. On multivariable logistic regression analysis, $\text{TBR}_{\text{blood}}$ ($P = 0.046$) was an independent prognostic factor for short-term outcome. **Conclusion:** A higher baseline $\text{TBR}_{\text{blood}}$ on ^{18}F -FAPI-04 PET/CT scans was associated with a poor response to CCRT in LA-ESCC patients, and thus, $\text{TBR}_{\text{blood}}$ may be useful for screening LA-ESCC patients before CCRT treatment.

Key Words: fibroblast activation protein; PET; concurrent chemoradiotherapy; esophageal squamous cell carcinoma

J Nucl Med 2023; 64:625–631

DOI: 10.2967/jnumed.122.264638

Received Jul. 8, 2022; revision accepted Oct. 4, 2022.
For correspondence or reprints, contact Yuchun Wei (yuchunwei0000@foxmail.com) or Shuanghu Yuan (yuanshuanghu@sina.com).
Published online Oct. 13, 2022.
COPYRIGHT © 2023 by the Society of Nuclear Medicine and Molecular Imaging.

Esophageal cancer is one of the most common malignant tumors of the digestive system in the world, ranking seventh in terms of incidence and sixth in mortality overall in 2020 (1,2). Squamous cell carcinoma is the main histologic type of esophageal cancer in central and southeast Asia (3), and radical concurrent chemoradiotherapy (CCRT) has been recognized by the Radiation Therapy Oncology Group as the first-line treatment for locally advanced esophageal squamous cell carcinoma (LA-ESCC) (4).

Fibroblast activation protein (FAP) is a member of the dipeptidyl peptidase 4 protein family and has both endopeptidase and dipeptidyl peptidase activities. FAP is highly expressed in the stromal fibroblasts of more than 90% of epithelial carcinomas (5–7). Research has shown that high expression of FAP in the stromal fibroblasts of breast cancer, colon cancer, esophageal cancer, and other malignant tumors is related to poor prognosis (8–11). As a means of visualizing FAP expression, a previous study demonstrated that uptake of FAP inhibitor (FAPI) can accurately reflect the biologic distribution of FAP (12). In addition, use of a FAPI-based tracer, ^{68}Ga -DOTA-FAPI-04, in PET/CT was able to clearly identify 12 types of malignant tumors with favorable tumor-to-background contrast (12). We previously performed a pilot clinical study in which ^{18}F -FAPI-04, a novel tracer, was proven to be safe and to offer high specificity for FAP imaging (13). Accordingly, to some extent, parameters on ^{18}F -FAPI-04 PET/CT are expected to predict the outcome of CCRT. However, the efficacy of ^{68}Ga -FAPI/ ^{18}F -FAPI-04 PET/CT for the prediction of treatment response needed to be verified by prospective studies.

The aim of the present study was to identify imaging parameters that can predict tumor response to CCRT by comparing ^{18}F -FAPI-04 PET/CT parameters between LA-ESCC patients classified as responders and nonresponders. The ability to identify patients with a poor prognosis in advance via imaging will help to realize individualized treatment of tumors.

MATERIALS AND METHODS

Patient Cohort

Potentially eligible LA-ESCC patients were recruited in Shandong Cancer Hospital and Institute from June 2021 to February 2022 (Table 1). All patients volunteered to participate in this prospective study and gave written informed consent. The study was approved by the local ethics committee of Shandong Cancer Hospital and Institute.

TABLE 1

Characteristics of Enrolled LA-ESCC Patients (n = 18)

Characteristic	Patients (n)
Age (y)	
>60	12 (66.67%)
≤60	6 (33.33%)
Sex	
Male	12 (66.67%)
Female	6 (33.33%)
Eastern Cooperative Oncology Group score	
0	11 (61.11%)
1	7 (38.89%)
T stage	
T2	1 (5.56%)
T3	14 (77.78%)
T4	3 (16.67%)
N stage	
N0	5 (27.78%)
N1	8 (44.44%)
N2	5 (27.78%)
Tumor site	
Cervical	3 (16.67%)
Upper	4 (22.22%)
Middle	2 (11.11%)
Lower	9 (50.00%)
Concomitant chemotherapy	
Docetaxel + carboplatin/nedaplatin	2 (11.11%)
Paclitaxel + nedaplatin/carboplatin/cisplatin	5 (27.78%)
Paclitaxel	7 (38.89%)
Capecitabine	1 (5.56%)
Tegafur	1 (5.56%)
None	2 (5.56%)
Short-term outcome (RECIST)	
Complete response	0
Partial response	11 (61.11%)
Stable disease	7 (38.89%)
Progressive disease	0

Patients were enrolled according to the following criteria: histopathologically confirmed esophageal squamous cell carcinoma (T3~4N0~2M0~1); an age of at least 18 y; an Eastern Cooperative Oncology Group score of no more than 1; the presence of measurable primary tumors according to RECIST (version 1.1); readiness to undergo CCRT without prior surgery, chemotherapy, or radiotherapy for thoracic tumors; and ¹⁸F-FAPI-04 PET/CT scanning performed before CCRT. The exclusion criteria included pregnancy or breastfeeding and unwillingness to participate. A flowchart of the study design is shown in Figure 1.

CCRT

Patients were scanned within 1 wk before the start of CCRT. The total radiotherapy dose ranged from 50.4 to 60 Gy, and intensity-modulated radiotherapy was delivered to all patients with megavoltage equipment (6 MV). Radiotherapy was given as the conventionally

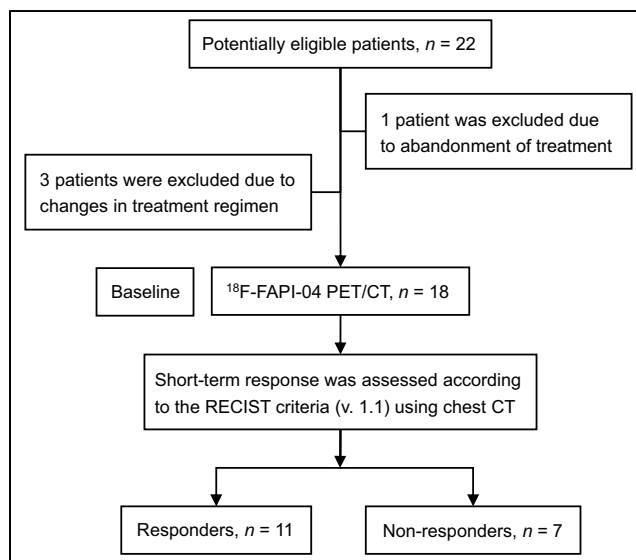


FIGURE 1. Research flowchart.

fractionated regimen, 1.8–2.0 Gy for 5 d per week. The specific chemotherapy regimens that followed are listed in Supplemental Table 1 (supplemental materials are available at <http://jnm.snmjournals.org>).

¹⁸F-FAPI-04 PET/CT Scanning

¹⁸F-FAPI-04 was synthesized as described previously (14). Patients were not required to fast or undergo blood glucose measurement before scanning. After receiving an intravenous injection of ¹⁸F-FAPI-04 (4.81 MBq/kg), the patients rested for approximately 1 h. Scanning was then performed with an integrated in-line PET/CT system (Gemini TF Big Bore; Philips Healthcare). Whole-body CT scans were obtained using a low-dose protocol (300 mAs, 120 kV, 512 × 512 matrix, rotation time of 1.0 s, and pitch index of 0.688; reconstructed with a soft-tissue kernel to a slice thickness of 2 mm) for attenuation correction. PET data were acquired in 3-dimensional mode using a 200 × 200 matrix with an imaging time of 1 min per bed position. During image acquisition, the patients maintained normal shallow breathing. Subsequently, after attenuation correction (Body-ctac-SB. Lstcln, Biograph 3-dimensional iterative reconstruction software, time-of-flight correction), we reviewed the PET, CT, and PET/CT images.

Imaging Analysis

The attenuation-corrected PET images, CT images, and PET/CT images, displayed as coronal, sagittal, and transaxial slices, were viewed and analyzed on a Nuclear Medicine Information System (Beijing Mozi Healthcare Ltd.). Two experienced nuclear medicine physicians visually assessed the ¹⁸F-FAPI-04 PET/CT images and reached consensus on interpretations for primary and metastatic tumors. Regions of interest were drawn around tumor lesions with higher uptake in transaxial sections, and ¹⁸F-FAPI-04 PET/CT parameters were generated by an automated 3-dimensional contouring program with a 30% isocontour. The uptake values within regions of interest were normalized to the injected dose per kilogram of patient body weight to derive the SUVs, according to the following formula: [measured activity concentration (Bq/mL) × body weight (g)]/injected activity (Bq). Regions of interest were drawn around the primary tumor lesion, and the obtained parameters, including SUV_{max}, SUV_{mean}, SUV_{peak}, metabolic tumor volume (MTV), and total lesion FAP expression, were generated by an automated contouring program provided by the vendor. We also measured the SUV_{mean} of 1-cm³ areas in the pulmonary aortic trunk and erector spinae. Then, the ratio of the SUV_{max} of the primary tumor to the SUV_{mean}

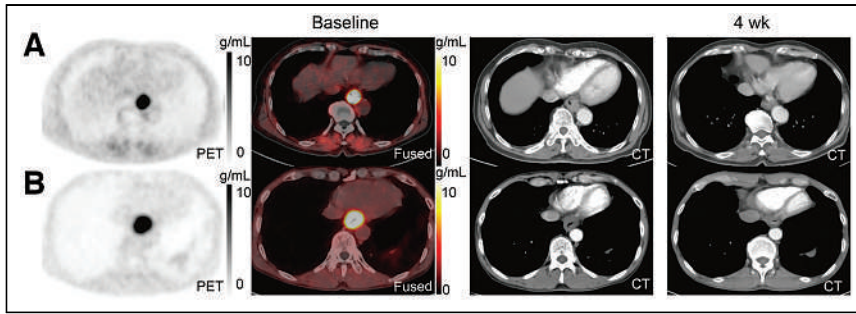


FIGURE 2. ^{18}F -FAPI-04 PET/CT and CT images of LA-ESCC patients with outcome classified as partial response (A) and stable disease (B).

of normal tissue (blood and muscle) was calculated, denoted as tumor-to-background ratio ($\text{TBR}_{\text{blood}}$ and $\text{TBR}_{\text{muscle}}$). For controversial lesions, discussion among the imaging experts with consideration of the results from other imaging modalities proceeded until a final consensus was reached.

Response Evaluation and Survival Assessments

Two imaging specialists independently reviewed the contrast-enhanced CT images obtained at baseline and at 4 wk of follow-up. The specialists knew that all patients had pathologically confirmed cancer but not the clinical, laboratory, or follow-up results. The reviewers recorded the primary tumor location and size in the axial plane. Short-term outcome was assessed at 4 wk after CCRT according to the revised RECIST using thoracic CT. According to RECIST, patients with an outcome of complete response or partial response were classified as responders, and patients with an outcome of stable disease or progressive disease were classified as nonresponders.

Statistical Analysis

Statistical analysis was performed using SPSS Statistics (version 25.0; IBM) for Microsoft Windows. Quantitative data for SUV_{max} , SUV_{mean} , SUV_{peak} , MTV, total lesion FAP expression, $\text{TBR}_{\text{blood}}$, and $\text{TBR}_{\text{muscle}}$ were expressed as mean \pm SD. Mann–Whitney U tests were used to compare the ^{18}F -FAPI-04 PET/CT parameters between responders and nonresponders. Logistic regression analyses were performed to identify the relationships between tumor site, degree of differentiation, and ^{18}F -FAPI-04 PET/CT parameters and short-term outcomes. Receiver-operating-characteristic curve analysis was used to determine the thresholds with the maximum Youden index as well as the predictive accuracy of ^{18}F -FAPI-04 PET/CT parameters for treatment response. Spearman rank correlation

coefficients were calculated to assess the relationships between biomarkers. All tests were 2-sided, and a P value of less than 0.05 was considered statistically significant.

RESULTS

Characteristics and Outcomes of Enrolled Patients

From June 2021 to March 2022, 18 patients diagnosed with LA-ESCC on the basis of histologic examinations at Shandong Cancer Hospital and Institute were enrolled in this study. The characteristics of the patients are presented in Table 1.

Among all patients, 11 were classified as responders and 7 as nonresponders (Table 1). Figure 2 shows representative ^{18}F -FAPI-04 PET/CT imaging results for a responder and a nonresponder.

Quantitative ^{18}F -FAPI-04 PET/CT Parameters

The quantitative baseline ^{18}F -FAPI-04 PET/CT parameters SUV_{max} , SUV_{mean} , SUV_{peak} , MTV, total lesion FAP expression, $\text{TBR}_{\text{blood}}$, and $\text{TBR}_{\text{muscle}}$ are shown in Table 2 for all patients, responders, and nonresponders. $\text{TBR}_{\text{blood}}$, $\text{TBR}_{\text{muscle}}$, and SUV_{mean} were significantly higher in nonresponders than in responders (12.53 ± 1.11 vs. 10.29 ± 1.54 , $P = 0.008$; 12.24 ± 1.08 vs. 9.81 ± 1.62 , $P = 0.006$; and 14.30 ± 8.83 vs. 6.30 ± 4.25 , $P = 0.010$, respectively) (Table 2). None of the other parameters showed a significant difference between responders and nonresponders.

Correlations Between ^{18}F -FAPI-04 PET/CT Parameters and Short-Term Outcome

Receiver-operating-characteristic curves were generated to evaluate the predictive accuracy of ^{18}F -FAPI-04 PET/CT parameters for identifying responders and nonresponders (Table 3; Fig. 3). The area under the curve (AUC) for $\text{TBR}_{\text{blood}}$ (AUC, 0.883) was higher than those for $\text{TBR}_{\text{muscle}}$ (AUC, 0.896) and SUV_{mean} (AUC, 0.870) (Table 4), and the AUCs for all 3 parameters were significant ($P = 0.008$, $P = 0.006$, and $P = 0.010$, respectively) (Table 3). The cutoffs for $\text{TBR}_{\text{blood}}$, $\text{TBR}_{\text{muscle}}$, and SUV_{mean} , based on the Youden indices, were 10.68, 10.96, and 6.88, respectively (Table 4). The calculated values for the sensitivity, specificity, positive predictive value, negative predictive value, and accuracy of these 3 parameters also are presented in Table 4.

TABLE 2
Parameters Calculated from Pretreatment ^{18}F -FAPI-04 PET/CT Scans

Parameter	All patients ($n = 18$)	Nonresponders ($n = 11$)	Responders ($n = 7$)	P
SUV_{max}	15.31 ± 11.31	20.33 ± 15.38	12.11 ± 6.81	0.085
$\text{SUV}_{\text{mean}}^*$	9.41 ± 7.37	14.30 ± 8.83	6.30 ± 4.25	0.010
SUV_{peak}	11.23 ± 8.53	14.44 ± 11.79	9.18 ± 5.33	0.298
MTV	13.55 ± 11.74	13.94 ± 13.53	13.30 ± 11.15	0.892
TLF	140.84 ± 159.61	217.40 ± 219.29	92.12 ± 88.00	0.221
$\text{TBR}_{\text{blood}}^*$	11.16 ± 1.76	12.53 ± 1.11	10.29 ± 1.54	0.008
$\text{TBR}_{\text{muscle}}^*$	10.76 ± 1.86	12.24 ± 1.08	9.81 ± 1.62	0.006

* $P < 0.05$.

TLF = total lesion FAP expression (^{18}F -FAPI-04).

TABLE 3
Areas Under Curve for Ability of SUV_{max}, SUV_{mean}, SUV_{peak}, MTV, TLF, TBR_{blood}, and TBR_{muscle} to Predict LA-ESCC Tumor Response to CCRT

Parameter	Area	SE*	Asymptotic significance [†]	Asymptotic 95% CI	
				Lower bound	Upper bound
SUV _{max}	0.747	0.120	0.085	0.512	0.981
SUV _{mean} [‡]	0.870	0.088	0.010	0.698	1.000
SUV _{peak}	0.649	0.143	0.298	0.369	0.929
MTV	0.481	0.144	0.892	0.198	0.763
TLF	0.675	0.134	0.221	0.414	0.937
TBR _{blood} [‡]	0.883	0.080	0.008	0.725	1.000
TBR _{muscle} [‡]	0.896	0.074	0.006	0.750	1.000

*Under nonparametric assumption.

[†]Null hypothesis: true area = 0.5.

[‡] $P < 0.05$.

TLF = total lesion FAP expression (¹⁸F-FAPI-04).

Correlations Between Biomarkers

The observed correlations between ¹⁸F-FAPI-04 PET/CT biomarkers, extracted from tumor lesions and variables of interest, are presented in Figure 4. TBR_{blood}, TBR_{muscle}, and SUV_{mean} showed significant correlations with each other. However, none of the ¹⁸F-FAPI-04 parameters correlated with any clinical variables.

Associations Between Baseline ¹⁸F-FAPI-04 PET/CT Parameters, Clinical Variables, and Short-Term Treatment Response

According to univariate logistic regression analyses, TBR_{blood} ($P = 0.026$), TBR_{muscle} ($P = 0.036$), SUV_{mean} ($P = 0.045$), and tumor site ($P = 0.032$) were independently associated with the

short-term treatment response in LA-ESCC patients. Because of the significantly positive correlation among TBR_{blood}, TBR_{muscle}, and SUV_{mean}, we included only TBR_{blood} and tumor site in the multivariate analysis. Finally, only TBR_{blood} ($P = 0.046$) remained significant as a prognostic factor for short-term outcome in these patients (Table 5).

DISCUSSION

The results of the present study indicate that certain parameters derived from baseline ¹⁸F-FAPI-04 PET/CT scans, specifically the baseline TBR_{blood}, TBR_{muscle}, and SUV_{mean}, as well as the tumor site, are potentially valuable for predicting the response to CCRT in patients with LA-ESCC. Moreover, TBR_{blood} was an independent predictor of short-term CCRT efficacy in these patients by multivariable logistic regression analysis.

In clinical practice, we observed different outcomes in patients with LA-ESCC treated with CCRT—differences that may be related to the heterogeneity of the tumor microenvironment (15,16). Previous studies reported that FAP is expressed mainly by interstitial cells of the tumor microenvironment, including cancer-associated fibroblasts and tumor-associated macrophages (17,18). It has been confirmed that FAP plays a key role in chemotherapy resistance (19–21), radiotherapy resistance (22), and immune escape (23–25). Furthermore, FAP can promote tumor cell invasion, migration, and tumor angiogenesis (26–28). In a previous report of 2 cases, 1 patient with peritoneal carcinomatosis who experienced disease progression after 4 mo of chemotherapy showed an increase in the average SUV_{max} compared with before chemotherapy, whereas the other patient, who achieved partial remission after 5 mo of treatment, showed a decrease in the average SUV_{max} relative to baseline (29). Accordingly, ¹⁸F-FAPI-04 uptake within the tumor was considered potentially valuable for predicting the short-term response to CCRT in patients with LA-ESCC.

A series of studies found that in esophageal cancer patients treated with chemoradiotherapy, the metabolic parameters on pretreatment ¹⁸F-FDG PET are reliable predictors of prognosis and survival (30–32). However, at present, the value of ¹⁸F-FDG PET/CT

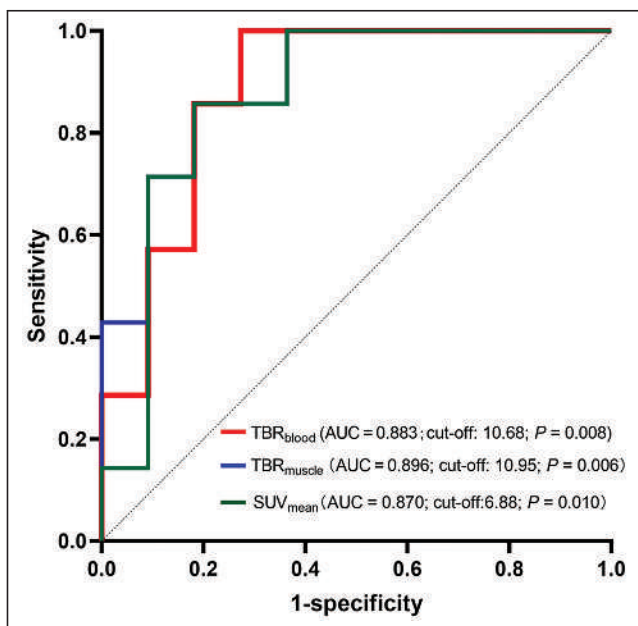


FIGURE 3. Receiver-operating-characteristic curves for ability of ¹⁸F-FAPI-04 PET/CT parameters to predict short-term response to CCRT.

TABLE 4
Specificity, Sensitivity, PPV, NPV, and Accuracy of SUV_{max}, SUV_{mean}, SUV_{peak}, MTV, TLF, TBR_{blood}, and TBR_{muscle} for Predicting LA-ESCC Tumor Response to CCRT

Parameter	Threshold	Sensitivity (%)	Specificity (%)	PPV (%)	NPV (%)	Accuracy (%)
SUV _{max}	14.86	71.4	81.8	71.4	81.8	77.8
SUV _{mean}	6.88	85.7	81.8	75.0	90.0	83.3
SUV _{peak}	9.57	71.4	72.7	62.5	80	72.2
MTV	5.91	85.7	36.4	46.2	80	55.6
TLF	103.20	71.4	63.6	55.6	77.8	66.7
TBR _{blood}	10.68	100.0	72.7	66.7	88.9	77.8
TBR _{muscle}	10.95	100.0	72.7	66.7	88.9	77.8

PPV = positive predictive value; NPV = negative predictive value; TLF = total lesion FAP expression (¹⁸F-FAPI-04).

parameters for predicting tumor prognosis remains controversial. Caresia Aroztegui et al. found that the evidence for the prognostic value of SUV_{max} in axillary lymph nodes derived from ¹⁸F-FDG PET/CT is limited, although higher values have been associated with higher recurrence rates (33). Research also has demonstrated that the application of ¹⁸F-FDG PET parameters in breast cancer prognosis is

still limited, and the criteria for these parameters have not been established (34). Thus, the urgent need to find a new imaging agent with higher diagnostic and predictive efficiency persists.

Several studies have demonstrated that high tumor MTV and total lesion glycolysis, derived from ¹⁸F-FDG PET/CT scans, are independent predictors in patients with esophageal cancer treated with chemoradiotherapy (32) and definitive chemoradiotherapy (31). However, in our cohort, the baseline tumor MTV and total lesion FAP expression from ¹⁸F-FAPI-04 PET/CT did not provide significant prognostic information. We consider that this difference between the results for ¹⁸F-FAPI-04 PET/CT and ¹⁸F-FDG PET/CT may be related to the imaging principle of ¹⁸F-FDG PET/CT, which is based on the level of glucose metabolism within tumor cells.

The main limitations of the present study included its single-center design and relatively small sample size. Further large-scale, multi-center clinical studies are needed to confirm our findings before clinical application. Additionally, the fact that this study included a heterogeneous population consisting of patients treated with total radiation doses of 50 and 60 Gy might affect the outcome. However, Xu et al. reported no significant difference in survival endpoints between groups that received 60 and 50 Gy (35), and Minsky et al. reported that higher radiotherapy doses do not lead to better outcomes (36). Additionally, the ARTDECO study found that increasing the radiation dose from 50.4 to 60 Gy did not improve local control in esophageal cancer (37). Overall, further prospective trials are required to confirm the role of ¹⁸F-FAPI-04 PET/CT in the treatment of patients with LA-ESCC.

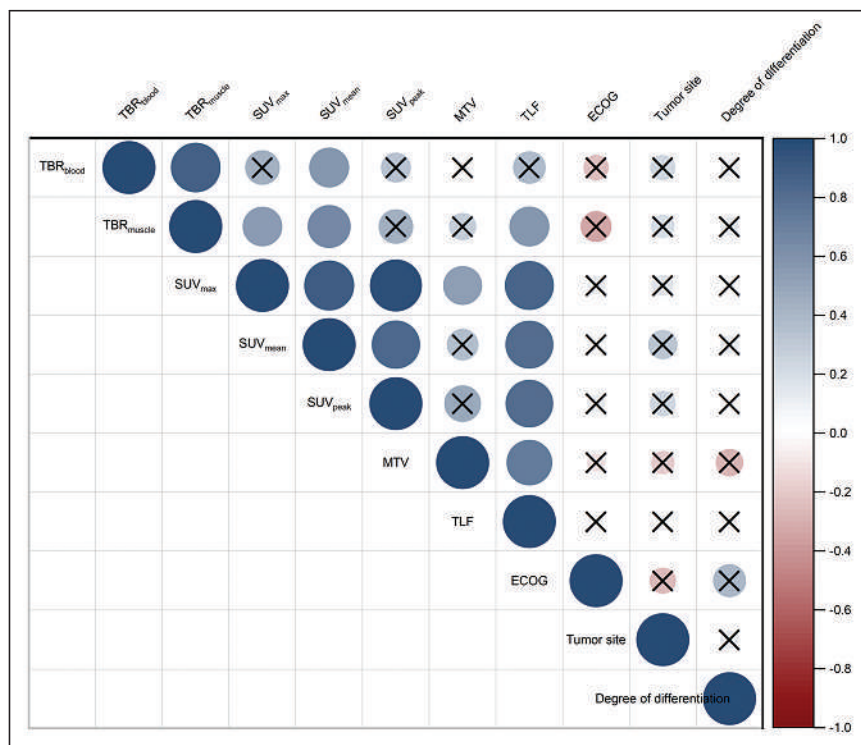


FIGURE 4. Correlations between ¹⁸F-FAPI-04 PET/CT parameters and clinical or biologic variables (Spearman coefficient). Those with $P < 0.05$ are marked by circles. Blue represents positive correlation between 2 variables, and red represents negative correlation. The stronger the correlation, the darker the color. Those with $P > 0.05$, indicating no correlation, are recorded as X. As example, SUV_{max} showed positive correlation with MTV. ECOG = Eastern Cooperative Oncology Group; TLF = total lesion FAP expression (¹⁸F-FAPI-04).

TABLE 5

Univariate and Multivariate Logistic Regression Analyses of ¹⁸F-FAPI-04 PET/CT Parameters and Clinical Factors Able to Predict Short-Term Outcomes in LA-ESCC Patients

Factor	Univariate analysis		Multivariate analysis	
	OR (95% CI)	P	OR (95% CI)	P
SUV _{max}	1.09 (0.96–1.23)	0.192	—	—
SUV _{mean} *	1.31 (1.01–1.71)	0.045	—	—
SUV _{peak}	1.09 (0.95–1.25)	0.241	—	—
MTV	1.01 (0.93–1.09)	0.908	—	—
TLF	1.01 (1.00–1.02)	0.157	—	—
TBR _{blood} *	3.04 (1.01–6.44)	0.026	2.75 (1.02–7.43)	0.046
TBR _{muscle}	3.99 (1.09–14.55)	0.036	—	—
ECOG score	1.31 (0.19–9.10)	0.783	—	—
Differentiation degree	2.26 (0.68–7.57)	0.186	—	—
Tumor site*	3.32 (1.11–9.89)	0.032	3.47 (0.77–15.66)	0.105

*P < 0.05.

OR = odds ratio; TLF = total lesion FAP expression (¹⁸F-FAPI-04); ECOG = Eastern Cooperative Oncology Group. Data in parentheses are 95% CIs.

CONCLUSION

The baseline TBR_{blood} on ¹⁸F-FAPI-04 PET/CT was associated with the short-term response to CCRT in patients with LA-ESCC. Combined with clinical prognostic factors, including tumor site, pretreatment ¹⁸F-FAPI-04 PET/CT can potentially improve the selection of candidates for CCRT and identify patient groups with markedly different prognoses.

DISCLOSURE

This work was funded by the Natural Science Foundation of China (NSFC81872475, NSFC82073345), the Jinan Clinical Medicine Science and Technology Innovation Plan (202019060), the Natural Science Foundation of Shandong Province (ZR2021QH008), and the Bethune Charitable Foundation (flzh202116). No other potential conflict of interest relevant to this article was reported.

KEY POINTS

QUESTION: Can ¹⁸F-FAPI-04 PET/CT parameters predict the short-term response to CCRT in patients with LA-ESCC?

PERTINENT FINDINGS: Baseline TBR_{blood} on ¹⁸F-FAPI-04 PET/CT was associated with short-term outcome in patients with LA-ESCC treated with CCRT.

IMPLICATIONS FOR PATIENT CARE: On the basis of the encouraging results of this analysis, ¹⁸F-FAPI-04 PET/CT may offer a standardized and reproducible technique for identifying LA-ESCC patients most likely to respond to CCRT.

REFERENCES

1. Siegel RL, Miller KD, Fuchs HE, Jemal A. Cancer statistics, 2022. *CA Cancer J Clin.* 2022;72:7–33.

2. Sung H, Ferlay J, Siegel RL, et al. Global cancer statistics 2020: GLOBOCAN estimates of incidence and mortality worldwide for 36 cancers in 185 countries. *CA Cancer J Clin.* 2021;71:209–249.

3. Arnold M, Soerjomataram I, Ferlay J, Forman D. Global incidence of oesophageal cancer by histological subtype in 2012. *Gut.* 2015;64:381–387.

4. Cooper JS, Guo MD, Herskovic A, et al. Chemoradiotherapy of locally advanced esophageal cancer: long-term follow-up of a prospective randomized trial (RTOG 85-01). Radiation Therapy Oncology Group. *JAMA.* 1999;281:1623–1627.

5. Hamson EJ, Keane FM, Tholen S, Schilling O, Gorrell MD. Understanding fibroblast activation protein (FAP): substrates, activities, expression and targeting for cancer therapy. *Proteomics Clin Appl.* 2014;8:454–463.

6. Zi F, He J, He D, Li Y, Yang L, Cai Z. Fibroblast activation protein alpha in tumor microenvironment: recent progression and implications. *Mol Med Rep.* 2015;11:3203–3211.

7. Altmann A, Haberkorn U, Siveke J. The latest developments in imaging fibroblast activation protein. *J Nucl Med.* 2021;62:160–167.

8. Cohen SJAR, Palazzo I, Meropol NJ, et al. Fibroblast activation protein and its relationship to clinical outcome in pancreatic adenocarcinoma. *Pancreas.* 2008;37:154–158.

9. Shi M, Yu DH, Chen Y, et al. Expression of fibroblast activation protein in human pancreatic adenocarcinoma and its clinicopathological significance. *World J Gastroenterol.* 2012;18:840–846.

10. Saigusa S, Toiyama Y, Tanaka K, et al. Cancer-associated fibroblasts correlate with poor prognosis in rectal cancer after chemoradiotherapy. *Int J Oncol.* 2011;38:655–663.

11. Ariga N, Ohuchi ESN, Nagura H, Ohtani H. Stromal expression of fibroblast activation protein/seprase, a cell membrane serine proteinase and gelatinase, is associated with longer survival in patients with invasive ductal carcinoma of breast. *Int J Cancer.* 2001;95:67–72.

12. Chen X, Liu X, Wang L, et al. Expression of fibroblast activation protein in lung cancer and its correlation with tumor glucose metabolism and histopathology. *Eur J Nucl Med Mol Imaging.* 2022;49:2938–2948.

13. Wei Y, Zheng J, Ma L, et al. [¹⁸F]AIF-NOTA-FAPI-04: FAP-targeting specificity, biodistribution, and PET/CT imaging of various cancers. *Eur J Nucl Med Mol Imaging.* 2022;49:2761–2773.

14. Wei Y, Cheng K, Fu Z, et al. [¹⁸F]AIF-NOTA-FAPI-04 PET/CT uptake in metastatic lesions on PET/CT imaging might distinguish different pathological types of lung cancer. *Eur J Nucl Med Mol Imaging.* 2022;49:1671–1681.

15. Wolf Y, Bartok O, Patkar S, et al. UVB-induced tumor heterogeneity diminishes immune response in melanoma. *Cell.* 2019;179:219–235.e21.

16. Junttila MR, de Sauvage FJ. Influence of tumour micro-environment heterogeneity on therapeutic response. *Nature.* 2013;501:346–354.

17. Cremasco V, Astarita JL, Grauel AL, et al. FAP delineates heterogeneous and functionally divergent stromal cells in immune-excluded breast tumors. *Cancer Immunol Res.* 2018;6:1472–1485.
18. Mei S, Zhang Y, Yu L, Chen G, Zi F. Expression and role of fibroblast activation protein alpha in acute myeloid leukemia. *Oncol Rep.* 2021;45:641–651.
19. Mhaweche-Fauceglia P, Yan L, Sharifian M, et al. Stromal expression of fibroblast activation protein alpha (FAP) predicts platinum resistance and shorter recurrence in patients with epithelial ovarian cancer. *Cancer Microenviron.* 2015;8:23–31.
20. Zhai Y, Zhang J, Wang H, et al. Growth differentiation factor 15 contributes to cancer-associated fibroblasts-mediated chemo-protection of AML cells. *J Exp Clin Cancer Res.* 2016;35:147.
21. Katsube R, Noma K, Ohara T, et al. Fibroblast activation protein targeted near infrared photoimmunotherapy (NIR PIT) overcomes therapeutic resistance in human esophageal cancer. *Sci Rep.* 2021;11:1693.
22. Huang W, Zhang L, Yang M, et al. Cancer-associated fibroblasts promote the survival of irradiated nasopharyngeal carcinoma cells via the NF-kappaB pathway. *J Exp Clin Cancer Res.* 2021;40:87.
23. Wong PF, Wei W, Gupta S, et al. Multiplex quantitative analysis of cancer-associated fibroblasts and immunotherapy outcome in metastatic melanoma. *J Immunother Cancer.* 2019;7:194.
24. Chen L, Qiu X, Wang X, He J. FAP positive fibroblasts induce immune checkpoint blockade resistance in colorectal cancer via promoting immunosuppression. *Biochem Biophys Res Commun.* 2017;487:8–14.
25. Yang X, Lin Y, Shi Y, et al. FAP promotes immunosuppression by cancer-associated fibroblasts in the tumor microenvironment via STAT3-CCL2 signaling. *Cancer Res.* 2016;76:4124–4135.
26. Chen WTKT. Seprase complexes in cellular invasiveness. *Cancer Metastasis Rev.* 2003;22:259–269.
27. Kelly T. Fibroblast activation protein-alpha and dipeptidyl peptidase IV (CD26): cell-surface proteases that activate cell signaling and are potential targets for cancer therapy. *Drug Resist Updat.* 2005;8:51–58.
28. Huang Y, Wang S, Kelly T. Seprase promotes rapid tumor growth and increased microvessel density in a mouse model of human breast cancer. *Cancer Res.* 2004;64:2712–2716.
29. Kuten J, Levine C, Shammi O, et al. Head-to-head comparison of [⁶⁸Ga]Ga-FAPI-04 and [¹⁸F]-FDG PET/CT in evaluating the extent of disease in gastric adenocarcinoma. *Eur J Nucl Med Mol Imaging.* 2022;49:743–750.
30. Wang C, Zhao K, Hu S, et al. A predictive model for treatment response in patients with locally advanced esophageal squamous cell carcinoma after concurrent chemoradiotherapy: based on SUVmean and NLR. *BMC Cancer.* 2020;20:544.
31. Takahashi N, Umezawa R, Takanami K, et al. Whole-body total lesion glycolysis is an independent predictor in patients with esophageal cancer treated with definitive chemoradiotherapy. *Radiother Oncol.* 2018;129:161–165.
32. Nakajo M, Jinguji M, Nakabeppu Y, et al. Texture analysis of ¹⁸F-FDG PET/CT to predict tumour response and prognosis of patients with esophageal cancer treated by chemoradiotherapy. *Eur J Nucl Med Mol Imaging.* 2017;44:206–214.
33. Caresia Aroztegui AP, Garcia Vicente AM, Alvarez Ruiz S, et al. ¹⁸F-FDG PET/CT in breast cancer: evidence-based recommendations in initial staging. *Tumour Biol.* 2017;39:1010428317728285.
34. Kim J, Yoo SW, Kang SR, et al. Prognostic significance of metabolic tumor volume measured by ¹⁸F-FDG PET/CT in operable primary breast cancer. *Nucl Med Mol Imaging.* 2012;46:278–285.
35. Xu Y, Dong B, Zhu W, et al. A phase III multicenter randomized clinical trial of 60 Gy vs 50 Gy radiation dose in concurrent chemoradiotherapy for inoperable esophageal squamous cell carcinoma. *Clin Cancer Res.* 2022;28:1792–1799.
36. Minsky BD, Pajak TF, Ginsberg RJ, et al. INT 0123 (Radiation Therapy Oncology Group 94-05) phase III trial of combined-modality therapy for esophageal cancer: high-dose versus standard-dose radiation therapy. *J Clin Oncol.* 2002;20:1167–1174.
37. Hulshof MC, Geijsen ED, Rozema T, et al. Randomized study on dose escalation in definitive chemoradiation for patients with locally advanced esophageal cancer (ARTDECO Study). *J Clin Oncol.* 2021;39:2816–2824.

¹⁸F-AIF-NOTA-Octreotide Outperforms ⁶⁸Ga-DOTATATE/ NOC PET in Neuroendocrine Tumor Patients: Results from a Prospective, Multicenter Study

Elin Pauwels¹, Frederik Cleeren², T rence Tshibangu², Michel Koole¹, Kim Serdons¹, Lennert Boeckxstaens¹, Jeroen Dekervel³, Timon Vandamme^{4,5}, Willem Lybaert⁵, Bliede Van den Broeck⁶, Annouschka Laenen⁷, Paul M. Clement⁸, Karen Geboes⁹, Eric Van Cutsem³, Sigrid Stroobants¹⁰, Chris Verslype³, Guy Bormans², and Christophe M. Deroose¹

¹Nuclear Medicine, University Hospitals Leuven, and Nuclear Medicine and Molecular Imaging, Department of Imaging and Pathology, KU Leuven, Leuven, Belgium; ²Radiopharmaceutical Research, Department of Pharmacy and Pharmacology, KU Leuven, Leuven, Belgium; ³Digestive Oncology, University Hospitals Leuven, Leuven, Belgium; ⁴Center for Oncological Research (CORE), Integrated Personalized and Precision Oncology Network (IPPON), University of Antwerp, Antwerp, Belgium; ⁵Oncology, NETwerk Antwerpen-Waasland CoE, Edegem, Belgium; ⁶Nuclear Medicine, Ghent University Hospital, Ghent, Belgium; ⁷Leuven Biostatistics and Statistical Bioinformatics Center, KU Leuven, Leuven, Belgium; ⁸General Medical Oncology, University Hospitals Leuven, Leuven, Belgium; ⁹Digestive Oncology, Department of Gastroenterology, Ghent University Hospital, Ghent, Belgium; and ¹⁰Nuclear Medicine, Antwerp University Hospital, and Molecular Imaging and Radiology, Faculty of Medicine and Health Sciences, University of Antwerp, Wilrijk, Belgium

¹⁸F-labeled somatostatin analogs (SSAs) could represent a valid alternative to the current gold standard, ⁶⁸Ga-labeled SSAs, for somatostatin receptor imaging in patients with neuroendocrine tumors (NETs), given their logistic advantages. Recently, ¹⁸F-AIF-NOTA-octreotide (¹⁸F-AIF-OC) has emerged as a promising candidate, but a thorough comparison with ⁶⁸Ga-DOTA-SSA in large patient groups is needed. This prospective, multicenter trial aims to demonstrate noninferiority of ¹⁸F-AIF-OC compared with ⁶⁸Ga-DOTA-SSA PET in NET patients (ClinicalTrials.gov, NCT04552847). **Methods:** Seventy-five patients with histologically confirmed NET and routine clinical ⁶⁸Ga-DOTATATE ($n = 56$) or ⁶⁸Ga-DOTA-NOC ($n = 19$) PET, performed within a 3-mo interval of the study scan (median, 7 d; range, -30 to +32 d), were included. Patients underwent a whole-body PET 2 h after intravenous injection of 4 MBq/kg of ¹⁸F-AIF-OC. A randomized, masked consensus read was performed by 2 experienced readers to count tumor lesions. After unmasking, the detection ratio (DR) was determined for each scan, that is, the fraction of lesions detected on a scan compared with the union of lesions of both scans. The differential DR (DDR; difference in DR between ¹⁸F-AIF-OC and ⁶⁸Ga-DOTATATE/NOC) per patient was calculated. Tracer uptake was evaluated by comparing SUV_{max} and tumor-to-background ratios in concordant lesions. **Results:** In total, 4,709 different tumor lesions were detected: 3,454 with ⁶⁸Ga-DOTATATE/NOC and 4,278 with ¹⁸F-AIF-OC. The mean DR with ¹⁸F-AIF-OC was significantly higher than with ⁶⁸Ga-DOTATATE/NOC (91.1% vs. 75.3%; $P < 10^{-5}$). The resulting mean DDR was 15.8%, with a lower margin of the 95% CI (95% CI, 9.6%–22.0%) higher than -15%, which is the prespecified boundary for noninferiority. The mean DDRs for the ⁶⁸Ga-DOTATATE and ⁶⁸Ga-DOTA-NOC subgroups were 11.8% (95% CI, 4.3–19.3) and 27.5% (95% CI, 17.8–37.1), respectively. The mean DDR for most organs was higher than zero, except for bone lesions (mean DDR, -2.8%; 95% CI, -17.8 to 12.2). No significant differences in mean SUV_{max} were observed ($P = 0.067$), but mean tumor-to-background ratio was significantly higher with

¹⁸F-AIF-OC than with ⁶⁸Ga-DOTATATE/NOC (31.7 ± 36.5 vs. 25.1 ± 32.7 ; $P = 0.001$). **Conclusion:** ¹⁸F-AIF-OC is noninferior and even superior to ⁶⁸Ga-DOTATATE/NOC PET in NET patients. This validates ¹⁸F-AIF-OC as an option for clinical practice somatostatin receptor PET.

Key Words: ¹⁸F-AIF-NOTA-octreotide; ⁶⁸Ga-DOTATATE; ⁶⁸Ga-DOTA-NOC; neuroendocrine tumor; somatostatin receptor

J Nucl Med 2023; 64:632–638

DOI: 10.2967/jnumed.122.264563

Neuroendocrine tumors (NETs) are part of a heterogeneous group of relatively rare tumors that develop from cells of the diffuse neuroendocrine system and are mainly found in the gastrointestinal and respiratory tracts. Many NETs show an overexpression of the somatostatin receptor (SSTR), a G-protein-coupled membrane receptor that makes an excellent target for molecular imaging and therapy with radiolabeled somatostatin analogs (SSAs) (1). SSTR imaging plays a crucial role in the diagnostic work-up, treatment selection, follow-up, and recurrence detection of NETs (1). ⁶⁸Ga-DOTATATE, ⁶⁸Ga-DOTATOC, and ⁶⁸Ga-DOTANOC, which can be collectively referred to as ⁶⁸Ga-DOTA-SSAs, are considered as the current gold standard for SSTR imaging (1,2). However, their widespread clinical implementation faces challenges inherent to the use of ⁶⁸Ge/⁶⁸Ga generators, such as limited availability, high associated costs, and low activity yield per elution (3). These challenges can be largely overcome by an ¹⁸F-labeled alternative. In particular, the high activity yield in combination with a favorable half-life of 109.8 min enables centralized production of ¹⁸F-labeled tracers followed by distribution to distant PET centers without cyclotron access (3). Furthermore, ¹⁸F has a shorter positron range than ⁶⁸Ga and is therefore more suitable for high-spatial-resolution imaging on modern PET cameras (3).

Recently, ¹⁸F-AIF-NOTA-octreotide (¹⁸F-AIF-OC) has emerged as a promising ¹⁸F-labeled SSA for SSTR imaging (4,5). ¹⁸F-AIF-OC is synthesized using the chelator-based Al¹⁸F-method (6).

Received Jun. 23, 2022; revision accepted Oct. 4, 2022.

For correspondence or reprints, contact Christophe M. Deroose (christophe.deroose@uzleuven.be).

Published online Oct. 20, 2022.

COPYRIGHT   2023 by the Society of Nuclear Medicine and Molecular Imaging.

To allow clinical implementation, a fast and robust automated good-manufacturing-practice-compliant process was recently developed (7). Two independently performed first clinical translations of ^{18}F -AIF-OC in healthy volunteers and NET patients have reported favorable dosimetry, biodistribution, tracer kinetics, and lesion targeting (4,5). First comparisons of ^{18}F -AIF-OC with ^{68}Ga -DOTATATE in 2 small NET patient groups ($n = 6$ and $n = 20$) have shown similar lesion detection rates and tumor uptake (5,8). However, a thorough head-to-head comparison with ^{68}Ga -DOTA-SSA PET in large patient groups is still lacking.

This prospective multicenter trial aimed to demonstrate that the diagnostic performance of ^{18}F -AIF-OC PET is equivalent or superior to the current gold standard, ^{68}Ga -DOTA-SSA PET, in NET patients (noninferiority trial).

MATERIALS AND METHODS

A full version of the Materials and Methods section is provided in the supplemental information (supplemental materials are available at <http://jnm.snmjournals.org>).

Study Population

In the main part (part A) of this prospective multicenter trial, 75 NET patients, 18 y of age or older, were included. The main inclusion criteria were as follows: histologically or cytologically confirmed NET of all grades of gastroenteropancreatic, pulmonary, neural crest, or unknown primary origin; routine clinical ^{68}Ga -DOTA-SSA PET/CT scheduled within 3 mo before or after the study scan; and at least 1 known tumor lesion below the level of the submandibular and parotid glands, with either a minimum size of 1 cm in at least 1 dimension on morphologic imaging (CT, MRI, or ultrasound) or an SUV_{max} of at least 10 on ^{68}Ga -DOTA-SSA PET. The main exclusion criterion was previous or ongoing recurrent or chronic disease at high risk to interfere with the performance or evaluation of the trial. The PET/MRI part (part B) of the trial in 10 NET patients will be presented elsewhere.

The study was performed at University Hospitals Leuven in collaboration with University Hospital Antwerp and University Hospital Ghent after approval by the Ethics Committee of all 3 institutes, and all subjects gave written informed consent (ClinicalTrials.gov identifier, NCT04552847; EudraCT, 2020-000549-15).

PET/CT Acquisition

We previously identified 2 h after injection to be the optimal time point for imaging (5). Patients underwent whole-body PET (from mid thigh to vertex) 2 h after intravenous injection of 4 MBq/kg of ^{18}F -AIF-OC, preceded by a low-dose CT scan for attenuation correction and anatomic information.

For both the routine and study scans, patients were asked to avoid long-acting SSA treatment, except in cases of uncontrolled hormonal symptoms, for 4–6 wk before the scan.

Image Analyses

All image analyses were done using MIM, version 7.1.5 (MIM Software Inc.). Tumor lesions were counted in consensus by 2 experienced readers, and the patient data and radiopharmaceutical that was used were masked from the reader. Routine and study scans were randomized per group of 20 patients (40 scans per group), and information regarding patient and radiopharmaceutical was removed from the Digital Imaging and Communications in Medicine headers. Furthermore, since normal salivary gland uptake is markedly higher with ^{68}Ga -DOTATATE than with ^{18}F -AIF-OC (5,8), all PET datasets were trimmed by an independent operator to remove the head region. A positive lesion was defined as a volume of increased tracer uptake, compared with background, that was deemed to be caused by the presence of NET cells and was unlikely to

be attributed to a physiologic or benign etiology (e.g., inflammation, blood pool retention, or excretion). A detailed description of the consensus read is provided in the supplemental information.

After unmasking, the detection ratio (DR) was determined for each scan, that is, the fraction of lesions detected on that scan, using the union of lesions detected by both tracers (^{68}Ga -DOTATATE/NOC and ^{18}F -AIF-OC) in a patient as the reference. Finally, the differential DR (DDR), which is the difference in DR between ^{18}F -AIF-OC and ^{68}Ga -DOTATATE/NOC, was calculated for each patient. The DR at organ level was determined as the number of lesions detected with 1 tracer divided by all lesions detected by both tracers in a specific organ.

For each lesion, the SUV_{max} was measured, and the tumor-to-background ratio (TBR) was calculated by dividing the SUV_{max} of that lesion by the SUV_{mean} of relevant background tissue (liver for liver lesions, bone for bone lesions, and gluteal muscle for all other lesions). In patients for whom no healthy liver ($n = 1$) or bone tissue ($n = 2$) could be delineated, the mean background value of all other patients was used instead to determine TBRs. Lesions with incorrect attenuation correction because of PET/CT misregistration were excluded from semiquantitative analysis.

TABLE 1
Patient and Clinical Characteristics ($n = 75$)

Characteristic	Data
Age (y)	65 (37–84)
Sex	
Male	46 (61.3%)
Female	29 (38.7%)
Primary tumor	
Intestine	45 (60.0%)
Pancreas	18 (24.0%)
Lung	7 (9.3%)
CUP	4 (5.3%)
Paraganglioma	1 (1.3%)
Tumor grade	
Grade 1	35 (46.7%)
Grade 1/2 (i.e., Ki-67 < 5%)	2 (2.7%)
Grade 2	34 (45.3%)
Grade 3	2 (2.7%)
NA	2 (2.7%)
Ki-67 (%)	2.5 (0.4–29)
Ongoing therapies	
SSA	44 (58.7%)
SSA and everolimus	10 (13.3%)
Everolimus	2 (2.7%)
Sunitinib	2 (2.7%)
None	17 (22.7%)
Interval between ^{18}F -AIF-OC and ^{68}Ga -DOTA-TATE/NOC scan (d)	7 (–30 to 32)

CUP = cancer of unknown primary; NA = not available; Ki-67 = Ki-67 proliferation index.

Qualitative data are number and percentage; continuous data are median and range.

TABLE 2
Comparison Between Mean DR with ^{68}Ga -DOTATATE/NOC (DR_{Ga}) and ^{18}F -AIF-OC (DR_{F}) and Mean DDR with 95% CI for Most Relevant Organs

Organ	Mean DR_{Ga} (%)	Mean DR_{F} (%)	<i>P</i>	Mean DDR (%)	95% CI (%)
Liver	60.3	93.3	$<10^{-5}$	33.1	21.7–44.4
Bone	79.8	77.0	0.78	–2.8	–17.8–12.2
Lymph nodes	74.1	96.0	$<10^{-5}$	21.9	14.0–29.8
Lung	73.6	98.1	0.027	24.6	3.3–45.8
Peritoneum	55.5	89.3	0.008	33.8	11.7–55.9
Pancreas	84.6	100.0	0.10	15.4	–3.7–34.4
All*	75.3	91.1	$<10^{-5}$	15.8	9.6–22.0

*Lesions in head region are not included.

Outcomes

The primary outcome measure was the DDR. The primary objective, that is, noninferiority of ^{18}F -AIF-OC compared with ^{68}Ga -DOTATATE/NOC, would be met if the lower margin of the 95% CI for the mean DDR was higher than –15%.

Secondary outcome measures included the following: lesion uptake in matched pairs of lesions (SUV_{max} and TBR), DR and DDR at organ level, DDR in function of the specific ^{68}Ga -DOTA-SSA used (^{68}Ga -DOTATATE or ^{68}Ga -DOTANOC) and tumor grade, and impact of ^{18}F -AIF-OC administration on blood pressure and heart rate. A post hoc analysis according to primary tumor site (for $n > 10$) was performed as well.

Lesion uptake was assessed, first, at the patient level; second, for 2 subsets of hottest lesions (i.e., 20 lesions per patient and a maximum of 5 lesions per organ, at the patient level); and third, at the lesion level. For secondary outcome measures, tumor lesions in the head region, identified through a nonmasked consensus read, were added in the analyses. The safety evaluation is provided in the supplemental information.

RESULTS

Patients and ^{18}F -AIF-OC Administration

Patient and clinical characteristics are shown in Table 1. The median time between the ^{18}F -AIF-OC and routine ^{68}Ga -DOTATATE/NOC scan was 7 d (range, –30 to 32 d), with 52 patients (78.7%)

having both scans within a 15-d interval (Supplemental Fig. 1). No therapeutic changes occurred between the scans, except in 3 patients: in 1 patient, everolimus was added 2 d before the second scan (^{18}F -AIF-OC); in 1 patient, everolimus was added 7 d before the second scan (^{18}F -AIF-OC); and in 1 patient, SSA treatment was reinitiated 13 d before the second scan (^{18}F -AIF-OC). The mean injected activity and peptide mass of ^{18}F -AIF-OC were 295 ± 60 MBq and 11.2 ± 6.8 μg , respectively.

Detection Rate Analysis

During the masked consensus read, 4,709 different tumor lesions were counted: 3,454 with ^{68}Ga -DOTATATE/NOC and 4,278 with ^{18}F -AIF-OC. In 48 patients, ^{18}F -AIF-OC detected more lesions than ^{68}Ga -DOTATATE/NOC, whereas ^{68}Ga -DOTATATE/NOC detected more lesions in only 15 patients. The mean DR with ^{18}F -AIF-OC was significantly higher than with ^{68}Ga -DOTATATE/NOC (91.1% vs. 75.3%; $P < 10^{-5}$). The resulting mean DDR was 15.8% (95% CI, 9.6%–22.0%). As the lower margin of the 95% CI was higher than –15%, the primary objective of the trial was met. DDRs ranged from –74.2% to 77.5% (interquartile range, 0.0%–32.7%; Supplemental Fig. 2).

In the head region, 214 additional lesions were counted. A summary of results for the most relevant organs is provided in

TABLE 3
Comparison Between Mean DR with ^{68}Ga -DOTATATE/NOC (DR_{Ga}) and ^{18}F -AIF-OC (DR_{F}) and Mean DDR with 95% CI for Different Subgroups of Patients According to Routine ^{68}Ga -DOTA-SSA Tracer, Tumor Grade, and Primary Tumor Site

Subgroup	<i>n</i>	Mean DR_{Ga} (%)	Mean DR_{F} (%)	<i>P</i>	Mean DDR (%)	95% CI (%)
^{68}Ga -DOTATATE	56	77.5	89.4	0.002	11.8	4.3–19.3
^{68}Ga -DOTANOC	19	68.9	96.4	$<10^{-3}$	27.5	17.8–37.1
Grade 1	35	75.0	89.9	0.003	14.9	6.0–23.8
Grade 2	34	75.5	92.1	0.002	16.6	6.3–27.0
Grade 3	2	62.0	97.4	NA	35.4	NA
Intestine	45	72.6	90.4	$<10^{-3}$	17.8	9.2–26.4
Pancreas	18	84.2	92.7	0.087	8.4	–1.2–18.0

NA = not applicable.

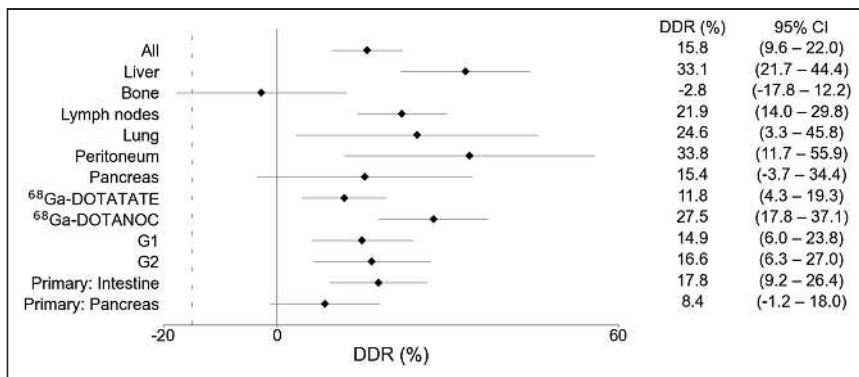


FIGURE 1. Forest plot summarizing mean DDR and 95% CI overall and for different subgroups of lesions and patients. Dashed vertical line represents prespecified boundary (−15%) for noninferiority for lower margin of 95% CI. G1 = grade 1; G2 = grade 2.

Table 2. A full analysis at the organ level is shown in Supplemental Table 1. Organs where most lesions were observed were bone (2,012 lesions in 50 patients), followed by liver (1,739 lesions in 54 patients), lymph nodes (602 lesions in 63 patients), peritoneum (275 lesions in 28 patients), and lung (195 lesions in 18 patients). The mean DR for these sites was significantly higher with ¹⁸F-AIF-OC than with ⁶⁸Ga-DOTATATE/NOC, with mean DDRs well above zero, except for bone, where the DR with both tracers was similar (79.8% vs. 77.0%; mean DDR, −2.8%; 95% CI, −17.8 to 12.2).

Both within the ⁶⁸Ga-DOTATATE and within the ⁶⁸Ga-DOTA-NOC subgroups, the mean DR with ¹⁸F-AIF-OC was significantly higher than with ⁶⁸Ga-DOTATATE/NOC (Table 3). The mean DDR for the ⁶⁸Ga-DOTATATE subgroup was 11.8% (95% CI, 4.3–19.3) versus 27.5% (95% CI, 17.8–37.1) for the ⁶⁸Ga-DOTANOC subgroup. The detailed analysis is shown in Supplemental Tables 2 and 3.

Subgroup analysis according to tumor grade showed a similar mean DDR for grade 1 and grade 2 tumors (14.9% [95% CI, 6.0–23.8] vs. 16.6 [95% CI, 6.3–27.0], respectively; Table 3). The mean DDR for the grade 3 subgroup was 35.4%. However, because this group contained only 2 patients, no statistics could be applied. No significant correlation was observed between Ki-67 proliferation index and DDR (Spearman correlation coefficient [ρ] = 0.075, P = 0.54; Supplemental Fig. 3).

Finally, the mean DR for patients with a NET from intestinal origin was significantly higher with ¹⁸F-AIF-OC than with ⁶⁸Ga-DOTATATE/NOC (mean DDR, 17.8%; 95% CI, 9.2–26.4), whereas no significant differences were observed for patients with a pancreatic NET (Table 3).

The forest plot in Figure 1 summarizes the results of the DR analysis. Head-to-head comparisons with examples of missed lesions are shown in Figures 2 and 3.

Lesion Uptake

Mean SUV_{max} at the patient level showed a trend toward lower values with ¹⁸F-AIF-OC than with ⁶⁸Ga-DOTATATE/NOC, but this was not statistically significant (20.0 vs. 22.4; P = 0.067). Conversely, TBR was significantly higher with ¹⁸F-AIF-OC (31.7 vs. 25.1; P = 0.001; Table 4; Fig. 4). Of note, background uptake was significantly lower with ¹⁸F-AIF-OC than with ⁶⁸Ga-DOTATATE/NOC (4.2 ± 1.7 vs. 6.3 ± 2.5 [$P < 10^{-7}$], 0.7 ± 0.2 vs. 1.2 ± 0.5 [$P < 10^{-7}$], and 0.4 ± 0.1 vs. 0.6 ± 0.2 [$P < 10^{-7}$]) for healthy liver, bone, and muscle, respectively; Supplemental Table 4). At the lesion level,

SUV_{max} was significantly lower and TBR was significantly higher with ¹⁸F-AIF-OC than with ⁶⁸Ga-DOTATATE/NOC (mean difference, −2.21 [95% CI, −4.28 to −0.15; P = 0.036] and 8.47 [95% CI, 3.46–13.49; P = 0.001] for SUV_{max} and TBR, respectively). Similar results were observed for a subset of a maximum of the 20 hottest lesions per patient and 5 hottest lesions per organ (Table 4). Of note, considerable variation in lesion uptake was also observed within the same patient, with a higher SUV_{max} with ¹⁸F-AIF-OC in some lesions and a higher SUV_{max} with ⁶⁸Ga-DOTATATE/NOC in others. Lesion uptake (at the patient level) per organ is shown in Table 4 and Supplemental Table 5. For the 3 most common metastatic sites (liver, bone, and lymph nodes), TBR was

significantly higher with ¹⁸F-AIF-OC than with ⁶⁸Ga-DOTATATE/NOC. However, only bone lesions showed a significantly lower SUV_{max} with ¹⁸F-AIF-OC. Lesion uptake at the patient level for patient subgroups according to routine ⁶⁸Ga-DOTA-SSA tracer, tumor grade, and primary is summarized in Table 5 and (per organ analysis) Supplemental Table 6. Most strikingly, mean SUV_{max} with ⁶⁸Ga-DOTANOC was significantly lower than with ¹⁸F-AIF-OC overall and also for liver, lymph node, and peritoneal lesions. Other subgroup results were in line with results for the whole patient group.

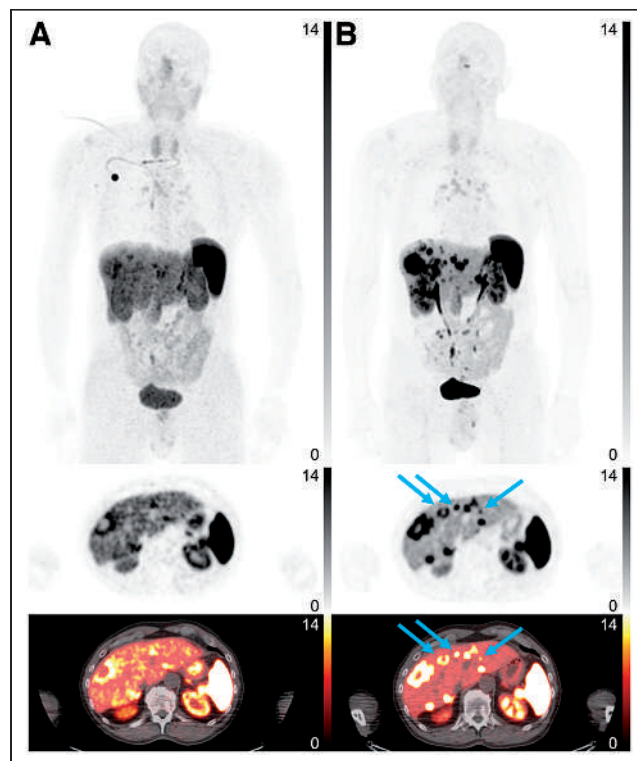


FIGURE 2. ⁶⁸Ga-DOTATATE (A) and ¹⁸F-AIF-OC (B) images (from top to bottom: maximum-intensity projection PET, transversal PET, and fused PET/CT images) of 64-y-old male patient with pancreatic NET and liver, lymph node, and peritoneal metastases. Multiple lesions in all 3 sites were missed by ⁶⁸Ga-DOTATATE. Arrows indicate missed liver lesions. Lookup tables apply to PET images (SUV). Intensity scale bars indicate SUVs.

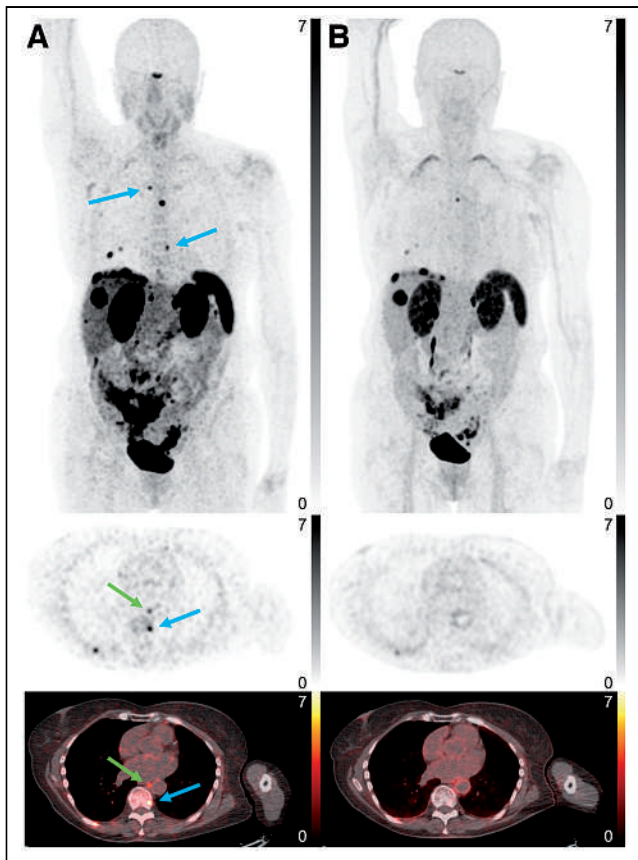


FIGURE 3. ^{68}Ga -DOTATATE (A) and ^{18}F -AIF-OC (B) images (from top to bottom: maximum-intensity projection PET, transversal PET, and fused PET/CT images) of 74-y-old female patient with intestinal NET and bone, liver, lymph node, and peritoneal metastases. Multiple lesions in all 3 sites were missed by ^{18}F -AIF-OC. Blue and green arrows indicate missed bone and lymph node lesions, respectively. Lookup tables apply to PET images (SUV). Intensity scale bars indicate SUVs.

The Bland–Altman plot showed fair agreement between mean SUV_{max} with ^{18}F -AIF-OC and ^{68}Ga -DOTATATE/NOC, with a bias toward an increased SUV_{max} in the ^{68}Ga -DOTATATE

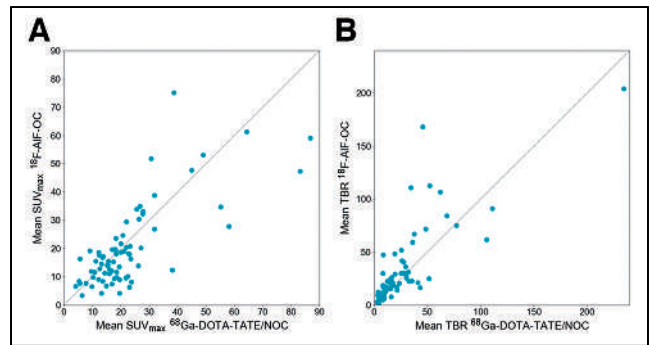


FIGURE 4. Mean SUV_{max} (A) and TBR (B) at patient level with ^{18}F -AIF-OC as function of mean SUV_{max} and TBR with ^{68}Ga -DOTATATE/NOC. Gray line represents unity line.

subgroup and a decreased SUV_{max} in the ^{68}Ga -DOTANOC subgroup compared with ^{18}F -AIF-OC (Supplemental Fig. 4).

DISCUSSION

This prospective trial aimed to demonstrate noninferiority of ^{18}F -AIF-OC compared with ^{68}Ga -DOTA-SSA PET in NET patients. The objective would be met if the lower margin of the 95% CI for the mean DDR were higher than -15% . We observed a mean DDR of 15.8% (95% CI, 9.6% – 22.0%), demonstrating superiority of ^{18}F -AIF-OC compared with ^{68}Ga -DOTATATE/NOC. Per-organ analysis showed that ^{18}F -AIF-OC outperforms ^{68}Ga -DOTATATE/NOC, with DRs of around 90% or higher for most sites and with bone being the most important exception. Overall, lesions missed by ^{18}F -AIF-OC were mainly situated in bone, in line with our previous findings (5). Nevertheless, the diagnostic performance for bone lesions of ^{18}F -AIF-OC was similar to that of ^{68}Ga -DOTATATE/NOC (DR, $\sim 80\%$; mean DDR, -2.8%). Results for the ^{68}Ga -DOTATATE and ^{68}Ga -DOTANOC subgroups were more or less in line with the results for the total patient group, except for bone lesions, for which ^{68}Ga -DOTATATE showed a significantly higher DR than did ^{18}F -AIF-OC whereas ^{68}Ga -DOTANOC had a significantly lower DR. The DDR was higher in the ^{68}Ga -DOTANOC subgroup than in the

TABLE 4
 ^{68}Ga -DOTATATE/NOC Mean SUV_{max} ($\text{SUV}_{\text{max_Ga}}$) and TBR (TBR_{Ga}) and ^{18}F -AIF-OC Mean SUV_{max} ($\text{SUV}_{\text{max_F}}$) and TBR (TBR_{F}) at Patient Level for All Concordant, Quantifiable Lesions ($n = 3,034$) and Different Subsets of Lesions

Organ	$\text{SUV}_{\text{max_Ga}}$	$\text{SUV}_{\text{max_F}}$	P	TBR_{Ga}	TBR_{F}	P
Liver	22.4 ± 11.4	21.5 ± 12.4	0.76	4.8 ± 3.8	6.7 ± 5.2	$<10^{-4}$
Bone	11.4 ± 8.3	8.6 ± 6.3	0.001	10.1 ± 7.3	13.8 ± 9.9	$<10^{-3}$
Lymph nodes	20.9 ± 14.3	19.9 ± 16.9	0.19	36.5 ± 24.2	49.9 ± 40.8	0.001
Lung	24.8 ± 29.5	16.9 ± 17.0	0.088	44.0 ± 61.2	42.7 ± 50.4	0.95
Peritoneum	16.3 ± 11.9	14.9 ± 9.9	0.87	29.2 ± 24.4	33.7 ± 25.6	0.091
Pancreas	51.1 ± 38.6	51.9 ± 45.6	0.94	90.3 ± 65.4	141.1 ± 113.8	0.006
Maximum 20 per patient	27.7 ± 16.9	24.7 ± 16.3	0.036	29.2 ± 33.1	37.6 ± 40.0	0.001
Maximum 5 per organ	28.9 ± 17.9	25.3 ± 16.2	0.032	33.0 ± 33.1	42.3 ± 40.0	0.002
All	22.4 ± 15.6	20.0 ± 14.5	0.067	25.1 ± 32.7	31.7 ± 36.5	0.001

Data are mean \pm SD.

TABLE 5
⁶⁸Ga-DOTATATE/NOC Mean SUV_{max} (SUV_{max_Ga}) and TBR (TBR_{Ga}) and ¹⁸F-AIF-OC Mean SUV_{max} (SUV_{max_F}) and TBR (TBR_F) at Patient Level for Different Subgroups of Patients According to Routine ⁶⁸Ga-DOTA-SSA Tracer, Tumor Grade, and Primary

Subgroup	SUV _{max_Ga}	SUV _{max_F}	P	TBR _{Ga}	TBR _F	P
⁶⁸ Ga-DOTATATE	23.3 ± 16.9	19.0 ± 14.8	0.002	26.6 ± 36.4	31.8 ± 38.9	0.12
⁶⁸ Ga-DOTANOC	19.6 ± 11.2	23.1 ± 13.7	<10 ⁻³	20.7 ± 17.7	31.2 ± 29.2	<10 ⁻³
Grade 1	22.9 ± 16.8	17.9 ± 11.5	0.008	26.7 ± 41.4	27.9 ± 36.1	0.20
Grade 2	22.1 ± 14.5	22.4 ± 17.7	0.90	23.3 ± 22.5	35.8 ± 39.2	0.003
Grade 3	15.2 ± 4.2	19.0 ± 0.6	NA	10.3 ± 9.5	15.3 ± 8.7	NA
Intestine	17.8 ± 6.0	16.3 ± 9.4	0.18	17.8 ± 13.0	22.6 ± 20.2	0.008
Pancreas	28.0 ± 16.7	26.9 ± 19.9	0.40	26.3 ± 26.6	40.7 ± 43.9	0.043

Data are mean ± SD.

⁶⁸Ga-DOTATATE subgroup, implying that ¹⁸F-AIF-OC outperforms ⁶⁸Ga-DOTANOC even more than ⁶⁸Ga-DOTATATE. The grade 1 and grade 2 subgroups had a similar DDR (insufficient data for grade 3 tumors), and no associations between the Ki-67 proliferation index and DDR were observed. The DR analysis for patients with a NET from intestinal origin was similar to that for the whole patient cohort, whereas for patients with a pancreatic NET, ¹⁸F-AIF-OC and ⁶⁸Ga-DOTATATE/NOC performed equally well.

Lesion uptake in terms of TBR, which is the most important parameter for lesion detectability, was significantly higher for ¹⁸F-AIF-OC than for ⁶⁸Ga-DOTATATE/NOC, both at the patient level and at the lesion level, as well as for most organs, including bone. This is reflected in the overall higher DRs for ¹⁸F-AIF-OC. Conversely, in comparison with SUV_{max} with ⁶⁸Ga-DOTATATE/NOC, SUV_{max} with ¹⁸F-AIF-OC was either significantly lower (e.g., at the lesion level, for subsets of hottest lesions per patient and for bone lesions) or similar (e.g., at the patient level and for most organs). These results are in line with our previous findings (5) but slightly differ from those of Hou et al. (8) because they observed not only higher TBRs but also a higher SUV_{max} with ¹⁸F-AIF-OC than with ⁶⁸Ga-DOTATATE, although the latter was not statistically significant. Nevertheless, higher TBRs for ¹⁸F-AIF-OC are mainly explained by significantly lower background uptake. In particular, the lower background uptake with ¹⁸F-AIF-OC in the liver significantly improves detection of liver metastases as reflected by the high DDR of 33.1% (95% CI, 21.7%–44.4%), which is consistent with previous observations (5,8). Tracer clearance may partly explain the lower background values for ¹⁸F-AIF-OC, as ¹⁸F-AIF-OC imaging was done at a later time point (2 h after injection) than was ⁶⁸Ga-DOTATATE (45–60 min after injection) or ⁶⁸Ga-DOTANOC (45–60 min after injection) imaging. However, Hou et al. (8) also reported a 1.5 times lower liver background with ¹⁸F-AIF-OC at 60 min after injection than with ⁶⁸Ga-DOTATATE at 50 min after injection, as well as significantly lower bone background.

Lesion uptake for the ⁶⁸Ga-DOTATATE subgroup was similar to that for the whole patient cohort. Conversely, in the ⁶⁸Ga-DOTANOC subgroup the mean SUV_{max} was significantly lower with ⁶⁸Ga-DOTANOC than with ¹⁸F-AIF-OC, in line with findings from a head-to-head comparison between ⁶⁸Ga-DOTANOC

and ⁶⁸Ga-DOTATATE, where a significantly lower lesion SUV_{max} was reported with ⁶⁸Ga-DOTANOC (9). This can most likely be explained by differences in the SSTR affinity profile, because ⁶⁸Ga-DOTATATE has an almost 10-fold higher affinity for SSTR2, which is the SSTR subtype that is most frequently expressed in NETs, than does ⁶⁸Ga-DOTANOC (9–11).

In accordance with Hou et al. (8), we observed considerable variability in lesion uptake both between and within patients. Differences in SSTR affinity profile between ¹⁸F-AIF-OC and ⁶⁸Ga-DOTATATE/NOC (to our knowledge, the exact affinity profile for ¹⁸F-AIF-OC is still unknown) in combination with NET heterogeneity may lie at the basis of this finding. Of note, this variability has also been reported in a head-to-head comparison between ⁶⁸Ga-DOTATATE and ⁶⁸Ga-DOTANOC (12). In particular, the Bland–Altman plot of mean differences in mean SUV_{max} with ⁶⁸Ga-DOTATATE and ⁶⁸Ga-DOTANOC showed a similar range between the limits of agreement, as we observed for mean SUV_{max} with ¹⁸F-AIF-OC and ⁶⁸Ga-DOTATATE (12). As ⁶⁸Ga-DOTATATE and ⁶⁸Ga-DOTANOC are considered equivalent in clinical practice, we believe that the uptake variability for ¹⁸F-AIF-OC will also be of limited relevance for implementation in routine practice. Furthermore, especially in cases of disseminated disease, it is likely that ¹⁸F-AIF-OC and ⁶⁸Ga-DOTATATE/NOC could be used interchangeably without clinical impact. A population that might benefit from ¹⁸F-AIF-OC is patients with confined liver disease in whom liver-directed therapies are considered.

The most important limitation of this trial is the lack of histologic confirmation of all detected lesions; such confirmation was not possible for ethical and practical reasons. Therefore, we did not have a perfect reference for evaluation of diagnostic performance because some lesions may have been false-positive. However, false-positive lesions are considered rare, because in most cases, additional lesions with 1 tracer compared with the other were observed in organs already known to be metastatically involved. Furthermore, in some cases, additional lesions observed with ¹⁸F-AIF-OC in previously unknown disease sites were later confirmed on ⁶⁸Ga-DOTATATE/NOC follow-up imaging (Supplemental Fig. 5). Second, for practical reasons, it was not possible to organize the study scan within a day of the routine scan. Although the interval between scans was kept to a minimum, in about 20% of patients the interval was more than 15 d (≤32 d).

However, as most patients had stable disease, especially those with a longer time between scans, the influence of the scan interval on the results of the trial is deemed negligible. Third, the time between long-acting SSA intake and the scan was not standardized. However, a recent prospective study reported no significant changes in tumor uptake depending on the time since last SSA intake (13). Fourth, in 3 patients, a therapeutic change occurred between the 2 scans. Because the same number of, or more, lesions were observed on the second scan, this will have no significant impact on the results of the study.

Finally, it is important to note the differences in imaging parameters, for example, the increased administered activity and time between tracer administration and imaging with ^{18}F -AIF-OC compared with ^{68}Ga -DOTATATE/NOC, because these most likely benefit the diagnostic performance of ^{18}F -AIF-OC. However, these are examples of the advantages of ^{18}F -labeled tracers over ^{68}Ga -labeled tracers that should be exploited, because the ultimate aim is to provide an alternative tracer for clinical practice with beneficial manufacturing properties and increased cost-effectiveness compared with the current gold standard. Of note, the effective dose per injected activity is similar for ^{18}F -AIF-OC and ^{68}Ga -DOTA-SSAs (22.4 vs. 21 $\mu\text{Sv}/\text{MBq}$, respectively) (3,5). Future trials may focus on identifying the optimal activity in combination with PET acquisition time for ^{18}F -AIF-OC.

CONCLUSION

^{18}F -AIF-OC demonstrated an excellent diagnostic performance, meeting our prespecified criterion for noninferiority, and showed superiority compared with ^{68}Ga -DOTATATE/NOC in NET patients. This validates ^{18}F -AIF-OC as an option for clinical practice SSTR PET.

DISCLOSURE

This research was funded by the project from Kom op tegen Kanker: "PET/MRI of the Norepinephrine Transporter and Somatostatin Receptor in Neural Crest and Neuroendocrine Tumors for Better Radionuclide Therapy Selection." Christophe M. Deroose is a senior clinical investigator at Research Foundation-Flanders (FWO). No other potential conflict of interest relevant to this article was reported.

ACKNOWLEDGMENTS

We thank Prof. Kristof Baete, Wies Deckers, and Stijn De Schep- per of the medical physics team of UZ Leuven and UZ Antwerp; Kwinten Porters and Jef Van Loock; and the PET radiopharmacy team of UZ Leuven for their skilled contributions.

KEY POINTS

QUESTION: Is the diagnostic performance of ^{18}F -AIF-OC PET equivalent or superior to the current gold standard, ^{68}Ga -DOTA-SSA PET, in NET patients?

PERTINENT FINDINGS: In this prospective, multicenter study in 75 NET patients, a randomized, masked consensus read was performed to count tumor lesions on ^{18}F -AIF-OC and ^{68}Ga -DOTATATE/NOC PET/CT scans of each patient. The mean DDR between ^{18}F -AIF-OC and ^{68}Ga -DOTATATE/NOC was 15.8% (95% CI, 9.6%–22.0%), meeting the primary noninferiority objective of the trial and even demonstrating superiority of ^{18}F -AIF-OC PET.

IMPLICATIONS FOR PATIENT CARE: ^{18}F -AIF-OC is a validated alternative for clinical practice SSTR PET. These results could facilitate widespread implementation of this tracer and increase accessibility for patients.

REFERENCES

1. Bozkurt MF, Virgolini I, Balogova S, et al. Guideline for PET/CT imaging of neuroendocrine neoplasms with ^{68}Ga -DOTA-conjugated somatostatin receptor targeting peptides and ^{18}F -DOPA. *Eur J Nucl Med Mol Imaging*. 2017;44:1588–1601.
2. Hope TA, Bergsland EK, Bozkurt MF, et al. Appropriate use criteria for somatostatin receptor PET imaging in neuroendocrine tumors. *J Nucl Med*. 2018;59:66–74.
3. Pauwels E, Cleeren F, Bormans G, Deroose CM. Somatostatin receptor PET ligands: the next generation for clinical practice. *Am J Nucl Med Mol Imaging*. 2018;8:311–331.
4. Long T, Yang N, Zhou M, et al. Clinical application of ^{18}F -AIF-NOTA-octreotide PET/CT in combination with ^{18}F -FDG PET/CT for imaging neuroendocrine neoplasms. *Clin Nucl Med*. 2019;44:452–458.
5. Pauwels E, Cleeren F, Tshibangu T, et al. [^{18}F]AIF-NOTA-octreotide PET imaging: biodistribution, dosimetry and first comparison with [^{68}Ga]Ga-DOTATATE in neuroendocrine tumour patients. *Eur J Nucl Med Mol Imaging*. 2020;47:3033–3046.
6. Laverman P, McBride WJ, Sharkey RM, et al. A novel facile method of labeling octreotide with ^{18}F -fluorine. *J Nucl Med*. 2010;51:454–461.
7. Tshibangu T, Cawthorne C, Serdons K, et al. Automated GMP compliant production of [^{18}F]AIF-NOTA-octreotide. *EJNMMI Radiopharm Chem*. 2020;5:4.
8. Hou J, Long T, He Z, et al. Evaluation of ^{18}F -AIF-NOTA-octreotide for imaging neuroendocrine neoplasms: comparison with ^{68}Ga -DOTATATE PET/CT. *EJNMMI Res*. 2021;11:55.
9. Kabasakal L, Demirci E, Ocak M, et al. Comparison of ^{68}Ga -DOTATATE and ^{68}Ga -DOTANOC PET/CT imaging in the same patient group with neuroendocrine tumours. *Eur J Nucl Med Mol Imaging*. 2012;39:1271–1277.
10. Reubi JC, Schar JC, Waser B, et al. Affinity profiles for human somatostatin receptor subtypes SST1–SST5 of somatostatin radiotracers selected for scintigraphic and radiotherapeutic use. *Eur J Nucl Med*. 2000;27:273–282.
11. Wild D, Macke HR, Waser B, et al. ^{68}Ga -DOTANOC: a first compound for PET imaging with high affinity for somatostatin receptor subtypes 2 and 5. *Eur J Nucl Med Mol Imaging*. 2005;32:724.
12. Poeppel TD, Binse I, Petersehn S, et al. ^{68}Ga -DOTATOC versus ^{68}Ga -DOTATATE PET/CT in functional imaging of neuroendocrine tumors. *J Nucl Med*. 2011;52:1864–1870.
13. Gálne A, Almquist H, Almquist M, et al. A prospective observational study to evaluate the effects of long-acting somatostatin analogs on ^{68}Ga -DOTATATE uptake in patients with neuroendocrine tumors. *J Nucl Med*. 2019;60:1717–1723.

Preclinical Evaluation of ^{68}Ga - and ^{177}Lu -Labeled Integrin $\alpha_v\beta_6$ -Targeting Radiotheranostic Peptides

Tanushree Ganguly¹, Nadine Bauer², Ryan A. Davis¹, Cameron C. Foster³, Rebecca E. Harris², Sven H. Hausner², Emilie Roncali^{1,3}, Sarah Y. Tang², and Julie L. Sutcliffe^{1,2,4}

¹Department of Biomedical Engineering, University of California Davis, Davis, California; ²Division of Hematology/Oncology, Department of Internal Medicine, University of California Davis, Sacramento, California; ³Division of Nuclear Medicine, Department of Radiology, University of California Davis, Sacramento, California; and ⁴Center for Molecular and Genomic Imaging, University of California Davis, Davis, California

The integrin $\alpha_v\beta_6$, an epithelium-specific cell surface receptor, is overexpressed on numerous malignancies, including the highly lethal pancreatic ductal adenocarcinomas. Here, we developed and tested a novel $\alpha_v\beta_6$ -targeting peptide, DOTA-5G (**1**) radiolabeled with ^{68}Ga , for PET/CT imaging and ^{177}Lu for treatment. With the goal to develop a radiotheranostic, further modifications were made for increased circulation time, renal recycling, and tumor uptake, yielding DOTA-albumin-binding moiety-5G (**2**). **Methods:** Peptides **1** and **2** were synthesized on solid phase, and their affinity for $\alpha_v\beta_6$ was assessed by enzyme-linked immunosorbent assay. The peptides were radiolabeled with ^{68}Ga and ^{177}Lu . In vitro cell binding, internalization, and efflux of ^{68}Ga -**1** and ^{177}Lu -**2** were evaluated in $\alpha_v\beta_6$ -positive BxPC-3 human pancreatic cancer cells. PET/CT imaging of ^{68}Ga -**1** and ^{68}Ga -**2** was performed on female nu/nu mice bearing subcutaneous BxPC-3 tumors. Biodistribution was performed for ^{68}Ga -**1** (1 and 2 h after injection), ^{68}Ga -**2** (2 and 4 h after injection), and ^{177}Lu -**1** and ^{177}Lu -**2** (1, 24, 48, and 72 h after injection). The ^{177}Lu -**2** biodistribution data were extrapolated for human dosimetry data estimates using OLINDA/EXM 1.1. Therapeutic efficacy of ^{177}Lu -**2** was evaluated in mice bearing BxPC-3 tumors. **Results:** Peptides **1** and **2** demonstrated high affinity (<55 nM) for $\alpha_v\beta_6$ by enzyme-linked immunosorbent assay. ^{68}Ga -**1**, ^{68}Ga -**2**, ^{177}Lu -**1**, and ^{177}Lu -**2** were synthesized in high radiochemical purity. Rapid in vitro binding and internalization of ^{68}Ga -**1** and ^{177}Lu -**2** were observed in BxPC-3 cells. PET/CT imaging and biodistribution studies demonstrated uptake in BxPC-3 tumors. Introduction of the albumin-binding moiety in ^{177}Lu -**2** resulted in a 5-fold increase in tumor uptake and retention over time. Based on the extended dosimetry data, the dose-limiting organ for ^{177}Lu -**2** is the kidney. Treatment with ^{177}Lu -**2** prolonged median survival by 1.5- to 2-fold versus controls. **Conclusion:** ^{68}Ga -**1** and ^{177}Lu -**2** demonstrated high affinity for the integrin $\alpha_v\beta_6$ both in vitro and in vivo, were rapidly internalized into BxPC-3 cells, and were stable in mouse and human serum. Both radiotracers showed favorable pharmacokinetics in preclinical studies, with predominantly renal excretion and good tumor-to-normal-tissue ratios. Favorable human dosimetry data suggest the potential of ^{177}Lu -**2** as a treatment for pancreatic ductal adenocarcinoma.

Key Words: integrin $\alpha_v\beta_6$; ^{68}Ga ; ^{177}Lu ; theranostics; albumin-binding moiety

J Nucl Med 2023; 64:639–644

DOI: 10.2967/jnumed.122.264749

Received Aug. 5, 2022; revision accepted Sep. 28, 2022.
For correspondence or reprints, contact Julie L. Sutcliffe (jsutcliffe@ucdavis.edu).

Published online Oct. 7, 2022.

COPYRIGHT © 2023 by the Society of Nuclear Medicine and Molecular Imaging.

Despite exhaustive testing and some encouraging advances in first- and second-line treatments, pancreatic ductal adenocarcinoma (PDAC) remains the fourth leading cause of cancer-related deaths, with a 5-y survival below 10% (1,2). This dire reality is also in part due to diagnosis at an advanced stage of the disease and the poor reliability of current standard imaging approaches. Therefore, there clearly remains an urgent unmet clinical need for more effective molecularly targeted diagnostics and therapeutics.

The heterodimeric transmembrane receptor integrin $\alpha_v\beta_6$ has been identified as a potential molecular target; it is an epithelium-specific cell surface receptor that is undetectable in healthy adult epithelium but is significantly upregulated in a wide range of epithelium-derived cancers, including PDAC (3–10). In fact, $\alpha_v\beta_6$ was initially identified in PDAC with nearly uniform high expression among patient samples screened; moreover, metastatic lesions demonstrate further highly upregulated expression of $\alpha_v\beta_6$ when compared with the primary tumor, and $\alpha_v\beta_6$ is undetectable in normal pancreas (11). These traits further underscore the potential of $\alpha_v\beta_6$ as an attractive target for both early detection and targeted delivery of a therapeutic payload in PDAC.

Radiotheranostics combines molecular imaging with targeted radionuclide therapy, often using the same targeting ligand, and has shown efficacy in several cancers (12,13). Over the last few years, we have seen an exponential growth in the development and acceptance of radiotheranostics for applications in oncology. For example, ^{68}Ga -DOTATATE for imaging of neuroendocrine tumors and ^{177}Lu -DOTATATE for peptide receptor radionuclide therapy were the first radiotheranostic peptides to be approved by the Food and Drug Administration, in 2018 (14). More recently, ^{18}F -DCFPyL and ^{68}Ga -PSMA-11 gained approval for imaging, as did ^{177}Lu -PSMA-617 for treatment of prostate-specific membrane antigen-positive metastatic castration-resistant prostate cancer (15).

Several groups, including our own, have developed molecular imaging agents to target the integrin $\alpha_v\beta_6$, and several promising agents have advanced to clinical trials for imaging cancer and fibrosis (16–20). Building on over a decade of work by the Sutcliffe laboratory to develop $\alpha_v\beta_6$ -targeted molecular imaging agents (17,21,22), we now propose to address the clear unmet need for new therapies for PDAC using a radiotheranostic strategy. We present a novel molecularly targeted radiotheranostic approach via the integrin $\alpha_v\beta_6$ for peptide receptor radionuclide therapy. DOTA-5G (**1**) was designed to selectively target the integrin $\alpha_v\beta_6$; in addition, with the goal to increase blood residence time, tumor uptake, and renal recycling, an albumin-binding moiety (ABM) was incorporated in

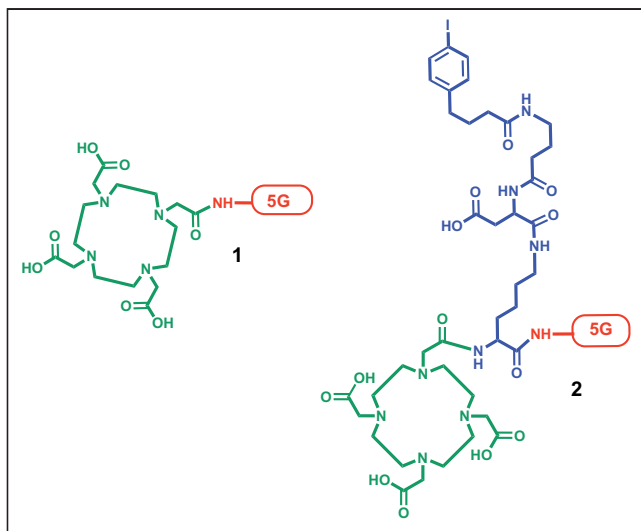


FIGURE 1. Chemical structures of **1** and **2**. The peptide is indicated in red, DOTA chelator in green, and ABM in blue.

the peptide to yield DOTA-ABM-5G (**2**) (Fig. 1). The peptides were synthesized on solid phase, labeled with ^{68}Ga (half-life, 68 min; E_{β^+} [max], 900 keV [23%]) for imaging and ^{177}Lu (half-life, 6.7 d; E_{β^-} [max], 490 keV; E_{γ} , 208 keV [11%]) for therapy, and evaluated in vitro (for cell binding, internalization, and efflux) in $\alpha_v\beta_6$ -expressing BxPC-3 human pancreatic cancer cells. Albumin binding and stability in mouse and human serum were determined. In vivo PET/CT imaging and biodistribution studies were performed on mice bearing BxPC-3 tumors xenografts, and $\alpha_v\beta_6$ -specific targeting was confirmed by blocking studies. Human dosimetry was estimated from the extended biodistribution data, and therapeutic efficacy was evaluated in mice bearing BxPC-3 tumors.

MATERIALS AND METHODS

Chemistry and Radiochemistry

Peptide synthesis on solid phase (23) and radiolabeling and formulation of ^{68}Ga - and ^{177}Lu -labeled peptides are described in Supplemental Section 2 (supplemental materials are available at <http://jnm.snmjournals.org>).

In Vitro Experiments

Enzyme-linked immunosorbent assays (ELISA) (23,24) and cell binding and internalization, albumin binding (23), and serum stability (25) tests followed previously published procedures as described in Supplemental Section 3.

In Vivo Imaging, Biodistribution, and Targeted Radionuclide Therapy

All animal studies were performed according to procedures approved by the University of California Davis Institutional Animal Care and Use Committee. BxPC-3 cells (5×10^6) were implanted subcutaneously into the left shoulder of 6- to 8-wk-old female nu/nu nude mice (Charles River Laboratories) and allowed to grow for 3 wk (imaging and biodistribution) or approximately 2 wk (therapy).

For imaging, the radiotracer (^{68}Ga -**1** or ^{68}Ga -**2**, 7.4–9.25 MBq) in phosphate-buffered saline (PBS) solution (150 μL , pH 7.2) was injected into the tail vein of mice ($n = 3/\text{time point}/\text{radiotracer}$) anesthetized with 3% isoflurane in medical-grade oxygen. After conscious uptake periods of 1 and 2 h, the animals were anesthetized and imaged 2 at a time, side by side in a feet-first prone position as previously described (26).

For biodistribution, the radiotracer (3–3.7 MBq in 100 μL of PBS) was injected into the tail vein, followed by conscious uptake periods of

1 and 2 h (^{68}Ga -**1**), 2 and 4 h (^{68}Ga -**2**), or 1, 24, 48, and 72 h (^{177}Lu -**1** and ^{177}Lu -**2**). For blocking studies, the respective peptides **1** and **2** (48 mg/kg, 16 mg/mL solution in PBS) were injected 10 min before the radiotracer. At each time point, the mice ($n = 3/\text{time point}/\text{radiotracer}$) were anesthetized and sacrificed, tissues were collected and rinsed with PBS, and the radioactivity was measured with a γ -counter. Radioactivity concentrations were calibrated, decay-corrected, and expressed as percentage injected dose per gram of tissue (%ID/g).

An extended biodistribution study was performed for ^{177}Lu -**2**. In 100 μL of PBS, 3.7–5.55 MBq were injected into the tail vein of male ($n = 4/\text{time point}$) and female ($n = 4/\text{time point}$) mice, followed by conscious uptake periods of 24 h, 48 h, 72 h, 1 wk, and 2 wk. The dosimetry values for ^{177}Lu -**2** were computed using OLINDA/EXM1.1 using a female or male model with organ mass scaling, and effective doses were reported as mSv/MBq.

For the therapeutic efficacy study, mice were randomly chosen and divided into 4 treatment groups: control saline (group 1, $n = 5$), control peptide **2** (group 2, $n = 6$), 74 MBq of ^{177}Lu -**2** (group 3, $n = 10$), and 2×37 MBq of ^{177}Lu -**2** (group 4, $n = 7$). Tumor volumes at the start of the treatment ranged from 14 to 218 mm^3 . Group 2 received 20 μg of peptide **2**, group 3 received a single dose of 74 MBq (20 μg of peptide **2**) on day 14 after tumor implantation (treatment day 0), and group 4 received 1 dose of 37 MBq (10 μg of peptide **2**) on days 14 and 21 after tumor implantation (treatment days 0 and 7). Body weights and tumor volumes were measured the day before treatment and twice a week after treatment throughout the study.

Statistical Analysis

All statistical data are reported as mean \pm SD. Paired, 2-tailed Student t tests were used to evaluate statistical significance, with a P value of less than 0.05 being considered statistically significant.

RESULTS

Synthesis of **1** and **2** and Respective ^{nat}Ga and ^{nat}Lu Analogs

Peptides **1** and **2** were synthesized by solid-phase peptide synthesis and obtained in high purity (>98%) after high-performance liquid chromatography purification, and ^{nat}Ga -**1**, ^{nat}Ga -**2**, ^{nat}Lu -**1**, and ^{nat}Lu -**2** were obtained in at least 98% purity. The analytic data are provided in Supplemental Section 2. ^{nat}Ga -**1**, ^{nat}Ga -**2**, ^{nat}Lu -**1**, and ^{nat}Lu -**2** were used in an ELISA for half-maximal inhibitory concentration determination and as reference standards for high-performance liquid chromatography coinjection to confirm the identity of the ^{68}Ga - and ^{177}Lu -labeled peptides.

Radiochemical Synthesis

^{68}Ga -**1** and ^{68}Ga -**2** were obtained in at least 98% radiochemical purity after semipreparative high-performance liquid chromatography purification. ^{177}Lu -**1** and ^{177}Lu -**2** were obtained in at least 97% radiochemical purity.

Half-Maximal Inhibitory Concentration Determinations

The half-maximal inhibitory concentration of ^{nat}Ga -**1**, ^{nat}Ga -**2**, ^{nat}Lu -**1**, and ^{nat}Lu -**2** for integrin $\alpha_v\beta_6$ determined by ELISA were 33.2 ± 1.5 nM, 37.2 ± 3.5 nM, 50.0 ± 4.4 nM, and 29.0 ± 0.6 nM, respectively. The binding affinities for integrin $\alpha_v\beta_3$ were more than 100 μM for all peptides.

Cell Binding, Internalization, and Efflux

For ^{68}Ga -**1**, $16.1\% \pm 0.3\%$ of total radioactivity bound to the BxPC-3 cells, of which $71.5\% \pm 0.6\%$ internalized into the cells. For ^{177}Lu -**2**, $31.5\% \pm 0.6\%$ bound, of which $72.3\% \pm 1.0\%$ internalized, and minimal efflux was observed for ^{177}Lu -**2** at 1 h ($\sim 20\%$ of internalized radioactivity) (Fig. 2).

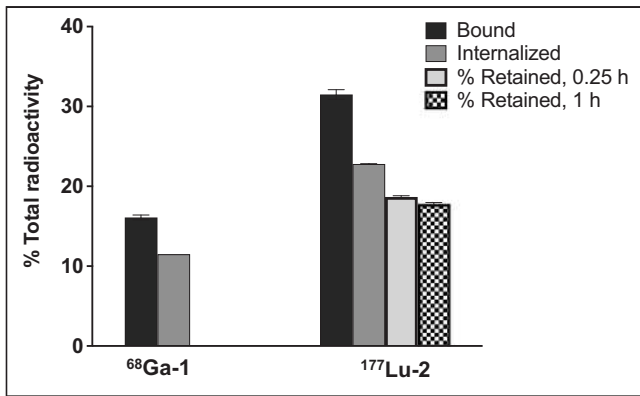


FIGURE 2. Cell binding and internalization of ⁶⁸Ga-1 and ¹⁷⁷Lu-2 at 1 h to BxPC-3 cells at 37°C, and percentage radioactivity of ¹⁷⁷Lu-2 retained in BxPC-3 cells after internalization. Internalization is expressed as fraction of total radioactivity ($n = 3$ /tracer; 1 h of incubation).

Albumin Binding

Albumin binding of ¹⁷⁷Lu-2 was $54.4\% \pm 2.8\%$ and $58.1\% \pm 0.4\%$ for mouse and human serum, respectively, compared with $18.1\% \pm 0.2\%$ and $16.2\% \pm 0.4\%$, respectively, for ¹⁷⁷Lu-1.

Serum Stability

⁶⁸Ga-1 and ⁶⁸Ga-2 were 100% intact at 2 h in both mouse and human serum. At 24 h, ¹⁷⁷Lu-1 and ¹⁷⁷Lu-2 were 72% and 78% intact, respectively, in mouse serum and at least 97% intact (both) in human serum.

In Vivo Imaging and Biodistribution

Imaging and Biodistribution of ⁶⁸Ga-1 and ⁶⁸Ga-2. Imaging and biodistribution were performed in the subcutaneous BxPC-3 tumor model at 1 and 2 h after injection for ⁶⁸Ga-1 and at 2 and 4 h after injection for ⁶⁸Ga-2 (Fig. 3; Supplemental Table 1). Uptake and retention in the tumor were evident at all time points for both ⁶⁸Ga-1 and ⁶⁸Ga-2. However, whereas ⁶⁸Ga-1 cleared from key organs such as the kidneys by 2 h, uptake of ⁶⁸Ga-2 continued to trend upward. Tumor uptake was $2.6\% \pm 0.8\%$ at 1 h and $2.0\% \pm 0.6\%$ at 2 h after injection for ⁶⁸Ga-1 and $9.4\% \pm 1.9\%$ at 2 h and $10.4\% \pm 2.6\%$ at 4 h after injection for ⁶⁸Ga-2.

Renal uptake of ⁶⁸Ga-1 was $23 \pm 3\% \text{ID/g}$ at 1 h, dropping to $14 \pm 4\% \text{ID/g}$ at 2 h ($P = 0.032$). For ⁶⁸Ga-2, renal uptake was $20 \pm 3\% \text{ID/g}$ at 2 h, increasing to $26 \pm 2\% \text{ID/g}$ at 4 h ($P = 0.039$). As depicted in Figure 3D, tumor-to-organ ratios at 2 h after injection for ⁶⁸Ga-1 and ⁶⁸Ga-2, respectively, were 0.75 ± 0.23 and 0.88 ± 0.25 for stomach, 1.6 ± 0.5 and 1.3 ± 0.3 for small intestine, 0.98 ± 0.26 and 1.2 ± 0.3 for large intestine, 20 ± 7 and 6 ± 0.9 for liver, 21 ± 2 and 7.2 ± 2.5 for pancreas, and 22 ± 3.9 and 1.1 ± 0.2 for blood. Collectively, these data suggest that ⁶⁸Ga-1 has the most favorable biodistribution properties for a PDAC imaging agent, clearing rapidly from key organs while being retained by the tumor.

Biodistribution of ¹⁷⁷Lu-1 and ¹⁷⁷Lu-2.

Uptake and retention in the BxPC-3 tumor were at least 4-fold greater for ¹⁷⁷Lu-2 than for ¹⁷⁷Lu-1, with ¹⁷⁷Lu-2 remaining at $5 \pm 0.8\% \text{ID/g}$ at 72 h (Figs. 4 and 5; Supplemental Tables 2 and 3). Both ¹⁷⁷Lu-1 and ¹⁷⁷Lu-2 demonstrated washout from key organs over time, resulting in tumor-to-kidney ratios for ¹⁷⁷Lu-1 of 0.08 ± 0.05 at 1 h and 0.14 ± 0.05 at 72 h; for ¹⁷⁷Lu-2, the ratios were 0.22 ± 0.05 at 1 h and 0.60 ± 0.02 at 72 h (Fig. 5B). For the same time points, tumor-to-stomach ratios were, respectively, 0.31 ± 0.06 and 0.87 ± 0.28 for ¹⁷⁷Lu-1 and 0.50 ± 0.08 and 1.16 ± 0.30 for ¹⁷⁷Lu-2 (Fig. 5C). Likewise, tumor-to-pancreas ratios were 5 ± 3 and 9 ± 1.4 for ¹⁷⁷Lu-1 and 5 ± 0.06 and 16 ± 5 for ¹⁷⁷Lu-2 (Fig. 5D); tumor-to-large intestine ratios were 0.31 ± 0.02 and 1.74 ± 0.39 for ¹⁷⁷Lu-1 and 0.77 ± 0.25 and 1.77 ± 0.26 for ¹⁷⁷Lu-2. Collectively, these data suggest that ¹⁷⁷Lu-2 has the most favorable pharmacokinetics to advance to therapeutic efficacy studies.

Blocking Studies. Preadministration of the respective blocking peptide (1 or 2) 10 min before administration of ⁶⁸Ga-1, ¹⁷⁷Lu-1, or ¹⁷⁷Lu-2 resulted in reduced tumor uptake. Tumor uptake dropped from $2.6 \pm 0.8\% \text{ID/g}$

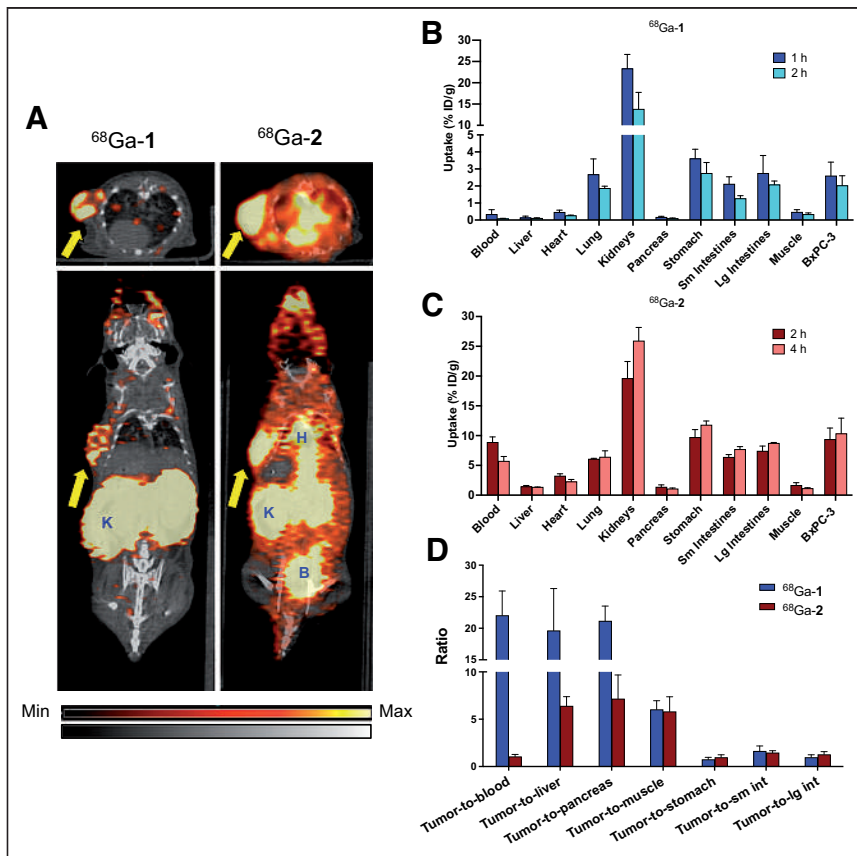


FIGURE 3. (A) Representative transaxial (top) and coronal (bottom) PET/CT cross sections of mice bearing BxPC-3 tumors (arrows) obtained at 2 h after injection. Both images are presented on same scale. Red is PET, and gray is CT. (B–D) Biodistribution showing uptake (%ID/g) of ⁶⁸Ga-1 (B) and ⁶⁸Ga-2 (C) in selected organs and $\alpha_v\beta_6$ -positive BxPC-3 tumors ($n = 3$ /group/time point) and tumor-to-tissue ratios 2 h after injection (D). B = bladder; K = kidney; H = heart; int = intestines; lg = large; sm = small.

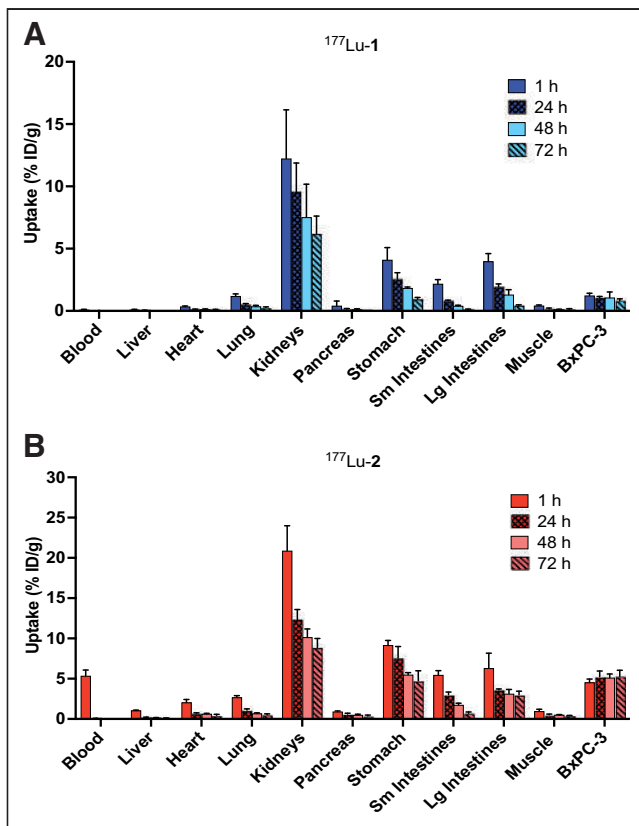


FIGURE 4. Biodistribution showing uptake (%ID/g) of $^{177}\text{Lu-1}$ (A) and $^{177}\text{Lu-2}$ (B) in selected organs and $\alpha_v\beta_6$ -positive BxPC-3 tumors ($n = 3/\text{group/time point}$). Lg = large; sm = small.

(unblocked) to $0.27 \pm 0.02\% \text{ID/g}$ for $^{68}\text{Ga-1}$ (1 h, -86% change); for $^{177}\text{Lu-1}$, tumor uptake dropped from $1.2 \pm 0.2\% \text{ID/g}$ to $0.3 \pm 0.02\% \text{ID/g}$ (1 h, -75% change); and for $^{177}\text{Lu-2}$, tumor uptake dropped from $7.2 \pm 3.0\% \text{ID/g}$ to $4.1\% \text{ID/g}$ (4 h, -42% change; Supplemental Figs. 1–3).

Therapeutic Efficacy

A significant delay in tumor growth was observed in treatment groups 3 (74 MBq $^{177}\text{Lu-2}$) and 4 ($2 \times 37 \text{ MBq } ^{177}\text{Lu-2}$) versus control groups 1 and 2 (Fig. 6A). All mice in groups 1 and 2 had met the endpoint criteria (tumor $\geq 2 \text{ cm}$ in any direction or ulceration) by days 63 and 68 from the start of treatment, respectively. In contrast, the mice in groups 3 and 4 had 30% and 43% survival rates, respectively, at the end of the study (120 d; Fig. 6B). The median survival was 56 d for mice in groups 1 and 2, versus 82 d for group 3 and 113 d for group 4. No treatment-related adverse effects (weight loss or signs of distress) were evident during the course of the study (Supplemental Fig. 4).

Dosimetry

The highest estimated dose, as expected from the imaging and biodistribution data, was to the kidneys. On the basis of the

extrapolated values obtained in OLINDA, the effective dose from $^{177}\text{Lu-2}$ to the kidneys would be 1.31 mSv/MBq and 1.14 mSv/MBq for a woman and man, respectively (Supplemental Tables 4 and 5).

DISCUSSION

There has been increasingly rapid growth in the field of radiotheranostics, fueled in part by the many successful clinical outcomes, significant investments by the pharmaceutical industry, and recent regulatory approvals (27). Numerous novel radiotheranostics for a wide range of clinically relevant targets are now under investigation (28). Here, we describe the development of peptide-based radiotheranostics to target the integrin $\alpha_v\beta_6$, an epithelium-specific receptor that has been identified as a relevant molecular target for both the detection and the treatment of cancer (29). Several $\alpha_v\beta_6$ -targeting imaging agents have demonstrated utility in the clinic for a range of carcinomas, including breast, colon, head and neck, lung, and pancreas (16–19). In view of the functional relevance of the integrin $\alpha_v\beta_6$, it is anticipated to become an important target for future radiotheranostics (30).

Building on over a decade of research and development of $\alpha_v\beta_6$ -targeted peptides for imaging by our group, we designed and report here a radiotheranostic strategy using ^{68}Ga for PET imaging and ^{177}Lu for both treatment and imaging with SPECT. We developed DOTA-5G (1), a peptide with high affinity and selectivity for the integrin $\alpha_v\beta_6$ and, with the goal to increase tumor uptake and reduce renal retention, further incorporated a 4-(*p*-iodophenyl) butyryl-containing ABM—based on prior literature showing favorable pharmacokinetics for targeting ligands such as folates, octreotides, and PSMA-targeting phosphoramidates (31–33)—to yield DOTA-ABM-5G (2). Given the notable presence of the integrin $\alpha_v\beta_6$ in PDAC, we evaluated 1 and 2 in a pancreatic mouse model (11,34,35).

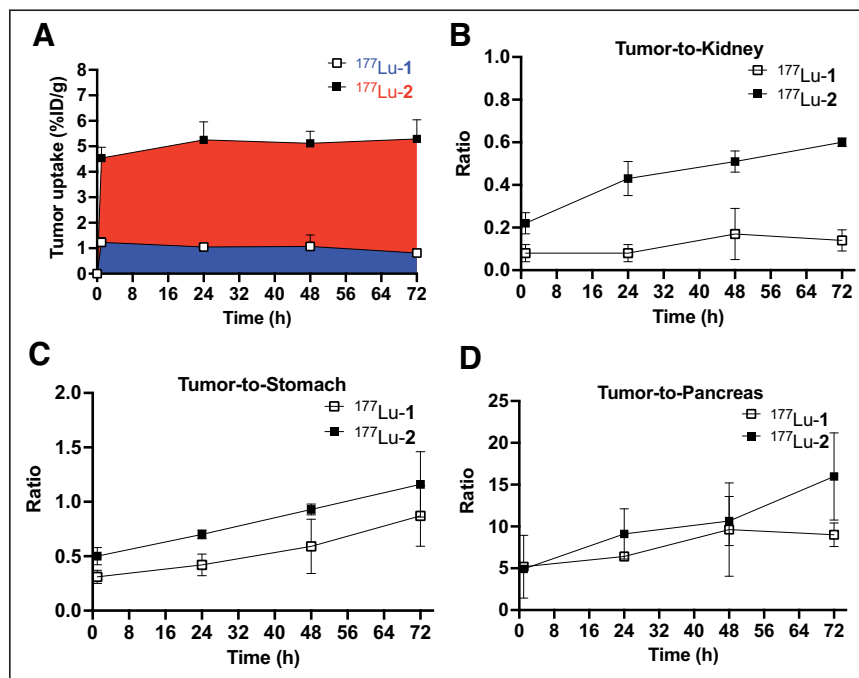


FIGURE 5. Uptake of $^{177}\text{Lu-1}$ and $^{177}\text{Lu-2}$ in BxPC-3 tumor (A) and tumor-to-organ ratios for kidney (B), stomach (C), and pancreas (D) derived from biodistribution data.

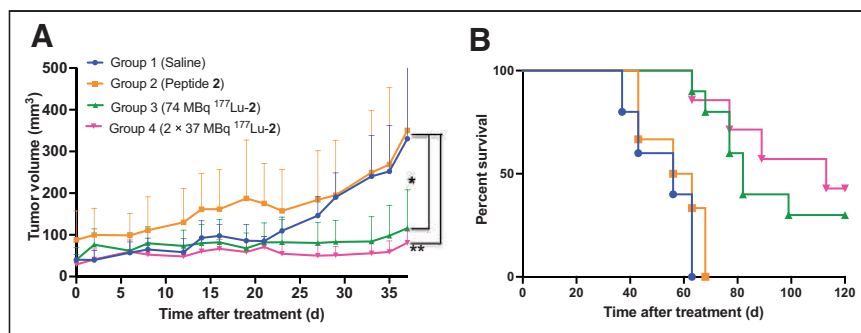


FIGURE 6. Therapeutic efficacy of $^{177}\text{Lu-2}$ in mice bearing $\alpha_v\beta_6$ -positive BxPC-3 tumors, as determined by tumor growth (average tumor volume ≤ 37 d after treatment) (A) and survival data (B). * $P = 0.0077$. ** $P = 0.0064$.

$^{nat}\text{Ga-1}$, $^{nat}\text{Ga-2}$, $^{nat}\text{Lu-1}$, and $^{nat}\text{Lu-2}$ demonstrated high affinity and selectivity for the integrin $\alpha_v\beta_6$, similar to our previously published $\alpha_v\beta_6$ -targeting peptides (23,26). Tumors were clearly detected with $^{68}\text{Ga-1}$ and $^{68}\text{Ga-2}$ by PET (Fig. 3A) and showed uptake similar to other ^{68}Ga -peptides reported in the literature (19,36). Both $^{68}\text{Ga-1}$ and $^{68}\text{Ga-2}$ show predominantly renal excretion, as commonly reported for radiolabeled peptides (37,38). Compared with $^{68}\text{Ga-2}$, $^{68}\text{Ga-1}$ was cleared rapidly from the blood and other nontarget tissues, including healthy pancreas (Fig. 3D), resulting in improved contrast. These data reaffirmed our previous reports that although the inclusion of an ABM into targeting ligands increases circulation and tumor uptake, this might not be desirable for short-lived (diagnostic) radioisotopes such as ^{68}Ga (39) or ^{18}F (23). Overall, $^{68}\text{Ga-1}$ compared favorably to other noteworthy examples, including ^{68}Ga -cycratide (36), ^{68}Ga -DOTA-SFITGv6 (16), and ^{68}Ga -trivehexin (19), and was therefore chosen as the clinical candidate for PET imaging.

In vitro studies showed $\alpha_v\beta_6$ -targeted cell binding and internalization with minimal efflux of the $^{177}\text{Lu-2}$ from cells. $^{177}\text{Lu-2}$ also demonstrated good stability ($>97\%$ at 24 h) in human serum. Compared with $^{177}\text{Lu-1}$, the addition of the ABM expectedly resulted in longer circulation of $^{177}\text{Lu-2}$, which, in combination with the long half-life of 6.7 d for ^{177}Lu , was highly beneficial as demonstrated by the biodistribution studies (Fig. 5). Lu-2 was rapidly taken up by and retained in the tumor over the 72-h window, along with significant washout from all key organs over this time frame. By the 72-h time point, only the kidneys showed higher uptake of $^{177}\text{Lu-2}$ than the tumor; notably, no renal clearing agents were used in this preclinical study. To further mitigate the high kidney activity, other complementary approaches such as coinjection of positively charged amino acids such as lysine and arginine and pretargeting will be explored. Biodistribution data were extrapolated to obtain estimated human dosimetry using OLINDA/EXM1.1, showing the highest dose to be to the kidney—as expected from the imaging and biodistribution data—at 1.31 mSv/MBq (female) and 1.14 mSv/MBq (male). These values are considerably lower than those reported for other ^{177}Lu -compounds currently under investigation in the clinic (e.g., CTT1403, an agent for the treatment of prostate cancer, was reported as 5.18 mSv/MBq (40)). For $^{177}\text{Lu-2}$, the estimated dose would equate to approximately a 1.21-Gy (female) and a 1.05-Gy (male) dose to the kidneys, based on a 925 MBq (25 mCi) starting injected dose for our proposed clinical trial, and is significantly lower than the current 23-Gy threshold.

On the basis of the in vitro and in vivo data, it was hypothesized that significant tumor killing could be achieved from selective

uptake and retention of $^{177}\text{Lu-2}$ in $\alpha_v\beta_6$ -positive cells; therefore, the therapeutic efficacy of $^{177}\text{Lu-2}$ was evaluated in the BxPC-3 tumor xenograft model. Two treatment doses were tested, a high single dose of 74 MBq and a fractionated dose of 2 times 37 MBq, 7 d apart. Both cohorts showed significantly increased survival above the control groups. While all mice in the control groups had reached endpoint criteria by day 68, the mice in the treatment groups had 80%–86% survival rates at that time point and showed 1.5- to 2.0-fold increased median survival times compared with the controls. Importantly, mice in both treatment groups maintained a healthy weight during the study, confirm-

ing no adverse effects from either the single dose (74 MBq) or the fractionated double dose (2×37 MBq) of $^{177}\text{Lu-2}$ (Supplemental Fig. 4). These results were highly encouraging and were contrary to the recently published data by Huynh et al., who reported severe weight loss and death due to kidney toxicity within the first 14 d in mouse cohorts receiving a 37 MBq dose of $^{177}\text{Lu-IBA-DOTA-(PEG28)}_2\text{-A20FMDV2}$ (35).

Overall, the relevance of integrin $\alpha_v\beta_6$ in cancer, the high binding of $^{177}\text{Lu-2}$ to the integrin $\alpha_v\beta_6$, and its excellent stability in human serum, along with the therapeutic efficacy and favorable estimated dosimetry, collectively suggest the utility of $^{177}\text{Lu-2}$ as a therapeutic. $^{177}\text{Lu-2}$ was therefore selected as the treatment candidate for our first-in-humans radiotherapeutics study alongside $^{68}\text{Ga-1}$ as the imaging agent (NCT04665947).

CONCLUSION

$^{68}\text{Ga-1}$ and $^{177}\text{Lu-2}$ demonstrated high affinity (low nM) and selectivity for the integrin $\alpha_v\beta_6$ in both in vitro assays and in vivo mouse models, were rapidly internalized, and were stable in human serum. Both radiotracers showed favorable pharmacokinetics in preclinical studies, with predominantly renal excretion and good tumor-to-organ ratios. Favorable human dosimetry data calculated from the murine biodistribution data for $^{177}\text{Lu-2}$ suggest the potential for this treatment. On the basis of these data, a first-in-humans study in patients with locally advanced or metastatic pancreas cancer is under way.

DISCLOSURE

This work was supported by Stand Up To Cancer and Lustgarten Foundation Pancreatic Cancer Collective (PCC) New Therapies Challenges (SU2C-AACR-PCC-06-18). Sven Hausner is a coinventor of intellectual property related to **1** and **2**. Julie Sutcliffe is founder and chief executive officer, and holds ownership interest (including patents) in, Luminance Biosciences, Inc., and is a coinventor of intellectual property related to **1** and **2**. No other potential conflict of interest relevant to this article was reported.

ACKNOWLEDGMENT

We thank Charles Smith and Sarah Tam of the Center for Molecular and Genomic Imaging at the University of California Davis for their technical support.

KEY POINTS

QUESTION: Can ^{68}Ga - and ^{177}Lu -radiolabeled integrin $\alpha_v\beta_6$ -targeting peptides detect and treat $\alpha_v\beta_6$ -positive cancers?

PERTINENT FINDINGS: ^{68}Ga -radiolabeled integrin $\alpha_v\beta_6$ -targeting peptides could detect $\alpha_v\beta_6$ -positive tumors, and the ^{177}Lu -radiolabeled $\alpha_v\beta_6$ -targeting peptide ^{177}Lu -2 demonstrated therapeutic efficacy in a pancreas cancer mouse model.

IMPLICATIONS FOR PATIENT CARE: This $^{68}\text{Ga}/^{177}\text{Lu}$ -radiolabeled $\alpha_v\beta_6$ -targeting theranostic pair holds significant promise for patients with locally advanced or metastatic pancreas cancer or other $\alpha_v\beta_6$ -positive solid tumors.

REFERENCES

- Siegel RL, Miller KD, Jemal A. Cancer statistics, 2018. *CA Cancer J Clin*. 2018; 68:7–30.
- Thomas JK, Kim MS, Balakrishnan L, et al. Pancreatic cancer database: an integrative resource for pancreatic cancer. *Cancer Biol Ther*. 2014;15:963–967.
- Berghoff AS, Kovanda AK, Melchardt T, et al. $\alpha_v\beta_3$, $\alpha_v\beta_5$ and $\alpha_v\beta_6$ integrins in brain metastases of lung cancer. *Clin Exp Metastasis*. 2014;31:841–851.
- Allen MD, Marshall JF, Jones JL. $\alpha_v\beta_6$ expression in myoepithelial cells: a novel marker for predicting DCIS progression with therapeutic potential. *Cancer Res*. 2014;74:5942–5947.
- Yang GY, Guo S, Dong CY, et al. Integrin $\alpha_v\beta_6$ sustains and promotes tumor invasive growth in colon cancer progression. *World J Gastroenterol*. 2015;21:7457–7467.
- Niu J, Li Z. The roles of integrin $\alpha_v\beta_6$ in cancer. *Cancer Lett*. 2017;403:128–137.
- Peng C, Zou X, Xia W, et al. Integrin $\alpha_v\beta_6$ plays a bi-directional regulation role between colon cancer cells and cancer-associated fibroblasts. *Biosci Rep*. 2018;38: BSR20180243.
- Cantor DI, Cheruku HR, Nice EC, Baker MS. Integrin $\alpha_v\beta_6$ sets the stage for colorectal cancer metastasis. *Cancer Metastasis Rev*. 2015;34:715–734.
- Ahmed N, Pansino F, Clyde R, et al. Overexpression of $\alpha_v\beta_6$ integrin in serous epithelial ovarian cancer regulates extracellular matrix degradation via the plasminogen activation cascade. *Carcinogenesis*. 2002;23:237–244.
- Kawashima A, Tsugawa S, Boku A, et al. Expression of α_v integrin family in gastric carcinomas: increased $\alpha_v\beta_6$ is associated with lymph node metastasis. *Pathol Res Pract*. 2003;199:57–64.
- Reader CS, Vallath S, Steele CW, et al. The integrin $\alpha_v\beta_6$ drives pancreatic cancer through diverse mechanisms and represents an effective target for therapy. *J Pathol*. 2019;249:332–342.
- Herrmann K, Schwaiger M, Lewis JS, et al. Radiotheranostics: a roadmap for future development. *Lancet Oncol*. 2020;21:e146–e156.
- Jadvar H, Chen X, Cai W, Mahmood U. Radiotheranostics in cancer diagnosis and management. *Radiology*. 2018;286:388–400.
- Maqsood MH, Tameez Ud Din A, Khan AH. Neuroendocrine tumor therapy with lutetium-177: a literature review. *Cureus*. 2019;11:e3986.
- Sun M, Niaz MO, Nelson A, Skafida M, Niaz MJ. Review of ^{177}Lu -PSMA-617 in patients with metastatic castration-resistant prostate cancer. *Cureus*. 2020;12:e8921.
- Flechsigs P, Lindner T, Loktev A, et al. PET/CT imaging of NSCLC with a $\alpha_v\beta_6$ integrin-targeting peptide. *Mol Imaging Biol*. 2019;21:973–983.
- Hausner SH, Bold RJ, Cheuy LY, Chew HK, Daly ME, Davis RA. Preclinical development and first-in-human imaging of the integrin $\alpha_v\beta_6$ with [^{18}F] $\alpha_v\beta_6$ -binding peptide in metastatic carcinoma. *Clin Cancer Res*. 2019;25:1206–1215.
- Nakamoto R, Ferri V, Duan H, et al. Pilot-phase PET/CT study targeting integrin $\alpha_v\beta_6$ in pancreatic cancer patients using the cystine-knot peptide-based ^{18}F -FP-R01-MG-F2. *Eur J Nucl Med Mol Imaging*. 2022;50:184–193.
- Quigley NG, Steiger K, Hoberück S, et al. PET/CT imaging of head-and-neck and pancreatic cancer in humans by targeting the “Cancer Integrin” $\alpha_v\beta_6$ with Ga-68-Trivehexin. *Eur J Nucl Med Mol Imaging*. 2022;49:1136–1147.
- Lukey PT, Coello C, Gunn R, et al. Clinical quantification of the integrin $\alpha_v\beta_6$ by [^{18}F]FB-A20FMDV2 positron emission tomography in healthy and fibrotic human lung (PETAL Study). *Eur J Nucl Med Mol Imaging*. 2020;47:967–979.
- Hausner SH, Bauer N, Hu LY, Knight LM, Sutcliffe JL. The effect of bi-terminal PEGylation of an integrin $\alpha_v\beta_6$ -targeted ^{18}F peptide on pharmacokinetics and tumor uptake. *J Nucl Med*. 2015;56:784–790.
- Hausner SH, Abbey CK, Bold RJ, et al. Targeted in vivo imaging of integrin $\alpha_v\beta_6$ with an improved radiotracer and its relevance in a pancreatic tumor model. *Cancer Res*. 2009;69:5843–5850.
- Hausner SH, Bauer N, Davis RA, Ganguly T, Tang SYC, Sutcliffe JL. The effects of an albumin binding moiety on the targeting and pharmacokinetics of an integrin $\alpha_v\beta_6$ -selective peptide labeled with aluminum [^{18}F]fluoride. *Mol Imaging Biol*. 2020;22:1543–1552.
- Hausner SH, DiCara D, Marik J, Marshall JF, Sutcliffe JL. Use of a peptide derived from foot-and-mouth disease virus for the noninvasive imaging of human cancer: generation and evaluation of 4-[^{18}F]fluorobenzoyl A20FMDV2 for in vivo imaging of integrin $\alpha_v\beta_6$ expression with positron emission tomography. *Cancer Res*. 2007; 67:7833–7840.
- Hausner SH, Bauer N, Sutcliffe JL. In vitro and in vivo evaluation of the effects of aluminum [^{18}F]fluoride radiolabeling on an integrin $\alpha_v\beta_6$ -specific peptide. *Nucl Med Biol*. 2014;41:43–50.
- Ganguly T, Bauer N, Davis RA, Hausner SH, Tang SY, Sutcliffe JL. Evaluation of copper-64-labeled $\alpha_v\beta_6$ -targeting peptides: addition of an albumin binding moiety to improve pharmacokinetics. *Mol Pharm*. 2021;18:4437–4447.
- Bodei L, Herrmann K, Schöder H, Scott AM, Lewis JS. Radiotheranostics in oncology: current challenges and emerging opportunities. *Nat Rev Clin Oncol*. 2022;19:534–550.
- Rangger C, Haubner R. Radiolabelled peptides for positron emission tomography and endoradiotherapy in oncology. *Pharmaceuticals (Basel)*. 2020;13:22.
- Bandyopadhyay A, Raghavan S. Defining the role of integrin $\alpha_v\beta_6$ in cancer. *Curr Drug Targets*. 2009;10:645–652.
- Steiger K, Quigley NG, Groll T, et al. There is a world beyond $\alpha_v\beta_3$ -integrin: multimeric ligands for imaging of the integrin subtypes $\alpha_v\beta_6$, $\alpha_v\beta_8$, $\alpha_v\beta_3$, and $\alpha_5\beta_1$ by positron emission tomography. *EJNMMI Res*. 2021;11:106.
- Rousseau E, Lau J, Zhang Z, et al. Effects of adding an albumin binder chain on [^{177}Lu]Lu-DOTATATE. *Nucl Med Biol*. 2018;66:10–17.
- Lau J, Jacobson O, Niu G, Lin KS. Bench to bedside: albumin binders for improved cancer radioligand therapies. *Bioconjug Chem*. 2019;30:487–502.
- Brandt M, Cardinale J, Giammei C, et al. Mini-review: targeted radiopharmaceuticals incorporating reversible, low molecular weight albumin binders. *Nucl Med Biol*. 2019;70:46–52.
- Tummers WS, Farina-Sarasqueta A, Boonstra MC, et al. Selection of optimal molecular targets for tumor-specific imaging in pancreatic ductal adenocarcinoma. *Oncotarget*. 2017;8:56816–56828.
- Huynh TT, Sreekumar S, Mpoy C, Rogers BE. Therapeutic efficacy of ^{177}Lu -labeled A20FMDV2 peptides targeting $\alpha_v\beta_6$. *Pharmaceuticals (Basel)*. 2022;15:229.
- Feng X, Wang Y, Lu D, et al. Clinical Translation of a ^{68}Ga -labeled integrin $\alpha_v\beta_6$ -targeting cyclic radiotracer for PET imaging of pancreatic cancer. *J Nucl Med*. 2020;61:1461–1467.
- de Jong M, Breeman WA, Bernard BF, et al. [^{177}Lu -DOTA₀Tyr₃] octreotate for somatostatin receptor-targeted radionuclide therapy. *Int J Cancer*. 2001;92:628–633.
- Notni J, Reich D, Maltsev OV, et al. In vivo PET imaging of the cancer integrin $\alpha_v\beta_6$ using ^{68}Ga -labeled cyclic RGD nonapeptides. *J Nucl Med*. 2017;58:671–677.
- Farkas R, Siwowska K, Ametamey SM, Schibli R, van der Meulen NP, Muller C. ^{64}Cu - and ^{68}Ga -based PET imaging of folate receptor-positive tumors: development and evaluation of an albumin-binding NODAGA-folate. *Mol Pharm*. 2016; 13:1979–1987.
- Ling X, Latoche JD, Choy CJ, et al. Preclinical dosimetry, imaging, and targeted radionuclide therapy studies of Lu-177-labeled albumin-binding, PSMA-targeted CTT1403. *Mol Imaging Biol*. 2020;22:274–284.

Myocardial External Efficiency in Asymptomatic Severe Primary Mitral Regurgitation Using ^{11}C -Acetate PET

Jens Sorensen¹, Johannes Bergsten², Tomasz Baron^{2,3}, Lovisa Holm Orndahl², Tanja Kero¹, Tomas Bjerner¹, Eva-Maria Hedin², Hendrik J. Harms¹, Rafael Astudillo⁴, and Frank A. Flachskampf²

¹Division of Nuclear Medicine and PET, Department of Surgical Sciences, Uppsala University, Uppsala, Sweden; ²Division of Cardiology and Clinical Physiology, Department of Medical Sciences, Uppsala University Hospital and Uppsala University, Uppsala, Sweden; ³Uppsala Clinical Research Center, Uppsala University, Uppsala, Sweden; and ⁴Division of Thoracic Surgery, Department of Surgical Sciences, Uppsala University, Uppsala, Sweden

Subjects with asymptomatic moderate-to-severe or severe primary mitral regurgitation are closely observed for signs of progression or symptoms requiring surgical intervention. The role of myocardial metabolic function in progression of mitral regurgitation is poorly understood. We used ^{11}C -acetate PET to noninvasively measure myocardial mechanical external efficiency (MEE), which is the energetic ratio of external cardiac work and left ventricular (LV) oxygen consumption. **Methods:** Forty-seven patients in surveillance with mitral regurgitation and no or minimal symptoms prospectively underwent PET, echocardiography, and cardiac MRI on the same day. PET was used to simultaneously measure cardiac output, LV mass, and oxygen consumption to establish MEE. PET findings were compared between patients and healthy volunteers ($n = 9$). MEE and standard imaging indicators of regurgitation severity, LV volumes, and function were studied as predictors of time to surgical intervention. Patients were followed a median of 3.0 y (interquartile range, 2.0–3.8 y), and the endpoint was reached in 22 subjects (47%). **Results:** MEE in patients reaching the endpoint ($23.8\% \pm 5.0\%$) was lower than in censored patients ($28.5\% \pm 4.5\%$, $P = 0.002$) or healthy volunteers ($30.1\% \pm 4.9\%$, $P = 0.001$). MEE with a cutoff lower than 25.7% was significantly associated with the outcome (hazard ratio, 7.5; 95% CI, 2.7–20.6; $P < 0.0001$) and retained independent significance when compared with standard imaging parameters. **Conclusion:** MEE independently predicted time to progression requiring valve surgery in patients with asymptomatic moderate-to-severe or severe primary mitral regurgitation. The study suggests that inefficient myocardial oxidative metabolism precedes clinically observed progression in mitral regurgitation.

Key Words: myocardial efficiency; mitral regurgitation; cardiovascular MR; PET

J Nucl Med 2023; 64:645–651
DOI: 10.2967/jnumed.122.264945

Primarily mitral valve regurgitation affects close to 2% of the overall population, increasing to 10% among the elderly. Surgical repair or replacement are the treatments of choice (1). Assessment of mitral regurgitation is an important task of cardiac imaging. In clinical routine, this is usually accomplished by integrating echocardiographic findings with the clinical picture (2,3). To determine

the impact of moderate or severe mitral regurgitation on left ventricular (LV) structure and function, the current recommendation is evaluation of LV diameters or volumes and LV ejection fraction (LVEF), with cardiovascular MRI (CMR) being considered the gold standard for such evaluations (4). A novel and theoretically attractive measure of LV performance in valvular heart disease is myocardial mechanical external efficiency (MEE), based on PET. MEE relates the mechanical energetic output of the left ventricle, measured as forward cardiac output times mean arterial blood pressure, to its chemical input from oxidative acetate metabolism, measured by PET (5). MEE decreases in heart failure (6) and in symptomatic primary and secondary mitral regurgitation (7–9), but data are scarce.

Given the increasing prevalence of moderate and severe mitral regurgitation, and the increasing complexity of therapeutic options (valve replacement and surgical and different types of interventional repair, including percutaneous edge-to-edge repair), the need to detect an adverse impact on LV performance early has gained urgency. We therefore set out to evaluate the impact of severe asymptomatic primary mitral regurgitation on MEE, its relation to quantitative measures of mitral regurgitation magnitude and LV remodeling by echocardiography and CMR (the standard imaging techniques in mitral regurgitation), and the role of myocardial metabolic integrity in predicting time to progression mandating surgical intervention.

MATERIALS AND METHODS

In total, 47 asymptomatic or mildly symptomatic patients (class I or II according to New York Heart Association Functional Classification) confirmed by bicycle exercise testing to have severe degenerative and chronic primary mitral regurgitation by echocardiographic criteria (2) were evaluated and included in the study between October 2013 and March 2018 at the Department of Cardiology, Uppsala University Hospital. Patients with other concomitant moderate or severe valve disease, nonsinus rhythm, a history of coronary artery disease, chronic renal disease, symptomatic or severe lung disease, and method-specific contraindications were excluded. All patients underwent ^{11}C -acetate PET, echocardiography, and CMR on the same day. CMR and PET were performed 1 h apart with no intake of food or fluids between scans to avoid hemodynamic alterations. Additionally, a group of healthy volunteers ($n = 9$) underwent same-day ^{11}C -acetate PET and echocardiography. The healthy volunteers had no signs or symptoms of cardiovascular disease or other chronic diseases. The study was approved by the Regional Ethical Review Board at Uppsala University (diarienummer 2012/543), and all subjects provided written informed consent.

Received Sep. 20, 2022; revision accepted Nov. 17, 2022.
For correspondence or reprints, contact Jens Sorensen (jens.sorensen@pet.uu.se).
Published online Jan. 5, 2023.
COPYRIGHT © 2023 by the Society of Nuclear Medicine and Molecular Imaging.

PET

PET/CT scanning was performed with a GE Healthcare Discovery ST16 or DMI20. After a scout CT scan, a low-dose CT scan (120 kV, 20 mAs) was performed. After this, a 27-min list-mode emission scan was performed, starting simultaneously with automated injection of a 5-MBq dose of ^{11}C -acetate per kilogram of body weight as a 5-mL bolus (1 mL s^{-1}) in an antecubital vein, followed by a 30-mL saline flush (2.0 mL s^{-1}). The collected list-mode emission data were used to create a dynamic image series consisting of 29 time frames using all data with 5-s frame lengths during the first minute. PET data were analyzed using software developed in-house (8) with full automation (Fig. 1).

MEE was calculated by a standard formula (incorporating caloric conversion factors) as proposed by Bing et al. in 1949 (10):

$$\text{MEE}(\%) = \frac{\text{MAP} \times \text{forward SV} \times \text{HR} \times 1.33 \times 10^{-4}}{\text{MVO}_2 \times \text{LVM} \times 20},$$

where MAP is mean arterial pressure (mm Hg), SV is stroke volume (mL/beat), HR is heart rate (beats/min), MVO_2 is mean myocardial oxygen uptake (mL/g/min), and LVM is LV mass (g).

The dynamic PET dataset was used to measure forward cardiac output (aortic flow) with an indicator dilution approach, as previously described (8,11). Heart rate and blood pressure were measured non-invasively at the time of PET scanning. Heart rate was used to calculate forward stroke volume from forward cardiac output. The full dynamic dataset was used to obtain the denominator of the MEE equation, mean myocardial oxygen uptake, and LV mass, as previously described (8,12). PET postprocessing was fully automated and produced identical results when iterated. Test-retest results using this

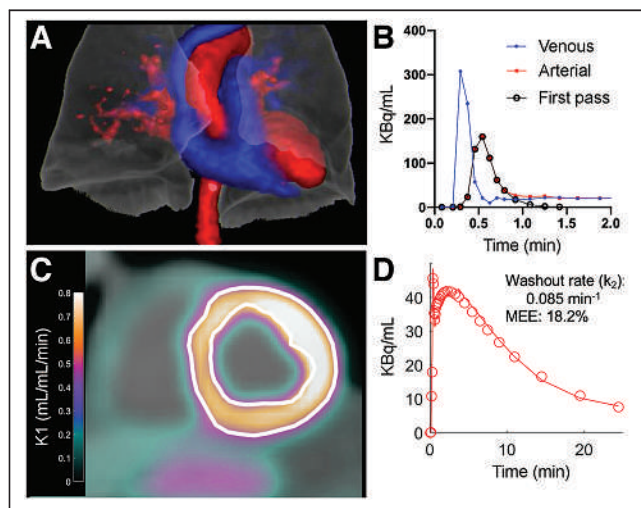


FIGURE 1. Automatic postprocessing of cardiac ^{11}C -acetate PET/CT images. (A) First-pass analysis after intravenous bolus injection of a few micrograms of ^{11}C -acetate. Arterial clusters (red) indicate left atrium, left ventricle, and aorta, whereas venous clusters (blue) indicate vena cava, right atrium, right ventricle, and pulmonary artery. (B) Time-activity curves of clusters for arterial and venous blood, and corresponding isolated first-pass peaks, from which cardiac output and external work (cardiac output \times mean arterial pressure) are calculated as in reference 11. (C) LV mass is measured by delineating LV endo- and epicardial contours by thresholding myocardium on parametric image representing myocardial blood flow (12). (D) Kinetics of radioactive content over time in myocardium is measured from region in C (8). ^{11}C -acetate is trapped intracellularly as ^{11}C -acetyl-coenzyme A and converted to ^{11}C - CO_2 by myocardial mitochondria; washout rate of radioactivity is directly proportional to mean myocardial oxygen uptake. Total LV oxygen consumption is measured as mean myocardial oxygen uptake \times LV mass. External work and total LV mean myocardial oxygen uptake are converted to Joules, the ratio of both yields MEE (8).

technique were previously published, showing a 9% coefficient of variance for MEE in healthy volunteers (13).

Echocardiography

Echocardiography (Vivid-7; GE Vingmed Ultrasound AS) was performed according to current guidelines. All studies were performed by experienced sonographers and interpreted by a single experienced physician.

LV end-diastolic volume, LV end-systolic volume, and LVEF were assessed using the biplane Simpson method. Left atrial volume was calculated by the biplane area length method. LV end-diastolic volume, LV end-systolic volume, and left atrial volume were indexed to the body surface area. Total stroke volume was calculated as the difference between LV end-diastolic and end-systolic volumes. Aortic forward stroke volume was calculated using the Doppler velocity time integral method, using the aortic annulus diameter for LV outflow tract diameter. Mitral regurgitant volume was estimated by both the proximal isovelocity surface area method and the volumetric method (total stroke volume – forward stroke volume). LV global longitudinal strain was measured by strain rate imaging.

Cardiovascular Mitral Regurgitation (CMR)

CMR studies were performed using an Ingenia 3-T whole-body scanner (Philips Healthcare) with an $80\text{ mT}\cdot\text{m}^{-1}$ gradient system. Short- and long-axis cine images were acquired using a steady-state free-precession pulse sequence. LV volumes and mass were manually segmented from short-axis stack images using long-axis images to define the basic slice. End-diastolic endocardial and epicardial contours were propagated, with manual readjustments performed as required. Papillary muscles and adnexal muscle tissue were included in LV mass. Phase-contrast images were acquired perpendicular to the proximal ascending aorta to quantify aortic flow (forward stroke volume), using a semiautomated algorithm. Images were analyzed using commercial software (CVI42; Circle Cardiovascular Imaging). Mitral regurgitant volume was calculated by subtracting aortic forward stroke volume from total LV stroke volume. End-systolic wall stress was estimated using the thick-wall sphere model (14), for which end-systolic cavity pressure was substituted with systolic brachial pressure obtained at PET. A CMR-based MEE ($\text{MEE}_{\text{CMR/PET}}$) was constructed using aortic forward stroke volume and LV mass from CMR with mean arterial pressure, HR, and mean myocardial oxygen uptake from PET.

Outcomes

For outcome analysis, patients were followed regularly at our clinic or affiliated hospitals until March 2021. Time from inclusion to mitral valve intervention was recorded. The decision for mitral valve intervention was at the discretion of a multidisciplinary conference and in most cases (19 of 22) triggered by a combination of echocardiographic progression of mitral regurgitation and heart failure symptoms.

Statistical Methods

Categorical variables are presented as number and frequency. Continuous variables are presented as mean \pm SD or as median and interquartile range. Correlations were assessed using linear regression. The agreement of corresponding parameters from PET and CMR was studied using Bland-Altman plot analyses, and the significance of bias was studied with paired t tests.

PET results were compared between patients and healthy volunteers using t tests. The relation of outcome data toward MEE and standard imaging parameters was analyzed by univariate Cox proportional hazards. Multivariate Cox models were experimentally performed using the best MEE cutoff and significant univariate predictors from echocardiography (end-systolic volume, mitral regurgitant volume, maximum tricuspid jet velocity) or CMR (end-diastolic volume, end-systolic volume, mitral regurgitant volume).

TABLE 1
Baseline Patient Characteristics (*n* = 47)

Characteristic	Data
Age (y)	62 ± 10
Male (<i>n</i>)	43 (91%)
Body surface area (m ²)	2.0 ± 0.2
Body mass index (kg/m ²)	25 ± 3
History of hypertension (<i>n</i>)	28 (60%)
N-terminal pro-brain natriuretic peptide* (ng/L)	
Median	99
Interquartile range	67–183
Medication at inclusion	
Renin-angiotensin-aldosterone system inhibitors	25 (53%)
β-receptor inhibitors	9 (19%)
Calcium channel inhibitors	7 (15%)
Diuretics	4 (9%)
Digoxin	2 (4%)

*Upper reference limit < 230.

P values of less than 0.05 were considered significant. Statistical analyses were performed using JMP, version 16 (SAS Institute Inc.), and Prism, version 9 (GraphPad Software).

RESULTS

Clinical and laboratory findings are shown in Table 1. The mean age of the study population was 59.4 ± 11.0 y, and 91% (*n* = 44)

were men. All patients met echocardiographic criteria for severe degenerative mitral regurgitation at the time of inclusion. The most common valve defect was an isolated or dominant P2-segment prolapse of the posterior leaflet (78%, *n* = 39), followed by Barlow disease (14%, *n* = 7)

A history of hypertension was present in 60% (*n* = 28). Symptoms were categorized as New York Heart Association class I in 89% (*n* = 42) and class II in 11% (*n* = 5) at referral. One patient did not complete the CMR scan because of claustrophobia; this patient did undergo PET. Healthy volunteers (*n* = 9, 54 ± 8 y, 3 men) had no history of cardiac disease and had normal echocardiographic findings.

Myocardial Efficiency

Table 2 shows the results of MEE and associated PET measurements in healthy volunteers, compared with mitral regurgitation patients. There were significant differences in age and sex distribution between the groups. Average MEE in patients (26.3% ± 5.3%) was significantly reduced compared with healthy volunteers (30.1% ± 5.0%, *P* = 0.048; Table 2). MEE in patients who reached an endpoint was lower than in censored patients (mean difference, −4.6%; 95% CI, −7.4 to −1.8; *P* = 0.002), whereas MEE in censored patients was similar to that in healthy volunteers (mean difference, −1.7%; 95% CI, −5.4% to 2.1; *P* = 0.37), as shown in Figure 2.

The results of linear correlation analyses of MEE with parameters from echocardiography and CMR are given in Table 3, showing inverse weak but significant correlations with indices associated with regurgitation, remodeling severity, and LV global longitudinal strain. Notably, MEE did not correlate with LVEF or end-systolic wall stress.

The MEE equation includes forward stroke volume and LV mass, here obtained by PET by an automated image analysis procedure. Both these parameters were also available from the same-day CMR

TABLE 2

¹¹C-Acetate PET/CT Comparison of Healthy Controls and Patients with Asymptomatic Severe Primary Mitral Regurgitation

Characteristic	Healthy controls	Patients	<i>P</i>
<i>N</i>	9	47	
Sex (<i>n</i>)			0.0002
Male	3	43	
Female	6	4	
Age (y)	55 ± 8	62 ± 10	0.03
Heart rate (min ^{−1})	62 ± 10	59 ± 10	0.50
Mean arterial pressure (mm Hg)	97 ± 11	100 ± 13	0.42
PET parameters			
Cardiac index (L/m ²)	2.8 ± 0.4	2.5 ± 0.3	0.054
Forward stroke volume index (mL/m ²)	45 ± 5	43 ± 7	0.29
MVO ₂ (mL/min/100 g)	10 ± 2	10 ± 2	0.50
LV mass index (g/m ²)	55 ± 8	83 ± 16	<0.0001
External work (J/min/m ²)	35 ± 3	34 ± 8	0.32
LV energy consumption (J/min/m ²)	114 ± 22	163 ± 45	<0.0001
MEE (%)	30 ± 5	26 ± 5	0.048

MVO₂ = mean myocardial oxygen uptake.

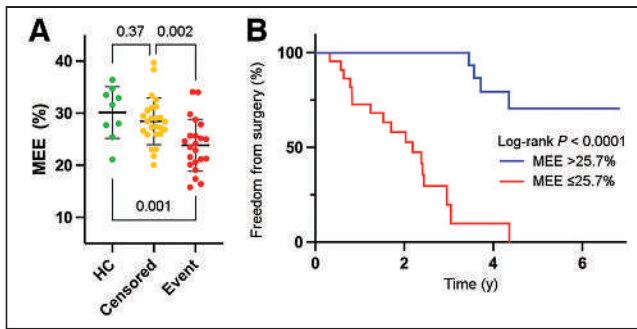


FIGURE 2. (A) Plots of MEE comparing healthy controls (HC) and study patients who were followed without (censored) or with (event) progression mandating surgical intervention. (B) Kaplan–Meier plot showing that patients with MEE below 25.7% at inclusion required valvular surgery significantly sooner than patients with MEE above 25.7%.

in mitral regurgitation patients, and cross-modality correlations and agreement were good (forward stroke volume: $r = 0.88$ [95% CI, 0.79–0.93; $P < 0.0001$] and bias = -1 ± 8 mL [$P = 0.52$]; LV mass: $r = 0.91$ [95% CI, 0.84–0.95; $P < 0.0001$] and bias = 0 ± 15 g [$P = 0.9$]). When CMR-based forward stroke volume and LV mass were inserted into the MEE equation, the correlation remained good ($r = 0.76$; 95% CI, 0.61–0.86; $P < 0.0001$), but MEE values from PET alone were higher (bias = $4.6\% \pm 3.5\%$,

$P < 0.0001$). A residual analysis showed that differences in both forward stroke volume and LV mass contributed significantly to MEE variance. Use of 2 different PET scanners in the study did not impact bias toward CMR-based MEE.

Clinical Outcomes

The median duration of follow-up was 2.7 y (interquartile range, 1.9–3.2 y). The endpoint of surgical intervention was reached in 21 subjects. One subject experienced disease progression and developed characteristic symptoms. Intervention was recommended, but the patient rejected surgery; cardiovascular death occurred 5 y after inclusion, and the time point of recommendation for surgery was used as an endpoint surrogate. Thus, the final number of subjects considered reaching the endpoint in statistical analyses was 22.

The indication for intervention was at the discretion of the treating physicians and followed guidelines available at the time of the study (15). Occurrence of symptoms during surveillance was noted in 17 of 22 (77%) in whom surgery was eventually recommended.

Univariate analysis showed that MEE as a continuous variable predicted outcome; a decrease in MEE by 1% increased the relative hazard of the outcome within the next year by 19% (hazard ratio, 0.84; 95% CI, 0.75–0.93; $P = 0.0004$). ROC analysis provided an MEE cutoff for event prediction at 25.7%, close to the lower limit of normalcy, which was associated with a risk ratio of

TABLE 3
Echocardiography and CMR: Mean Values, Linear Correlations with MEE, and Univariate Cox Proportional-Hazards Analysis

Parameter	Mean \pm SD	Pearson correlation with MEE (r)	Hazard ratio*	P
Echocardiography				
LV end-diastolic diameter (cm)	5.5 \pm 0.5	-0.35 ($P = 0.02$)	2.9 (1.3–6.9)	0.01
LV end-systolic diameter (cm)	3.4 \pm 0.4	-0.24 ($P = 0.10$)	3.0 (1.0–9.6)	0.05
Left atrial volume index (mL/m ²)	35 (interquartile range, 31–52)	-0.53 ($P = 0.0001$)	1.01 (1.00–1.03)	0.08
Maximum tricuspid jet velocity (m/s)	2.6 \pm 0.4	-0.51 ($P = 0.0003$)	6.2 (2.5–15.2)	0.0002
EROA (cm ²)	0.65 \pm 0.39	-0.40 ($P = 0.005$)	2.2 (0.89–4.6)	0.09
Regurgitant volume by PISA (mL)	106 \pm 60	-0.37 ($P = 0.01$)	1.01 (1.00–1.01)	0.07
LV end-diastolic volume index (mL/m ²)	98 \pm 18	-0.51 ($P = 0.0003$)	1.05 (1.02–1.07)	0.0002
LV end-systolic volume index (mL/m ²)	34 \pm 7	-0.35 ($P = 0.01$)	1.13 (1.06–1.21)	0.0001
LVEF (%)	66 \pm 4	-0.13 ($P = 0.35$)	0.97 (0.88–1.07)	0.48
Regurgitant volume volumetric (mL)	51 \pm 31	-0.44 ($P = 0.002$)	1.02 (1.01–1.04)	0.001
LV global longitudinal strain (%)	-21.5 \pm 2.6	0.44 ($P = 0.003$)	0.93 (0.79–1.09)	0.37
Cardiac MRI				
LV end-diastolic volume index (mL/m ²)	122 \pm 26	-0.53 ($P = 0.0002$)	1.03 (1.01–1.04)	0.001
LV end-systolic volume index (mL/m ²)	39 \pm 11	-0.47 ($P = 0.001$)	1.08 (1.04–1.12)	0.0004
Regurgitant volume (mL)	81 \pm 35	-0.47 ($P = 0.001$)	1.02 (1.00–1.03)	0.01
Regurgitant fraction (%)	47 \pm 12	-0.54 ($P = 0.0001$)	1.08 (1.03–1.13)	0.001
LVEF (%)	68 \pm 4	0.09 ($P = 0.57$)	0.91 (0.82–1.02)	0.1
End-systolic wall stress (kPa)	20 \pm 4	-0.10 ($P = 0.53$)	1.08 (0.96–1.22)	0.21
MEE _{CMR/PET} (%)	22 \pm 5	0.76 ($P < 0.0001$)	0.85 (0.77–0.93)	0.0002

*Data in parentheses are 95% CIs.

EROA = effective regurgitant orifice area; PISA = proximal isovelocity surface area.

7.5 (95% CI, 2.7–21; $P < 0.0001$) in a univariate Cox model. A Kaplan–Meyer plot is shown in Figure 2B.

Table 3 shows univariate baseline predictors of outcome by Cox proportional-hazards analysis from echocardiography and CMR. $MEE_{CMR/PET}$ performed similarly to MEE from PET alone, both as a continuous variable (hazard ratio, 0.85; 95% CI, 0.77–0.93) and as a binary cutoff, established as an $MEE_{CMR/PET}$ of less than 22.2% (hazard ratio, 5.9; 95% CI, 2.0–17.8).

The echocardiographic and CMR-based severity of mitral regurgitation were also predictive ($P < 0.05$) in univariate Cox analyses (Table 3). Furthermore, and likely mediated by guideline-based management, LV volumes by standard imaging were significantly predictive of outcomes. LVEF, end-systolic wall stress, and global longitudinal strain had no significant association with outcome.

MEE remained a significant independent predictor when adjusted for any of the standard imaging parameters—more pronounced when a cutoff MEE of less than 25.7% was used. Table 4 shows the results of 2 experimental Cox multivariate models, in which an MEE of less than 25.7% was adjusted for the parameters with the highest univariate predictive capacity from either echocardiography or CMR. In a Cox model of MEE corrected for anamnestic presence of hypertension, MEE remained highly predictive ($P = 0.0002$), whereas history of hypertension did not reach statistical significance ($P = 0.9$).

DISCUSSION

Our study shows for the first time, to our knowledge, the relation of MEE to mitral regurgitation severity, LV remodeling, and progression requiring surgical intervention in asymptomatic severe primary mitral regurgitation. Importantly, the predictive value of MEE was proportional and persisted after correction for standard objective estimators of mitral regurgitation severity, suggesting that MEE offers information that is orthogonal to the estimators recommended in current guidelines. These observations suggest that reduction of myocardial efficiency precedes progression to symptomatic mitral regurgitation requiring intervention.

MEE predicted outcome independently of standard clinical, laboratory, echocardiographic, and CMR parameters collected at the time of PET. This result can be partially explained by the fact that MEE is calculated from parameters that are typically not part of

standard guideline-oriented mitral regurgitation evaluation, such as cardiac forward work and myocardial oxygen consumption. However, none of the functional parameters used in the MEE equation were significant predictors of outcome on their own.

Clinically, our data confirm the prognostic impact of well-established regurgitation parameters such as mitral regurgitant volume and LV volumes for both echocardiography and CMR. LVEF did not correlate with MEE in this cohort and was not predictive, probably because LVEF was within the reference range in all subjects.

Maximum tricuspid jet velocity and left atrial volume, the echocardiographic estimates of backward volume loading recommended in guidelines, were both significantly correlated with MEE and significant predictors in univariate analyses. Both, however, lost predictive significance when adjusted for MEE in multivariate models. A potential explanation for these results is that a poorer metabolic efficiency might have a culprit role in reducing diastolic LV function, which drives the backward failure and results in earlier symptom occurrence.

The experimental multivariate Cox analyses showed that end-systolic volume from echocardiography, but not from CMR, had independent predictive capacity. This is confusing, since CMR is the gold standard. A potential explanation could be that treating physicians had access to serial echocardiography data according to guidelines but were masked to CMR and PET.

Although MEE showed independent predictive value for outcomes, the modest size of our cohort, as well as the limited availability of ^{11}C -acetate PET, does not allow us to predict the potential future role of MEE in the routine management of patients with asymptomatic severe mitral regurgitation. Still, the orthogonal perspective on progression offered by MEE might be useful for research into optimizing decision-making algorithms based on clinical data and for developing surrogate markers of MEE from standard imaging modalities. One such opportunity could be to study MEE in mitral regurgitation patients with concomitant cardiovascular or metabolic diseases to see if comorbidities contribute to mitral regurgitation progression by augmenting disturbances in oxidative metabolism beyond what is caused by volume overload. Hypertension is common in mitral regurgitation, and patients who have both disease entities are potentially prone to more rapid symptomatic progression, but there is no clear evidence for benefit of

TABLE 4
Experimental Multivariate Cox Proportional-Hazards Models of MEE with Adjustments for Standard Outcome Parameters from Either Echocardiography or CMR

Parameter	Hazard ratio	<i>P</i>
MEE and echocardiography (whole-model $P < 0.0001$)		
MEE < 25.7%	3.7 (1.1–12.8)	0.03
Regurgitant volume volumetric (mL)	1.37 (0.17–13.8)	0.77
LV end-systolic volume index (mL/m ²)	1.08 (1.01–1.17)	0.03
Maximum tricuspid jet velocity (m/s)	2.2 (0.70–6.64)	0.17
MEE and CMR (whole-model $P = 0.0002$)		
MEE < 25.7%	5.9 (1.7–20.3)	0.005
LV end-diastolic volume index (mL/m ²)	1.00 (0.93–1.07)	0.94
LV end-systolic volume index (mL/m ²)	1.04 (0.95–1.14)	0.39
Regurgitant volume (mL)	1.00 (0.97–1.03)	0.87

Data in parentheses are 95% CIs.

antihypertensive therapy (16). The fact that MEE is lowered in hypertension with LV hypertrophy (17) suggests that a history of hypertension might predispose a reduction of MEE in mitral regurgitation and contribute to the more rapid symptomatic progression in a subset of patients found in this study. On the basis of this hypothesis, we tested the association of hypertension and MEE for predicting progression but found no significant interaction in this cohort.

In patients with overt heart failure, MEE is significantly associated with LV hypertrophy and end-systolic wall stress (6). Among the individual parameters used in the MEE equation, LV mass was the only one that was significantly increased in mitral regurgitation patients, compared with healthy controls in our study. The hypertrophy seen in mitral regurgitation is generally regarded as an adaptive mechanism that reduces wall stress, secondary to LV dilatation. We did not find any association of end-systolic wall stress toward MEE or outcome, probably because the hypertrophic adaptation matched the dilatation sufficiently overall. However, this adaptation is apparently not sustainable in a subset of mitral regurgitation patients and causes a lowered metabolic efficiency even before major adverse changes in wall stress and systolic function occur. This may relate to metabolic alterations found in failing myocardium, including in the setting of mitral regurgitation (18), and points to a poorly understood variation in phenotypic susceptibility. MEE was in the reference range in mitral regurgitation subjects that did not experience early progression despite LV hypertrophy, suggesting that early adaptations to chronic volume overloading in subjects without increased susceptibility include a potentially improved efficiency of oxidative metabolism. This is analogous to previous findings in subjects with LV hypertrophy due to aortic stenosis and pressure overload, where MEE was in the reference range until symptom occurrence (19).

¹¹C-acetate PET has been used to study MEE at a later stage in mitral regurgitation progression in small studies of symptomatic primary (7) and secondary (9) mitral regurgitation, showing MEE improvements after surgery in parallel with normalization of forward stroke volume. In the current study, external cardiac work and forward stroke volume in patients who reached the endpoint was not significantly different from that in patients who were censored or healthy volunteers, and symptom burden was minimal, suggesting that our cohort was studied at an earlier disease state than in previous ¹¹C-acetate PET studies on mitral regurgitation. Moreover, it is difficult to draw conclusions from comparisons between our study and previous knowledge because guideline criteria for recommending surgical intervention have become more aggressive in the recent decade. Hence, studies with serial PET measurements might be required to understand the dynamics of myocardial metabolic efficiency, during progression leading to an intervention and during recovery after surgery, and to what extent the presumably distinct predictive value of MEE found in this study can be used for therapeutic decision making or as an outcome surrogate in drug trials. For such studies, PET-MEE has the advantage of simultaneous acquisition and automated analysis of all required parameters. The data show, however, that combined CMR and PET with careful avoidance of hemodynamic alterations between scans is not inferior to PET alone for predictive purposes, but MEE quantification appear to be method-dependent.

Several limitations of our study should be recognized. The number of patients included was modest, but nevertheless this was potentially the largest study evaluating primary mitral regurgitation severity with same-day PET, echocardiography, and CMR. Most importantly,

this was a study on patients with moderate-to-severe or severe primary mitral regurgitation, which does not address lesser degrees of mitral regurgitation or secondary mitral regurgitation.

An important fundamental limitation was the nature of our endpoint, which was mitral valve intervention. The decision to proceed with intervention followed current guidelines at the time of the study and thus was triggered by the emergence of symptoms or N-terminal pro-brain natriuretic peptide increase, progressive LV dilatation, reduction in LVEF exceeding guideline-specified echocardiographic limits, or some combination of these features. Hence, it is not surprising that volumetric indices such as mitral regurgitant volume and LV end-diastolic volume were prognostic of outcomes. One patient was recommended for surgery but declined and died of cardiovascular causes. Of interest, this patient had the lowest MEE (15.7%) of all subjects in the cohort. Removal of this patient from outcome analyses did not change results or conclusions.

We acknowledge that MEE is a simplified approach to measuring myocardial efficiency and that comparisons to invasive approaches with pressure–volume loop analyses and direct measurement of mean myocardial oxygen uptake are relevant for future studies. Pump work did not include the product of regurgitant volume and end-systolic left atrial pressure; it is unclear whether this addition would alter the predictive value of MEE.

CONCLUSION

MEE by ¹¹C-acetate PET was reduced in asymptomatic chronic degenerative mitral valve in proportion to the severity of mitral regurgitation measured by multiparametric echocardiography and CMR, and MEE predicted time to progression triggering surgical intervention, independently of standard imaging parameters of mitral regurgitation severity, LV function, and size.

DISCLOSURE

This study was supported by research grants 20130631 and 20190593 from the Swedish Heart-Lung Foundation, Stockholm, Sweden. No other potential conflict of interest relevant to this article was reported.

KEY POINTS

QUESTION: What is the role of MEE measured with ¹¹C-acetate PET in progression of asymptomatic moderate-to-severe or severe primary mitral valve insufficiency?

PERTINENT FINDINGS: MEE was proportional to standard imaging indicators of regurgitation severity and volume overload. MEE was independently predictive of time to progression requiring surgical intervention.

IMPLICATIONS FOR PATIENT CARE: MEE might provide an objective and early indication of deteriorating myocardial energetics in mitral valve disease.

REFERENCES

1. Nkomo VT, Gardin JM, Skelton TN, Gottdiener JS, Scott CG, Enriquez-Sarano M. Burden of valvular heart diseases: a population-based study. *Lancet*. 2006;368:1005–1011.
2. Lancellotti P, Tribouilloy C, Hagendorff A, et al. Recommendations for the echocardiographic assessment of native valvular regurgitation: an executive summary

- from the European Association of Cardiovascular Imaging. *Eur Heart J Cardiovasc Imaging*. 2013;14:611–644.
3. Zoghbi WA, Adams D, Bonow RO, et al. Recommendations for noninvasive evaluation of native valvular regurgitation: a report from the American Society of Echocardiography developed in collaboration with the Society for Cardiovascular Magnetic Resonance. *J Am Soc Echocardiogr*. 2017;30:303–371.
 4. Myerson SG, d'Arcy J, Christiansen JP, et al. Determination of clinical outcome in mitral regurgitation with cardiovascular magnetic resonance quantification. *Circulation*. 2016;133:2287–2296.
 5. Sørensen J, Harms HJ, Aalen JM, Baron T, Smiseth OA, Flachskampf FA. Myocardial efficiency: a fundamental physiological concept on the verge of clinical impact. *JACC Cardiovasc Imaging*. 2020;13:1564–1576.
 6. Hansen KB, Sorensen J, Hansson NH, et al. Myocardial efficiency in patients with different aetiologies and stages of heart failure. *Eur Heart J Cardiovasc Imaging*. 2022;23:328–337.
 7. Chow BJ, Abunassar JG, Aseah K, et al. Effects of mitral valve surgery on myocardial energetics in patients with severe mitral regurgitation. *Circ Cardiovasc Imaging*. 2010;3:308–313.
 8. Harms HJ, Hansson NHS, Kero T, et al. Automatic calculation of myocardial external efficiency using a single ¹¹C-acetate PET scan. *J Nucl Cardiol*. 2018;25:1937–1944.
 9. Sugiki T, Naya M, Manabe O, et al. Effects of surgical ventricular reconstruction and mitral complex reconstruction on cardiac oxidative metabolism and efficiency in nonischemic and ischemic dilated cardiomyopathy. *JACC Cardiovasc Imaging*. 2011;4:762–770.
 10. Bing RJ, Hammond MM, Handelsman JC, et al. The measurement of coronary blood flow, oxygen consumption, and efficiency of the left ventricle in man. *Am Heart J*. 1949;38:1–24.
 11. Harms HJ, Tolbod LP, Hansson NH, et al. Automatic extraction of forward stroke volume using dynamic PET/CT: a dual-tracer and dual-scanner validation in patients with heart valve disease. *EJNMMI Phys*. 2015;2:25.
 12. Harms HJ, Stubkjaer Hansson NH, Tolbod LP, et al. Automatic extraction of myocardial mass and volume using parametric images from dynamic nongated PET. *J Nucl Med*. 2016;57:1382–1387.
 13. Hansson NH, Harms HJ, Kim WY, et al. Test-retest repeatability of myocardial oxidative metabolism and efficiency using standalone dynamic ¹¹C-acetate PET and multimodality approaches in healthy controls. *J Nucl Cardiol*. 2018;25:1929–1936.
 14. Alter P, Rupp H, Rominger MB, Klose KJ, Maisch B. A new methodological approach to assess cardiac work by pressure-volume and stress-length relations in patients with aortic valve stenosis and dilated cardiomyopathy. *Pflugers Arch*. 2008;455:627–636.
 15. Vahanian A, Iung B. The new ESC/EACTS guidelines on the management of valvular heart disease. *Arch Cardiovasc Dis*. 2012;105:465–467.
 16. Katsi V, Georgiopoulos G, Magkas N, et al. The role of arterial hypertension in mitral valve regurgitation. *Curr Hypertens Rep*. 2019;21:20.
 17. Laine H, Katoh C, Luotolahti M, et al. Myocardial oxygen consumption is unchanged but efficiency is reduced in patients with essential hypertension and left ventricular hypertrophy. *Circulation*. 1999;100:2425–2430.
 18. Conway MA, Bottomley PA, Ouwerkerk R, Radda GK, Rajagopalan B. Mitral regurgitation: impaired systolic function, eccentric hypertrophy, and increased severity are linked to lower phosphocreatine/ATP ratios in humans. *Circulation*. 1998;97:1716–1723.
 19. Hansson NH, Sorensen J, Harms HJ, et al. Myocardial oxygen consumption and efficiency in aortic valve stenosis patients with and without heart failure. *J Am Heart Assoc*. 2017;6:e004810.

Deep Learning Coronary Artery Calcium Scores from SPECT/CT Attenuation Maps Improve Prediction of Major Adverse Cardiac Events

Robert J.H. Miller*^{1,2}, Konrad Pieszko*^{1,3}, Aakash Shanbhag¹, Attila Feher⁴, Mark Lemley¹, Aditya Killekar¹, Paul B. Kavanagh¹, Serge D. Van Kriekinge¹, Joanna X. Liang¹, Cathleen Huang¹, Edward J. Miller⁴, Timothy Bateman⁵, Daniel S. Berman¹, Damini Dey¹, and Piotr J. Slomka¹

¹Departments of Medicine (Division of Artificial Intelligence in Medicine), Imaging, and Biomedical Sciences, Cedars-Sinai Medical Center, Los Angeles, California; ²Department of Cardiac Sciences, University of Calgary, Calgary, Alberta, Canada; ³Department of Interventional Cardiology and Cardiac Surgery, University of Zielona Góra, Zielona Góra, Poland; ⁴Section of Cardiovascular Medicine, Department of Internal Medicine, Yale University School of Medicine, New Haven, Connecticut; and ⁵Cardiovascular Imaging Technologies LLC, Kansas City, Missouri

Low-dose ungated CT attenuation correction (CTAC) scans are commonly obtained with SPECT/CT myocardial perfusion imaging. Despite the characteristically low image quality of CTAC, deep learning (DL) can potentially quantify coronary artery calcium (CAC) from these scans in an automatic manner. We evaluated CAC quantification derived with a DL model, including correlation with expert annotations and associations with major adverse cardiovascular events (MACE). **Methods:** We trained a convolutional long short-term memory DL model to automatically quantify CAC on CTAC scans using 6,608 studies (2 centers) and evaluated the model in an external cohort of patients without known coronary artery disease ($n = 2,271$) obtained in a separate center. We assessed agreement between DL and expert annotated CAC scores. We also assessed associations between MACE (death, revascularization, myocardial infarction, or unstable angina) and CAC categories (0, 1–100, 101–400, or >400) for scores manually derived by experienced readers and scores obtained fully automatically by DL using multivariable Cox models (adjusted for age, sex, past medical history, perfusion, and ejection fraction) and net reclassification index. **Results:** In the external testing population, DL CAC was 0 in 908 patients (40.0%), 1–100 in 596 (26.2%), 100–400 in 354 (15.6%), and >400 in 413 (18.2%). Agreement in CAC category by DL CAC and expert annotation was excellent (linear weighted κ , 0.80), but DL CAC was obtained automatically in less than 2 s compared with about 2.5 min for expert CAC. DL CAC category was an independent risk factor for MACE with hazard ratios in comparison to a CAC of zero: CAC of 1–100 (2.20; 95% CI, 1.54–3.14; $P < 0.001$), CAC of 101–400 (4.58; 95% CI, 3.23–6.48; $P < 0.001$), and CAC of more than 400 (5.92; 95% CI, 4.27–8.22; $P < 0.001$). Overall, the net reclassification index was 0.494 for DL CAC, which was similar to expert annotated CAC (0.503). **Conclusion:** DL CAC from SPECT/CT attenuation maps agrees well with expert CAC annotations and provides a similar risk stratification but can be obtained automatically. DL CAC scores improved classification of a significant proportion of patients as compared with SPECT myocardial perfusion alone.

Key Words: cardiology; artificial intelligence; coronary artery calcification; deep learning; myocardial perfusion imaging; risk stratification

J Nucl Med 2023; 64:652–658

DOI: 10.2967/jnumed.122.264423

SPECT myocardial perfusion imaging (MPI) is a well-established and widely used noninvasive imaging modality for the diagnosis and prognostication of coronary artery disease (1,2). SPECT MPI is frequently obtained with ungated, unenhanced CT attenuation correction (CTAC) scans. SPECT/CT scanners use a common bed to move the patient sequentially through both scanners (3), with some models incorporating solid-state detector arrays. CTAC allows correction for soft-tissue attenuation artifacts, leading to improved diagnostic accuracy of SPECT MPI (4).

However, CTAC scans can also potentially be used to provide an anatomic assessment that includes evaluation of coronary artery calcium (CAC) (5). CAC scores are a well-established marker of the extent of coronary atherosclerosis (6–8). Integrating CAC scores from dedicated, gated CT scans with assessments of myocardial perfusion can improve the diagnostic accuracy of SPECT (7) and PET MPI (9). Additionally, CAC from dedicated electrocardiography-gated scans can provide incremental risk stratification when combined with SPECT MPI perfusion (10,11). However, CTAC scans are typically acquired with lower radiation doses and without cardiac gating, leading to worse image quality and often thicker slices than for dedicated CAC scans, which may influence CAC scores (12). Although it is possible to quantify CAC manually from CTAC scans, this can be time-consuming and is not common. It is also possible to visually estimate CAC (13,14), but visual estimation is inherently subjective and requires experience to be performed accurately. Deep learning (DL) has been applied to image segmentation, including models for automated measures of CAC primarily from dedicated CAC scans. We developed a novel convolutional long short-term model (convLSTM) that integrates adjacent image slices, mimicking the clinical approach of scrolling between slices, to quantify CAC more efficiently. We evaluated the correlation between DL and expert annotated CAC scores in patients undergoing SPECT/CT MPI. We then evaluated the prognostic significance of DL and expert annotated CAC scores for major adverse cardiovascular events (MACE), including incremental risk

Received May 20, 2022; revision accepted Oct. 4, 2022.
For correspondence or reprints, contact Piotr J. Slomka (piotr.slomka@cshs.org).
*Contributed equally to this work.
Published online Oct. 7, 2022.
COPYRIGHT © 2023 by the Society of Nuclear Medicine and Molecular Imaging.

stratification over traditional SPECT MPI parameters, in an external population imaged with solid-state SPECT/CT MPI.

MATERIALS AND METHODS

Study Population

Patients who underwent SPECT/CT MPI with CTAC at 1 of 2 centers (Yale and Cardiovascular Imaging Technologies) were used to train the convLSTM. Patients who underwent SPECT/CT MPI from a third center (University of Calgary) were used as an external testing cohort. Patients without CTAC were excluded. For external testing, patients with a history of coronary artery disease ($n = 673$), defined as previous myocardial infarction or revascularization with either percutaneous coronary intervention or coronary artery bypass grafting (15), were excluded. Details of the clinical data acquisition are provided in the supplemental materials (available at <http://jnm.snmjournals.org>). The study protocol complied with the Declaration of Helsinki. The study was approved by the institutional review board at all sites. To the extent allowed by data sharing agreements and institutional review board protocols, data and codes used in this article will be shared on written request.

Image Acquisition and Interpretation

Details of MPI and CTAC image acquisition and interpretation are available in the supplemental materials (16). Additional details on the training population are in Supplemental Table 1.

Two separate cohorts (each comprising 10% of the total number of available scans, $n = 661$) of the initial training cohort were sampled, with an equal number of cases in each CAC score category. One of those cohorts was held out as a validation set during training, and the model parameters were tuned to this set, whereas the second was held out for internal testing.

All the training, internal validation, internal testing, and external testing cases were annotated on-site by 2 expert readers with at least 5 years of experience in CAC scoring using dedicated quantitative software (Cardiac Suite; Cedars Sinai Medical Center). DL annotations were processed using a custom-developed pipeline, and both expert and DL annotated CAC scores were calculated according to the standard clinical algorithm (6), with additional details in the supplemental materials.

The DL and expert annotated cases were categorized on the basis of the CAC score (category 1, CAC score = 0; category 2, CAC score = 1–100; category 3, CAC score = 101–400; category 4, CAC score > 400).

Model Architecture

The model architecture is outlined in Figure 1. The model was built using PyTorch, version 3.7.4. We automatically segmented CAC from CTAC using a cascaded convLSTM system (17). This system consists of 2 networks, the first of which was trained for segmentation of the

heart silhouette and the second of which was trained to segment the CAC. The heart convLSTM was trained on a subset of training data with expert reader annotations from QFAT software (18). A supervised learning regime was used for both segmentation networks. The heart mask was applied to the final CAC prediction to reduce any spurious bone overcalling or calcification in noncardiac regions. To imitate the physician approach of aggregating information from adjacent slices, 3 slices were provided to both networks as input (19). This network architecture was shown previously to have significantly reduced memory consumption and to have inference times almost 2 times faster, with similar accuracy to U-Net on a typical central processing unit (17). Case examples with expert and DL annotations are shown in Figure 2.

Statistical Analysis

Details of the statistical analysis are provided in the supplemental materials (20,21). The Proposed Requirements for Cardiovascular Imaging–Related Machine Learning Evaluation (22) checklist is shown in Supplemental Table 2. Improvements in likelihood ratio χ^2 and area under the receiver-operating-characteristic curve were also assessed.

RESULTS

Population Characteristics

In total, 6,608 patients were included in the training population. The external testing population included 2,271 patients, with population characteristics by DL CAC category shown in Table 1. On the basis of the DL model results, CAC was 0 in 908 (40.0%) patients, 1–100 in 596 (26.2%) patients, 100–400 in 354 (15.6%) patients, and more than 400 in 413 (18.2%) patients.

DL Versus Expert Annotated CAC

DL CAC was obtained fully automatically in less than 2 s per scan (time required to load the study, select slices, and annotate lesions for the entire CTAC volume). This compares with approximately 2.5 min for expert annotations, including the time required to load the study, review all slices, and annotate lesions on selected slices. Figure 3 outlines concordance between DL CAC and expert annotation CAC categories. The categorywise agreement (Fig. 3) between DL CAC and expert CAC was excellent (linear weighted κ , 0.80). There was also good pairwise correlation between DL CAC and expert annotated CAC as continuous measures ($r^2 = 0.693$, $P < 0.001$; Supplemental Fig. 1). Summary of categorization by visual CAC estimation compared with DL and expert annotated CAC is shown in Supplemental Table 3. Review of discrepant cases is shown in the Supplemental Results and Supplemental Figure 2.

Associations with MACE

During a median follow-up of 2.8 years (interquartile range, 1.7–4.1 years), 320 patients experienced at least 1 MACE. Supplemental Table 4 outlines the characteristics of patients who experienced MACE compared with those who did not. Patients who experienced MACE had a higher median CAC (178 vs. 11, $P < 0.001$) and were more likely to have a CAC of more than 400 (35.9% vs. 15.3%, $P < 0.001$). Patients who experienced MACE were also older (median, 70.7 vs. 66.1; $P < 0.001$) and more likely to have a history of diabetes

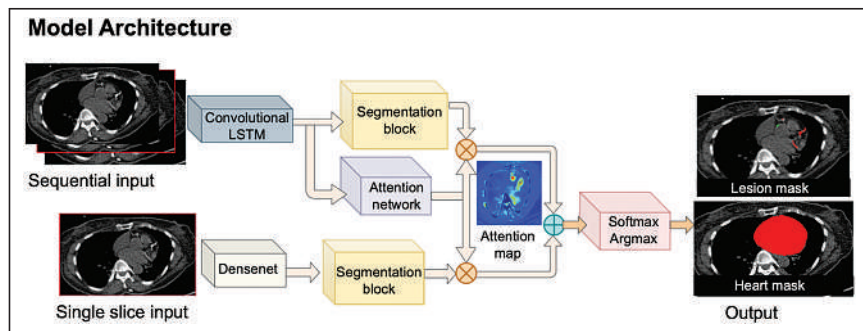


FIGURE 1. Outline of model architecture. ConvLSTM includes network trained to segment CAC, as well as second network for segmentation of heart, which limits CAC scoring. Softmax argmax function normalizes output of network to expected probabilities. Model identifies coronary calcium (red) and noncoronary calcium (green) within heart mask.

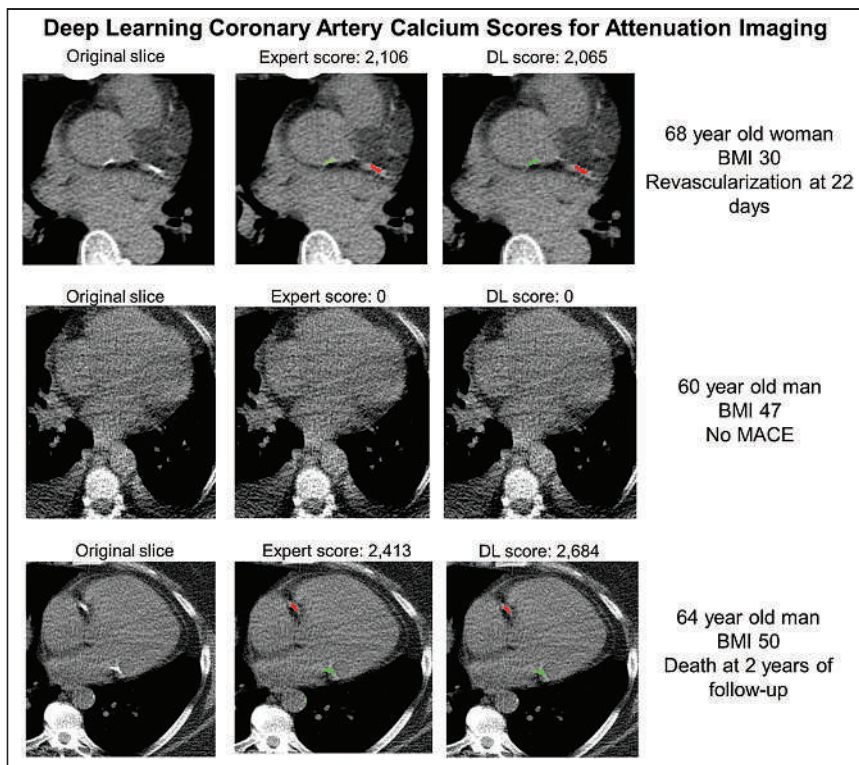


FIGURE 2. Examples of expert scores compared with DL CAC scores. Model identifies coronary calcium (red) and noncoronary calcium (green). In case 1, expert and DL annotations identified similar left circumflex CAC as well as ascending aorta calcium. No CAC was identified by either expert or DL scoring in case 2. In case 3, expert and DL annotations identified similar right coronary artery CAC as well as mitral annular calcification. BMI = body mass index.

(31.6% vs. 22.1%, $P < 0.001$) in addition to higher rates of other cardiovascular risk factors.

Increasing DL CAC and expert CAC category were associated with an increased risk of MACE (Fig. 4). Compared with patients with a DL CAC of 0, patients with scores of 1–100 (unadjusted hazard ratio [HR], 2.20; 95% CI, 1.54–3.14), 101–400 (unadjusted HR, 4.58; 95% CI, 3.23–6.48), and more than 400 (unadjusted HR, 5.92;

95% CI, 4.27–8.22) were at significantly increased risk of MACE. The risk was similar across categories of expert annotated CAC categories. Kaplan–Meier survival curves stratified by visually estimated CAC are shown in Supplemental Figure 3.

Associations with MACE in the multivariable model are outlined in Table 2. DL CAC category continued to be associated with an increased risk of MACE in adjusted analyses for patients with a CAC of 1–100 (adjusted HR, 1.90; 95% CI, 1.32–2.73; $P < 0.001$), 101–400 (adjusted HR, 3.32; 95% CI, 2.29–4.81; $P < 0.001$), and more than 400 (adjusted HR, 3.58; 95% CI, 2.47–5.19; $P < 0.001$) compared with a CAC of 0. This risk stratification was similar to the risk associated with mild stress perfusion abnormalities (stress total perfusion deficit, 5%–10%; adjusted HR, 1.70; 95% CI, 1.19–2.44; $P = 0.004$) and moderate to severe stress perfusion abnormalities (stress total perfusion deficit, >10%; adjusted HR, 4.73; 95% CI, 3.02–7.46; $P < 0.001$). The risk associated with expert annotated CAC categories was similar to DL categories (CAC of 1–100: adjusted HR, 2.20; 95% CI, 1.52–3.19; $P < 0.001$; CAC of 101–400: adjusted HR, 3.57; 95% CI, 2.45–5.20; $P < 0.001$; CAC > 400: adjusted HR, 4.05; 95% CI, 2.78–5.90; $P < 0.001$).

Associations with primary outcome were similar if patients who underwent early revascularization were excluded (DL CAC of 1–100: adjusted HR, 2.00; 95% CI, 1.34–2.94; $P = 0.001$; DL CAC of 101–400: adjusted HR, 2.98; 95% CI, 1.97–4.49; $P < 0.001$; DL CAC > 400: adjusted HR, 3.07; 95% CI, 2.03–4.66; $P < 0.001$). Results were also similar for associations with death or myocardial infarction as well as associations with death (Supplemental Table 5).

TABLE 1
External Testing: Patient Characteristics According to CAC Category Determined by Deep-Learning Model

Characteristic	CAC < 1	CAC 1–100	CAC 100–400	CAC > 400	<i>P</i>
<i>n</i>	908 (40.0%)	596 (26.2%)	354 (15.6%)	413 (18.2%)	
Age (y)	61.9 (55.1–69.3)	66.4 (57.3–74.2)	70.8 (65.3–77.3)	72.3 (66.3–77.9)	<0.001
Male	368 (40.5%)	293 (49.2%)	200 (56.5%)	286 (69.2%)	<0.001
BMI	29.3 (25.1–32.6)	30 (25.8–34.4)	29.3 (25.4–32.9)	29.4 (25.2–32.4)	0.048
Past medical history					
Hypertension	423 (46.6%)	355 (59.6%)	240 (67.8%)	268 (64.9%)	<0.001
Diabetes	136 (15.0%)	146 (24.5%)	111 (31.4%)	140 (33.9%)	<0.001
Dyslipidemia	334 (36.8%)	246 (41.3%)	187 (52.8%)	236 (57.1%)	<0.001
Family history	453 (49.9%)	305 (51.2%)	155 (43.8%)	205 (49.6%)	0.20
Smoking	67 (7.4%)	35 (5.9%)	21 (5.9%)	27 (6.5%)	0.67

BMI = body mass index.

Qualitative data are number and percentage; continuous data are median and interquartile range.

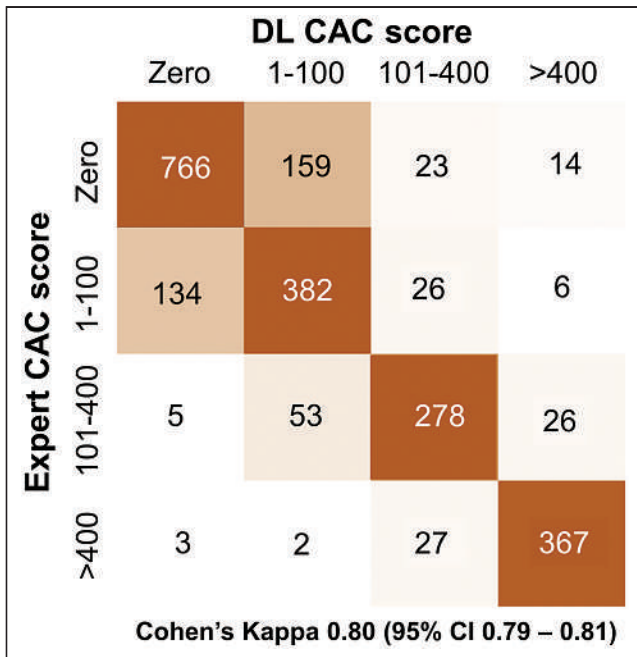


FIGURE 3. Concordance matrix between DL and expert CAC categories in external testing population.

Net Reclassification

We assessed patient reclassification with the addition of CAC categories to all other components of the multivariable model outlined in Table 2. The results of the net reclassification index (NRI) analysis are shown in Figure 5. Both DL CAC and expert annotated CAC significantly improved model fit and AUC (all $P < 0.01$) (Supplemental Table 6). DL CAC categories improved the risk classification of patients with events (event NRI, 0.230; 95% CI, 0.142–0.314), patients without events (nonevent NRI, 0.264; 95% CI, 0.204–0.309), and overall patient classification (overall NRI, 0.494; 95% CI, 0.363–0.607). Event, nonevent, and overall NRI were similar for both measures, as shown in Supplemental Table 6. Additionally, overall NRI was lower for visually estimated CAC (overall NRI, 0.409; 95% CI, 0.278–0.537).

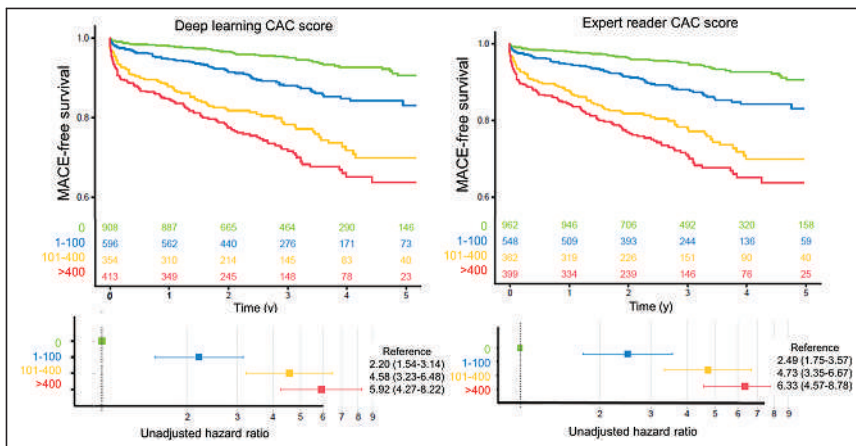


FIGURE 4. Kaplan-Meier survival curves for MACE. Increasing CAC category was associated with increasing risk of MACE for DL and expert annotated CAC scores on SPECT/CT attenuation maps.

DISCUSSION

We demonstrated that DL-derived CAC scores from CTAC imaging could be used to stratify the risk of MACE, with scores derived rapidly (~2 s) in a completely automated manner. There was good agreement between CAC score categorization by DL and expert annotations, as evaluated in a large external population with different characteristics. Lastly, we demonstrated that DL CAC categories provided prognostic information additional to clinical information and quantitative assessment of perfusion and ventricular function, with improved classification of a quarter of patients who experienced MACE and a quarter of patients who did not experience MACE. DL CAC scores from CTAC could be used clinically to significantly improve risk stratification in patients undergoing SPECT/CT MPI, without the need for physician or technician time for manual annotation.

We demonstrated that the convLSTM network was able to quantify CAC from CTAC imaging, with excellent agreement with and risk stratification similar to expert annotated CAC. Importantly, the model was trained with data from 2 sites that have CTAC imaging protocols different from that of the external testing site. This training has not been commonly done in other studies reported in the existing literature, providing evidence that the convLSTM and associated DL CAC scores should be generalizable to a variety of acquisition protocols. We also previously demonstrated that this approach has faster inference times than a U-net model and therefore should not negatively impact clinical workflow. Another major strength of the current study is the large number of expert annotations performed on CTAC scans, which are not typically performed clinically. This strength allowed us to evaluate agreement with expert CAC scores more precisely and to robustly compare the risk stratification provided by the 2 measures, including their improvements for risk prediction of traditional SPECT/CT variables.

Several other approaches to CAC scoring with artificial intelligence have been applied previously (23–27). The agreement between CAC categories in our study (Cohen κ , 0.80) is similar to agreement demonstrated using dedicated electrocardiography-gated scans with other DL approaches (25). Isgum et al. developed a convolutional neural network that quantified CAC from low-dose CT scans obtained for lung cancer screening (26). When the same model was applied to patients undergoing PET MPI, the agreement between manual and automated scoring in CTAC

was lower than in the present study (linear weighted κ , 0.70–0.74), and the testing was on a much smaller patient population ($n = 133$) (28). Sartoretto et al. also demonstrated good agreement between expert annotated and DL CAC scores in a cohort of 56 patients undergoing SPECT/CT MPI (29). Importantly, these methods demonstrate rates of agreement similar to what would be expected between 2 expert readers scoring CAC from low-dose CT scans (30). High noise levels and partial-volume effects impact the appearance of CAC lesions (12), leading to frequent false-negative physician interpretations, as evidenced by our finding that physician interpretation of the presence or absence of calcium was discrepant in about 10% of patients. Additionally, we identified cases in which DL annotations differed

TABLE 2
Associations with MACE

Association	Unadjusted HR		Adjusted HR	
	95% CI	P	95% CI	P
DL CAC categories				
<1	Reference	—	Reference	—
1–100	2.20 (1.54–3.14)	<0.001	1.90 (1.32–2.73)	<0.001
101–400	4.58 (3.23–6.48)	<0.001	3.32 (2.29–4.81)	<0.001
>400	5.92 (4.27–8.22)	<0.001	3.58 (2.47–5.19)	<0.001
Age (per 10 y)	1.37 (1.24–1.52)	<0.001	1.12 (1.00–1.26)	0.046
Male	1.75 (1.39–2.19)	<0.001	1.11 (0.86–1.43)	0.418
BMI (per kg/m ²)	0.98 (0.96–1.00)	0.021	0.99 (0.97–1.01)	0.157
Hypertension	1.22 (0.98–1.53)	0.079	0.98 (0.77–1.25)	0.862
Diabetes	1.60 (1.26–2.02)	<0.001	1.28 (0.99–1.64)	0.060
Dyslipidemia	1.34 (1.08–1.67)	0.008	1.00 (0.78–1.27)	0.997
Family history	0.82 (0.65–1.02)	0.071	0.90 (0.72–1.13)	0.353
Smoking	1.18 (0.81–1.72)	0.389	1.18 (0.80–1.74)	0.415
Stress AC TPD category				
< 1%	Reference	—	Reference	—
1–<5%	1.28 (0.96–1.71)	0.097	1.22 (0.90–1.65)	0.200
5–<10%	2.06 (1.46–2.90)	<0.001	1.70 (1.19–2.44)	0.004
≥10%	7.52 (5.43–10.4)	<0.001	4.73 (3.02–7.46)	<0.001
Rest AC TPD	1.07 (1.05–1.08)	<0.001	1.00 (0.97–1.03)	0.836
Stress LVEF	0.97 (0.97–0.98)	<0.001	0.99 (0.98–1.00)	0.293

BMI = body mass index; AC = attenuation correction; TPD = total perfusion deficit; LVEF = left ventricular ejection fraction.

from expert annotations for calcium in coronary ostia versus adjacent aorta and for valvular calcification versus adjacent coronary arteries.

Although agreement between DL and expert CAC categories is important in itself, we demonstrated that significant improvements in risk stratification are possible with DL annotated CAC scores. We demonstrated that increasing DL CAC category was associated with an increased risk of MACE, similar to recent findings

from Zeleznik et al. in both symptomatic and asymptomatic populations (27). However, in the present study we demonstrated that the risk associated with each category was similar to the corresponding category of expert annotated CAC. Additionally, both DL and expert reader CAC categories were significantly associated with MACE after correcting for relevant confounders, including age, sex, medical history, and SPECT MPI results. Lastly, we

demonstrated that improvement in patient risk classification with DL CAC was similar to that achieved by expert annotated categories of CAC, with both being higher than is possible with subjective expert visual estimates. Importantly, visually estimated CAC was performed at the time of clinical reporting and was informed by clinical history and perfusion findings. Improved classification compared with expert visual estimate is particularly relevant since nuclear cardiology laboratories more frequently rely on this method for CAC classification given the time required for expert annotation. Although Dekker et al. found that DL CAC scores had an NRI of 0.13 in patients undergoing PET MPI (31), in our study about 1 in 4 patients who experienced MACE would have their risk correctly reclassified, with a

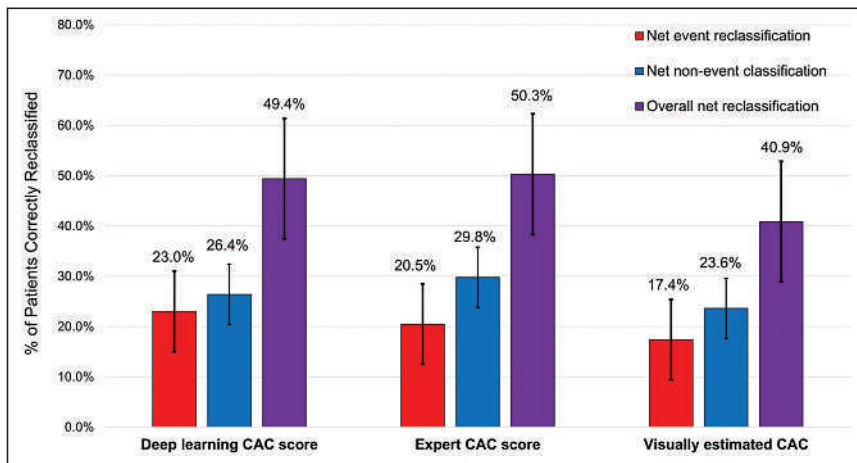


FIGURE 5. Results of net-reclassification analysis. We assessed addition of CAC categories to full multivariable model outlined in Table 2.

similar proportion of patients who did not experience MACE correctly reclassified. Therefore, this approach could be applied to automatically improve risk classification in a substantial proportion of patients.

Our work adds to a growing body of literature supporting integration of CAC scores when interpreting MPI. Chang et al. demonstrated that quantitative CAC combined with SPECT MPI findings provided independent and complementary prognostic information among a cohort of 1,126 patients without prior coronary artery disease (11). Engbers et al. evaluated a combination of the Agatston CAC score and SPECT MPI in 4,897 symptomatic patients without prior coronary artery disease (10), demonstrating a stepwise increase in MACE with increasing CAC score among patients with both normal and abnormal perfusion. Visually estimated CAC (13) can also provide risk stratification in patients undergoing SPECT/CT MPI (14). However, in the present work we demonstrate that the improvement in risk classification is higher with DL CAC, which is rapidly and automatically derived from SPECT/CT attenuation maps.

Our study had a few important limitations. CT attenuation imaging was used clinically to visually assess coronary calcification, and knowledge of CAC can influence patient management (32). However, results were similar for associations with hard outcomes, and this bias would be expected to—if anything—decrease the associations between CAC and hard outcomes. Additionally, it is unknown whether associations with outcomes would differ significantly between CAC from dedicated gated studies and CAC from CT attenuation imaging; however, previous studies have demonstrated close agreement between the measures (33). We trained the convLSTM model using scans with acquisition parameters different from those for the external testing population. More precise quantification of CAC may be possible if the model is trained with similar data, but this also suggests that the model should be broadly generalizable. The model was trained to differentiate coronary from noncoronary calcifications using expert annotations. However, some lesions are challenging for expert readers to annotate (such as ostial calcium compared with adjacent aortic calcifications), and the DL model would also be expected to have difficulties with these areas. Although the DL method provides fully automated results, they will still need to be verified by a physician. The training population included patients with previous revascularization; however, we excluded patients with known coronary artery disease from the external testing population, and dedicated studies are needed to evaluate the model's ability to differentiate CAC from coronary stents. Lastly, we were not able to ascertain cardiovascular mortality in this large, retrospective population.

CONCLUSION

DL CAC derived from SPECT/CT attenuation maps agrees well with expert CAC annotations. DL and expert annotated CAC are associated with MACE, but DL scores can be obtained automatically in a few seconds. DL CAC scores can be quantified automatically after SPECT/CT MPI, without impeding clinical workflow, to improve classification of a significant proportion of patients.

DISCLOSURE

This research was supported in part by grants R01HL089765 and R35HL161195 from the National Heart, Lung, and Blood Institute/National Institutes of Health (NHLBI/NIH) (principal investigator, Piotr Slomka). The content is solely the responsibility

of the authors and does not necessarily represent the official views of the National Institutes of Health. Robert Miller has received consulting fees and research support from Pfizer. Daniel Berman, Piotr Slomka, and Paul Kavanagh participate in software royalties for QPS software at Cedars-Sinai Medical Center. Piotr Slomka has received research grant support from Siemens Medical Systems. Daniel Berman and Edward Miller have served as consultants for GE Healthcare. No other potential conflict of interest relevant to this article was reported.

KEY POINTS

QUESTION: Do CAC scores quantified automatically with a DL model provide risk stratification similar to that of expert annotated scores?

PERTINENT FINDINGS: In this retrospective multicenter study with dedicated training and external testing populations, DL CAC scores agreed well with expert annotated scores. DL and expert annotated CAC are associated with MACE, but DL scores can be obtained automatically in a few seconds.

IMPLICATIONS FOR PATIENT CARE: DL CAC scores could be used to improve risk prediction of a significant proportion of patients, without impeding clinical workflow.

REFERENCES

1. Berman DS, Hachamovitch R, Kiat H, et al. Incremental value of prognostic testing in patients with known or suspected ischemic heart disease. *J Am Coll Cardiol.* 1995;26:639–647.
2. Fihn SD, Gardin JM, Abrams J, et al. 2012 ACCF/AHA/ACP/AATS/PCNA/SCAI/STS guideline for the diagnosis and management of patients with stable ischemic heart disease. *J Am Coll Cardiol.* 2012;60:e44–e164.
3. Dorbala S, Di Carli MF, Delbeke D, et al. SNMMI/ASNC/SCCT guideline for cardiac SPECT/CT and PET/CT 1.0. *J Nucl Med.* 2013;54:1485–1507.
4. Huang JY, Huang CK, Yen RF, et al. Diagnostic performance of attenuation-corrected myocardial perfusion imaging for coronary artery disease. *J Nucl Med.* 2016;57:1893–1898.
5. Patchett ND, Pawar S, Miller EJ. Visual identification of coronary calcifications on attenuation correction CT improves diagnostic accuracy of SPECT/CT myocardial perfusion imaging. *J Nucl Cardiol.* 2017;24:711–720.
6. Agatston AS, Janowitz WR, Hildner FJ, Zusmer NR, Viamonte M, Detrano R. Quantification of coronary artery calcium using ultrafast computed tomography. *J Am Coll Cardiol.* 1990;15:827–832.
7. Schepis T, Gaemperli O, Koepfli P, et al. Added value of coronary artery calcium score as an adjunct to gated SPECT for the evaluation of coronary artery disease in an intermediate-risk population. *J Nucl Med.* 2007;48:1424–1430.
8. Blaha MJ, Blankstein R, Nasir K. Coronary artery calcium scores of zero and establishing the concept of negative risk factors. *J Am Coll Cardiol.* 2019;74:12–14.
9. Brodov Y, Gransar H, Dey D, et al. Combined quantitative assessment of myocardial perfusion and coronary artery calcium score by hybrid ⁸²Rb PET/CT improves detection of coronary artery disease. *J Nucl Med.* 2015;56:1345–1350.
10. Engbers EM, Timmer JR, Ottervanger JP, Mouden M, Knollemans S, Jager PL. Prognostic value of coronary artery calcium scoring in addition to single-photon emission computed tomographic myocardial perfusion imaging in symptomatic patients. *Circ Cardiovasc Imaging.* 2016;9:e003966.
11. Chang SM, Nabi F, Xu J, et al. The coronary artery calcium score and stress myocardial perfusion imaging provide independent and complementary prediction of cardiac risk. *J Am Coll Cardiol.* 2009;54:1872–1882.
12. Mühlenbruch G, Thomas C, Wildberger JE, et al. Effect of varying slice thickness on coronary calcium scoring with multislice computed tomography in vitro and in vivo. *Invest Radiol.* 2005;40:695–699.
13. Einstein AJ, Johnson LL, Bokhari S, et al. Agreement of visual estimation of coronary artery calcium from low-dose CT attenuation correction scans in hybrid PET/CT and SPECT/CT with standard Agatston score. *J Am Coll Cardiol.* 2010;56:1914–1921.

14. Trpkov C, Savtchenko A, Liang Z, et al. Visually estimated coronary artery calcium score improves SPECT-MPI risk stratification. *Int J Cardiol Heart Vasc.* 2021;35:100827.
15. Miller RJH, Klein E, Gransar H, et al. Prognostic significance of previous myocardial infarction and previous revascularization in patients undergoing SPECT MPI. *Int J Cardiol.* 2020;313:9–15.
16. Slomka PJ, Nishina H, Berman DS, et al. Automated quantification of myocardial perfusion SPECT using simplified normal limits. *J Nucl Cardiol.* 2005;12:66–77.
17. Pieszko K, Shanbhag A, Killekar A, et al. Calcium scoring in low-dose ungated chest CT scans using convolutional long-short term memory networks. *Proc SPIE Int Soc Opt Eng.* 2022;12032:120323A.
18. Eisenberg E, McElhinney PA, Commandeur F, et al. Deep learning-based quantification of epicardial adipose tissue volume and attenuation predicts major adverse cardiovascular events in asymptomatic subjects. *Circ Cardiovasc Imaging.* 2020;13:e009829.
19. Lin TY, Goyal P, Girshick R, He K, Dollar P. Focal loss for dense object detection. *IEEE Trans Pattern Anal Mach Intell.* 2020;42:318–327.
20. Miller RJH, Bonow RO, Gransar H, et al. Percutaneous or surgical revascularization is associated with survival benefit in stable coronary artery disease. *Eur Heart J Cardiovasc Imaging.* 2020;21:961–970.
21. Azadani PN, Miller RJH, Sharir T, et al. Impact of early revascularization on major adverse cardiovascular events in relation to automatically quantified ischemia. *JACC Cardiovasc Imaging.* 2021;14:644–653.
22. Sengupta PP, Shrestha S, Berthon B, et al. Proposed requirements for cardiovascular imaging-related machine learning evaluation (PRIME). *JACC Cardiovasc Imaging.* 2020;13:2017–2035.
23. Kurkure U, Chittajallu DR, Brunner G, Le YH, Kakadiaris IA. A supervised classification-based method for coronary calcium detection in non-contrast CT. *Int J Cardiovasc Imaging.* 2010;26:817–828.
24. Isgum I, Rutten A, Prokop M, van Ginneken B. Detection of coronary calcifications from computed tomography scans for automated risk assessment of coronary artery disease. *Med Phys.* 2007;34:1450–1461.
25. Wolterink JM, Leiner T, de Vos BD, et al. An evaluation of automatic coronary artery calcium scoring methods with cardiac CT using the orCaScore framework. *Med Phys.* 2016;43:2361.
26. Isgum I, Prokop M, Niemeijer M, Viergever MA, van Ginneken B. Automatic coronary calcium scoring in low-dose chest computed tomography. *IEEE Trans Med Imaging.* 2012;31:2322–2334.
27. Zeleznik R, Foldyna B, Eslami P, et al. Deep convolutional neural networks to predict cardiovascular risk from computed tomography. *Nat Commun.* 2021;12:715.
28. Işgum I, de Vos BD, Wolterink JM, et al. Automatic determination of cardiovascular risk by CT attenuation correction maps in Rb-82 PET/CT. *J Nucl Cardiol.* 2018;25:2133–2142.
29. Sartoretti T, Gennari AG, Sartoretti E, et al. Fully automated deep learning powered calcium scoring in patients undergoing MPI. *J Nucl Cardiol.* May 17, 2022 [Epub ahead of print].
30. Jacobs PC, Isgum I, Gondrie MJ, et al. Coronary artery calcification scoring in low-dose ungated CT screening for lung cancer. *AJR.* 2010;194:1244–1249.
31. Dekker M, Waissi F, Bank IEM, et al. The prognostic value of automated coronary calcium derived by a deep learning approach on non-ECG gated CT images from ⁸²Rb-PET/CT MPI. *Int J Cardiol.* 2021;329:9–15.
32. Rozanski A, Gransar H, Shaw Leslee J, et al. Impact of coronary artery calcium scanning on coronary risk factors and downstream testing. *J Am Coll Cardiol.* 2011;57:1622–1632.
33. Pieszko K, Shanbhag AD, Lemley M, et al. Reproducibility of quantitative coronary calcium scoring from PET/CT attenuation maps: comparison to ECG-gated CT scans. *Eur J Nucl Med Mol Imaging.* June 25, 2022 [Epub ahead of print].

Fast and Accurate Amyloid Brain PET Quantification Without MRI Using Deep Neural Networks

Seung Kwan Kang^{1,2}, Daewoon Kim^{3,4}, Seong A Shin¹, Yu Kyeong Kim^{5,6}, Hongyoon Choi^{2,5}, and Jae Sung Lee¹⁻⁵

¹Brightonix Imaging Inc., Seoul, Korea; ²Institute of Radiation Medicine, Medical Research Center, Seoul National University College of Medicine, Seoul, Korea; ³Interdisciplinary Program of Bioengineering, Seoul National University, Seoul, Korea; ⁴Artificial Intelligence Institute, Seoul National University, Seoul, Korea; ⁵Department of Nuclear Medicine, Seoul National University College of Medicine, Seoul, Korea; and ⁶Department of Nuclear Medicine, Seoul Metropolitan Government–Seoul National University Boramae Medical Center, Seoul, Korea

This paper proposes a novel method for automatic quantification of amyloid PET using deep learning–based spatial normalization (SN) of PET images, which does not require MRI or CT images of the same patient. The accuracy of the method was evaluated for 3 different amyloid PET radiotracers compared with MRI-parcellation–based PET quantification using FreeSurfer. **Methods:** A deep neural network model used for the SN of amyloid PET images was trained using 994 multicenter amyloid PET images (367 ¹⁸F-flutemetamol and 627 ¹⁸F-florbetaben) and the corresponding 3-dimensional MR images of subjects who had Alzheimer disease or mild cognitive impairment or were cognitively normal. For comparison, PET SN was also conducted using version 12 of the Statistical Parametric Mapping program (SPM-based SN). The accuracy of deep learning–based and SPM-based SN and SUV ratio quantification relative to the FreeSurfer-based estimation in individual brain spaces was evaluated using 148 other amyloid PET images (64 ¹⁸F-flutemetamol and 84 ¹⁸F-florbetaben). Additional external validation was performed using an unseen independent external dataset (30 ¹⁸F-flutemetamol, 67 ¹⁸F-florbetaben, and 39 ¹⁸F-florbetapir). **Results:** Quantification results using the proposed deep learning–based method showed stronger correlations with the FreeSurfer estimates than SPM-based SN using MRI did. For example, the slope, *y*-intercept, and *R*² values between SPM and FreeSurfer for the global cortex were 0.869, 0.113, and 0.946, respectively. In contrast, the slope, *y*-intercept, and *R*² values between the proposed deep learning–based method and FreeSurfer were 1.019, –0.016, and 0.986, respectively. The external validation study also demonstrated better performance for the proposed method without MR images than for SPM with MRI. In most brain regions, the proposed method outperformed SPM SN in terms of linear regression parameters and intraclass correlation coefficients. **Conclusion:** We evaluated a novel deep learning–based SN method that allows quantitative analysis of amyloid brain PET images without structural MRI. The quantification results using the proposed method showed a strong correlation with MRI-parcellation–based quantification using FreeSurfer for all clinical amyloid radiotracers. Therefore, the proposed method will be useful for investigating Alzheimer disease and related brain disorders using amyloid PET scans.

Key Words: amyloid PET; spatial normalization; deep learning; quantification

Received May 20, 2022; revision accepted Oct. 19, 2022.
For correspondence or reprints, contact Jae Sung Lee (jaes@snu.ac.kr).
Published online Nov. 3, 2022.
Immediate Open Access: Creative Commons Attribution 4.0 International License (CC BY) allows users to share and adapt with attribution, excluding materials credited to previous publications. License: <https://creativecommons.org/licenses/by/4.0/>. Details: <http://jnm.snmjournals.org/site/misc/permission.xhtml>.

COPYRIGHT © 2023 by the Society of Nuclear Medicine and Molecular Imaging.

J Nucl Med 2023; 64:659–666

DOI: 10.2967/jnumed.122.264414

Because of the nature of brain diseases, the pathologic condition of the brain should be evaluated noninvasively. PET is a useful imaging tool for assessing the functional and molecular status of the brain (1,2). The application of brain PET imaging in the diagnosis and treatment of degenerative brain diseases is widely increasing (3–5). In Alzheimer disease (AD), the most common degenerative brain disease, brain deposition of fibrillar amyloid β -plaques is a neuropathologic hallmark for diagnosis. Therefore, amyloid PET has significantly contributed to the diagnosis and treatment of AD.

Visual assessment of PET images by nuclear medicine physicians or radiologists is the standard method for clinical neuroimaging interpretation. Nevertheless, quantitative and statistical analyses of PET images are widely used in brain disease research (1,2,6–9) because such analyses provide useful information for objective interpretation of the PET images of individual patients. The most prevalent method of quantitative image analysis is evaluating regional uptake of radiotracers by manually drawing a region of interest or volume of interest (VOI) on individual brain PET images. Another common method for brain PET image analysis is voxelwise statistical analysis, which is based on spatial normalization (SN) of images (10–12). Furthermore, brain PET SN allows the use of predefined VOIs, which are a suitable alternative to laborious and time-consuming manual VOI drawing (13–19).

Monoclonal antibodies such as aducanumab and donanemab are emerging as AD treatment drugs that target aggregated amyloid β to reduce its buildup in the brain (20,21). Therefore, the importance of quantification methods for amyloid brain PET images with high objectivity, accuracy, and reproducibility is increasing. Although voxelwise statistical analysis and predefined-VOI–based automated anatomic labeling are objective and efficient methods for amyloid brain PET image analysis, their reliability depends primarily on the accuracy of the SN procedure. However, accurate amyloid PET SN without the complementary use of anatomic images, such as MRI or CT, is technically challenging because of the large discrepancy in amyloid deposit patterns between cognitively normal and abnormal cases (22–24). Additionally, severe cerebral atrophy and hydrocephalus, which are frequently observed in older patients, complicate SN. Previously, we proposed 2 deep-learning–based amyloid PET SN

TABLE 1
Demographic and Clinical Diagnosis of Training and Test Datasets

Parameter	n	Age (y)	Sex		Diagnosis			Tracer	
			M	F	NC	MCI	AD	FMM	FBB
Training set	994	73.2 ± 5.6	318	676	200	543	251	367	627
Test set	148	74.8 ± 6.6	75	73	26	85	37	64	84

NC = cognitively normal control; MCI = mild cognitive impairment; FMM = ¹⁸F-flutemetamol; FBB = ¹⁸F-florbetaben.

methods that did not require matched MRI or CT data (25,26). In one of these approaches (25), we used a generative adversarial network to generate pseudo-MRI data from amyloid PET and applied spatial transformation parameters—obtained by performing SNs of pseudo-MR images on the MRI template—to amyloid PET images. In the second approach (26), we used deep neural networks (DNNs) to generate adaptive PET templates for individual amyloid PET images and performed SN of amyloid PET images using individual adaptive templates. Both approaches showed a strong correlation of regional SUV ratio (SUVr) relative to cerebellar activity with the matched MRI-based PET SN and outperformed the MRI-less SN with the average amyloid PET template. However, these methods have the following limitations: first, the process of generating a pseudo-MRI or adaptive template using DNNs and the SN process are separated. Second, we used the SN algorithm provided by the Statistical Parametric Mapping (SPM; Wellcome Centre for Human Neuroimaging) software, which iteratively applies image registration and segmentation algorithms (27). Therefore, the accuracy and speed of the entire SN pipeline depend on the SN performance and computation time of SPM. These limitations undermine the advantage of not requiring matched MRI for amyloid PET SN in both approaches.

Therefore, in this study, we developed a novel MRI-less amyloid PET SN method that allows 1-step generation of spatially normalized PET images using cascaded DNNs that estimate linear and nonlinear SN parameters from individual amyloid PET images. Furthermore, we evaluated the accuracy of the proposed method for 3 different amyloid PET radiotracers compared with MRI-parcellation-based PET quantification using FreeSurfer (28), which has shown a strong correlation with a manual-drawing method in cortical thickness and volume measurement (29–31) and in regional amyloid load estimation (32,33) but requires a significantly longer computation time (~8 h).

TABLE 2
Demographic and Clinical Diagnosis of External Test Dataset

Tracer	n	Diagnosis	
		Young control	Elderly
¹⁸ F-florbetaben	30	8	22
¹⁸ F-flutemetamol	67	22	45
¹⁸ F-florbetapir	39	12	27

Age and sex were anonymized.

MATERIALS AND METHODS

Datasets

To train and test the DNN model for PET SN, we used an open-access dataset provided by the National Information Society Agency (<https://aihub.or.kr/>). This internal dataset comprised pairs of multicenter amyloid PET scans (¹⁸F-florbetaben or ¹⁸F-flutemetamol) and structural T1-weighted 3-dimensional MRI scans of patients with AD or mild cognitive impairment and cognitively normal subjects. The image data were acquired from 6 university hospitals in South Korea. The demographic information and clinical diagnoses of the training and test sets are summarized in Table 1. A public institutional bioethics committee designated by the Ministry of Health and Welfare of South Korea approved the retrospective use of the scan data and waived the need for informed consent.

Furthermore, the trained network was evaluated using an external dataset obtained from the Global Alzheimer Association Interactive Network (<http://www.gaain.org/centiloid-project>). The trained network was tested for 3 different Food and Drug Administration–approved amyloid tracers: ¹⁸F-florbetaben, ¹⁸F-flutemetamol, and ¹⁸F-florbetapir. Originally, this dataset, comprising young controls and elderly subjects, was acquired for the centiloid calibration of each tracer (34–36). The demographic information is summarized in Table 2.

Network Model

The proposed DNN model, comprising cascaded U-nets (37,38), takes an affine-registered amyloid PET image as input and generates local displacement fields for nonlinear registration (Supplemental Fig. 1; supplemental materials are available at <http://jnm.snmjournals.org>). The generated displacement fields were then applied to the coregistered MR images in the training phase, and the cross-correlation loss between the spatially normalized MR images and the T1 template (individual

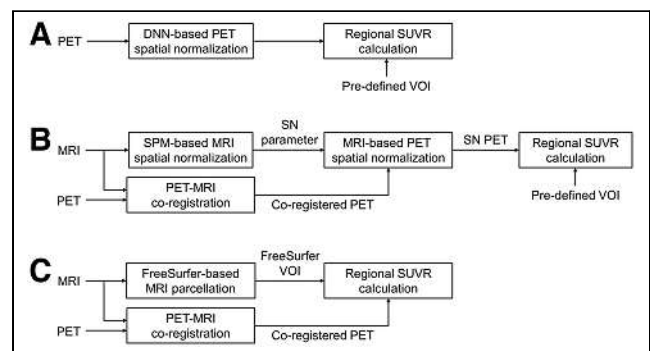


FIGURE 1. Three approaches used to estimate regional SUVr from amyloid PET images are compared in this study: DNN-based PET SN (A), PET/MRI coregistration and MRI-based PET SN using SPM (B), and PET/MRI coregistration and MRI parcellation using FreeSurfer (C).

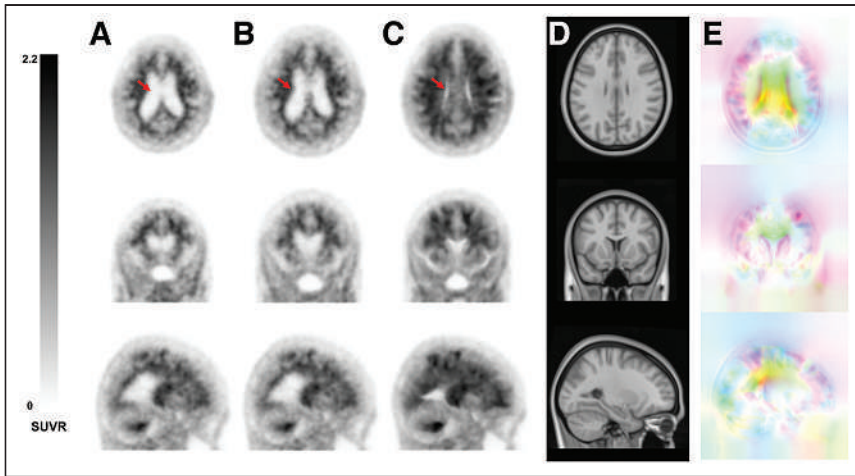


FIGURE 2. SN of ^{18}F -florbetaben PET in amyloid-positive case: input image in individual space (A), MRI-based SN using SPM (B), PET SN using DNN (C), T1 MRI template (D), and estimated deformation fields using DNN (E). Red arrows indicate the enlarged ventricles, which are not properly deformed by SPM.

Montreal Neurological Institute [MNI] 152) was minimized by error back propagation. Additionally, the gray matter segment of each MR image was used to improve the performance of the trained network and deformed using the same displacement fields as shown in Supplemental Figure 1. Dice loss was calculated between the deformed gray matter segment and the gray matter of the MNI 152 template, which was minimized along with the cross-correlation loss. On-the-fly data augmentation was applied when training the network model to prevent parameter overfitting. Spatially normalized PET images were not required in the training phase, and only PET images in individual spaces were used to create deformation fields. When the DNN model was trained, only PET images in an individual space were fed into the DNN model to generate SN images in the template space (Fig. 1A).

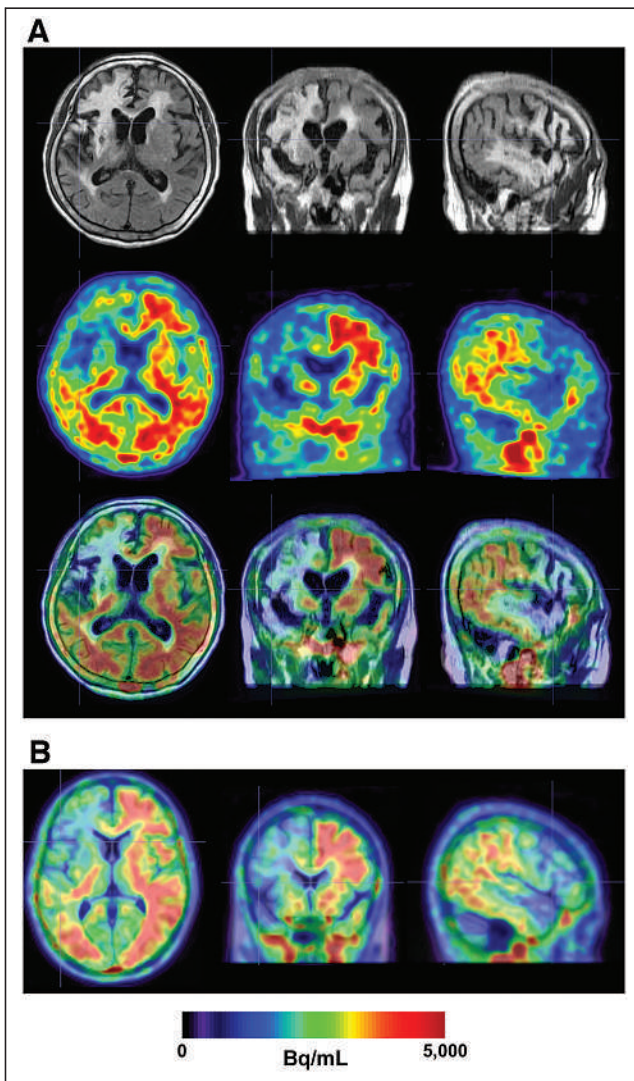


FIGURE 3. SN result of patient with chronic stroke lesion using proposed method. (A) Patient's original FLAIR MRI (top), ^{18}F -florbetaben PET (middle), and PET/MRI fusion (bottom). (B) SN PET overlaid on standard T1 MRI template.

Quantification of Amyloid Load

SN was conducted using the SPM program (version 12; <https://www.fil.ion.ucl.ac.uk/spm>) for comparison (Fig. 1B). Using the SPM program, PET and MRI pairs were coregistered, and the MR images

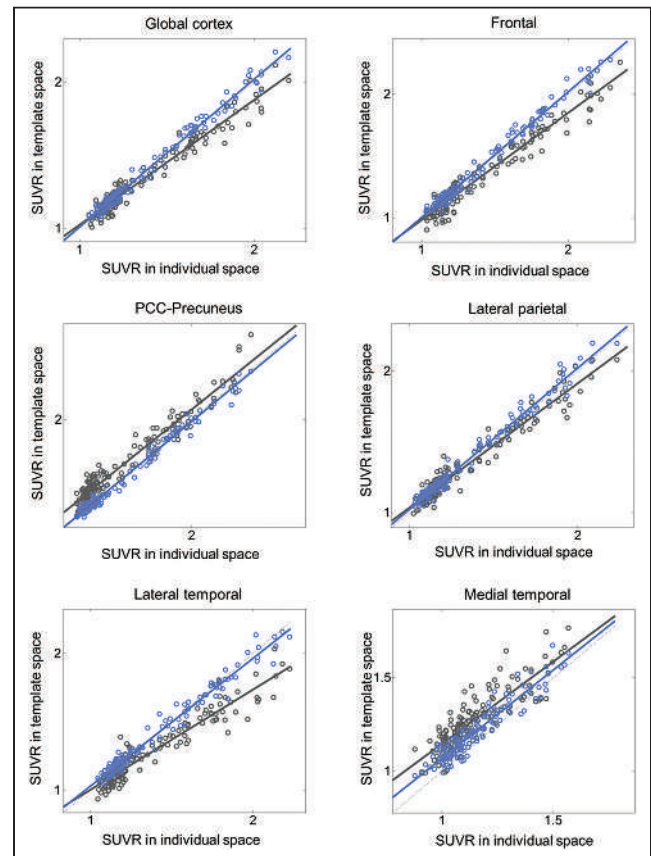


FIGURE 4. Internal validation: SUVR comparison in ^{18}F -florbetaben and ^{18}F -flutemetamol ($n = 148$). x-axis represents ground truth SUVR estimated in individual space using FreeSurfer VOI, whereas y-axis represents SUVR estimated in template space using coregistered MRI and SPM (black symbols and lines) or proposed DNN (blue symbols and lines). PCC = posterior cingulate cortex.

were spatially normalized. MRI SN was performed using a unified segmentation method that applies tissue probability maps as deformable spatial priors for regularization of the nonlinear deformations (27). The PET images were then spatially normalized using the deformation fields estimated from the paired MRI.

Using the VOIs predefined in the template space, regional PET counts were extracted from spatially normalized images using DNN or SPM. The predefined VOIs were generated by applying automatic MRI parcellation using FreeSurfer software (version 7.1.0; Martinos Center for Biomedical Imaging) to the MNI template (39,40). The cortical and subcortical structures segmented and parcellated by FreeSurfer were grouped into 6 composite VOIs: global cerebral cortex, frontal lobe, posterior cingulate cortex and precuneus, lateral parietal, lateral temporal, and medial temporal. The counts of the VOIs were then divided by the counts of the cerebellar gray matter to calculate SUVR.

As a reference, SUVRs in individual brain spaces were estimated using T1-weighted 3-dimensional MR images and FreeSurfer (Fig. 1C). The results of the FreeSurfer segmentation of MR images were visually inspected by a neuroscience expert to ensure the quality of all datasets. About 10% of the datasets were excluded because of incomplete cortex segmentation or cessation of the FreeSurfer program. Cases of failure were higher in elderly subjects (young controls, 8.7%; elderly, 10.5%). Finally, the 6 composite VOIs were applied to the coregistered amyloid brain PET images to calculate SUVR. FreeSurfer SUVR estimated in individual space was regarded as ground truth because FreeSurfer and

manual-drawing approaches achieved nearly identical estimates of amyloid load (32).

Statistical Analysis

The correlation between SN-based approaches (DNN or SPM) and the FreeSurfer approach was evaluated using Pearson correlation. Furthermore, we performed a Bland–Altman analysis on the SUVR. Additionally, intraclass correlation coefficients were calculated to assess the consistency of the quantification results.

RESULTS

After network training, the proposed DNN method successfully generated displacement fields for SN and achieved accurate spatially normalized PET images, as shown in Figure 2 and Supplemental Figure 2. However, the SPM SN was not sufficiently accurate for patients with severe ventricular enlargement (Fig. 2; Supplemental Fig. 2); nonetheless, the ventricular enlargement did not degrade the performance of the proposed method. Figure 2 and Supplemental Figure 2 show a representative amyloid-positive case and an amyloid-negative case with a global SUVR of 1.889 (73-y-old woman; diagnosis, AD; tracer, ^{18}F -florbetaben) and 1.318 (80-y-old woman; cognitively normal; tracer, ^{18}F -florbetaben), respectively.

The proposed DNN method is also robust in the SN of lesioned brains. Figure 3 and Supplemental Figure 3 show the SN result for

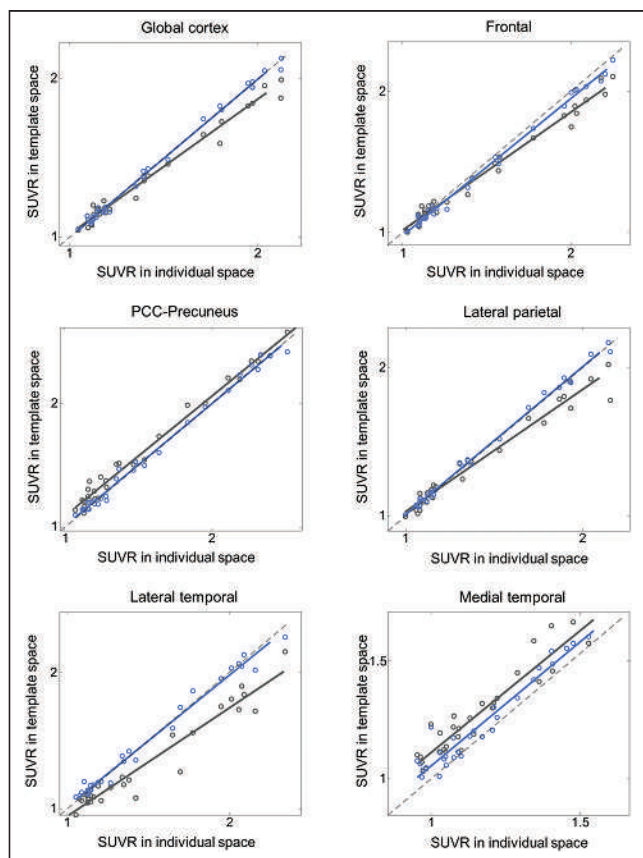


FIGURE 5. External validation: SUVR comparison in ^{18}F -florbetaben ($n = 30$). x -axis represents ground truth SUVR estimated in individual space using FreeSurfer VOI, whereas y -axis represents SUVR estimated in template space using coregistered MRI and SPM (black symbols and lines) or proposed DNN (blue symbols and lines). PCC = posterior cingulate cortex.

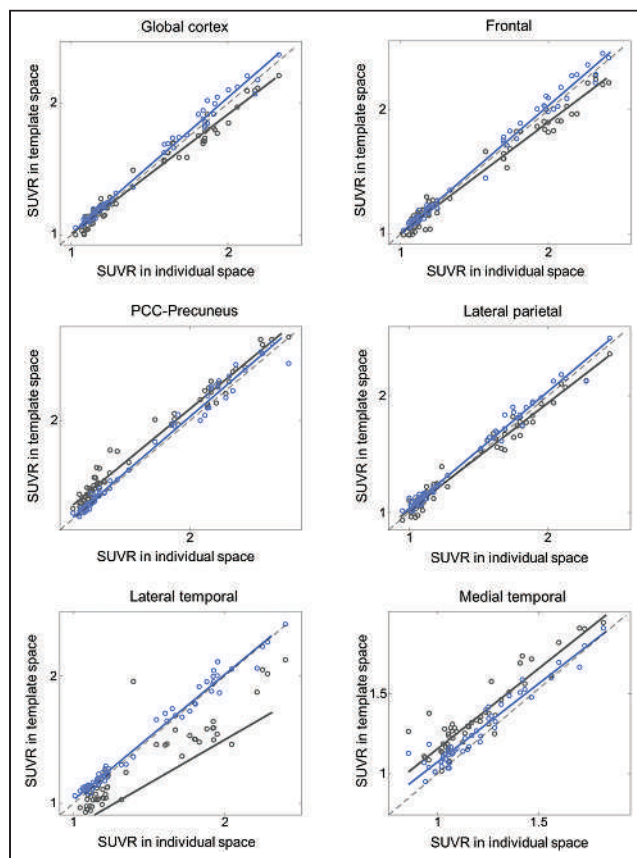


FIGURE 6. External validation: SUVR comparison in ^{18}F -flutemetamol ($n = 67$). x -axis represents ground truth SUVR estimated in individual space using FreeSurfer VOI, whereas y -axis represents SUVR estimated in template space using coregistered MRI and SPM (black symbols and lines) or proposed DNN (blue symbols and lines). PCC = posterior cingulate cortex.

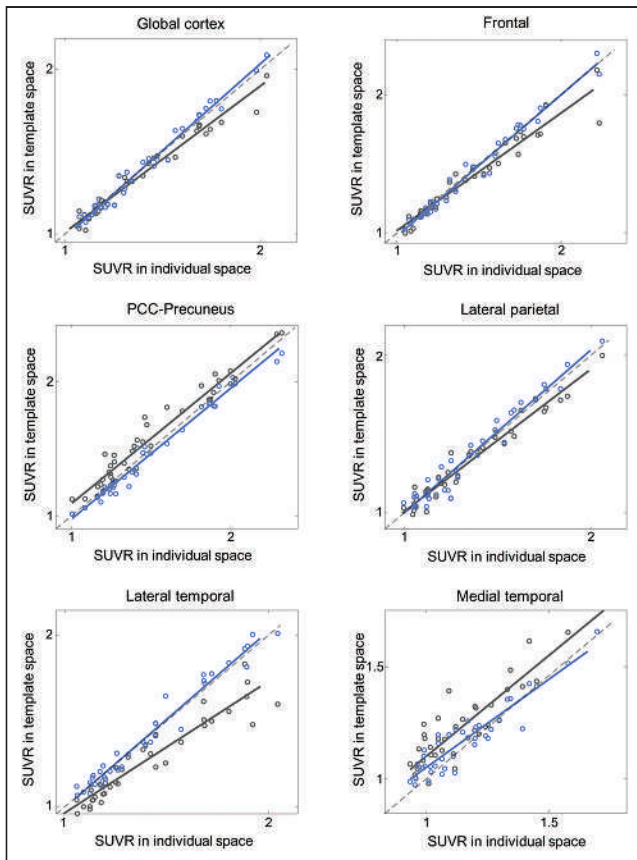


FIGURE 7. External validation: SUVR comparison in ^{18}F -florbetapir ($n = 39$). x -axis represents ground truth SUVR estimated in individual space using FreeSurfer VOI, whereas y -axis represents SUVR estimated in template space using coregistered MRI and SPM (black symbols and lines) or proposed DNN (blue symbols and lines). PCC = posterior cingulate cortex.

a patient (84-y-old woman; tracer, ^{18}F -florbetaben) with a chronic stroke lesion using the proposed method, thereby enabling accurate SN with no shrinkage in lesion volume.

Additionally, the proposed DNN method correlated better with the FreeSurfer approach than did SPM SN for all 3 tested radiotracers and most of the tested VOIs (Figs. 4–7; Tables 3–6). Furthermore, the proposed method yielded higher intraclass correlation coefficient

results than did SPM in almost all comparisons (Tables 3–6). Moreover, the proposed method showed a lower bias in SUVR estimation in the Bland–Altman analysis (Supplemental Figs. 4–7). No remarkable differences were observed between the internal and external validation results. Although the ^{18}F -florbetapir data were not used in the DNN training, the proposed method showed no performance degradation for the external ^{18}F -florbetapir dataset. The results of separate analysis for amyloid-positive and -negative cases, which were divided by a global SUVR of 1.5, are summarized in Supplemental Tables 1–4.

The computation time required for PET SN using the proposed method was approximately 1 s. Conversely, SPM required more than 60 s for the batch operation, which included coregistration between PET and MRI, SN parameter estimation from MRI, and writing of the spatially normalized PET image. FreeSurfer required approximately 8 h for automatic MRI parcellation.

DISCUSSION

In this study, we developed a fast amyloid brain PET SN method based on DNNs to overcome the limitations of existing approaches based on paired anatomic images or patient-specific templates (25,26,32). Furthermore, we assessed the correlation and measurement consistency between the proposed method and FreeSurfer-based SUVR quantification, which showed a strong correlation with the manual VOI approach (32). In terms of correlation and consistency with the FreeSurfer-based approach, the DNN-based PET SN method outperformed MRI-based PET SN conducted using the coregistration and SN routines of SPM, which is one of the most widely used pipelines for amyloid brain PET research.

The DNN model trained in this study allowed a robust SN of amyloid PET images without MRI. The superiority of the SN performance of the proposed method compared with that of SPM SN using MRI was most pronounced in cases with hydrocephalus, as shown in Figure 2 and Supplemental Figure 2. The DNN model trained using nearly 1,000 datasets with on-the-fly data augmentation was able to generate SN PET images that were morphologically consistent with the standard MRI template. Although the DNN model was trained using a Korean dataset, no performance difference was observed when it was applied to external datasets obtained from other countries. Accurate SN of the lesioned brain was also possible, as shown in Figure 3, without shrinkage of the lesion volume, which is frequently observed in conventional SN

TABLE 3

Internal Validation: Pearson Correlation and ICC Analysis for SUVR of Internal ^{18}F -Florbetaben and ^{18}F -Flutemetamol Dataset ($n = 148$) Relative to FreeSurfer Approach

Parameter	SPM				Proposed			
	Slope	y -intercept	R^2	ICC	Slope	y -intercept	R^2	ICC
Global	0.869	0.113	0.946	0.965	1.019	−0.016	0.986	0.992
Frontal	0.956	0.183	0.947	0.946	0.983	0.019	0.987	0.992
PCC–precuneus	0.877	0.158	0.950	0.921	0.998	0.026	0.981	0.993
Lateral parietal	0.734	0.267	0.910	0.970	0.936	0.092	0.977	0.988
Lateral temporal	0.853	0.173	0.957	0.865	1.008	0.003	0.987	0.987
Medial temporal	0.879	0.269	0.732	0.554	0.944	0.125	0.891	0.861

PCC = posterior cingulate cortex.

TABLE 4
External Validation: Pearson Correlation and ICC Analysis for SUVR of External ¹⁸F-Florbetaben Dataset (*n* = 30)
Relative to FreeSurfer Approach

Parameter	SPM				Proposed			
	Slope	<i>y</i> -intercept	<i>R</i> ²	ICC	Slope	<i>y</i> -intercept	<i>R</i> ²	ICC
Global	0.853	0.167	0.979	0.972	1.003	−0.006	0.995	0.998
Frontal	0.836	0.181	0.983	0.966	0.970	0.010	0.995	0.994
PCC–precuneus	0.970	0.121	0.986	0.981	0.990	0.019	0.993	0.996
Lateral parietal	0.821	0.209	0.965	0.961	0.994	0.016	0.996	0.998
Lateral temporal	0.794	0.151	0.936	0.879	0.963	0.054	0.986	0.993
Medial temporal	0.972	0.134	0.898	0.800	0.990	0.062	0.931	0.927

PCC = posterior cingulate cortex.

approaches (41). However, despite the use of MRI, SPM SN could not compensate for the large morphologic differences between the input images and the template. In the SN algorithm used in SPM, the images are deformed by the linear combination of 1,000 cosine transform bases, which allowed only a limited amount of image deformation.

A potential alternative approach to the proposed method is generating spatially normalized amyloid PET images directly from individual PET inputs using DNNs. This method is faster than the proposed method considering it directly conducts SN without generating explicit deformation fields. However, direct SN methods are more susceptible to the perturbation of input images because of noise. Therefore, it is difficult to ensure maintenance of regional count rate concentrations after the direct SN of brain PET images. However, the DNN model used in the proposed method does not directly provide the intensity of SN images. The intensities were calculated by interpolating neighbor voxel values using DNN-generated deformation fields, which reduced the risk of erroneous intensity mapping by the SN. In addition, the DNN model trained for deformation field generation using amyloid PET images can be used for transfer learning on other radiotracers with small datasets available. Our preliminary (unpublished data, June 2022) study on ¹⁸F-flortaucipir showed

that the transfer learning allows for highly accurate quantification of ¹⁸F-flortaucipir brain PET using the proposed method.

The proposed fast and reliable deep-learning–based SN of amyloid PET images can potentially be used to improve inter-reader agreement on, and confidence in, amyloid PET interpretation. In our previous study (42), when visual amyloid PET interpretation was supported by a deep-learning model that directly estimated regional SUVR from input images (43), inter-reader agreement (Fleiss κ -coefficient) and the confidence score increased from 0.46 to 0.76 and from 1.27 to 1.66, respectively. The method proposed here requires a longer computation time for regional SUVR calculation than the direct end-to-end SUVR estimation, mainly because of the voxel-by-voxel multiplication of SN results and the predefined brain atlas. However, the reliability of the amyloid burden estimation based on the proposed method is higher, considering that the proposed method allows visual confirmation of SN results and exclusion of cases with erroneous SNs. Furthermore, accurate automatic quantification of amyloid burden can be used in longitudinal follow-up studies on patients with AD and mild cognitive impairment. Several dementia treatment drugs based on the amyloid hypothesis are now emerging, and amyloid PET scans are important for

TABLE 5
External Validation: Pearson Correlation and ICC Analysis for SUVR of External ¹⁸F-Flutemetamol (*n* = 67)
Relative to FreeSurfer Approach

Parameter	SPM				Proposed			
	Slope	<i>y</i> -intercept	<i>R</i> ²	ICC	Slope	<i>y</i> -intercept	<i>R</i> ²	ICC
Global	0.907	0.104	0.979	0.977	1.033	−0.020	0.990	0.989
Frontal	0.893	0.117	0.976	0.975	1.025	−0.015	0.990	0.987
PCC–precuneus	0.978	0.150	0.978	0.945	1.024	−0.032	0.985	0.984
Lateral parietal	0.919	0.103	0.975	0.969	1.001	0.036	0.987	0.979
Lateral temporal	0.794	0.136	0.946	0.844	0.986	0.042	0.984	0.984
Medial temporal	0.943	0.206	0.857	0.758	0.921	0.149	0.926	0.931

PCC = posterior cingulate cortex.

TABLE 6
External Validation: Pearson Correlation and ICC Analysis for SUVR of External ¹⁸F-Florbetapir Dataset (n = 39)
Relative to FreeSurfer Approach

Parameter	SPM				Proposed			
	Slope	y-intercept	R ²	ICC	Slope	y-intercept	R ²	ICC
Global	0.888	0.123	0.961	0.979	1.082	-0.071	0.982	0.985
Frontal	0.851	0.166	0.940	0.974	1.022	-0.045	0.980	0.989
PCC-precuneus	0.973	0.119	0.948	0.940	0.975	0.001	0.980	0.982
Lateral parietal	0.905	0.102	0.949	0.981	1.037	-0.039	0.958	0.978
Lateral temporal	0.768	0.196	0.892	0.854	1.029	-0.034	0.970	0.990
Medial temporal	0.977	0.128	0.798	0.742	0.855	0.199	0.864	0.936

PCC = posterior cingulate cortex.

monitoring the efficacy of treatments. The proposed method will enable an objective measurement of drug-induced amyloid clearance without requiring additional 3-dimensional structural MRI.

CONCLUSION

We evaluated a novel deep-learning-based SN method that allows quantitative analysis of amyloid brain PET images without structural MRI. The quantification results using the proposed method correlated strongly with MRI-parcellation-based quantification using FreeSurfer for all clinical amyloid radiotracers. Therefore, the proposed method will be useful for investigating AD and related brain disorders using amyloid PET scans.

DISCLOSURE

This research was supported by the Seoul R&BD Program (BT200151) through the Seoul Business Agency (SBA) funded by the Seoul Metropolitan Government. No other potential conflict of interest relevant to this article was reported.

KEY POINTS

QUESTION: Is quantification of amyloid PET images without MRI feasible?

PERTINENT FINDINGS: A method based on deep learning allowed fast and reliable amyloid PET SN and quantification without MRI.

IMPLICATIONS FOR PATIENT CARE: The proposed method will be useful for interpreting amyloid PET scans in AD and related brain disorders.

REFERENCES

- Kwon JS, Kim JJ, Lee DW, et al. Neural correlates of clinical symptoms and cognitive dysfunctions in obsessive-compulsive disorder. *Psychiatry Res.* 2003;122:37-47.
- Lee DS, Lee JS, Oh SH, et al. Deafness: cross-modal plasticity and cochlear implants. *Nature.* 2001;409:149-150.
- Nordberg A, Rinne JO, Kadir A, Långström B. The use of PET in Alzheimer disease. *Nat Rev Neurol.* 2010;6:78-87.
- Rowe CC, Ng S, Ackermann U, et al. Imaging β -amyloid burden in aging and dementia. *Neurology.* 2007;68:1718-1725.
- Oh M, Kim JS, Kim JY, et al. Subregional patterns of preferential striatal dopamine transporter loss differ in Parkinson disease, progressive supranuclear palsy, and multiple-system atrophy. *J Nucl Med.* 2012;53:399-406.
- Wong DF, Rosenberg PB, Zhou Y, et al. In vivo imaging of amyloid deposition in Alzheimer disease using the radioligand ¹⁸F-AV-45 (florbetapir F 18). *J Nucl Med.* 2010;51:913-920.
- Choi H, Cheon GJ, Kim HJ, et al. Gray matter correlates of dopaminergic degeneration in Parkinson's disease: a hybrid PET/MR study using ¹⁸F-FP-CIT. *Hum Brain Mapp.* 2016;37:1710-1721.
- Small GW, Ercoli LM, Silverman DHS, et al. Cerebral metabolic and cognitive decline in persons at genetic risk for Alzheimer's disease. *Proc Natl Acad Sci USA.* 2000;97:6037-6042.
- Förster S, Grimmer T, Miederer I, et al. Regional expansion of hypometabolism in Alzheimer's disease follows amyloid deposition with temporal delay. *Biol Psychiatry.* 2012;71:792-797.
- Ashburner J, Friston KJ. Nonlinear spatial normalization using basis functions. *Hum Brain Mapp.* 1999;7:254-266.
- Lancaster JL, Glass TG, Lankipalli BR, Downs H, Mayberg H, Fox PT. A modality-independent approach to spatial normalization of tomographic images of the human brain. *Hum Brain Mapp.* 1995;3:209-223.
- Minoshima S, Koeppe RA, Frey KA, Kuhl DE. Anatomic standardization: linear scaling and nonlinear warping of functional brain images. *J Nucl Med.* 1994;35:1528-1537.
- Kang KW, Lee DS, Cho JH, et al. Quantification of F-18 FDG PET images in temporal lobe epilepsy patients using probabilistic brain atlas. *Neuroimage.* 2001;14:1-6.
- Lee JS, Lee DS, Kim S-K, et al. Localization of epileptogenic zones in F-18 FDG brain PET of patients with temporal lobe epilepsy using artificial neural network. *IEEE Trans Med Imaging.* 2000;19:347-355.
- Evans AC, Janke AL, Collins DL, Baillet S. Brain templates and atlases. *Neuroimage.* 2012;62:911-922.
- Caviness VS, Meyer J, Makris N, Kennedy DN. MRI-based topographic parcellation of human neocortex: an anatomically specified method with estimate of reliability. *J Cogn Neurosci.* 1996;8:566-587.
- Eickhoff SB, Stephan KE, Mohlberg H, et al. A new SPM toolbox for combining probabilistic cytoarchitectonic maps and functional imaging data. *Neuroimage.* 2005;25:1325-1335.
- Tzourio-Mazoyer N, Landeau B, Papathanassiou D, et al. Automated anatomical labeling of activations in SPM using a macroscopic anatomical parcellation of the MNI MRI single-subject brain. *Neuroimage.* 2002;15:273-289.
- Lee JS, Lee DS. Analysis of functional brain images using population-based probabilistic atlas. *Curr Med Imaging Rev.* 2005;1:81-87.
- Mintun MA, Lo AC, Duggan Evans C, et al. Donanemab in early Alzheimer's disease. *N Engl J Med.* 2021;384:1691-1704.
- Sevigny J, Chiao P, Bussière T, et al. The antibody aducanumab reduces A β plaques in Alzheimer's disease. *Nature.* 2016;537:50-56.
- Barthel H, Gertz H-J, Dresel S, et al. Cerebral amyloid- β PET with florbetaben (¹⁸F) in patients with Alzheimer's disease and healthy controls: a multicenter phase 2 diagnostic study. *Lancet Neurol.* 2011;10:424-435.

23. Klein A, Andersson J, Ardekani BA, et al. Evaluation of 14 nonlinear deformation algorithms applied to human brain MRI registration. *Neuroimage*. 2009;46:786–802.
24. Klunk WE, Engler H, Nordberg A, et al. Imaging brain amyloid in Alzheimer's disease with Pittsburgh compound-B. *Ann Neurol*. 2004;55:306–319.
25. Choi H, Lee DS. Generation of structural MR images from amyloid PET: application to MR-less quantification. *J Nucl Med*. 2018;59:1111–1117.
26. Kang SK, Seo S, Shin SA, et al. Adaptive template generation for amyloid PET using a deep learning approach. *Hum Brain Mapp*. 2018;39:3769–3778.
27. Ashburner J, Friston KJ. Unified segmentation. *Neuroimage*. 2005;26:839–851.
28. Fischl B. FreeSurfer. *Neuroimage*. 2012;62:774–781.
29. Clerx L, Gronenschild EH, Echavarrri C, Verhey F, Aalten P, Jacobs HI. Can FreeSurfer compete with manual volumetric measurements in Alzheimer's disease? *Curr Alzheimer Res*. 2015;12:358–367.
30. Kuperberg GR, Broome MR, McGuire PK, et al. Regionally localized thinning of the cerebral cortex in schizophrenia. *Arch Gen Psychiatry*. 2003;60:878–888.
31. Salat DH, Buckner RL, Snyder AZ, et al. Thinning of the cerebral cortex in aging. *Cereb Cortex*. 2004;14:721–730.
32. Su Y, D'Angelo GM, Vlassenko AG, et al. Quantitative analysis of PiB-PET with FreeSurfer ROIs. *PLoS One*. 2013;8:e73377.
33. Tuszynski T, Rullmann M, Luthardt J, et al. Evaluation of software tools for automated identification of neuroanatomical structures in quantitative β -amyloid PET imaging to diagnose Alzheimer's disease. *Eur J Nucl Med Mol Imaging*. 2016;43:1077–1087.
34. Rowe CC, Doré V, Jones G, et al. ^{18}F -florbetaben PET beta-amyloid binding expressed in centiloids. *Eur J Nucl Med Mol Imaging*. 2017;44:2053–2059.
35. Battle MR, Pillay LC, Lowe VJ, et al. Centiloid scaling for quantification of brain amyloid with [^{18}F]flutemetamol using multiple processing methods. *EJNMMI Res*. 2018;8:107.
36. Navitsky M, Joshi AD, Kennedy I, et al. Standardization of amyloid quantitation with florbetapir standardized uptake value ratios to the centiloid scale. *Alzheimers Dement*. 2018;14:1565–1571.
37. Ronneberger O, Fischer P, Brox T. U-net: convolutional networks for biomedical image segmentation. Arxiv website. <https://arxiv.org/abs/1505.04597>. Published May 18, 2015. Accessed December 12, 2022.
38. Balakrishnan G, Zhao A, Sabuncu MR, et al. VoxelMorph: a learning framework for deformable medical image registration. *IEEE Trans Med Imaging*. 2019;38:1788–1800.
39. Fonov V, Evans AC, Botteron K, et al. Unbiased average age-appropriate atlases for pediatric studies. *Neuroimage*. 2011;54:313–327.
40. Fonov VS, Evans AC, McKinstry RC, Almlí C, Collins D. Unbiased nonlinear average age-appropriate brain templates from birth to adulthood [abstract]. *Neuroimage*. 2009;47(suppl):S102.
41. Ripollés P, Marco-Pallarés J, de Diego-Balaguer R, et al. Analysis of automated methods for spatial normalization of lesioned brains. *Neuroimage*. 2012;60:1296–1306.
42. Kim JY, Oh D, Sung K, et al. Visual interpretation of [^{18}F]florbetaben PET supported by deep learning-based estimation of amyloid burden. *Eur J Nucl Med Mol Imaging*. 2021;48:1116–1123.
43. Kim JY, Suh HY, Ryo HG, et al. Amyloid PET quantification via end-to-end training of a deep learning. *Nucl Med Mol Imaging*. 2019;53:340–348.

Detecting CXCR4 Expression in Meningioma on ^{68}Ga -Pentixafor PET/MRI

Simone Krebs¹⁻³, Jazmin Schwartz⁴, Christian Grommes⁵, Robert J. Young⁶, Heiko Schöder^{1,2}, and Marius E. Mayerhoefer^{1,2,7}

¹Molecular Imaging and Therapy Service, Department of Radiology, Memorial Sloan Kettering Cancer Center, New York, New York; ²Department of Radiology, Weill Cornell Medical College, New York, New York; ³Radiochemistry and Imaging Sciences Service, Department of Radiology, Memorial Sloan Kettering Cancer Center, New York, New York; ⁴Department of Medical Physics, Memorial Sloan Kettering Cancer Center, New York, New York; ⁵Department of Neurology, Memorial Sloan Kettering Cancer Center, New York, New York; ⁶Neuroradiology Service, Department of Radiology, Memorial Sloan Kettering Cancer Center, New York, New York; and ⁷Body Imaging Service, Department of Radiology, Memorial Sloan Kettering Cancer Center, New York, New York

The C-X-C chemokine receptor 4 (CXCR4) is crucial for tumor proliferation, migration, and angiogenesis in many different cancers. Recently, ^{68}Ga -pentixafor, a radiotracer comprising a synthetic, cyclic pentapeptide analog of stromal cell-derived factor 1, a ligand for CXCR4, has been successfully introduced for assessment of hematologic malignancies, including lymphomas of the body and central nervous system, myeloma, and leukemia (1,2). Furthermore, ^{68}Ga -pentixafor uptake has been described in various solid tumors but not yet in meningioma.

We report the case of a 67-y-old woman with newly diagnosed primary central nervous system lymphoma who was referred for ^{68}Ga -pentixafor PET/MRI (NCT05093335) 2 d after MRI was performed with intravenously injected gadopentetate dimeglumine (Magnevist; Bayer Healthcare Pharmaceuticals). PET imaging was acquired for 15 min starting 15 min after intravenous injection of 150 MBq of ^{68}Ga -pentixafor on a hybrid device (Signa PET/MR; GE Healthcare). PET demonstrated a homogeneously enhancing lesion in the right temporal lobe with an SUV_{max} of 5.3 (Fig. 1). Incidentally, slightly lower uptake, with an SUV_{max} of 4.8, was observed in a dura-based extraaxial homogeneously enhancing mass in the left middle cranial fossa, a known meningioma.

Here, we show that ^{68}Ga -pentixafor can detect not only central nervous system lymphoma but also meningioma with a high tumor-to-background activity ratio on PET, given the minimal uptake of this radiotracer in brain parenchyma. A recent analysis in 55 meningioma specimens showed that CXCR4 messenger RNA was expressed in 43 (78%) of the tumor specimens, and CXCR4 stimulation led to extracellular signal-regulated protein kinase 1 and 2 phosphorylation/activation and cell proliferation (3). CXCR4 and stromal cell-derived factor 1 were often detected in the same tumor tissues, suggesting an autocrine-paracrine feedback loop potentially promoting the phenotypic behavior of the tumor, such as the ability to grow autonomously.

Our findings suggest that ^{68}Ga -pentixafor PET may be useful for delineation of meningioma and for elucidating biologic characteristics

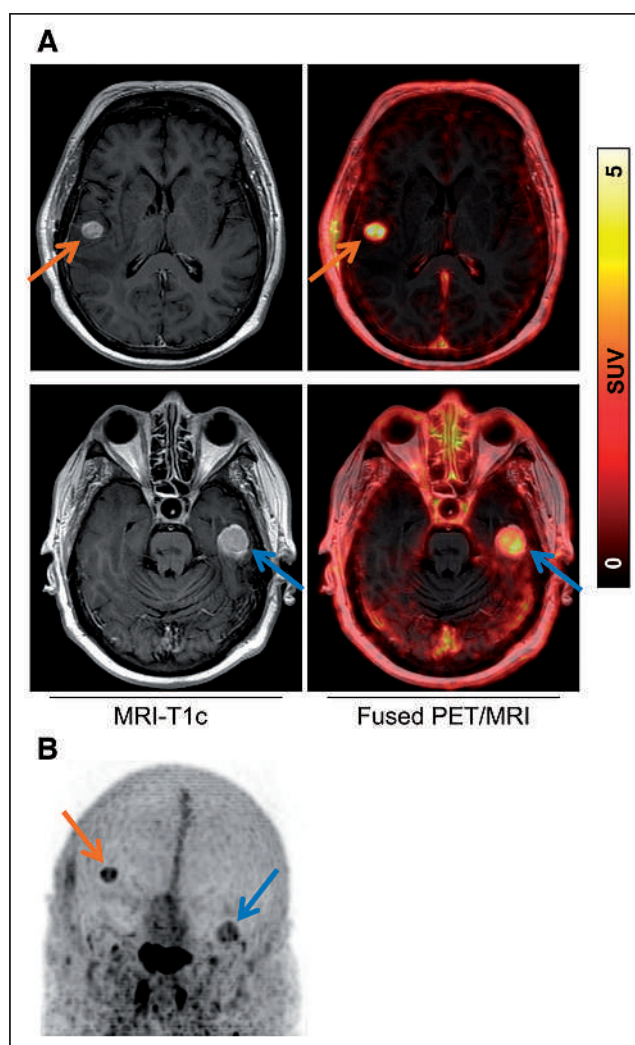


FIGURE 1. Contrast-enhanced T1-weighted MR images showing enhancing lesions with focal ^{68}Ga -pentixafor uptake on axial PET/MRI (A) and on maximum-intensity-projection PET (B), corresponding to biopsy-proven lymphoma (orange arrows) and known meningioma (blue arrows).

Received Nov. 1, 2022; revision accepted Nov. 7, 2022.

For correspondence or reprints, contact Simone Krebs (krebss@mskcc.org).

Published online Nov. 10, 2022.

COPYRIGHT © 2023 by the Society of Nuclear Medicine and Molecular Imaging.

DOI: 10.2967/jnumed.122.265127

and that, especially in treatment-refractory meningiomas, ^{68}Ga -pentixafor PET may guide CXCR4-based theranostic approaches with pentixather that were previously evaluated in blood cancers (4).

DISCLOSURE

This study was supported in part by NIH/NCI Cancer Center support grant P30 CA008748. Marius Mayerhoefer received speaker honoraria from GE Healthcare, Siemens Healthineers, and Bristol Myers Squibb. No other potential conflict of interest relevant to this article was reported.

REFERENCES

1. Starzer AM, Berghoff AS, Traub-Weidinger T, et al. Assessment of central nervous system lymphoma based on CXCR4 expression in vivo using ^{68}Ga -pentixafor PET/MRI. *Clin Nucl Med.* 2021;46:16–20.
2. Mayerhoefer ME, Jaeger U, Staber P, et al. [^{68}Ga]Ga-pentixafor PET/MRI for CXCR4 imaging of chronic lymphocytic leukemia: preliminary results. *Invest Radiol.* 2018;53:403–408.
3. Bajetto A, Barbieri F, Pattarozzi A, et al. CXCR4 and SDF1 expression in human meningiomas: a proliferative role in tumoral meningeothelial cells in vitro. *Neuro-oncol.* 2007;9:3–11.
4. Hänscheid H, Schirbel A, Hartrampf P, et al. Biokinetics and dosimetry of ^{177}Lu -pentixather. *J Nucl Med.* 2022;63:754–760.

EARLY-BIRD DEADLINE: APRIL 27, 2023

June 24-27
2023

SNMMI ANNUAL MEETING

Chicago, Illinois, USA



Register Today

WWW.SNMMI.ORG/AM2023





SPECTRUM
DYNAMICS MEDICAL

VERITON-CT[®]

DIGITAL SPECT/CT



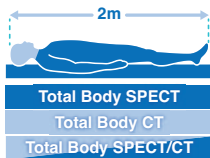
Optimization of Every Step

Spectrum Dynamics has integrated its ground-breaking BroadView Technology design into the VERITON-CT system, providing a digital platform enabling routine 3D imaging in Nuclear Medicine. The result is optimization of every step, from image acquisition to interpretation.

VERITON-CT digital SPECT/CT combines the best-in-class CZT detectors, novel system design, high resolution CT, and advanced software technology to elevate the performance of 360° digital SPECT/CT.



BroadView Technology
Proprietary swiveling detector design provides increased sensitivity for faster scans



Total Body 3D Imaging
200cm continuous coverage vertex to feet
SPECT | CT | SPECT/CT



80cm NM and CT bore
Wide Bore SPECT/CT
80cm NM and CT bore



Choice of 16/64 slice
Choice of high-resolution CT for diagnostic applications and low dose total body CTAC



TruView Console
One platform, one location for clinical care decision-making:
1. Acquisition
2. Advanced quantitative reconstruction
3. Both 3D and 4D data analysis and review

VERITON-CT Feature Application: 3D Dynamic Imaging

TruFlow for VERITON-CT offers real-time 3D in-vivo fast dynamic imaging to capture the radiopharmaceutical distribution, uptake, or clearance over time in 3D SPECT/CT parametric imaging.

TruFlow



The Journal of Nuclear Medicine

April 2023 • Vol. 64 • Pages 503-668